HEAT TRANSFER AND FLUID FLOW ASPECTS OF FUEL - COOLANT INTERACTIONS

BY

MICHAEL LOUIS CORRADINI

B.S., Mechanical Engineering, Marquette University
(1975)

S.M., Massachusetts Institute of Technology
(1977)

SUBMITTED IN PARTIAL FULFILLMENT
OF THE REQUIREMENTS FOR THE
DEGREE OF

DOCTOR OF PHILOSOPHY

at the

MASSACHUSETTS INSTITUTE OF TECHNOLOGY

SEPTEMBER, 1978

Signature redacted
Signature of Author.....
Department of Nuclear Engineering, September, 1978

Signature redacted
Certified by.....
Thesis Supervisor

Signature redacted
Certified by.....
Thesis Supervisor

Signature redacted
Accepted by.....
Chairman, Department Committee on Graduate Students

HEAT TRANSFER AND FLUID FLOW ASPECTS OF FUEL - COOLANT INTERACTIONS

by

MICHAEL LOUIS CORRADINI

Submitted to the Department of Nuclear Engineering
on September 29, 1978, in partial fulfillment of the requirements
for the Degree of Doctor of Philosophy

ABSTRACT

A major portion of the safety analysis effort for the LMFBR is involved in assessing the consequences of a Hypothetical Core Disruptive Accident (HCDA). The thermal interaction of the hot fuel and the sodium coolant during the HCDA is investigated in two areas.

A postulated loss of flow transient may produce a two-phase fuel at high pressures. The thermal interaction phenomena between fuel and coolant as the fuel is ejected into the upper plenum are investigated, and three major conclusions are reached: (1) Small-scale unheated experiments and analysis indicate that a dominant mechanism for coolant entrainment into the expanding fuel bubble is due to Taylor Instabilities; (2) Analysis of small heated noncondensible and condensible tests indicate that the characteristic size of the entrained coolant in droplet form is between the critical Taylor Instability wavelength (λ_c) and the fastest growing wavelength ($\lambda_m = \sqrt{3}\ \lambda_c$); (3) Analysis of full scale reactor conditions indicates that the dominant heat transfer mechanism is radiation, and coolant vaporization is small due to vapor diffusion effects. The net effect is to reduce the fuel vapor pressure and reduce the expansion work by a factor of 2. Small-scale simulant experiments utilizing refrigerants could confirm the vaporization behavior, while reactor materials tests must be done to investigate the radiation heat transfer mechanism.

A postulated transient overpower accident may produce molten fuel being released into sodium coolant in the core region. An energetic coolant vapor explosion for these reactor materials does not seem likely. However, experiments using other materials (e.g. Freon/water, tin/water) have demonstrated the possibility of this phenomenon. Models are proposed which explain, for molten metal/water systems in the drop mode of contact, (1) that a fuel-coolant interaction can occur even though the bulk of the fuel is above the critical temperature of the coolant, and (2) the observed upper boundary on a T_{c_i} vs. T_{H_i} plot above which no self-triggered fragmentation occurs.

Thesis Supervisor: Professor Neil E. Todreas, Professor of Nuclear Engineering
Thesis Supervisor: Professor Warren M. Rohsenow, Professor of Mechanical Engineering

ACKNOWLEDGEMENTS

It is quite hard to thank all the people who have helped me through my thesis, so I hope that my errors by omission are pardoned. I would like to thank Mr. Joseph A. (Tiny) Caloggero, whose advice during the design and operation of the experiment was invaluable. Also thanks goes to Michael McNallon, whose photographic advice expedited many long hours and to Ray Rothrock, whose tireless efforts were an inspiration to me.

Thanks also goes to Professors Mujid Kazimi, Borivoje Mikic, and Ain Sonin. Each graciously gave of their time by answering the questions of the author and giving valuable advice to help in formulating the problem and the analysis in specific areas.

Finally, special thanks goes to my advisors, Professor Warren Rohsenow, and Neil Todreas. Professor Rohsenow's constant good cheer, patience, and insight were invaluable when the results seemed unclear. Professor Todreas' assistance was indeed indispensable because his grasp of the overall picture of reactor safety and the key issues involved gave meaning to my work. The educational experience I received from both men is something of great value that I hope to carry with me throughout my life.

The financial support for my thesis by the Department of Energy through Los Alamos Scientific Laboratories is gratefully acknowledged. Also thanks goes to Rockwell International and Dr. D. Camnon for financial support for my first two years of graduate school.

This thesis and my career at MIT was not possible without the help of my beautiful wife, Debi.

TABLE OF CONTENTS

LIST OF FIGURES

LIST OF TABLES

NOMENCLATURE

B_i - scaling law

b - scaling factor

A_p - projected area of reactor vessel

a - acceleration

B_i - Biot No. $\frac{\bar{h}D}{k}$

c_a - acoustic velocity

c_p - specific heat at constant pressure of vapor

c_v - specific heat at constant volume of vapor

c - specific heat of liquid or solid

D_p - diameter or width of chamber

d_i - initial depth of liquid slug for the entrainment experiment

d - depth of liquid slug for the entrainment experiment

$\Delta d_i = d_i - d$

D_d - diameter of the entrained coolant drop

D_b - diameter of expanding bubble

D_t - travel distance of the liquid slug for the entrainment experiment

E - total energy

e - specific energy per unit mass; $u + \frac{v^2}{2} + x$

f - frequency

$\bar{h}$ - heat transfer coefficient

h - specific enthalpy per unit mass (h_{fg}, h_f, h_g)

h_f - enthalpy of saturated liquid

h_g - enthalpy of saturated vapor

h_{pl} - Planck's constant

k_B - Boltzman constant 1.38 (10^{-23}) $\frac{w\text{-}s}{^oK}$

k - thermal conductivity

K - wave number - $2\pi/\lambda$

L_s - latent heat of solidification

l - length

L_o - axial non-entrainment length

$\dot{m}_f$ - mass flow rate of fuel from core

$\dot{m}_e$ - mass flow rate of entrained coolant

M_{slug} - mass of the coolant slug

MW - molecular weight of substance

$\dot{M}$ - rate of change of momentum (mom. flux)

Nu - Nusselt No - $\frac{\bar{h}D}{k}$

P_∞ - pressure of the ambient (.1MPa)

P - pressure

P_{pl} - pressure in the upper plenum

Pr - Prandtl number $c_p\mu/k$

$\dot{q}$ - heat transfer rate

ΔQ - total heat transferred

Re - Reynolds No. $\frac{\rho_v D}{\mu}$

R_o - universal gas constant

R_i - R_o/MW_i

R_b - radius of the bubble

r - radius

S - LaPlace Transform variable

s - entropy

s_e - statistical deviation

T - temperature

t - time

τ_i - characteristic time of ith process

T_l - initial temperature of liquid coolant

T_m - melting temperature

U - total internal energy

u - specific internal energy per unit mass

u_{b_i} - bubble rise velocity

v_i - velocity - (i - vel - relative value, slug - coolant slug value)
- g - gas value

V - volume

v_{rel} - relative velocity

v_r - relative penetration velocity of a Taylor Instability

$v_{f,c}$ - specific volume of the fuel or coolant

W - work transport of energy

w - dimensionless parameter

x - axial distance

X - mass thermodynamic quality

α - thermal diffusivity

$\bar{\alpha}$ - void fraction

β - ratio of thermophysical properties

ε - radiative emissivity or absorbtivity for a gray surface or gas

η - amplitude of wavelength at gas-liquid interface

γ - ratio of specific heats

δ - film thickness

λ - wavelength

λ_c - critical Taylor Instability wavelength

λ_m - fastest growing Taylor Instability wavelength

λ_i - initial wavelength imposed

λ_o - observed wavelength at a given time, t

κ_l, κ_s - dimensionless parameters for conduction models

ρ - density

μ - viscosity

σ_r - Stephan Blotzman constant - $5.67(10^{-8}) \frac{w}{m^2 o_K^4}$

σ - surface tension

ϕ - velocity potential

Ψ - mole fraction

Θ - dimensionless temperature

$\bar{\Theta}$ - dimensionless temperature in LaPlace Transform variable

SUBSCRIPTS

br - break up value

b - bubble value

c - coolant value

crit - critical values

co or core - core value

d - drop value

e - entrained value

ex - exit conditions

exp - expansion or experimental value

f - fuel value

F - fin value

g - gas or vapor value

H - hot fuel value

i - initial value

l - liquid value

o - orifice value

pl - plenum value

s - solid value

SH - spontaneous nucleation

HH - homogeneous nucleation

sat - saturation value

HC - homogeneous crystallization

sl - coolant slug value

OPERATORS

$\bar{x}$ - time average

$\dot{x}$ - $\frac{\partial x}{dt}$ - time derivative

* - nondimensional

$\langle x \rangle$ - spatial average

1. INTRODUCTION

1.1 Foreword

In the context of reactor safety, various types of phenomena have been considered in the analysis of low probability accidents for both Light Water Reactors (LWR) and the Liquid Metal Fast Breeder Reactor (LMFBR). These accidents are investigated because although their probabilities of occurrence are very small (1 chance in 20,000 per reactor per year), the possible consequences to the public health and safety are large (possibly hundreds of fatalities) [1,2].

One such phenomenon that is possible during these accident scenarios involves a thermal interaction when the more volatile coolant in the reactor and the hot core materials (e.g. UO_2) within the core come into contact and become intermixed. It is imagined that this "fuel-coolant interaction" (FCI) may result in the rapid vaporization of the coolant and the possible formation of shock waves, as the coolant becomes a high pressure two-phase expanding fluid. This energetic event may possibly occur only if the fuel is initially molten (MFCI) or if the fuel is itself a two-phase expanding mixture of fuel liquid and vapor intermixing with coolant (e.g. occurring from a hydrodynamic disassembly in an LMFBR).

Cho and Epstein [3] conservatively estimated that intermixing the coolant could double the disruptive work potential of an expanding source of two-phase fuel for the LMFBR loss of flow accident. This interaction could then represent a doubling of the thermal to mechanical energy conversion efficiency (from ~5% to 10%).

Hick and Menzies [4] performed a similar parametric study for a molten fuel-coolant interaction between liquid UO_2 and sodium in the LMFBR. The fuel and coolant are adiabatically mixed at constant volume to an equilibrium temperature; then the sodium is expanded down to one atmosphere continually keeping the fuel and sodium in equilibrium. In this ideal process as much as 30% of the thermal energy of the molten fuel can be converted to disruptive mechanical work by heat transfer to the sodium. Experimental verification of these theoretical maximums has not been demonstrated with LMFBR materials although experiments using simulant materials (Freon-22 & Water) by Armstrong and Anderson [5] do demonstrate the possibility of these high efficiencies for MFCI's.

It should be emphasized that the MFCI is common to many industries. Light water reactor safety is also concerned with MFCI's as Appendix VIII of Wash 1400 indicates. "Steam explosions" or "vapor explosions," as MFCI's are often called, have occurred in other industries where hot molten metals or materials can become accidentally intermixed with coolants (e.g. water); aluminum, titanium, smelt, and paper industries. Good reviews of molten fuel-coolant interaction accidents and experiments in many industries, including nuclear energy are given by Reid [6] and Board and Caldarola [7].

1.2 Consideration of Initial Conditions, Independent Variables and Physical Mechanisms

To determine the possible consequences of both types of these interactions in the reactor environment, the possible ranges of significant initial conditions and independent variables should be identified, i.e., size of fuel and coolant masses, initial temperature and quality of fuel,

length and time scales of the interaction, thermophysical properties of the constituents, surrounding reactor geometry and possible initiating events leading to the interaction. The initiating events in the LMFBR for a MFCI are different from those contributing to the formation of a fuel (UO_2) vapor-liquid expansion and subsequent sodium interaction.

The two-phase UO_2 fuel source is envisioned to be formed from a low probability accident (Hypothetical Core Disruptive Accident - HCDA) designated as a Loss of Flow transient with failure to scram. The reactor is assumed to have experienced a loss of flow coincident with a failure to shut down power by the control rods. This situation could cause a series of events: voiding of the core's sodium coolant causing a rise in reactor power and fuel temperature, fuel rod melting and slumping causing further power increases and subsequent fuel vaporization and expansion.

The Transient Overpower HCDA is envisioned as one possible initiating event for a MFCI. This scenario assumes an initial core power increase (e.g. due to control rod withdrawal), again with a failure to scram. The major difference is that the sodium coolant remains in the core as the fuel melts due to the overpower condition, giving a pre-mixed condition of liquid fuel and coolant. For the LWR the initiating event for the MFCI can be different, for example the loss of coolant accident scenario where water is the coolant, but the possible phenomenon remains the same.

The initial conditions have a noticeable effect in the consequences of the interaction between the two-phase fuel and the sodium coolant. As Cho and Epstein [3] indicated, if sodium coolant is considered, it can be

viewed as a work enhancing fluid or as a quenching liquid depending upon the relative mass of sodium coolant intermixed with the two-phase fuel and the characteristic length scale for heat transfer between the constituents (i.e. sodium drop diameter). If the entrained mass is small and the characteristic size small, the sodium can vaporize and become the working fluid enhancing the disruptive expansion work (~double) [3]; whereas, if the mass and characteristic size are large, the sodium can act as a non-vaporizing quenching liquid reducing the UO_2 fuel pressure and the expansion work. In safety analyses for the Fast Flux Test Facility (FFTF) [8] and the Clinch River Breeder Reactor (CRBR) [9], the two-phase fuel expansion has been modeled as an isentropic expansion maximizing work output and neglecting sodium entrainment and heat transfer. Recently though, work at Los Alamos Laboratories on a computer code, SIMMER II, [10] has indicated that there is a possibility of a number of phenomena that could mitigate the expansion work of the fuel: sodium entrainment and the associated vapor-liquid heat transfer, heat transfer effects to the solid structure in the reactor, frictional effects on the fuel vapor pressure. It is in this context that the effect of the coolant entrainment is investigated.

The sequence of physical events leading to an energetic molten fuel-coolant interaction (MFCI) are not completely known but could be characterized by a three-stage process [7,11]; (1) coarse intermixing of the molten fuel and coolant, (2) a trigger mechanism that initiates the interaction between the constituents, (3) propagation of the interaction to an explosive nature (possible shock wave production). This process is analogous to the

to the preparation of chemical explosions where chemical fuels and oxygen are uniformly and finely intermixed. Here the fuel and coolant must be finely intermixed to obtain large heat transfer rates in short time scales to give an "explosive" result. At present, the details of each stage specifically in regard to the fragmentation and mixing of fuel and coolant are being disputed. There are two theories being advanced to describe this physical process.

The spontaneous nucleation theory [12] is based on the concept that there is a lower temperature threshold for energetic MFCI's, that being the spontaneous nucleation temperature (T_{SN}). This temperature is based on the properties of the coolant and fuel-coolant wetting behavior. If the interface temperature (T_I) of the liquid-liquid pair of fuel and coolant is above T_{SN}, then the possibility exists for a coherent energetic MFCI. Thus the three-stage process is viewed as occurring only if $T_I > T_{SN}$, whereby this "explosive" boiling, fragmentation, intermixing and heat transfer occur simultaneously. For UO_2 and sodium in the LMFBR $T_I << T_{SN}$ due to the thermophysical properties of the constituents, seemingly excluding energetic interactions in the reactor.

A hydrodynamic and vapor collapse model is postulated [13,14] whereby fragmentation of fuel and coolant can take place not due to an explosive boiling phenomenon as described before but based upon purely liquid-liquid hydrodynamic fragmentation (Taylor Instability Helmholtz instabilities), or fragmentation due to the collapse of a vapor film between the constituents. In this case the fragmentation and intermixing can occur prior to explosive boiling or heat transfer thereby implying no temperature threshold. This then would imply energetic MFCI's cannot be ruled out in the LMFBR.

Experimentation with LMFBR materials [15,16] have not indicated that energetic MFCI's are possible, although it has been Armstrong's contention [15] that small vapor explosions have been observed when sodium is injected into UO_2. Simulant materials have been experimentally used to investigate the MFCI phenomenon. In particular, a large amount of data has been accumulated using molten metals as the fuel and water as the coolant. It is these experiments that particular emphasis is placed in this research. These other experiments - molten metal and water - were conducted as simulant experiments, but their subsequent behavior does not simulate the UO_2-sodium system behavior. However, because these experiments were run and produced interactions, they should be explained in an attempt to learn more about the MFCI process.

1.3 Present Work

The purpose of this research work is twofold:

(1) Investigate the effects of cold liquid heat transfer during a two-phase expansion of the hot fuel. This specifically addresses the effects of sodium entrained during a two-phase UO_2 expansion.

(2) To propose a model for molten fuel-coolant interactions specifically in regard to small scale molten metal/water systems in drop experiments.

The course of investigation into coolant entrainment and heat transfer during a two-phase fuel expansion is depicted in Figure 1.1. The entrainment phenomena is investigated by performing simple experiments to determine an entrainment model based on Taylor Instabilities. Vapor-liquid heat transfer models are then developed to be applied to both small scale experiments and possible full scale conditions. The application of these models are in three areas. Small scale experiments have been performed by other

investigators which indicate that liquid entrainment and heat transfer could be substantial. The models developed are applied to these experiments to determine their validity and usefulness in application to full scale calculations using reactor materials. Finally, these models along with the governing equations can be used to give an indication of the possible governing dimension less groups and type of simulant fluid combinations needed for small scale experimentation.

For MFCI's it has been noted that for some simulant materials (e.g. tin/water, bismuth/water, lead/water) random self-triggered fuel-coolant interactions only occur for a specific range of fuel and coolant initial temperatures, for small scale experiments in the drop mode of contact. As Figure 1.2 indicates these small scale experiments in particular are examined in this work. For these material combinations the major investigation has been in regard to the triggering of the interaction. This work proposes a model for these interactions which indicates: (1) the fuel surface temperature in the region of a self-triggered interaction is below the critical temperature of the coolant; (2) the upper diagonal cutoff for the self triggered interaction can be explained by a non-condensible gas film which allows quiescent coolant vaporization and film boiling thereby precluding a self triggered event.

It is hoped that the present work will be useful in assessing the consequences of the phenomena of fuel-coolant interactions.

FIGURE 1.1

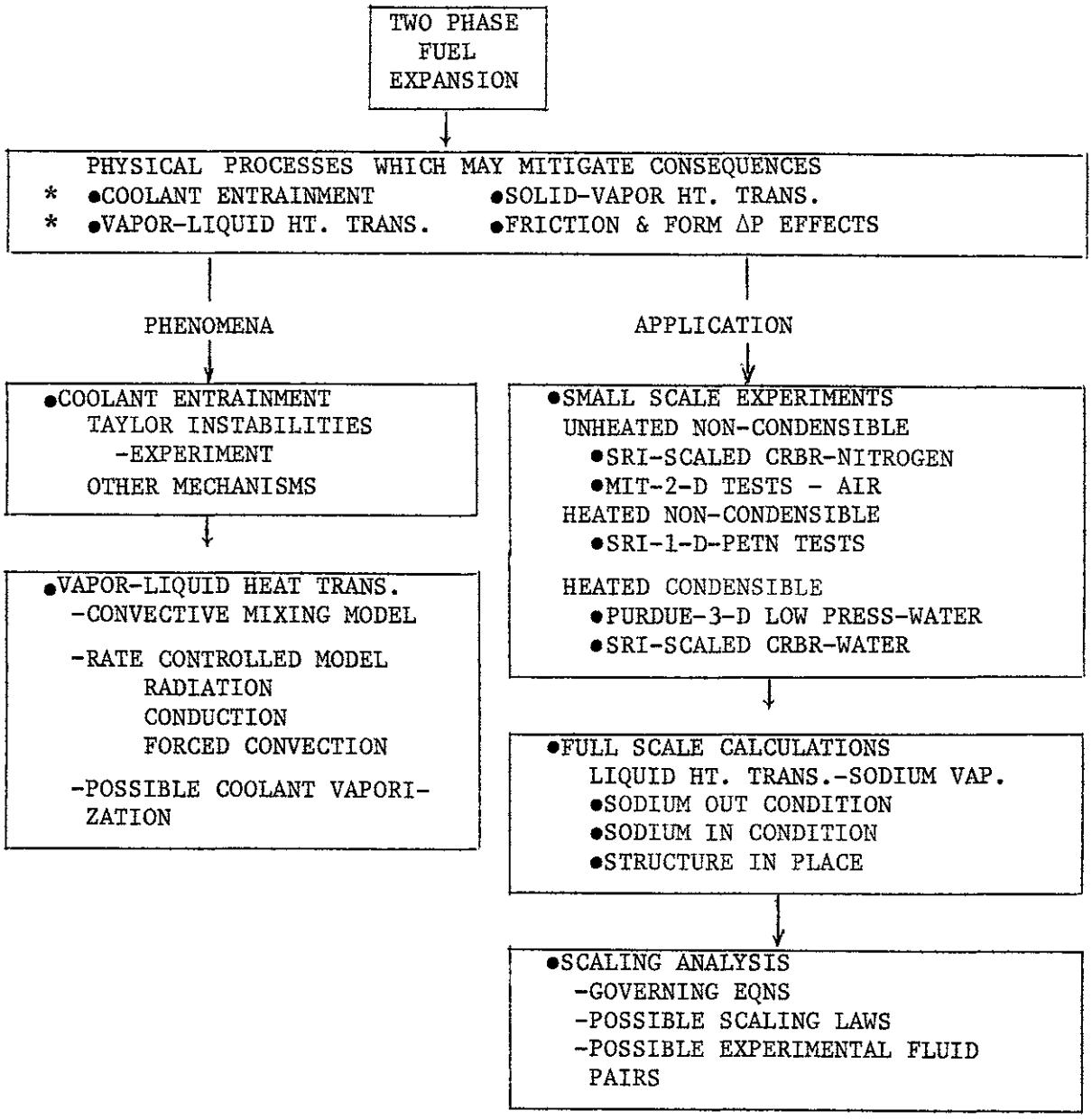

AREAS OF INVESTIGATION FOR TWO-PHASE FUEL EXPANSION

FIGURE 1.2

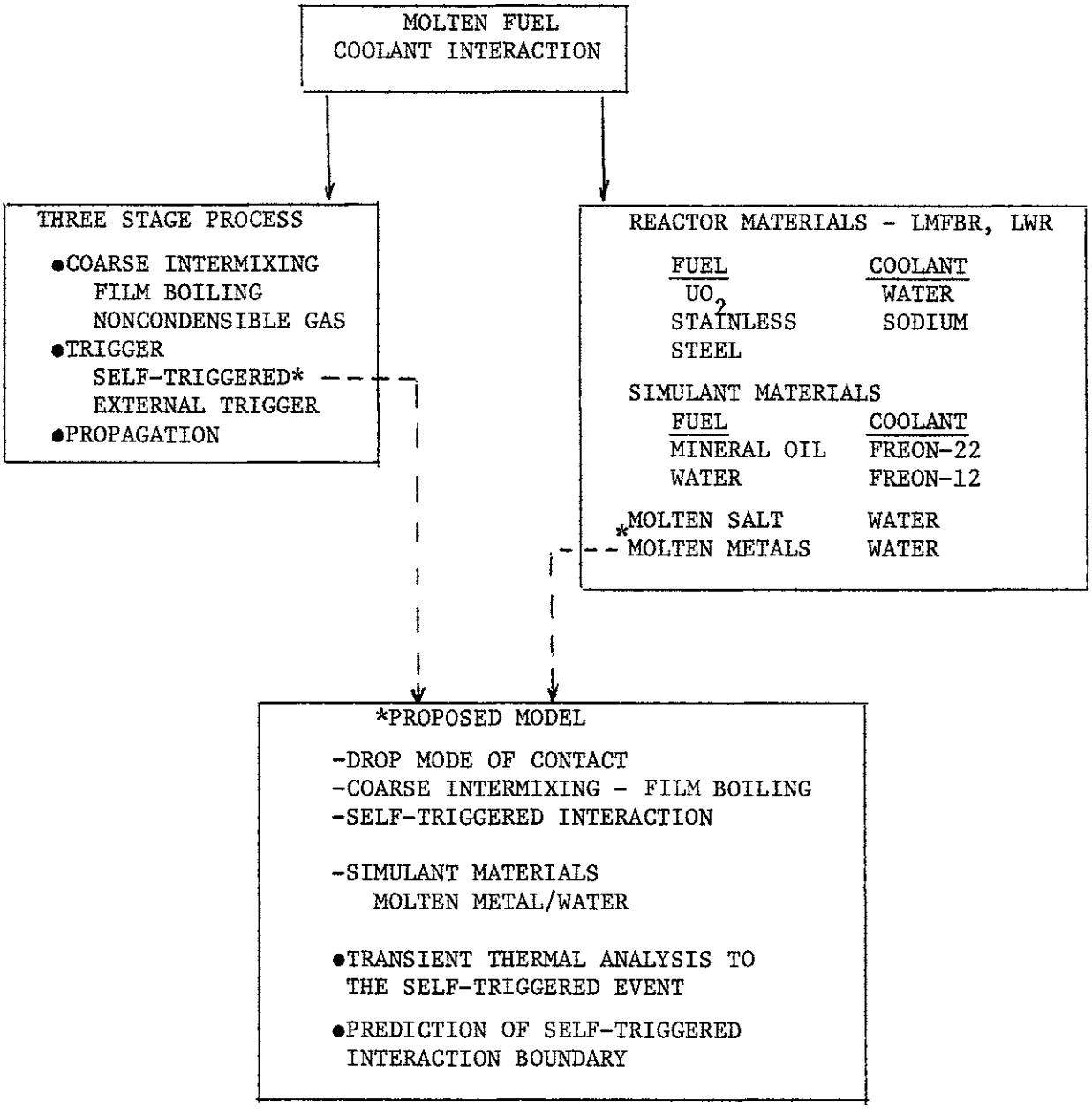

AREAS OF INVESTIGATION FOR MOLTEN FUEL-COOLANT INTERACTIONS

PART I

TWO-PHASE FUEL AND COOLANT HEAT TRANSFER

2. A REVIEW OF EXPERIMENTAL AND THEORETICAL INVESTIGATIONS INTO TWO-PHASE FUEL AND COOLANT HEAT TRANSFER

2.1 Overview

The existence of a two-phase fuel source during an HCDA is possible only in a fast breeder reactor. Because the fuel is not in its most nuclear reactive state in the core geometry, possible fuel material motions during the accident could lead to a prompt critical condition and high energy deposition in a short time, resulting in some fuel vaporization. The present design concept for the LMFBR in the U.S. is a loop type primary system where the sodium coolant is circulated through the core within the reactor vessel (Figure 2.1) to cool the fuel and then out to intermediate heat exchangers. The initiating event that is assumed to occur during full power operation is a loss of primary flow in the core with a failure to scram. This initiating event and the full spectrum of consequences has been extensively analyzed for the FFTF and CRBR [2,8,9] and only a brief review is given here.

Given the initiator of a loss of coolant flow in the core, sodium will start to boil out. This voiding behavior causes an increase in the power of the core because of the positive sodium void coefficient. Thus effective fuel rod cooling ceases and the power increases causing a rise in fuel temperature and eventual melting of the fuel rod. The coolable geometry of the core begins to deteriorate and the spectrum of possible consequences becomes large. Figure 2.2 gives a conceptual view of the possible paths of the accident. The initiation phase can lead to early termination if a coolable geometry is maintained, but this is unlikely for

the present design. Once fuel and clad motion begins due to melting, there are two general directions the accident can take. If the fuel motion is outward from the core or if the generated vapor from boiling steel keeps the fuel in a dispersed state (high void fraction) the core power will not increase significantly and may decrease due to high neutron leakage. This transition phase then will lead to an eventual boil out of the fuel and steel in the core at low power levels so that vapor pressures in the core are low and the disruptive mechanical work is small. This path of the accident is viewed by some [17] in the reactor safety community as the most likely consequence, because a steel and fuel mixture is considered to be inherently dispersive. This is due to the fact that the boiling point of steel is the same as the melting point of fuel, thereby giving a dispersed (high void fraction) regime during the accident and negligible energetics. This physical model though has not yet been conclusively proven. On the other hand, if the transition phase results in a slumping of the fuel to the central region of the core or if this occurs directly after the accident initiation, core power will dramatically increase because of a prompt critical condition. This increase will deposit a large amount of energy in a short time. The fuel will then partially vaporize at high pressures and the core will physically disassemble under a high pressure two-phase fuel expansion as core neutronic power falls to near zero.

This final HCDA scenario will result in a disruptive work expansion being exerted upon the core and the reactor vessel. The work done is taken up in deforming the vessel and accelerating the sodium above the core as a slug, impacting upon the reactor vessel head. If this energetic

expansion is severe enough, the primary containment can be breached and some of the radioactive fuel released in a highly mobile vapor form. This represents the most immediate and catastrophic method of radioactivity release from an accident. It is this final scenario of two-phase fuel expansion that will be considered here. Although it is recognized that it is by far the least probable accident path [2], it does possibly pose significant public health consequences.

Given this two-phase expansion, there are a significant number of physical phenomena that may be operative in this short time period (20 - 200 msec) that could reduce the pressure of the two-phase mixture and thereby reduce the disruptive work. If the solid structure (e.g. fission gas plenum, upper internals) above the core is remaining after the accident initiation and disassembly, then it could serve as a large heat sink and as a throttling valve to reduce the pressure of the expansion due to friction and form drag. The fission gas plenum and upper axial blanket represent sizable masses with a large exposed surface area for efficient heat transfer. In addition, the effective L/D_e for this geometry is large implying a possibly large pressure drop as the core materials are discharged through this area. Non-equilibrium effects can also have a large effect during the expansion. If the amount of fuel liquid-vapor surface area is large (e.g. dispersed flow regime) or the time scale long (exp. time >> char. length/acoustic vel.), then the two-phase blowdown out of the core may be near equilibrium. This would imply that a significant amount of liquid is being expelled with the vapor, thereby tending to keep the expansion pressure higher, near equilibrium and give larger expansion work. If, however, the flow geometry is more

stratified or the time scale smaller, then the blowdown may have a non-equilibrium nature with lower pressures and less expansion work. In addition, self-mixing of the fuel within the core may alleviate core thermal gradients and may also tend to reduce the work output of the expansion because the resultant pressure of the two-phase mixture could be reduced significantly. Another phenomenon to consider is the two-phase fuel-liquid sodium interaction as the coolant is entrained during the expansion. This phenomenon can transfer a significant fraction of the energy of the fuel to the coolant and possibly reduce the work output. It is this phenomenon that will be examined in this study. To illustrate the interaction of these possible events, consider Figure 2.3 which gives a possible event tree following the generation of the two-phase fuel source. This will be used later in Chapter 6 to select some key full scale calculations incorporating liquid heat transfer effects. Let us now turn to a review of experimental and theoretical investigations of the fuel vapor and liquid heat transfer.

2.2 Experiments Utilizing Reactor Materials

There have not been any experimental programs which have directly investigated the phenomenon of two-phase fuel expansion using UO_2 or other reactor materials (e.g. stainless steel) and possible sodium heat transfer. Because of this there are no experimental data or results that can be used as a physical basis for phenomenelogical modeling or analysis. There have been, though, some experiments that have generated a two-phase fuel expansion as a component in a larger test. These experiments will be briefly mentioned as well as some future experimental plans in this area.

Tests have been performed at Argonne National Laboratory at the TREAT reactor facility where small amounts of two-phase fuel were generated [18]. This occurred in the TREAT S-series experiments where steel clad UO_2 fuel pins were melted down in a stagnant sodium column under energetic power transients. The tests were designed to observe possible molten fuel-coolant interactions (MFCI) which did not occur. Instead, pressure pulses (~5 - 20 MPa) were noted during the experiment and were attributed to some localized fuel vaporization and subsequent condensation due to two-phase fuel-sodium heat transfer. The test is not prototypic of the accident discussed because geometry, and sodium and fuel mass ratios are much different.

In-pile experiments conducted under Nuclear Regulatory Commission (NRC) sponsorship at Sandia Laboratories [19] are underway. Some tests have been completed in the ACPR reactor where a single clad fuel pin in a stagnant sodium column undergoes a severe power transient and significant fuel vapor is generated. At the present time, results from these tests have not been released due to continued data reduction and in any case, the geometry and fuel-sodium masses are not prototypic. Future tests in the program will be conducted with new geometries to try to get some results which are prototypic of the full scale fuel expansion both with and without sodium present.

Out of pile experiments are being planned at Oak Ridge National Laboratory using an electrical capacitive discharge system to vaporize fuel in various coolant environments. Past experiments have been conducted at ORNL using this system [20] for the purposes of studying fuel aerosol transport, where fuel is vaporized in an argon atmosphere.

2.3 Experiments Utilizing Simulant Materials at Small Scale

There has been more extensive experimentation performed using simulant materials at small scales. The phenomenon that has been mainly examined is the rate of coolant entrainment in the expanding fuel vapor bubble and the fuel-coolant heat transfer that occurs. Table 2.1 gives a listing of these experiments and some of the key initial conditions of each.

SRI International has been conducting a research program for the Department of Energy (DOE) over the past few years on Hypothetical Core Disruptive Accidents. The objectives of the research is twofold:

(1) Experimentally determine the structural response of an LMFBR to a simulated HCDA. These tests are done to enable a verification of computer codes which predict the reactor vessel structural response (e.g. REXCO [21]);

(2) To develop a basic understanding of the dynamics and thermodynamics of expanding bubbles similar to that in a two-phase fuel expansion in an LMFBR, to predict eventually core material transport in the vessel.

The first objective was originally pursued in the analysis of the FFTF. The core disruptive accident analyzed in the Final Safety Analysis Report [8] was an MFCI with two-phase expansion of sodium. SRI's objective was to develop a high pressure gas source which would produce the pressure-volume curve of an isentropic MFCI expansion [22-24]. An explosive non-condensible source (PETN) was developed and in the process it was noted that when water was inserted in the experiment to simulate the cold sodium slug above the core [22], significant heat transfer between the hot gas and cold water occurred reducing the work output by 50%. Cagliostro [22] suggested that Taylor Instabilities may be the mechanism which caused a large amount of water entrainment in the hot gas, thereby generating a large surface area for efficient heat transfer. These small scale tests were done in

planar geometries (30 tests) as well as geometrically scaled FFTF reactor vessel geometries (6 tests) and the heat transfer phenomenon consistently occurred. No attempt was made at that time to analyze the phenomenon but at present they are being reviewed by SRI under the second research objective previously mentioned. It was this series of experiments that initially motivated this investigation of vapor-liquid heat transfer and these experiments will be analyzed in more detail in Chapter 4.

More recently SRI has initiated work on the second objective aimed at understanding the behavior of a fuel vapor expansion by performing both isothermal and heated experiments [25,26]. The experiments are geometrically scaled (1/30 scale) to the CRBR in the fission gas plenum and upper plenum regions. The simulant fluids presently being used do not thermodynamically model the fuel and coolant, although this goal is ultimately being sought. Three experiments have been performed: nitrogen gas as the fuel and water as the coolant in an adiabatic expansion; two experiments employing hot two-phase water as the fuel and subcooled water as the coolant. The initial experiments are aimed at the mechanisms of entrainment and liquid heat transfer with future tests being devoted to the solid heat transfer phenomenon. The preliminary conclusions of the work were that significant entrainment did occur (~30% by volume) into the expanding bubble both in the isothermal and heated experiments, and that this led to significant heat transfer in the two-phase blowdown. In addition, non-equilibrium effects were noted in the two-phase expansion. These tests are also evaluated in Chapter 5.

Argonne National Laboratory working in conjunction with Purdue University performed a series of small scale experiments investigating the transient

behavior of two-phase jets [27,28]. The geometry was similar to the CRBR although not exactly scaled. Both isothermal (compressed air) and heated (two-phase water) experiments were performed at low pressures ($\sim$ .4MPa) ejecting the vapor source into a subcooled water pool. The conclusions indicated that significant coolant entrainment again occurred (30 - 50% by volume), and that this probably generated a large surface area which aided heat transfer. In addition, it was noted that growth of the transient bubble first behaved as spherically symmetric bubble growth later changing into a planar (jet-like) expansion. Specific entrainment or heat transfer mechanisms were not investigated and these tests will also be examined in Chapter 5.

2.4 Theoretical Studies of the Two-Phase Fuel Expansion

The analysis of this phenomenon has generally taken one of two routes within the safety research community. One route attempts to look at the two-phase expansion and develop simple phenomenological models which describe the dominant physical processes and come to some conclusion as to the likely consequences. The other avenue has been to develop the governing equations of the phenomenon on a more general basis and attempt to analyze the transient process by development of large computer codes which account for many physical processes simultaneously. Each route has drawbacks. Phenomenological modeling demands some prior knowledge of dominant processes, while large computer models inherently lack some rate coefficients (heat transfer coefficient, flow regimes) that are based on a knowledge of the individual phenomena. The two approaches can compliment each other. For instance, a parametric analysis with computer codes to see the dominant processes and their key uncertainties may lead to

identification of key phenomena to study and perform separate effects tests. It appears that contemporary analysis presently rests at this juncture for these phenomena.

The safety analysis reports for the FFTF and CRBR [8,9] view the hypothetical two-phase fuel source in a conservative way by looking at an isentropic disruptive work output of the expansion. The computer codes employed in the CRBR analysis (e.g. SAS3A) use a spectrum of possible initial conditions and parametric rate coefficients to determine the initial conditions for the two-phase isentropic expansion in the work-energy slug expansion phase.

A parametric analysis by Cho and Epstein [3] represents one of the initial attempts to include the effect of possible sodium entrainment and heat transfer during a two-phase fuel expansion. The analysis took the model of a spherically symmetric two-phase UO_2 bubble (Figure 2.4) being formed above the core and expanding causing sodium entrainment until the sodium slug impacts the reactor vessel head. The mechanism for possible entrainment was not investigated, and a parametric calculation was used requiring: (1) the coolant mass entrained; (2) its characteristic size; (3) the rate mechanism for vapor-liquid heat transfer. The rate of coolant mass entrainment ($\dot{m}_e$) was modeled as a constant times the fuel mass flow rate from core blowdown ($\dot{m}_e = W\dot{m}_f$) and this constant was parametrically varied. The mechanism of heat transfer between the fuel and coolant was modeled as vapor-liquid heat transfer by assuming that small coolant droplets (~100 μm) are entrained and come instantaneously to their saturation temperature at the vapor pressure of the fuel and are vaporized

and superheated at a rate governed by black body radiation heat flux. The interesting point to emphasize about this fuel-coolant pair is that sodium is a more volatile fluid; its vapor pressure at a given temperature is higher than UO_2, thus it can act as a work enhancing fluid. This behavior is seen in Figure 2.5. If the amount of sodium liquid entrained is small, then it is almost totally vaporized at high fuel temperatures and the pressure in the expanding bubble increases thereby increasing the expansion work, making sodium a work enhancing fluid. This occurs because the quality of the two-phase fuel is quite low (1 - 10%) which gives a large saturated liquid reservoir that can evaporate and give up its latent heat. If the amount of sodium entrained increases, then it not only vaporizes but can substantially cool the fuel thereby reducing the pressure and the expansion work. Thus the analysis by using a very large heat transfer rate took a conservative view of the effect of sodium entrainment. The conclusion of the analysis was that in the worst case of optimum sodium entrainment mass the coolant could increase the expansion work by a factor of 1.4 to 2 (Figure 2.6), but with large amount of entrainment could become a quenching liquid.

There have been other simple parametric investigations [29,30] into the effect of heat transfer from the two-phase source to the solid structure that may be present above the core (fission gas plenum, upper intervals). These analyses have indicated that the possible heat transfer to the solid structure can be large because the exposed surface area is great and the major heat transfer resistance is within the solid. The major question that has not been answered is whether the structure will be present after

the accident initiation and disassembly occurs. The possibility exists that the structure may be melted out or pushed out of the way before the energetic disassembly occurs thereby removing it as a possible heat sink.

A large research effort is being maintained at Los Alamos Laboratories to develop a computer code (SIMMER I) which will be able to follow the LMFBR core from accident initiation to its termination after slug impact. The important feature of the code is that it attempts to model some of the various phenomena that may affect the isentropic work expansion of the two-phase fuel source. As mentioned before some of these phenomena that may mitigate the fuel expansion work are sodium entrainment and heat transfer, heat transfer to solid structure, friction and form pressure losses due to the structure fuel self-mixing. The major drawback of such an approach is that there are a number of heat transfer and momentum rate coefficients that are difficult to determine and are needed as input to the code. To illustrate the possible combined effect of these phenomena [10], consider the reactor geometry model of Figure 2.7. The structure is assumed to be present and the initial conditions are depicted for an initial core two-phase fuel temperature of $4800^{o}K$. Figure 2.8 gives the results of a best estimate prediction of the expansion work at the time of sodium slug impact for a variety of participating phenomena. The major conclusion to date of this method of analysis by LASL researchers is that the isentropic work expansion is a very conservative upper limit and the mitigating phenomena should be investigated further. Particular emphasis is now being placed on phenomenological modeling of effects such as sodium entrainment, solid heat transfer, structure friction effects.

From this review of previous work, it is quite apparent that phenomenological modeling of the various possible effects during two-phase fuel expansion is quite sparse. In addition, there has not been a unified evaluation of small non-scaled experiments (e.g. SRI & Purdue tests) to determine the physical mechanisms that may be involved. This is especially needed due to the present lack of experimental data using reactor materials. It is this area which will be described, specifically in regard to the phenomena of coolant entrainment and two-phase fuel-coolant heat transfer.

TABLE 2.1

SUMMARY OF SIMULANT SMALL SCALE EXPERIMENTS
CONCERNING COOLANT ENTRAINMENT AND
FUEL-COOLANT HEAT TRANSFER

	NONCONDENSIBLE UNHEATED	NONCONDENSIBLE HEATED	CONDENSIBLE HEATED
1-D		SRI [22] 30 tests PETN source Press. (10-40MPa)	
2-D			
3-D NON-SCALE	ANL-PURDUE [27,28] 3 tests AIR source Press. (.4MPa)		ANL-PURDUE [27, 28] 12 tests HOT WATER (2ϕ) Press. (.4MPa)
SCALED GEOMETRY	SRI-[25,26] CRBR 1 test Nitrogen source Press. (10MPa)	SRI [23,24] FFTF 6 tests PETN Source Press. (10-40MPa)	SRI [25,26] CRBR-2 tests HOT WATER (2ϕ) Press. (8.2MPa)

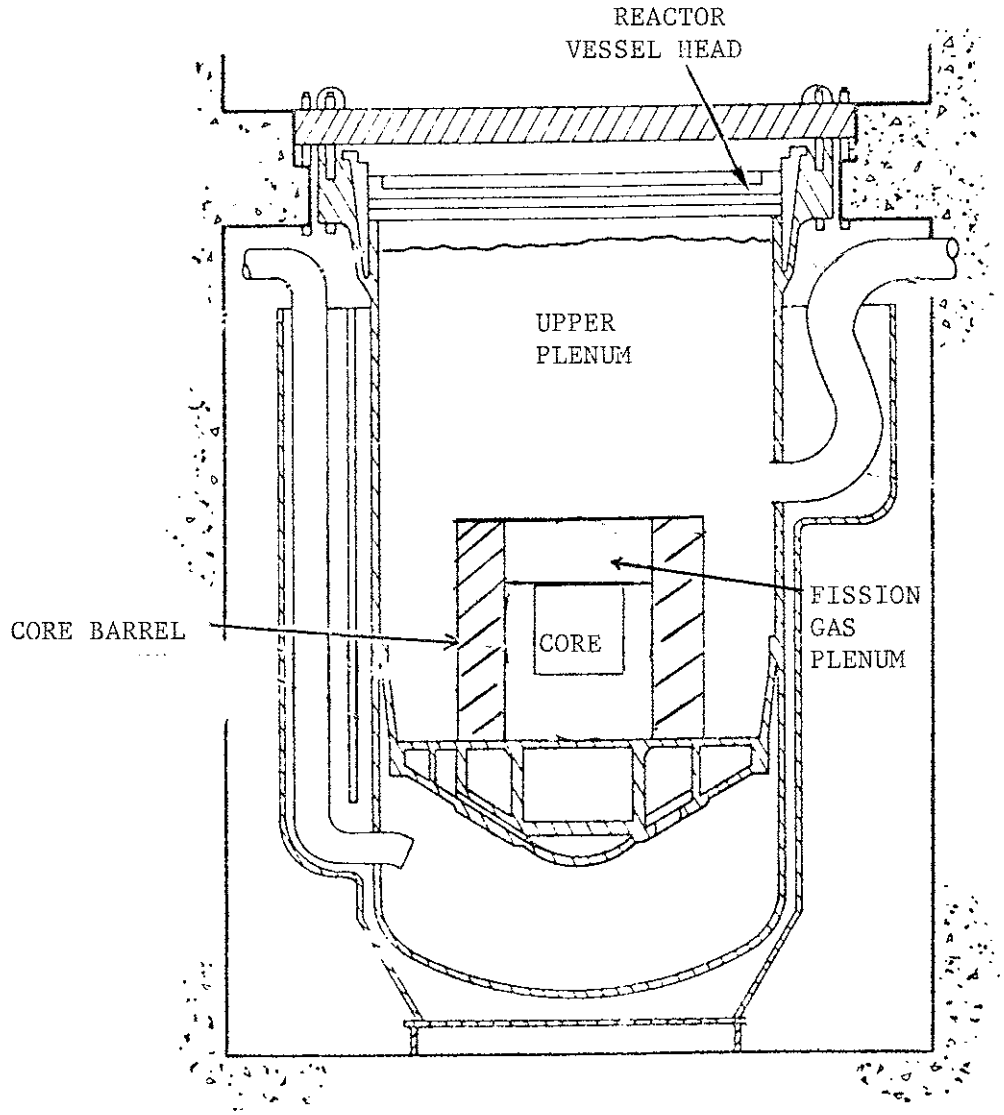

FIGURE 2.1

GENERAL PICTURE OF LMFBR REACTOR VESSEL AND CORE

COMPREHENSIVE APPROACH TO LOF HCDA ANALYSIS

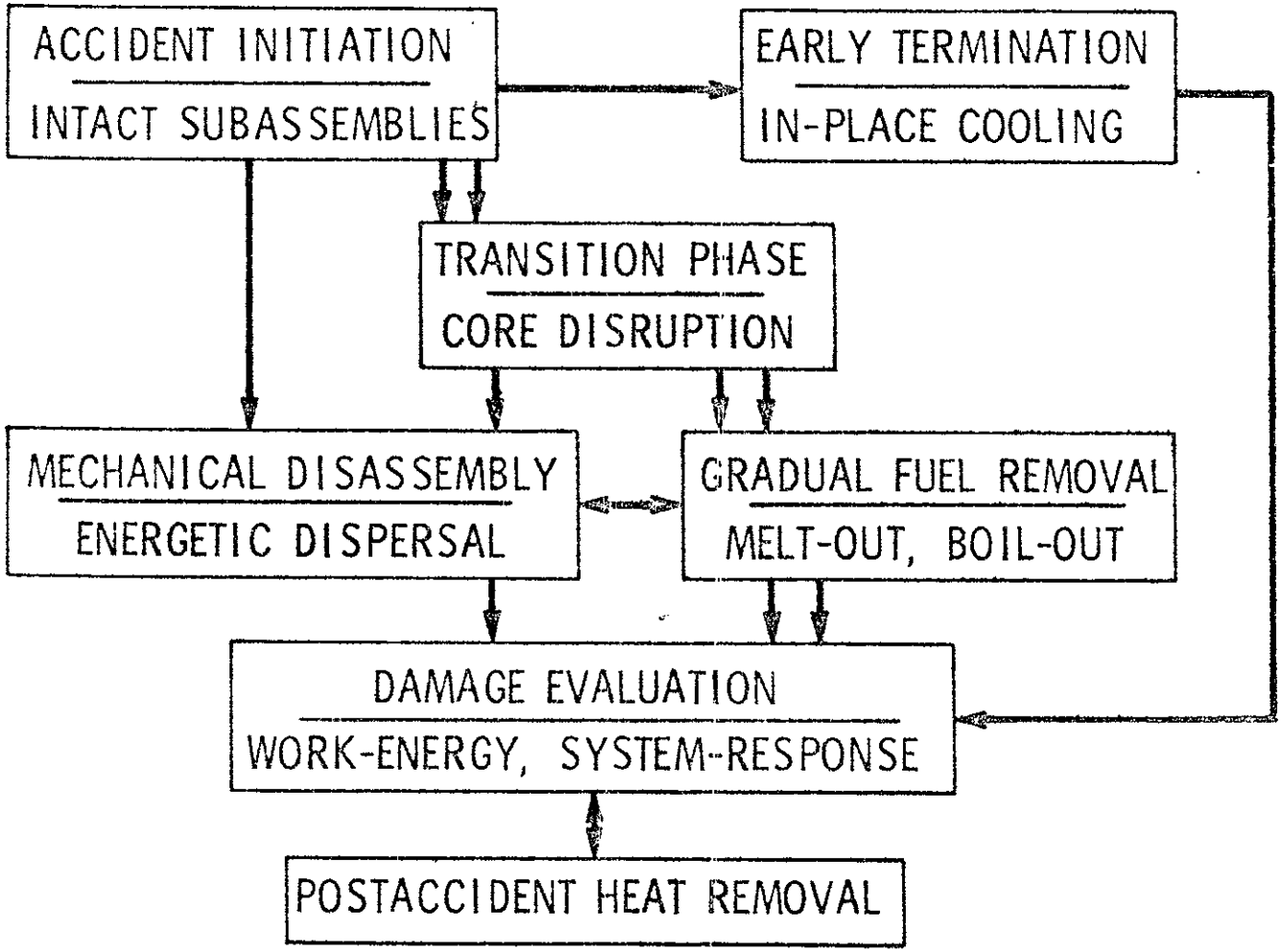

FIGURE 2.2

FIGURE 2.3

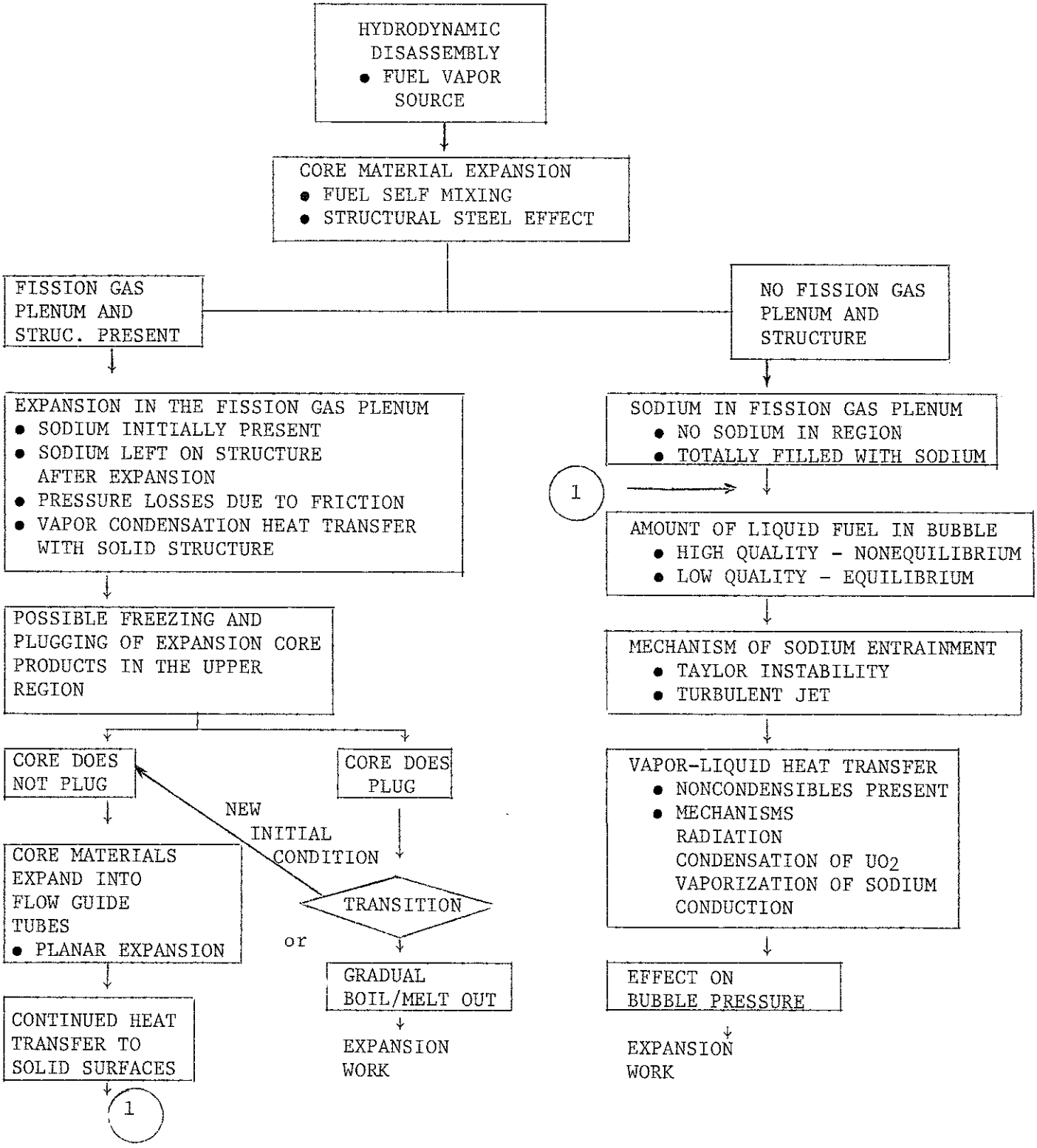

POSSIBLE EVENT TREE FOR A HYDRODYNAMIC DISASSEMBLY

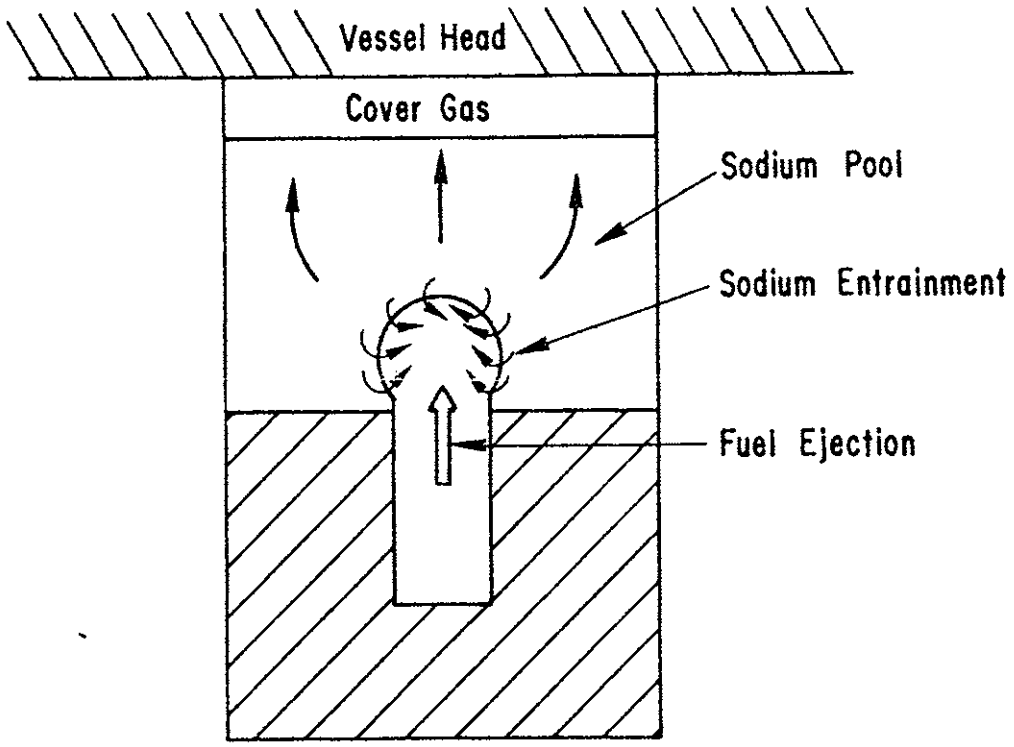

FIGURE 2.4

CHO-EPSTEIN MODEL FOR TWO-PHASE FUEL EXPANSION AND SODIUM ENTRAINMENT

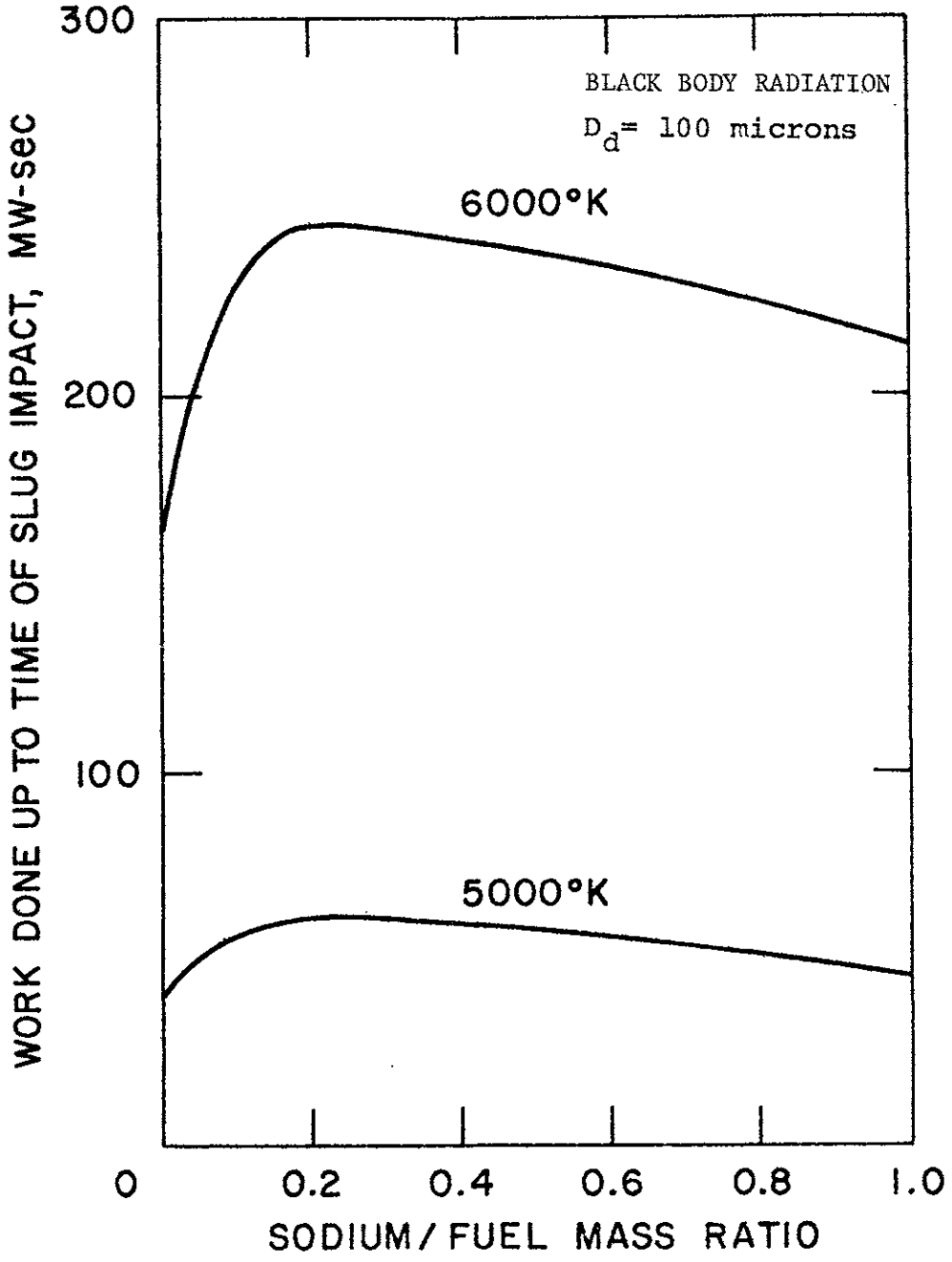

FIGURE 2.5

EXPANSION WORK DONE UP TO SLUG IMPACT AND THE EFFECT OF SODIUM ENTRAINMENT

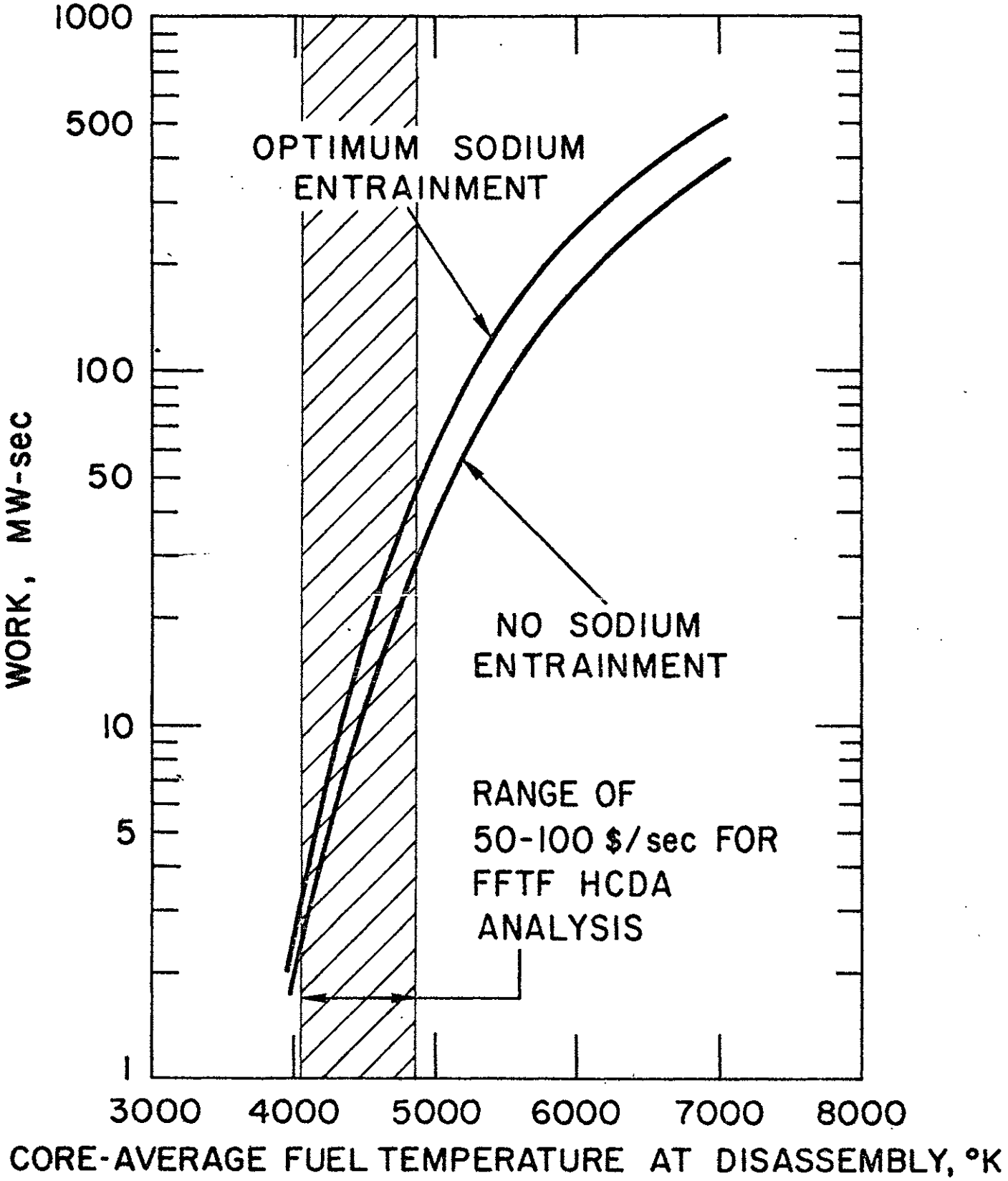

FIGURE 2.6

SUMMARY OF OPTIMUM ADVERSE EFFECT OF SODIUM ENTRAINMENT ON EXPANSION WORK

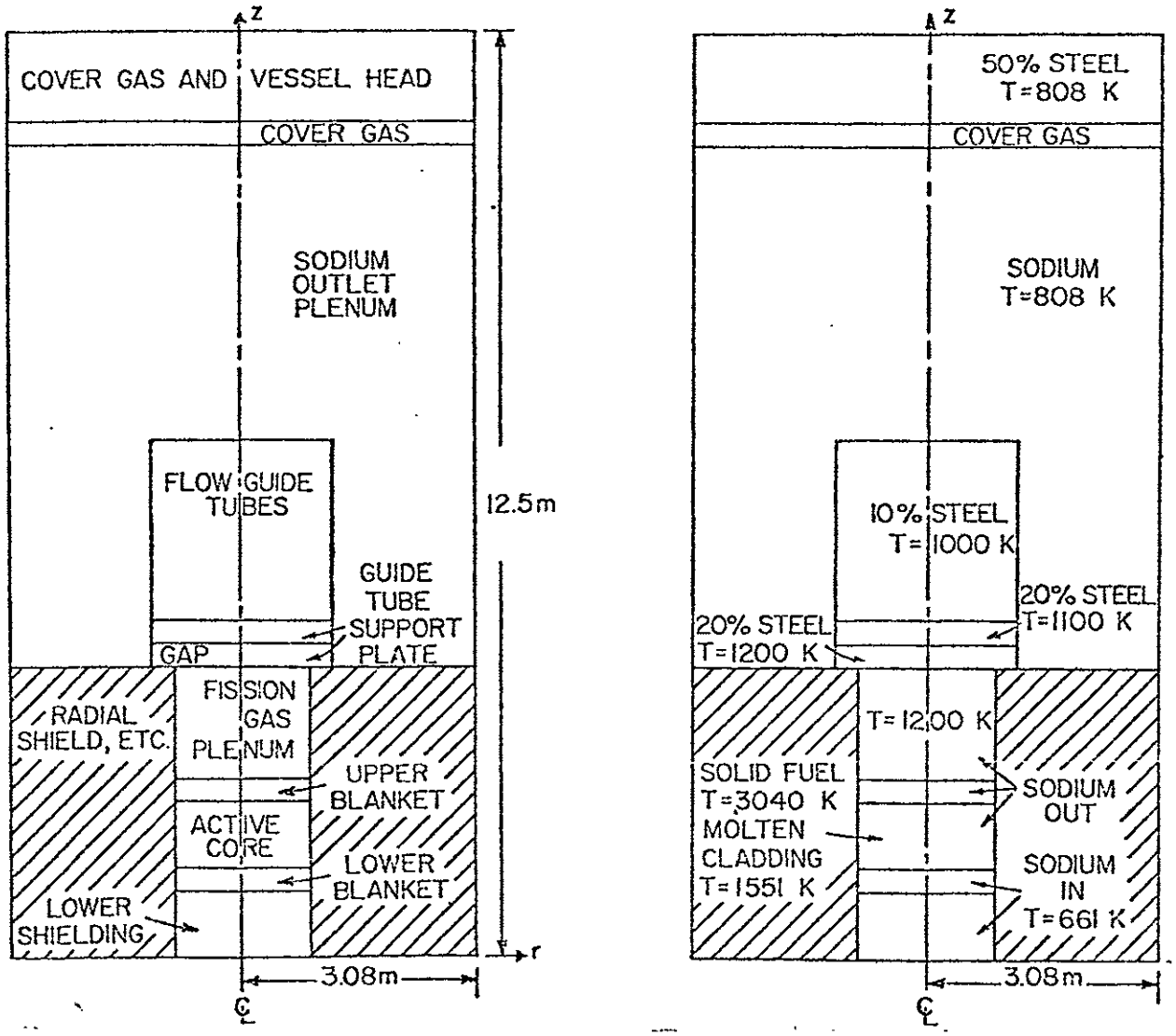

FIGURE 2.7

SIMMER MODELING PICTURE OF THE REACTOR VESSEL

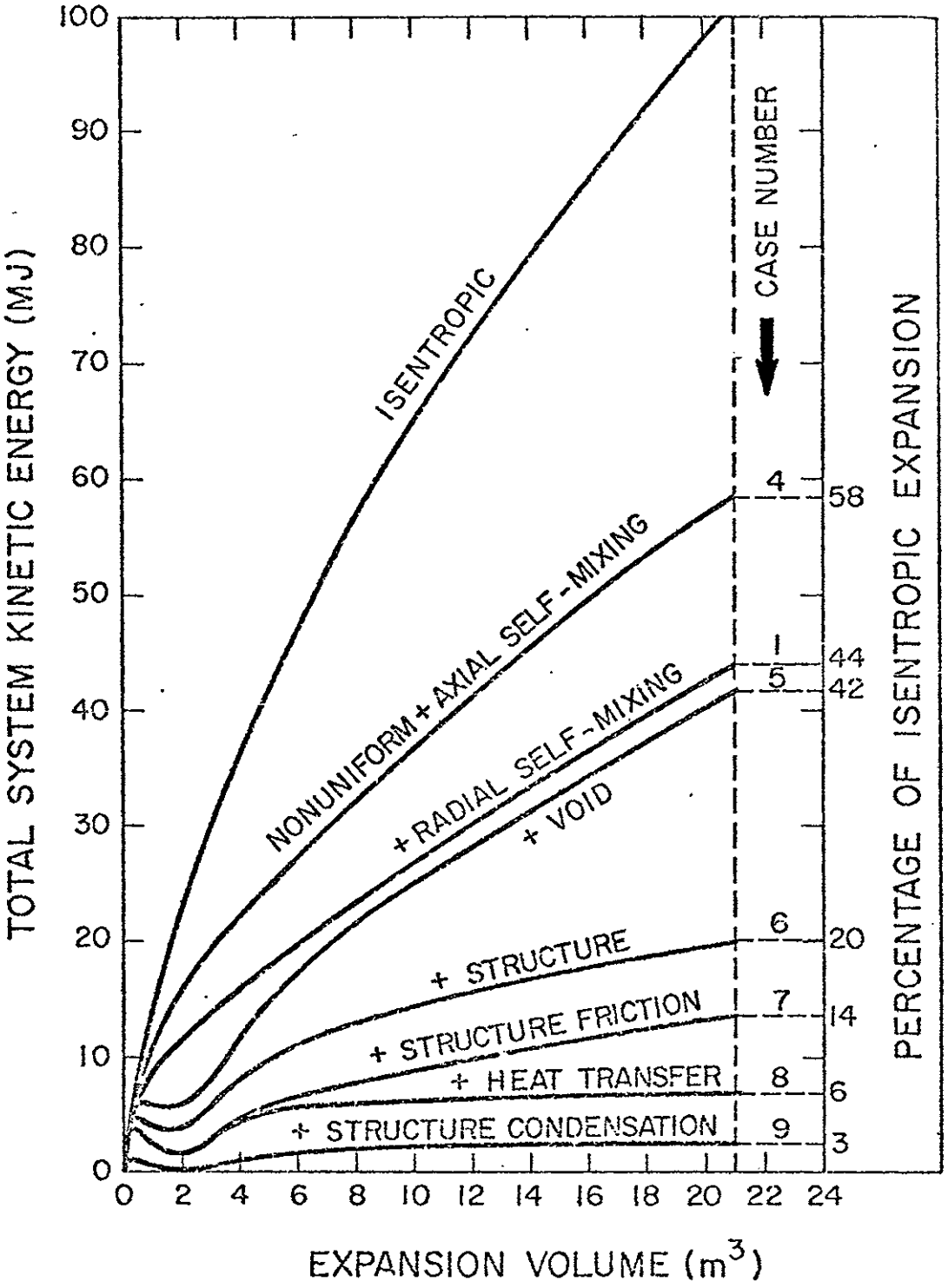

FIGURE 2.8

EFFECT OF VARIOUS PHENOMENA ON THE EXPANSION WORK AT SLUG IMPACT

3. EXPERIMENTS AND PHENOMENOLOGICAL MODELING CONCERNING LIQUID ENTRAINMENT

3.1 Introduction

There are a number of mechanisms that may cause entrainment during the vapor expansion into the coolant pool above the core. Two fundamental ways in which entrainment can occur are illustrated in Figure 3.1.

Given two different fluids if an acceleration (a) is imposed which is perpendicular to their interfaces and is from the less dense fluid to the more dense, the fluid interface is unstable. Given a random perturbation of the interface, the perturbation will grow with time and the more dense fluid will be entrained in the less dense fluid. This phenomenon was originally studied by Sir Geoffrey Taylor and has come to be known as a Taylor fluid instability. It is one fundamental mechanism by which two fluids of differing densities can become intermixed. If, however, the acceleration is from the more dense to the less dense fluid, it can be shown that the fluid interface is stable and no intermixing occurs. This Taylor Instability mechanism may be operative in the full scale reactor accident scenario (Figure 3.2) and in the small scale experiments. Cagliostro [22] and Epstein [31] have suggested this in particular for the 1-D SRI tests.

Another possible situation is shown at the bottom of Figure 3.1 where a gas stream exits from a hole into a reservoir. Initially, waves are formed at the fluid interface as on the ocean surface by the wind. If the parallel velocity becomes large enough, the interface will become unstable and the waves will grow. This situation is known as a Kevin-Helmholtz

instability. As the velocity increases, the waves grow and turn over on themselves forming a churning vortex at the fluid interface and some of this fluid can be entrained in the gas flow. This entrainment is caused by the flow of this turbulent jet out of the hole. This mechanism may also be operative in the full scale accident scenario (Figure 3.2) again depending upon the initial conditions and geometry. This may also be an operative mechanism in the small scale tests as Tobin [32] from SRI has suggested.

These two possible mechanisms are investigated in the following sections. First, a review of past experiments involving these mechanisms is presented. Special emphasis is placed on Taylor Instabilities because it is believed that this mechanism plays a more dominant role during the transient. The indication from this review is that Taylor Instabilities can be an operative mechanism although no entrainment model now exists. To determine such a model, a series of experiments were undertaken to investigate the possible variables affecting this entrainment mechanism.

3.2 General Overview of Past Analysis and Experiments Concerning Entrainment

3.2.1 Turbulent Jet Entrainment

The phenomenon of fluid entrainment by the discharge of jets into a reservoir has been extensively studied in the steady state mode, thus only a brief review of pertinent analysis is given here. Schlichting [33] gives an excellent review of basic models to describe the induced mass flow caused by a steady state jet discharging into a reservoir. The most useful concept to retain from this treatment is that the volumetric rate of flow of the entrained fluid ($\dot{V}_e$) increases with the axial distance (x) away from the discharge point (Figure 3.3),

$$\dot{V}_e \sim x \tag{3.1}$$

whether this be for a laminar or turbulent jet.

There are other functional dependencies which must be included to obtain a workable formulation for entrainment. Spalding [34] performed a series of experiments where a noncondensible gas as a steady jet was discharged into a reservoir of various other gases, in an apparatus similar to Figure 3.3. He measured the rate of entrainment of the gas in the reservoir by installing a cylindrical porous wall around the jet and measuring the entrained flow through it as a function of axial distance. The experiment was conducted with various gas density ratios ($\frac{1}{15} < \rho_g/\rho_e < 2$) and the resultant relation that Spalding suggested from dimensional analysis was

$$\dot{V}_e = .32 \frac{x}{D_o} \left(\frac{\rho_g}{\rho_e}\right)^{\frac{1}{2}} \dot{V}_e \qquad (3.2)$$

for $x >> D_o$. This dependence of $\dot{V}_e$ on $\dot{V}_g$ can be physically visualized as a rate of transfer of axial momentum ($\dot{M}_i$) from the turbulent jet to the stationary fluid in the reservoir,

$$\dot{M}_{in} = \dot{M}_{out}$$

$$\dot{m}_g v_{g_{in}} = (\dot{m}_g + \dot{m}_e) v_{out}.$$

However, since $\dot{m}_g << \dot{m}_e$ for $x >> D_o$, this equation can be approximated as

$$\dot{m}_g v_{g_{in}} = \dot{m}_e v_{out}$$

$$\rho_g A_{g_{in}} v_{gin}^2 = \rho_e A_e v_{out}^2$$

$$\dot{V}_e^2 = \frac{A_e}{A_g} \frac{\rho_g}{\rho_e} \dot{V}_g^2$$

where

$$\dot{V}_e = A_e v_{out}$$

$$V_g = A_g v_{in}$$

now

$$A_g = \frac{\pi}{4} D_o^2$$

$$A_e \simeq x^2 \tan\alpha_J$$

Therefore,
$$\dot{V}_e \sim \frac{x}{D_o} \left(\frac{\rho_g}{\rho_e}\right)^{\frac{1}{2}} \dot{V}_g \tag{3.3}$$

For small values of x, no entrainment occurs. This non-entrainment length (L_o) in these experiments was found to be small and neglected.

Chawla [35-37] performed a theoretical analysis of a sonic turbulent steady state gas jet discharging into a liquid reservoir and developed an entrainment model. The physical model visualized was to consider that Helmholtz instabilities generate the initial waves on the liquid surface from the gas jet discharge and can be used as the model for the resultant vortex motion and entrainment rate. The analysis is quite complicated and lengthy, but two fundamental dependencies of the model are similar to Spalding's results; the rate of entrainment is proportional to the axial distance ($\dot{V}_e \sim x$), and the initial non-entrainment length (L_o) remains unknown and must be empirically determined for an experiment, or considered small as Spalding had done.

Analysis or experiments concerning the transient development of jets is not extensive. Abramovich [39] has performed some transient experiments of laminar jets by injecting noncondensible gases into a water pool. The main experimental interest though is not the rate or mechanism of entrainment but the transient movement of the jet. This type of analysis has some relevance to the investigation of vapor-liquid heat transfer but not concerning entrainment. It will be returned to in later analysis. Therefore, as a first approximation for the rate of entrainment due to a discharging turbulent jet, the relation suggested by Spalding is used. Because the equation is based on steady state experiments, some characteristic entrainment length ($x = x_o$) must be utilized when applying this relation to transient experiments. This length may vary depending on the geometry of the experiments and must be determined when the model is applied.

3.2.2 Taylor Instability Mechanism for Entrainment

The instability of liquid surfaces when accelerated in a direction perpendicular to their interfaces was originally investigated by Taylor [40]. In particular, what was evaluated was the initial growth rate of the fluid interface (Figure 3.4) under this instability condition by the use of the linearized hydrodynamic equations for incompressible and inviscid flow. For each fluid the equations are

$$\frac{\partial v_x}{\partial x} + \frac{\partial v_y}{\partial y} = 0 \qquad (3.4.1)$$

$$\frac{\partial v_x}{\partial t} + \frac{1}{\rho}\frac{\partial P}{\partial x} = 0 \qquad (3.4.2)$$

$$\frac{\partial v_y}{\partial t} + \frac{1}{\rho}\frac{\partial P}{\partial y} + g + a = 0 \qquad (3.4.3)$$

The initial perturbation is assumed to be small ($\eta_o << \lambda$) and is of the wave form $\eta_o \sim \cos Kx$.

The goal of this investigation is to find the amplitude of and shape of the interface as time progresses. These equations can be solved by making the substitution [40]

$$v_x = -\frac{\partial \phi}{\partial x} \qquad v_y = -\frac{\partial \phi}{\partial y} \qquad (3.5.1)$$

$$P = P_{ref} - (g+a)\rho y + \rho\frac{\partial \phi}{\partial t} \qquad (3.5.2)$$

with the potential functions (ϕ) being related to v_x and v_y and p_{ref} being the reference pressure at the interface. By direct substitution, it can be shown that the solutions in the upper fluid are

$$\phi_1 = A\, f(t)\, e^{-Ky} \cos Kx \qquad (3.6.1)$$

$$P_1 = P_{ref} - (g+a)\rho_1 y + \rho_1 \frac{\partial \phi_1}{\phi t} \qquad (3.6.2)$$

and in the lower fluid are

$$\phi_2 = -Ae^{Ky} f(t) \cos Kx \tag{3.7.1}$$

$$p_2 = p_{ref} - (g+a)\rho_2 y + \rho_2 \frac{\partial \phi}{\partial t} \tag{3.7.2}$$

where $K = {}^{2\pi}/\lambda$. These potential functions satisfy the condition that velocities are finite as $y \to \pm\infty$, and that the velocities are equal at the interface. The expression for η can be found by taking the linear approximation [40] that

$$\frac{\partial \eta}{\partial t} \doteq v_y = AK f(t) \cos Kx \tag{3.8}$$

This gives

$$\eta = KA\left(\int_{t_o}^{t} f(t)\, dt\right) \cos Kx \tag{3.9}$$

Now to find the time function (f(t)) the final physical condition can be invoked at the interface

$$p_1 \simeq p_2; \tag{3.10.1}$$

note that this neglects the effect of surface tention. Substituting in for the pressure, results in

$$-(g+a)\ (\rho_2-\rho_1)y = \left(\rho_1 \frac{\partial \phi_1}{\partial t} - \rho_2 \frac{\partial \phi_2}{\partial t}\right)$$

By substituting for ϕ and y and taking the derivative with respect to time, the result is

$$-Kf\ (g+a)\ (\rho_2-\rho_1) = (\rho_1+\rho_2) \frac{d^2 f}{dt^2} \tag{3.10.2}$$

The sinh (nt) and cosh (nt) functions will satisfy this differential equation with sinh (nt) matching the initial condition that

$$\frac{\partial \eta}{\partial t} = 0 \ @\ t = 0 \tag{3.11}$$

This leaves an algebraic expression for n

$$n = \sqrt{\frac{-(g+a)(\rho_2-\rho_1)K}{\rho_1+\rho_2}} \tag{3.12}$$

and gives for η (x,t)

$$\eta = \frac{AK}{n} \cosh(nt) \cos Kx \qquad (3.13)$$

where $K = 2\pi/\lambda$. Note the physical significance of this mathematical description of the instability; if the acceleration is negative [(a+g)<0], then n is real and the disturbance will grow with time $\eta \sim \cosh(nt)$. This corresponds to an acceleration from the less dense fluid into the more dense one. If, on the other hand, the acceleration is positive [(a+g)>0], then n is complex and $\eta \sim \cosh(nt)$ which indicates a stable situation where the interface will oscillate with time in the absence of viscosity. This situation is physically analogous to the acceleration being from the more dense to the less dense fluid.

This linear analysis is for the initial stage of growth of the instability in the absence of compressibility, viscous, and surface tension effects. Subsequent analysis by Bellman and Pennington [41] have included the effect of viscosity and surface tension. Physically, it would be expected that viscous forces would tend to slow the amplitude growth rate of the interfacial instability, and this is, in fact, the case as experiments have shown. To illustrate this mathematically though becomes quite complicated and is not pertinent to the investigation at hand. The physical effect of surface tension is somewhat different in that it will have its greatest effect at small wavelengths where not only does it slow the growth rate as viscosity does but if the wavelength is small enough, its force dominates over pressure forces and the wavelengths are stable. This can quite easily be seen mathematically by reexamining equation 3.10 where $p_1 = p_2$. This condition is not exactly true because the surface tension affects the pressure due to the curvature of the interface (Figure 3.5)

and can be represented by,

$$p_1 - p_2 = \sigma \frac{\partial^2 \eta}{\partial x^2} \tag{3.14}$$

When values for the pressure are inserted and manipulated as before with f(t) taken equal to sinh (nt), the result is

$$-(g+a)(\rho_2+\rho_1)\frac{AK}{n} \sinh (nt) \cos Kx$$
$$-(\rho_2+\rho_1)An \sinh nt \cos Kx - \sigma \frac{AK^3}{n} \sinh (nt) \cos Kx = 0$$

Solving for n, the result is

$$n = \sqrt{\left(\frac{-(g+a)(\rho_2-\rho_1)}{\rho_1+\rho_2}\right)K - \frac{\sigma}{\rho_1+\rho_2}K^3} \tag{3.15}$$

Again note that the original value of n appears but now with the surface tension correction. The term n will be complex (and hence the interface stable) when the acceleration is from the more dense to the less dense (see Figure 3.4). Also when the acceleration is from the less dense into the more dense fluid, n is real when

$$\frac{\sigma}{\rho_1+\rho_2} K^3 \leq \frac{-(g+a)(\rho_2-\rho_1)}{\rho_1-\rho_2} K$$

or by rearranging (note $K = 2\pi/\lambda$),

$$\lambda \geq 2\pi \sqrt{\frac{\sigma}{(a+g)(\rho_1-\rho_2)}} \tag{3.16}$$

For this latter case, then a lower cutoff wavelength (λ_c) exists, below which the instability will oscillate without growth (i.e., stable interface). The second physical effect of the surface tension is similar to viscosity in that as λ_c is approached, the rate of growth of the amplitude slows down, thus making the growth rate go through a maximum at a given wavelength (a maximum value of n). This can be found by differentiating equation 3.15 with respect to K and solving for the fastest growing wavelength (λ_m).

This results in

$$\lambda_m = 2\pi\sqrt{\frac{3\sigma}{(g+a)(\rho_1-\rho_2)}} \qquad (3.17)$$

These results indicate some basic properties of the instability for a planar geometry for its initial growth phase and wavelength limits. Birkhoff [42,43] extended this stability analysis to spherical geometries. What he theoretically proposed was that the stability criterion of Taylor was also valid for a spherical geometry, but collapsing spherical bubbles are also unstable. This "positive damping" phenomenon as Birkhoff termed it suggests that even if acceleration is from the more dense to the less dense fluid, if the velocity of a spherical bubble is inward (collapsing bubble), the interface is unstable and will distort. Physically, this occurs because the liquid interface is moving inward attempting to occupy a smaller surface area. The initial area is then distorted to fit into this smaller area. This situation is not relevant to our physical situation because the fuel two-phase source is expanding, whether under a planar or spherical constraint, thus only the acceleration stability criterion is important.

More complex analyses have been done for the initial theoretical stage of growth of the Taylor Instability [44-48]. Both Nayfeh [44] and Kiang [47] have analytically considered a non-linear solution to this first stage growth rate considering surface tension. Their conclusions do not markedly alter the past results. For example, Nayfeh [44] suggests a correction to λ_c as

$$2\pi/\lambda_c(\text{non-linear}) = \frac{2\pi}{\lambda_c}\left[1 + \frac{3}{8}\left(\frac{2\pi\eta_o}{\lambda_c}\right)^2 + \frac{51}{512}\left(\frac{2\pi\eta_o}{\lambda_c}\right)^4\right]^{\frac{1}{2}}$$

(3.18)

One major investigation of these non-linear analyses is the behavior of the interface near $\lambda \leq \lambda_c$, when the interface oscillates rather than grows exponentially. Daly [45,46] investigated the instability phenomenon by incorporating the complete 2-D governing equations and solving these numerically by using the Marker and Cell numerical technique. The main conclusion in regard to the first stage growth was that non-linear effects can be modeled well by this numerical technique and that predicted growth rates are shown to be in good agreement with analytical models.

Experiments concerning Taylor Instabilities have been performed, but different investigators focused on different aspects of the phenomenon. Lewis [50] performed concurrently with Taylor's analysis a large number of experiments. The basic design of the apparatus is shown in Figure 3.6. A slug of liquid of a known depth is supported on a thin surface, while a pressure difference (Δp) is created across the slug. This Δp causes the liquid slug to break through the supporting surface and accelerate through a planar channel. The interfacial instability grows with time on the upper surface and is photographed to quantitatively analyze the growth rate. The experiment was essentially a planar expansion in two dimensions, because the width of the expansion chamber was small (~.625 cm) to allow for ease in photography methods and analysis. Lewis imposed an initial wave length on the upper surface by means of oscillating a paddle to generate standing waves. The fluid combinations used in the experiment were mainly air and water, although he did perform an experiment with glycerine to examine any viscosity effects. The imposed accelerations were over a range of 5-100 g and the imposed wavelengths (λ_i) were approximately five times the critical wavelength (λ_c). The major conclusion of the experiment was that the simple model of the initial amplitude growth

rate proposed by Taylor matched the experimental results quite well, and the main deviation for the glycerine run was attributed to the retarding effect of viscosity. Lewis also noted that this rate of growth changed when the amplitude (η) grew to a size comparable to $.4\lambda$ and resulted in a constant velocity growth of the amplitude when $\eta \geq \frac{3}{4}$. At this point, the physical appearance of the instability looks like a spike of gas penetrating the water slug (Figure 3.1). Lewis suggested that this stage of growth be modeled by the bubble rise velocity analysis which Taylor [49] had developed ($u_b = C\sqrt{aD_b}$). Thus, the constant relative penetration velocity (v_r) was correlated as

$$v_r \sim \sqrt{a\lambda_o} \tag{3.19}$$

where λ_o is the experimentally observed wavelength. Lewis reports the proportionality constant to be $C = .78$. Because the change to this constant velocity growth phase occurs quite early in the relative size of the amplitude, it is probably the main mechanism by which the liquid becomes entrained in the gas.

Emmons [52] performed a series of experiments to investigate Taylor Instabilities using an apparatus shown in Figure 3.6. A chamber filled with a liquid (methanol or carbon tetrachloride) and a gas (air) was accelerated downward on a metal track by elastic bands. This again created Taylor instabilities at the top surface given an initial perturbation (λ_i) by a paddle. This method of instability generation allowed a finer control of the acceleration magnitude at low values ($1<a/g<10$). The purpose of the experimentation was to look at growth rates near the critical wavelength (λ_c), particularly during the first stage of growth. Emmons observed a damped oscillatory motion ("overstability") when $\lambda \lesssim \lambda_c$ in accordance with

Taylor's model and the expected influence of viscosity effects. In regard to the non-linear final growth stage, Emmons notes a constant velocity again and correlated it with the bubble rise velocity as Lewis did, reporting the constant to be .3. No reason for the difference from Lewis' result was noted, although it was emphasized that the scatter in the data was quite large and that it functionally agreed with a theoretical estimate by Birkhoff [48].

Cole [53] performed an experiment which was similar to that of Emmons (Figure 3.6) but used a different technique to measure the rate of growth of the amplitude. The purpose of the experiment again centered on observing the instability at low accelerations ($5 < a/g < 20$) and initial wavelengths near the critical value ($1 < \lambda/\lambda_c < 5$). The technique used to measure $\eta(t)$ was to fit the interface surface profile at each experimental time by a sine wave function and thereby not measure the amplitude directly. The results indicated that by using this technique the scatter of the growth data for small amplitudes was reduced, and compared well with Emmons' results. Cole did not investigate the final non-linear growth stage of the instability.

A summary of these experiments is given in Table 3.1 to illustrate the range of variables over which this phenomenon has been tested and to give a view of where current experiments undertaken at MIT fit in. Our fundamental interest in Taylor Instabilities relates to utilizing the phenomenon in developing a liquid entrainment model to predict the entrainment observed during a transient expansion of a vapor source into a liquid pool. To do this, the final stage growth appears to be the dominant growth for long times compared to the time for $\eta \simeq \lambda$, and thus useful in entrainment modeling. However, Lewis' correlation using the observed wavelength (λ_o) during an experiment is not suitable because it requires prior knowledge

of λ_o to use it in a predictive entrainment model. In addition, the ratios of λ_i/λ_c and a/g investigated are small in relation to what may appear in a large scale system so it is unclear that the phenomenon may have the same behavior with these different parameters. Therefore, an experiment was performed at what is considered to be representative parameters ($100<a/g<1000$; $\lambda_i/\lambda_c>10$) to gain further understanding of the phenomena. In addition, experiments by Rothrock [54] were performed in a two dimensional reactor scaled geometry to observe any differences in the entrainment behavior at a larger geometric scale.

3.3 Taylor Instability Experiment

The purpose of this experiment is twofold: (1) to develop a model for liquid entrainment that is based on independent variables that can be determined irrespective of the randomness of the interaction; (2) determine if the phenomenon is altered at larger ratios of a/g or λ_i/λ_c. Lewis originally correlated the relative velocity of penetration of the air into the liquid by the bubble rise velocity using λ_o for the characteristic length,

$$v_r \sim \sqrt{a\lambda_o}$$

where λ_o is the observed wavelength at some time in the experiment. The rate of entrainment then could be modeled as

$$\dot{V}_e \sim A_p \sqrt{a\lambda_o} \tag{3.20}$$

However, using λ_o does not lend this model to be a predictive tool because λ_o is a dependent variable of the phenomenon. Instead, another characteristic length should be utilized that is an independent variable. Epstein [31] has suggested that this length scale be λ_c. Another possibility is the physical size of the system (D_p) or the initial imposed wavelength at the

at the start of the transient (λ_i - although this cannot be known a priore during any full scale accident condition). The range of parameters for a/g and λ_i/λ_c was low in past experiments. For the small scale experiments examined (SRI,Purdue) and for possible reactor conditions, the acceleration can lie in the range $100<a/g<1000$. In addition, at these accelerations λ_i/λ_c cannot be assumed to be small, thus the effect of larger ratios should be examined.

The experimental design of the apparatus was similar to the pressure acceleration approach of Lewis (Figure 3.6). Figure 3.7 illustrates the experimental apparatus, which was based on a shock tube arrangement. Two rupture disks were installed at the bottom of the assembly with a small volume between them fed by an air source and hooked to a solenoid valve. The liquid slug of a measured depth was supported in the upper chamber by an aluminum foil membrane, with air below in the plexiglas viewing chamber and above in the upper chamber and surge volume. A motorized paddle was used to generate an initial standing wave (λ_i) on the upper liquid interface.

The experiment was started by pressurizing the upper and lower chamber to the same predetermined value (.2-.7MPa), and the volume between the rupture disks to half this pressure. The apparatus was then isolated from the air source and the experimental transient initiated. This was done by an electrical signal to open the solenoid valve and to start depressurizing the zone between the rupture disks. The calibrated disks were made to only maintain half of the chamber pressure, thus they break almost instantaneously, depressurizing the lower chamber to a value near ambient. The foil breaks due to the imposed pressure difference and the liquid slug is accelerated downward as upper interfacial instability grows with time and the gas penetrates the liquid slug and entrains liquid.

The event is photographed by a HyCam high speed movie camera, and a transient pressure signal is used to monitor the starting time (Figure 3.8). The experiment is started automatically by the camera which contains an internal trigger circuit to energize the solenoid valve at a predetermined point in the film. The upper chamber is made large so that it acts as a constant pressure surge tank during the transient. The magnitude of the acceleration can be controlled by the initial pressure (p_{max}) in the chamber or the initial height (d_i). The initial wavelength (λ_i) is controlled by the speed of motor allowing a range of wavelengths between $.64<\lambda_i<2.54$cm. The internal dimensions of the chamber are 1.9 x 13 x 71cm giving a two dimensional geometry for a planar expansion. More detailed information concerning the apparatus or experimental procedure is provided in Appendix B.

The raw data collected from the experiment consisted of the hi-speed movie of the transient. By projection of the film and measurement of the distances during the transient and the timing marks on the film, the travel distance of the slug (D_t) and the penetration distance into the slug ($\Delta d_i = d_i - d$) could be determined as a function of time. These data were then plotted as in Figure 3.9 to determine the slug acceleration (a) and the penetration velocity of the instability (v_r). By plotting $\sqrt{2D_t}$ vs. t, the acceleration (a^2) becomes the slope of the line. This time average value $\bar{a}$ was graphically measured and compared to a least squares fit of the experimental points to assure consistent results. A similar procedure was done to find the relative penetration velocity ($\bar{v}_r$). Using this method to measure the rate of the penetration of the instability into the water slug implies that the amount of water left on the walls of the channel is insignificant. This assumption is impossible to verify in this

apparatus and is, incidentally, assumed in the other Taylor Instability experiments. The only test of the entrainment model developed with this assumption is to apply it to entrainment experiments where the air bubble does not reach the walls (SRI, Purdue).

In addition, as the instability at the interface grew into the liquid slug, the characteristic wavelength initially imposed grew with time (λ_i changing to λ_o). The observed wavelength (λ_o) was also monitored with time to follow its growth behavior. Forty experiments were attempted. A summary of the successful experimental runs is given in Table 3.2.

Qualitatively a number of interesting results were noted that had not been observed or emphasized before in Taylor Instability experiments. The initial growth of the instability was monitored in a few experiments and it was consistently found that not only did the initial wavelength (λ_i) begin to penetrate the surface but smaller wavelengths near the critical size (λ_c) also appeared and grew into the liquid. As time progressed the region above these penetrating spikes turned dark, and the initially visible small wavelengths were hard to detect leaving only the noticeable outline of the large gas spikes penetrating the liquid slug. Because backlighting was used in these experiments, it was felt that the dark area represented a region of entrained water in the gas stream in the form of droplets. This would explain the dark visual image, because the large surface area would refract the light from the view of the camera. The size of these droplets could not be determined because of the inherent film qualities. The final qualitative behavior noted was that the observed wavelengths (λ_o) became bigger with time. For example, if the initial wavelength was 2.54 cm and five standing waves were originally formed, at the end of the viewing chamber, only two or three large gas penetrations would be remaining across the

width (D_p) of the chamber. Thus, it appeared as though both the small wavelengths (harmonic sizes) as well as the initial large ones aided in the entrainment of water in the gas stream in droplet form.

The main fluid pair used in the experiments was air-water. To investigate the effects of different fluid properties, the liquid was changed to alter the viscosity (water-glycerine) and surface tension (soap-water; "photoflow"). As in Lewis' experiment, glycerine would be expected to slow the rate of entrainment due to an increased viscosity, and as Figure 3.11 illustrates, a slight trend in this direction is indicated. The breakage of the foil in Runs 5 and 15 was not uniform; therefore, the water slug did not accelerate uniformly until later in the experiment. This may have caused larger than normal errors in the distance measurements, thus the lower data point in Figure 3.11 at 1 centapoise may be more uncertain than the others. The surface tension effect is illustrated in Figure 3.12. A soap-water photographic solution ("photoflow") was used to reduce the surface tension of the liquid by about a factor of four ($\sigma \doteq$ 17-20 dynes/cm). Again the lower point for the water tests (σ = 73 dyne/cm) corresponds to Run #15 which may have a larger error in the results. The general trend of the velocity is slightly upward for increasing σ, although no statistically conclusive trend is indicated. This is consistent with the observations of Emmons [52] that using methanol ($\sigma \doteq$ 22 dynes/cm) and carbon tetrachloride ($\sigma \simeq$ 23 dynes/cm) the coefficient (C=.3) for $v_r = C\sqrt{a\lambda_o}$ was lower than that used by Lewis [50] for water (C-.78). However, this difference of 50% in constant values can no way be totally explained by this upward trend.

The effect of the initially imposed wavelength (λ_i) and the behavior of it as it grows during experimental observation (λ_o) is illustrated in Figures 3.13 and 3.14. The observed wavelength (λ_o) at two fixed slug depths

($\Delta d_i = d_i - d(t)$) are plotted as a function of the acceleration ($\bar{a}$) during the experiment. The initially imposed wavelength corresponding to each run is depicted by the different shape symbols. One result which appears is that the observed wavelength (λ_o) at a fixed Δd_i does not seem to be greatly affected by the initial wavelength (λ_i). All the values of λ_o appear to cluster around $4cm<\lambda_o<5cm$ for $\Delta d_i \simeq 5cm$, and $5<\lambda_o<7cm$ for $\Delta d_i \simeq 8.5cm$. The different initial wavelengths caused no significant stratification of λ_o for a given acceleration, although for $\lambda_i = .64cm$, the λ_o values are consistently on the lower edge of this range. In addition, λ_o appears to be constant with a change in the acceleration. Therefore, it does not seem to be a useful endeavor to correlate the penetration velocity (v_r) with the observed wavelength or the initial wavelength for two reasons: (1) the dependence upon either quantity is not statistically significant, (2) both quantities cannot be known a priore during an integral experiment or during a full scale accident. Thus, it would not be useful to use these values in trying to predict v_r for a new set of initial conditions. However, as a check of the results of this experiment in relation to the reported results of Lewis [50], the proportionality constant (C) for

$$\bar{v}_r = C\sqrt{a\lambda_o}$$

was computed (Figure 3.15). The constant found was .65±.22 for air-water which compares well with Lewis' value of .78.

The dependence of the penetration velocity of the instability ($\bar{v}_r$) on the acceleration ($\bar{a}$) is depicted on Figure 3.16. The data was fitted to an equation of the form

$$\bar{v}_r = C\,\bar{a}^m \qquad (3.21)$$

by a least squares method. The results of the correlation of course are dependent upon the data chosen and in this experiment there are three possibilities as Table 3.3 indicates. If all the data is included, this results in m = .33. This is altered slightly if the runs where the foil broke unevenly are excluded from the data m = .35. Finally, if a differentiation is maintained between the different liquids used, the air-water runs indicate that m = .31. The variance of this mean value dependence for a 95% confidence interval is .27. This indicates that the data spread was large between different runs as past experimenters have noted and that the exclusion of some experiments with larger errors does not noticeably alter the spread in the data. Another point to be made is that for all three groups, m is not found to be .5 as was assumed by Lewis [50] originally, although this value lies within the statistically possible range.

A possible correlation for the penetration velocity ($\bar{v}_r$) incorporating a length scale could be

$$\bar{v}_r = C\sqrt{\bar{a}\lambda_c} \tag{3.22}$$

as Figure 3.17 illustrates, where the most critical wavelength is given by

$$\lambda_c = 2\pi\sqrt{\frac{\sigma}{\bar{a}\,(\rho_l-\rho_g)}} \tag{3.24}$$

This would incorporate a length scale dependent only upon properties. When this relation is inserted into equation 3.22, the result is

$$\bar{v}_r = C\,(2\pi)^{\frac{1}{2}}\left(\frac{\sigma a}{\rho_l-\rho_g}\right)^{\frac{1}{4}} \tag{3.24}$$

which implies

$$\bar{v}_r \sim \bar{a}^{\frac{1}{4}} \tag{3.25}$$

This dependence was suggested by Epstein [31], but as the range of possible exponents (Table 3.3) indicates, it is below the average values, again still within a statistically possible range. This behavior may also account for the slight decrease in $\bar{v}_r$ as the surface tension (σ) was decreased (Figure 3.12). A factor of four decrease in surface tension would correspond to a 40% decrease in the relative velocity which is a slightly greater decrease than is experimentally observed.

Another possibility for a known length scale to incorporate in the correlation for v_r, is the characteristic length scale of the system (D_p)

$$\bar{v}_r = C \sqrt{\bar{a} D_p} \qquad (3.26)$$

This would assume $v_r \sim a^{\frac{1}{2}}$ and suggest that the growth of the instability is locally affected by the overall global geometry of the system; perhaps through the growth behavior of the large observed wavelengths (λ_o). To prove this relation the instability phenomenon at different experimental scales should be observed. Figure 3.18 illustrates an attempt to view this dependence. If the quantity $\bar{v}_r / \bar{a}$ is plotted as a function of $(D_p)^{\frac{1}{2}}$, then the resultant line should have a noticeable positive slope ($C \simeq .37$). The data of Lewis and Taylor [50] is plotted here for the length scale of 6.35 cm (2.5 in.). These data were obtained by reviewing the photographs in the published paper and making measurement estimates of the relative penetration velocity ($\bar{v}_r$) and the acceleration ($\bar{a}$). The data from the present experiments is also plotted for the length scale of 12.7 cm (5 in.). The scatter in the data is large for both length scales and thus no statistically significant trend can be determined.

The phenomenon may also be described by a combination of local and global effects. This view would support the claim that entrainment would be caused

by both the observed large penetrating spikes (λ_o) of gas as well as the small wavelengths near λ_c which were initially observed in the experiment until clouded by the entrainment process. Thus neither process may dominate and the relative velocity would be described by

$$\bar{v}_r = C_1 \sqrt{a\lambda_c} + C_2 \sqrt{aD_p} \tag{3.27}$$

The entrainment rate would then be predicted by the model

$$\dot{V}_e = C_1 A_p \sqrt{a\lambda_c} \text{ - Local Mechanism} \tag{3.28.1}$$

$$C_2 A_p \sqrt{aD_p} \text{ - Global Mechanism} \tag{3.28.2}$$

In either case the models are useful as predictive tools for entrainment in that all the variables are independent of the phenomena and can be determined during the transient.

One further task was undertaken to settle this uncertainty. A series of experiments are being conducted at MIT [54] to investigate the integral entrainment phenomenon in planar and spherical geometries near the geometric shapes of the CRBR upper plenum. The application is again in regard to the two-phase fuel source expansion into the upper plenum during an accident. Unheated tests are being initially performed using an air-water system in a geometry where D_p is two and one-half times as big as the present experiment and employs lower accelerations (10-50g). Predicting the entrainment rates of these experiments using the local or global models would imply a dominance of either mechanism. This will then give an indication of which mechanism dominates with a change in the geometric scale.

The concern for a correct predictive model is again motivated by the fact that it will be applied to full scale conditions to view the effect of sodium entrainment and heat transfer from a two-phase UO_2 fuel source. This can be accomplished given an appropriate length scale for the entrainment

model. The need for this is not important for the small scale experiments (using water) because their characteristic sizes ($7.6<D_p<17.7$cm) are close to the size of the Taylor Instability experiment ($D_p \sim 12.7$); thus the entrainment rates will be nearly the same regardless of the effect of D_p.

3.4 Unheated Noncondensible Gas Entrainment Experiments

The entrainment models previously developed (equations 3.28.1, 3.28.2) will now be applied to a series of experiments where the major mechanism studied is liquid entrainment. The tests presently underway at MIT [54] are reviewed first in hopes of determining which version of the Taylor Instability model is appropriate with a change in geometric scale of the system. The experimental testing program at SRI International is also underway and one experiment using nitrogen as the pressure source is also analyzed. Finally, a brief review of tests done by Christopher [28] at Purdue is presented.

3.4.1 MIT Tests

The experiments underway at MIT seek to understand the phenomenon of entrainment in geometry shapes similar to those of the CRBR. The experimental apparatus is depicted in Figure 3.19. The upper plenum region of the CRBR is simulated without the upper internal structure present to a geometric scale of 1/20. This is done in two dimensions with the third dimension (thickness) being made small (1.27 cm) to facilitate observation of the entrainment phenomenon. It is as if a central section of the three dimensional structure was sliced out and taken for observation. The height of the upper plenum was lengthened to allow for variability in liquid water pool height. The entrance chute to the upper plenum is not scaled although it is similar in height and width to the fission gas plenum and upper blanket

region of the vessel. Below the entrance chute an unscaled core region contains the pressurized air source and the rupture disk assembly needed to start the transient experiment. Details of the design and building of the experimental apparatus can be found in Rothrock's report [54].

The water is held in an upper plenum by an aluminum foil membrane at the bottom of the entrance chute. This situation would then correspond to sodium in the fission gas region for the full scale initial conditions. A double rupture disk assembly is below the foil membrane and holds two rupture disks. The general procedure to start the experiment is similar to that of the Taylor instability apparatus. The core region is pressurized to some initial pressure while the region between the disks is raised to about 1/2 this value, while the region between the upper disk and foil is near atmospheric pressure. Each rupture disk can only bear half of the core pressure. A Hycam high speed movie camera is used to photograph the transient and trigger the experiment. As the camera starts and gets up to a predetermined speed, a trigger circuit is energized which opens the solenoid valve between the rupture disks. This depressurizes this zone and the rupture disks break allowing the core gas to break the foil and expand into the chute and upper plenum thereby moving the water slug and entraining liquid.

The amount of entrained water is determined by taking the difference between the rise of the liquid pool level which indicates the change in the gas volume and the observed bubble volume which contains both entrained water and the expanding gas. With these parameters measured as a function of time during the expansion, the entrainment behavior can be determined.

To model the transient a simple isentropic expansion model is employed (Figure 3.20). The air is modeled as a perfect gas with constant properties. The expansion is assumed to be isentropic. The core and the expanding gas volume are treated as one lumped volume system (V_g) with a common uniform pressure (P_g) and temperature (T_g). This assumption is valid because the characteristic time for a pressure signal to tranverse the core (t_t) is shorter than the expansion time of the experiment (τ_{exp}), where

$$t_t = \frac{2l}{C_a} = \frac{2l}{\sqrt{\gamma RT}} \doteq \frac{2(.305\ m)}{\sqrt{1.4(296)(300\quad)}} = 1.7\ \text{msec}$$

and $\tau_{exp} \simeq 30$ msec. The expansion geometry is assumed to be one dimensional and occurs in two stages. As the gas source expands through the entrance chute, the mass of the liquid slug is taken as the mass of the water in the chute. When the gas expands beyond this volume change, the gas is assumed to act across the whole cross sectional area of the upper pool and the mass of the liquid slug is taken as the total upper pool volume including the liquid mass of the chute. The cover gas region which is being compressed by the gas expansion is also modeled as one lumped volume (V_{pl}) isentropic compression. Therefore, the governing momentum equation is given by

$$a = \frac{d^2x}{dt^2} = \frac{(P_g - P_{pl})A_p}{M_{slug}} \tag{3.29}$$

where

$$P_g = \frac{m_g R_g T_g}{V_g} \tag{3.30}$$

$$R_g = R_o/MW_{air} \tag{3.31}$$

$$V_g = A_p\, x \tag{3.32}$$

$$P_{pl} = P_{pl_i} (V_{pl_i}/V_{pl})^{\gamma} \tag{3.33}$$

$$V_{pl} = V_{TOT} - V_g \tag{3.34}$$

$$V_{TOT} = \text{constant} = V_{g\,i} + V_{pl_i} \tag{3.35}$$

The initial conditions then are the volume of the core initially ($V_{g\,i}$), the gas plenum volume (V_{pl_i}), the mass of gas (m_g) and the temperature (T_g). The energy equation for an adiabatic expansion is

$$\frac{dU}{dt} = \frac{-dW}{dt} \tag{3.36}$$

$$\frac{d}{dt}\left(\frac{m_g R_g T_g}{\gamma-1}\right) = -P_g \frac{d}{dt} V_g$$

$$\frac{dT_g}{dt} = -\left(\frac{\gamma-1}{m_g R}\right) P_g A_p \frac{dx}{dt} \tag{3.36}$$

These non-linear differential equations and the entrainment equations are solved by using a numerical integration technique known as a "modified Euler Predictor-Corrector" integration scheme. This solution technique is incorporated as a library subroutine for the MIT IBM 370/168 computer. A more detailed explanation of its use is given in Appendix F. It should suffice to emphasize here that this is a standard process for the solution of a system of non-linear differential equations.

The two models used for entrainment are for turbulent jet entrainment,

$$\dot{V}_e = .32 \frac{x_o}{D_o} \left(\frac{\rho_g}{\rho_1}\right)^{\frac{1}{2}} \frac{dV}{dt}_{gas} \tag{3.37}$$

and for the Taylor Instability entrainment

$$\dot{V}_e = A_p \sqrt{a\lambda_c} \tag{3.38}$$

The characteristic length (x_o) for turbulent length entrainment is assumed to be the height of the chute while D_o is the hydraulic diameter of the chute. Usage of this ratio is viewed as the maximum entrainment possible due to this phenomena and as will be seen still does not predict a large amount of entrained liquid compared to what is experimentally measured. The Taylor Instability entrainment model incorporating the local effect of λ_c is used here and if the measured entrainment is substantially smaller, then it will be definitive proof that the global model is more applicable.

The coupling of the stage 1 expansion to the stage 2 expansion entails two main points. The final velocity of stage 1 is inputed as the initial velocity of Stage 2 with the correction

$$v|_{2_i} = \frac{dx}{dt} = v_1 \left(\frac{A_{p_{chute}}}{A_{p_{upper\ plenum}}}\right) \qquad (3.39)$$

The acceleration in stage 2 is changed from stage 1 by

$$a|_1 = \frac{dx^2}{dt^2}_{stage\ 1} = (P_g - P_{p1})\left(\frac{A_p}{M_{slug}}\right)_{chute}$$

and

$$a_2 = \frac{d^2x}{dt^2}_{stage\ 2} = (P_g - P_{p1})\left(\frac{A_p}{M_{slug}}\right)_{upper\ plenum} \qquad (3.40)$$

The final conditions of stage 1 are then input as the initial conditions for Stage 2.

The results of some of the experiments are illustrated in Figure 3.21, 22 and 23. The gas expansion tests were repeated two or three times at each

pressure level to ensure that reproducibility could be attained. A listing of all the unheated experiments performed is given in Table 3.4. On each graph the gas volume (V_g) is plotted as a function of time on the left ordinate and the amount of entrained water is plotted on the right ordinate.

The isentropic expansion model for the gas volume (V_g vs. t) is in good agreement with the experimental data within the estimated error. The initial conditions of the experiment are input as initial conditions for the computer prediction directly with a slight correction for initial pressure. This correction is necessary because only the compressed air below the pair of rupture disks is at the high initial pressure (P_{g_i}). After the disks break, the pressure decreases slightly because it expands into the zone above the disks as the foil membrane breaks. Thus, the input pressure to the computer model is decreased by the volume ratio increase between the core before the disks break to the whole volume in the core below the foil membrane. Thus the initial pressure is reduced to

$$P_{i_{comp}} \doteq P_{g_i} \left(\frac{4660}{5819cc}\right)^{1.4} \doteq .74 P_{g_i} \qquad (3.41)$$

This is the only correction used in the computer model calculation.

Before examining the experimental entrainment behavior, it is important to point out that the steady state turbulent jet entrainment model predicts a much lower value of entrainment than is observed and thus is not viewed as a dominant mechanism. The steady state model for entrainment is

$$\dot{V}_e = .32 \frac{x_o}{D_{ch}} \left(\frac{\rho g}{\rho_l}\right)^{\frac{1}{2}} \frac{dV}{dt}_{gas} \qquad (3.37)$$

where for this geometry

$$\frac{X_o}{D_{ch}} = \frac{7.3cm}{2.18cm} = 3.35$$

Therefore, the model becomes

$$\dot{V}_e = 1.07 \left(\frac{\rho g}{\rho_l}\right)^{\frac{1}{2}} \frac{dV}{dt}_{gas}$$

The entrainment by this mechanism only occurs as the gas is expanding through the entrance chute and initially into the upper plenum. The reason for this is that the experimentally observed expansion characteristics show no jet-like behavior in the gas bubble except when the bubble is ejected into the upper plenum. After that time, the gas bubble laterally grows out to the walls of the upper plenum region and a planar expansion begins again. No jet-like parallel flow geometry is seen at the abrupt change in area (Figure 3.2) except at the beginning of the bubble's emergence. Thus, the length to diameter ratios used (x_o/D_d - 3.35) is a maximum for these series of experiments. In addition, the characteristic time for this entrainment rate is only the time for the bubble to expand through the entrance chute. This time is a function of the initial pressure but has values between $5.<t<9.$ msec. Also the ratio of densities is a function of the initial pressure and varies between $5/1000<\rho_g/\rho_l<2/1000$. Therefore, the range of entrainment rates due to this mechanism is given by

$$\dot{V}_e \doteq .075 \frac{dV}{dt}_{gas} \quad \text{for } P_{g_i} = .6\text{MPa}, \; t \simeq 5 \text{ msec}$$

$$\dot{V}_e \doteq .048 \frac{dV}{dt}_{gas} \quad \text{for } P_{g_i} = .3\text{MPa}, \; t \simeq 9 \text{ msec}$$

and the volume entrained being

$$3.4<\Delta V_e<5.3 \text{ cc},$$

and can be neglected.

A few qualitative characteristics of the experiment should be emphasized as the Taylor entrainment model is applied. Although the expansion is being modeled as a one dimensional planar expansion, in reality some

spherical growth characteristics exist (Figure 3.24). The gas expansion in the entrance chute is truly a planar expansion and some water is entrained during this time due to Taylor instabilities. This is evident because when the bubble appears in the plexiglas upper plenum, by measurement of volume differences water has already been entrained. This is the first data point indicated for the entrained water volume. The emergence of the bubble can be distinctly seen because it visually appears to be black due to the entrained water volume in droplet form. However, once the 2-D bubble enters the upper plenum, its growth is now mainly lateral (Figure 3.24); no entrainment should occur. The reason for this is that the exit velocity from the chute is high and as the surface area of the bubble expands laterally to fill the whole upper plenum, the acceleration becomes negative as in spherical growth. The velocity decreases until the bubble fills the majority of the upper plenum cross sectional area. During this time, the acceleration is from the more dense water into the gas; therefore, no entrainment due to the Taylor instability mechanism is expected. This behavior is repeatedly demonstrated in the data in Figures 3.21-23. The transition point back to planar growth is difficult to predict because it is a function of the density ratio of the gas source, and the pool liquid and the geometry. Appendix D presents a discussion of various models which attempt to determine the transition point. However, for this geometry and density ratio pair none of the models are applicable. What has been observed in all the tests is that the entrainment rate is zero until $V_g/V_{g_i} \doteq 1.04$ and then entrainment begins again. This volume ratio consistently corresponds to a point where the bubble cross sectional area has been observed to occupy approximately 2/3 of the upper plenum area (A_p). Therefore, this transition point is empirically assumed to be the realistic

beginning of one dimensional growth in the upper plenum. At this point the acceleration is positive, again from the less dense gas into the water and the Taylor instability entrainment mechanism is operative.

Later in the expansion (Stage 2), the entrainment rate again falls to zero and the amount entrained remains constant until the water slug impacts the upper plenum roof. This behavior is explained by the fact that the acceleration again becomes negative and thus the interfacial surface is stable (from water toward the gas bubble). The reason in this instance is that the upper plenum cover gas region is being compressed as the gas bubble is expanding. Thus the plenum pressure (P_{pl}) at some point becomes greater than the gas bubble pressure (P_g) and the planar acceleration becomes negative. The point when this occurs varies with the initial gas pressure (P_{g_i}) because at higher P_{g_i} the compressed volume can be smaller before $P_{pl} > P_g$.

The Taylor Instability model incorporating the local effect for entrainment ($v_r \sim \sqrt{a\lambda_c}$) is used to predict the water entrainment. As Figures 3.21, 3.22 and 3.23 indicate, the general qualitative behavior of the experimental data is exhibited by the model. An initial amount of water is entrained in the entrance chute and then the first plateau of a constant entrained water volume occurs due to the lateral growth of the two-dimensional bubble (when the acceleration is from the water into the gas). Once the growth is again one dimentional, the acceleration turns positive and the Taylor Instability entrainment begins and continues until the plenum pressure is greater than the bubble pressure, the acceleration is reversed, and the second constant entrained water volume plateau occurs. Quantatively two observations can be seen that consistently occur in all the test predictions:

1. The prediction of water entrainment during the time when the entrance chute is cleared of water by the gas falls below the experimental values, and the difference increases from a negligible amount (P_{g_i} = .3MPa) to almost 40cc (P_{g_i} = .6MPa which is 20% of all water entrainment.

2. The prediction of the net amounts of water entrainment during the time of one dimensional bubble growth in the upper plenum shows good agreement with experiments, and this indicates that the local model of Taylor instability entrainment seems to govern with a change of scale.

The local mechanism model ($\dot{V}_e \sim \sqrt{a\lambda_c}$) for entrainment due to Taylor Instabilities seems to be dominant with a change in the initial conditions. This is indicated by the experiment because if the global model ($\dot{V}_e \sim \sqrt{aD_p}$) were dominant, the water entrainment values would be smaller by 50% due to the large change in the initial conditions of the MIT tests [54]. To understand this scale effect, let us form the ratio of the entrainment rate per unit area ($\frac{\dot{V}e}{A}$) for values employed in our experiment (100g<a<1000g; D_p = .127m) to those employed in the tests by Rothrock (1g<a<50g; D_p = .305m), for both the local and global models.

$$\left.\frac{(\dot{V}_e/A_p)_{ROTH.}}{(\dot{V}_e/A_p)_{CORR.}}\right|_{local} = \frac{\sqrt{a\lambda_c}}{\sqrt{a\lambda_c}} = \left(\frac{a_{ROTH.}}{a_{CORR.}}\right) \doteq .31\text{-}.44 \qquad (3.42.1)$$

$$\left.\frac{(\dot{V}_e/A_p)_{ROTH.}}{(\dot{V}_e/A_p)_{CORR.}}\right|_{global} = \frac{\sqrt{aD_p}}{\sqrt{aD_p}} = .16\text{-}.31 \qquad (3.42.2)$$

As these ratios indicate when the experimental conditions are changed, the global model will predict a lower entrainment than the local model by about 50% because the decrease in acceleration affects $\dot{V}_{eglobal} \sim (a)^{\frac{1}{2}}$ to a larger extent than it does $\dot{V}_{elocal} \sim (a^{\frac{1}{4}})$ even with an increase in the scale of the system. This smaller amount of liquid entrainment is not observed in the

data even with the consideration of the experimental error. Thus in spite of the entrance effect anamolies, the results of the experiment indicate the appropriate Taylor Instability entrainment model would be

$$\dot{V}_e = 4.65\ A_p \sqrt{a\lambda_c}.$$

The lack of agreement between the Taylor Instability model and the experimental data for the entrance chute expansion could be attributed to two reasons: (1) another transient entrainment mechanism is operative during this time when the chute water volume is accelerated or (2) the dynamic analysis of this expansion time period needs to be revised for Taylor Instability entrainment.

The major assumption utilized in the first stage analysis of the gas expansion was that the slug mass of water being accelerated by the gas was a constant. This mass was taken to be the mass of water initially in the entrance chute (.07kg). The actual dynamics are more complicated because as the gas expands against the slug, the water is ejected into the upper plenum and some is entrained, and both effects reduce the slug mass and increase the acceleration. This in turn will increase the entrained water volume over that which is predicted. However, it is felt that the underestimate error incurred by this analysis method is not large and does not totally account for the entrainment underprediction noted. As the initial pressure is increased, this underprediction would increase because the acceleration increases. The amount of underprediction could be estimated. Let us assume the actual inertial slug mass that opposes gas expansion is 1/2 the water mass in the entrance chute. (Note: this is an average slug value over the expansion distance.) The acceleration would increase by a factor of 2. The increase in entrainment rate is proportional to $(a)^{1/4}$ which indicates that the entrained volume would at most increase by 20%

(~10cc for P_{g_i} = .6MPa) which does not account for the total discrepancy of 40 cc for P_{g_i} = .6MPa.

A transient entrainment mechanism operative during this expansion time may be a more feasible possibility. The qualitative expansion behavior of the emergence of the bubble as the chute is cleared of water does not seem to change dramatically as the pressure increases. At all times the entrained water (appearing to be black) is near the upper part of the bubble. The only noticeable difference is that as the initial pressure increases, the time at which the observed bubble interface emerges into the upper plenum is shorter than what is expected due the gas expansion and its water penetration due to Taylor instabilities. As the initial pressure goes up, acceleration increases, and thus the penetration velocity ($v_r = 4.65\sqrt{a\lambda_c}$) of the Taylor Instability increases. The interface motion (Δd) of the gas and liquid interface taking into account the relative velocity of entrainment is

$$\Delta d = v_r t + \frac{1}{2}at^2 \qquad (3.43)$$

where

$$v_r = 4.65\sqrt{a\lambda_c}$$

$$a = \frac{(P_g - P_{pl})A_{chute}}{M_{slug\ chute}}$$

For the lower pressure experiments (e.g. .4MPa), the observed time of bubble emergence and that predicted by equation 3.43 for the chute length (Δd_i = 7.3cm) are in agreement. For the higher pressure runs (i.e., .6MPa) the bubble emerges faster (t = 1.88 msec) than is predicted (t = 3.5 msec). This behavior occurs for all the high pressure tests indicating that it is probably not due to the randomness of the start of the experiment with the foil breakage, but due probably to a different transient entrainment mechanism

which becomes operative after P_{g_i} = .3 - .4MPa. The bubble shape as it initially emerges seems to expand faster laterally as the pressure increases as if there are two jets coming out of the chute going toward the wall and a transient rolling vortex motion over the abrupt corner change from chute to the upper is more noticeable at higher pressures. Thus as Figure 3.24 illustrates the gas flow path could be initially viewed as a recirculating flow and the transient mechanism of entrainment could be due to parallel flow entraining water not only on the chute walls as was assumed previously in the steady state model but across the upper interface of the bubble. This parallel flow geometry could aid in the entrainment as the gas initially comes out of the chute because the lateral velocity would be high when the bubble volume is small and Helmholtz instabilities could be initiated.

There exists a lower limit for this parallel flow velocity below which no entrainment should occur [35] due to Helmholtz Instabilities and is given by

$$v_g - v_l = \sqrt{\frac{\sigma 2\pi(\rho_l+\rho_g)}{\lambda \rho_l \rho_g}} \qquad (3.44)$$

where

$$\lambda \doteq \lambda_c = 2\pi\sqrt{\frac{\sigma}{g(\rho_l-\rho_g)}}$$

For the low pressure experiments discussed here, this relative velocity is mainly a function of the air density and lies in the range 4-8 m/s. This velocity corresponds to the average slug velocity in the entrance chute for P_{g_i} = .3 - .4MPa. Thus, it appears that the parallel flow entrainment mechanism is operative for these experiments at higher pressures ($P_{g_i} \geq$ .4MPa). The steady state jet entrainment model did not predict the experimentally observed values. The entrainment by this transient mechanism should only be

operative as the gas is expanding out of the entrance and laterally in the plenum because the internal gas velocity will be high. After this point the lateral velocity would decrease as the bubble volume increases and the entrained water volume becomes constant as observed. Also this effect should be more pronounced in this two-dimensional geometry than in spherical geometries because the lateral expansion is not radial but one dimensional. A spherical expansion would cause lower gas velocities because as the bubble expands radially, the gas velocity decreases by $1/r$. Thus this entrainment mechanism would probably be less effective in the actual reactor geometries.

3.4.2 SRI Tests

The experimental program at SRI International has two main purposes one of which is the investigation of the thermodynamics of a transient two-phase fuel bubble source during the expansion in the reactor vessel. Initially SRI is not using any fluids that can be considered to thermodynamically scale the phenomena, but has begun by looking at the transient in both unheated and heated CRBR scaled geometries to determine the separate effects of coolant entrainment and vapor-liquid heat transfer. The geometrical arrangement is depicted in Figure 3.25. This 1/30 scale model of the CRBR has a scaled upper plenum and fission gas-upper blanket region with the initial condition of the upper internal structure being removed and the coolant (subcooled water) in the fission gas plenum region. The unscaled core region is separated from the upper plenum region by thin sliding steel doors. A detailed description of this starting mechanism is given by Ploeger [26]. The experiment is begun by the doors opening by an explosive charge, and the high pressure core expanding into the water filled fission gas region.

One unheated noncondensible gas experiment has been performed and reported using nitrogen gas. The same assumptions and models used in the analysis of the MIT experiments are used here. The experimental results are given in Figure 3.26 for V_g vst, Figure 3.27 for P_g vst, Figure 3.28 for ΔV_e and $(1-\bar{\alpha})$vst. The liquid fraction $(1-\bar{\alpha})$ is defined as

$$1-\bar{\alpha} = \frac{\Delta V_e}{\Delta V_g + \Delta V_e} \tag{3.40}$$

The amount of water entrainment is again found by the difference between the photographically observed bubble volume and the displaced volume of the water pool.

The isentropic planar model again shows good agreement with the experimental volume and pressure data. This expansion had no cover gas volume as in the MIT tests, thus $P_{pl} = P_\infty$ (1 bar). The behavior of the entrainment rate (Figure 3.28) then shows no upper plateau as in the MIT tests. However, the lower plateau of entrained volume as the N_2 gas bubble exits the fission gas region still is apparent although the time span (.25 - .5 msec) is smaller because of the larger initial pressures. Remember that the entrainment rate falls to zero in this region because the growth is spherical with a high initial exit velocity, thus the acceleration is negative and no entrainment is expected due to Taylor Instabilities. The transition point though for this case can be approximately estimated by using the criterion presented in Appendix F. In particular, Christopher and Theofanous [28] performed a parametric calculation for the CRBR geometry to determine when the spherical to planar transition occurs. A potential flow solution of the expansion for a constant pressure gas bubble was run in a CRBR geometry. The initial condition was for P_{g_i} = 20MPa. Their conclusion was that the bubble growth ceased to

be spherical after the volume change was about 1/9 of that to slug impact. This was concluded to occur because the bubble would sense the presence of the wall at this point and the radial expansion would decrease significantly. If this estimate is applied here, it is predicted that no entrainment occurs for the gas bubble from the time it enters the upper plenum for about $\Delta V_g \sim 90cc$. If this criterion is incorporated into the Taylor Instability model ($\dot{V}_e = C\ A_p\sqrt{a\lambda_c}$), then the predicted entrained water volume is in good agreement with what is seen experimentally. Figure 3.28 indicates this by the plateau for the entrained water plot ($1.2<V_g/V_{g_i}<1.3$) and by the sharp drop in the ($1-\bar{\alpha}$) value over this region. The agreement between the experimental entrainment data and the prediction using the Taylor Instability local mechanism model ($\dot{V}_e \sim \sqrt{a\lambda_c}$) seems to be a further indication that the local mechanism is dominant with a change in the scale of the system rather than the global model ($\dot{V}_e \sim \sqrt{aD_p}$). In this case the diameter of upper plenum ($D_p \sim 20cm$) is not so different from the MIT tests [54], but the shape of the upper plenum has changed markedly from a rectangle with a high aspect ratio to a circle. Even with this change, the use of the local entrainment model to predict the entrained water volume is successful.

The steady state turbulent jet entrainment model [36] is also employed to predict the observed entrained water volume. In this case, the momentum of the gas jet is high enough so that the bubble growth takes place with an observed jet-like base attached to the bubble (Figure 3.2). Thus, the entrainment length (x_o) does not only exist for the short time of the fission-gas volume but for the whole experiment. The size of x_o was estimated from the experimental photographs and was assumed to be acting over the whole transient. This amount of entrained water is also plotted in Figure 3.28 and it can be seen that this volume is small compared to what is predicted by

Taylor Instabilities, again implying that this mode of entrainment is a second order effect.

The underprediction of the initial entrainment when the scaled fission gas plenum is cleared of water is again noted as in the MIT tests. The volume amount of error though (30cc) in comparison to the total amount of water which is entrained (~400cm) is small. One reason for this could be that the bubble emergence is now spherical, thus the gas velocity of the bubble on the average would be lower as it flows over the surface area of the bubble because of its 1/r dependence. This decrease in velocity in turn would decrease the entrainment by this mechanism. The conclusion of this analysis is that the Taylor Instability model appears to be the dominant mechanism for coolant entrainment in a geometric scale similar to the reactor.

3.4.3 Purdue-ANL Tests

A series of tests were conducted at Argonne by Christopher and Theofanous [28] using compressed air expanding into a water pool. Based on the results, it was concluded (Figure 3.29) that no water entrainment occurred at low pressures (.4MPa), in a non-scaled geometry similar to the CRBR upper plenum with no structure present. This result and conclusion cannot be explained because entrainment did occur in MIT experiments at this pressure range although the plenum was a two dimensional scaled version of CRBR. One possibility is that since this was a three dimensional upper plenum pool and the possible entrainment volumes are small at this pressure ($1-\overline{\alpha} \doteq .15$), the reported experimental error swamped any significant results.

Other than this experiment, all other unheated noncondensible tests seem to confirm the result that the Taylor Instability entrainment mechanism is the dominant mode for coolant entrainment in the gas bubble for these small scale tests.

TABLE 3.1

SUMMARY OF PAST TAYLOR INSTABILITY EXPERIMENTS PERFORMED

λ_i/λ_c \ a/g	1-10	10-100	100-1000
1-2	•EMMONS [52] PLANAR D_p -13cm AIR-METHANOL •COLE [53] PLANAR D_p -7.5cm AIR-WATER		
2-10	•ALLRED [51] PLANAR AIR-HEPTANE	•LEWIS [50] PLANAR D_p -6.5cm AIR-WATER AIR-GLYCERINE	
>10		•ROTHROCK [54] SPHERICAL-2D PLANAR D_p -7.5 D_p -30.5cm AIR-WATER	•CORRADINI PLANAR D_p -13cm AIR-WATER AIR-GLYCERINE AIR-PHOTOFLOW

*D_p - width of chamber (or diameter)

RUN	Film Sp(fps)	Time Sp(mps)	P_{max}(MPa)	λ_i(cm)	λ_{o_e}(cm)	d_i(cm)	d_e(cm)	$\bar{v}_r$	$\bar{a}$
2	2500	1000	.405	1.27	4.45	6.35	.95	827	442
3	4500	1000	.432	1.27	5.72	11.43	1.91	1100	439
4	4500	1000	.678	1.27	5.08	13.97	1.43	1063	511
5	4500	1000	.652	--	6.99	11.43	.94	1200	143
6	4900	1000	.680	.64	4.45	10.16	5.72	860	380
7	4500	1000	.687	.64	3.18	8.89	1.91	969	778
8	4750	1000	.687	.64	4.45	7.62	2.14	650	132
9	4500	1000	.687	.64	4.76	6.35	1.19	1190	994
10	4750	1000	.653	2.54	6.35	15.24	8.10	670	103
11	4900	1000	.673	2.54	6.35	10.16	2.54	950	527
12	5000	1000	.667	2.54	4.45	6.35	1.91	537	215
15	5000	1000	.639	1.27	5.08	15.24	--	450	148
16	4000	1000	.653	1.27	7.62	10.48	1.91	687	380
17	3500	1000	.687	1.27	5.08	6.67	1.43	1085	1021
18	3800	1000	.667	1.27	6.99	12.7	2.86	760	135
19	3500	1000	.660	2.54	5.40	12.7	1.43	926	631
20	4000	1000	.653	2.54	5.08	8.26	1.43	1300	1425
21	3800	1000	.660	1.27	5.08	8.26	1.43	868	227
22 G	4000	1000	.653	1.27	5.08	7.62	.48	472	150
23 G	4000	1000	.653	1.27	6.99	12.07	2.86	455	120
25	5000	1000	.391	1.27	5.08	6.99	0	400	117
26 P	5000	1000	.391	1.27	3.81	6.99	1.19	455	126
27 P	5000	1000	.391	1.27	5.08	10.48	.95	580	75

G - AIR - GLYCERINE
P - AIR - PHOTOFLOW

TABLE 3.2

SUMMARY OF EXPERIMENTAL RESULTS FROM PRESENT TAYLOR INSTABILITY EXPERIMENTS

TABLE 3.3

CORRELATION OF RELATIVE PENETRATION VELOCITY(v_r) TO THE SLUG ACCELERATION(a)

$$v_r = C\,\bar{a}^{\,m}$$

DATA EXCLUDED	m ± 95% CONFIDENCE VALUE
no data excluded 23 runs	$m = .332 \pm .27$ $C = .54$ (a - m/s^2)
Runs 5 & 15 excluded due to partial foil blockage 21 runs	$m = .35 \pm .26$ $C = .42$ (a - m/s^2)
Run 5 & 15 Run 22 & 23 glycerine Run 26 & 27 photoflow	$m = .311 \pm 27$ $C = .656$ (a - m/s^2)

FOR AIR-WATER IF $\bar{v}_r \sim \bar{a}^{\frac{1}{2}}$ $C = .14$ (a-m/s^2)

$\bar{v}_r \sim \bar{a}^{\frac{1}{4}}$ $C = 1.08$ (a-m/s^2)

TABLE 3.4

SUMMARY OF MIT EXPERIMENTS AND INITIAL CONDITIONS PERFORMED BY ROTHROCK[54]

RUN NO.	P_{g_i}	$P_{g_{comp}}$ (MPa)	M_{slug}(kg)
9	.3	.225	1.25
10	.3	.255	1.25
11	.4	.3	1.25
12	.4	.3	1.25
13	.4	.3	1.25
14	.6	.45	1.25
15	.6	.45	1.25
17	.8	.6	1.25
21	.8	.6	1.25
24	1.0	.75	1.25
26	1.0	.75	1.25

FIGURE 3.1
TWO FUNDAMENTAL GEOMETRIES FOR LIQUID ENTRAINMENT

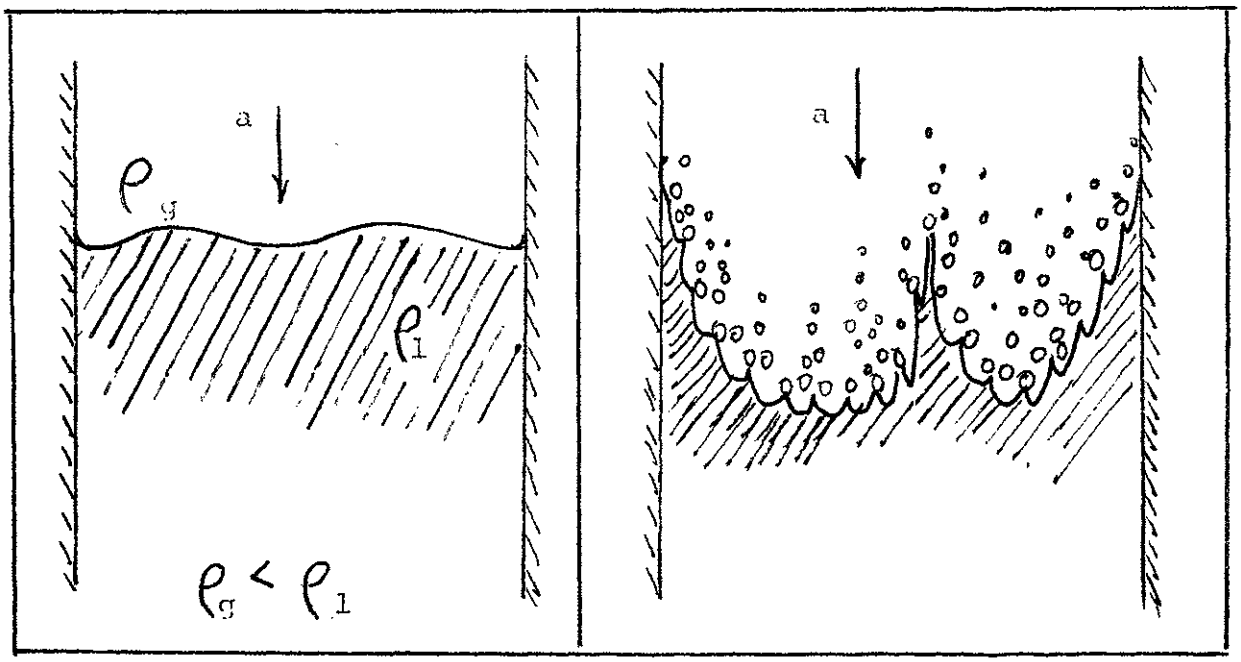

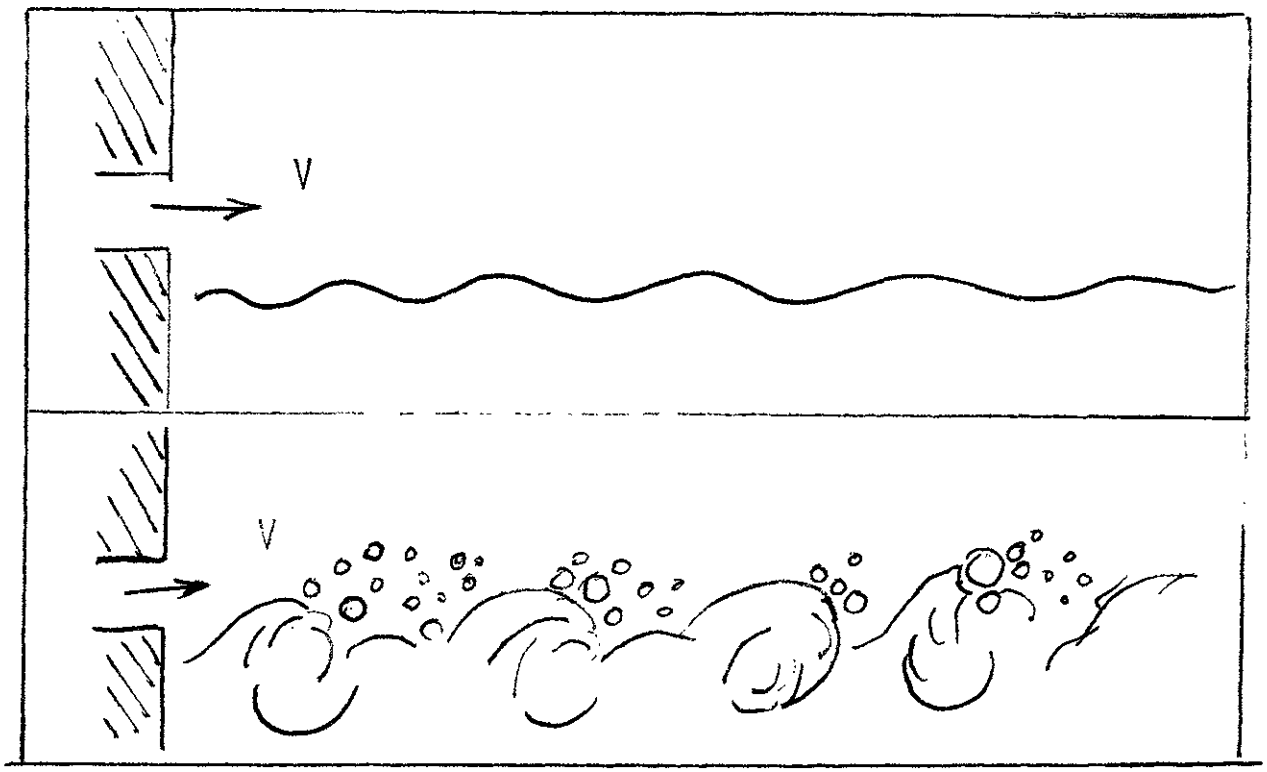

FIGURE 3.2

TWO TYPES OF ENTRAINMENT POSSIBLE IN REACTOR GEOMETIES

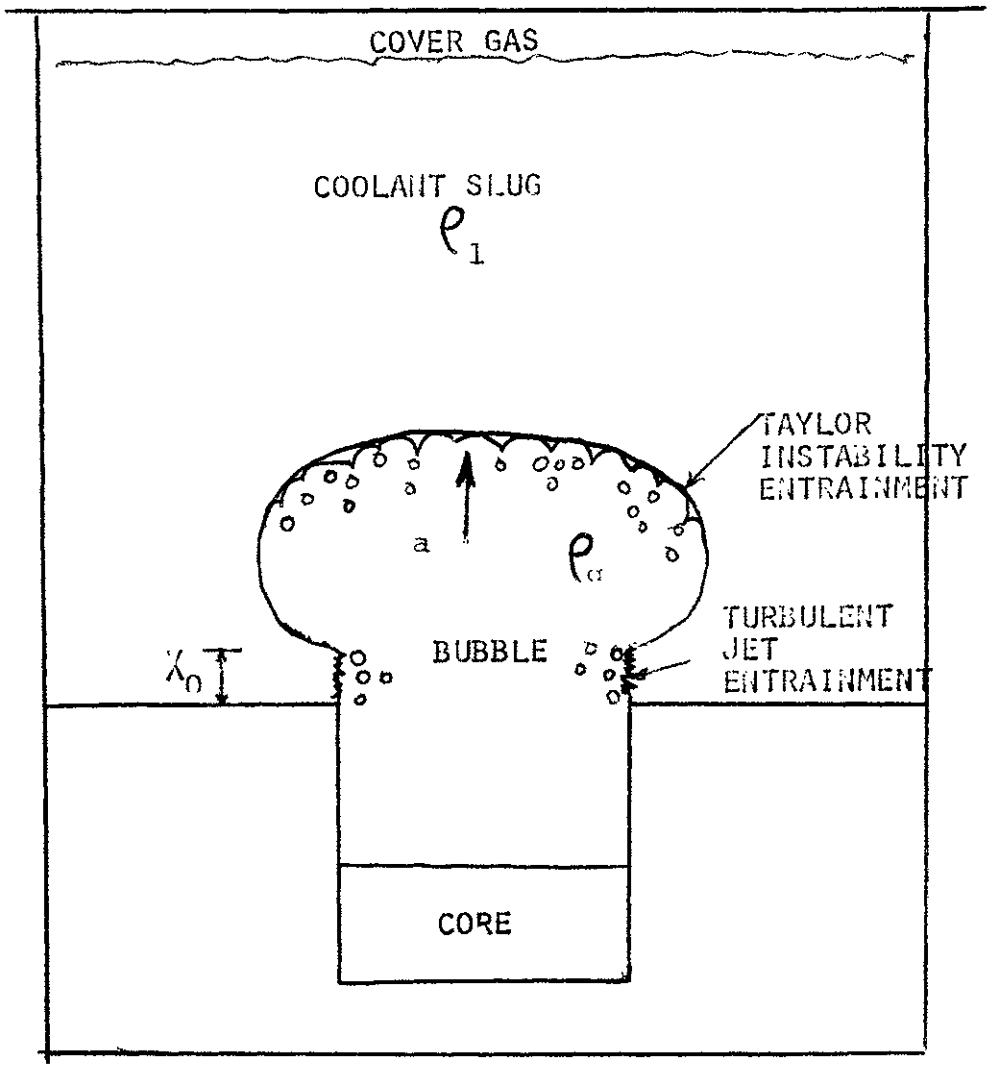

FIGURE 3.3

CONCEPTUAL PICTURE OF A STEADY STATE TURBULENT JET

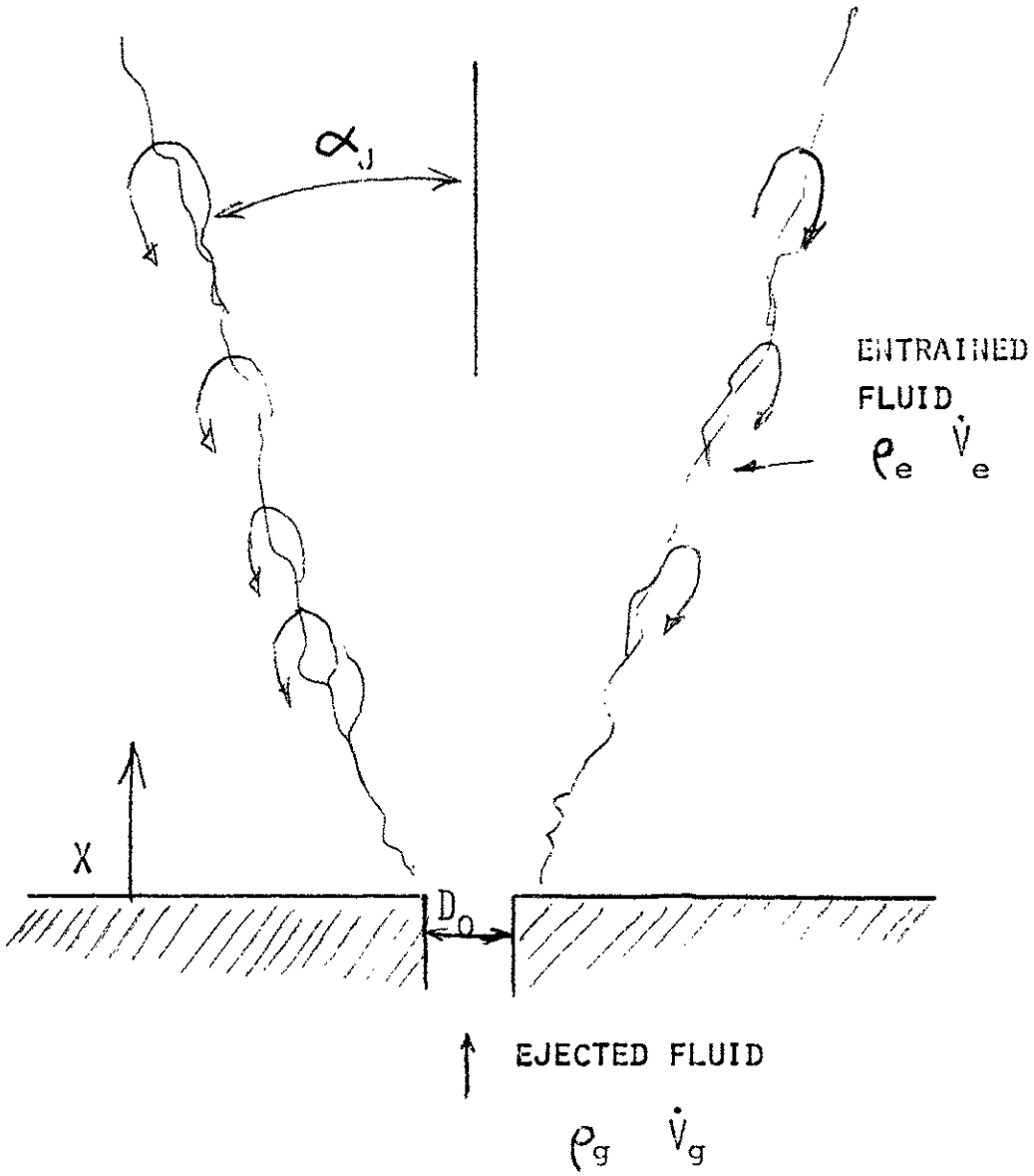

FIGURE 3.4

CONCEPTUAL PICTURE OF A TAYLOR INSTABILITY AT A FLUID INTERFACE

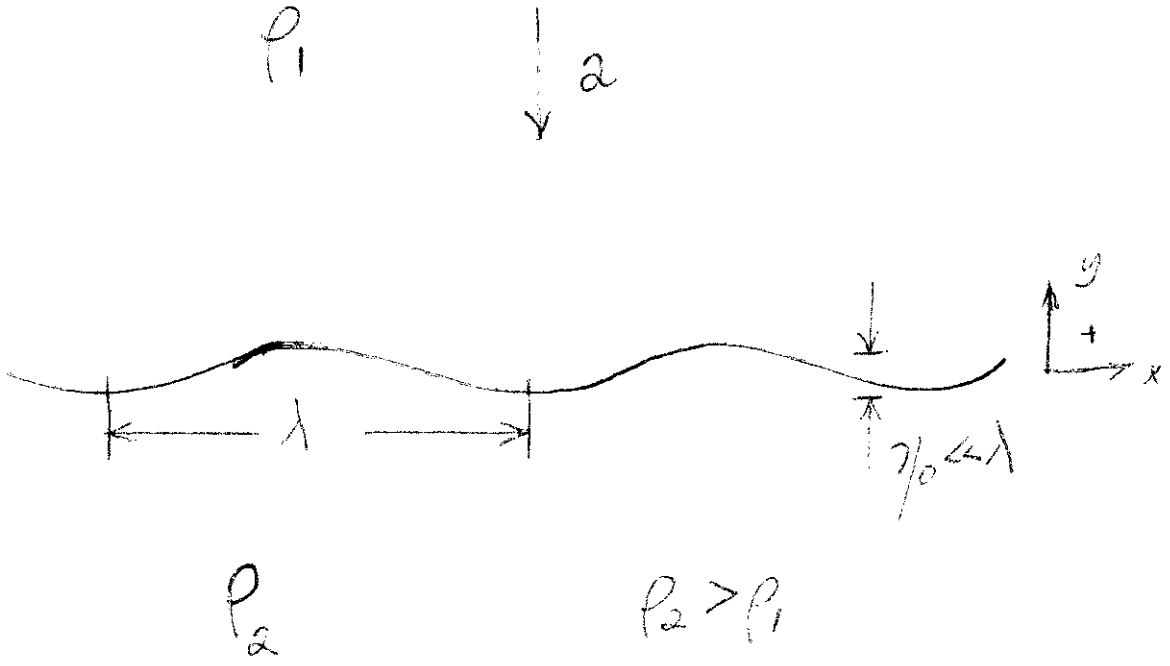

V_x - X VELOCITY COMPONENT

V_y - Y VELOCITY COMPONENT

FIGURE 3.5

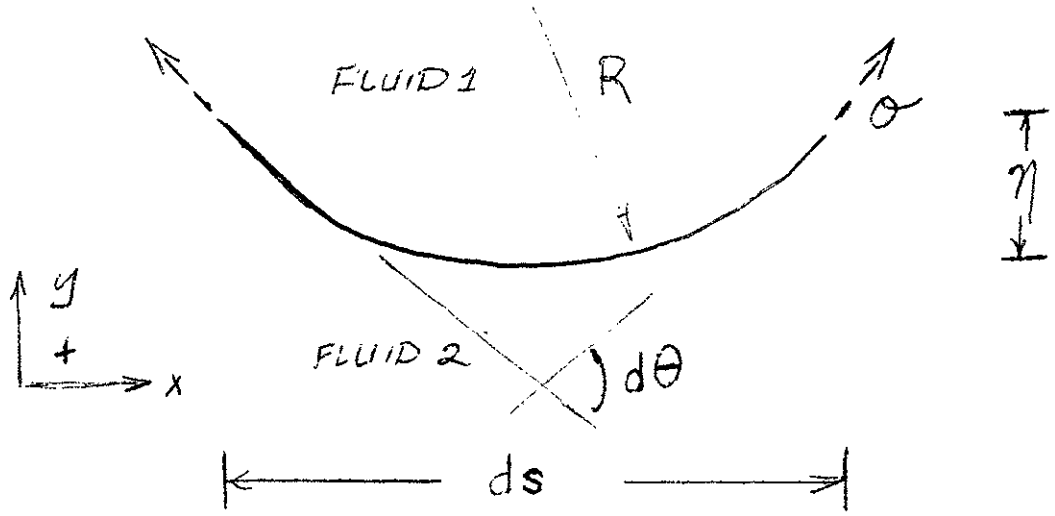

$$(P_1 - P_2)\, ds = \sigma \sin d\theta$$

$$\simeq \sigma\, d\theta$$

$$(P_1 - P_2) \simeq \sigma \frac{d\theta}{ds}$$

$$\frac{d\theta}{ds} = \frac{1}{R} \simeq \frac{\Delta\eta}{\Delta x}\left(\frac{1}{\Delta x}\right)$$

$$\simeq \frac{d^2\eta}{dx^2}$$

$$(P_1 - P_2) = \sigma \frac{d^2\eta}{dx^2}$$

SURFACE TENSION CORRECTION TO THE INTERFACE PRESSURE

FIGURE 3.6

TWO BASIC DESIGNS FOR TAYLOR INSTABILITY EXPERIMENTS

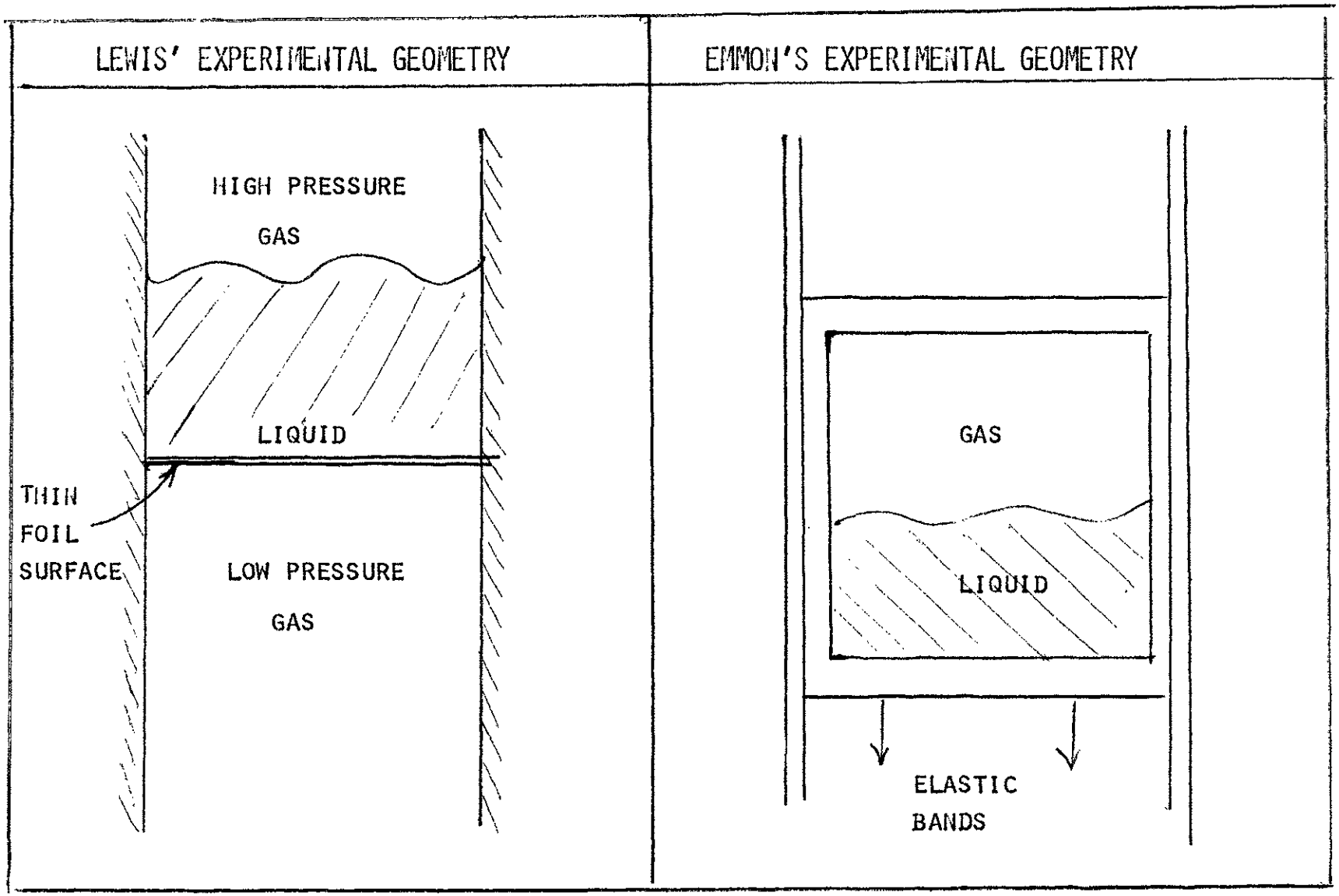

FIGURE 3.7

EXPERIMENTAL APPARATUS USED IN THE TAYLOR INSTABILITY TESTS

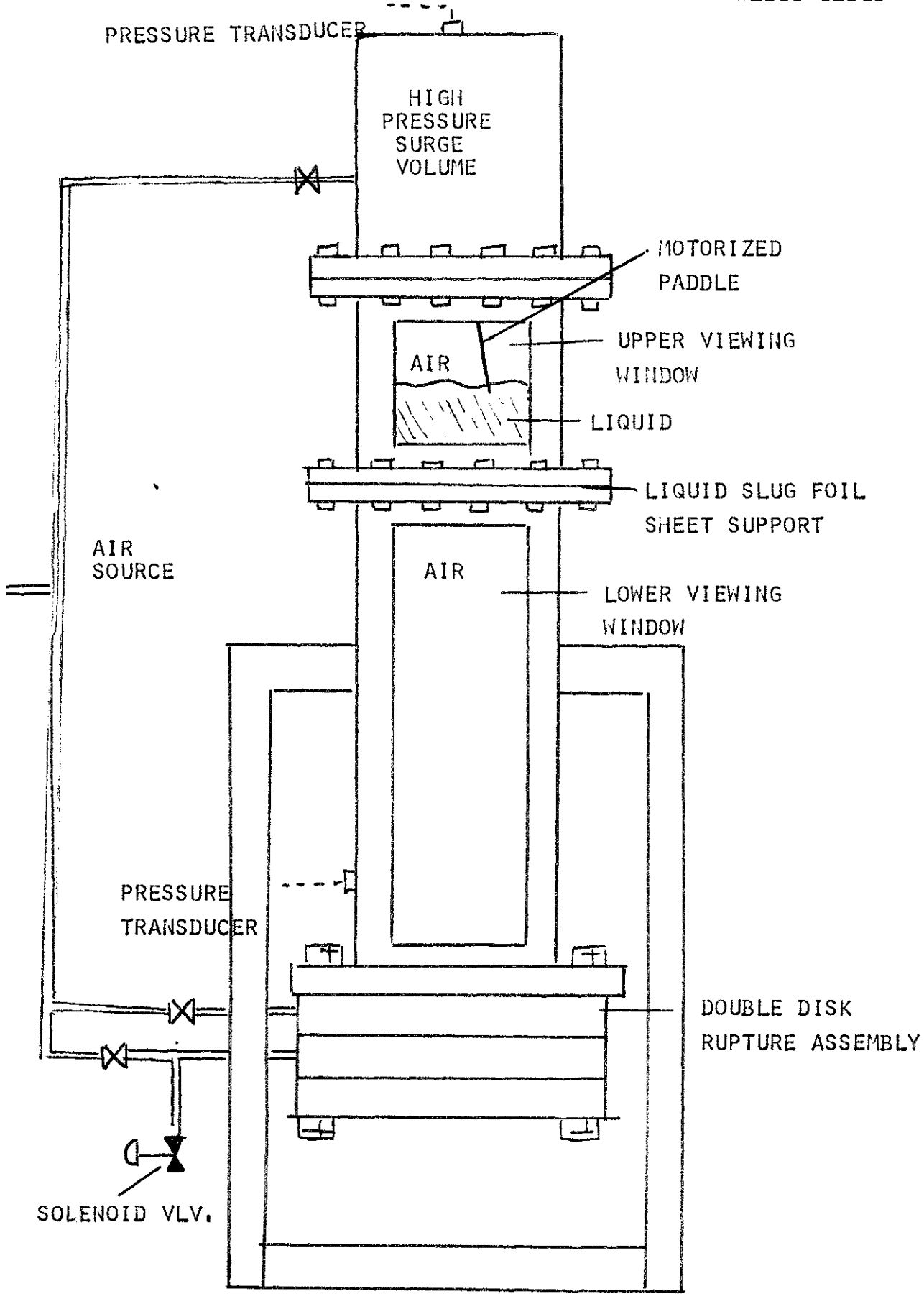

FIGURE 3.8

SCHEMATIC OF THE DATA ACQUISITION SYSTEM

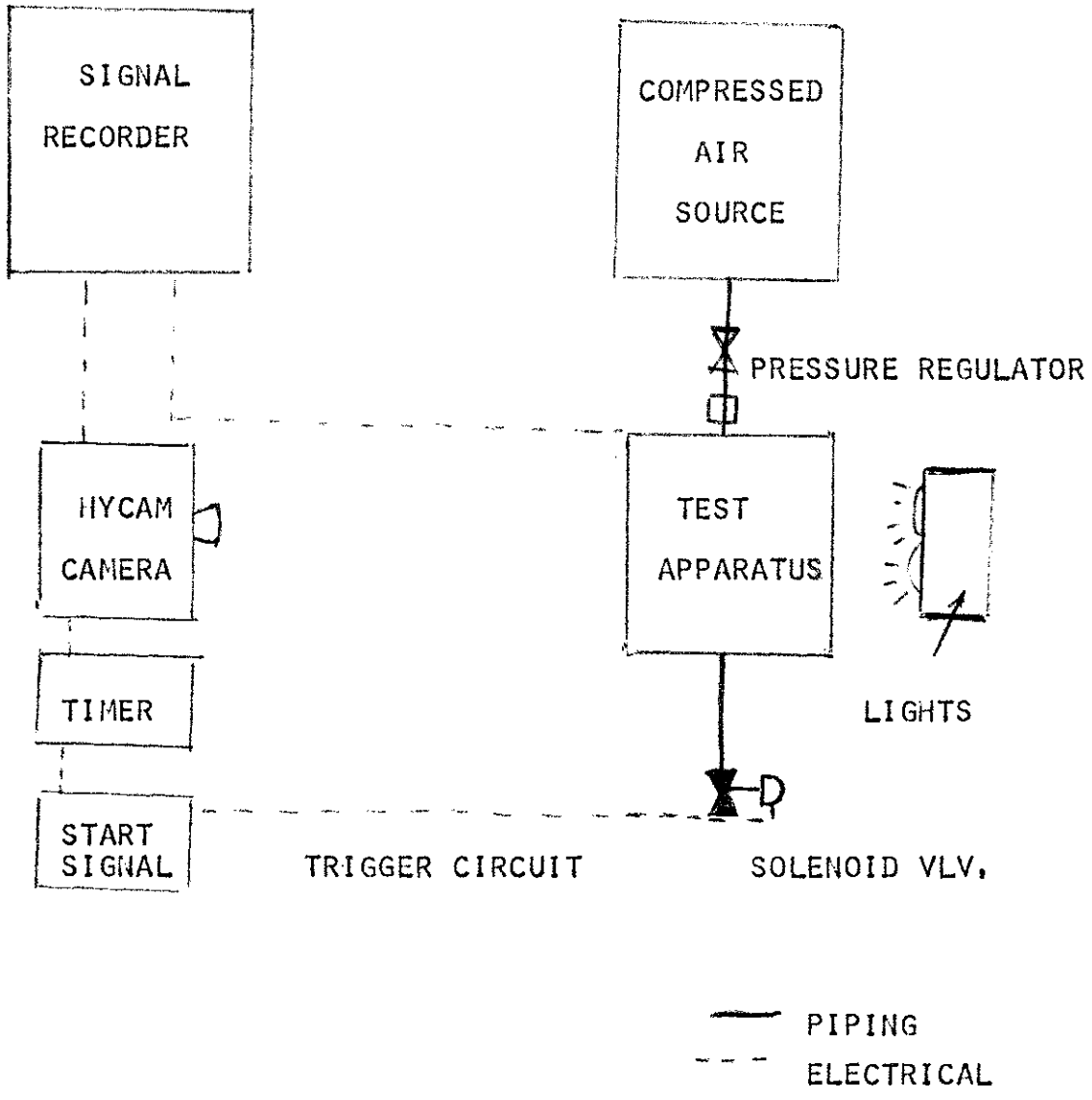

FIGURE 3.9

SLUG TRAVEL DISTANCE (D_t) AND SLUG PENETRATION DEPTH (Δd_i) RAW DATA

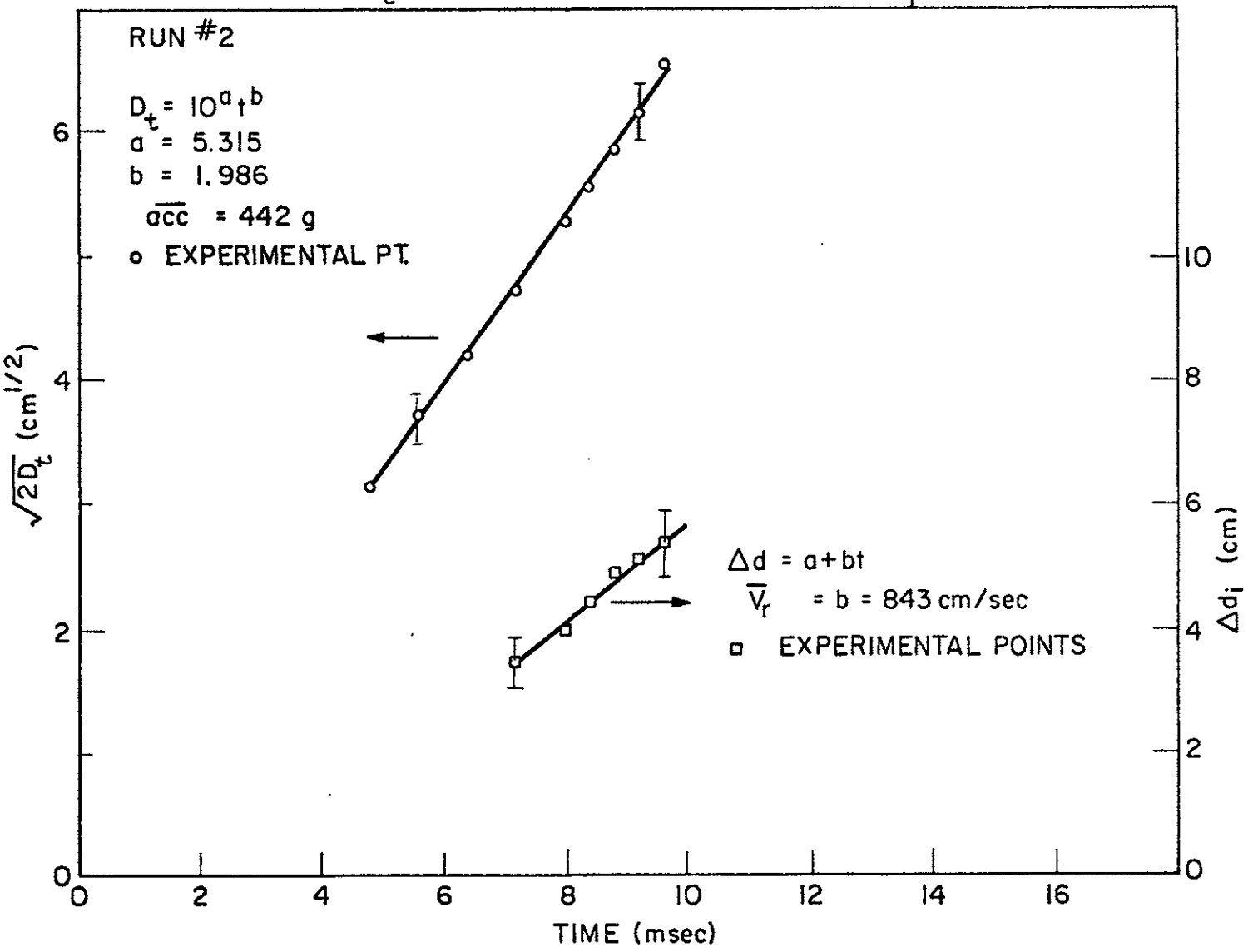

FIGURE 3.10

QUALITATIVE PICTURE OF THE INITIAL GROWTH OF THE INSTABILITY

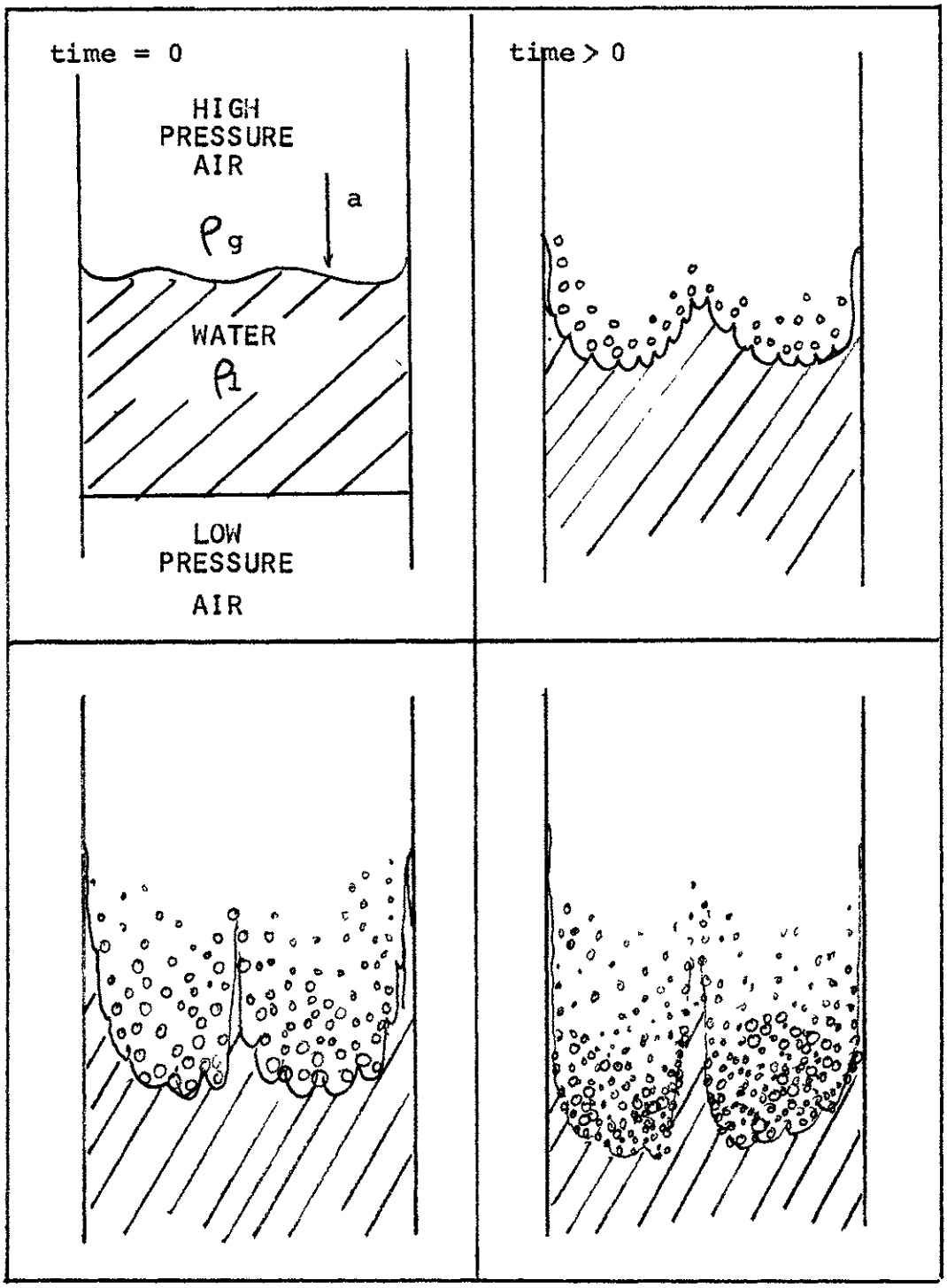

FIGURE 3.11

EFFECT OF INCREASING THE LIQUID VISCOSITY

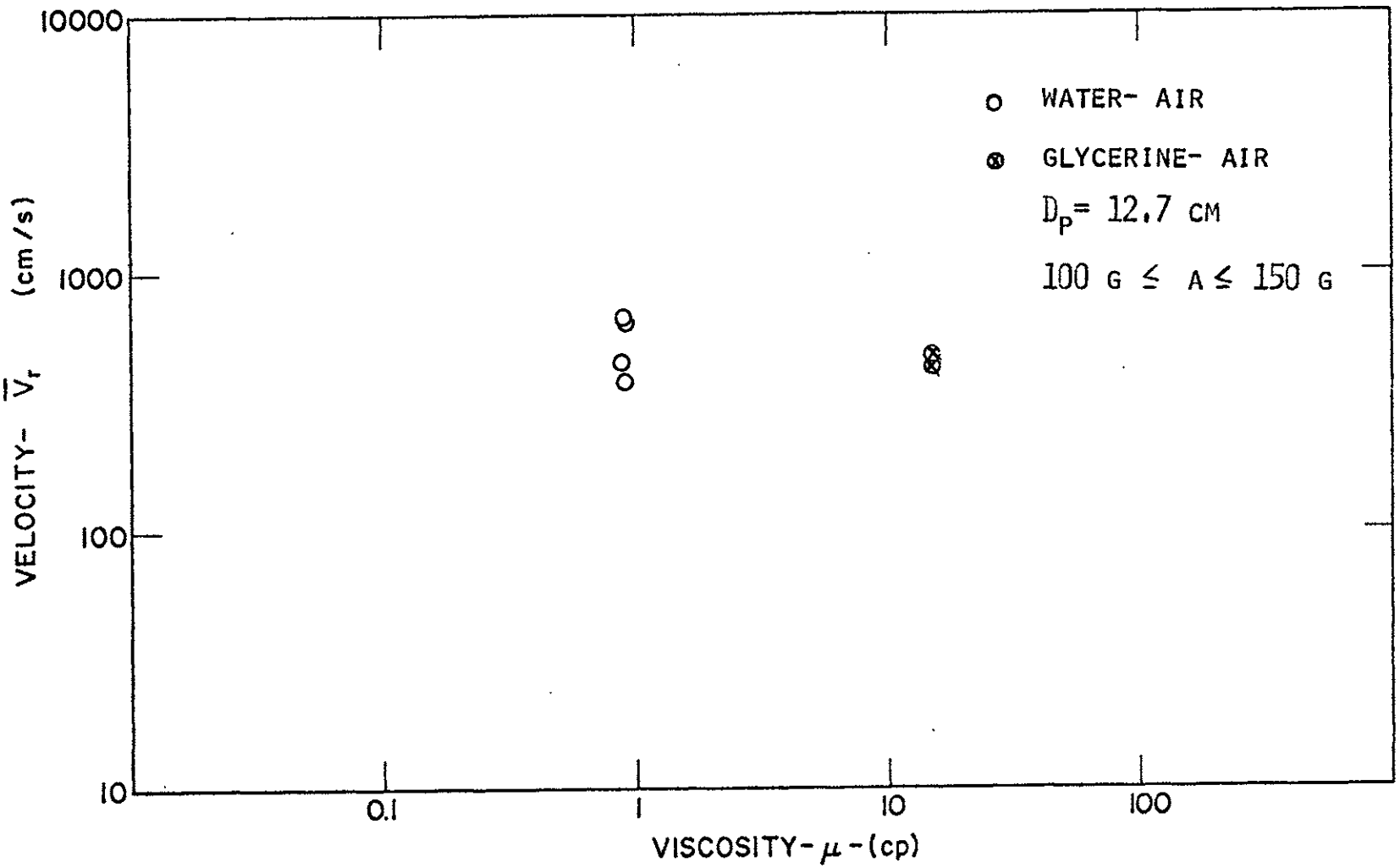

FIGURE 3.12

EFFECT OF DECREASING THE LIQUID SURFACE TENSION

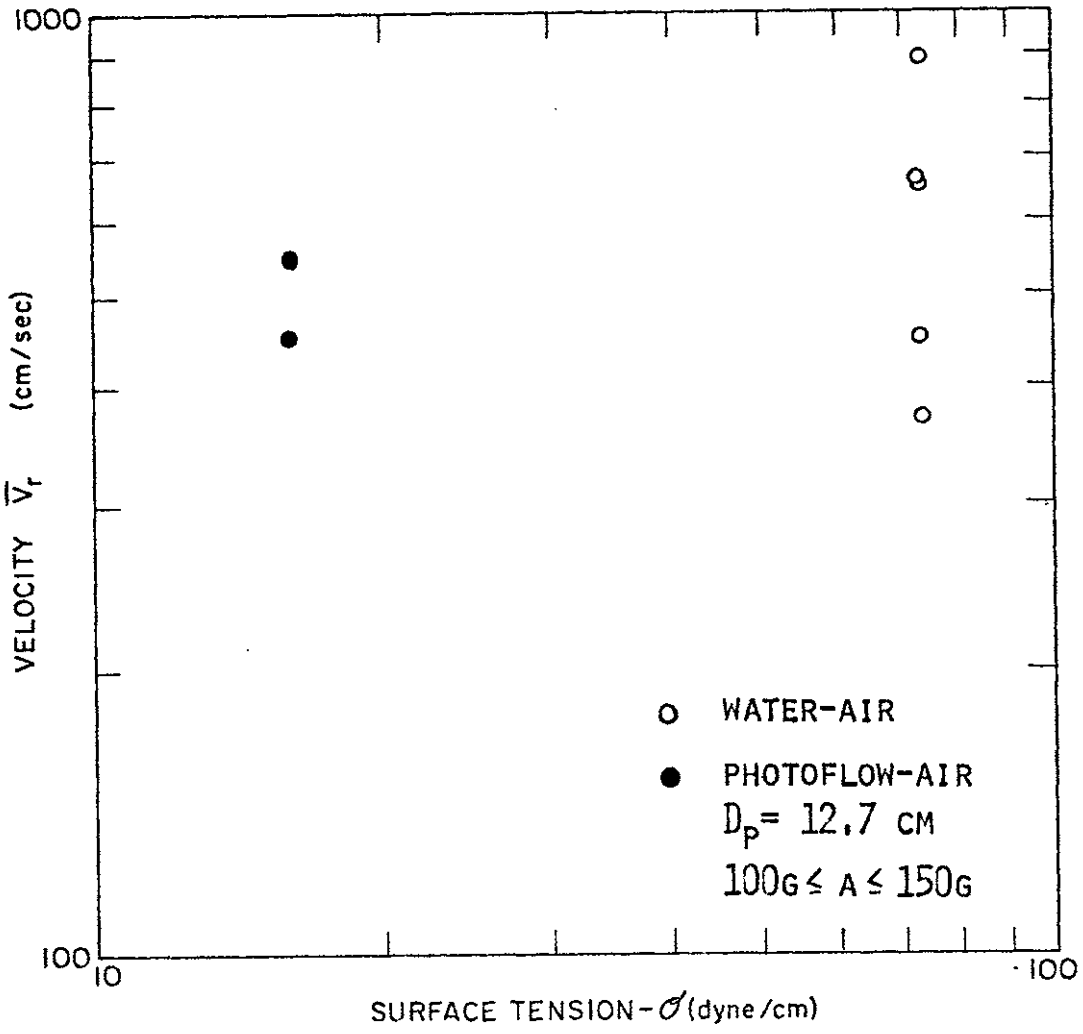

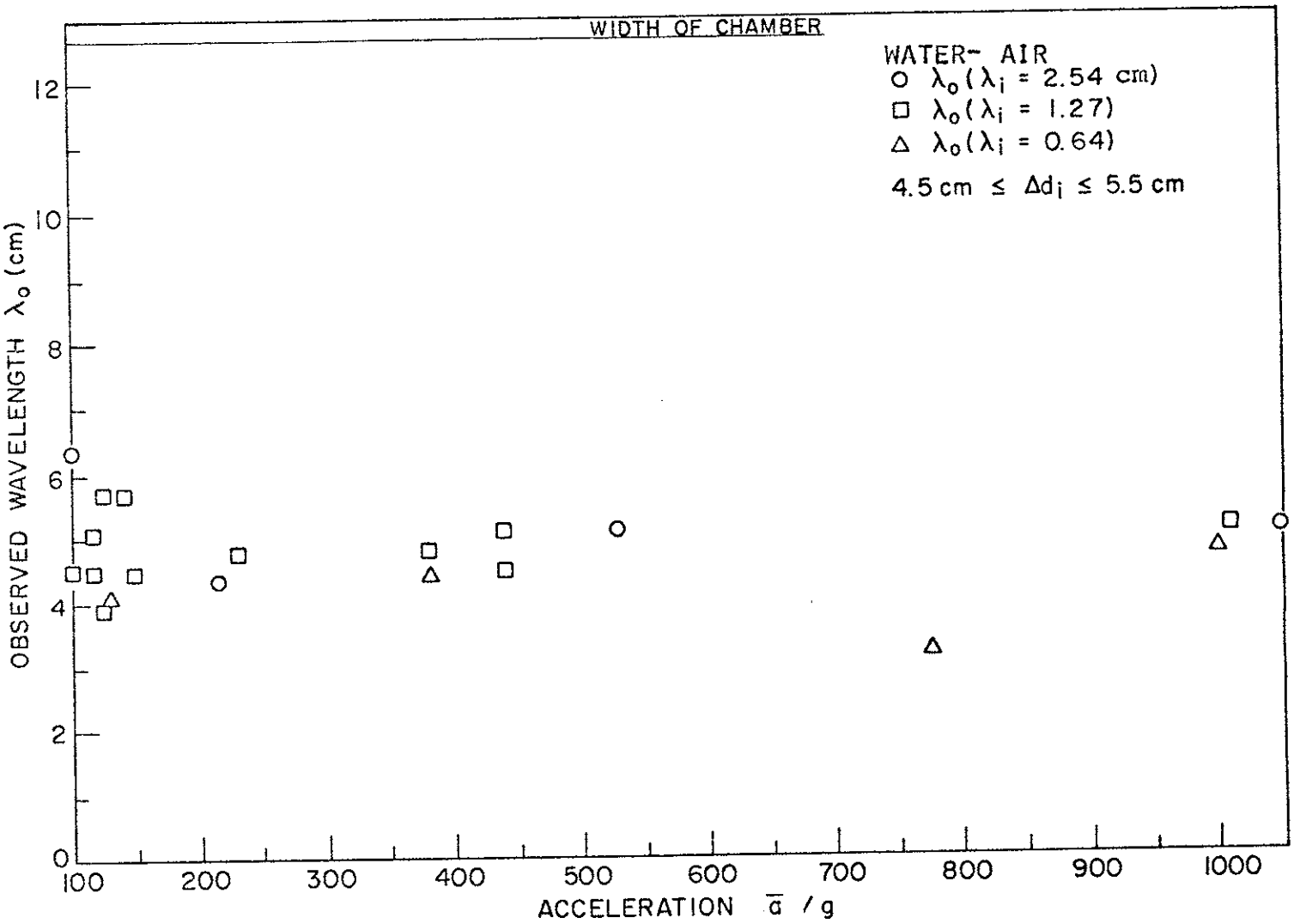

FIGURE 3.13 BEHAVIOR OF THE OBSERVED WAVELENGTH (λ_o) IN REGARD TO ITS INITIALLY IMPOSED WAVELENGTH (λ_i) AND SLUG ACCELERATION (a) AT $4 < \Delta d_i < 5$ cm.

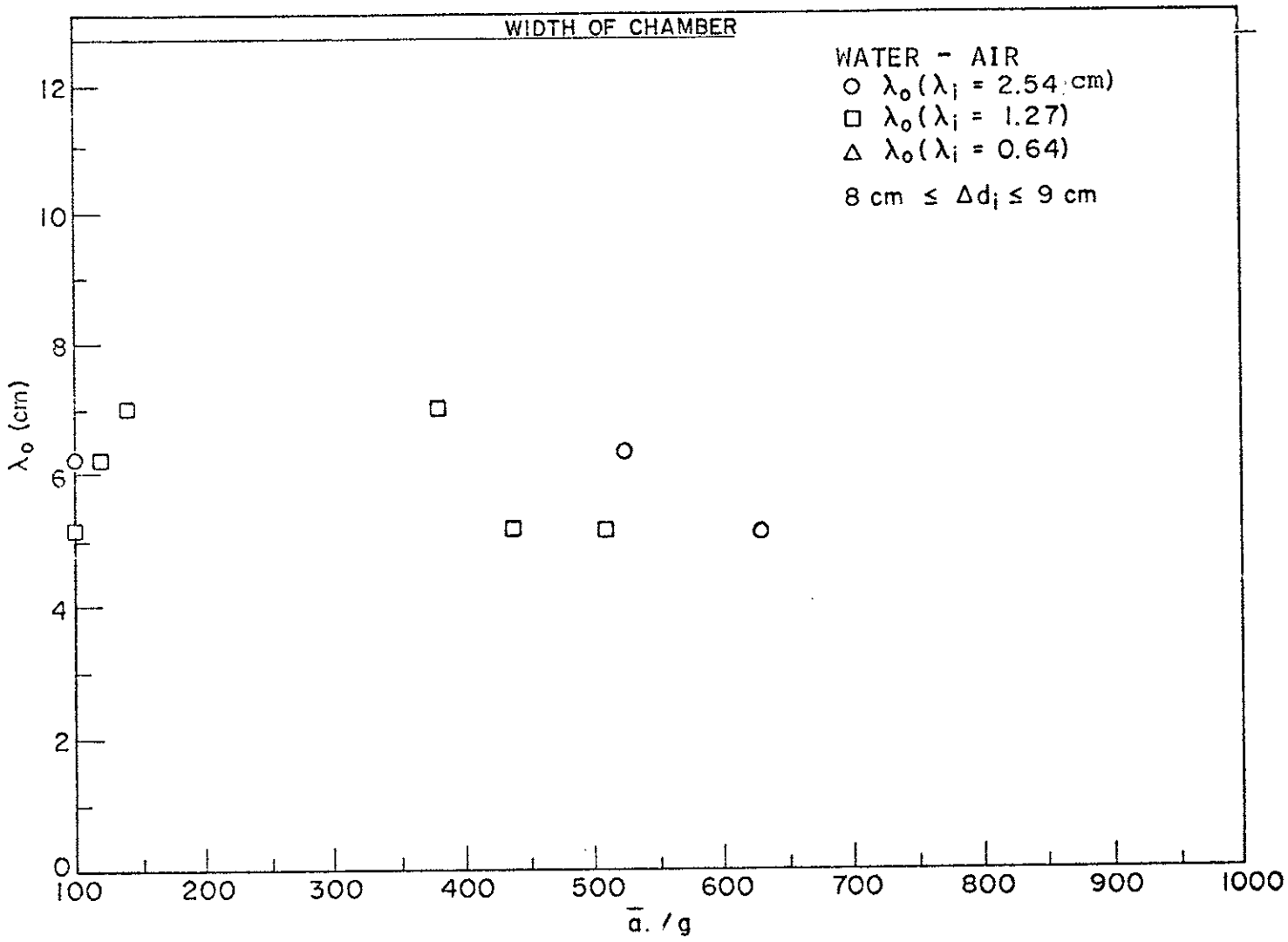

FIGURE 3.14 BEHAVIOR OF THE OBSERVED WAVELENGTH (λ_o) IN REGARD TO ITS INITIALLY IMPOSED WAVELENGTH (λ_i) AND SLUG ACCELERATION (a) AT $8 < \Delta d_i < 9$ cm.

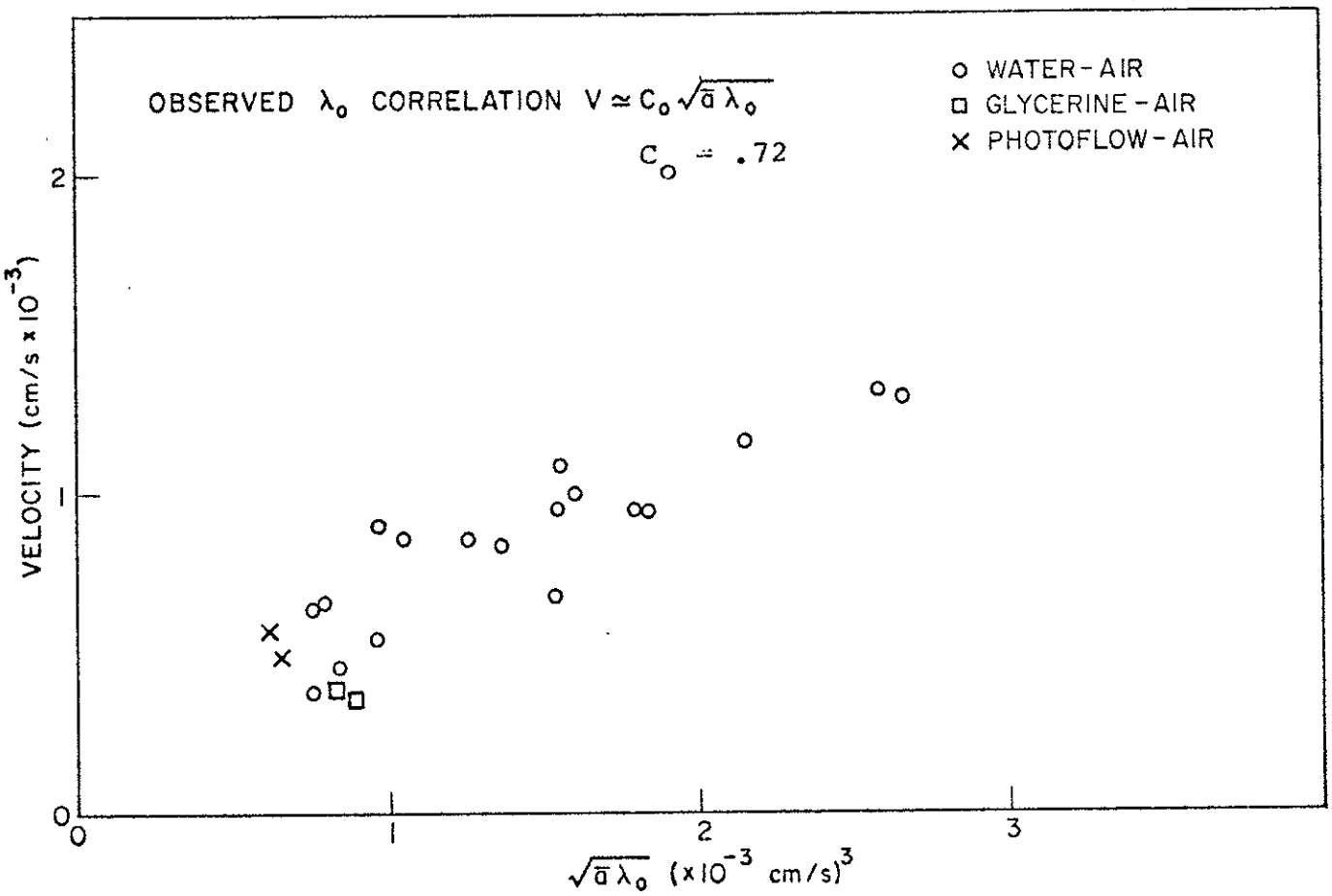

FIGURE 3.15 CORRELATION OF $\bar{v}_r \sim \sqrt{a\lambda_o}$ AS PROPOSED BY LEWIS [50] FOR THE PRESENT EXPERIMENT

FIGURE 3.16

DEPENDENCE OF $\bar{v}_r$ ON $\bar{a}$ FOR THE PRESENT EXPERIMENT

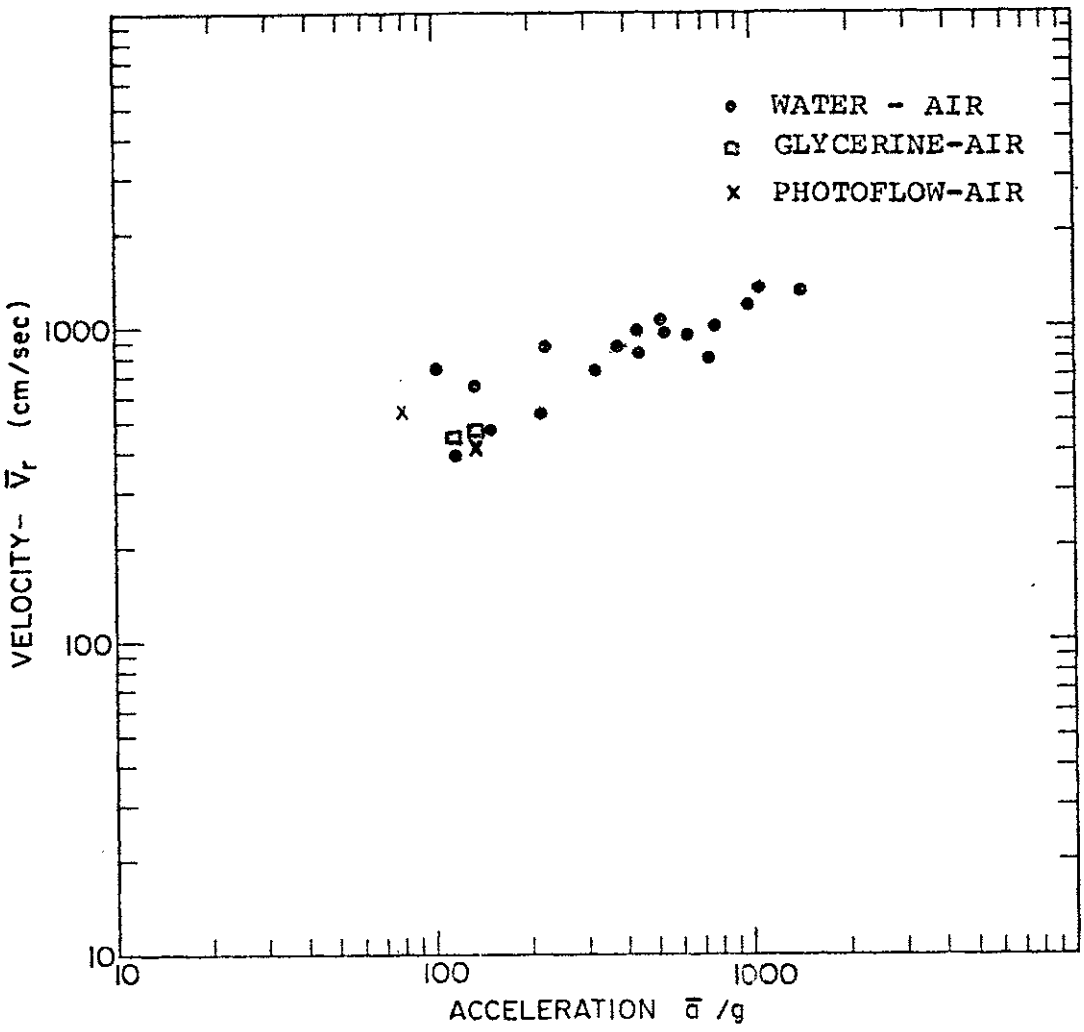

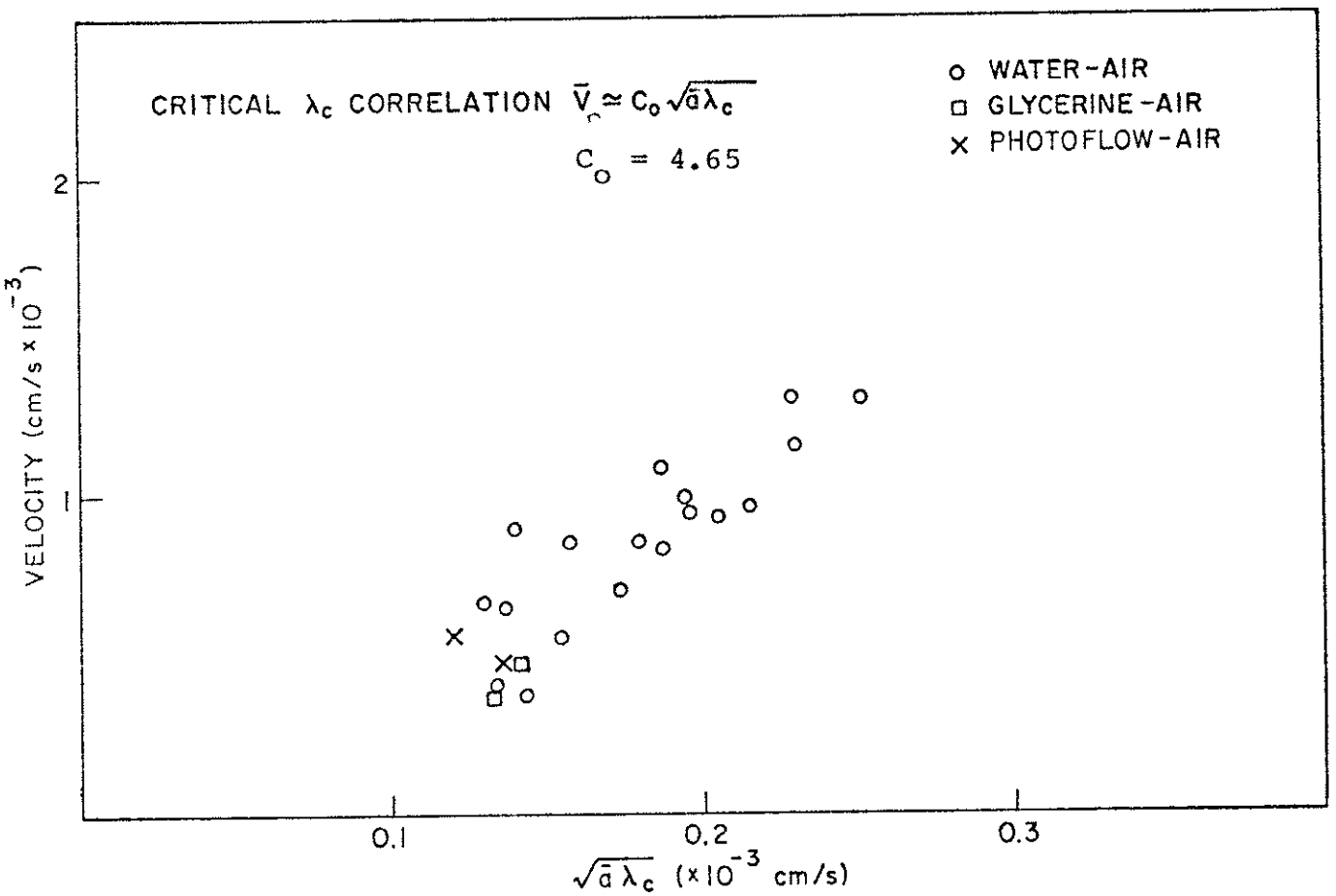

FIGURE 3.17 POSSIBLE CORRELATION OF $\bar{v}_r \sim \sqrt{\bar{a}\lambda_c}$ FOR THE PRESENT EXPERIMENT

FIGURE 3.18

DEPENDENCE OF $\bar{v}_r$ ON THE WIDTH OF THE CHAMBER(D_p)

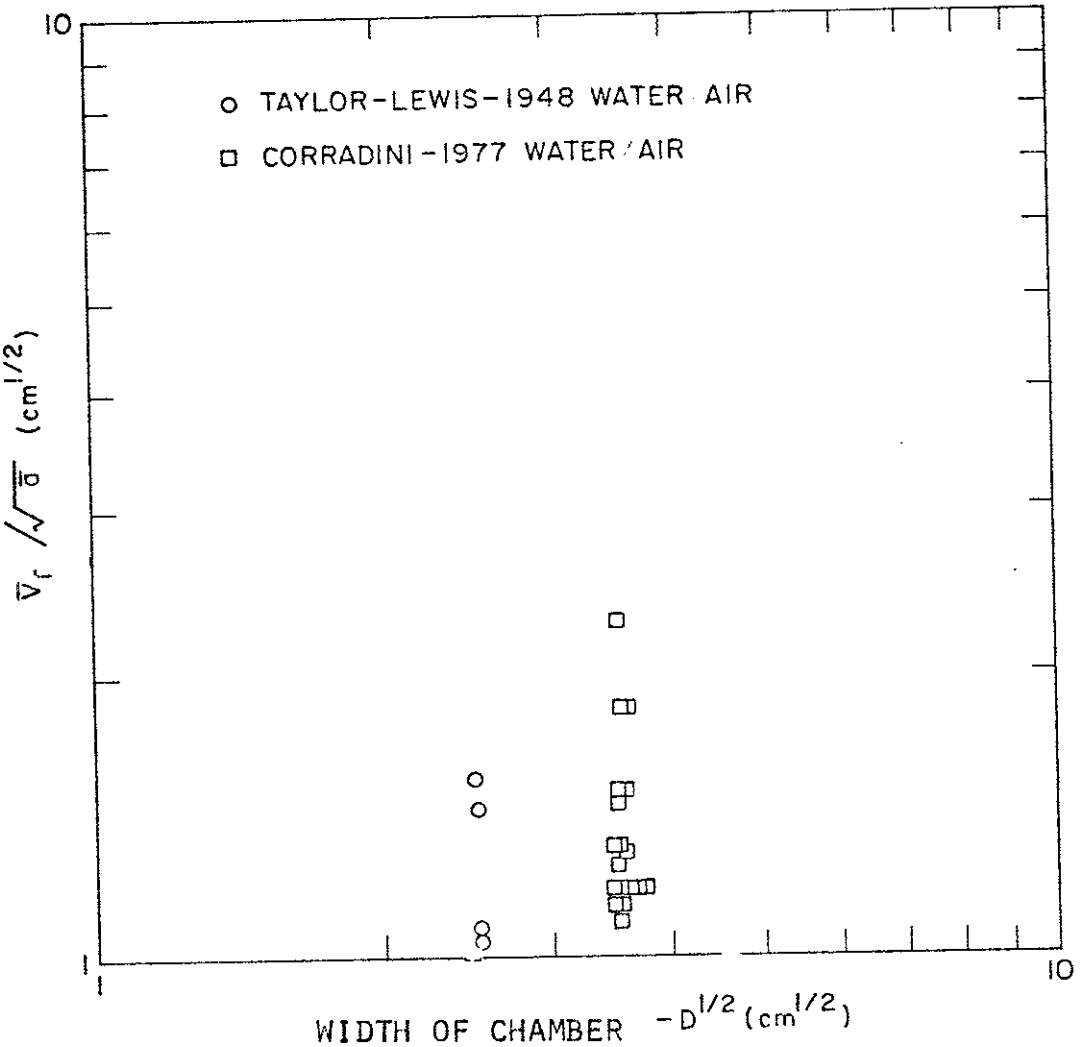

FIGURE 3.19

CONCEPTUAL PICTURE OF THE MIT EXPERIMENTS [54]

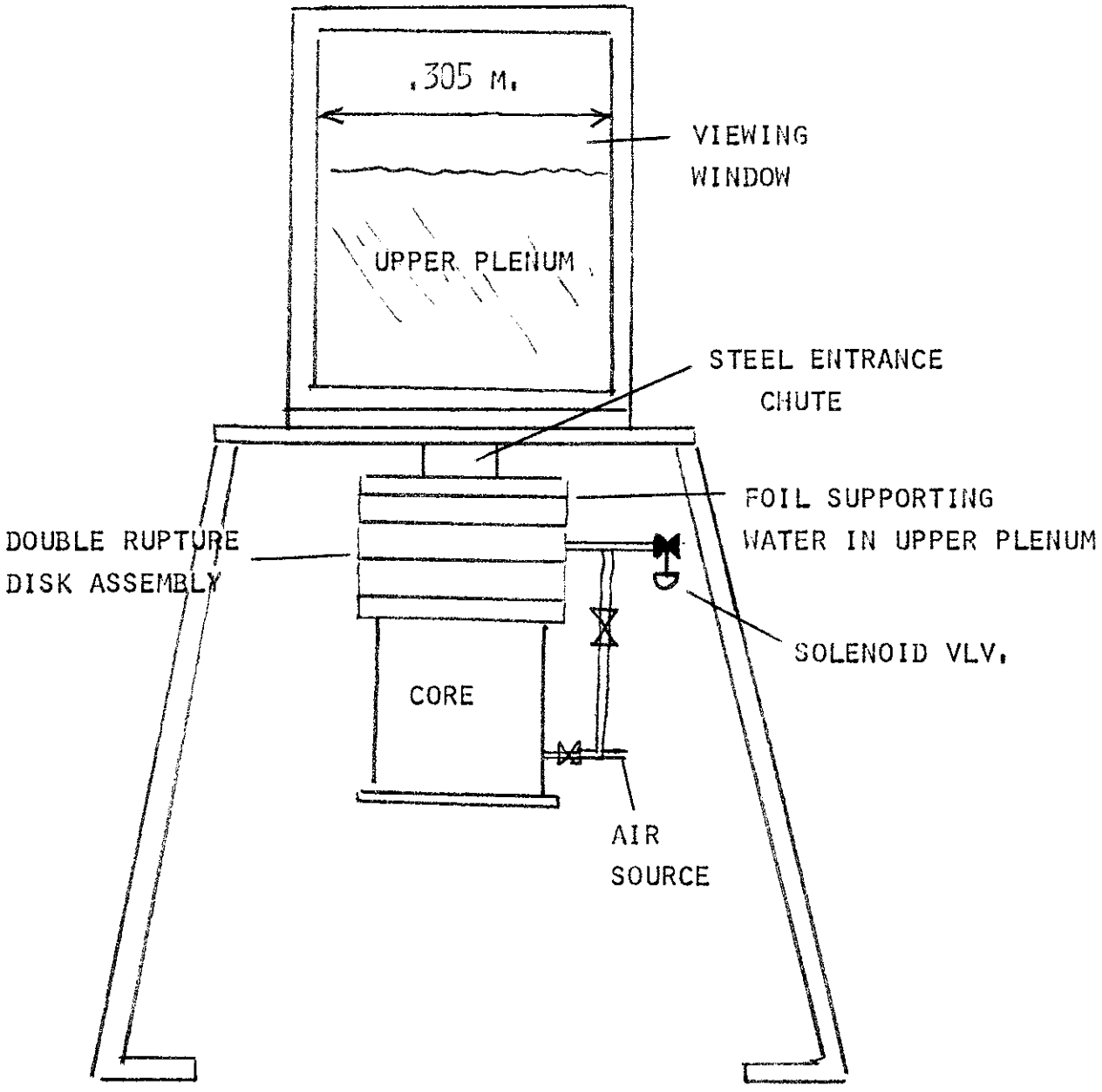

FIGURE 3.20

ANALYSIS METHOD FOR ENTRAINMENT PREDICTION OF THE MIT EXPERIMENTS

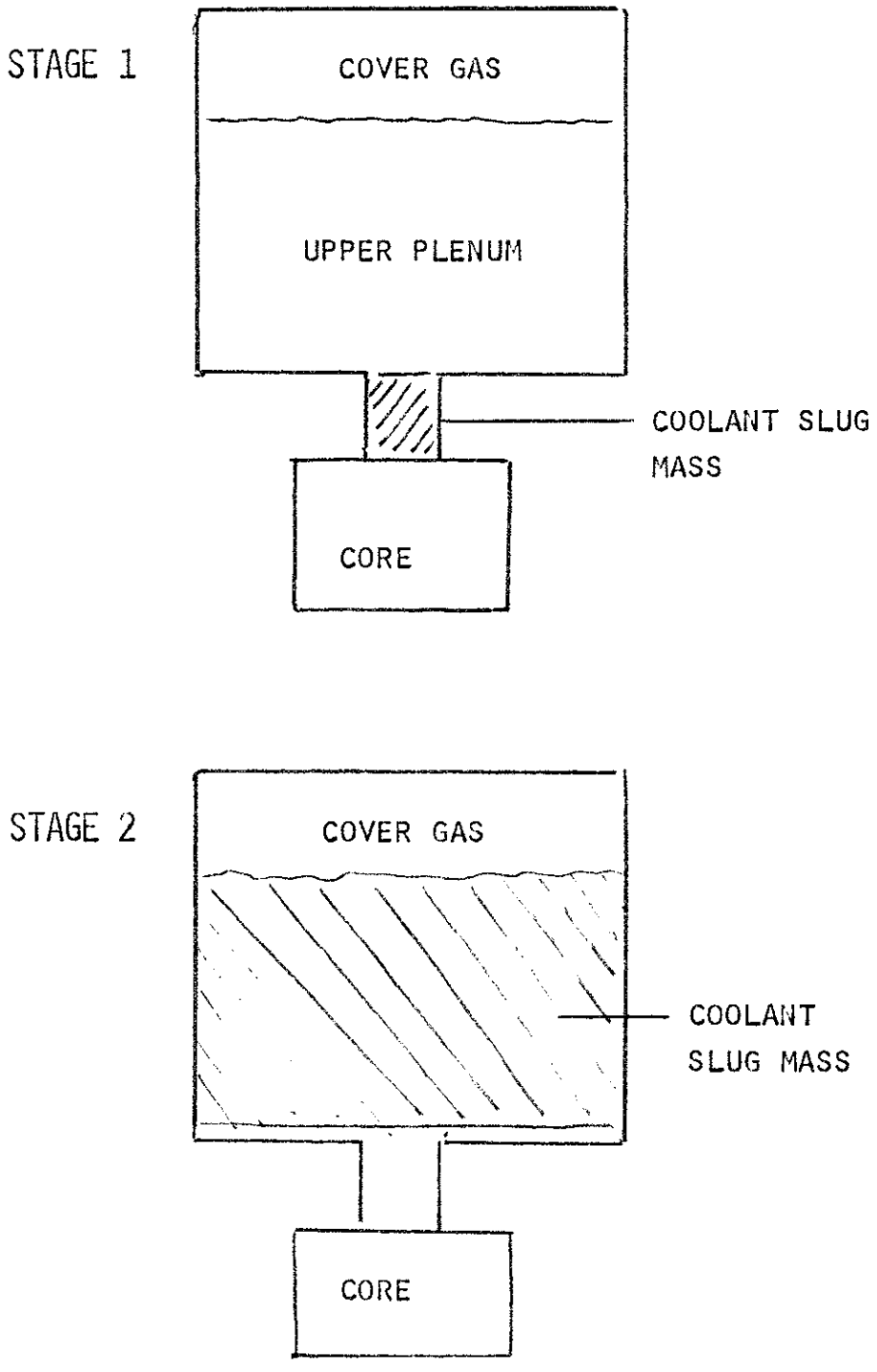

FIGURE 3.21

GAS EXPANSION BEHAVIOR AND COOLANT ENTRAINMENT

FOR P_{gi}= .3MPa - MIT SCALED TESTS

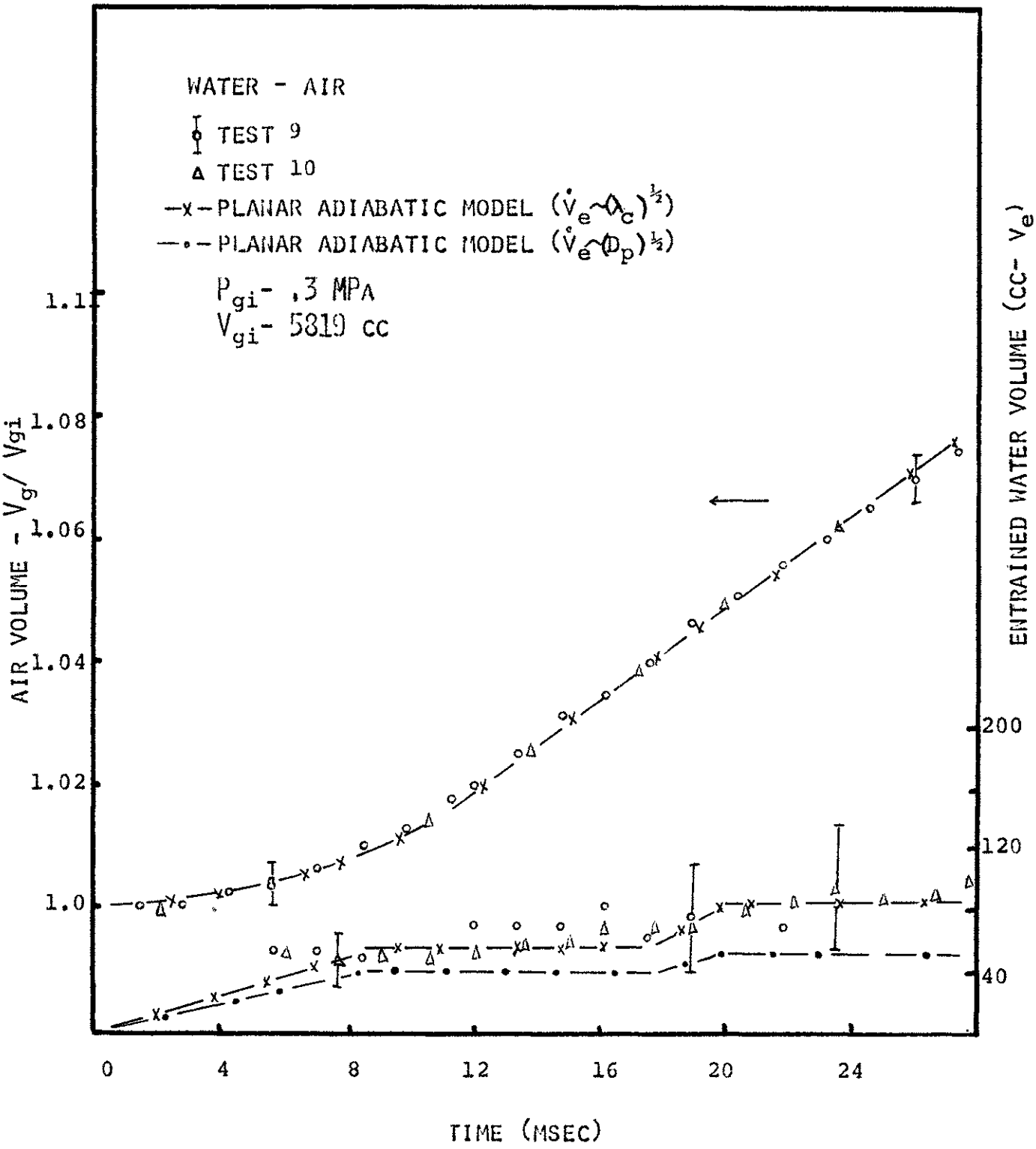

FIGURE 3.22

GAS EXPANSION BEHAVIOR AND COOLANT ENTRAINMENT

FOR P_{gi} = .4MPa - MIT SCALED TESTS

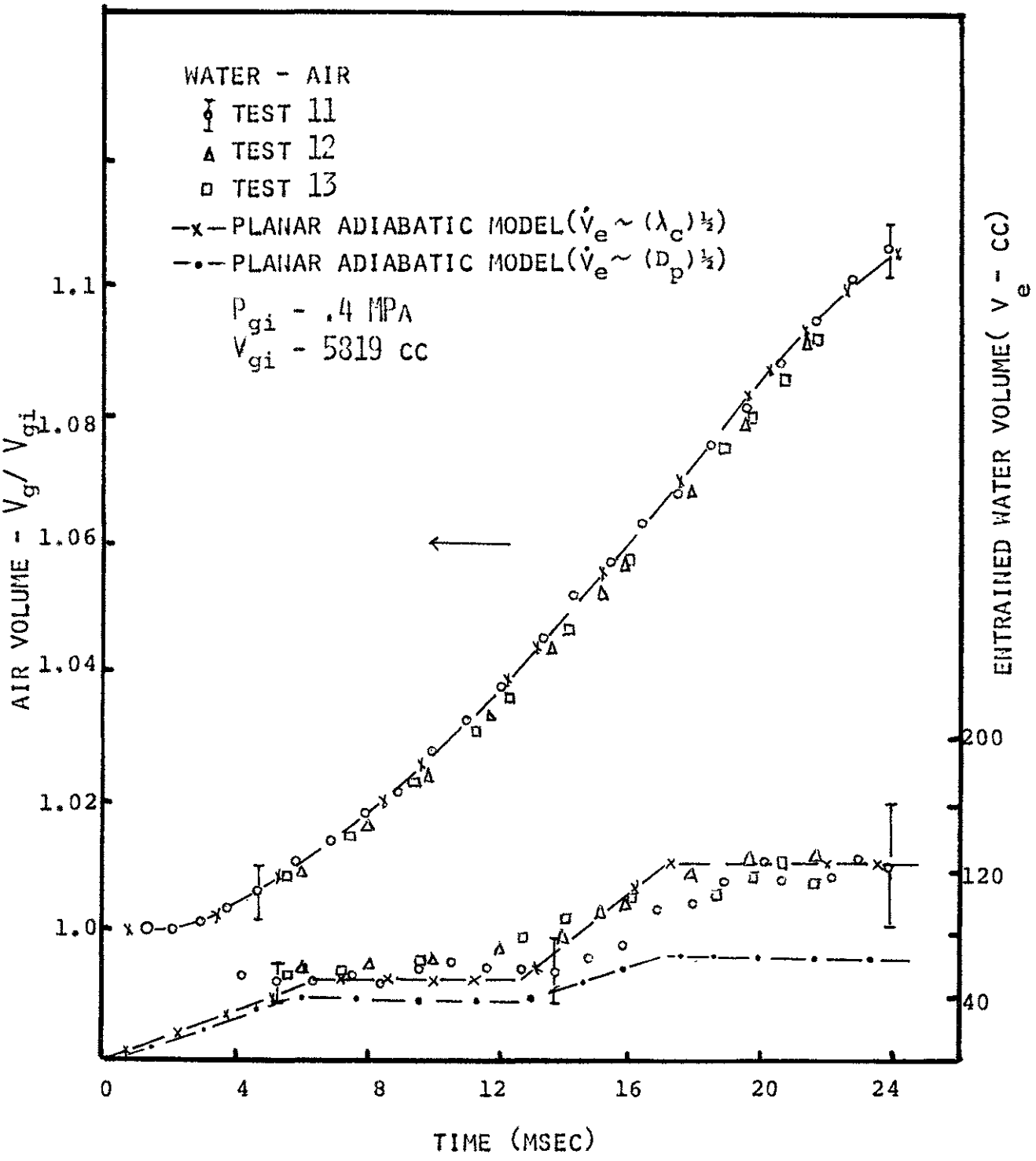

FIGURE 3.23

GAS EXPANSION BEHAVIOR AND COOLANT ENTRAINMENT

FOR P_{gi}= .6MPa - MIT SCALED TESTS

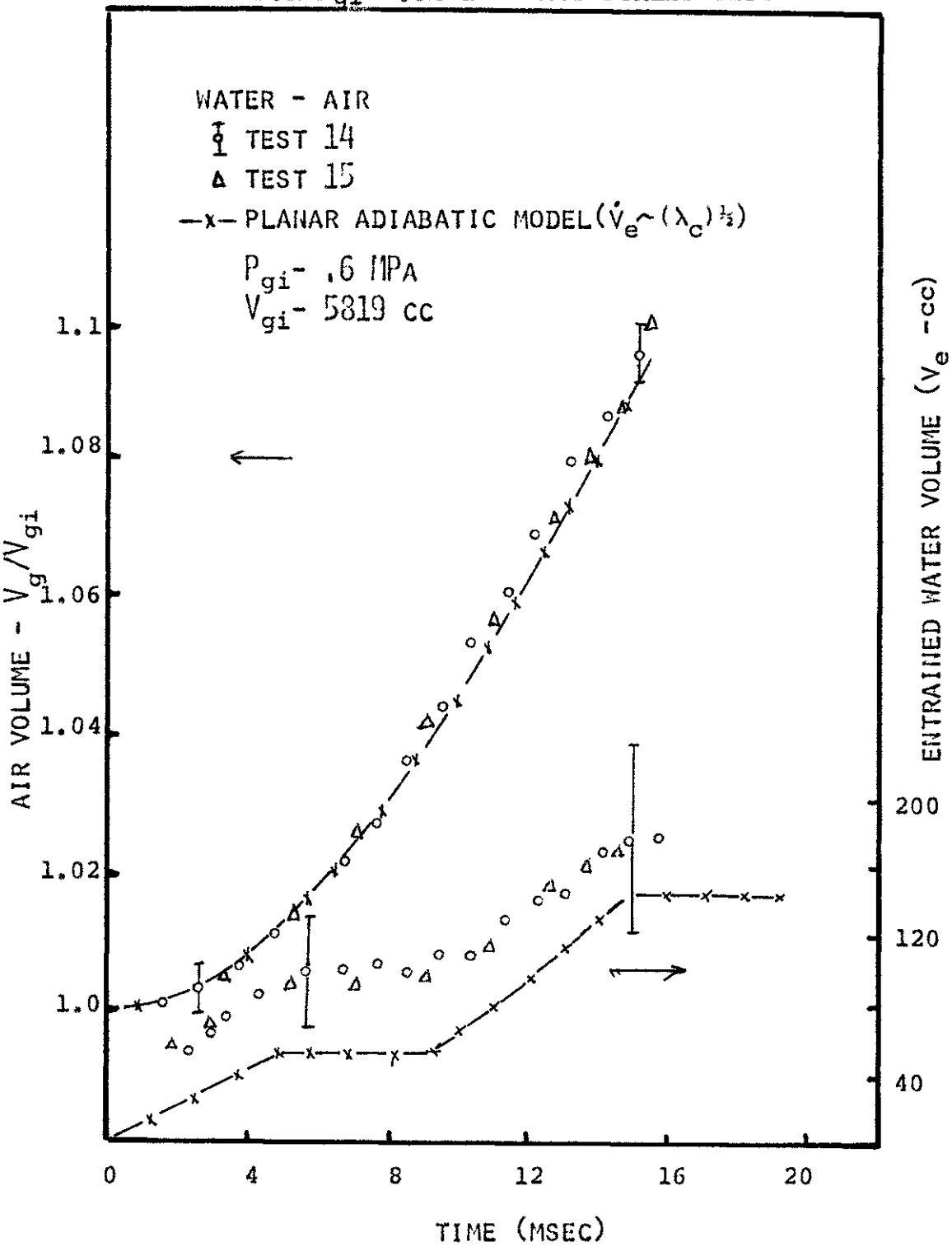

FIGURE 3.24

QUALITATIVE PICTURE OF ACTUAL BUBBLE EXPANSION

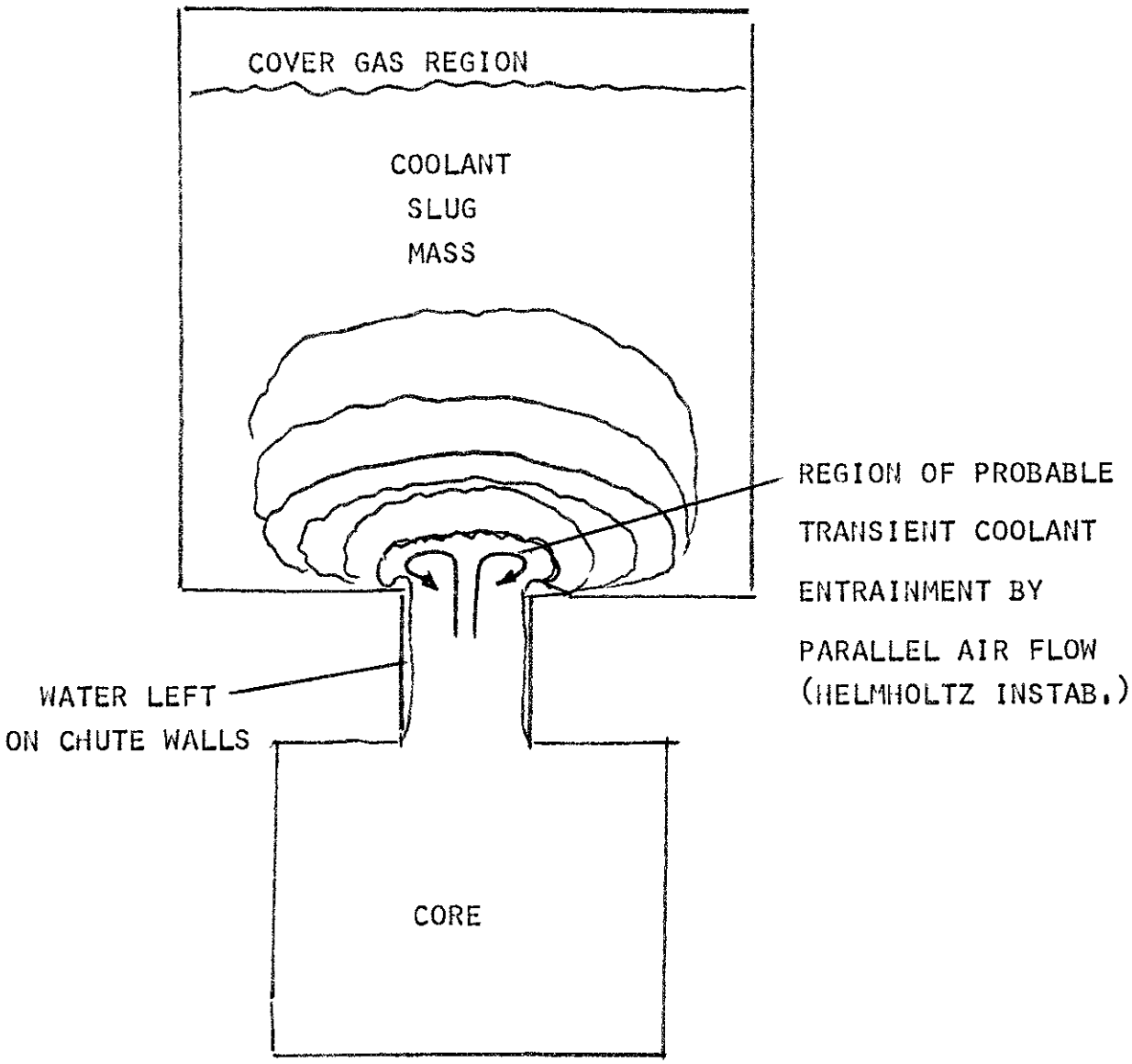

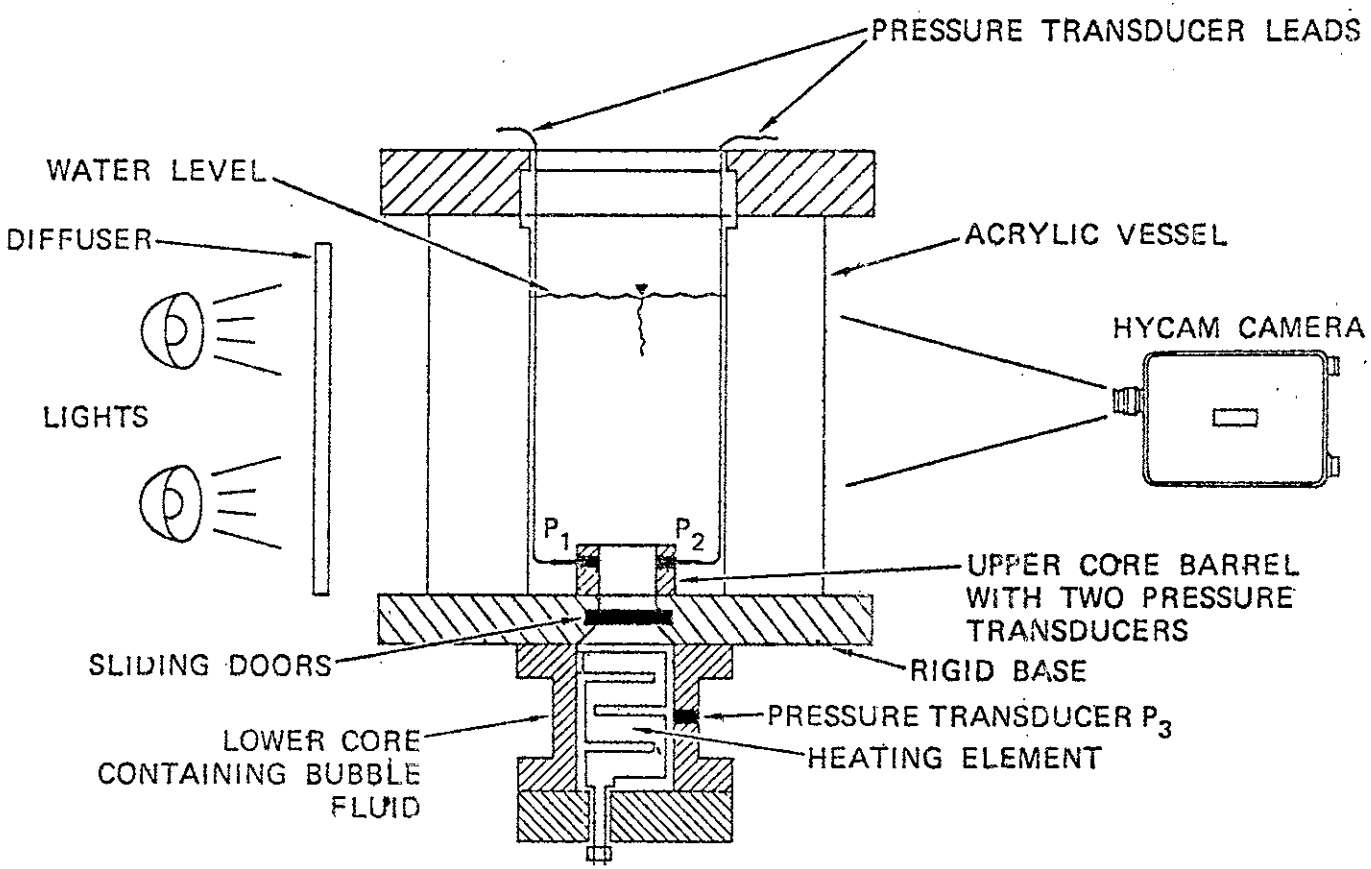

FIGURE 3.25 SRI APPARATUS FOR THE UNHEATED N_2 EXPERIMENT

FIGURE 3.26

GAS VOLUME EXPANSION BEHAVIOR FOR N_2 TEST

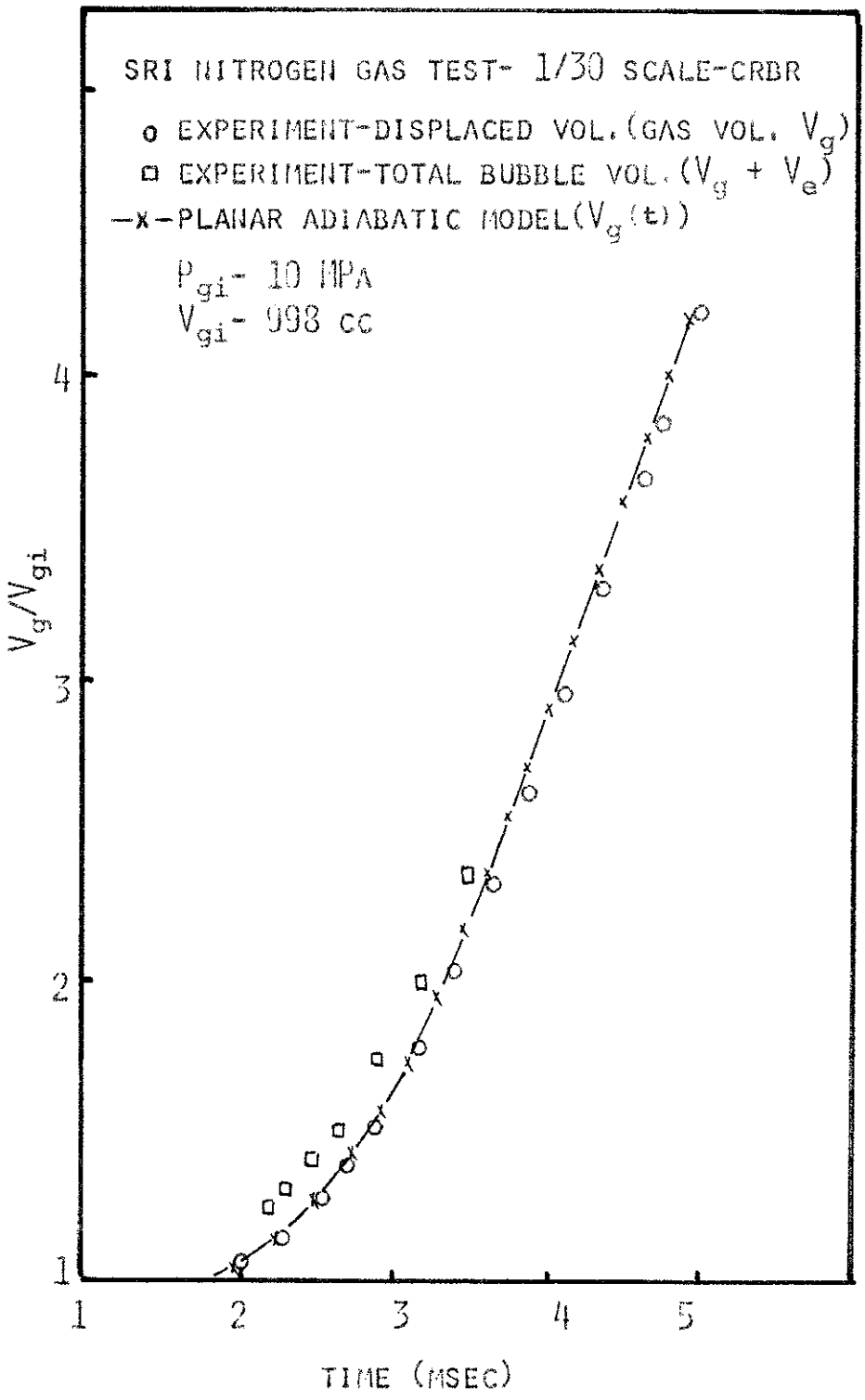

FIGURE 3.27

PRESSURE BEHAVIOR FOR THE N_2 TEST

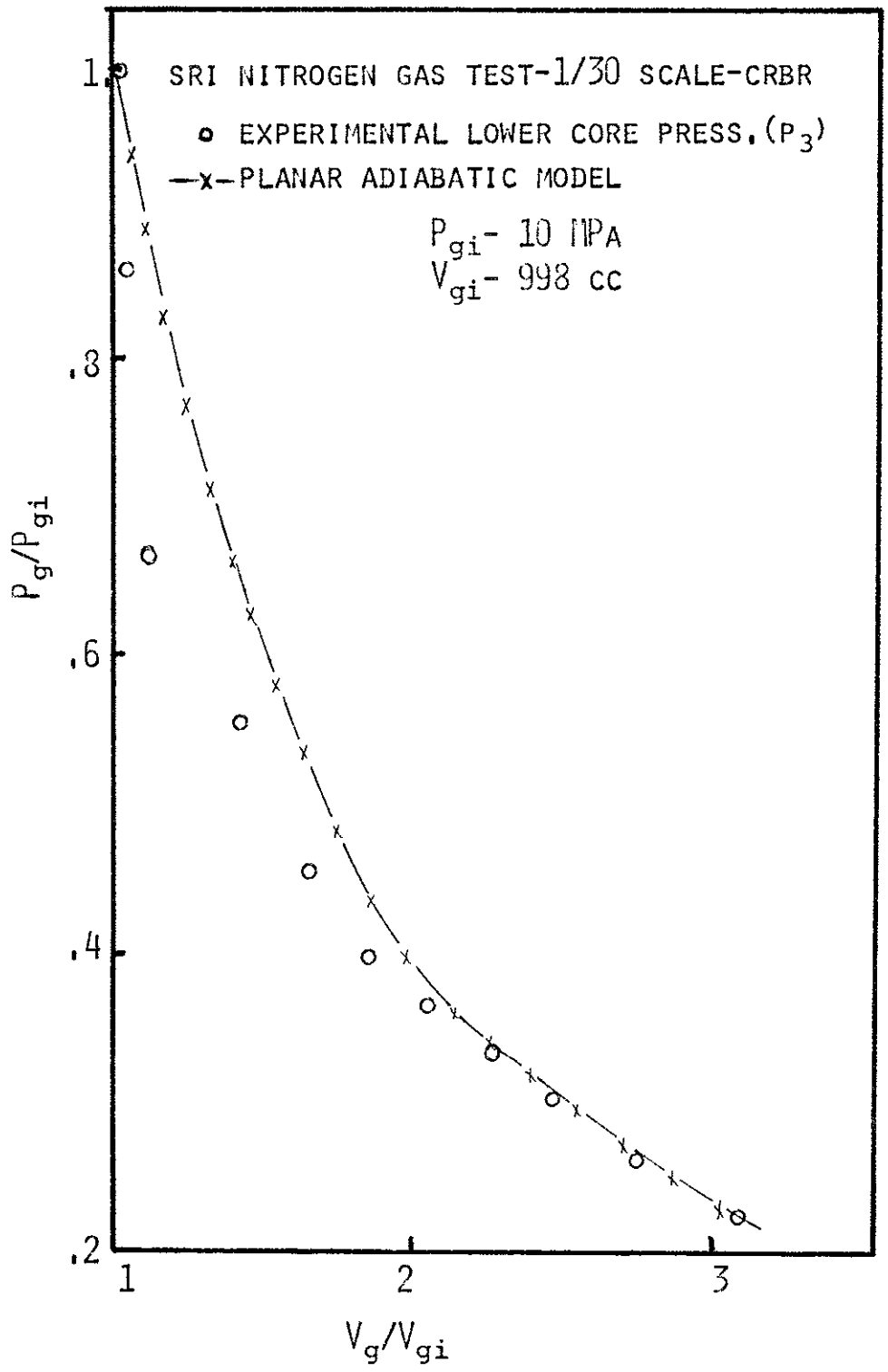

FIGURE 3.28

COOLANT ENTRAINMENT AND VOLUME FRACTION ($1-\bar{\alpha}$) FOR N_2 TEST

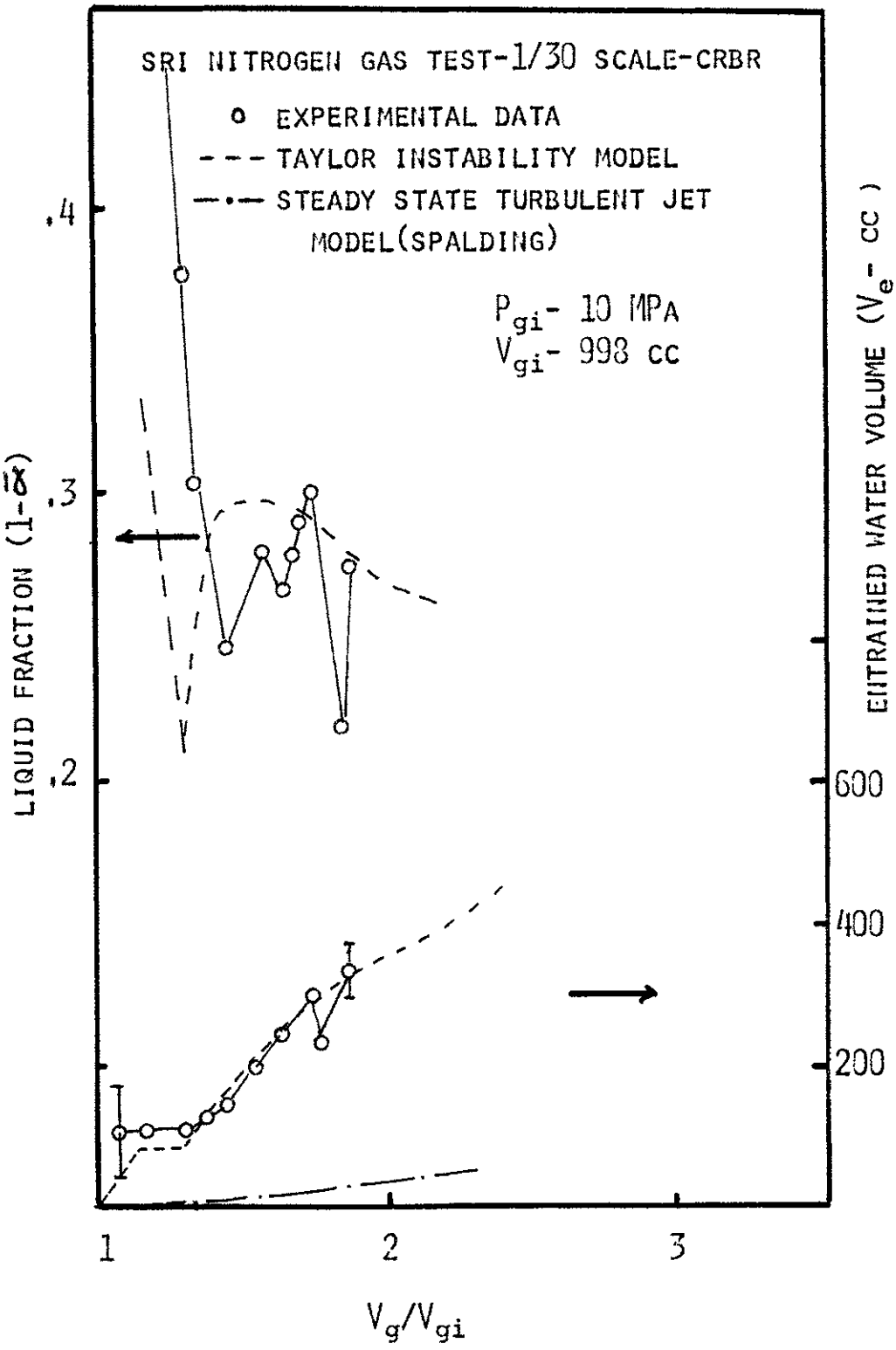

FIGURE 3.29

COOLANT ENTRAINMENT VOLUME FRACTION FOR PURDUE AIR TEST

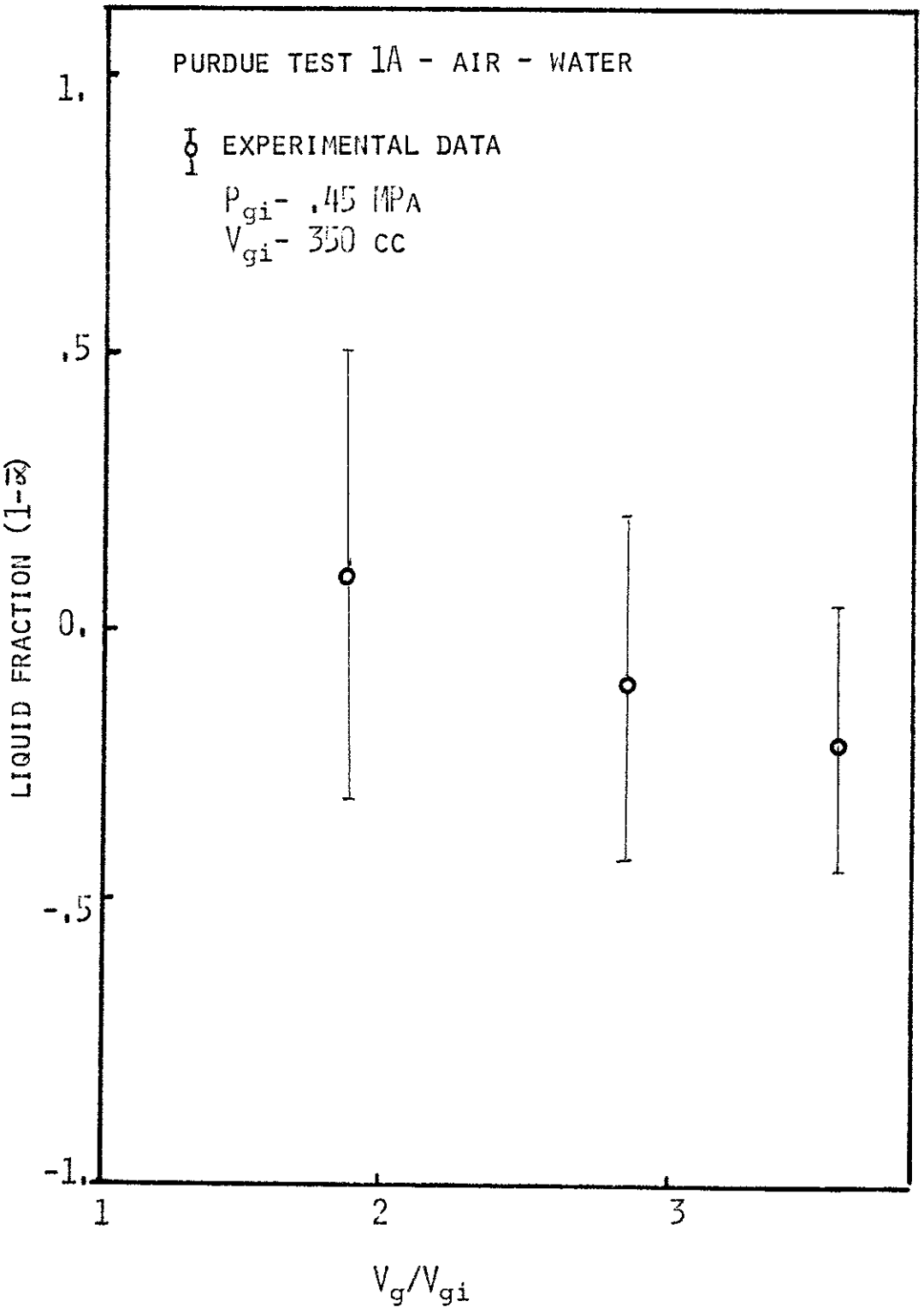

4. PHENOMENOLOGICAL MODELING OF HEATED NONCONDENSIBLE GAS EXPERIMENTS

4.1 Introduction

Noncondensible gas heated tests conducted by SRI International originally served the purpose of simulating a pressure-volume behavior similar to that of an isentropically expanding two-phase source during an HCDA for the FFTF. During this source calibration phase of development, it was noted that significant heat transfer occurred between the hot gas (PETN $\simeq 3000^{o}K$) and the simulant coolant (water - $300^{o}K$) reducing the work output by 50% from near isentropic. Cagliostro [22] and Epstein [31] suggested that the phenomenon which may have created significant surface area for heat transfer was coolant entrainment caused by Taylor Instabilities, and Epstein suggested that $\dot{V}_e \sim \sqrt{a\lambda_c}$. Holten [55] performed a first law analysis utilizing the SRI data and determined the heat transfer from the hot gas by the differences between internal energy and work output. He also concluded that area enhancement was the key to explaining the large heat transfer; however, no modeling of this component was pursued. Corradini and Sonin [56,57] suggested that $\dot{V}_e \sim \sqrt{aD_p}$ and demonstrated with a simple entrainment controlled heat transfer model that the experimental results could be predicted. However, up to the present time, the available tests from SRI have not been consistently predicted without utilizing empirical constants to quantitatively match the data.

To develop a heat transfer model a few fundamental physical phenomena must be identified and modeled: (1) the amount of coolant which becomes entrained in the hot gas to enhance heat transfer; (2) the relative velocity between coolant and gas; (3) the characteristic size of the coolant-

gas system for the heat transfer process; (4) the appropriate rate mechanism which controls the heat transfer-conduction, convection, or radiation; (5) the possibility of coolant vaporization during the process and the consequences of this; (6) the contribution of the heat transfer to the solid structure during the transient. This analysis is presented in the following chapter after a review of the SRI apparatus and tests is given.

4.2 SRI Experiments

These noncondensible source calibration tests were performed at two different scales and in two different geometries. The majority of these gas expansion tests were performed in a one dimensional cylindrical tube arrangement [22] (Figure 4.1) where the diameter of the tube was scaled to be 1/30 or 1/10 of the core diameter for the FFTF. Thirty-five experiments were run in the 1/30 scale geometry (Table 4.1) while twelve were performed at 1/10 scale (Table 4.2). The three main variables which were investigated during the tests were the effects of water addition as part of the inertial slug mass, the effect of initial pressure and the effect of the size of the inertial slug mass on the gas expansion. Four tests were performed in geometric scale models of the FFTF (Figure 4.2) at both 1/30 and 1/10 scales (Table 4.3), the purpose being to verify that the source expansion characteristics remained unchanged (4 tests), and to assess the structural response of a structurally scaled vessel to a simulated "isentropic expansion" (2 tests).

The explosive source developed to produce the noncondensible gas expansion was PETN (pentaerythritol tetranitrate) and a mixture of glass microspheres. It was mixed with the glass microspheres (35%) to reduce the initial shock wave nature of the explosion and give a smoother pressure transient as was expected from a flashing two-phase mixture. The chemical

reaction which produces the hot product gases is

$$C_5H_8O_{12}N_{4(s)} \rightarrow 3CO_{2(g)} + 2CO_{(g)} + 4H_2O_{(g)} + 2N_{2(g)}$$

and as Holten has illustrated [55], the mixture of product gases can be considered to a good approximation to be a perfect gas. The gas properties used for analysis are given in Appendix A. The explosive charge is placed in a louvered canister in an air space inside the apparatus (Figure 4.1 or 4.2) and ignited by an electrical signal. The canister is used to add another damping barrier for the shock waves initially generated by the explosive charge. The canister is attached to the top of the one dimensional apparatus, thus no membrane is needed to separate the initial air space from the water and the piston slug. For the scaled FFTF tests, the charge is placed in the core and a Mylar plastic sheet is used to initially isolate the gas space from the water pool. For the source calibration tests the pressures were monitored by piezoelectric pressure transducers and the piston displacement (or water pool displacement) was measured by a calibrated light ladder crossing a light beam. From these experimental measurements P_g vs. t, V_s vst and ΔW vs t could be obtained.

Because of the pressure shock waves that are characteristic of the explosion and hot gas generation, an average initial pressure for the experiments must be determined for model analysis. A graphing technique was used to estimate this value. The product of the experimental pressure and volume values were plotted as a function of time (Figure 4.3). The curve becomes smooth as the time of the transient becomes long compared to the transient time of a pressure wave ($\frac{2l}{c_a} << t$) and this curve is extrapolated back to the origin to determine an average initial pressure. Given this pressure, volume and the mass of the gas, the initial state is known

for the gas expansion. Table 4.4 gives the initial conditions for the experiments to be analyzed.

The SRI experiments were designed with structural scaling tests as the final experimental goal, and because of this are based on certain scaling laws:

$$B_{D_p} = \frac{\text{Length Prototype}}{\text{Length Model}} = b$$

$$B_m = \frac{\text{Mass Proto.}}{\text{Mass Model}} = b^3 \qquad (4.1)$$

$$B_p = \frac{\text{Pressure Proto.}}{\text{Pressure Model}} = 1$$

This is reflected in Table 4.4 as the masses are scaled from 1/30 to 1/10 test sizes where b = 3. To get a physical feel for these choices, consider that one important variable that is involved in a structural analysis is the stress in a structural member. Now under the accident scenario being considered, this stress is being applied due to the movement of a slug of liquid upward toward the vessel head. Therefore, it could be assumed that

$$\text{Stress} = f(\rho_y, E_y, \nu_y, v, D_p, M_{slug}) \qquad (4.2)$$

where ρ_y, E_y, ν_y are the structural properties of the vessel. This gives four dimensionless groups

$$\frac{\text{Stress}}{v^2 \rho_y} = f\left(\nu_y, \frac{M_{Sl}}{\rho_y D_p^3} \frac{E_y}{\rho_y v^2}\right) \qquad (4.3)$$

For the structural response in the model to be similar to the full scale prototype, the dimensionless stress must be equal. Because there are six independent variables and three dimensionless groups, the scaling laws for these variables can be chosen. If the same structural material is used in

the test as in the prototype, then $B_{\nu} = B_{\rho} = B_{p} = 1$ and the remaining variables take on the scaling factors of

$$\begin{aligned} B_{D_p} &= b \\ B_{v} &= 1 \\ B_{m} &= b^3 \\ B_{stress} &= 1 \end{aligned} \tag{4.4}$$

Now the slug velocity is related to the pressure by the momentum equation (for one-dimension)

$$\frac{dv}{dt} \sim \frac{\Delta P \; D_p^2}{M_{slug}}$$

If this is non-dimensionalized by the factors

$$t^* = t\left[\frac{\Delta P D_p}{M_{slug}}\right]^{\frac{1}{2}} \qquad v^* = \frac{v}{D_p}\left[\frac{M_{slug}}{\Delta P D_p}\right]^{\frac{1}{2}} \tag{4.5}$$

then the result is

$$\frac{dv^*}{dt^*} \sim 1$$

Given the scaling laws in Equation 4.4, it can be seen that if these are applied to the terms in Equation 4.5, the resulting scaling laws are

$$\begin{aligned} B_{P} &= 1 \\ B_{t} &= b \end{aligned} \tag{4.6}$$

These are the resulting scaling factors which were used in the SRI tests, and it must be emphasized that they imply only structurally similar behavior between the model and prototype.

4.3 Heat Transfer Models

4.3.1 Convective Mixing Model

Previous analysis by Corradini, Sonin and Todreas [56,57] modeled the gas expansion tests by a convective mixing model for liquid heat transfer, where it was assumed that the rate of coolant entrainment controlled the rate of heat transfer from the gas to the water. The intent in briefly presenting this model is to note the assumptions involved in its derivation. The purpose of modeling the SRI tests is to predict the results without utilizing an empirical constant to quantitatively match the data. The convective mixing model shows good agreement with SRI data while using an empirical constant. The model does not specify a rate mechanism controlling the energy transfer process but assumes it is controlled by the rate of water entrainment.

The physical view of the process is that the coolant droplets are entrained in the gas near the interface (Figure 4.4). This convective mixing zone of the hot gas and cold water is created due to the water entrainment at a rate governed by Taylor Instabilities, specifically the final growth stage such that

$$\frac{dV_e}{dt} \sim A_p \sqrt{aL} \tag{4.7}$$

The length is viewed as the characteristic wavelength imposed by the transient and is assumed to be

$$L = K D_p \tag{4.8}$$

The convective mixing region can be considered to be some portion of the gas volume although not necessarily the whole volume. The hot gas which enters this mixing region is assumed to come to thermal equilibrium with the liquid entrained such that the energy transferred by the gas per unit

volume is

$$\frac{\Delta Q}{\Delta V} = \rho_g C_{p_g} (T_g - T_l) \tag{4.9}$$

The heat transfer rate then due to the water entrainment is formed by multiplying Equation 4.9 by rate of gas volume flow into the mixing zone

$$\dot{q} = \rho_g C_{p_g} (T_g - T_l) \frac{dV_g}{dt}$$

$$\dot{q} = C_o \rho_g C_{p_g} (T_g - T_l) A_p \sqrt{aD_p} \tag{4.10}$$

The constant C_o introduced here accounts for two unknowns in the volumetric rate of gas addition to the mixing zone. The first is the relation that the wavelength (L) which is growing and entraining water has to the diameter (D_p) of the apparatus. The second unknown is the relative amounts of the gas and liquid in this convective mixing zone and can be expressed as,

$$\left[\frac{\frac{dV_g}{dt}}{\frac{dV_e}{dt}}\right] = C = \left(\frac{\bar{\alpha}}{1-\bar{\alpha}}\right) \tag{4.11}$$

where $\bar{\alpha}$ is the void fraction in the zone, which is assumed constant during the gas expansion process. The constant (C_o) though can be estimated to be between .05 and 1 because of the physical bounds on the two unknowns

$$1 \leq C \leq 10$$

$$\lambda_c \leq KD_p < D_p \tag{4.12}$$

The results of this model will be discussed later in comparison to the proposed rate models but the conclusions reached previously [56] should be restated. The constant (C_o) fit to the experimental data lies in the range of .05 to 1 as was expected and is not a function of the geometric scale of experiment; however, it is not constant if the initial pressure or the mass of the slug (water and piston) is changed varying from $.5<C_o<.8$. This indicates that either the characteristic wavelength or

the void fraction in the convection mixing zone is altered in these transients. Perhaps a more detailed model will be able to differentiate these effects.

4.3.2 Models for Water Entrainment

In analyzing the SRI experiments based upon rate models to describe the gas-liquid heat transfer, the amount of water which interacts with the hot gas should be predicted. The geometry of the one-dimensional tests (Figure 4.1) and the scaled tests (Figure 4.2) indicate that the Taylor instability mechanism will be operative because of the acceleration from the gas to the water. Thus, the entrainment rate is modeled by

$$\dot{V}_e = 4.65\, A_p \sqrt{a\lambda_c} \tag{4.13}$$

The possibility also does exist for turbulent jet entrainment because as the hot gas is produced from the explosive chemical reaction, the flow is out of the canister and downward against the water and piston slug. The gas velocity could sweep across the water surface as the slug is accelerated initially entraining some liquid by the turbulent jet mechanism. The amount entrained can be estimated by the steady state model [34]

$$\dot{V}_e = .32\, \frac{x_o}{D_o} \left(\frac{\rho_g}{\rho_e}\right)^{\frac{1}{2}} \dot{V}_g \tag{4.14}$$

This can be rearranged to give

$$\dot{m}_e = .32\, \frac{x_o}{D_o} \left(\frac{\rho_e}{\rho_g}\right)^{\frac{1}{2}} \dot{m}_g$$

or approximately

$$\Delta m_e \doteq .32\, \frac{x_o}{D_o} \left(\frac{\rho_e}{\rho_g}\right)^{\frac{1}{2}} \Delta m_g \tag{4.15}$$

A sample calculation can be made to obtain the order of magnitude of entrainment by the mechanism. The ratio of $\frac{x_o}{D_o}$ would be expected to be near one because the initial length to diameter ratio in this apparatus is

near that value. This entrainment would only be operative during the time that the gas (Δm_g) exits the explosion canister because the circulating velocity in the initial volume before the piston moves would be high and entrainment a maximum. For the test AVG2 (Table 4.4) the values for these parameters are

$$\rho_{e/\rho_g} = 24/1000$$

$$\Delta m_g = 5.2 \text{ gm}$$

and therefore

$$\Delta m_e \simeq 11 \text{ gm (11cc)}$$

This amount of entrainment is small in comparison to that predicted by Taylor instabilities (~120cc). This will be seen later in the presentation of the results but it should suffice to emphasize here that the dominant entrainment mechanism again appears to be Taylor instabilities.

4.3.3 Determination of Dominant Rate Mechanism

The heat transfer between the hot gas (~3000°K) and the water (300°K) is due to a combination of processes forced convection, conduction and radiation. It is the intent here to perform some simple order of magnitude analyses to determine which mechanism may dominate during the gas expansion transient.

The physical picture of the gas and entrained water is one where the liquid is being entrained mainly due to Taylor Instabilities at the interface and interacts with the hot gas as spherical droplets. This view is partially based upon the qualitative experimental results of the entrainment experiments where black areas above the interface were thought to represent the entrained droplet volume. A relative velocity between the liquid

drops and the gas exists, initially caused by the relative entrainment velocity ($v_r \propto \sqrt{a\lambda_c}$) and later by a combination of the slug velocity and frictional drag on the drops. Because of this relative velocity it is expected that the process of conduction ($Nu \sim 2$) in the gas is not dominant and the other two processes, radiation and convection, are more significant. To estimate the heat flux of each of these processes, a simple analysis can be performed.

To estimate the magnitude of the forced convection heat flux, an estimate of the relative velocity between the gas and water drop and drop diameter is necessary. The relative velocity is initially caused by the Taylor Instability entrainment rate, thus it could be assumed that

$$v_{rel} \simeq 4.65 \sqrt{a\lambda_c} \tag{4.16}$$

The characteristic size can then be taken as the most critical wavelength

$$D_d \simeq \lambda_c = 2\pi\sqrt{\frac{\sigma}{a(\rho_l - \rho_g)}} \tag{4.17}$$

where the acceleration is caused by the pressure difference across the slug. For a sphere in a gas stream a Nusselt number correlation by McAdams [61,62] can be used to determine the heat transfer coefficient

$$\bar{h} = \frac{k_g}{D_d} Nu \tag{4.18}$$

where

$$Nu = .33\ Re^{.6} \tag{4.19}$$

$$Re = \frac{\rho_g\ v_{rel}\ D_d}{\mu_g} \tag{4.20}$$

for $Pr \simeq 1$ where

$$Pr = \frac{C_{p_g}\ \mu_g}{k_g} \tag{4.21}$$

The resistance to heat transfer caused by the water droplet is considered to be small because the transient Biot number is small ($\frac{\bar{h}\sqrt{\alpha t}}{k_g} \sim .1$). Appendix A lists the properties used for PETN product gases. Thermophysical properties not given by SRI (k_g, μ_g) were estimated by using relations based upon the kinetic theory of gases [60]. Using this approximate value of the heat transfer coefficient, the heat flux due to forced convection can be estimated and is listed for representative SRI experiments in Table 4.5.

For the black body radiation heat flux from the gas to the drop the basic rate equation is

$$\dot{q}/_A = \sigma_r (T_g^4 - T_l^4) \tag{4.22}$$

This represents the maximum energy that the gas can transmit and is not realistic because of the dilute radiative nature of the gas that affects the energy transfer process [59,62]. The two variables which can affect the actual radiative emissive power of the gas are the pressure (P_g) and the volume to area characteristics of the enclosure the gas occupies. As a first approximation the number of molecules of a gas in an enclosure that can radiate and the enclosure geometry determine the emissive power of the gas. The pressure of the gas in the volume (P_g) and a characteristic length of the volume (L_m - mean beam length) can be viewed as variables which set the magnitude of gas radiation. Hottel [63] utilizes this engineering approach to the phenomena and uses the concept of a gas emittance (ε_r) to characterize the variables of T_g, P_g, and L_m. The mean beam length for irregular geometries is given by Rohsenow [59] as

$$L_m = \frac{4V_g}{A_{surface}} \tag{4.23}$$

The product $P_g L_m$ is given as a variable along with the gas temperature

(T_g) to determine ε_r and this is given in tabular form by Rohsenow and Hottel [59] [62]. Considering the products of the PETN source, the radiating gases are CO_2, CO, and $H_2O_{(g)}$ and for a given set of initial conditions (Table 4.4), the partial pressures of these gases can be found. The mean beam length (L_m) is dependent upon how much water is entrained in the gas because as ΔV_e increases, the surface area greatly increases and thus L_m and thus ε_r decrease markedly. The two physical bounds on L_m are (1) when there is almost no entrainment the area is the surface area of the water and gas volume ($A_{slug} \sim 200$ cm^2) and then $L_m \sim 4.2$ cm (2) when there is a large amount of entrainment ($\Delta V_e \sim 100$ cc) during the expansion the surface area is large and mainly due to the entrained water droplets ($A \sim 30000$ cm^2) and L_m is small $\sim .03$ cm. Therefore, the maximum emissivity (ε_r) would occur at the beginning of the expansion when $P_g L_m$ and the gas temperature (T_g) are both at their maximum values. This value once found multiplies the black body radiation and gives an estimate of the absolute maximum radiation heat flux (Table 4.5). It should be emphasized that once the water entrainment becomes significant ($\Delta V_e > 10$ cc), then the emissivity of the gas should decrease substantially. As Table 4.5 indicates the forced convection heat flux is by far the dominant mechanism for possible energy transfer, and, therefore, will be the basis for the heat transfer modeling used here.

4.3.4 Vaporization Potential of Coolant

The final investigation that must be undertaken before a rate model for heat transfer is proposed is to assess the vaporization potential of the water coolant. If some of the water which is entrained by the Taylor Instability mechanism is vaporized, then the heat transfer and gas expansion characteristics can become complicated. The reason is that

depending upon the amount of water vaporized, the working fluid for the expansion can change: (1) if negligible vaporization occurs, then the noncondensible hot gas expands transferring heat to the water droplets; (2) if a large amount of water is predicted to vaporize, then the water vapor (saturated condition) not the noncondensible gas is the main pressure source and controls the expansion characteristics. This second possibility was suggested by Tobin [32] of SRI and should be considered in order to decide which process is probably occurring.

To understand how the thermodynamics of this process occurs, a simple model can be constructed. Consider a chamber of volume V_o filled with a hot noncondensible gas of a given mass (m_g), pressure (P_{g_i}) and temperature (T_{g_i}). This essentially is the initial condition of the SRI tests before the piston begins to move. To simplify the analysis assume the walls are adiabatic. To determine the effect of water vaporization assume that some liquid water at a given mass (m_w) and temperature (T_w) is introduced into the chamber and comes to thermodynamic equilibrium with the gas. A measure of the effect of the water addition would be to monitor the equilibrium pressure (P_e) and temperature (T_e) if the water is superheated and the pressure (P_e) and water quality (X_w) if the water is saturated when it equilibrates with the gas. If the thermodynamic system is taken to be the gas and water neglecting the initial volume of water, an energy balance gives

$$U_{g_i} + U_{w_i} = U_{g_{equil}} + U_{w_{equil}} \tag{4.24}$$

$$m_g c_{v_g} (T_g - T_{equil}) = m_w (u_{w_{equil}} - u_{w_i})$$

Now if the gas is modeled as a perfect gas and all the water introduced is assumed to be superheated ($X_w = 1$) and its vapor is modeled as a perfect

gas, then the energy equation becomes

$$m_g\left(\frac{R_g}{\gamma_g - 1}\right)(T_g - T_e) = m_w(u_{w_{equil}} - u_{w_i}) \tag{4.25}$$

where

$$u_w(equil) = \left(\frac{R_w}{\gamma_w - 1}\right)(T_{equil} - T_{crit_w}) +$$

$$c_w(T_{crit_w} - T_{ref}) + u_{ref}$$

$$u_{w_i} = c_w(T_w - T_{ref}) + u_{ref}$$

This relation approximately holds when the equilibrium temperature (T_e) is above the critical temperature of water (T_{crit_w}) and all the water introduced is vaporized. The equilibrium temperature is then

$$T_e = \frac{\left(\frac{R_g}{\gamma_g - 1}\right) T_g + \frac{m_w}{m_g}\left(\frac{R_w}{\gamma_w - 1}\right) T_{crit} - \frac{m_w}{m_g}(u_w - c(T_w - T_{ref}))}{\left(\frac{R_g}{\gamma_g - 1}\right) + \frac{m_w}{m_g}\left(\frac{R_w}{\gamma_w - 1}\right)} \tag{4.26}$$

The equilibrium pressure is then

$$P_e = P_g + P_w$$

$$P_e = \frac{m_g R_g T_e}{V_o} + \frac{m_w R_w T_e}{V_o} \tag{4.27}$$

or

$$\frac{P_e}{P_{g_i}} = \frac{T_e}{T_{g_i}} + \left[\frac{m_w R_w T_e}{m_g R_g T_{g_i}}\right] \tag{4.28}$$

Now if enough liquid water is introduced, the vaporized water will become saturated ($x < 1$ for $T_e = T_{sat_w}$) and the partial pressure of water vapor is determined by the equilibrium temperature. If the vapor and gas are again assumed to behave as perfect gases, the resulting energy equation is

$$m_g\left(\frac{R_g}{\gamma_g - 1}\right)(T_g - T_e) = m_w(u_{w_{equil}} - u_{w_i}) \tag{4.29}$$

where

$$u_{w_{equil}}(T_e) = X_w u_{fg} + c_w(T_e - T_{ref}) + u_{ref}$$

$$u_{w_i} = c_w(T_w - T_{ref}) + u_{ref}$$

$$X_w \triangleq \frac{P_w V_o}{m_w R_w T_e}$$

The equilibrium temperature ($T_e = T_{sat_w}$) can be solved for giving

$$T_e = \left[\frac{\left(\frac{R_g}{\gamma_g - 1}\right) T_g + \frac{m_w}{m_g} c_w T_w - \frac{m_w}{m_g} X_w u_{fg}}{\left(\frac{R_g}{\gamma_g - 1}\right) + \frac{m_w}{m_g} c_w}\right] \tag{4.30}$$

The equilibrium pressure is now

$$P_e = \frac{m_g R_g T_e}{V_o} + P_w(T_e) \tag{4.31}$$

This must be solved iteratively for the equilibrium conditions. The results of this analysis for a typical set of initial conditions is given in Table 4.6. This indicates that initially the water can act as a working enhancing fluid because P_e/P_{g_i} is greater than one, and as more water is added, the water then acts as a quenching fluid and reduces the pressure. This simple model presents the other possibility [32] to a gas expansion in the SRI tests. If enough water is quickly entrained ($\frac{m_w}{m_g} \sim 2$; $m_w \sim 12$ gm) at the initial stage of the transient before the piston starts to move and is vaporized to a saturated state ($P_e/P_{g_i} \sim 1$), then the expansion is controlled by a saturated water vapor expansion. The model presented gives

the possibility of this other explanation but it must be justified by a simple heat transfer rate calculation to establish its validity.

A comparison can be made between the predicted heat transfer coefficient from forced convection expected between the hot gas and water droplets and the heat transfer coefficient needed to accomplish this water vaporization. Using the same analysis as in the previous section, the forced convection heat transfer coefficient is determined by McAdams' correlation for a sphere in a gas

$$\bar{h} = \frac{K_g}{D_d} .33\left(\frac{\rho_g V_{rel} D_d}{\mu_g}\right)^{.6} \tag{4.32}$$

where

$$v_{rel} \sim 4.65 \sqrt{a\lambda_c}$$

$$D_d \sim \lambda_c = 2\pi\sqrt{\frac{\sigma}{a(\rho_l - \rho_g)}}$$

using the conditions for SRI tests AVG2

$$\bar{h} \simeq 1.65\ (10^4)\ w/_{m^2}\ ^oK$$

Now the estimate of the heat transfer coefficient needed for water vaporization can be obtained by using the results of the previous thermodynamic analysis to fix the state of the water when it is vaporized and saturated

$$m_w \sim 12 \text{ gm}$$

$$T_e = T_{sat} \sim 640^oK$$

$$X_w \sim 1$$

$$\Delta h \simeq 2.1(10^6)\frac{w\text{-}s}{kg}$$

The equation relating this to the heat transfer coefficient is

$$m_w \Delta h \simeq (\bar{h}\ (T_{g_i} - T_w))\ A\ \tau \tag{4.33}$$

where

$$A = \frac{6m_w}{\rho_l D_d} \tag{4.34}$$

The characteristic time (τ) for this heat transfer process should be of the same order of time as the time necessary for the gas to expand out of the explosion canister into the initial volume. This can be estimated by a transient isentropic blowdown calculation for the gas. A value for τ of .1 msec is used here which agrees well with Holten's [55] estimate of .05 msec. Inserting these values into Equation 4.34 gives an estimate for the needed heat transfer coefficient for vaporization of

$$\bar{h} \simeq 2.7(10^5) \ w/m^2 \ ^oK$$

This value is almost twenty times as large as what is expected due to the flow characteristics of the system and seems unrealistically high. Thus, it appears that the possibility of water vaporization is slight based upon heat transfer rate arguments.

4.3.5 Gas-Liquid Heat Transfer Model

The model used to describe the phenomenon of gas-liquid heat transfer during the transient expansion is based on the rate mechanism of forced convection and on the physical picture (Figure 4.5) that the hot gas transfers energy to the water in the form of spherical drops in the gas stream. The heat transfer rate to one drop can be characterized by

$$\dot{q}_{\substack{\text{one} \\ \text{drop}}} = \left[\frac{k_g \, Nu}{D_d} \right] \pi D_d^2 \, (T_g - T_l) \tag{4.35}$$

The assumption has been made that the heat transfer resistance due to the water droplet itself is small in comparison to that due to the gas. This is justifiable for two reasons: (1) the expected size of the water droplet $D_d \lesssim \lambda_c$ is much bigger than the penetration depth due to the

transient thermal response of the drop $x \sim \sqrt{\alpha t}$, $\frac{\sqrt{\alpha t}}{D_d} \sim .08$, thus the water droplet behaves as a semi-infinite mass; (2) the Biot number based on this penetration depth is small $\bar{h} \frac{\sqrt{\alpha t}}{k_g} < 1/6$, thus the controlling resistance is due to the gas. The total heat transfer rate then at any time (t) is just the sum of the heat transfer due to each drop

$$\dot{q}_l(t) = \sum_{\text{i-all drops}} \left(\frac{k_g}{D_{d_i}} Nu_i\right) \pi D_{d_i}^2 (T_g - T_l) \tag{4.36}$$

To find this heat transfer rate then, relative velocity between the drop and the gas must be found and the possible values of the drop diameter specified.

The relative velocity between the drop and the gas is expected to be a function of time (t) and the axial distance (x). When the drop is first formed due to the Taylor Instability mechanism, the relative velocity between it and the gas-liquid interface defined as $v_{rel}(x = x_{slug}, t) = v_g(x_{slug}, t) - v_d(t)$ can be written as

$$v_{rel}(x=x_{slug},t) = v_{slug}(t) + C\sqrt{a\lambda_c} - v_{slug}(t)$$

$$v_{rel}(x=x_{slug},t) = 4.65\sqrt{a\lambda_c} \tag{4.37}$$

As the interface passes by the drop, the relative velocity between the drop and the gas at x ($x < x_{slug}$) changes because of three factors: (1) The drop is being accelerated from its original velocity of $v_{slug}(t_o)$ at a past time, t_o, to a new velocity v_d due to frictional drag forces on the drop; (2) The slug velocity increases due to the acceleration caused by the differential pressure across the slug mass; (3) The gas velocity (v_g) behind the interface moves with some velocity less than $v_{slug}(t)$ and greater than zero at the base. If a linear dependence is

assumed, the gas velocity within the gas volume ($0<x<x_{slug}$) is

$$v_g(x,t) = \frac{x}{x_{slug}} (v_{slug}(t) + C\sqrt{a(t)\lambda_c}) \quad (4.38)$$

The drop velocity starts at some slug velocity ($v_{slug}(t_o)$) when it is formed and is accelerated by a drag force equal to

$$\frac{dv_d(x,t)}{dt} = \frac{3C_d}{4D_d} \frac{\rho_g}{\rho_l} (v_{rel}(x,t))^2 \quad (4.39)$$

which is found by a simple momentum balance on the spherical drop where C_d - drag coefficient = .5. Therefore, the relative velocity for a drop at any x and t is

$$v_{rel} = \frac{x}{x_{slug}} (v_{slug}(t) + C\sqrt{a(t)\lambda_c}) - v_d(t) \quad (4.40)$$

The drop diameter has two physical bounds which will determine its magnitude. The first is the size at which it is probably formed. Because the dominant mechanism of entrainment is due to Taylor instabilities, it seems that a characteristic size of formation should be equal to or less than the size of a fastest growing instability wavelength

$$D_d = \lambda_m = 2\pi\sqrt{\frac{3\sigma}{a(\rho_l - \rho_g)}} \quad (4.41)$$

The lower bound is if the characteristic Weber number for the drop is above the critical breakup value [64]

$$We = \frac{\rho_g (v_{rel}(x,t))^2 D_d}{\sigma} > We_{crit} \simeq 7\text{-}20 \quad (4.42)$$

then the droplet will begin to breakup until the kinetic energy and surface tension forces are balanced and the droplet Weber number is near the critical values. If the characteristic drop Weber number is below this range of values, then the drop is stable and will not decrease in size due to this mechanism.

The heat transfer coefficient for the drop at any x and t in the hot gas can again be determined by using McAdams' correlation for a sphere in a hot gas ($Pr_g \sim 1$)

$$\bar{h}(x,t) = \frac{k_g \quad Nu}{D_d\ (x,t)}$$

$$\text{where } Nu = .33\left[\frac{\rho_g(t)\ v_{rel}\ (x,t)\ D_d\ (x,t)}{\mu_g}\right]^{.6} \tag{4.43}$$

This description accurately gives the heat transfer from a drop at an axial distance x and at a time t. To get the total heat transferred in the whole gas volume, a summation over all the drops formed over a distance from $0 \leq x \leq x_{slug}$ must be done. The formal integration over all x is not possible; however, it can be approximated by finding the number of drops born over a discrete number of axial increments (Δx_i), forming the product of this number with heat transfer rate and summing over all Δx_i. The number of drops formed in a Δx_i is

$$\underset{\text{born}}{\text{No. } (\Delta x_i)} = \frac{\text{Vol. Entrained @ x in } \Delta t_i}{\text{Volume of one spherical drop}}$$

$$\underset{\text{born}}{\text{No. } (\Delta x_i)} = \frac{C\ \sqrt{a\lambda_c}\ A_p\ \Delta t_i}{\frac{\pi}{6} D_d^{\,3}} \tag{4.44}$$

Conbining this with Equation 4.35, the total heat transfer at a time (t) is given by

$$\dot{q} = \sum_{i=0}^{N} \underset{\text{born}}{\text{No. } (\Delta x_i)}\ \underset{\text{drop}}{\dot{q}\ \text{one}}\ ;\ N = \frac{x_{slug}}{\Delta x_i}$$

This gives

$$\dot{q} = \sum_{i=0}^{N}\left[\frac{\text{Vol}_{\text{born}}(\Delta x_i)}{\frac{\pi}{6}\ (D_d(x,t))^3}\right]\left[\frac{k_g}{D_d(x,t)} Nu\right]\ \pi\ D_d(x,t)^2 (T_g - T_l)$$

$$\dot{q}(t) = \sum_{i=0}^{N} \left[\frac{6\,Vol_{born}(\Delta x_i)}{D_d(x,t)}\right]\left[\frac{k_g\,Nu}{D_d(x,t)}\right](T_g - T_l) \tag{4.45}$$

where

$$Nu = .33\left(\frac{\rho_g\, v_{rel} D_d}{\mu_g}\right)^{.6}$$

Although this is an exact formulation of the heat transfer, it is unrealistic to solve because it requires a separate differential equation for each level of Δx_i to monitor the acceleration of the drops and determine the relative velocity. This presents an unwieldy set of equations to solve. Some approximations are attempted to make the problem tractable. The intent of this formulation is to insert this liquid heat transfer model into a set of governing equations and numerically solve the system on a computer.

4.3.5.1 Model #1 Variable Heat Transfer Coefficient and Drop Diameter

The first approximation that can be made is to obtain an average drop acceleration over all the drops and then integrate this one equation and add it to the individual velocities of each drop. The drop velocity at any time (t) is made up of the velocity it was born at, that being the slug velocity ($v_{slug}(t_o)$) at a past time (t_o), and the additional velocity caused by the frictional acceleration of the drag,

$$v = \int_o^t \frac{dV_d}{dt}\,dt \text{ where } \frac{dV_d}{dt}$$

is given by Equation 4.39. Now the velocity of the drop at its formation time can be approximated by

$$v_{slug}(t_o) \doteq a\,t_o = \frac{a\,t_o}{t}\,t$$

where it is assumed that the acceleration is constant

$$v_{slug}(t_o) \doteq \frac{t_o}{t}\,a\,t = \frac{t_o}{t}\,v_{slug}(t)$$

$$v_{slug}(t_o) \doteq \left[\frac{a\, t_o^2}{a\, t^2}\right]^{\frac{1}{2}} v_{slug}(t)$$

$$v_{slug}(t_o) \doteq \left[\frac{x - x(t=0)}{x_{slug} - x(t=0)}\right]^{\frac{1}{2}} v_{slug}(t) \tag{4.46}$$

The drop velocity is then

$$v_d(t) = \left[\frac{x - x(0)}{x_{sl} - x(0)}\right]^{\frac{1}{2}} v_{slug}(t) + v_f(t) \tag{4.47}$$

The velocity increase due to friction ($v_f(t)$) can be found by taking the acceleration at each Δx_i

$$\frac{dv_d}{dt}(x,t) = \frac{3C_D}{4} \frac{\rho_g}{D_d \rho_l} (v_{rel}(x,t))^2 \tag{4.39}$$

and finding the average drop acceleration

$$\left\langle \frac{dv_d(t)}{dt} \right\rangle = \frac{\Sigma \frac{dv_d(x,t)}{dt} \Delta x_i}{\Sigma \Delta x_i} \tag{4.48}$$

and integrating this one equation over time. The relative velocity then becomes

$$v_{rel}(x,t) = \frac{x}{x_{slug}} (c\sqrt{a\lambda_c} + v_{slug}(t)) - \left[\frac{x - x(t=0)}{x_{slug} - x(t=0)}\right]^{\frac{1}{2}} v_{slug}(t) - \int_o^t \left\langle \frac{dv_d}{dt} \right\rangle dt \tag{4.49}$$

where it is used in Equation 4.45.

The second approximation that can be made is to obtain a spatial average relative velocity and average drop diameter separately and then insert these values into the heat transfer rate equation and integrate it over time. The relative velocity can be averaged by taking the relation for relative velocity (Equation 4.49) and performing an average as

$$\left\langle v_{rel}(t) \right\rangle = \sum_{\Delta x_i} \frac{(v_{rel}(x,t))^{.6}}{\sum_{\Delta x_i} \Delta x_i} \Delta x_i \qquad (4.50)$$

The reason that the velocity is raised to the .6 power is that it appears in the heat transfer correlation to this exponent, therefore, requiring this non-linear averaging technique. Similarly for the drop diameter, the spatial average is

$$\left\langle D_d(t) \right\rangle = \frac{\sum_{\Delta x_i}^{N} \text{No.}_{\text{born}}(\Delta x_i)\, D_d(x,t)^{1.4}\, \Delta x_i^{\frac{1}{1.4}}}{\sum_{\Delta x_i} \text{No.}_{\text{born}}(\Delta x_i)\Delta x_i} \qquad (4.51)$$

where as before

$$\text{No.}_{\text{born}}(\Delta x_i) = \frac{C\sqrt{a\lambda_c}\, A_p\, \Delta t_i}{\frac{\pi}{6}(D_d(x,t))^3}$$

The exponent in the average is again used because of the correlation of the heat transfer dependence on D_d. These values can now be inserted into the heat transfer rate equation (Equation 4.45) and the expression reduces to

$$\dot{q}(t) = \frac{6\,\Delta V_e}{\left\langle D_d \right\rangle}\left[\frac{k_g}{\left\langle D_d \right\rangle} Nu\right](T_g - T_l) \qquad (4.52)$$

where

$$\Delta V_e = \int_o^t C\, A_p \sqrt{a\lambda_c}\, dt \qquad (4.53)$$

$$Nu = .33\left[\frac{\rho_g \left\langle v_{rel} \right\rangle \left\langle D_d \right\rangle}{\mu_g}\right]^{.6} \qquad (4.54)$$

This spatial averaging is first accomplished and then the average values are used in the rate equation for heat transfer. This numerical averaging technique is detailed in Appendix F. This technique is commonly used for all the heat transfer models in this work and a common description is given.

4.3.5.2 Model #2 Constant Drop Diameter

A further approximation can be added by simply calculating the spatial average relative velocity and utilizing one average value of the drop diameter for the whole transient. The characteristic Taylor Instability wavelength and the critical Weber number size can be used as the bounds on this diameter and a representative value can be inserted. The heat transfer rate then becomes

$$\dot{q}_1(t) = \frac{6\Delta V_e}{D_d} \left(\frac{k_g}{D_d} Nu\right)(T_g - T_1)$$

where

$$Nu = .33 \left(\frac{\rho_g \langle v_{rel} \rangle D_d}{\mu_g}\right)^{.6} \qquad (4.55)$$

$$D(We_{cr}) \leq D_d \leq \lambda_m$$

4.3.5.3 Model #3 Constant Heat Transfer Coefficient and Drop Diameter

The most approximate form of this model results when an average heat transfer coefficient and drop diameter are estimated and assumed to be constant throughout the transient expansion. Again the physical view of the relative velocity and the drop diameter would be used to obtain this average estimate but the values would not be updated during the expansion process, giving us

$$\dot{q}(t) = \frac{6\Delta V_e}{D_d} \bar{h} (T_g - T_1) \qquad (4.56)$$

$$\bar{h} = \frac{k_g}{D_d} .33 \left(\frac{\rho_g v_{rel} D_d}{\mu_g}\right)^{.6}$$

The gas-liquid heat transfer model presented assumes the energy transfer rate as being controlled by forced convection between the expanding gas and the entrained water in a droplet form. The main characteristics of the relative velocity and drop diameter are indicated along with three different levels of sophistication to the model. This model can now be

included into a set of governing equations to predict the transient process.

4.3.6 Gas-Solid Heat Transfer Model

During the expansion transient, it is expected that the solid structure also acted as a heat sink to the hot gas. The magnitude of this heat transfer is not expected to be as large as that due to the gas-liquid heat transfer simply because the exposed solid surface area is much smaller. However, it is felt that the magnitude of this energy transfer is not negligible and should be considered and analyzed. The heat transfer to the solid elements in the apparatus can be considered in two stages: (1) the heat transfer to the interior of the explosion canister and the glass microspheres as the detonation gas products leave the canister; (2) the heat transfer to the exposed solid surface area of the apparatus and the outer canister area during the rest of the transient.

The first heat transfer stage is difficult to determine because no instrumentation is located within the explosion canister to measure the pressure. Thus, the only measure of the heat transferred to the interior structure and the glass microspheres is to find the internal energy change between what is predicted as the initial internal energy (U_{g_p}) from the chemical explosion to what is measured (U_{g_i}) when the gas expands into the initial volume (P_g) of the apparatus and mixes with the air, that is

$$(U_{g_p} - U_{g_i}) + (U_{a_p} - U_{a_i}) = \Delta Q_{S_I}$$

This heat transfer is expected to occur before the piston moves, as the gas enters the initial expansion volume. The amount of heat transferred

can be found for one SRI test (AVG2). The reported energy release from the PETN reaction [23] is 3520 w-sec/gm of explosive. Thus the heat transferred to the interior structure is approximately,

$$(U_{g_p} - U_{g_{ref}} - m_g c_{v_g} (T_{g_i} - T_{ref}) + m_{air} c_{v_a} (T_p - T_{g_i})) = \Delta Q_{S_I}$$

$$T_{g_i} = \frac{P_{g_i} V_o}{(m_g + m_a) R_g} = 3050^{o}K \text{ (Table 4.4)}$$

$$U_{g_p} - U_{g_{ref}} = 28.1 \text{ kw - sec}$$

$$T_{ref} = 273^{o}k$$

$$m_{air} = .0003 \text{ kg}$$

$$m_g = .0052 \text{ kg}$$

Therefore,

$$\Delta Q_{S_I} \simeq 7. \text{ kw - sec}$$

This value of heat transfer is in good agreement with what has been estimated by Holten [55] and Cagliostro [68] over a range of 6-8 kw-s. The main energy transfer presumably occurs to the interior canister structure as the hot gas is expanding through the small slits into the expansion volume. At this point, the flow in the canister is near a choked flow condition ($v_{gas} \sim 1000$ m/s) and the density is quite high ($\rho_{gas} \sim 400$ kg/m^3). Thus the heat transfer coefficient would be high causing this large energy transfer. Thus at the start of the analysis presented here when the gas is in the initial apparatus volume, this process has occurred for all the SRI tests reducing the initial pressure to the level experimentally measured.

The second stage of heat transfer to the solid occurs when the gas has occupied the entire initial apparatus volume. The heat sink area has increased to the outer structural surface area and the exterior of the canister although the density, velocity, and temperature have markedly decreased. Because this heat transfer process occurs simultaneously with the gas-liquid process, a model needs to be devised to describe this phenomenon so that it can be included into the transient analysis of the test.

The surface area available for solid heat transfer is expected to be just the initially exposed area for the tests with water. The reason for this is that as the gas expands if water is present, it will most likely be left as a film on the walls of the apparatus. The heat transfer in this region will be to the water not to the wall because in the time of the transient (~2 msec), the penetration depth of a transient thermal wave will only penetrate a distance of

$$x \sim \sqrt{\alpha t} \tag{4.57}$$

which for water is

$$x \sim \sqrt{1.43(10^{-7})\ 2(10^{-3})} \simeq 20\ \mu m$$

This distance is much smaller than what the expected film thickness is

$$\delta_{film} \simeq .005 D_p \sim 400\ \mu m \tag{4.58}$$

as Ozgu suggests [69]. Thus for all the SRI tests the total solid heat transfer area is assumed to be same ($A_s \sim 700\ cm^2$).

The method used to find the magnitude of this heat transfer was to analyze the experiments performed with no water present (Table 4.4) and fit the solid heat transfer rate calculated to the equation

$$\dot{q}_{solid} = \bar{h}_{emp} A_s (T_g - T_l) \tag{4.59}$$

The energy equation applicable to these tests is

$$\Delta U = \Delta Q_s + \Delta W_{exp}$$

$$\Delta Q_s = (U_{g_i} - U) + \Delta W_{exp} \qquad (4.60.1)$$

The work output of the experiments is calculated by SRI from the pressure-volume experimental measurements and the initial internal energy (U_{g_i}) is known from the pressure and volume measurements. If the gas is modeled as a perfect gas, the solid heat transfer (ΔQ_s) is

$$\Delta Q_s = m_g c_{v_g} (T_{g_i} - T_g) + \Delta W_{exp}$$

$$\Delta Q_s = m_g \left(\frac{R_g}{\gamma_g - 1}\right) (T_{g_i} - T_g) + \Delta W_{exp} \qquad (4.60.2)$$

Therefore, the heat transfer rate is approximately

$$\dot{q}_s = \frac{\Delta Q_s}{\Delta t} \qquad (4.61)$$

In the experiments with no water the solid heat transfer area (A_s) increases with time, thus the amount of energy transferred is larger than that in the tests with water. What is assumed is that the empirical heat transfer coefficient determined by this method is valid for the SRI tests with water when the solid surface area is constant. The results of this analysis are presented in Table 4.7 along with two approximate models to account for this heat transfer rate.

The first model used to predict these results utilizes the Dittus Boelter correlation for the Nusselt number where

$$Nu = .023\ Re^{.8}\ Pr^{.4} \qquad (4.62)$$

using

$$Re = \frac{\rho_g v_{slug} D_p}{\mu_g}$$

$$Pr = \frac{c_{pg} \mu_g}{k_g}$$

The average properties during the transient were taken along with an average velocity of the slug during the experiment. This resulted in a predicted heat transfer coefficient about 50% of the empirical value utilized (Table 4.7). This lower value would be expected because the transient nature of the expansion would not give a fully developed condition near the wall where the heat transfer is taking place. Rather it would be expected that some stagnant hot zone of gas would give a higher initial temperature gradient near the wall for a higher energy transfer rate.

To investigate the possibility of a transient model a transient conduction solution between the gas and the solid wall was used. Here the assumption is the gas and solid wall behave as semi-infinite masses and conduction is the heat transfer mechanism. Carslaw and Jaeger [70] give the solution to this situation for the case of constant properties as

$$\Delta Q_s = \frac{2A_s k_s (T_I - T_s)}{\sqrt{\pi \alpha_s}} \sqrt{t} \qquad (4.63)$$

where T_s - initial solid temperature

T_I - interface temperature

$$T_I = \frac{T_g}{1+\beta} + \frac{\beta T_s}{1+\beta} \qquad (4.64)$$

$$\beta = \sqrt{\frac{k_s \rho_s c_{ps}}{k_g \rho_g c_{pg}}} \qquad (4.65)$$

The results of this model are also given in Table 4.7 and give about 60-65% of the experimental value. This model is approximately valid if the penetration depth of a transient thermal wave into the gas is of the same order of magnitude or less than the laminar sublayer of the flowing gas,

$$\sqrt{\alpha_g t} \lesssim y^+ \frac{\mu_g}{\rho_g v_*} \tag{4.66}$$

where y^+ is the dimensionless depth of the laminar sublayer [59] at a value

$$y+ = \frac{x_{lam} v_* \rho_g}{\mu_g} = x_{lam}\sqrt{\frac{\tau_o}{\rho_g}}\left(\frac{\rho_g}{\mu_g}\right) \doteq 5 \tag{4.67}$$

and τ_o - shear stress at the wall = $f \frac{\rho_g}{2} v_g^2$. If the mean properties of the transient for test AVG2 are used, it is found that

$$\sqrt{\alpha_g t} \sim 50\ \mu m$$

$$x_{lam} \sim 12\ \mu m$$

This indicates that conduction is not totally valid for the whole transient because some gas motion is expected to influence the heat transfer. Thus again this calculation is expected to be lower than the empirically found values as Table 4.7 illustrates.

These models then indicate that the solid heat transfer empirically calculated is probably due to both characteristics of a transient process and convective flow. In the subsequent transient analysis of the SRI tests containing water the empirical heat transfer coefficient values are used. However, it should be noted that the ratio of energy transferred by solid heat transfer compared to liquid heat transfer in these experiments is small (~ .05), thus any of the solid heat transfer models presented could be used without causing large errors.

4.4 Governing Equations

The heat transfer models previously described are now included into a set of governing equations to predict the transient gas expansion. The major assumptions of the model are:

1) The gas is modeled as a perfect gas with thermophysical properties listed in Appendix A.

2) The expanding gas volume is modeled as one lumped volume system (V_g) with a uniform pressure (P_g) and temperature (T_g).

The second assumption is valid because the characteristic time for a pressure signal to traverse the core (τ_t) is shorter than the expansion time of the experiment (τ_{exp}), where

$$\tau_t \simeq \frac{2l}{c_a} = \frac{2(.1m)}{\sqrt{\gamma_g R_g T_g}} \simeq .2 \text{ msec}$$

$$\tau_{exp} \simeq 2\text{-}3 \text{ msec.}$$

The acceleration of the slug mass can be described by a one-dimensional momentum equation for the planar SRI tests by

$$a = \frac{dv}{dt} = \frac{d^2x}{dt^2} = \left(\frac{P_g - P_\infty}{M_{slug}}\right) A_p \tag{4.68}$$

where

$$P_g = \frac{m_g R_g T_g}{V_g} \tag{4.69}$$

$$V_g = A_p x \tag{4.70}$$

The energy equation for this closed system is

$$\frac{dU}{dt} = \frac{dq}{dt} - \frac{dW}{dt}$$

where for a perfect gas

$$\frac{d}{dt}\left(m_g c_{v_g} (T_g - T_{ref}) + m_g u_{ref}\right) = -\dot{q}_s - \dot{q}_l - P_g \frac{dV_g}{dt}$$

$$\frac{dT_g}{dt} = \left(\frac{\gamma_g - 1}{m_g R_g}\right)\left[-\dot{q}_s - \dot{q}_l - P_g \frac{dV_g}{dt}\right] \tag{4.71}$$

The heat transfer to the solid ($\dot{q}_s$) is given by Equation 4.59. The liquid heat transfer model depending upon the level of approximation made is given by either Equation (4.52), (4.55), or (4.56). The relative gas velocity and the drop diameter used in determining the liquid heat transfer rate are given in Equations (4.49), (4.41) and (4.42). The liquid entrainment rate is given by Equation 4.13. Keep in mind that the drops are accelerated during the transient due to frictional drag according to relation (4.39) and this also must be solved as a function time.

For the two tests conducted in the scaled FFTF core (Table 4.4) the expansion characteristics are not completely one-dimensional for the initial portion of the gas expansion. As Christopher [28] indicates the reactor geometry will give a quasi-one dimensional expansion for at least 2/3 of the time to slug impact although the first portion is more spherical in nature. Thus, the tests in the FFTF geometry are analyzed in two ways. The one dimensional model presented is used with the projected area being the total area of the vessel (A_v). The second model developed with the aid of Mikic [71] is based on the concept of a quasi-spherical momentum equation (Figure 4.6). The acceleration of the slug of water above the gas bubble is given by

$$\frac{dv_{slug}}{dt} = \frac{(P_g - P_\infty)}{M_{slug}} A_b \tag{4.72}$$

During the transient the rate of volumetric flow of the gas and water is equal, thus

$$v_{slug} A_v = \frac{dR}{dt} A_b \tag{4.73}$$

where the area of the bubble (A_b) pushing against the water slug is

$$A_b = \left(\frac{R}{R_o}\right)^m A_p \tag{4.74}$$

A_p - original core area

R_o - equivalent radius of bubble of Volume $V_{g_i} = \cdot\frac{75}{\pi} (V_{g_i})^{\frac{1}{3}}$

The expression of Equation 4.73 with 4.74 inserted is differentiated giving

$$\frac{dv}{dt}_{slug} = \frac{A_p}{A_v} \left(\ddot{R}\left(\frac{R}{R_o}\right)^m + \frac{(\dot{R})^2 m}{R_o} \left(\frac{R}{R_o}\right)^{m-1}\right)$$

and the acceleration is also equal to

$$\frac{dv}{dt}_{slug} = \frac{(P_g - P_\infty)}{M_{slug}} A_p \left(\frac{R}{R_o}\right)^m \tag{4.72}$$

If these are equated and $\ddot{R}$ is solved for, the result is

$$\ddot{R} = \frac{(P_g - P_\infty)}{M_{slug}} A_p - \frac{m(\dot{R})^2}{R} \tag{4.75}$$

This is approximately the form of the Rayliegh equation for the growth of a spherically symmetric bubble in an infinite medium. The empirical coefficient m is determined such that the two physical limits on A_b are maintained

$$A_p \leq A_b \leq A_v \tag{4.76}$$

The behavior of equation is like the bubble growth equation in that as the bubble velocity ($\dot{R}$) increases, the acceleration falls to zero and becomes negative. This equation is used to model the initial expansion of the FFTF scaled SRI tests to compare to the one-dimensional model. If the pressure-volume characteristics are similar, then it appears the one dimensional model is apprxoimately valid for the initial volume expansion of the gas in these tests.

It should be noted that only the third approximate model for the liquid heat transfer can be used with this model because the linear model for relative velocity is not valid here. The relative velocity here can be approximated by $v_{rel} \sim \sqrt{a\lambda_c}$ to get an estimate of the heat transfer coefficient and drop diameter.

This system of non-linear first order differential equations in time are solved by utilizing an numerical integration technique known as a "modified Euler predictor-corrector" integration scheme. This solution technique is incorporated as a Library subroutine for the MIT IBM 370/168 computer. A more detailed explanation of its use along with a flow chart to describe the averaging logic for the relative velocity and drop diameter is given in Appendix F. Because this system of equations has the mathematical characteristic that all the dependent variables of time change nearly at the same rate (non-stiff system), this standard integration technique could be used. The results of these calculations in comparison to experimental results are presented in the following section.

4.5 Comparison of the Models to Experimental Results

The SRI experiments in the one dimensional geometry investigated the effects of three main variables; water depth, initial pressure, mass of the slug. The effect of water depth can be briefly illustrated in Figure 4.7. As the water depth is increased from .5 - 1.5 inches, the gas expansion work decreases markedly, from near isentropic values to 50% less for depths greater than 1.5 inches. Given the model of Taylor Instabilities there is a characteristic depth of water penetration that will be entrained in the gas through the expansion. This can be estimated by

$$\Delta d \simeq 4.65 \sqrt{\bar{a}\lambda_c}\ \tau_{exp} \tag{4.77}$$

For the tests in Figure 4.7 using PETN changes of 8 gms, the characteristic $\bar{a}$ and λ_c are

$$\bar{a} \doteq \frac{1}{2}\left(\frac{215(10^5)(.0045)}{1.348}\right) \simeq 3(10^4)\text{m/s}^2$$

$$\lambda_c = 2\pi\sqrt{\frac{.073}{30000(1000)}} = 200\mu\text{m}$$

The penetration depth of the instability is, for $\tau_{exp} \sim 2$ msec, $\Delta d \sim 1$ inch. This then suggests that the observed decrease, in the gas work for the range $.5 < \Delta d < 1.5$ inches, is related to this entrainment behavior. In fact, the entrainment early in the expansion is more important because the temperature is higher and the droplets are in the gas stream for the whole transient. This would justify the marked decrease in ΔW which occurs before $\Delta d \sim 1$ inch as shown in Figure 4.7.

Now let us consider the results for the average of three tests for fixed initial pressure AVG 2, illustrated in Figures 4.8, 4.9, 4.10, and 4.11. The experimental results are illustrated by the triangles with a 10% experimental error band as reported by SRI. The pressure at the end of the expansion ($V_g/V_{g_i} \simeq 3.14$) which corresponds to FFTF slug impact (Figure 4.8) is more than three times less than that for the no water tests (15 bars vs. 48). This indicates two facts: (1) The gas work output ($\int pdV$) is reduced by 50%; (2) The internal energy of the gas ($\Delta U \simeq m_g c_{v_g} \Delta T$) is much lower suggesting a large amount of liquid heat transfer ($\Delta Q_l \sim 18$ kw-s). Two of the liquid heat transfer models are shown to indicate the prediction of the volume and pressure behavior of the test. One is the convective mixing model developed previously by Corradini and Sonin [56] and the other is the rate model 2 using a constant drop diameter. Both models show good agreement with the data, and an empirical constant ($C_o = .75$) is used in the convective mixing model to quantitatively match the data. In the case of the rate model, the

the drop diameter empirically chosen was between the two physical bounds of the Weber drop size and the fastest growing Taylor wavelength (λ_m) for an average acceleration.

Figure 4.10 gives the experimental values for the gas expansion work and the predictions using all four of the liquid heat transfer models. Again all four models show good qualitative agreement with the data; however, the difference between them lies in the degree of empiricism needed to quantitatively match the data. The convective mixing model is empirically fit to the data by C_o and the bounds on the value for C_o are known over an order of magnitude ($.05 < C_o < 1$). The qualitative shape of the mixing model matches very well with experiments, and this seems to indicate that the heat transfer rate is largest at the beginning of the transient when the gas temperature is high and the entrainment rate is large. The rate model 3 using the constant heat transfer coefficient ($\bar{h}$) and diameter (D_d) is also empirically fit to the data with the relative velocity and diameter being estimated between known physical bounds. Again these bounds can be larger than an order of magnitude in cumulative effect. In addition, the shape of the gas work plot shows a higher work at small volumes, indicating that the heat transfer rate is lower than that occurring in the experiment at low V_g/V_{g_i}. This is due to the fact that the heat transfer coefficient is assumed to be constant, and thus at early times will underestimate the heat transfer rate and at long times overestimate it. The inclusion of a variable heat transfer rate with a constant diameter (D_d = 450 μm) correct most of this behavior as rate model 2 indicates. The range of physical bounds on the diameter of the Weber number and Taylor fastest growing wavelength (λ_m) is smaller, and the qualitative shape of the gas work plot is closer to experimental values at small volumes. The least approximate rate model 1 incorporates a variable drop diameter where

the characteristic Weber number (We = 34) is chosen to quantitatively fit the data. This model exhibits the best qualitative fit to the data. The characteristic Weber number is greater than the critical value and corresponds to a drop diameter in the range of the Taylor Instability wavelengths of $\lambda_c < D_d < \lambda_m$. To demonstrate these bounds the gas work is predicted using these two limits for the drop diameter in rate model 1, and is illustrated in Figure 4.11. The experimental data from both the 1/30 scale and 1/10 scale tests (reduced by a factor of $27 = (3)^3$) are seen to be bounded by these two limits on the drop diameter.

As the initial pressure is changed, the prediction of the gas work using the liquid heat transfer models exhibit the same trends as in the tests, AVG2. Three other initial pressures were tested as Table 4.4 indicates. For experiment A132 (Figure 4.12), the gas work data are shown with the predictions utilizing all the liquid heat transfer models. Again the same behavior as in AVG2 is observed. In this case, the more exact rate model 1 matches the data again for a constant characteristic Weber No. (We - 70) that corresponds to a drop diameter in the range of $\lambda_c < D_d < \lambda_m$. This is shown more clearly in Figure 4.13 where the two bounding cases of $D_d = \lambda_c$ and $D_d = \lambda_m$ are used to bracket the experimental work. A similar result is true for test A134 for both the 1/30 and 1/10 scales as Figure 4.14 indicates. It should be noted that the agreement between the experiments at different scales is the poorest for A134. Cagliostro [69] suggested that this may be due to some undetected experimental error, perhaps in the chemical reaction because the experimental deviation is greater than the 10% reproducibility margin exhibited in all other experiments. Experiment A143 gas work is also modeled quite well by the analysis using the liquid heat transfer models as Figure 4.15 depicts.

The worst agreement occurs when a constant heat transfer coefficient and diameter are used in rate model 3 and the best agreement occurs using model 1. Figure 4.16 depicts model 1 results using the bounds on drop diameter, $\lambda_c = D_d$ and $\lambda_m = D_d$, and again the data falls within this range. A summary of the empirical constants, for the convective mixing model and the characteristic Weber numbers, indicating $\lambda_c < D_d < \lambda_m$ for rate model #1, is presented in Figure 4.17.

SRI tests were also conducted to observe the effect of the mass of the piston slug (Table 4.4). As the mass increases, the acceleration decreases extending the time of the transient expansion (τ_{exp}). When this occurs, more energy can be dissipated as heat transferred to the coolant, and ΔW decreases as the experimental data shows on Figure 4.18. The gas work predictions for three liquid heat transfer models are also shown in the plot. The convective mixing model shows good agreement as does the rate model .2 for the constant diameter ($D_d \sim 450$ μm). What is again shown is that by using rate model .1, the experimental work data and the other model predictions are bracketed by the results for $D_d = \lambda_c$ and $D_d = \lambda_m$. Thus for all the one dimensional tests the forced convection rate model 1 can be used in the transient analysis to predict the gas work knowing that the characteristic drop diameters lie within the range of $\lambda_c < D_d < \lambda_m$.

One question that could be raised is why in our analysis we assume that the drop born at a size between λ_c and λ_m does not breakup due to Weber forces during the transient? All the tests indicated that the characteristic sizes of the water drop were between λ_c and λ_m but all had Weber numbers (see Figure 4.17) greater than We_{crit}. One reason for this result is that although $We > We_{crit}$, the characteristic time for droplet breakup (τ_{br}) is of the same order of magnitude as the expansion time of the experiments;

the majority of the drops do not breakup. Sonin [67] has suggested that the characteristic time for breakup can be modeled as

$$\tau_{br} = C \frac{D_d}{v_{rel}} \sqrt{\frac{\rho_l}{\rho_g 2C_D}} \qquad (4.78)$$

where C is a proportionality constant and where C_D is the drag coefficient for a drop ~ .5. Gordon [66] derived a quantity similar to this and noted that although this equation reflects the dependencies for the breakup time, the actual characteristic time could be an order of magnitude larger (C ~ 10). The reason for this value was that although the drop begins to deform in a time coincident with C=1, the whole breakup process will take much longer. How much longer is dependent on the breakup process and on magnitude of the Weber number. Gordon suggests that C could be as large as 10. This value for τ_{br} was calculated for a number of these experiments and are shown in Table 4.8. Two different relative velocities are used, the first being at the beginning of the transient when v_{rel} is near a maximum and the second being at the middle of the transient when v_{rel} is smaller. The diameter used is the average value for each test. This calculation indicates that the characteristic time for breakup is indeed of the same order of magnitude as the expansion time for the large relative velocity if C ~ 10. More important, regardless of the proportionality constant for the small v_{rel} which occurs for at least half of the expansion, the table indicates that perhaps the needed breakup time is not afforded during the transient tests.

The only test reported for the FFTF geometry scale was Test 180 which duplicated the initial conditions of Tests AVG2. The experimental results are illustrated in Figures 4.19 and 4.20 for volume as a function of time and the gas expansion work. Both the spherical and one dimensional models are used to predict the results using the convective mixing model and the forced convection rate model 3. All the models show good agreement although

the same behavior for a constant heat transfer coefficient and drop diameter is shown here where the initial heat transfer rate is lower than the experiment. The ratio of $\bar{h}/D_d$ for the spherical and one dimensional models differ slightly because the average acceleration in each case is different over the transient. The spherical expansion has a smaller acceleration because the bubble velocity reduces the value as time progresses. This in turn reduces the relative velocity and increases the characteristic drop diameter, since the $\bar{h}/D_d$ ratio from Equation 4.56 has the dependence of

$$\bar{h}/D_d \sim v_{rel}^{.6}/D_d^{1.4}.$$

This constant term will decrease a small amount to quantitatively match the experimental data. No other scale tests were reported in detail by SRI; however, the gas work at slug impact from two other scale tests CM-30-1 and 2 were given in the final report [24], and the results are shown on the plot. Test CM-30-2 reported a gas work of 3.7 kw-s at slug impact and this large deviation from other experimental results was not accounted for by Cagliostro [24]. It appears though that the one dimensional model does a good job of predicting this gas expansion, even though the initial volume expansion may be more spherical than one dimensional in nature.

The final point to emphasize is that the ratio of the energy transferred to the liquid in comparison to the energy transferred to the solid structure is large. Figure 4.21 and 4.22 gives representative values for the SRI tests AVG2. As can be seen, the energy transferred to the liquid is more than ten times as large as that to the solid. Thus the rate model used to describe the solid heat transfer has a small effect on the results.

The conclusion then from the analysis of SRI noncondensible heated experiments is that the Taylor instability mechanism appears to be the dominant mechanism for liquid entrainment, and in determining the size of

the entrained droplets. In addition, rate model 1 can best predict the experimental results of the tests for $\lambda_c < D_d < \lambda_m$.

TABLE 4.1

SUMMARY OF SRI 1/30 SCALE - PLANAR SOURCE CALIBRATION TESTS

Test	Charge Mass (g)	Water Height (in)	Water Mass	Projectile Mass (g)	Total Mass	Initial Volume (cm^3)	Remarks
A115	8	0	0	1,014	1,014	225	
A117	8	0.04	6	1,000	1,006	225	
A118	8	1.0	116	1,000	1,116	225	
A119	8	4.0	463	1,000	1,463	225	
A120	8	6.0	695	1,000	1,695	225	
A121	8	3.0	348	1,000	1,348	225	1-mil Mylar sheet on water
A122	8	3.0	348	1,000	1,348	225	
A123	8	3.0	348	1,000	1,348	225	1-mil Mylar sheet on water
A124	8	3.0	348	1,000	1,348	225	
A125	8	3.0	348	1,000	1,348	225	
A126	8	0.5	58	1,000	1,058	225	
A127	8	3.0	348	4,638	4,986	225	
A128	8	3.0	348	670	1,018	225	
A129	8	3.8*	78	1,679	2,718	225	* dia - 3/16"
A130	8	0	0	670	670	225	
A131	8	0	0	4,638	4,638	225	
A132	16	3	348	1,000	1,348	237	
A133	16	0	0	1,000	1,000	237	
A134	14	3	348	1,000	1,348	229	
A135	8	3	348	410	758	225	
A136	8	0	0	424	424	225	
A137	8	0	0	1,679	2,640	305	3" of (dia - 3/16")
A139	8	0	0	1,000	1,000	225	
A140	8	3	348	1,000	1,348	225	No pressure data available
A141	2	0	0	4,638	4,638	225	
A142	2	3	348	4,638	4,986	225	
A143	2	3	348	1,000	1,348	225	
A144	4	0.25	29	1,000	1,029	225	
A145	8	0	0	1,000	1,000	225	
A146	8	3	348	410	758	225	
A147	8	0	0	424	424	225	
A148	14	0	0	1,000	1,000	229	

* Steel balls

TABLE 4.2

SUMMARY OF SRI 1/10 SCALE - PLANAR SOURCE CALIBRATION TESTS

Test	Charge Mass (g)	Water Height (in.)	Water Mass (g)	Projectile Mass (g)	Total Mass (g)	Initial Volume (cm^3)
B101	216	9	9,380	27,480	36,860	6,026
B102	216	9	9,380	27,480	36,860	6,026
B103	216	9	9,380	27,480	36,860	6,026+
B104	216	12	12,510	27,480	39,990	6,026
B105	216	1.5	1,560	27,620	29,180	6,026
B106	216	0	0	27,620	27,620	6,026
B107	216	9*	2,100	37,850	72,150	6,070&
B108	216	9	9,380	10,690	20,070	6,026
B109	216	0	0	10,830	10,830	6,026
B110	378	9	9,380	27,530	36,910	6,026
B111	378	0	0	27,690	27,690	6,026
B112	378	9	9,380	27,530	36,910	6,026

* Steel balls

+ 3-mil Mylar sheet on water

& Steel balls diameter - 9/16"

TABLE 4.3

SUMMARY OF SRI 1/30 - 3D SCALED FFTF SOURCE CALIBRATION TESTS

TEST #	SCALE	GAS WORK (kw-s)	COMMENTS
180	1/30	2.98	Rigid models; only core and water slug
196	1/10	2.93 $(\frac{1}{27})$	
CM-30-1	1/30	2.83	Complex models with simulated structure and reactor vessel head in place
CM-30-2	1/30	3.7	

TABLE 4.4

INITIAL CONDITIONS OF THE SRI EXPERIMENTS ANALYZED

TEST NO.	SCALE	P_{g_i} (MPa)	V_{g_i} (cc)	m_g (gm)	M_{slug} (gm)	WATER DEPTH (cm)
A122						
A123 AVG2	1-D-1/30	21.5	225	5.5	1,348	7.62
A123 A143	1-D-1/30	10.6	225	2.9	1,348	7.62
A134	1-D-1/30	35.5	225	9.4	1,348	7.62
A132	1-D-1/30	41.2	237	10.7	1,348	7.62
B102	1-D-1/10	21.5	$225x(3)^3$	$5.5x(3)^3$	$1,348x(3)^3$	7.62x(3)
B112	1-D-1/10	35.5	$225x(3)^3$	$9.4x(3)^3$	$1,348x(3)^3$	7.62x(3)
A119	1-D-1/30	21.5	225	5.5	1,463	10.16
A120	1-D-1/30	21.5	225	5.5	1,695	15.24
A127	1-D-1/30	21.5	225	5.5	4,638	7.62
A182	1-D-1/30	21.5	225	5.5	1,018	7.62
A135	1-D-1/30	21.5	225	5.5	765	7.62
AVG1	1-D-1/30	21.5	225	5.5	1,000	0
A130	1-D-1/30	21.5	225	5.5	1,000	0
A136	1-D-1/30	21.5	225	5.5	1,000	0
A148	1-D-1/30	41.0	225	9.4	1,000	0
A133	1-D-1/30	41.8	237	10.7	1,000	0
180	FFTF 1/30	21.5	225	5.5	UPPER PLENUM	
CM-30-1,2	FFTF 1/30	21.5	225	5.5	UPPER PLENUM	

TABLE 4.5

ORDER OF MAGNITUDE ESTIMATE OF GAS HEAT FLUXES

		RADIATION		CONVECTION	
TEST #	TEMP. (^{o}K)	ε_r	$\dot{q}/A$ (w/m^2)	Nu	$\dot{q}/A$ (w/m^2)
AVG2	3050	.56	2.4 (10^6)	21	45 (10^6)
A132	3005	.62	2.8 (10^6)	29	86 (10^6)
A134	2945	.62	2.6 (10^6)	27	73 (10^6)
A143	2850	.34	1.2 (10^6)	17	24 (10^6)

TABLE 4.6

VAPORIZATION POTENTIAL OF WATER*

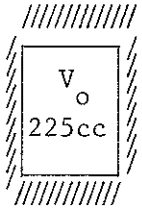

P_{g_i} - 21.5 MPa

T_{g_i} - 3050°K TESTS: AVG2

m_g - .0055 kg

m_w/m_g	X_w	T_e/T_{g_i}	P_e/P_{g_i}
0	1	1	1
.01	1	.98	1.005
.05	1	.95	1.025
.1	1	.90	1.05
.5	1	.83	1.09
1	1	.48	1.25
2	.99	.21	.92
3	.4	.18	.53
5	.057	.16	.23

* assumed $T_{crit_w} = 648°K$

u_{g_w} - $2.07(10^6)$ w-s/kg

u_{fg_w} - 462 w-s/kg

γ_w - 1.3

TABLE 4.7

COMPARISON OF SOLID HEAT TRANSFER PREDICTIONS TO EXPERIMENTAL DATA

TEST # NO WATER	$\bar{h}$ EMPIRICAL ($\frac{w}{m^2\ ^oK}$)	ΔQ_s EXPERIMENT (kw-s)	ΔQ_s TRANSIENT COND. MODEL (kw-s)	$\bar{h}$ DITTUS BOELTER ($\frac{w}{m^2\ ^oK}$)	ΔQ_s FORCED CONV. MODEL (kw-s)
AVG 1	6000	4.5	2.7	3000	2.3
A130	6000	4.2	2.7	3000	2.3
A136	6000	4.2	2.7	3000	2.3
A148	6500	7.2	4.3	3500	3.6
A133	7000	7.4	4.9	3500	4.2

TABLE 4.8

CALCULATED DROPLET BREAKUP TIMES

TEST	v_{rel}	D_d	τ_{br}^{*} (msec)	$\tau_{br}^{\#}$ (msec)	τ_{exp} (msec)
AVG2	17.7m/s	450μm	.2	2.0	2.25
	2 m/s		1.83	18.3	
A132	21.0	320μm	.087	.87	1.65
	3		.61	6.1	
A143	14.8	700μm	.514	5.14	3.42
	1.5		5.08	50.8	

* C= 1

C= 10

FIGURE 4.1

RIGID PISTON-CYLINDER APPARATUS FOR SRI SOURCE CALIBRATION TESTS

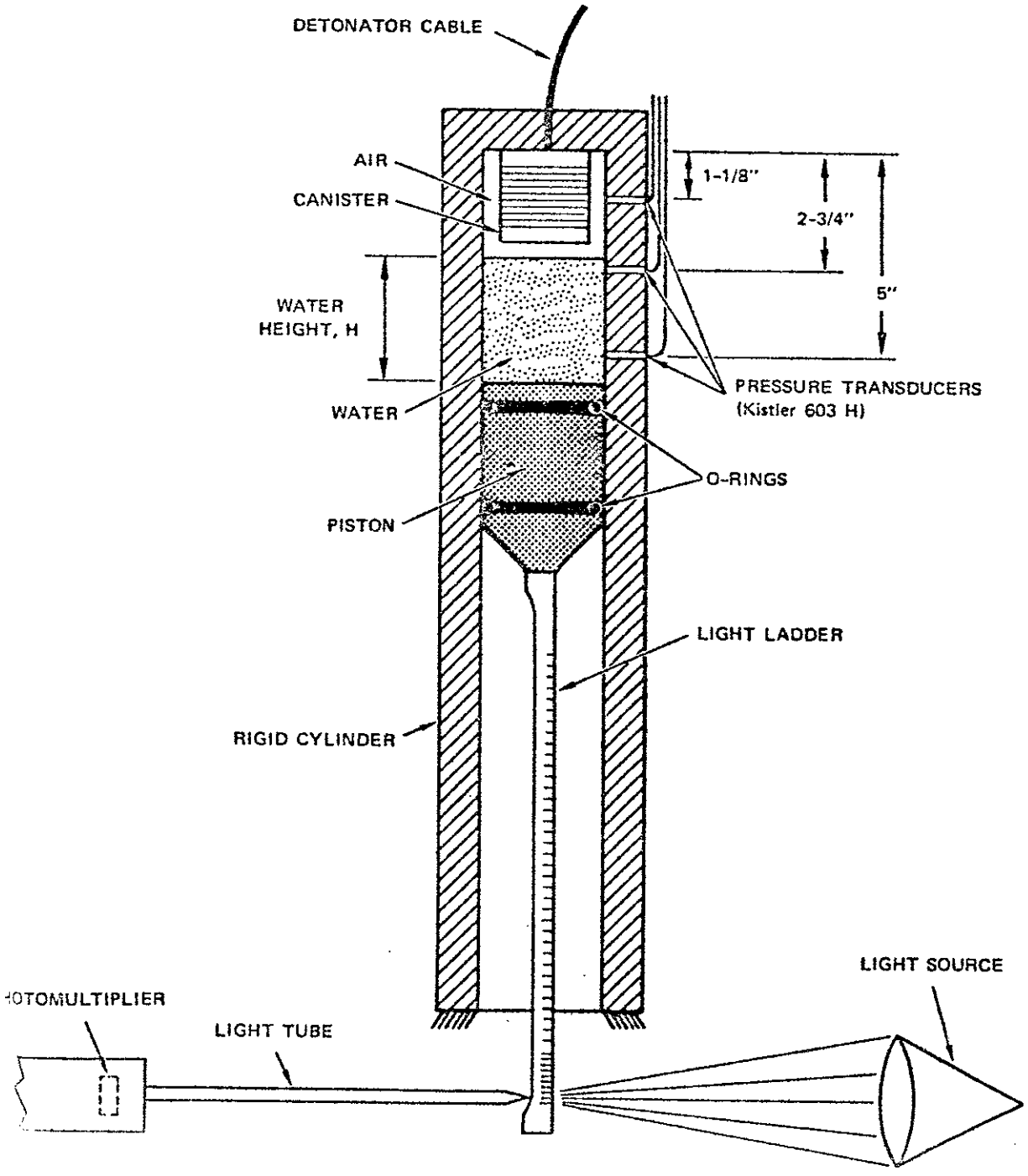

FIGURE 4.2

RIGID FFTF SCALE MODEL (1/30) FOR SRI SOURCE CALIBRATION TESTS

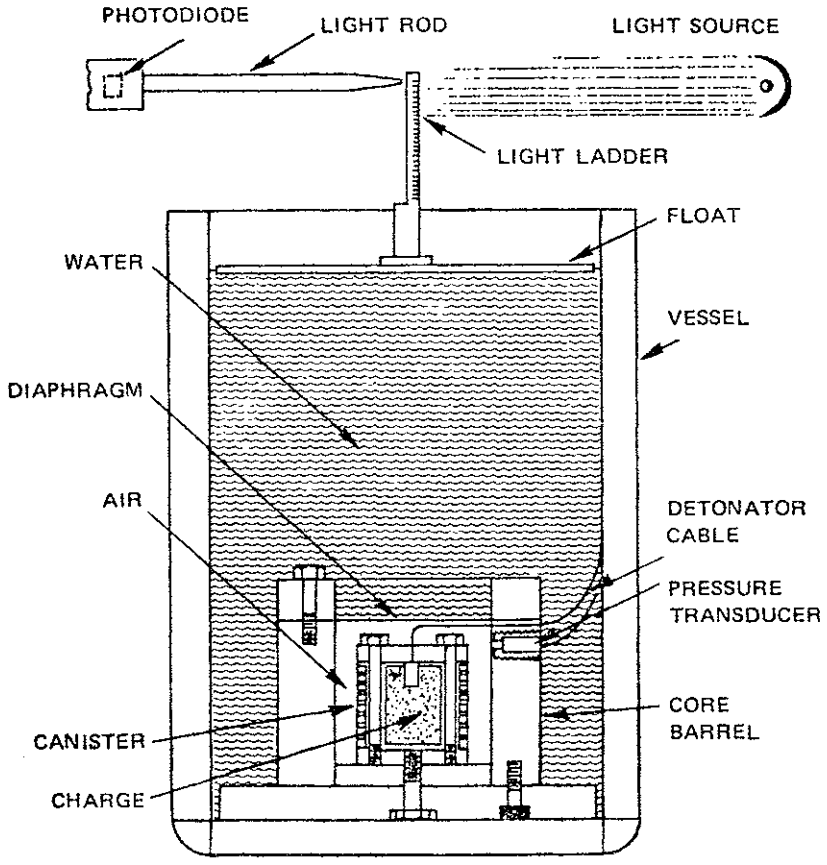

FIGURE 4.3

TIME-SMOOTHING PLOT USED TO DETERMINE INITIAL CONDITIONS

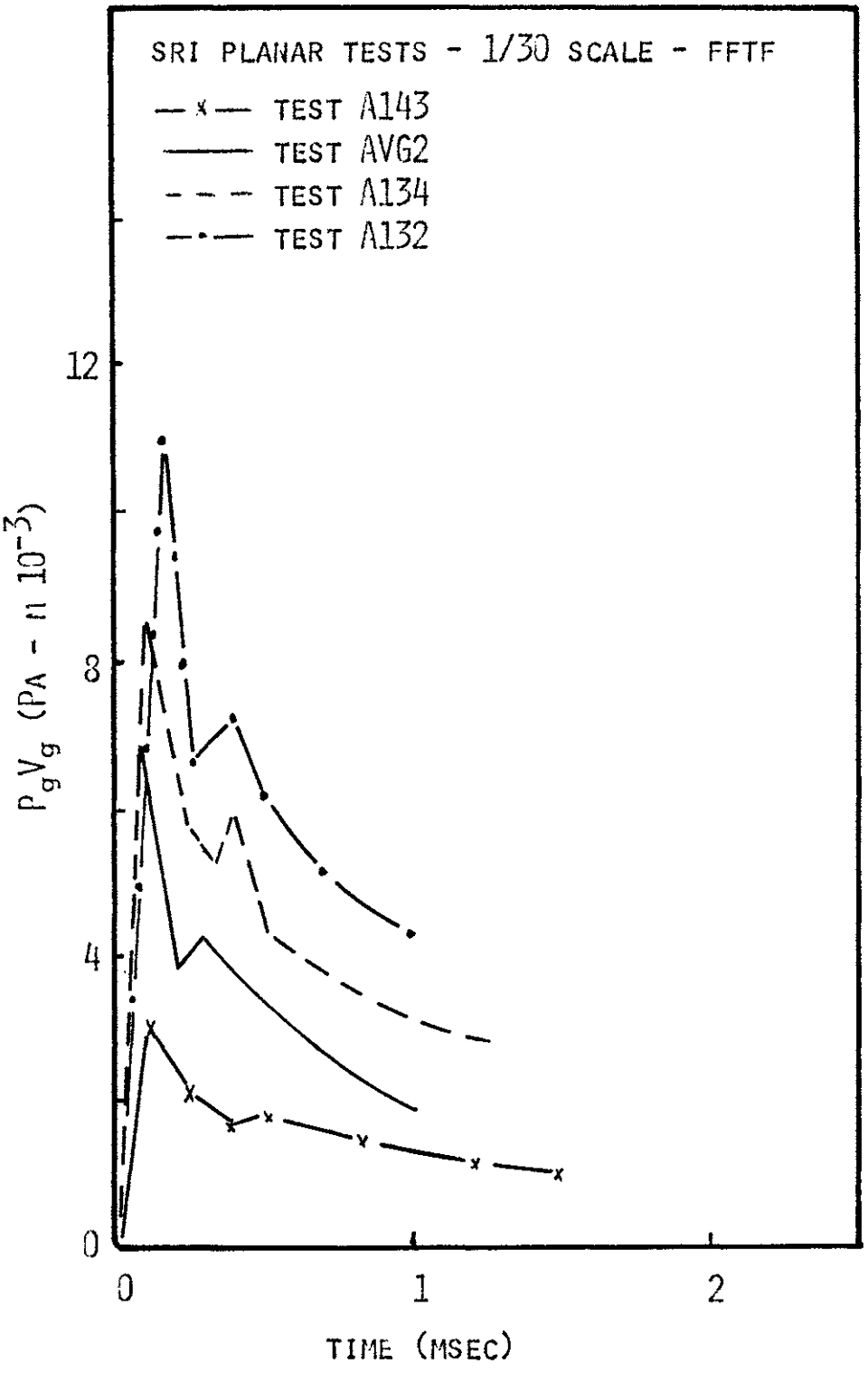

FIGURE 4.4

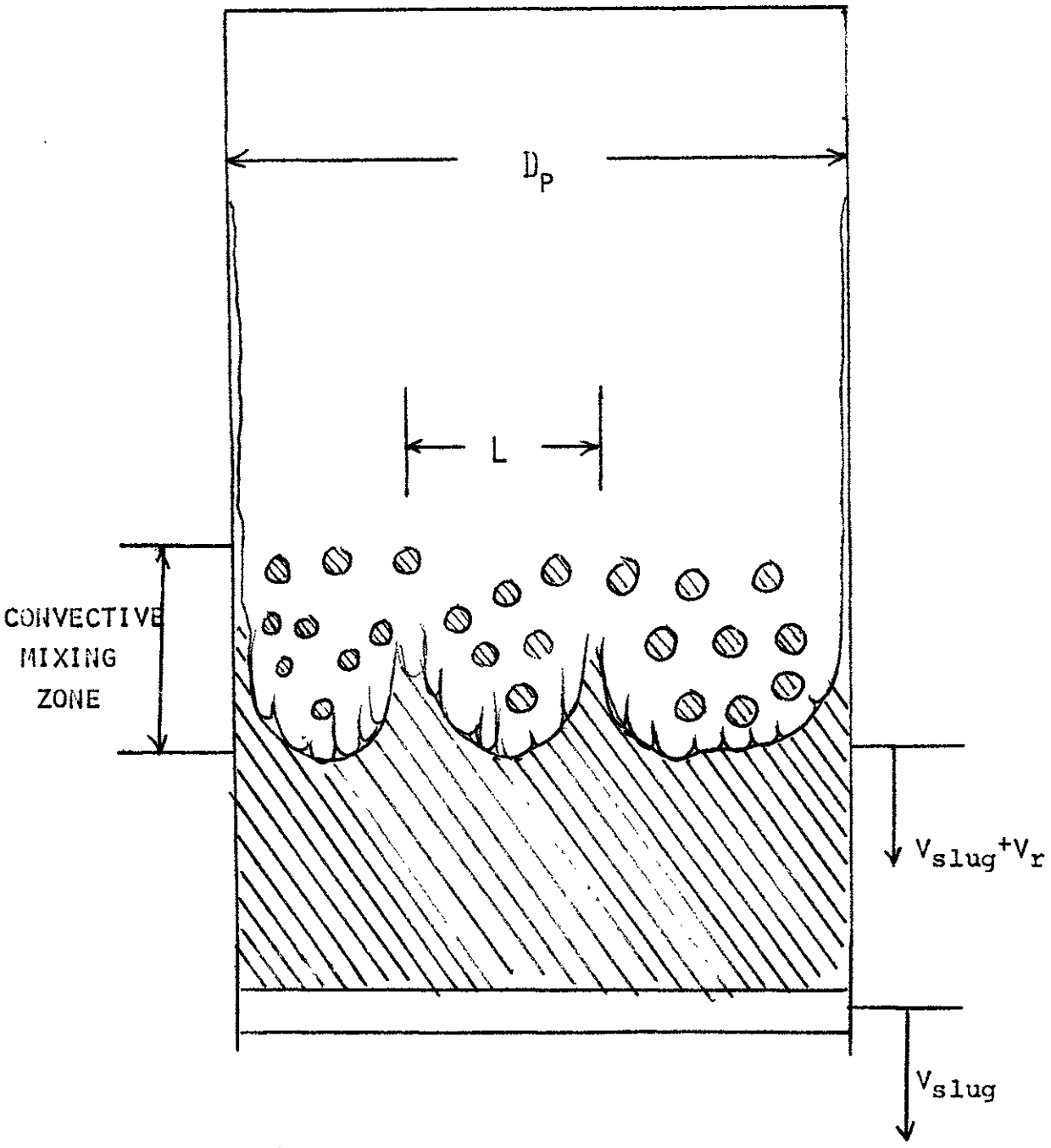

$$V_r \sim \sqrt{a_L}$$

$$L = K D_P$$

CONCEPTUAL VIEW OF THE CONVECTIVE MIXING MODEL

FIGURE 4.5

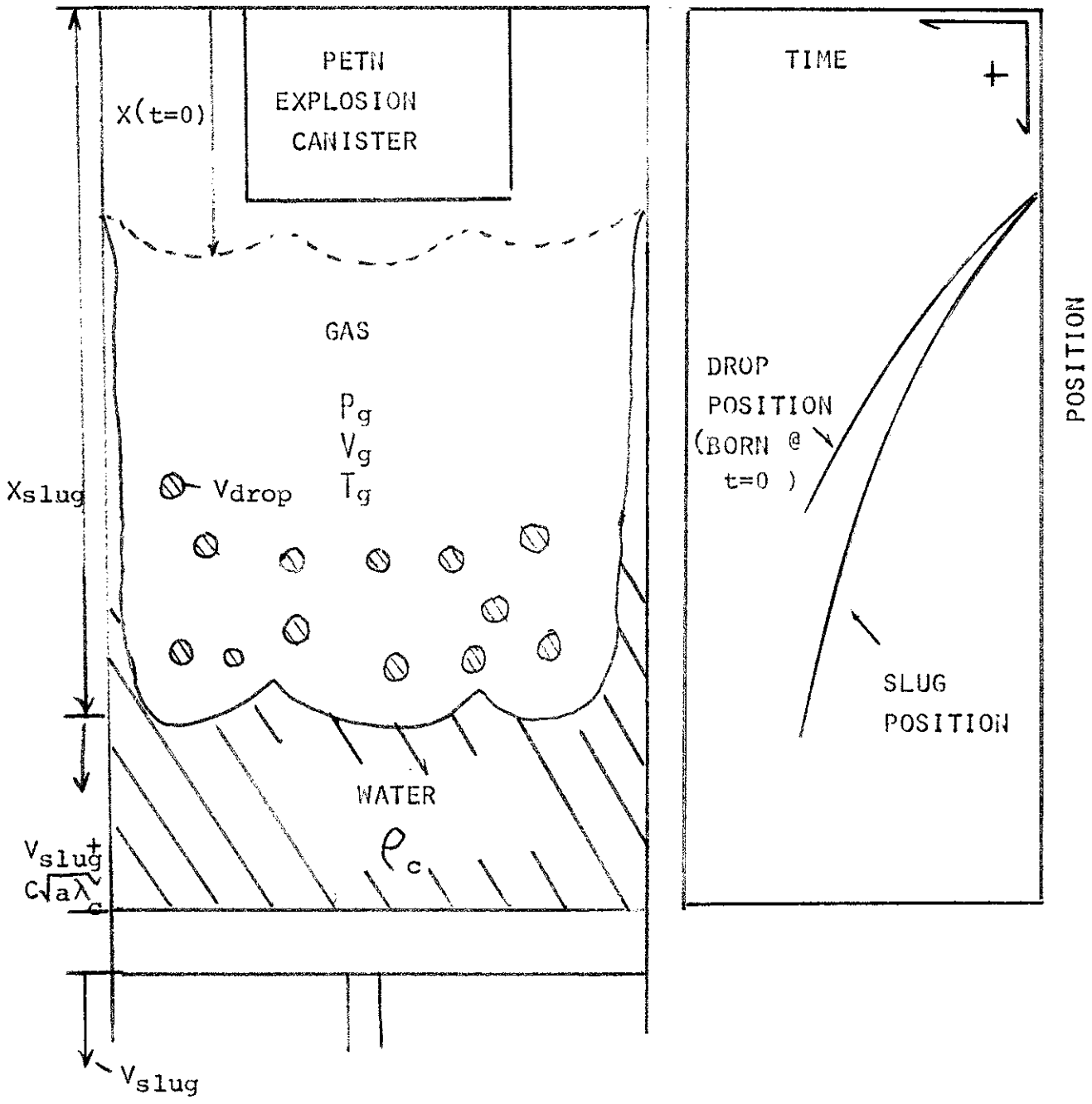

CONCEPTUAL VIEW OF FORCED CONVECTION HEAT TRANSFER MODEL

FIGURE 4.6

CONCEPTUAL VIEW OF FORCED CONVECTION HEAT TRANSFER IN THE EXPANDING BUBBLE

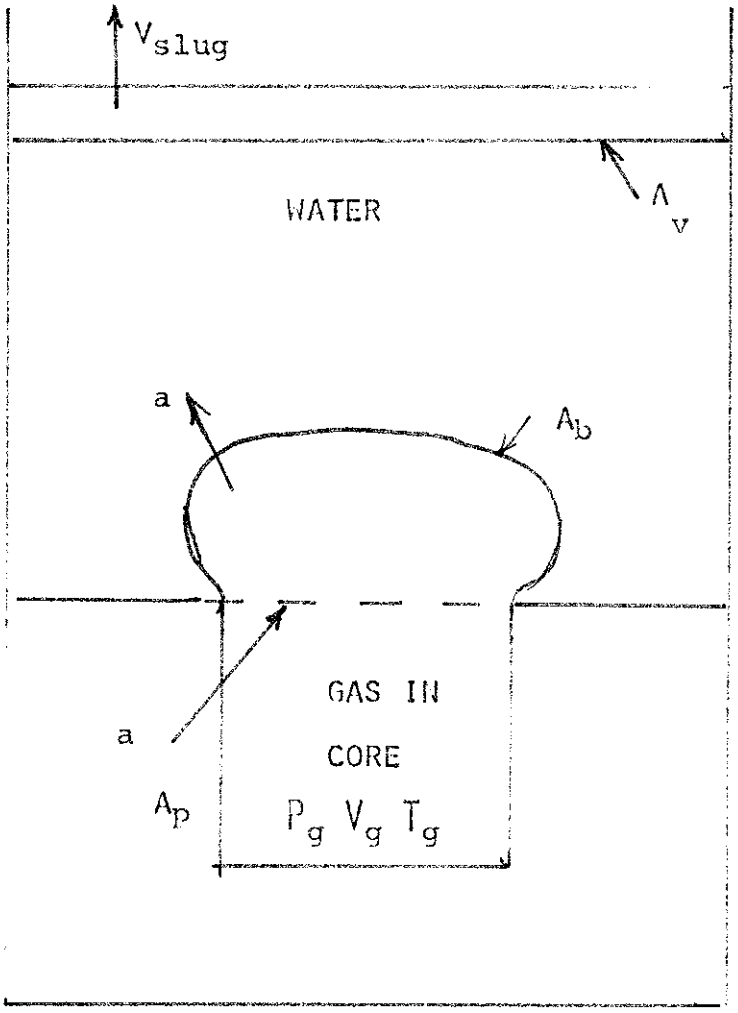

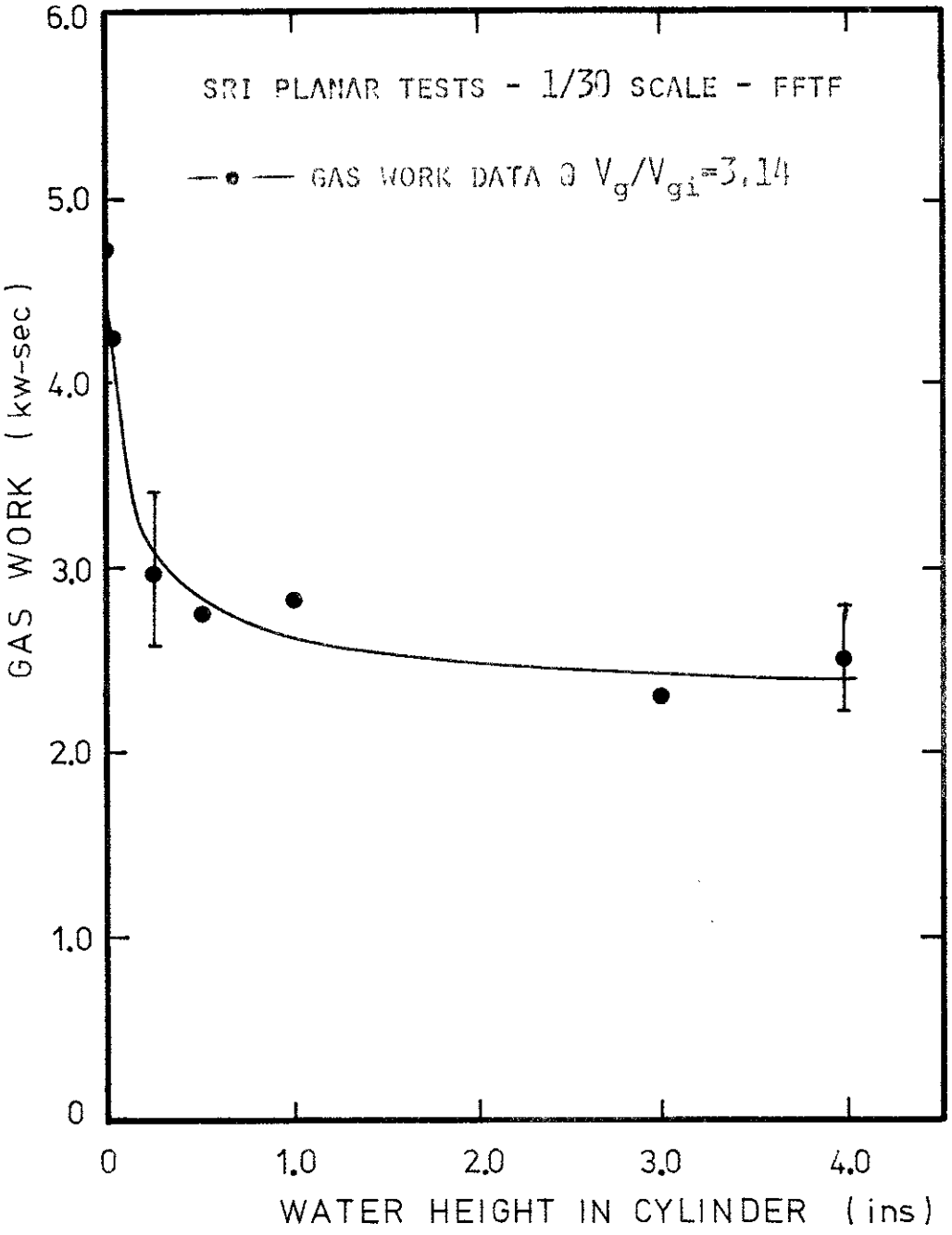

FIGURE 4.7 BEHAVIOR OF THE GAS WORK WITH A VARIATION OF THE COOLANT WATER DEPTH

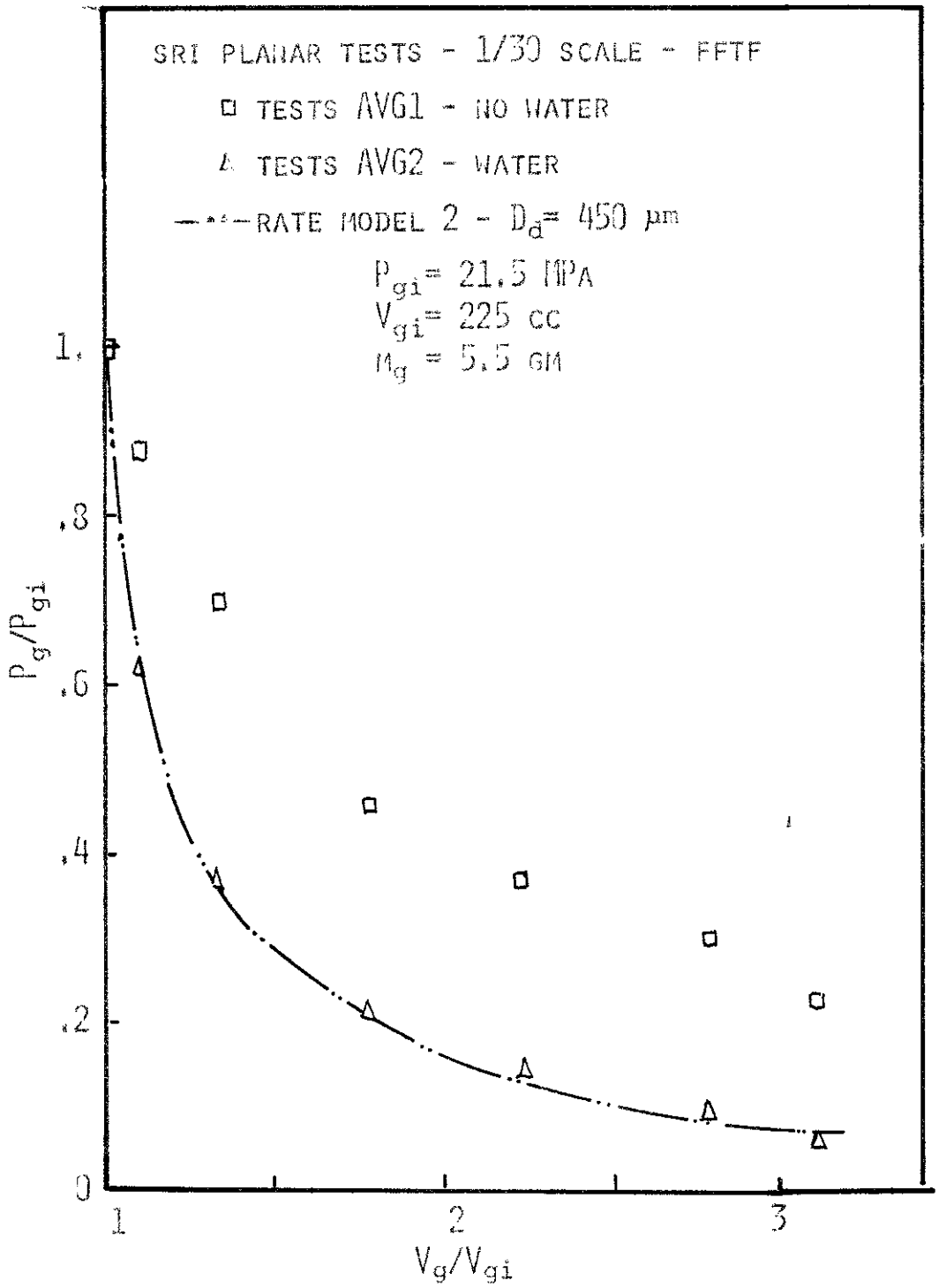

FIGURE 4.8 TESTS AVG2 TRANSIENT BEHAVIOR OF THE GAS PRESSURE

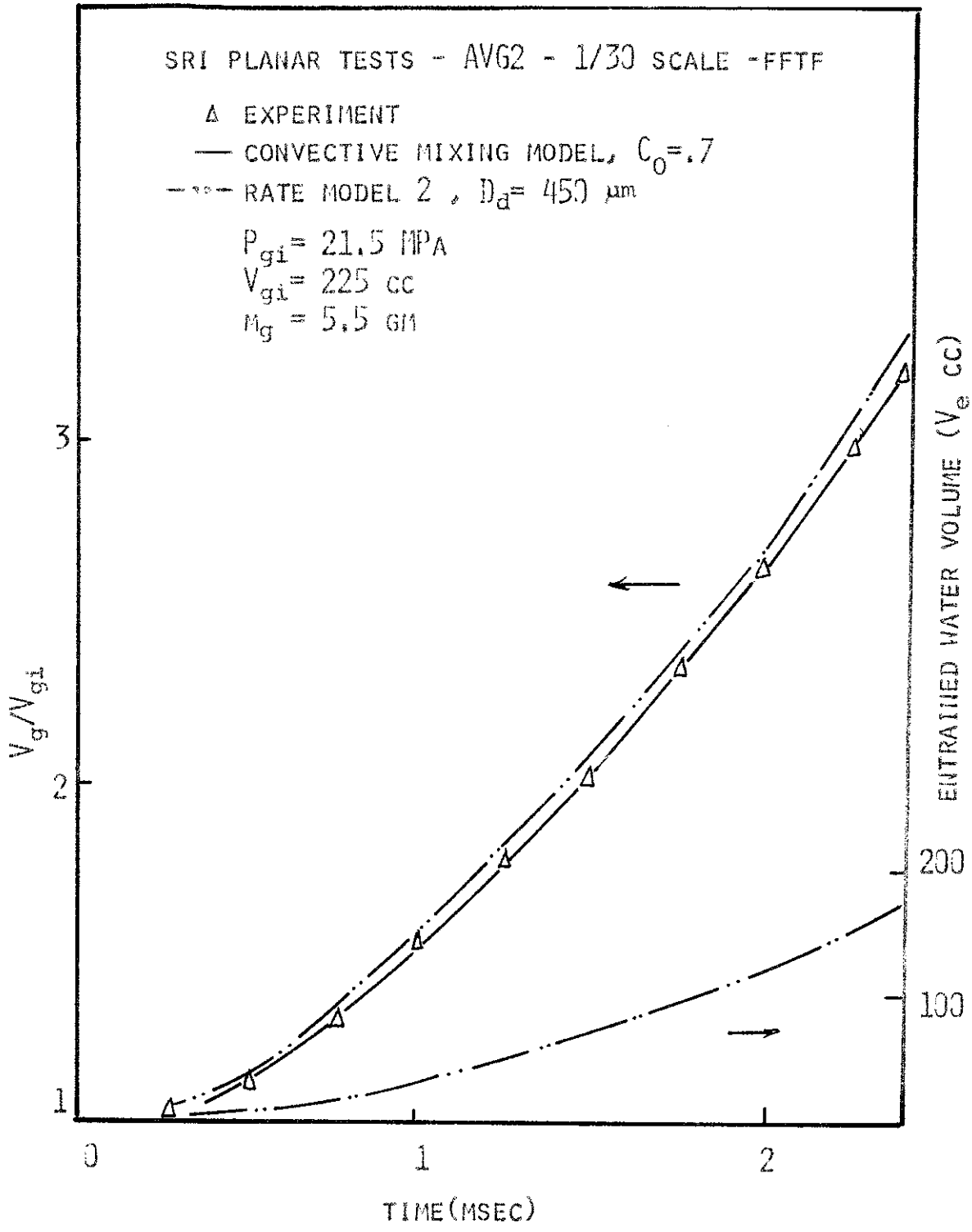

FIGURE 4.9 TESTS AVG2 EXPANSION BEHAVIOR OF THE GAS VOLUME

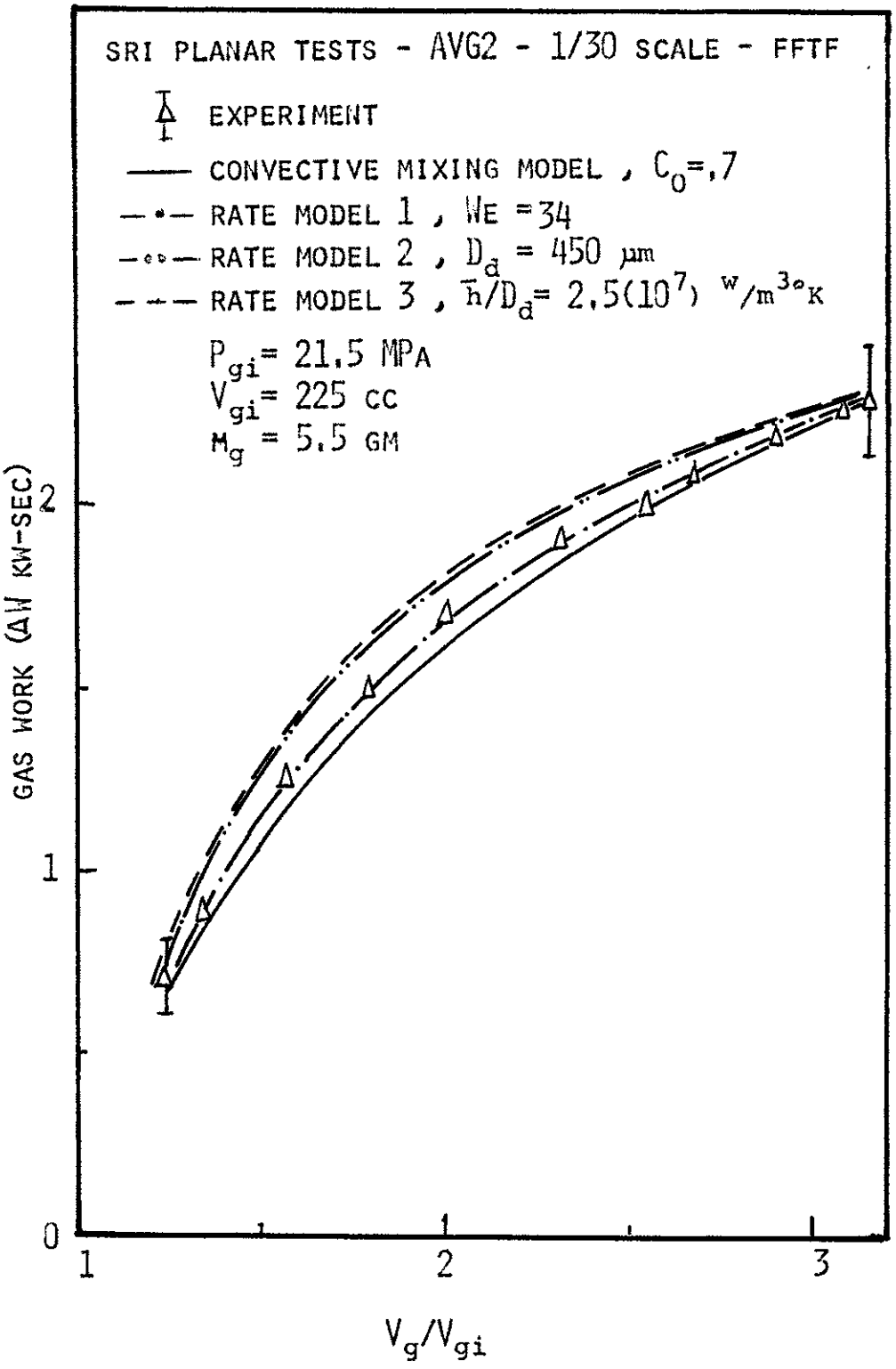

FIGURE 4.10 TESTS AVG2 EXPANSION GAS WORK COMPARISON

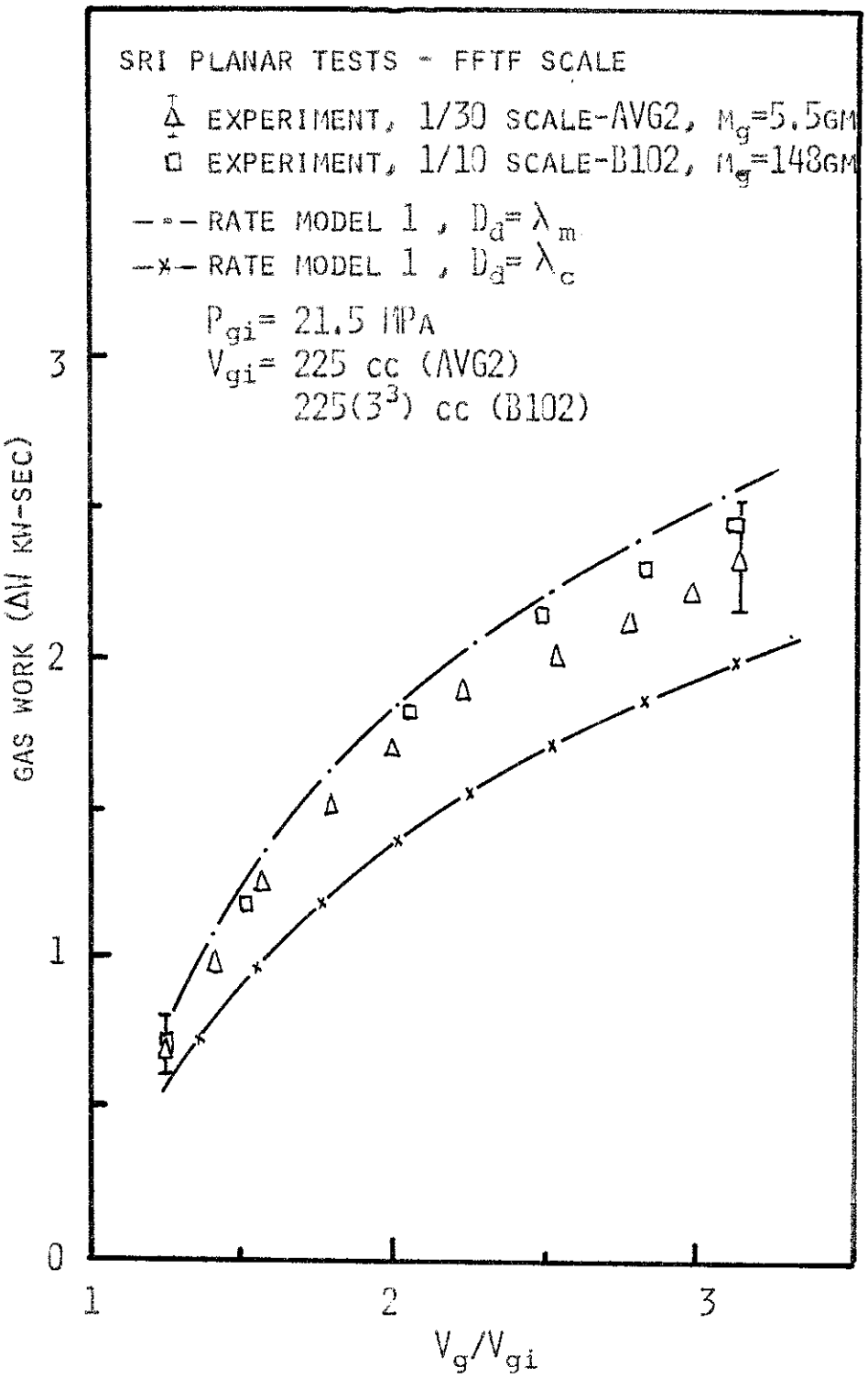

FIGURE 4.11 TESTS AVG2 EXPANSION GAS WORK COMPARED TO THE PREDICTION USING RATE MODEL 1 WITH $\lambda_c < D_d < \lambda_m$

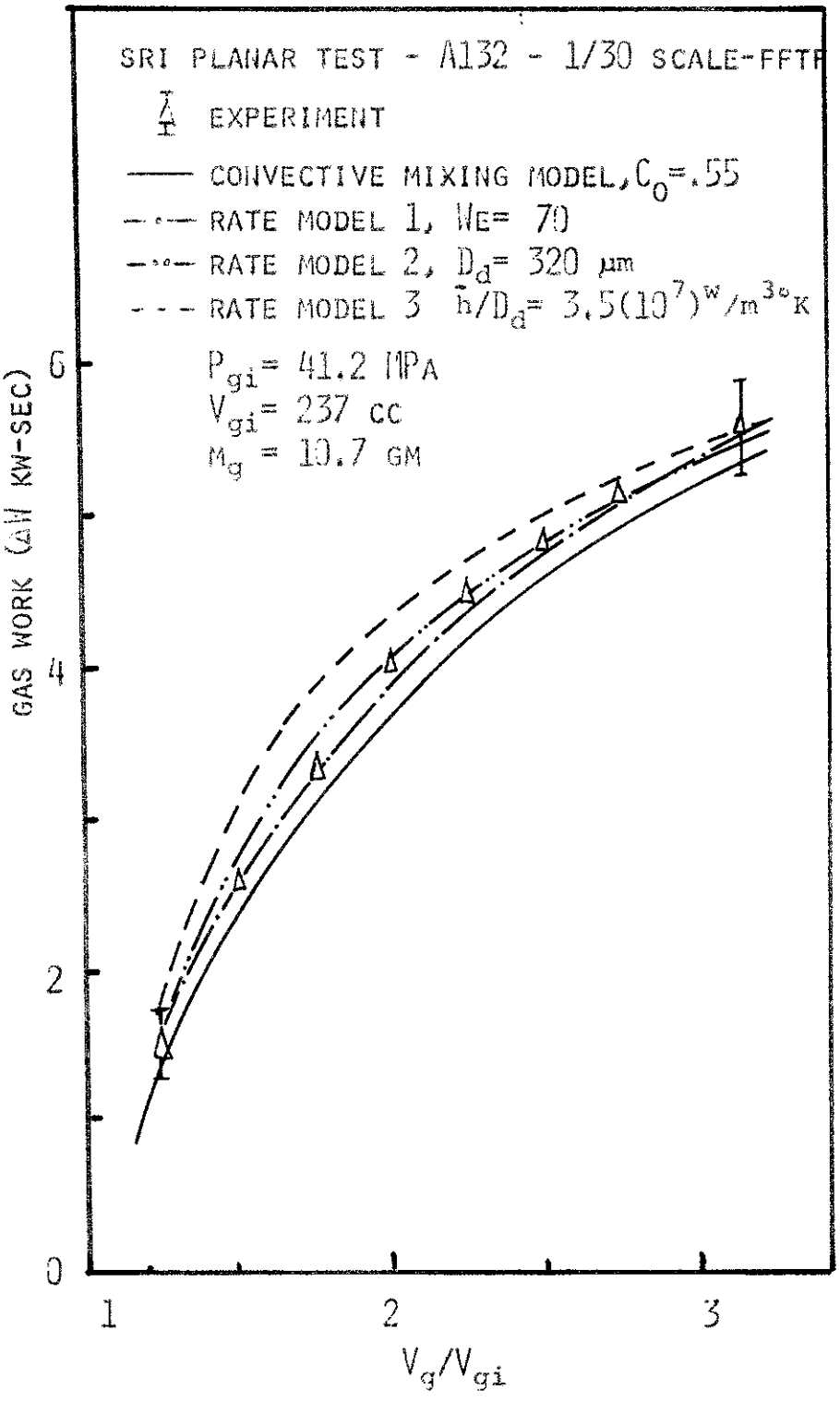

FIGURE 4.12 TEST A132 EXPANSION GAS WORK COMPARISON

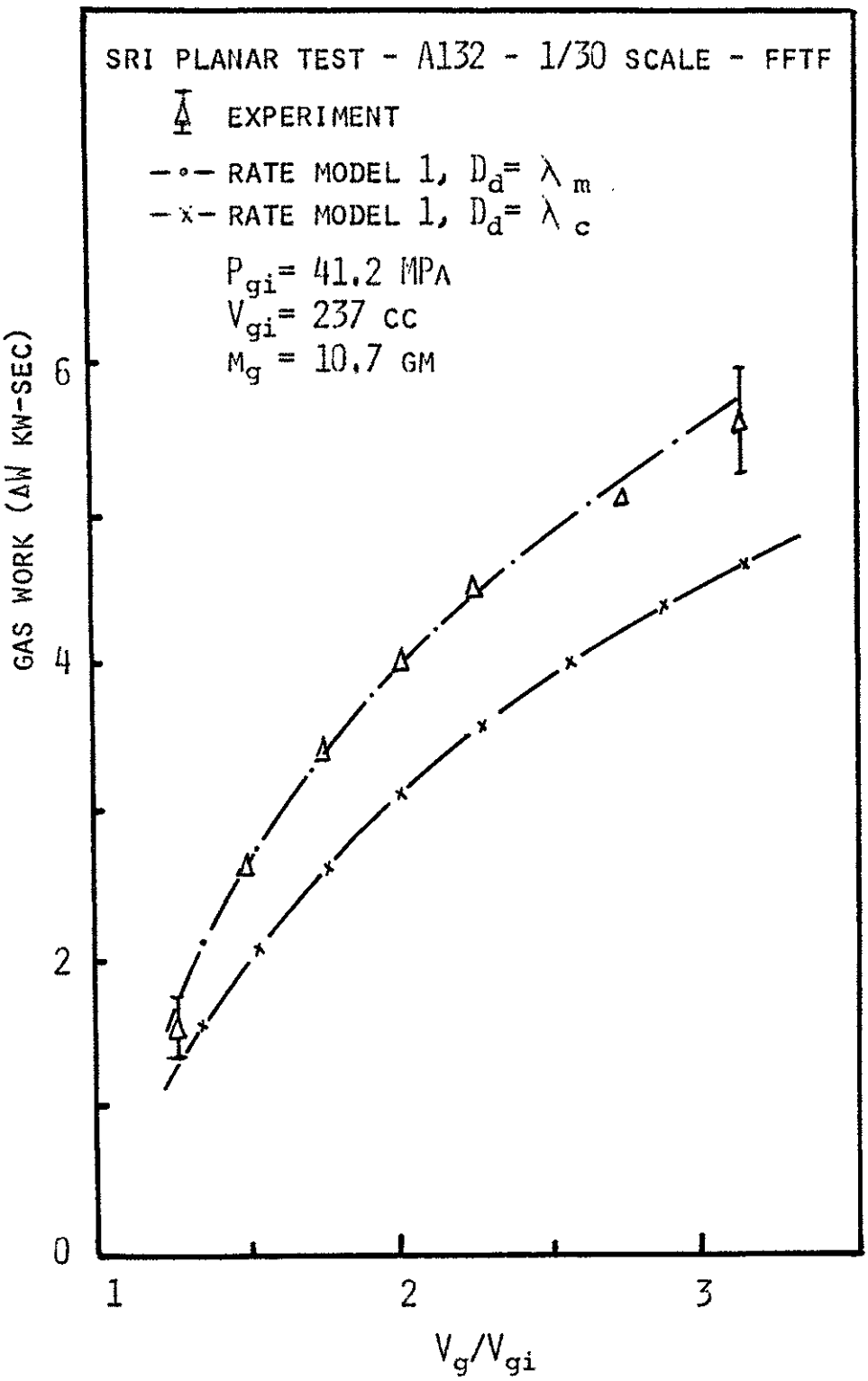

FIGURE 4.13 TEST A132 EXPANSION GAS WORK COMPARED TO THE PREDICTION USING RATE MODEL 1 WITH $\lambda_c < D_d < \lambda_m$

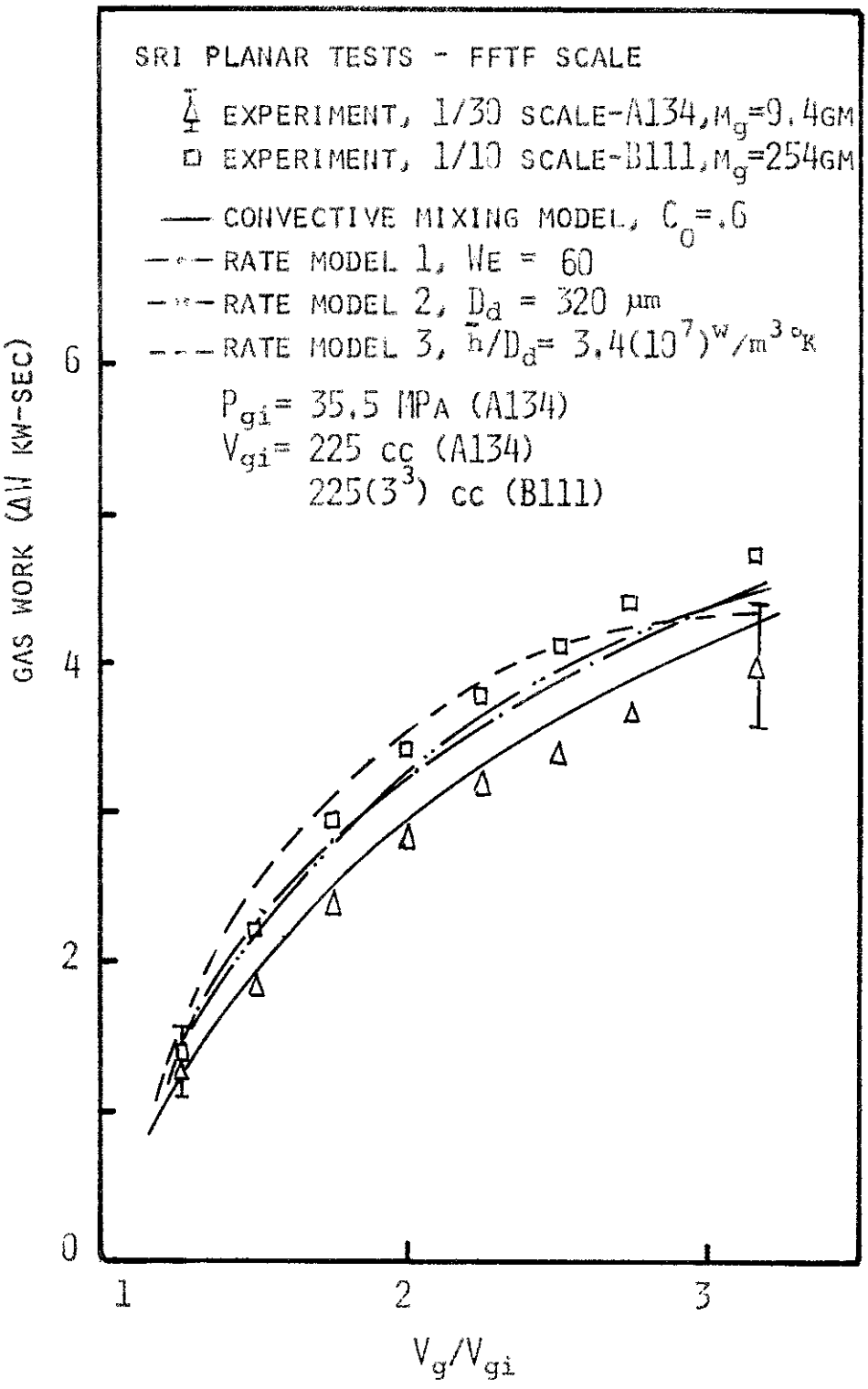

FIGURE 4.14 TEST A134 EXPANSION GAS WORK COMPARISON

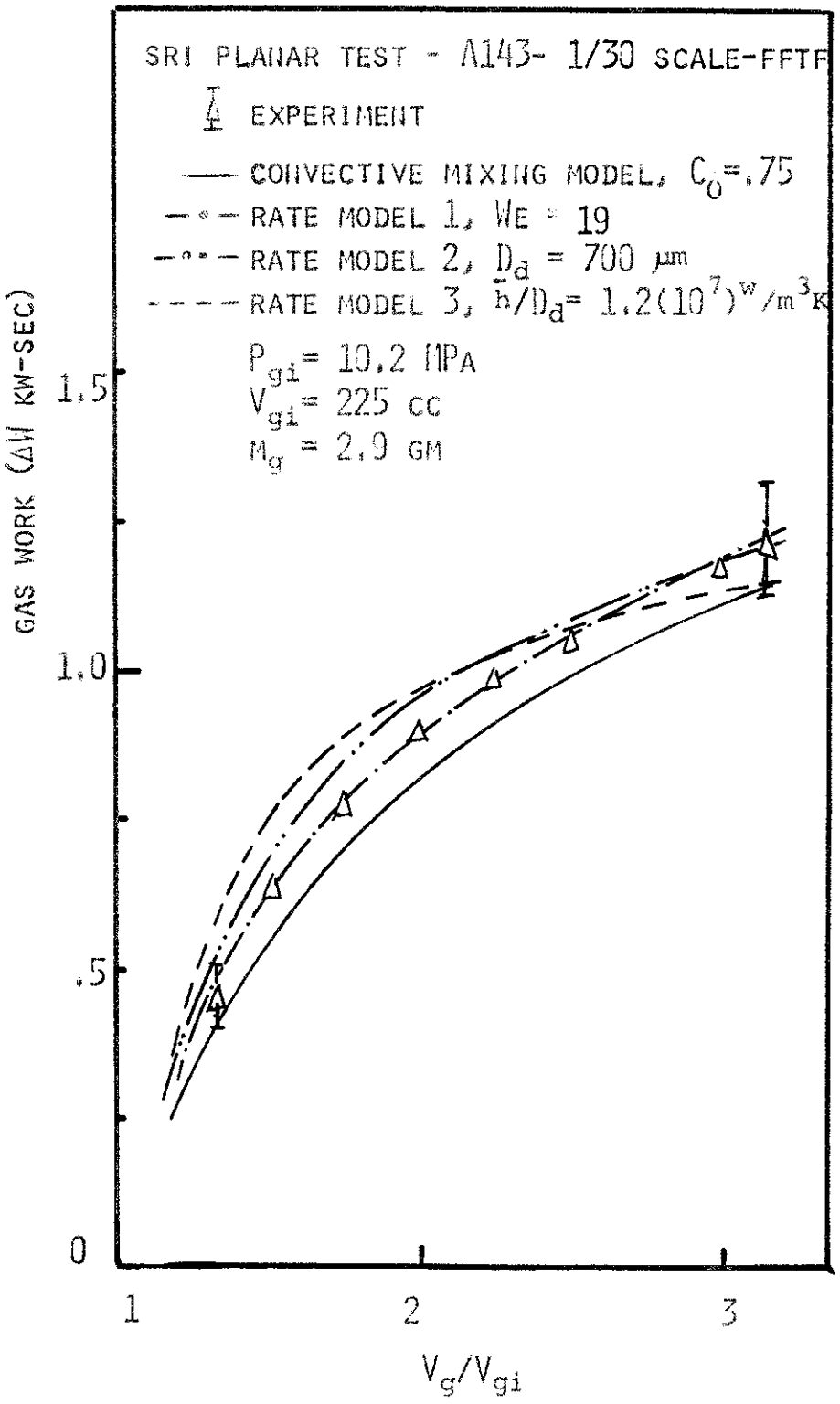

FIGURE 4.15 TEST A143 EXPANSION GAS WORK COMPARISON

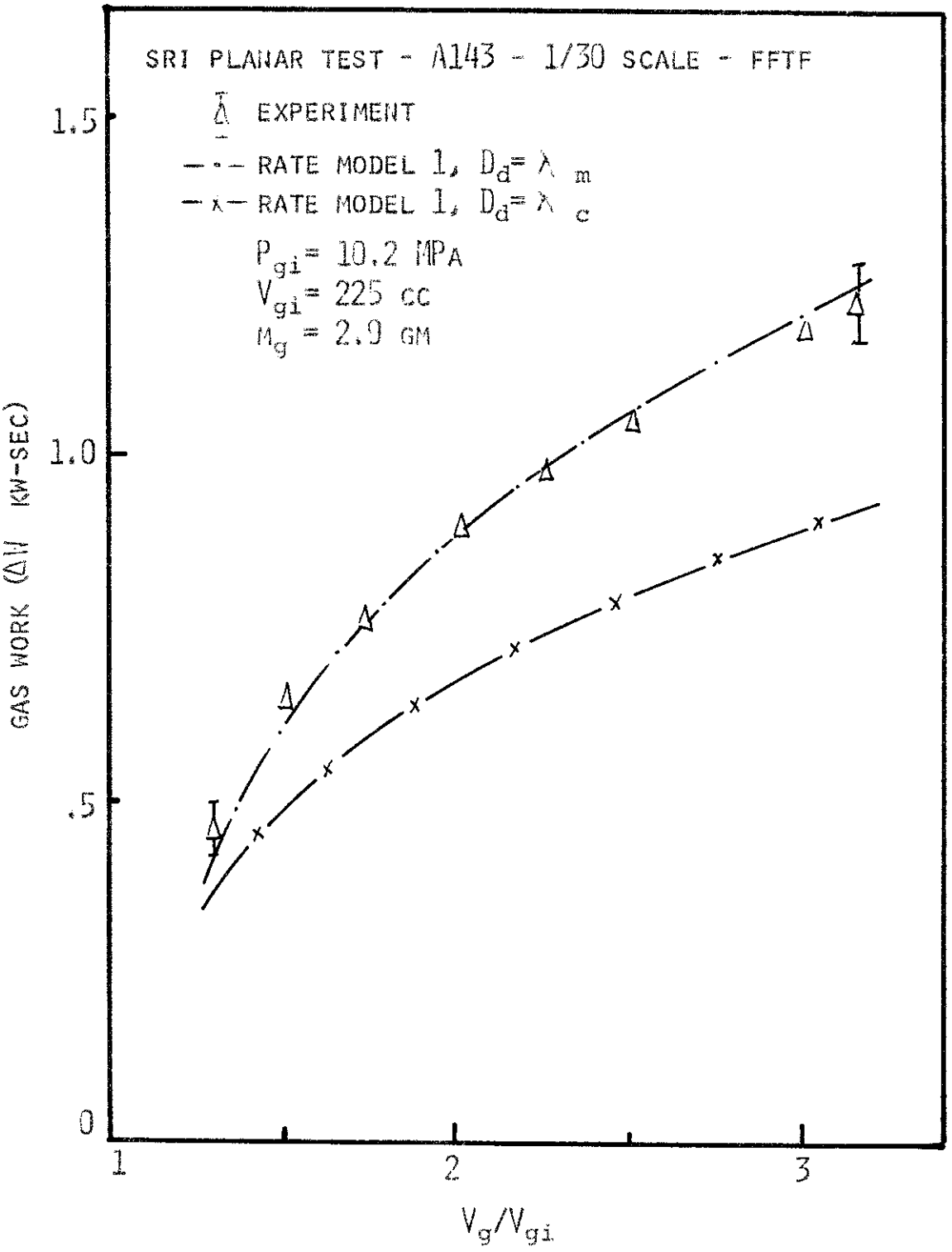

FIGURE 4.16 TEST A143 EXPANSION GAS WORK COMPARED TO THE PREDICTION USING RATE MODEL 1 WITH $\lambda_c < D_d < \lambda_m$

FIGURE 4.17

SUMMARY OF EMPIRICAL CONSTANTS FOR HEAT TRANSFER MODELS

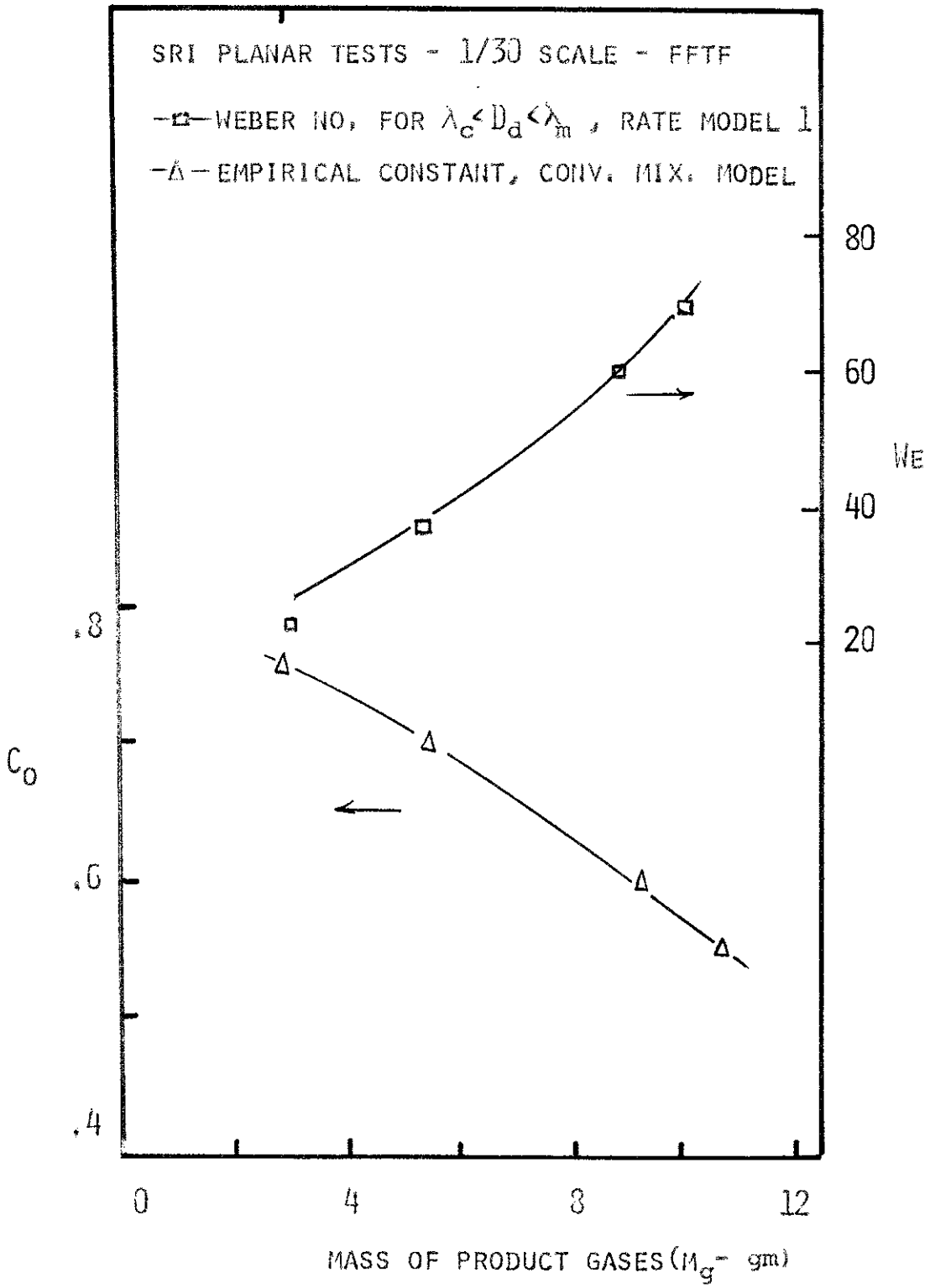

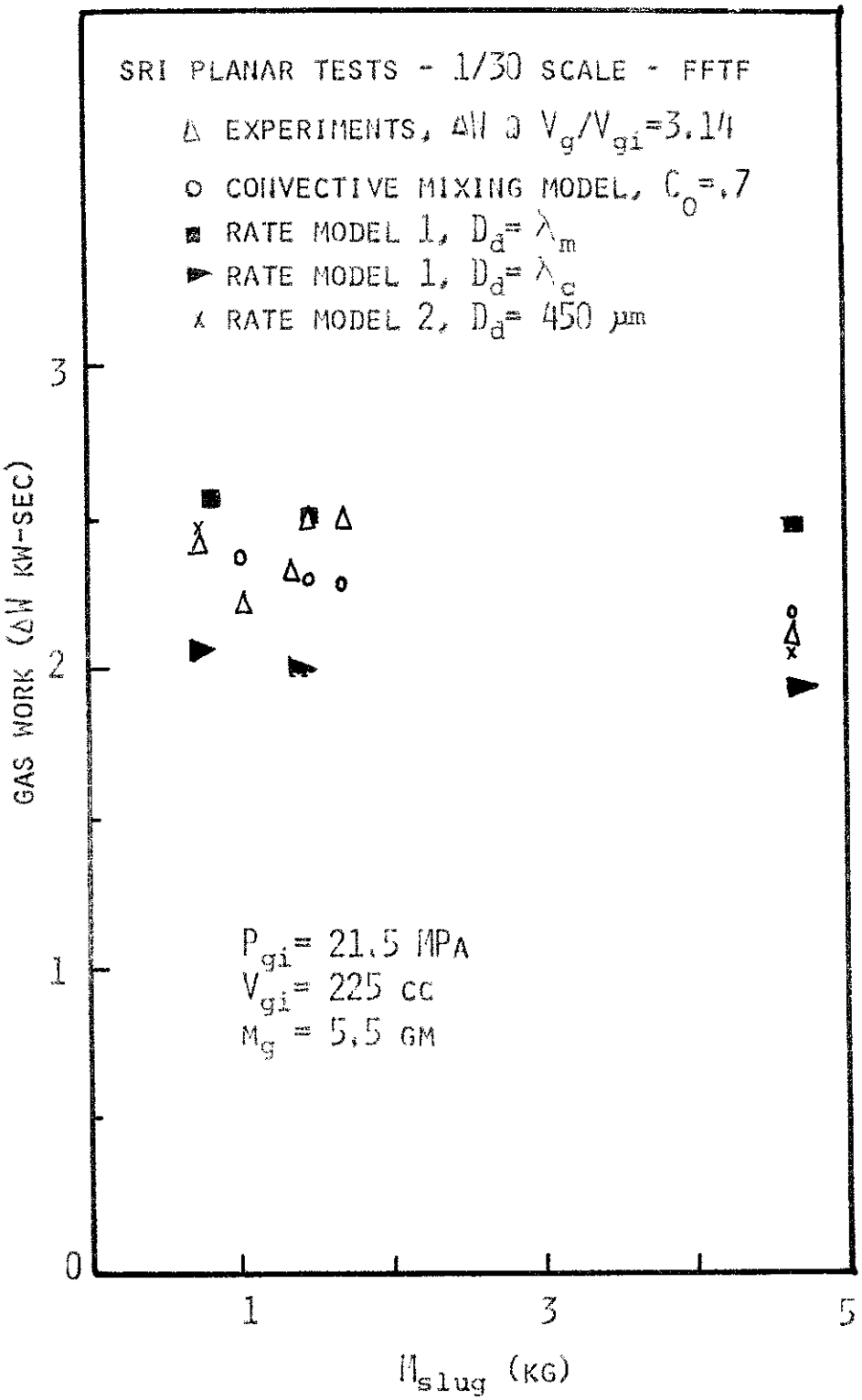

FIGURE 4.18 EXPANSION GAS WORK COMPARISON FOR VARIOUS SLUG MASSES

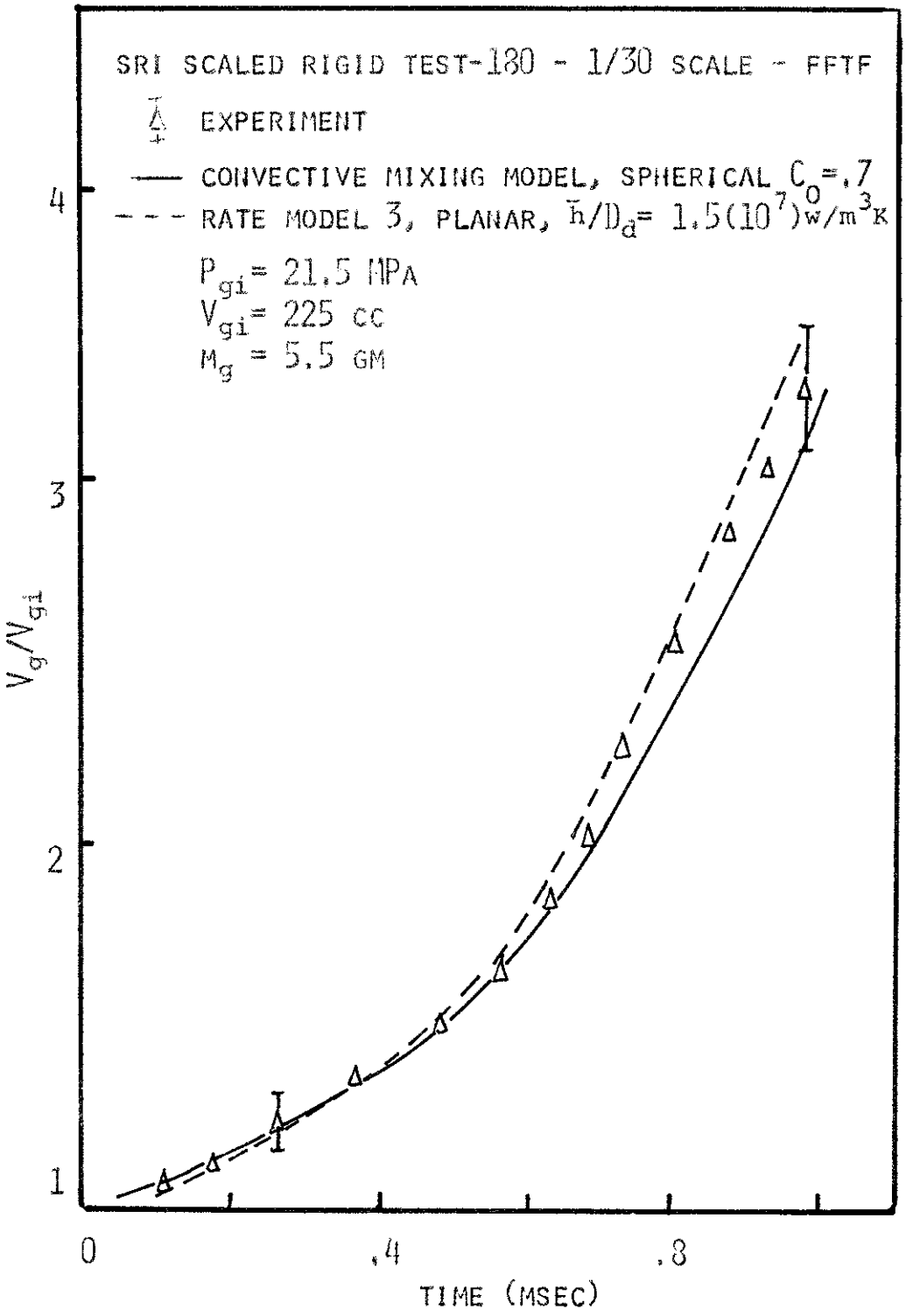

FIGURE 4.19 TEST 180 FFTF SCALE EXPANSION BEHAVIOR OF GAS VOLUME

FIGURE 4.20

TEST 180 FFTF SCALE EXPANSION GAS WORK COMPARISON

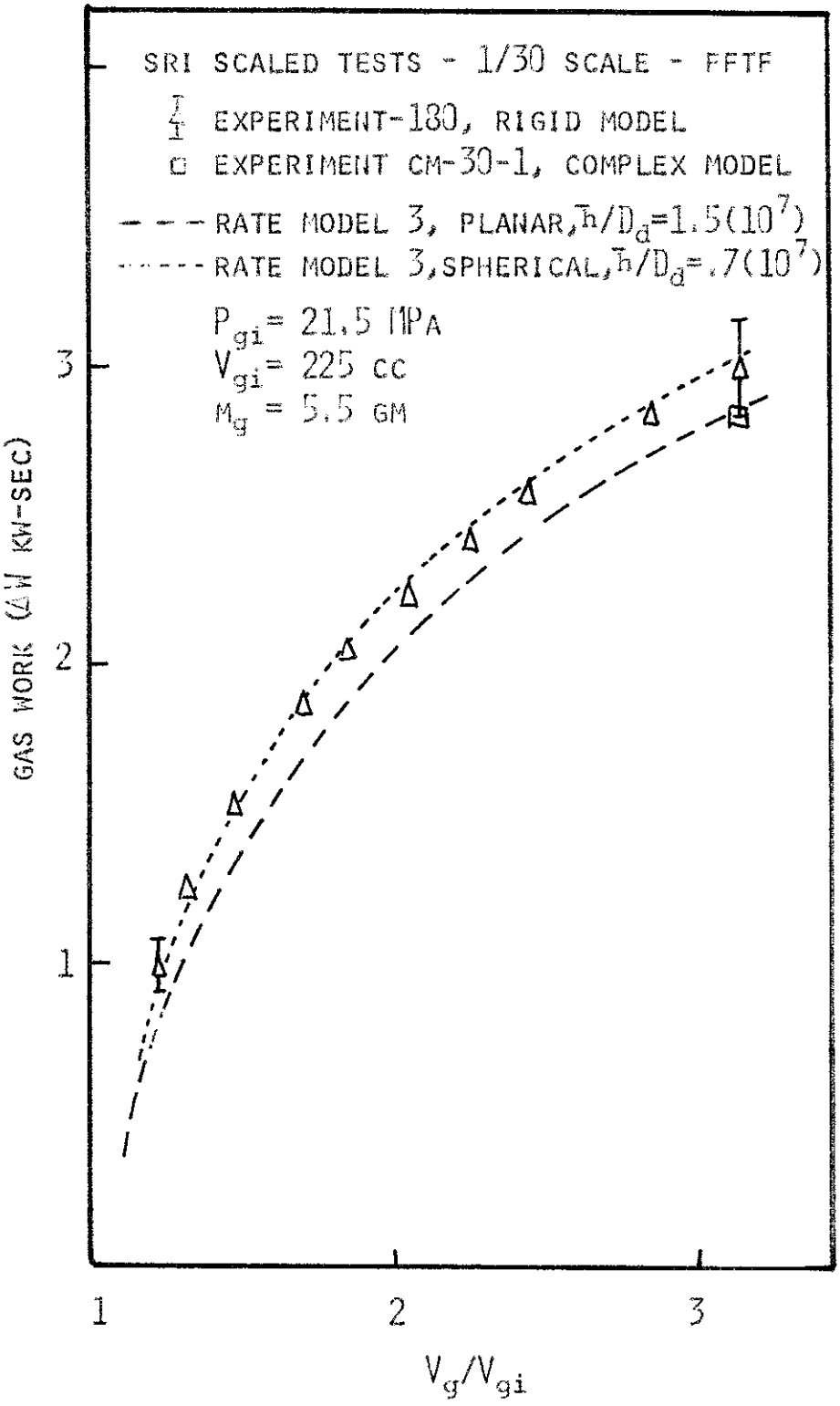

FIGURE 4.21

TESTS AVG2 ENERGY TRANSFERRED TO SOLID STRUCTURE

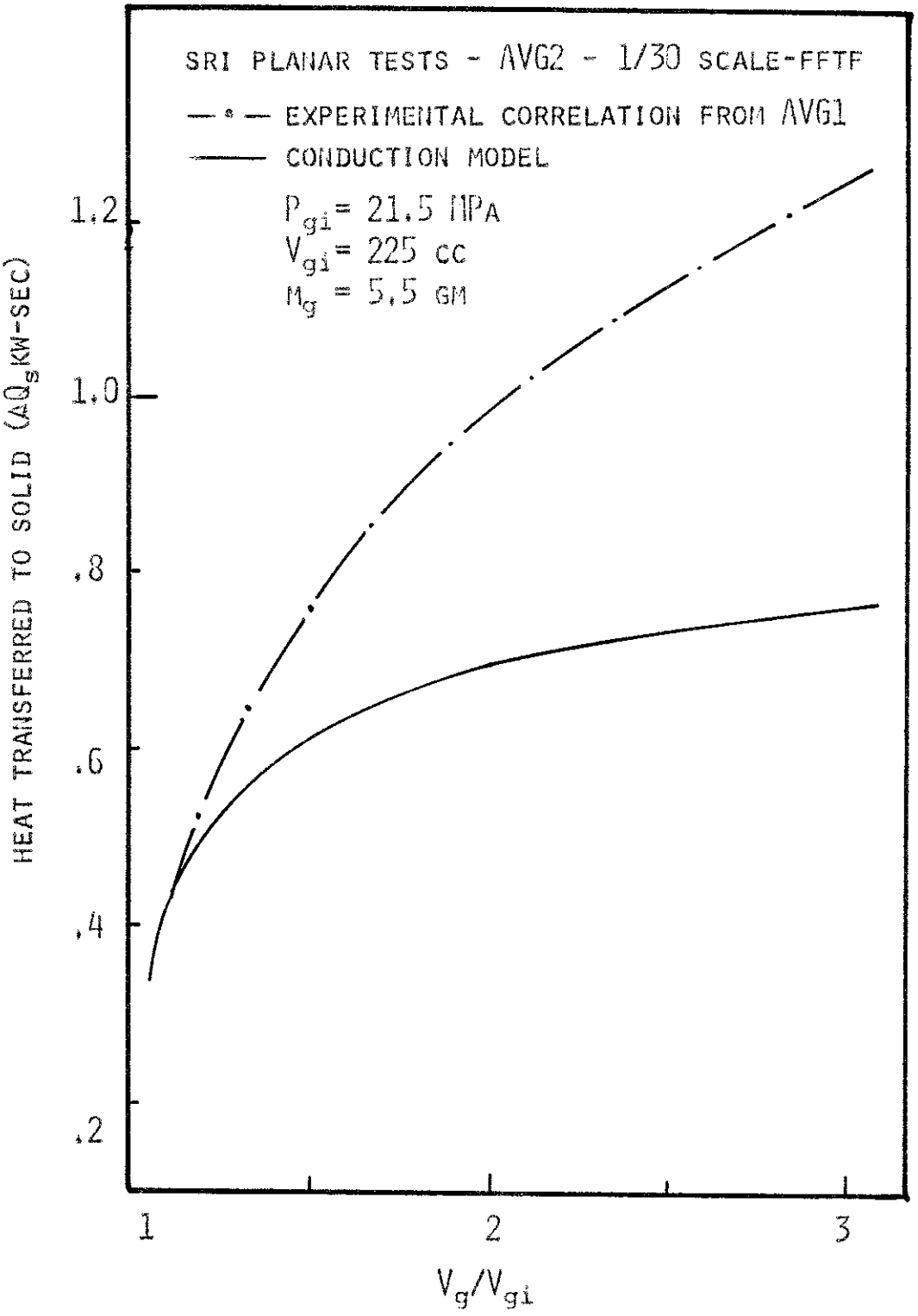

FIGURE 4.22

TESTS AVG2 ENERGY TRANSFERRED TO ENTRAINED WATER COOLANT

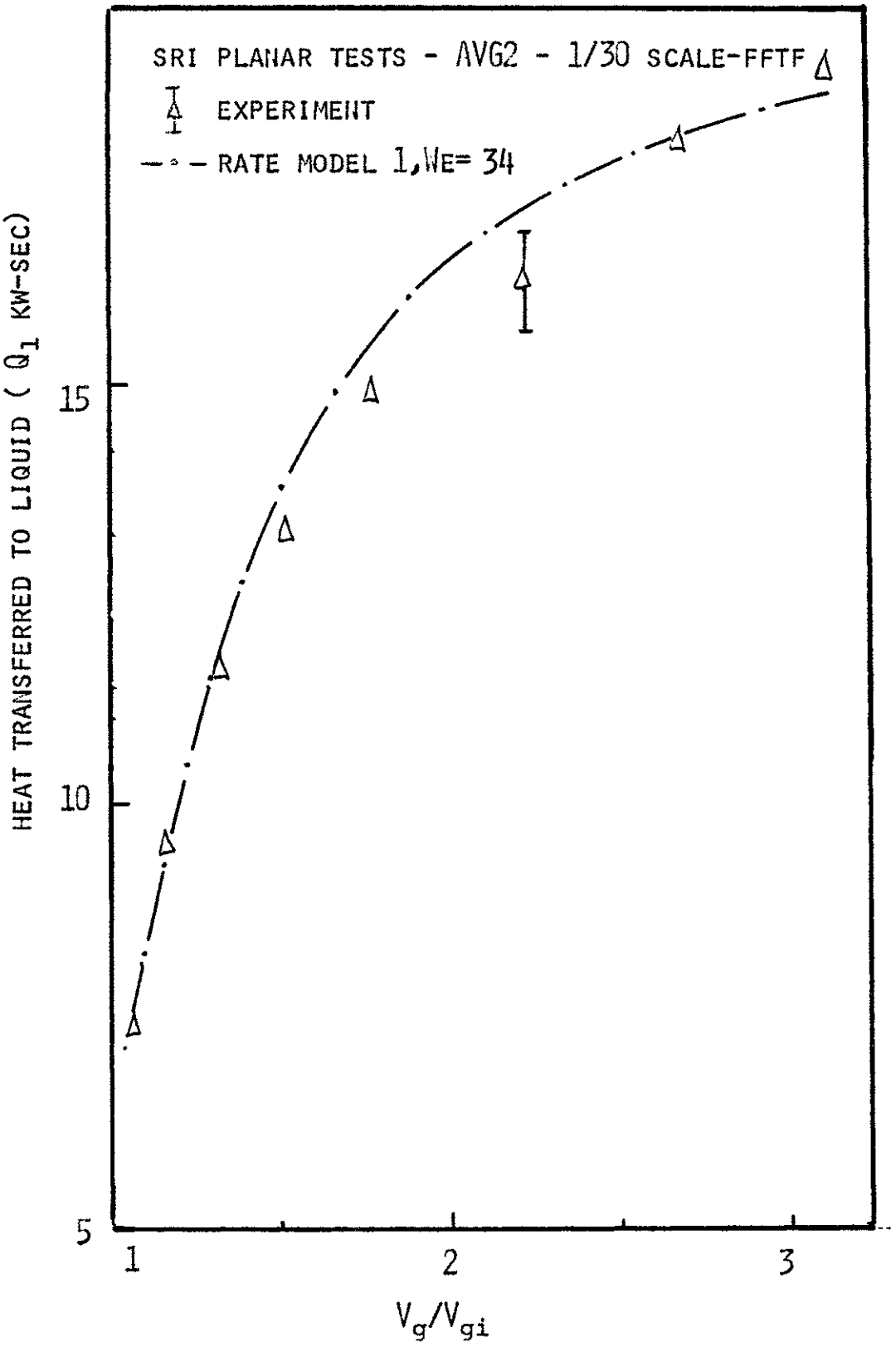

5. PHENOMENOLOGICAL MODELING OF CONDENSIBLE VAPOR SOURCE EXPERIMENTS

5.1 Introduction

Condensible vapor source experiments have been conducted by Theofanous et al at Purdue [27,28] and by Cagliostro at SRI International [25,26]. The purpose of both of these experimental programs has been to investigate the dynamic and thermodynamic behavior of a transient two-phase bubble expansion into a subcooled pool of liquid. The experiments at Purdue utilized a geometry which was similar to the CRBR upper plenum without the upper internal structure, although not geometrically scaled. SRI experiments were performed in a geometrically scaled (1/30) apparatus of the CRBR upper plenum without the upper internals present. Both experimental programs utilized two-phase water as the fuel vapor source and subcooled water coolant in the upper plenum pool. Thus, the behavior observed here was not intended to thermodynamically model the behavior of a UO_2 vapor source in a sodium pool. The tests rather should be viewed as separate effect experiments which investigated the phenomena of coolant entrainment and vapor-liquid heat transfer.

The entrainment model based on Taylor Instabilities will be applied as in the past tests to predict the observed entrainment rates along with a condensible vapor-liquid heat transfer model to describe the transient volume and pressure characteristics of the expansion. To accomplish this not only is the entrained coolant volume needed but also: 1) the relative velocity between the vapor and the entrained coolant; 2) the characteristic drop size of the coolant for the heat transfer process; 3) the mechanism which controls the condensation process; 4) knowledge of whether the two-phase vapor source expansion is equilibrium or non-equilibrium in nature.

This analysis is presented in the following sections after a brief review of the Purdue and SRI apparatus and tests.

5.2 Background on Condensible Vapor Experiments

5.2.1 Purdue-ANL Experiments

The experiments conducted by Theofanous and Christopher [27,28] were performed in an apparatus which had a geometrical shape similar to the core and the upper plenum of the CRBR without the internal structure present (Figure 5.1). The unscaled upper plenum was a plexiglas cylinder which contained the subcooled water and a large plenum volume of air above it (see Figure 5.1, s = 31 cm), which could be adjusted in height. The core was simulated by a steel pipe which contained the hot two-phase water which was kept at the desired saturated pressure and temperature by electric heaters. The core was separated from the upper plenum by a pair of rupture disks. A spring loaded rod in the core was used as the breaking mechanism. The core opening area was varied by changing an installed orifice plate above the upper rupture disk,and noncondensible gas (air) could be introduced at various pressures between the disks. The geometry then, although unscaled,was similar to the full scale reactor condition of the sodium coolant out of the core and fission gas region as the two-phase source expands out of the core.

Fifteen experiments were performed by Christopher [28] and are listed in Table 5.1. The main parameters which were varied in the tests were the steam void fraction in the core ($\bar{\alpha}$), the orifice area for blowdown and the pressure of noncondensible gas between the rupture disks. The variables which were experimentally measured were the pressure in the core and upper

plenum volumes by piezoelectric transducers, the displaced volume of the upper plenum pool and the bubble volume by hi-speed photography. The entrained water volume is the difference between the bubble and displaced volumes. A large experimental error (±15-20%) was reported for both the displaced plenum volume and the bubble volume measurements. The reasons cited for these errors are that the volumes are determined by visual measurements of hi-speed photographs and this measurement problem is compounded by the light refraction effects as the bubble grows bigger and the plexiglas cylinder visually distorts the actual volumes. The result is that the entrainment values reported have a large error (±20-30%).

The initial conditions of the experimental tests to be analyzed are given in Table 5.2. Although a large number of tests were performed only a few have been reported in the literature and these three tests give a representative sampling of the condensible source behavior in the Purdue experiments. When noncondensibles were added, the maximum expansion volume for a test increased as the initial gas pressure increased. This behavior would be expected for two reasons: the noncondensible may retard the condensation process, and at the later stages of the expansion, the bubble pressure could be largely due to noncondensible partial pressure. No other significant results were noted from the addition of noncondensible gases.

5.2.2 SRI Experiments

The SRI test program [25,26] is an ongoing effort to understand the key phenomena which occur during transient two-phase expansions similar in behavior to what is expected during an HCDA. Presently, only two experiments involving condensible sources have been reported, although more are planned and are being performed at the present time. One of the final goals of the

program is to perform small scale experiments which will be similar in some aspects to the UO_2 vapor expansion into a sodium pool. At present, only separate effect tests are being run in a 1/30 geometric scale model of the CRBR's upper plenum and fission gas plenum. Experiments performed to date do not have a scaled upper internal structure present in the vessel, thus the experiments model an initial condition similar to the sodium coolant being in the fission gas plenum without the structure. Future experiments are planned with the structure in place. The upper plenum region containing the subcooled water coolant is a plexiglas cylinder so that photographic techniques can be used to record the transient. The reactor vessel head can be installed at its scaled height or removed completely, and the two experiments analyzed represent these two alternatives. The unscaled core region contains the two-phase water under pressure conditions (8.2 MPa) similar in magnitude to those expected in the full scale accident (Figure 5.2). Immersion heaters keep the hot water at the prescribed saturated conditions and explosively triggered sliding doors separate the core region from the fission gas plenum.

The two experiments performed are listed in Table 5.1 while the initial conditions used for the analysis are given in Table 5.2. The experimental parameters measured were the pressure in the core, throat, and upper plenum region by piezoelectric transducers, the displaced volume of the upper plenum pool and bubble volume by hi-speed photography. As in the Purdue and MIT tests, the water entrainment volume is determined by the bubble and displaced volume difference. However, SRI employed a different data reduction technique to minimize the error incurred in measuring the bubble volume. The visual bubble image taken by the hi-speed camera was digatized and the volume was found by a computer calculation assuming a

symmetric body of revolution for the bubble. SRI estimates that the error in entrainment values using this technique is approximately ±5%. A more detailed description of the SRI experiments can be found in references 25 and 26. In particular, the development of the starting mechanism for the experiment is quite elaborate. The sliding doors separating core and plenum are opened in a very short time span (100-200 μs) by the use of a chemical explosive. This opening scheme gives a very reliable initial condition to the transient in contrast to rupture disk starting mechanisms (MIT, Purdue).

5.3 Heat Transfer Model

To analyze the transient expansion behavior in the SRI and Purdue condensible tests, the following phenomena occur during the experiments and need to be modeled: (1) Prediction of amount of coolant volume which is entrained as the two-phase water expands; (2) The two-phase fluid expulsion from the core to the bubble should be considered in regard to possible choked flow conditions and nonequilibrium behavior; (3) The condensation heat transfer from the vapor to the entrained coolant should be modeled in regard to the dominant heat transfer resistance, the diameter of the entrained coolant droplets and the relative velocity between the vapor and the coolant; (4) These individual models should be consolidated into a set of governing equations which when solved can describe the overall transient behavior of the experiment. Up to the present time no analysis of this transient heat transfer process has been attempted by other investigators. However, the vapor condensation models which are employed in the analysis are found in standard texts on heat and mass transfer [59,60].

5.3.1 Coolant Entrainment

The geometry of both sets of condensible experiments have the high pressure two-phase water source expanding from the core region into a larger upper plenum. While both mechanisms of turbulent jet entrainment and Taylor Instabilities entrainment are operative, it is again felt that the dominant mode of entrainment will be due to Taylor Instabilities modeled as

$$\dot{V}_e = 4.65\ A_p \sqrt{a\lambda_c} \tag{5.1}$$

The turbulent jet entrainment has been estimated in the past chapters by Spalding's steady state model

$$\dot{V}_e = .32 \frac{x_o}{D_o}\sqrt{\frac{\rho_g}{\rho_e}}\dot{V}_g \tag{5.2}$$

and can be used to estimate the magnitude of entrainment by this mechanism here. As an example, consider the SRI tests where the observed bubble growth indicated a region where jet-like entrainment could occur (Figure 3.2). This observed distance can be used as the value for $x_o \sim 3$ cm for possible entrainment over the whole transient expansion ($\tau_{exp} \sim 4$ msec). The pressure in the core during the expansion was approximately 49 bars (534^oK) which corresponds to a value of density of $\rho_g \sim 19$ kg/m^3. Thus, the maximum entrainment due to this mechanism ($D_o \sim 5.8$ cm) assuming the highest initial vapor density is

$$\dot{V}_e \simeq .32\ (\frac{3}{5.8})\sqrt{\frac{19}{1000}}\ \dot{V}_g$$

or

$$\Delta V_e \simeq .023 \Delta V_g \tag{5.3}$$

Thus for a vapor expansion to scaled CRBR slug impact ($\Delta V_g \sim 750$ cc), the maximum entrainment due to this mechanism is $\Delta V_e \sim 17$ cc. This amount of

coolant entrainment is much smaller than is seen experimentally (~300 cc) and thus does not appear to be a dominant mechanism for entrainment. This type of estimation gives the same conclusion for the Purdue condensible experiments.

Another possible transient mechanism of entrainment may exist in the SRI tests, as was shown in the MIT and the SRI noncondensible gas tests, when the vapor initially empties the fission gas plenum region. As Chapter 3 indicated, the possibility of additional entrainment beyond what is predicted by Taylor Instabilities may be caused by exceeding Helmholtz Instability limits causing transient jet entrainment as the water in the fission region is pushed out by the gas. The analysis indicated that the entrainment is probably due to the parallel flow of the vapor over the liquid left along the wall and at the vapor-liquid interface. This was indicated because the minimum relative velocity criterion for Helmholtz Instabilities is easily met for the SRI initial conditions. The condensible SRI tests also have similar initial conditions to the noncondensible N_2 test, thus this same mechanism may be operative. However, it will be seen when the results are presented that the amount of entrainment that could be attributed to this mechanism is still small (30 cc) in comparison to the total entrainment observed at scaled CRBR slug impact (~330 cc).

5.3.2 Two-Phase Mass Flow Rate from Core

The model utilized to predict the mass flow rate into the expanding bubble (i.e., from the core into the upper plenum) is an important component of the analysis. A review of the models available in the open literature is given in Appendix E, and those models which are used in the condensible test analysis are briefly described here. In the SRI and Purdue experiments a flow constriction exists between the core region and the upper plenum.

For the Purdue experiments this occurs because an orifice is placed at the opening between the core and the plenum to adjust the flow area. In the SRI tests the fission gas region acts as an orifice for most of the expansion because the L/D ratio is near one. Thus if the two-phase mass flow is near equilibrium conditions as it exits into the bubble, an orifice equation can be used to predict the mass flux (G) [72,73] as

$$G = .61 \sqrt{2\rho_{co}(P_{co} - P)} \tag{5.4}$$

where

ρ_{co}, P_{co} = core density and pressure

P = receiver pressure if $P > .55\ P_{co}$ or $.55\ P_{co}$ if $P < .55\ P_{co}$

The possibility also exists that the two-phase mixture is not at equilibrium conditions and nonequilibrium effects must be accounted for. This situation is experimentally observed in both SRI tests where the initial condition for the experiments is that P_{g_i} - 8.2 MPa at saturated conditions $T_{g_i} = 578^{o}K$. When the experiment begins the sliding doors separating the core and fission gas plenum open and as the two-phase vapor expands, the core pressure immediately falls to a constant value of 4.9 MPa (Figure 5.3). This behavior indicates that nonequilibrium effects are controlling the core blowdown and the rate of water evaporation. The probable reason for this is that the two-phase mixture is initially stratified and the area for evaporation is just the core area and the flow into the bubble is saturated vapor. Since the transient occurs so fast, the pressure drops until the evaporation off the water surface in the core (Figure 5.5) holds the core pressure constant through the transient. To model this nonequilibrium mass flow rate from the core, the maximum mass flux of water evaporation off the water surface in the core is [59]

$$G_{evap} = \frac{1}{\sqrt{2\pi R_g}} \left[\frac{P_{sat}(T_{g_i})}{\sqrt{T_{g_i}}} \right] \tag{5.5}$$

where the water vapor is modeled as a perfect gas, and T_{g_i} is the initial core temperature (saturation pressure P_{sat}). The maximum rate of condensation onto the surface of the water is

$$G_{cond} = \frac{1}{\sqrt{2\pi R_g}} \left[\frac{P_g}{\sqrt{T_{sat}(P_g)}} \right] \tag{5.6}$$

where P_g is the experimentally measured core pressure, for $t > 0$ (saturation temperature T_{sat}). Thus the net maximum rate of mass flux into the bubble is the difference between these two relations.

$$G = \frac{1}{\sqrt{2\pi R_g}} \left[\frac{P_{sat}(T_{g_i})}{\sqrt{T_{g_i}}} - \frac{P_g}{\sqrt{T_{sat}(P_g)}} \right] \tag{5.7}$$

This model is used for the SRI experiments to describe the mass flow rate of vapor into the bubble ($\dot{m}_{vap} = G\, A_{core}$).

This situation could also exist for the Purdue tests, because the initial two-phase water in the core is stratified with a low area for evaporation. However, the expansion time for the experiment is much longer than the SRI tests (~ 20 - 30 msec) so that the possibility of nucleation on the heater element surfaces and a more homogenous mixture in the two-phase expansion is more likely. The observed pressure traces (Figure 5.4 - Test 3V) from the Purdue experiments do not show a constant pressure behavior which would be an indication of the vapor expansion being mainly nonequilibrium. There is no constant pressure plateau during the expansion ($0 < t < 25$ msec) although there is one for a few milliseconds. Thus for the Purdue tests both equilibrium (orifice Equation 5.4) and nonequilibrium expansion (Equation 5.7) models are utilized to determine which model is needed for agreement with the experimental results.

The final consideration that must be mentioned in modeling the vapor expansion is how to treat the initially spherical growth of the two-phase bubble in the upper plenum. Appendix D gives a review of some published criteria and again for these geometries the conclusions of Christopher and Theofanous [28] are used. For the SRI condensible tests the scaled CRBR geometry will have an initial spherical growth for $1.2 < V_g/V_{g_i} < 1.3$. Because of the water pushed out of the fission gas region and its high exit velocity, the acceleration during this time is negative and no entrainment will occur. This is the same condition as was imposed in Chapter 3 on the SRI Nitrogen gas test. For the Purdue tests Theofanous' conclusion is that the condensible tests are mainly one-dimensional because the transition from spherical to planar bubble growth occurs very early in the expansion ($V_g/V_{g_i} < 1.1$) [28]. The reason for the difference is that the Purdue apparatus was not scaled to CRBR dimensions although it was similar in shape. The ratio of the upper plenum diameter to the core diameter is about three, while for the CRBR case it is four. The bubble is affected by the upper plenum wall sooner in the Purdue experiments causing the earlier transition to planar growth. Also, because there is no water filled fission gas region, the acceleration is always from the less dense to the more dense fluid throughout the expansion and Taylor Instability entrainment would always be operative.

5.3.3 Vapor-Liquid Heat Transfer Model

The vapor-liquid heat transfer that presumably occurs in this process is viewed as being due to the condensation of the saturated water vapor onto the entrained subcooled water which is in droplet form (Figure 5.5). The previous heat transfer models used in the noncondensible gas heated tests are not applicable here because the condensation process onto the

droplet surface is the dominant mechanism for energy transfer in these experiments. The model for heat transfer from the vapor to a liquid droplet can be represented as in Chapter 4 as

$$\dot{q}_{drop}(t) = \bar{h}\,\pi D_d^2 (T_{sat} - T_l) \tag{5.8}$$

where $\bar{h}$ is the heat transfer coefficient. T_{sat} is the saturation temperature of the vapor. The total heat transfer from the two-phase mixture is found by summing over all the entrained drops in the bubble giving

$$\dot{q}_l(t) = \sum_{\text{all drops}} \dot{q}_{\substack{\text{one}\\ \text{drop}}} \tag{5.9}$$

To utilize this model an estimation of the entrained coolant droplet size (D_d) is made. The two physical bounds on D_d, as described in Chapter 4, are: (1) The probable size at which the droplet is formed would be between the critical Taylor Instability wavelength and the fastest growing one (λ_m)

$$\lambda_c = 2\pi\sqrt{\frac{\sigma}{a(\rho_l - p_v)}} \tag{5.10}$$
$$\lambda_m = \sqrt{3}\lambda_c$$

(2) The lower bound would be the diameter corresponding to the critical Weber number (We_{crit}) indicating a balance between surface tension and inertial energy forces. Thus if the droplet diameter initially near λ_m in size has a Weber number below We_{crit}, then the droplet will not breakup. If, however, the Weber number for $D_d \sim \lambda_m$ is above We_{crit}, then the droplet will begin to breakup to a size

$$D_d = \frac{We_{crit}\,\sigma}{\rho_v (v_{rel}(x,t))^2} \tag{5.11}$$

The physical picture (Figure 5.7) of the expansion is similar to the development in Chapter 4 (Figure 4.5) except that the velocity of the vapor near x = 0 should be the velocity of the vapor from the core. Then if the linear velocity profile is again assumed the expression for v_{rel} is

$$v_{rel}(x,t) = \left(1 - \frac{x}{x_{slug}}\right) v_{core} + \frac{x}{x_{slug}} \left(v_{slug} + C\sqrt{a\lambda_c}\right) - v_d \quad (t) \qquad (5.12)$$

The droplet velocity ($v_d(t)$) initially starts with the value of the slug velocity at some past time ($v_{slug}(t_o)$) and is accelerated due to vapor drag forces by the momentum equation given as

$$\frac{dv_d(x,t)}{dt} = \frac{3}{4} C_d (v_{rel}(x,t)^2) \frac{\rho_g}{\rho_l D_d} \qquad (5.13)$$

The heat transfer coefficient ($\bar{h}$) for the condensation process is determined by three heat transfer resistances as Figure 4.6 illustrates. The condensation process onto the droplet surface at some mass flux (G_{cond}) is caused by a temperature difference between the vapor at T_{sat} and the condensate at T_i. Now to estimate this interface resistance an expression similar to Equation 5.7 can be used to estimate the maximum rate of condensation

$$G_{cond} = \frac{1}{\sqrt{2\pi R_g}} \left(\frac{P_{sat}(T_{sat})}{\sqrt{T_{sat}}} - \frac{P_{sat}(T_i)}{\sqrt{T_i}}\right) \qquad (5.14)$$

The heat transfer coefficient for this process could be found by an energy balance giving

$$G_{cond}\, h_{fg} = \bar{h}_{inter}(T_{sat} - T_i)$$

$$\bar{h}_{inter} = \frac{G_{cond}\, h_{fg}}{(T_{sat} - T_i)} \qquad (5.15)$$

The heat transfer resistance due to condensate buildup on the drop surface can be estimated by a quasi-steady process as

$$\bar{h}_{cond} = \frac{k_c}{\delta} \tag{5.16}$$

where δ is the thickness of condensate existing at a given time (t). The water droplet itself can provide a large resistance to heat transfer in a condensation process. The drop is modeled as a semi-infinite mass because

$$D_d >> \sqrt{\alpha_c t_{exp}} \tag{5.17}$$

where for typical values of α_c for water and $\tau_{exp} \sim 30$ msec, $\sqrt{\alpha_c \tau_{exp}} \sim 50 - 100$ μm, which is smaller than the predicted droplet sizes ($D_d > 500$ μm). The heat transfer coefficient for a semi-infinite mass is given by Carslaw and Jaeger [70] as

$$\bar{h}_{drop} = \frac{2k_c}{\sqrt{\pi \alpha_c t}} \tag{5.18}$$

Now a simple order of magnitude estimate can be used to determine which of these resistances are dominant. The SRI test conditions could be used for this estimation along with properties in Appendix A. The minimum value of $\bar{h}_{inter}$ would be when the interface temperature difference is large (e.g. $T_i = 373^oK$, $T_{sat_{max}} = 534^oK$)

$$\bar{h}_{inter} = \frac{1.57(10^6)(2\pi 462)^{\frac{1}{2}}\left(\frac{4.7(10^6)}{\sqrt{534}} - \frac{1(10^5)}{\sqrt{373}}\right)}{(534 - 373)}$$

$$\bar{h}_{inter} = 3.6\ (10^7)\ \frac{w}{m^{2o}K}$$

The minimum value of $\bar{h}_{water}$ would be at long times ($\tau_{exp} \sim 4$ msec) i.e.,

$$\bar{h}_{drop} \simeq \frac{2(.6)}{\sqrt{\pi(1.4(10^{-7}).004}} = 2.8\ (10^4)\ \frac{w}{m^{2o}K}$$

Therefore, from this simple calculation it is evident that the controlling resistance in forming the condensate film is $\bar{h}_{water}$ not $\bar{h}_{inter}$. Now this value needs to be compared to $\bar{h}_{cond}$ to determine if one of these resistances are negligible. To determine $\bar{h}_{cond}$ we can utilize a simple energy balance to find condensate film thickness (δ) based on $\bar{h}_{drop}$

$$\rho_c \delta h_{fg} = \int_o^t \bar{h}_{water}(T_{sat} - T_l)\, dt$$

$$\rho_c \delta h_{fg} = \frac{4k_c}{\sqrt{\pi\alpha_c}} (T_{sat} - T_l) \sqrt{t}$$

where for our case $t \sim \tau_{exp} = 4$ msec

$$\alpha_c \sim 1.41\ (10^{-7})\ m^2/_s$$

$$h_{f_g} \sim 1.57\ (10^6)\ \frac{w-s}{k_g}$$

$$\Delta T \sim 161^oK$$

$$\delta \simeq 23\ \mu m.$$

$$\bar{h}_{cond} \simeq 2.5\ (10^4)\ w/m^{2o}K$$

Therefore, the indication is that the heat transfer resistance is controlled by the condensate film and the transient resistance in the water drop. Thus the composite heat transfer coefficient for a drop is given by

$$\bar{h} = \left[\frac{k_c}{\delta + \frac{\sqrt{\pi\alpha_c t}}{2}} \right] \qquad (5.19)$$

The final task to perform in this exact model for the liquid heat transfer is to sum over all the drops that have been entrained. This can be done by finding the number of drops in an internal Δx_i and multiplying this by the heat transfer to one drop at that x and t. This number of drops is

$$No\ (\Delta x_i) = \frac{V_e(\Delta x_i)}{\frac{\pi}{6} D_d^{\,3}}$$

$$No\ (\Delta x_i) = \frac{(4.65\ A_p \sqrt{a\lambda_c})\ \Delta t}{\frac{\pi}{6} D_d^3} \tag{5.20}$$

By summing this product of No (Δx_i) and $\dot{q}_{drop}\ (\Delta x_i)$ over all the Δx_i from $0 \leq x \leq x_{slug}$, the result is the total heat transfer from the vapor to the liquid is given as

$$\dot{q}_l(t) = \sum_{i=1}^{N} No(\Delta x_i)\dot{q}_{drop}(\Delta x_i);\ N = \frac{x_{slug}}{\Delta x_i}$$

$$\dot{q}_l(t) = \sum_{i}^{N} \frac{6V_e(\Delta x_i)\bar{h}\ (T_{sat} - T_l)}{D_d(\Delta x_i, t)} \tag{5.21}$$

where

$$\bar{h}(\Delta x_i) = \left[\frac{k_c}{\delta\ (\Delta x_i) + \sqrt{\pi \alpha_c t}}\right] \tag{5.19}$$

Although this is the exact formulation of the heat transfer rate, it is quite impractical to compute. One reason is that for every axial increment (Δx_i) containing droplets a differential equation is needed to monitor the acceleration of the drop velocity due to drag forces. This makes the model in its present form quite unwieldy, and so some approximations are made.

5.3.3.1 Model #1 Variable Diameter and Heat Transfer Coefficient

The first approximation that can be made is similar to that used in Chapter 4 where an average drop acceleration is computed from all the intervals (Δx_i) and then can be integrated once. The drop velocity (v_d) can be separated into two components, one being the initial velocity at its formation $(v_{slug}(t_o))$, and the other being the velocity addition due to frictional drag forces accelerating the drop, $v = \int_o^t \frac{dv_d}{dt}\ dt$ where $\frac{dv_d}{dt}$ is given by Equation 5.13. The initial drop velocity $(v_{slug}(t_o))$ can be estimated as in Chapter 4.

$$v_{slug}(t_o) \doteq a\, t_o = a\, t\, t_o = v_{slug}(t)\, \frac{t_o}{t}$$

where it is assumed that acceleration (a) is constant giving

$$v_{slug}(t_o) = \left[\frac{x - x(t=0)}{x_{slug} - x(t=0)}\right]^{\frac{1}{2}} v_{slug}(t) \tag{5.22.1}$$

Therefore, the relative velocity is given as

$$v_{rel}(t) = \left(1 - \frac{x}{x_{slug}}\right) v_{core} + \frac{x}{x_{slug}} \left(v_{slug} + C\sqrt{a\lambda_c}\right)$$
$$- \int_o^t \left\langle \frac{dv_d}{dt} \right\rangle dt - \left[\frac{x - x(t=0)}{x_{slug} - x(t=0)}\right]^{\frac{1}{2}} (v_{slug}) \tag{5.22.2}$$

The average drop acceleration can be calculated by

$$\left\langle \frac{dv_d}{dt} \right\rangle = \frac{\sum_i \frac{dv_d}{dt}\, \Delta x_i}{\sum_i \Delta x_i} \tag{5.22.3}$$

where

$$\frac{dv_d}{dt}(\Delta x_i) = \frac{3}{4}\, \frac{C_D}{D_d}\, \frac{\rho_g}{\rho_e}\, (v_{rel}(\Delta x_i, t))^2 \tag{5.22.4}$$

This average velocity can then be used in the calculation of the lower bound for the droplet diameter based upon the Weber breakup criterion.

The second approximation that can be made is to spatially average the droplet diameter and the heat transfer coefficient separately and then insert these values into the liquid heat transfer model. To obtain a representative droplet diameter for the vapor bubble at any given time (t) the average model would be represented by

$$\left\langle D_d \right\rangle = \frac{\sum_i No(\Delta x_i) D_d(\Delta x_i)\, \Delta x_i}{\sum_i No\,(\Delta x_i) \Delta x_i} \tag{5.23}$$

where

$$No(\Delta x_i) = \frac{V_e(\Delta x_i)}{\frac{\pi}{6} D_d^3}$$

The diameter is averaged linearly in contrast to what was done in Chapter 4 because this model for the liquid heat transfer varies linearly with the droplet diameter.

The heat transfer coefficient can be averaged by looking at each heat transfer resistance separately. The thermal resistance at any time (t) due to the water droplet born at a past time (t_o) and an interval (Δx_i) is

$$\bar{h}_{drop} = \frac{2\, k_c}{\sqrt{\pi \alpha_c (t - t_o)}} \qquad (5.24.1)$$

Thus the average spatial resistance over the whole volume for all the droplets born from $0 < t_o < t$ in the axial distance $0 \leq x \leq x_{slug}$ is just

$$\bar{h}_{drop} = \frac{1}{t} \int_o^t \frac{2\, k_c\, dt_o}{\sqrt{\pi \alpha_c (t - t_o)}} \qquad (5.24.2)$$

$$\langle \bar{h}_{drop} \rangle = \frac{4\, k_c}{\sqrt{\pi \alpha_c t}}$$

Now to find the spatial average heat transfer coefficient including the effect of the condensate film an iteration technique is necessary. First, the average film thickness ($^1\delta$) can be calculated for a Δt using $\bar{h}_{drop}$ where

$$^1\delta = \frac{4\, k_c (T_{sat} - T_l)}{\rho_c h_{fg} \sqrt{\pi \alpha_c t}}\, \Delta t \qquad (5.25)$$

Then a new value for the average $\bar{h}$ can be calculated using '

$$\frac{1}{\bar{h}} = \frac{k_c}{{}^1\delta + \frac{\sqrt{\pi \alpha_c t}}{4}} \qquad (5.26)$$

With this new value of $\bar{h}$, a new film thickness ($^2\delta$) can be calculated

$$^2\delta = \frac{\bar{h}\,(T_{sat} - T_l)\Delta t}{\rho_c h_{f_g}} \qquad (5.27)$$

With this value a new value for $^2\bar{h}$ is calculated and this procedure continues until $^i\bar{h}$ does not change markedly from $^{i-1}\bar{h}$. This was found to occur after about 20 iterations.

If these two spatially averaged quantities are inserted into the liquid heat transfer model, the result is

$$\dot{q}_l(t) = \frac{6\,V_e}{\langle D_d \rangle} \langle \bar{h} \rangle (T_{sat} - T_l) \qquad (5.28)$$

where

$\langle D_d \rangle$ is given by Equation 5.23

$\langle \bar{h} \rangle$ is given by Equations 5.25-27

V_e by integration of Equation 5.1.

5.3.3.2 Model #2 Constant Drop Diameter

The next level of approximation that can be made is to assume one constant value for the droplet diameter for the entire time of the bubble expansion. The physical bounds of the fastest growing wavelength of the Taylor Instability and the critical Weber diameter can be estimated to establish a range of possible values. The liquid heat transfer rate would then be

$$\dot{q}_l(t) = \frac{6\,V_e}{D_d} \langle \bar{h} \rangle (T_{sat} - T_l) \qquad (5.29)$$

where

$\langle \bar{h} \rangle$ is given by Equations 5.25-27

V_e by integration of Equation 5.1.

5.3.3.3 Model #3 Constant Heat Transfer Coefficient and Drop Diameter

The most approximate model for heat transfer would be to assume a constant value for $\bar{h}$ and D_d giving

$$\dot{q}_l(t) = \frac{6V_e}{D_d} \bar{h} (T_{sat} - T_l) \qquad (5.30)$$

To determine an average $\bar{h}$ to use the thermal resistance due to the water droplet (Equation 5.24) can be evaluated near $t = \tau_{exp}/2$ and an iteration similar to that illustrated previously (5.25 - 5.27) can be done by hand to evaluate δ.

All three models are used in predicting the transient expansion behavior of these condensible tests. To accomplish this, these liquid heat transfer models are combined with a set of governing equations for energy and momentum.

5.4 Governing Equations

Before presenting the governing equations, it should be noted here that the heat transfer to solid surfaces is not considered because no exposed solid surfaces appear during the experiment. All surfaces are covered with water, thus it is the water not the solid surface with which energy transfer occurs. This is the case because the thermal penetration depth is small compared to the probable film size left on the solid surface (>1000 μm [69])

$$x_{pen} \sim \sqrt{\alpha_c \tau_{exp}} \leq 100 \text{ μm}$$

Figure 5.7 illustrates pictorially how the condensible tests are modeled. Two lumped parameter volumes are utilized to model the two-phase volume; one volume for the core region (adiabatic) and one for the expanding bubble. The assumptions utilized in this analysis are:

1. The thermophysical properties of water are assumed to be constant and are listed in Appendix A.

2. The water vapor can be modeled as a perfect gas.

3. The mass flow out of the core is modeled either as an orifice flow (equilibrium) or a nonequilibrium flow of saturated water vapor.

4. The inertial constraint is assumed to be one-dimensional.

5. The liquid and vapor water coming from the core are saturated and in equilibrium.

6. The volume of saturated liquid water is assumed to be small in comparison to the saturated vapor volume in the bubble.

7. The Clausius Clapeyron relation describes the slope of the saturation line.

For the core region under the assumption of an equilibrium blowdown, the equation for the conservation of mass is

$$\frac{d}{dt}(m_{f_{co}}) = -\dot{m}_f \tag{5.31}$$

where $\dot{m}_f$ is given by Equation 5.4.

Now the above equation can be rearranged by noting

$$m_{f_{co}} = V_{co}/v_{fco} \text{ inserting into} \tag{5.31}$$

$$\frac{d}{dt}\left(\frac{V_{co}}{v_{fco}}\right) = \frac{-V_{co}}{v_{fco}^2}\frac{d\,v_{fco}}{dt} = -\dot{m}_f$$

or

$$\frac{1}{v_{fco}}\frac{dv_{fco}}{dt} = \frac{1}{m_{fco}}\dot{m}_f \tag{5.32}$$

Now if the definition for v_{fco} is used

$$v_{fco} = v_f(1-X_{fco}) + v_g \tag{5.33}$$

where

$$v_g = \frac{R_f T_{fco}}{P_{fco}} \tag{5.34}$$

and substituted into the term dv_{fco}/dt, the result is

$$\frac{dv}{dt}_{fco} = \frac{dX_{fco}}{dt}\left[\frac{R_f T_{fco}}{P_{fco}} - v_f\right] + X_{fco}\left[\frac{R_f \dot{T}_{fco}}{P_{fco}} - \frac{R_f T_{fco}}{P_{fco}^2}\dot{P}_{fco}\right] \tag{5.35}$$

The Clausius Clapeyron relation can be utilized where

$$\frac{dP_{fco}}{dt} = \frac{dP_{fco}}{dT_{fco}}\frac{dT_{fco}}{dt} = \frac{h_{fg_f}}{v_g T_{fco}}\frac{dT_{fco}}{dt} \tag{5.36}$$

Inserting this into Equation 5.35 for $\dot{P}_{fco}$ and substituting Equation 5.35 into the left hand side of Equation (5.32), the result is

$$\frac{1}{v_{fco}}\left[\dot{X}_{fco}\left(\frac{R_f T_{fco}}{P_{fco}}\right) + \left(\frac{X_{fco} R_f}{P_{fco}} - \frac{h_{fg_f} X_{fco}}{P_{fco} T_{fco}}\right)\dot{T}_{fco}\right] = \frac{1}{m_{fco}}\dot{m}_f$$

Now solving for the rate of change of the core quality ($\dot{X}_{fco}$), the resulting equation is

$$\dot{X}_{fco} = \frac{P_{fco}}{R_f T_{fco}}\left[\frac{v_{fco}}{m_{fco}}\dot{m}_f + \left(\frac{X_{fco} h_{fg_f}}{P_{fco} T_{fco}} - \frac{X_{fco} R_f}{P_{fco}}\right)\dot{T}_{fco}\right] \tag{5.37}$$

The energy equation for the core can be expressed as

$$\frac{d}{dt}(m_{fco} u_{fco}) = -\dot{m}_f(u_{fco} + P_{fco} v_{fco}) \tag{5.38}$$

where

$$u_{fco} = X_{fco} u_{fg_f} + C_{lf}(T_{fco} - T_{ref}) + u_{ref}$$

By rearranging this equation and noting the continuity Equation (5.31), the result is

$$m_{fco} u_{fg_f} \dot{X}_{fco} + m_{fco} c_{lf} \dot{T}_{fco} = \dot{m}_{fco} P_{fco} v_{fco} \tag{5.39}$$

again noting that $P_{fco} = P_{sat}(T_{fco})$. Now there are two unknowns

(T_{fco}, X_{fco}) which are derivatives of time and two equations which describe their behavior. The core is coupled to the two-phase bubble by $\dot{m}_f$ and thus must be solved simultaneously with the governing equations for the bubble. For the core region under the assumption of a nonequilibrium blowdown into the bubble, the core conditions (T_{fco}, P_{fco}) are not in equilibrium, thus they are taken from the experimental conditions observed (e.g., SRI experiment). Thus the mass flow from the core ($\dot{m}_f$) is given by Equation 5.7 where

$$G_{core} = \frac{\dot{m}_f}{A_{core}} = \frac{1}{\sqrt{2\pi R_f}} \left[\frac{P_{sat}(T_{fco_i})}{\sqrt{T_{fco_i}}} - \frac{P_{fco}}{\sqrt{T_{sat}(P_{fco})}} \right] \tag{5.40}$$

and the flow is saturated vapor $X_{fco} = 1$. The energy transferred to the bubble by this convective flow is

$$\dot{m}_f h_{fco} = \dot{m}_f (X_{fco} h_{fg_f} + c_{lf} T_{sat}(P_{fco})) \tag{5.41}$$

The conservation of mass equation for the bubble is given by

$$\frac{dm_{fb}}{dt} = +\dot{m}_f$$

A one dimensional momentum equation is utilized to describe the bubble expansion given by

$$a = \frac{dv_{slug}}{dt} = \frac{d^2x}{dt^2} = \frac{(P_{fb} - P_\infty)}{M_{slug}} A_p \tag{5.42.1}$$

where

$$P_{fb} = P_{sat}(T_{fb}) \tag{5.42.2}$$

The energy equation for the bubble is given by

$$\frac{d}{dt}(m_{fb} u_{fb}) = -\dot{q}_l - P_b \frac{dV_b}{dt} + \dot{m}_f (u_{fc} + P_{fco} v_{fco})$$

where

$$u_{fb} = X_{fb}\ u_{fg_f} + c_{fl}(T_{fb} - T_{ref}) + u_{ref} \tag{5.43}$$

and where

$$X_{fb} = \frac{P_{fb}\ V_b}{m_{fb} R_f T_{fb}} \tag{5.44}$$

$$V_b = A_p\ x \tag{5.45}$$

The energy equation can be rearranged in terms of enthalpies to give

$$\frac{d}{dt}(m_{fb} h_{fb}) = -\dot{q}_l + V_b \frac{dP_{fb}}{dt} + \dot{m}_f(u_{fco} + P_{fco} v_{fco}) \tag{5.46}$$

where

$$h_{fb} = X_{fb}\ h_{fg_f} + c_f(T_{fb} - T_{ref}) + h_{ref} \tag{5.47}$$

Simplifying the result is

$$m_{fb}\dot{h}_{fb} = -\dot{q}_l + V_b \dot{P}_{fb} + \dot{m}_f\ (h_{fco} - h_{fb}) \tag{5.48}$$

Now the derivative of pressure can again be approximated by the Clausius Clapeyron relation

$$\frac{dP_{fb}}{dt} = \frac{dP_{fb}}{dT_{fb}} \quad \frac{dT_{fb}}{dt} = \frac{h_{fg_f}}{v_{gb} T_{fb}} \frac{dT_{fb}}{dt} = \frac{P_{fb}\ h_{fg_f}}{R_f T_{fb}^2} \dot{T}_{fb} \tag{5.49}$$

With these definitions for X_{fb}, V_b, h_{fb}, and $\dot{P}_{fb}$, the energy equation is only a function of the bubble saturation temperature (T_{fb}) and previously defined unknowns (x, $\dot{q}_l$, $\dot{m}_f$, X_{fco}, T_{fco}). Thus this set of nonlinear ordinary differential equations in time are a complete system of equations to describe the transient expansion given the initial conditions ($t = 0$) for x, v_{slug}, X_{fco}, T_{fco}, T_{fb}, q_l, m_{fco}, m_{fb}. For the SRI condensible

tests because water occupies the fission gas plenum region as in their N_2 test, a two stage expansion is used as in Chapter 3 which only modifies the momentum equation (Equation 5.42). The first stage is when the displaced volume is equivalent to the water expelled from the fission gas region, and there the mass of the slug (M_{slug}) and projected area (A_p) correspond to the water mass and area in the fission gas plenum. The second stage is the remainder of the expansion (majority of volume) where M_{slug} and A_p are taken to be the upper plenum water mass and area.

This system of non-linear ordinary differential equations are solved by using a numerical integration technique. The solution technique is especially designed to solve a "stiff" system of non-linear equations. The term "stiff" refers to the fact that the rate of change of some dependent variables (e.g. X_{fco}, T_{fco}) is quite slow with time while others (e.g. x, q_1) are fast. This solution technique is incorporated as a library subroutine for the MIT IBM 370/168 computer. A more detailed explanation of its use is given in Appendix F. It should suffice to emphasize here that the process is a standard scheme for solution of stiff systems. In addition, Appendix F contains a description of the averaging technique for D_d, $\bar{h}$ and $\frac{dv_d}{dt}$ used in the heat transfer models.

5.5 Comparison with Experimental Results

5.5.1 Purdue - ANL Experiments

The experimental results for the three condensible tests performed by Purdue are given in Figures 5.8 to 5.16 along with the analytical predictions based upon the liquid heat transfer model.

One observation should be noted before the data and predictions are compared. For the low pressures used in Purdue's experiments, it is found that the characteristic Weber number for drops being entrained at sizes between $\lambda_c \leq D_d \leq \lambda_m$ is lower than the critical Weber number for breakup. This can be shown by a simple estimate where

$$We = \frac{\rho_v (V_{rel})^2 D_d}{\sigma}$$

For the Purdue tests, from Table 5.2

$$a = \frac{dv_{slug}}{dt} = \left(\frac{P_{f_i} - P_\infty}{M_{slug}}\right) A_p = \frac{(.45 - .1)\ 10^6 (.0182)}{5.56}$$

$$\simeq 1145\ m/s^2$$

$$D_d \simeq \lambda_c \text{ to } \lambda_m \simeq 1500 \text{ to } 2800\ \mu m$$

$$v_{rel} \simeq 4.65 \sqrt{a\lambda_c} = 6.3\ m/s$$

$$\rho_g \sim 2.35\ kg/m^2$$

$$We(\lambda_m) = 3.5$$

$$We(\lambda_c) = 1.9$$

Thus once the drops are entrained, they do not breakup because they are below the critical Weber number range (7-20). Thus the droplet diameter range remains between $\lambda_c \leq D_d \leq \lambda_m$ for all the tests.

The first question that should be addressed here is whether the Purdue experiments are best represented by an equilibrium or nonequilibrium blowdown from the core. Both models for $\dot{m}_f$ were utilized to predict the experimental results and the conclusion arrived at was that the Purdue tests seemed to behave in an equilibrium manner. The reason for this conclusion is based upon two factors:

1) The pressure and volume behavior which is predicted by the use of a nonequilibrium flow rate from the core does not show good agreement with the experimental behavior.

2) The time for pressure relief and vapor nucleation and departure in comparison to the expansion time of the experiment indicates that there is sufficient time for vapor nucleation on the heater walls of the core during the transient implying an equilibrium condition.

The comparison between the experimental results and the nonequilibrium model for the pressure behavior is shown in Figures 5.10 and 5.15. The average constant core pressure used in the nonequilibrium prediction was found by taking the raw data traces, similar to Figure 5.4, and calculating an average core pressure for each pressure spike and obtaining a time averaged value for each test. This average value was used as the nonequilibrium pressure for the core. The pressure data (pressure spikes eliminated) do not appear to be qualitatively the same as the constant value assumed although a plateau for the core pressure is indicated. This nonequilibrium mass flow out of core is included in the governing equations with the least approximate model for the liquid heat transfer (Model 1) and two facts are observed in comparison to the data: (1) The prediction of the displaced volume in the upper plenum does not exhibit good qualitative agreement with the experimental data (Figure 5.8); (2) The Weber number needed to quantitatively match the experiment represents a drop diameter which is larger than λ_m by a factor of two to three (see Figure 5.12 and 5.13). The largest value for the Weber number if $D_d = \lambda_m$ is We $\simeq$ 3.5; whereas; the empirical values of We for tests 3L and 4L if a nonequilibrium expansion is assumed are We = 8 and 12 respectively. Therefore, it appears that the nonequilibrium model is not a reasonable explanation for the experimental behavior. Further proof for this conclusion can be gotten by comparing the expansion time of the experiment ($\tau_{exp} \sim 20 - 30$ msec) to the

time for a pressure pulse to traverse the core and the time for vapor bubble nucleation at a heater wall in the core (τ_{nuc}). If the characteristic time for a pressure wave to transverse the core ($\frac{21}{c_a}_{core}$) is short compared to τ_{exp}, then core pressure uniformly decreases and the evaporation of the saturated liquid in the core would not only occur from the surface but from the hotter core walls. Vapor generation would occur in both places thereby causing a more homogeneous and less stratified core mixture. The increased surface area for evaporation would bring the two-phase expansion closer to equilibrium conditions. Thus a measure of the time needed for this equilibrium state would be to compare $\frac{21}{c_a}_{core}$ and τ_{nuc} to τ_{exp}. If $21/c_a \ll \tau_{exp}$, then the whole core will depressurize uniformly allowing nucleation not only from the surface but the heater walls. In addition, if $\tau_{nuc} \ll \tau_{exp}$, then the vapor nucleation time will be small in comparison to the experimental expansion time. The value of $\frac{21}{c_a}_{core}$ is approximately

$$\frac{21}{c_a}_{core} \sim \frac{2(.3m)}{500\ m/s} \simeq 1\ msec$$

where c_a is taken to be about equal to the acoustic velocity in the vapor. The value for τ_{nuc} can be found by using known correlations for the nucleation and departure frequency of a bubble from a heater surface [59],

$$fD_b^{\frac{1}{2}} = (8/3\ g\ \frac{\rho_l - \rho_v}{\rho_l})^{\frac{1}{2}} \qquad (5.50)$$

where

D_b = bubble departure size

$$= \sqrt{\frac{\sigma}{g(\rho_e - \rho_v)}}\,[.000154\ (\frac{\rho_l c_{pl} T_{sat}}{\rho_v h_{fg_f}})^{\frac{5}{4}}] \qquad (5.51)$$

It has been assumed here that the time for bubble nucleation and departure are equal. For the Purdue initial conditions $\tau_{nuc} = \frac{1}{f}$, and can be found to be $\tau_{nuc} \simeq 1$ msec. Both of these characteristic times are small compared to τ_{exp} and the approximate conditions for an equilibrium expansion are satisfied, further implying that an equilibrium two-phase core blowdown is more likely.

The prediction of transient behavior for tests 3V, 3L, 4L using equilibrium core conditions was done for all three liquid heat transfer models. For test 3V with high initial void fraction the volume expansion rate ($V_b(t)$, Fig. 5.8 & 5.9) is well predicted using the more approximate liquid heat transfer models #2 and #3. Also the same behavior that is exhibited in the noncondensible heated SRI tests is shown here; the droplet diameter used in these more approximate models is again bounded by the two characteristic sizes for Taylor Instabilities $\lambda_c \leq D_d \leq \lambda_m$, when rate model #1 is utilized as Figure 5.9 illustrates. In addition, the prediction of the model for the volume of entrained water (V_e) shows good agreement with the experimental data (Figure 5.11). The ordinate in the figure is the entrained liquid volume fraction which is defined as

$$(1 - \bar{\alpha}_b) \equiv \frac{V_e}{V_b + V_e} \tag{5.52}$$

The trend in the data is a decrease in the volume fraction with time and this is matched by the prediction. However, this agreement between model and experiment is not crucial because predicted experimental error in entrainment values is quite large for all the Purdue tests.

The low void fraction tests are shown in Figures 5.12 - 5.16. Again, agreement is maintained between the experimental data and the transient prediction using the more approximate liquid heat transfer models, #2 and #3,

for the volume expansion rate (Figure 5.12 and 5.13). It should be noted that the reason test 4L shows a greater vapor volume (V_b-displaced volume) at a given time is that the core orifice area is larger than in test 3L. This allows more hot two-phase water from the core to be expelled into the bubble, holding the bubble pressure higher than test 3L at a given time (Figure 5.15). This will increase the slug acceleration and give larger vapor volumes in shorter times. The physical bounds for the droplet diameter $\lambda_c \leq D_d \leq \lambda_m$ using rate model #1 encompass the experimental behavior as Figure 5.14 illustrates. For these tests the drop diameter is much closer to λ_c than in the past experiments. The entrainment volume predicted by the models agrees with the data (Figure 5.16). However, the trend of entrainment data for experiment 4L differs from the model and from the other experiments in that $(1 - \overline{\alpha}_b)$ increases with time while the tests 3V, 3L data (also SRI data) and all the model predictions decrease with time. The reason for this difference is not apparent unless some water from the upper plenum pool leaked into the voided region between the disks. Then, when the experiment began, cool water existed in the region and was later expelled into the upper chamber and increased V_e and $(1 - \overline{\alpha}_b)$ over what was seen in other tests.

The conclusion from these comparisons is that again Taylor Instabilities appear to be the dominant mechanism for entrainment in these tests and when utilized with the liquid heat transfer model show reasonable agreement with the transient data.

5.5.2 SRI Tests

The experimental results for the two condensible tests performed by SRI are depicted in Figures 5.17 - 5.19. Two points should be noted before

a comparison between models and experiment is made. First, because the pressures are higher in these tests than in the Purdue tests, the critical Weber number again becomes a lower bound for D_d. However, the Weber number for λ_m is not far from the We_{crit} range as can be estimated below

$$We\ (\lambda_m) \simeq \frac{\rho_v\ v_{rel}^2\ \lambda_m}{\sigma}$$

$$\simeq \frac{20\ (13)^2\ 700(10^{-6})}{.073} \simeq 34$$

The second point is that the core two-phase blowdown into the expanding bubble is truly nonequilibrium as Figure 5.3 depicted. The values for the saturated vapor pressure above the core water surface used in Equation 5.7 are taken from the experimental data. The estimate used in the Purdue tests to check the characteristic times criterion for an equilibrium expansion can also be used here where $\tau_{exp} \sim 4$ msec. The time for a pressure wave to transverse the SRI core chamber is again

$$\frac{2l_{core}}{c_a} \sim \frac{2(.15\ cm)}{500} \sim .6\ msec$$

The time for τ_{nuc} is again given by Equations 5.50 and 5.51 and when using the SRI initial conditions (Table 5.2), the result is $\tau_{nuc} \simeq 1$ msec. Therefore, for these experiments, all the characteristic times

$$\frac{2l_{core}}{c_a} \simeq \tau_{nuc} \simeq \tau_{exp}$$

are of the same order of magnitude, and the expansion would be expected to be more nonequilibrium in nature.

The pressure behavior for both experiments is given in Figure 5.17 along with an analytical prediction using the assumption of an equilibrium core blowdown. It can be seen that the nonequilibrium core pressure behavior

is qualitatively different from the predicted equilibrium behavior.

The transient expansion rate for the vapor volume ($V_b(t)$ - displaced water volume) is shown in Figure 5.18 for the experiment and for the analysis prediction using the least approximate model 1 for the droplet diameter bounds of $\lambda_c \leq D_d \leq \lambda_m$. Again the use of these bounding sizes does a satisfactory job in predicting the experimental results.

The experimental values for the coolant entrainment volume are illustrated in Figure 5.19 along with the analysis prediction. Again the agreement is quite good. It should be remembered that the SRI tests are in a scaled CRBR geometry with water in the fission gas plenum region. When the water-vapor interface exits into the upper plenum at a high exit velocity, the acceleration will be from coolant slug into the vapor because the growth is initially spherical. The same assumption used in Chapter 3 is assumed here. The Taylor Instability entrainment rate is assumed to be zero for $1.2 < (V_b + V_{fco})/V_{fco} < 1.3$, which again corresponds to the criterion detailed in Appendix D.

The final point to note about the entrainment behavior is that as the vapor expands into the fission gas plenum region ($1.0 < V/V_i < 1.2$), the Taylor Instability model for entrainment again underpredicts the entrained water volume by about 30 cc. This same behavior due to other transient entrainment mechanisms was noted in the SRI N_2 tests and the MIT tests [54] in Chapter 3. This amount of entrainment is not large when compared to that predicted to be due to Taylor Instabilities (~330 cc).

The overall conclusion that can be drawn from these condensible experiments is that Taylor Instability entrainment appears to be the dominant mechanism for coolant entrainment in the expanding vapor bubble. Utilization of this phenomenon with a liquid heat transfer model, rate

model 1, for a range of droplet diameters $\lambda_c < D_d < \lambda_m$ does predict the experimental transient behavior for these condensible tests.

TABLE 5.1

SUMMARY OF PURDUE AND SRI EXPERIMENTS

TEST RUN PURDUE-ANL	INITIAL PRESSURE (P_{g_i}-MPa)	ORIFICE AREA (A_{core}-(cm^2))	INITIAL CORE VOID FRACTION (α)	NONCONDENSIBLE GAS PRESSURE (MPa)
1-V	.45	5.06	.95	~0
2-V	.45	9.5	.95	~0
3-V	.45	15.5	.95	~0
4-V	.69	15.5	.95	~0
1-L	.45	5.06	.1-.15	~0
2-L	.45	7.9	.1-.15	~0
3-L	.45	9.5	.1-.15	~0
4-L	.45	13.0	.1-.15	~0
5-L	.45	7.1	.1-.15	~0
1-V(A)	.45	15.5	.95	.0167
2-V(A)	.45	15.5	.95	.033
3-V(A)	.45	15.5	.95	.05
4-V(A)	.45	15.5	.95	.0667
5-V(A)	.45	15.5	.95	.078
6-V(A)	.45	15.5	.95	.083
7-V(A)	.45	15.5	.95	.092
SRI				
VESSEL TOP REMOVED	8.12	26.8	.04	-
VESSEL TOP IN PLACE	8.27	26.8	.04	-

TABLE 5.2

INITIAL CONDITIONS FOR THE TESTS ANALYZED

TEST	P_{g_i}	T_{g_i}	M_{slug}	A_{vessel}	m_{fcore}	X_{core}
PURDUE-ANL	(MPa)	(^oK)	(kg)	(cm^2)	(kg)	
3V	.45	421	5.56	182	.017	.0463
3L	.45	421	5.56	182	.210	.00044
4L	.45	421	5.56	182	.269	.00044
SRI						
VESSEL TOP REMOVED	8.12*	578*	8.15	341	.706	~0
VESSEL TOP IN PLACE	8.27*	578*	8.15	341	.706	~0

*NONEQUILIBRIUM EFFECTS REDUCE THE INITIAL CONDITIONS TO

$$P_{g_i} = 4.9 \text{ MPa}$$

$$T_{g_i} = 534^oK$$

FIGURE 5.1

PURDUE-ANL EXPERIMENTAL APPARATUS FOR CONDENSIBLE WATER TESTS

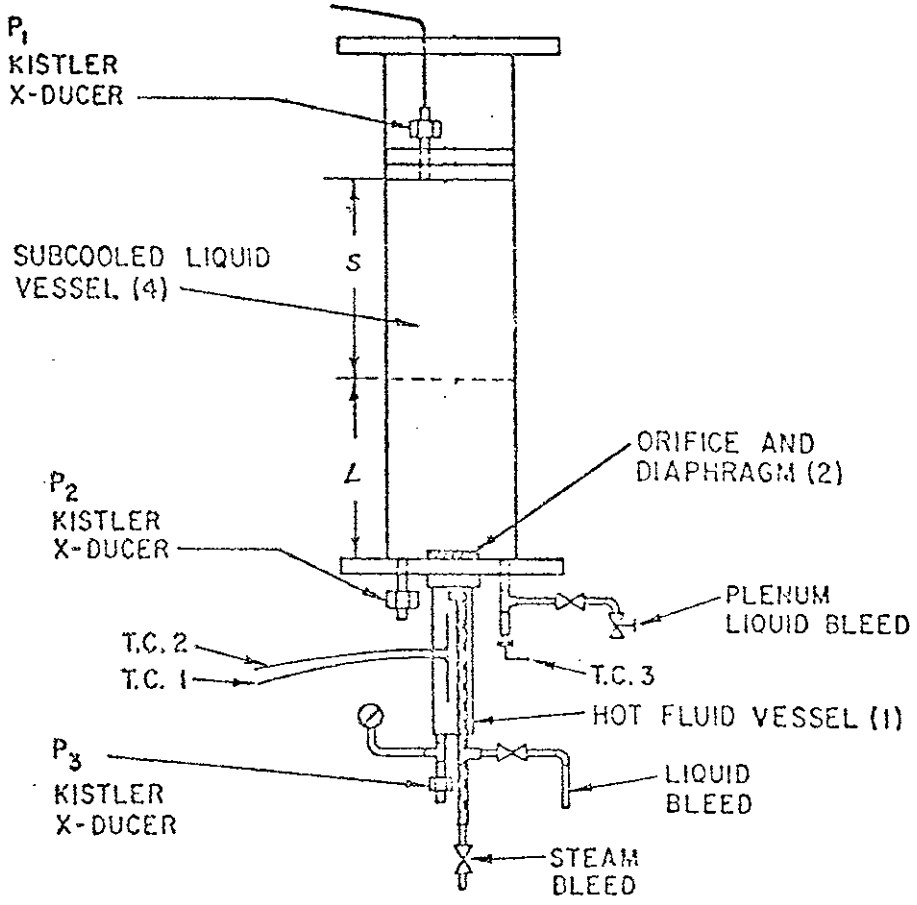

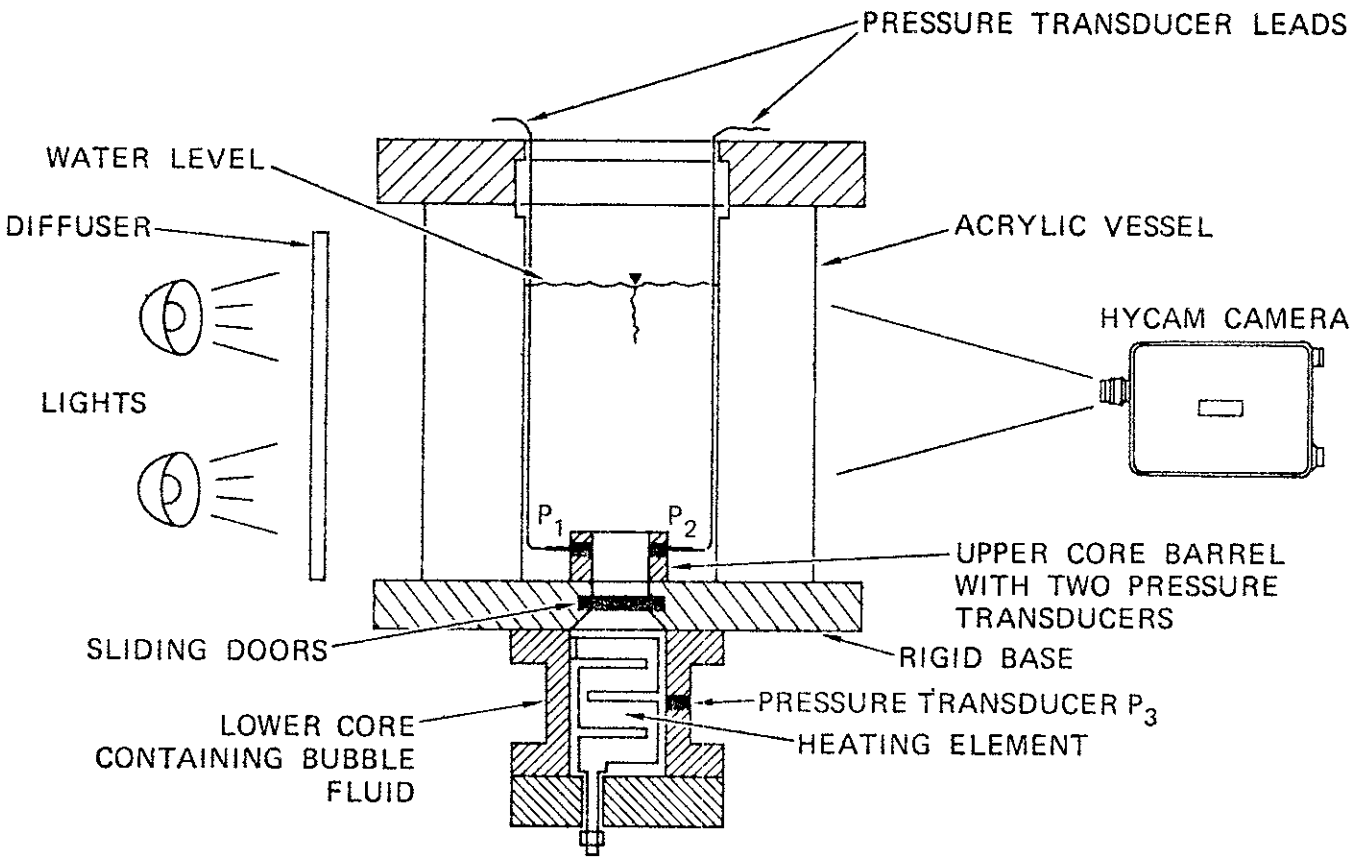

FIGURE 5.2 SRI EXPERIMENTAL APPARATUS FOR CONDENSIBLE WATER TESTS

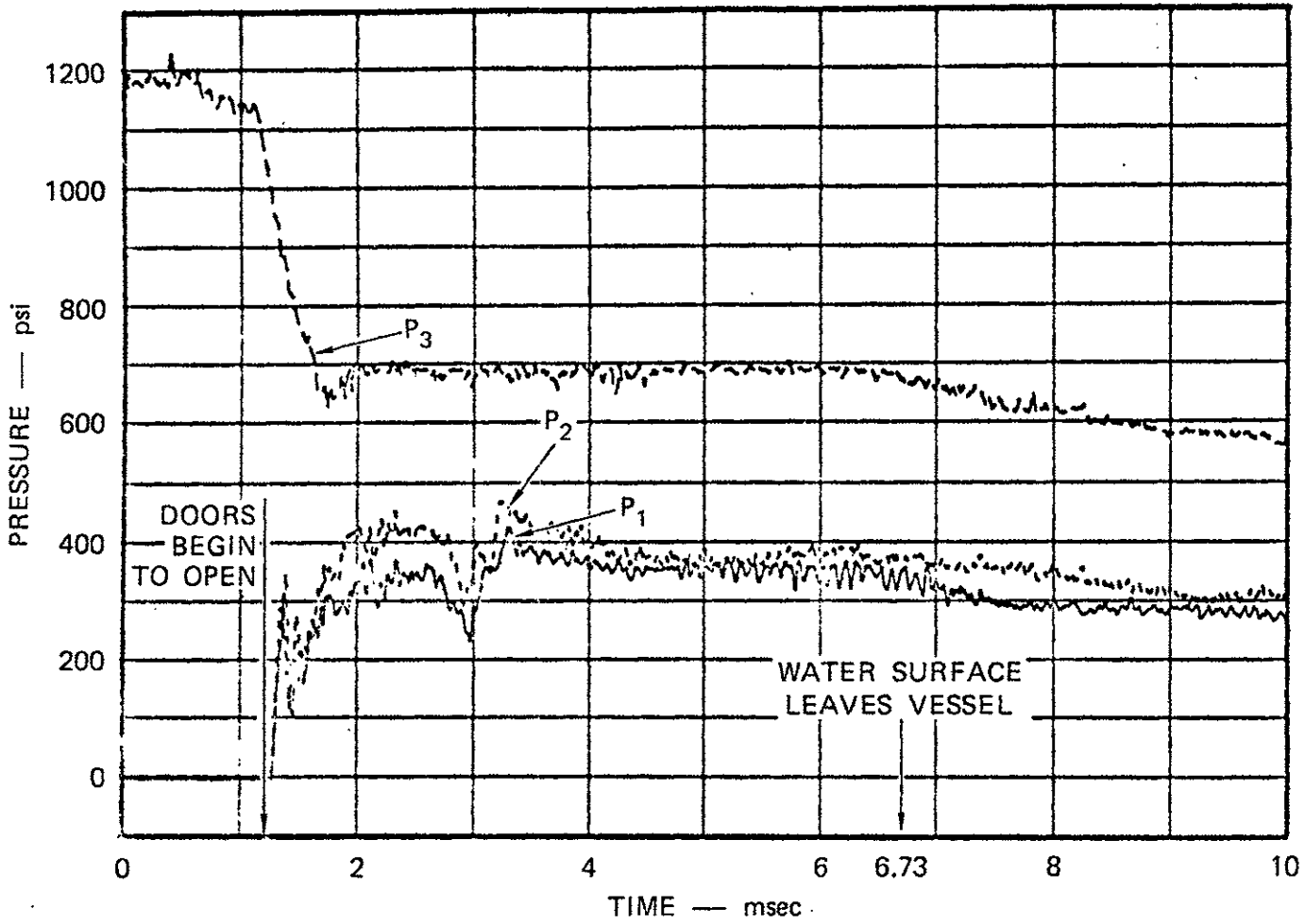

FIGURE 5.3 NON-EQUILIBRIUM PRESSURE BEHAVIOR FOR SRI TESTS

FIGURE 5.4 TRANSIENT PRESSURE BEHAVIOR FOR PURDUE TEST 3V

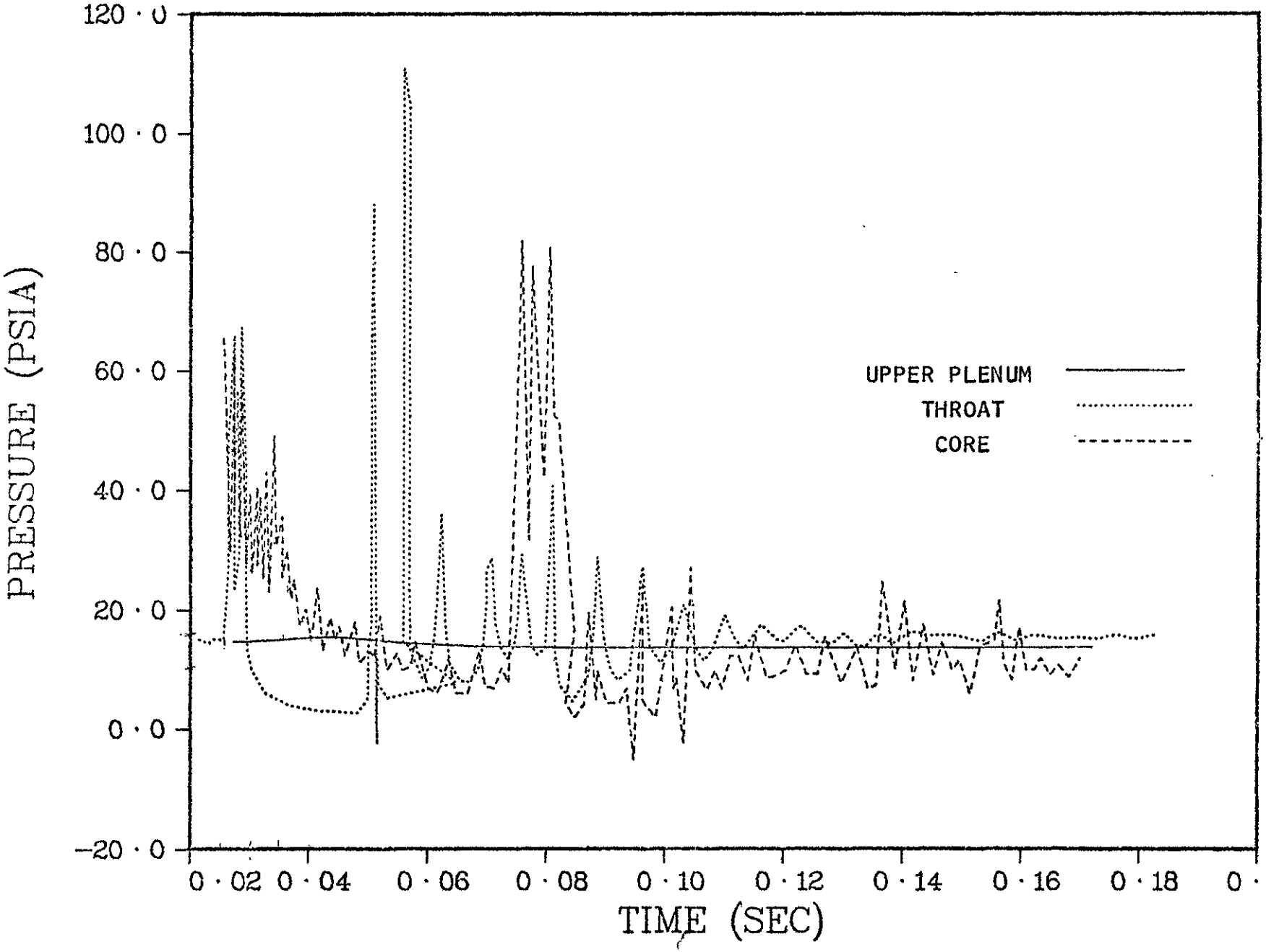

FIGURE 5.5

CONCEPTUAL VIEW OF THE INITIAL TWO-PHASE STRATIFICATION IN THE CORE

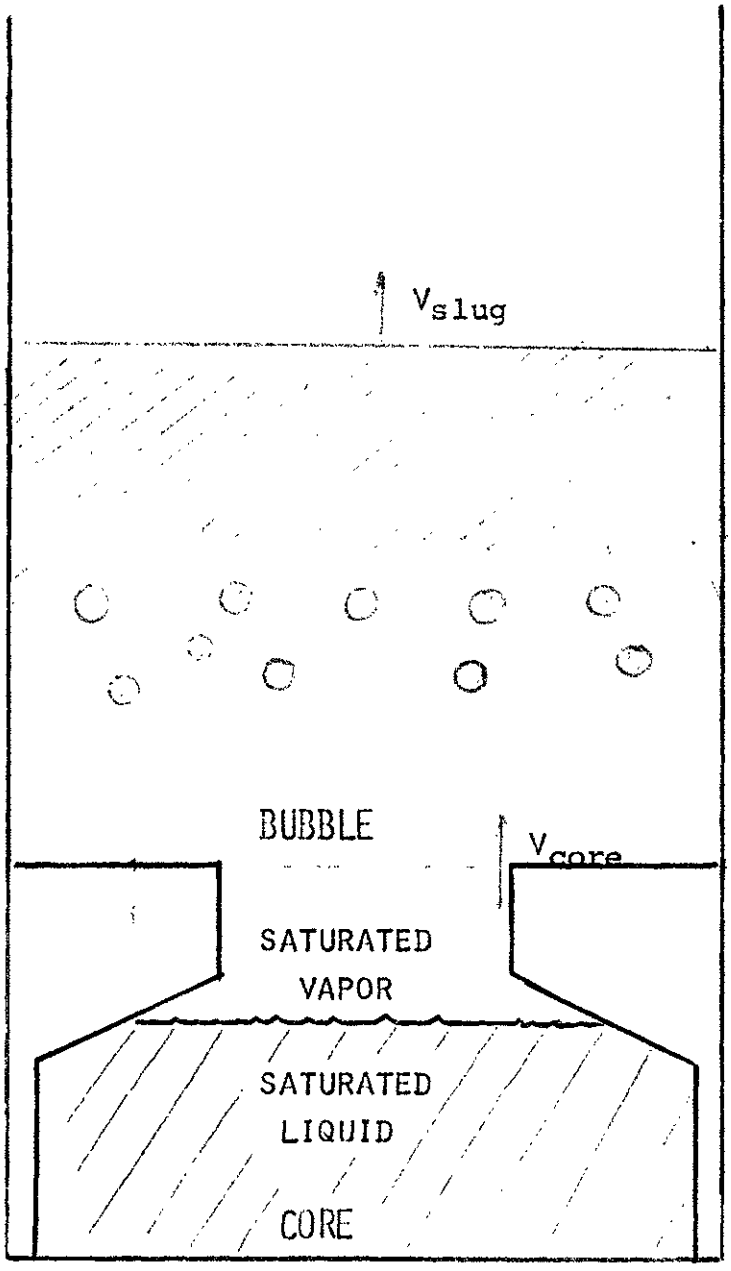

FIGURE 5.6

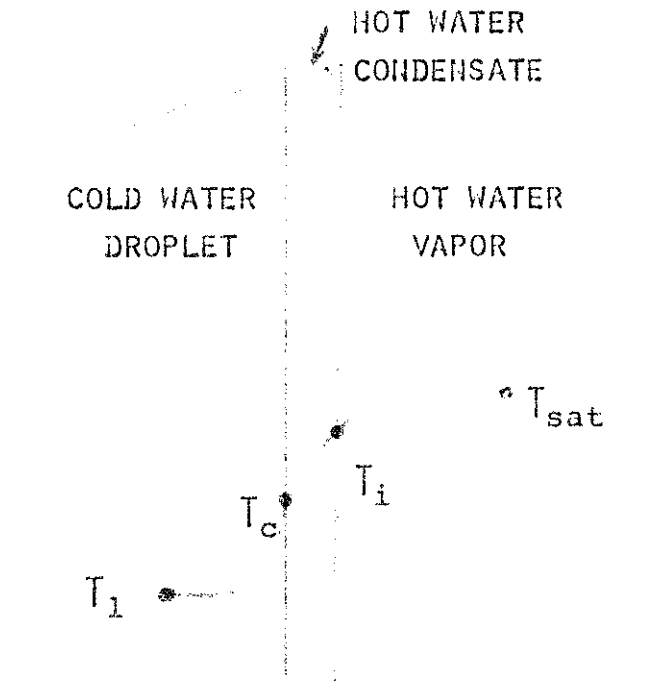

$$\bar{h} = \left[\frac{1}{\frac{1}{\bar{h}_{interf}} \quad \frac{1}{\bar{h}_{cond}} \quad \frac{1}{\bar{h}_{drop}}} \right]$$

CONCEPTUAL VIEW OF HEAT TRANSFER COEFFICIENT FOR CONDENSATION

FIGURE 5.7

CONCEPTUAL MODEL TO THE BUBBLE EXPANSION

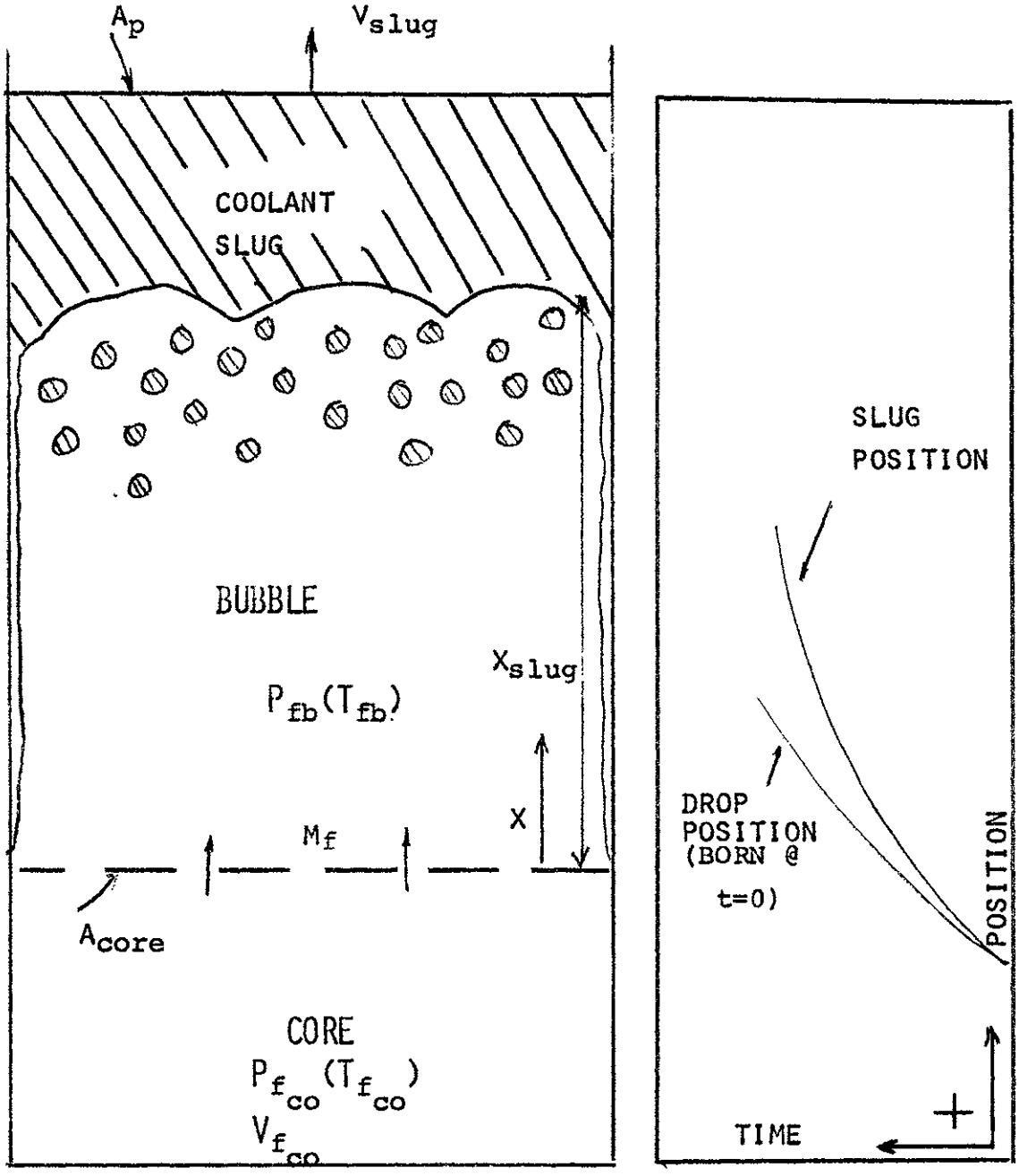

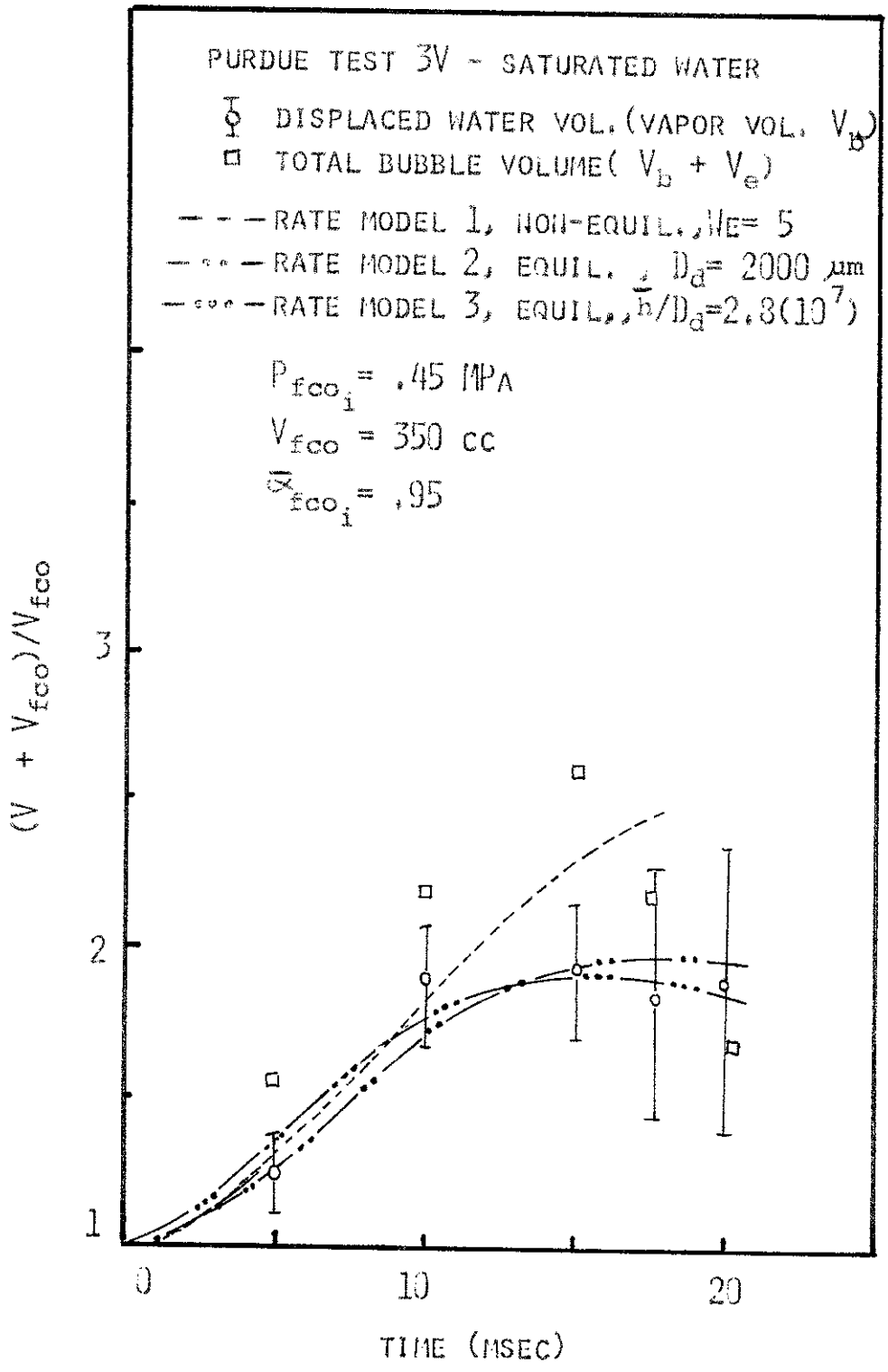

FIGURE 5.8 PURDUE TEST 3V, VOLUME EXPANSION BEHAVIOR DUE TO THE TWO-PHASE EXPANSION

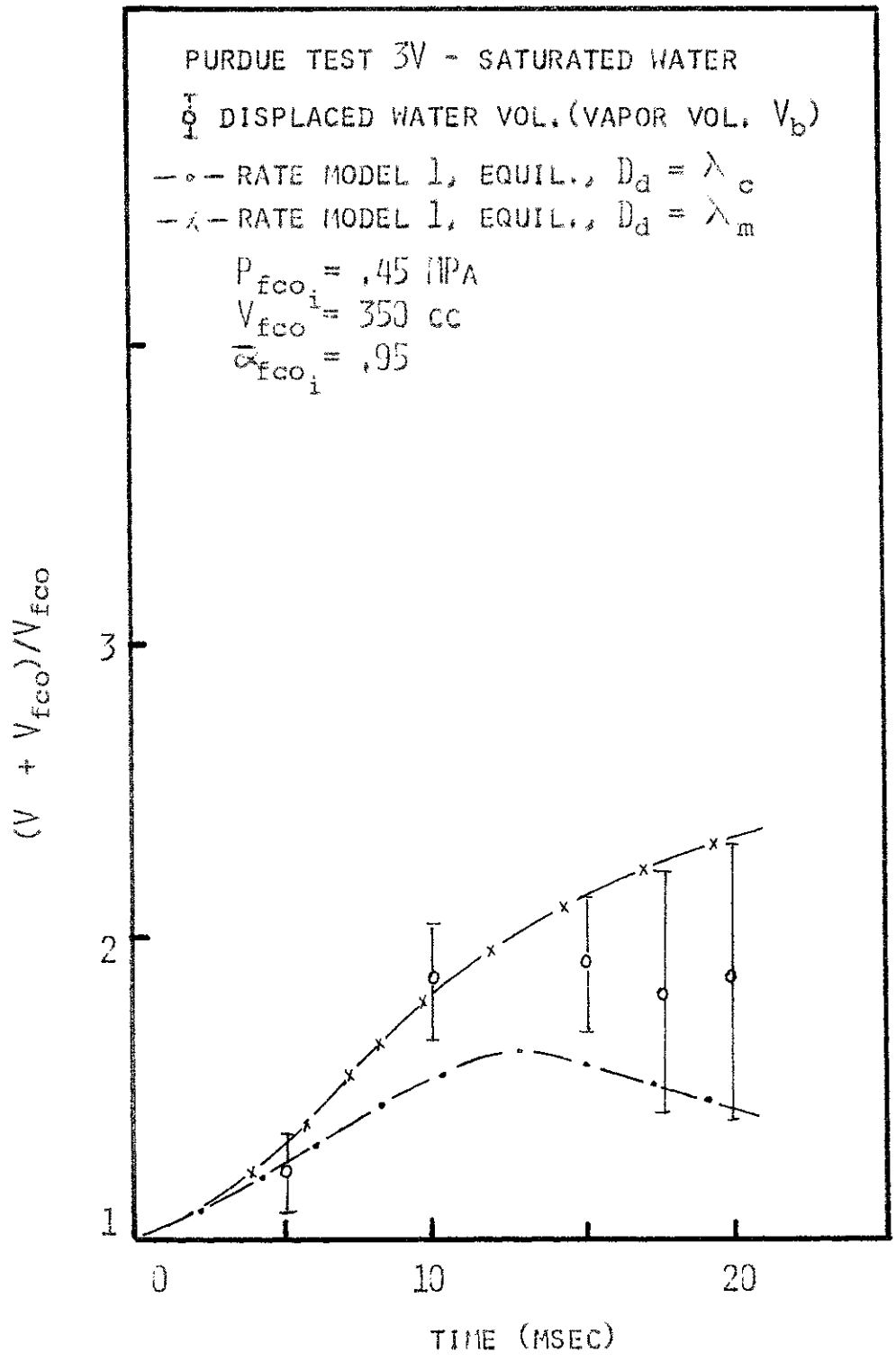

FIGURE 5.9 PURDUE TEST 3V, COMPARISON OF VOLUME EXPANSION BEHAVIOR FOR $\lambda_c < D_d < \lambda_m$

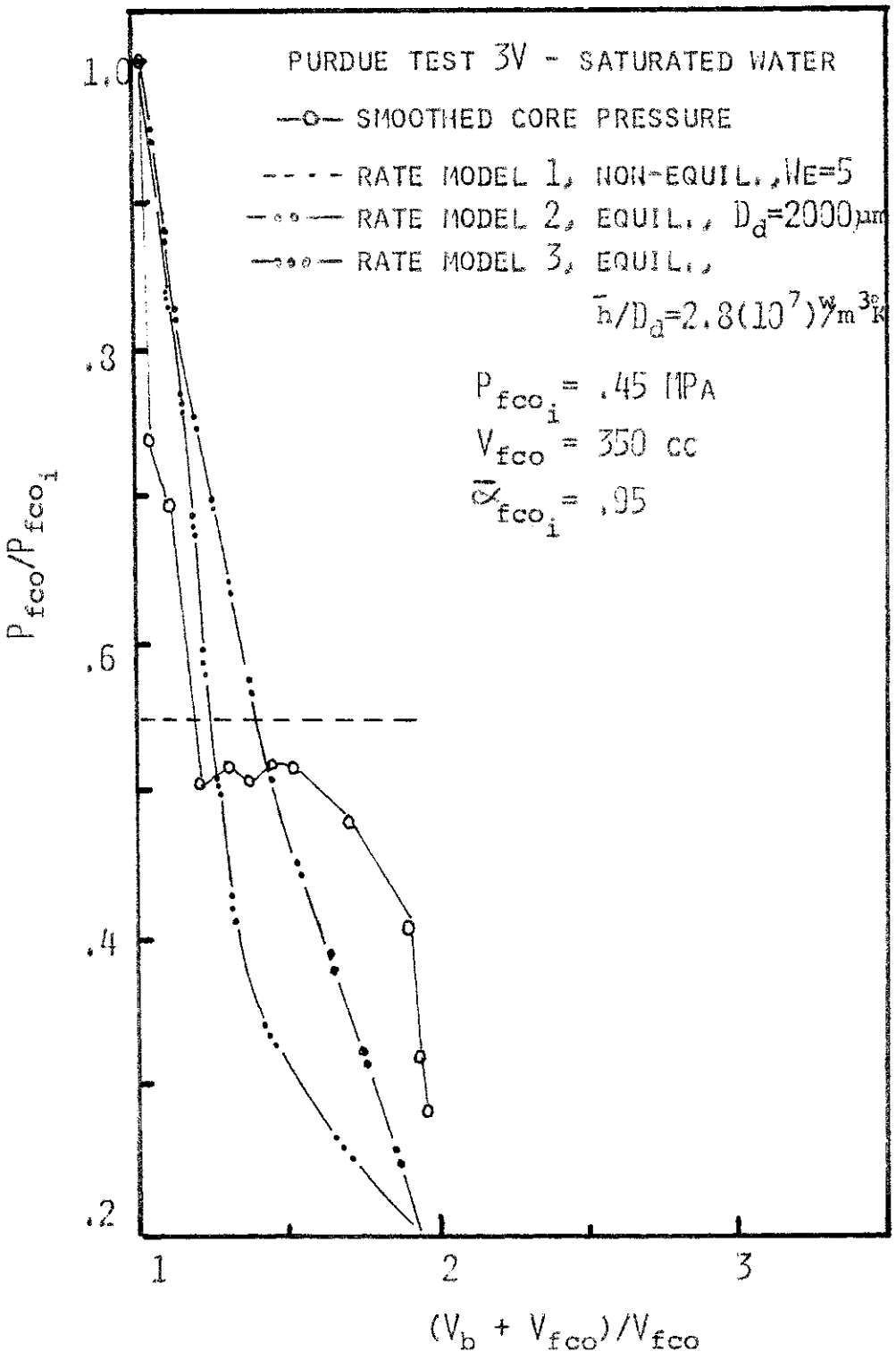

FIGURE 5.10 PURDUE TEST 3V, TRANSIENT PRESSURE BEHAVIOR

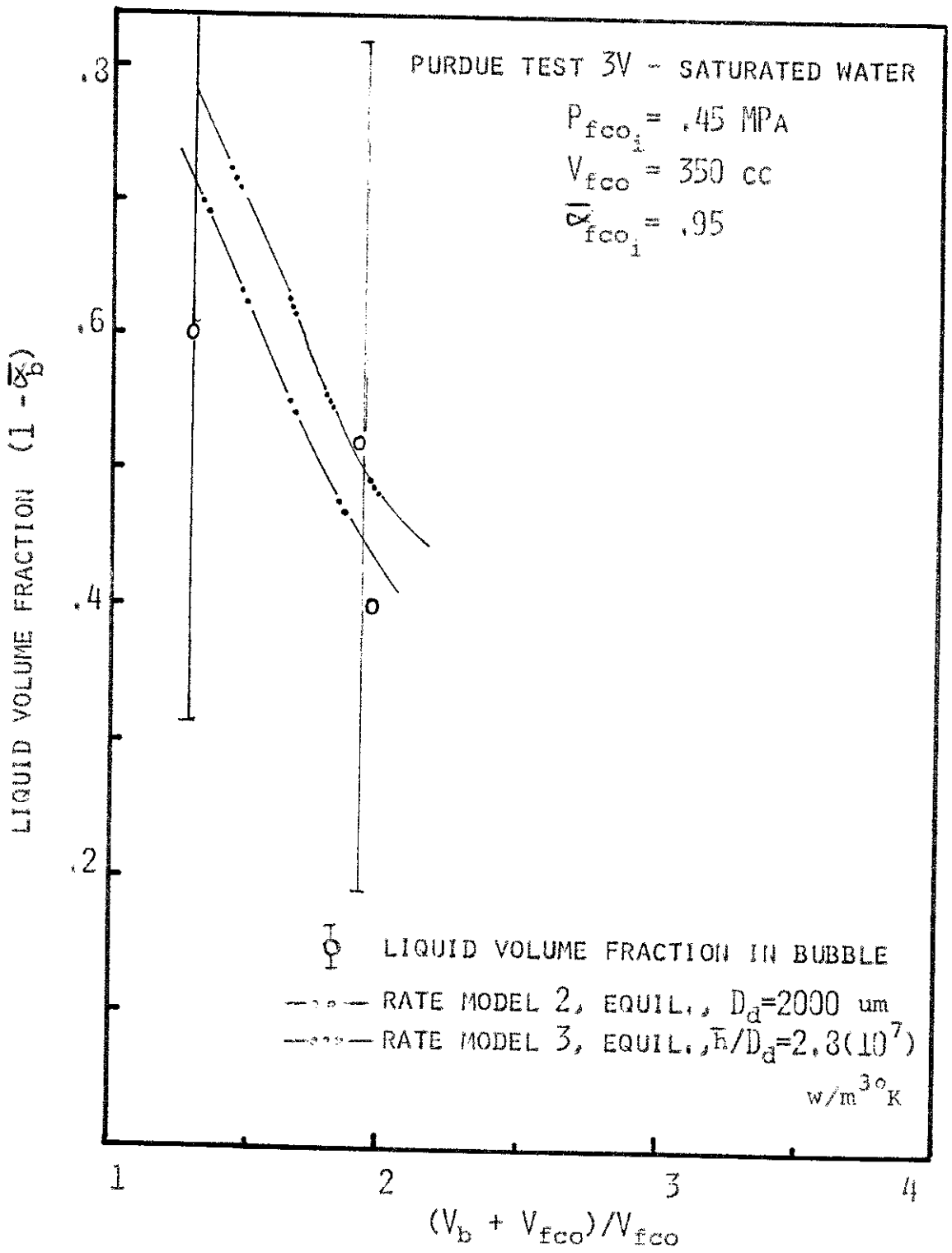

FIGURE 5.11 PURDUE TEST 3V, ENTRAINED COOLANT VOLUME FRACTION IN BUBBLE

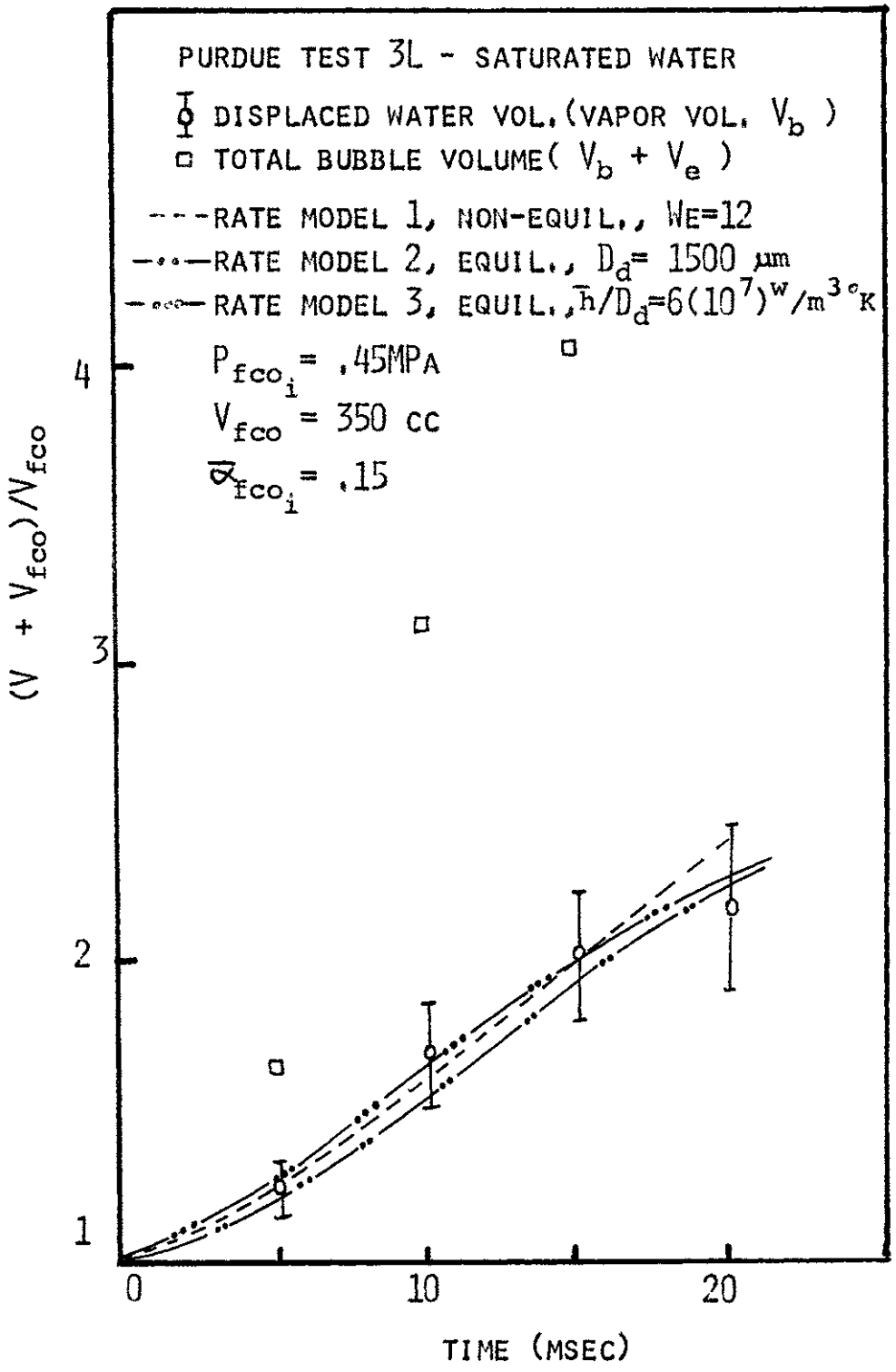

FIGURE 5.12 PURDUE TEST 3L,VOLUME EXPANSION BEHAVIOR DUE TO THE TWO-PHASE EXPANSION

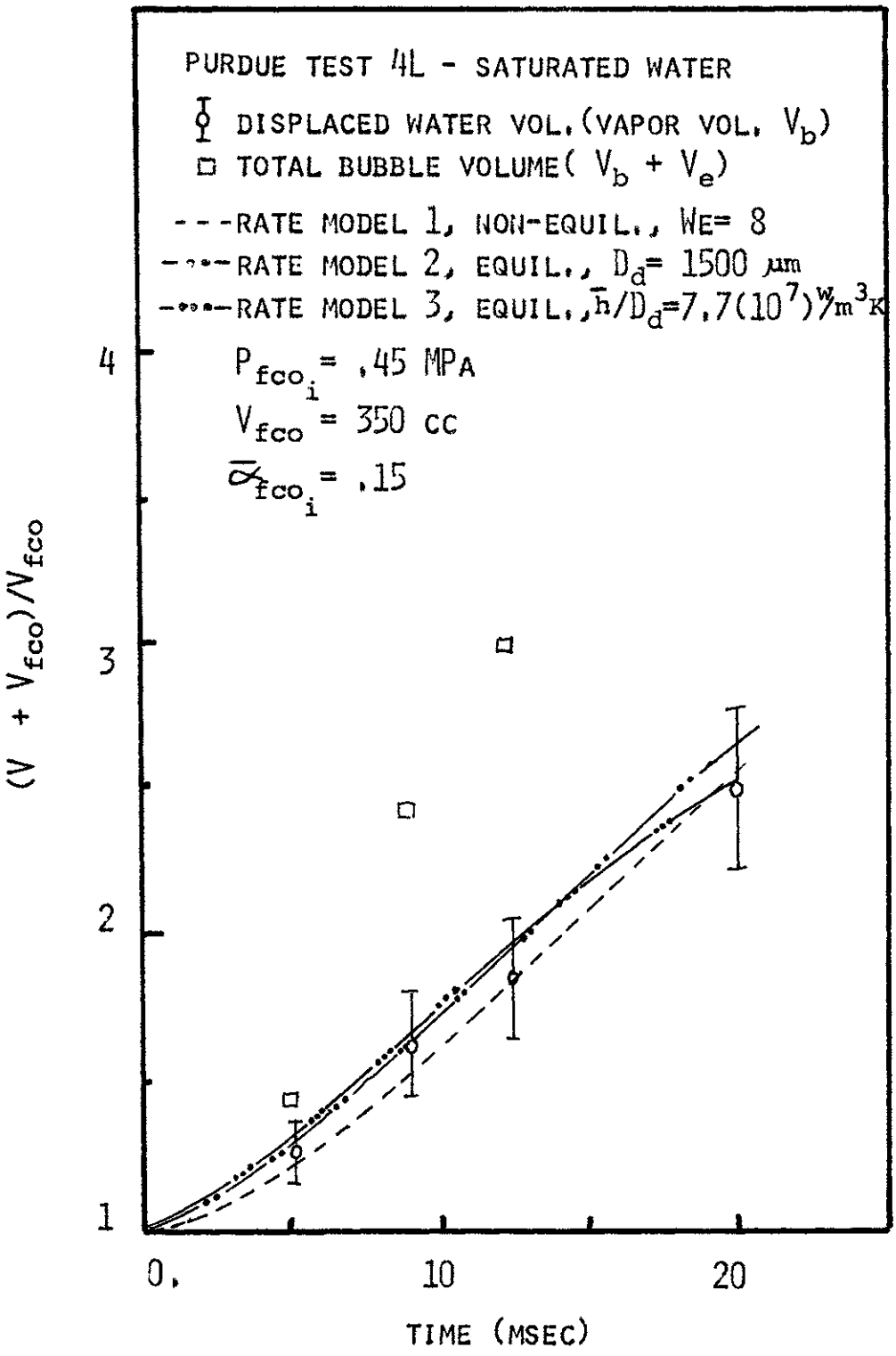

FIGURE 5.13 PURDUE TEST 4L, VOLUME EXPANSION BEHAVIOR DUE TO THE TWO-PHASE EXPANSION

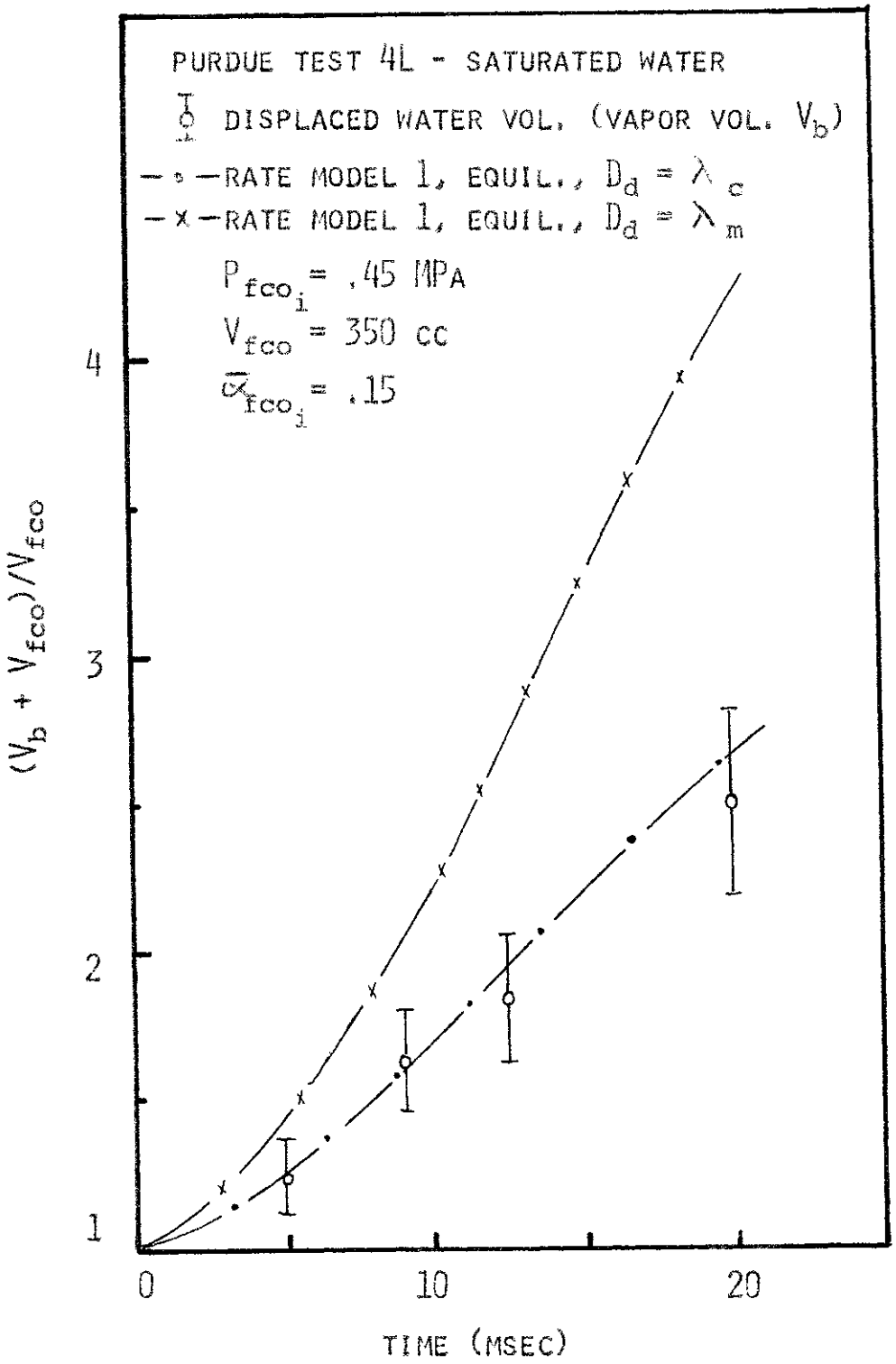

FIGURE 5.14 PURDUE TEST 4L, COMPARISON OF VOLUME EXPANSION BEHAVIOR FOR $\lambda_c < D_d < \lambda_m$

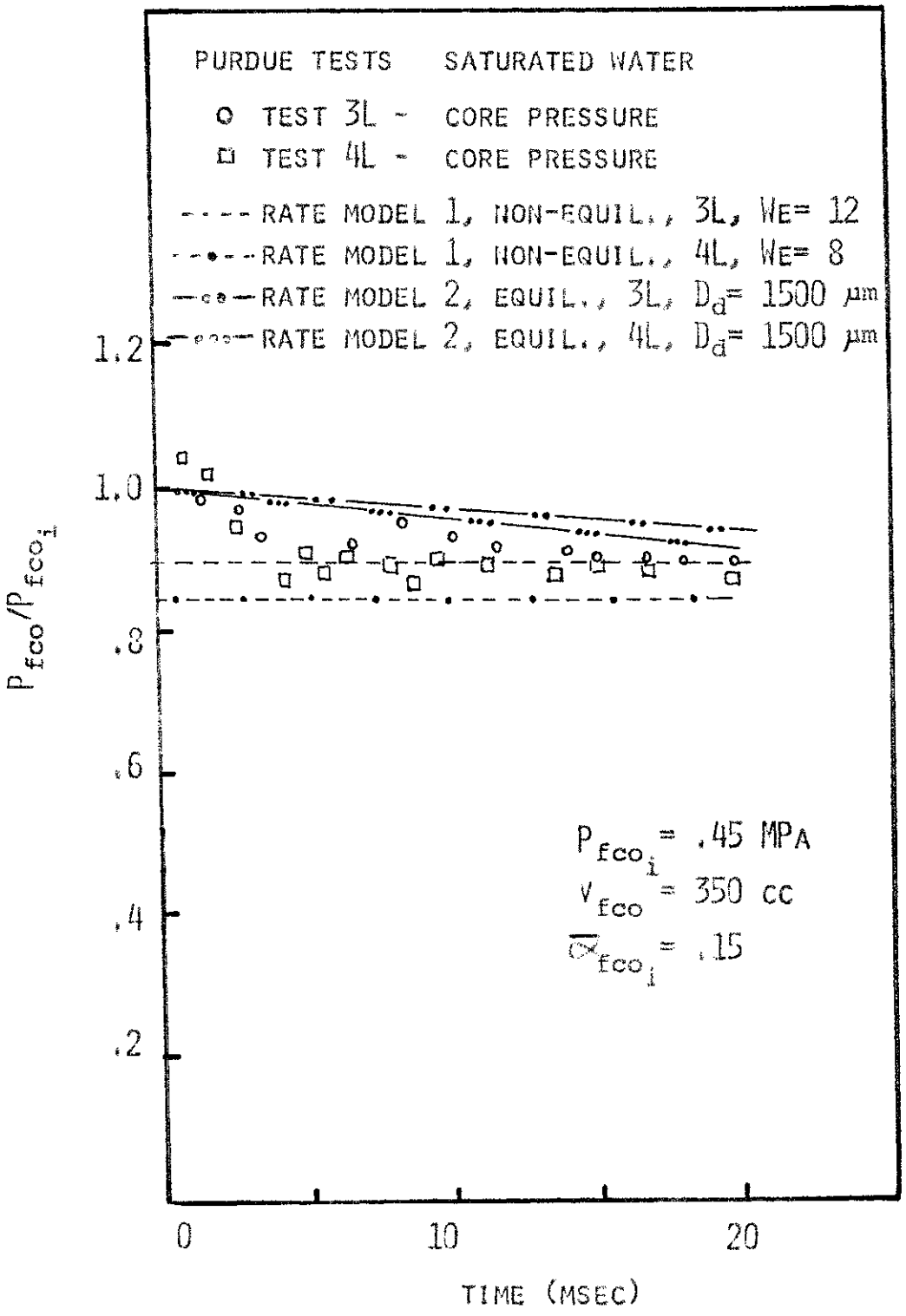

FIGURE 5.15 PURDUE TESTS 3L & 4L, COMPARISON OF THE TRANSIENT PRESSURE BEHAVIOR

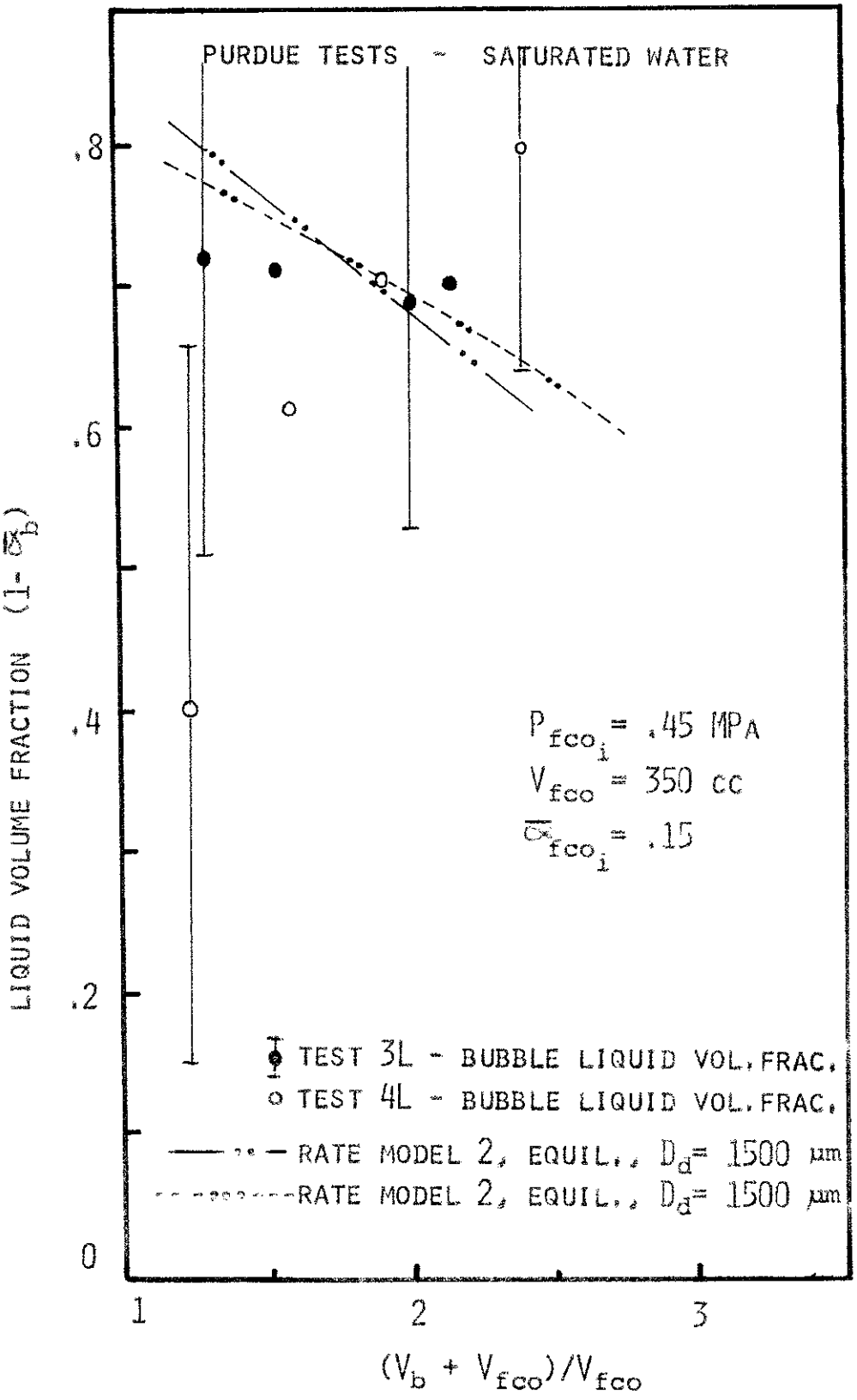

FIGURE 5.16 PURDUE TESTS 3L & 4L, ENTRAINED COOLANT VOLUME FRACTION IN THE BUBBLE

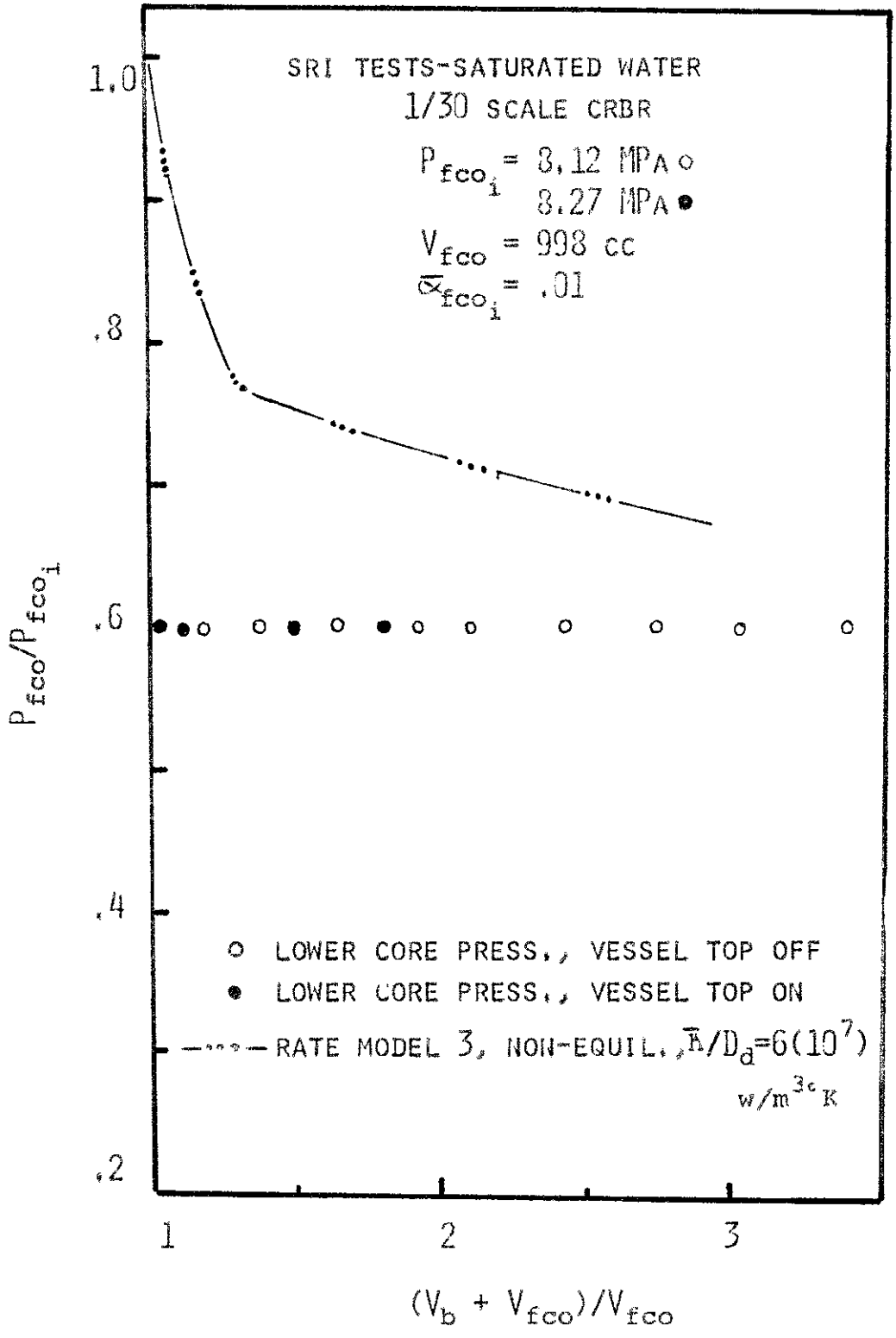

FIGURE 5.17 SRI TESTS TRANSIENT PRESSURE BEHAVIOR

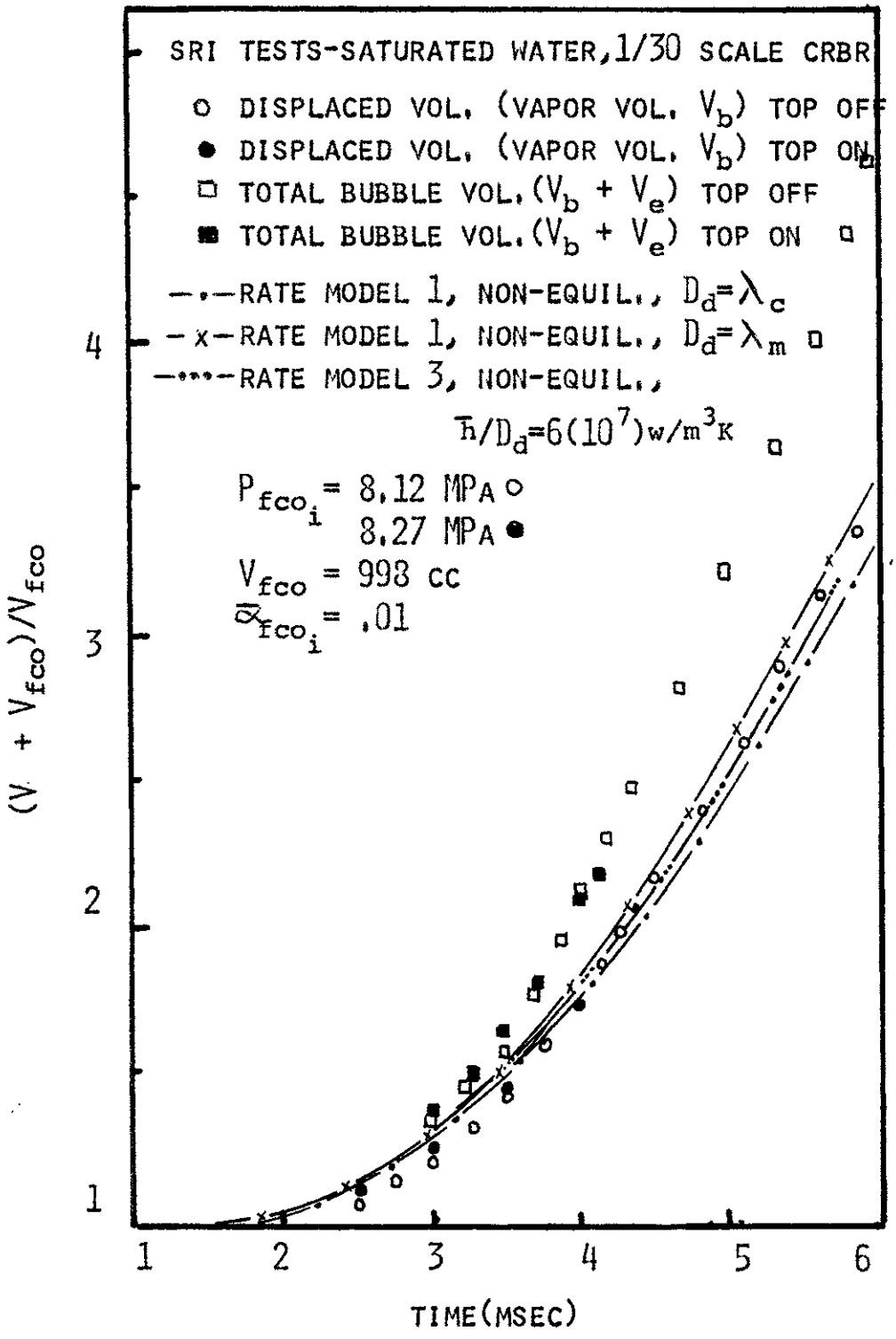

FIGURE 5.18 SRI TESTS VOLUME EXPANSION BEHAVIOR DUE TO THE TWO-PHASE EXPANSION

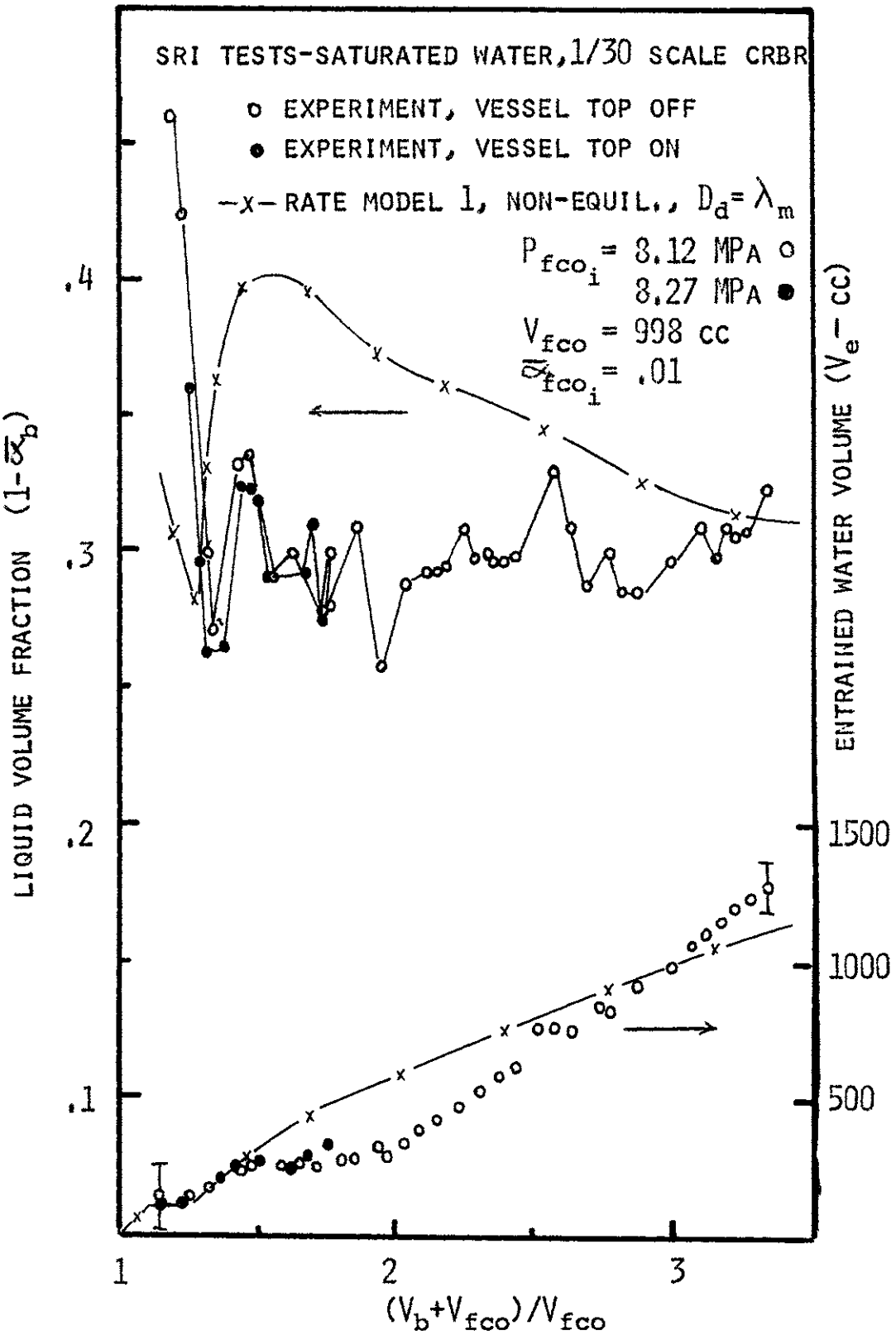

FIGURE 5.19 SRI TESTS ENTRAINED COOLANT VOLUME FRACTION

6. THE EFFECTS OF SODIUM ENTRAINMENT AND HEAT TRANSFER WITH TWO-PHASE UO_2 DURING AN HCDA

6.1 Overview

The hypothetical core disruptive accident (HCDA) which has been simulated in the separate effects experiments by Purdue and SRI is assumed to be initiated by a loss of flow incident in conjunction with a failure to shutdown the fast breeder reactor with its control rod system. This initiating event then can lead to a variety of consequences for the reactor core, the least probable and yet most catastrophic being a hydrodynamic disassembly. This accident path (Figure 2.2) leaves the core materials (steel, fuel) in a two-phase configuration at high pressures. A more extensive description of this phase of the accident is given in Chapter 2 and References 2 and 9.

Once this hypothetical accident has reached this stage of initial conditions, the prime concern is the damage potential of this high pressure source and the possible leak paths it may create to the environment for the transport of the radioactive fuel. A major avenue for this radioactivity transport would occur if the high pressure source expands and accelerates the sodium pool above it as a slug and impacts the reactor vessel head with enough kinetic energy to breach its containment capability (see Figure 6.1). This expansion work of the two-phase core materials is then a measure of the disruptive mechanical energy of this accident.

The magnitude of this expansion work is dependent upon the initial conditions of the two-phase core materials, the possible geometries of the system and other phenomena that could mitigate the effective work of this expansion. The possible interdependence of all these variables is given in Figure 6.2. Because the initiation of this accident is not determined mechanistically, the possible range of initial conditions for the two-phase

core materials is quite large. The amount of structural steel in the core and its physical state can affect the expansion work because it could provide a large heat sink. For the analysis done in this study, the steel in the core is conservatively neglected. Also the two-phase fuel initially is not at a uniform temperature but rather contains large spatial temperature pressure and void fraction gradients, with the hotter high pressure zones in the central region. This initial configuration could lead to a self-mixing phenomenon [10] whereby the hotter regions of fuel are cooled by the outer low temperature regions and reduce the pressure and the overall expansion work of the two-phase source. This phenomenon, being complex and not well understood, is conservatively neglected in this analysis and the two-phase fuel (UO_2) is assumed to be at a uniform saturation pressure and temperature.

One major question is the nature of the expansion of the two-phase fuel, whether it be equilibrium or non-equilibrium. If the initial two-phase fuel flow regime is homogeneous and the expansion time (τ_{exp}) is much longer than the time for a pressure wave to traverse the core ($\frac{21}{c_a}$), the the core expansion will be near equilibrium and transport both liquid and vapor upwards into the expanding bubble. This is the more likely situation because the hydrodynamic disassembly will probably leave the core initially in a homogeneous state. However, if the initial core two-phase geometry is stratified or if $\tau_{exp} << \frac{21}{c_a}$, then the expansion will have an inhomogeneous nature similar to the characteristics of the SRI two-phase water experiments in Chapter 5. SRI tests resulted in saturated vapor being expelled into the expanding bubble, and would represent a much lower work potential up to slug impact. The reason is that there was no saturated fuel liquid present to evaporate and support the bubble pressure as the vapor expands and cools down due to liquid-vapor or solid-vapor heat transfer. In all the analysis presented here, it is

conservatively assumed that the fuel expansion behaves in a homogeneous and equilibrium fashion.

There are three possible geometric configurations which can be visualized for the core expansion, and they are listed in Figure 6.2 and shown pictorially in Figure 6.3. If the above-core structure (i.e., fission gas plenum - upper axial blanket - coolant flow guide tubes and chimney) remains intact after the initial phases of the accident, then the two-phase fuel expansion will be one-dimensional in nature, with the two-phase fuel accelerating the sodium slug in this planar region. More importantly, the fission gas plenum can provide substantial surface area for solid heat transfer and a high L/D ratio for frictional pressure dissipation of the core expansion fluid. Both of these phenomena are quite complicated and are being investigated by others [10,26,30,32,78]. Therefore, these issues are not addressed in this study. In addition to the effects of the solid structure, liquid sodium entrainment would occur during this planar expansion through the flow guide tubes and chimney region. The fission gas plenum structure will suppress coolant entrainment in its volume because the spacing between the fuel pins (~1.5 mm) is of the same order of magnitude as the critical wavelength (λ_c) for Taylor Instabilities.

The above-core structure may also be removed from the expansion path because it has been melted away or pushed aside by the hot core materials. Then the sodium liquid pool above the core provides the only means of heat transfer by coolant entrainment in the two-phase expansion zone. This may occur with the sodium in or out of the fission gas plenum region. The major difference for these two initial conditions is found to be in the amount of coolant entrained during the fuel expansion up to slug impact.

It is this final phenomenon of coolant entrainment and heat transfer that is investigated in this chapter. In this regard the following specific

parameters should be considered: (1) the possible effect of sodium vaporization during the heat transfer process; (2) the possible controlling mechanisms occurring during this heat transfer process, conduction, sodium vaporization, radiation, fuel condensation; (3) the mechanism for sodium entrainment; (4) the characteristic size of the entrained coolant droplet; (5) the relative velocity between the fuel and coolant; (6) the mass flow rate of two-phase fuel from the core region. These concepts are addressed in the next section. After this ground work has been laid, the governing equations for the analysis are presented along with possible heat transfer models for the UO_2 vapor-sodium liquid interaction.

6.2 Models Utilized in the Heat Transfer Analysis

6.2.1 Isentropic Expansion Work of Two-Phase Fuel

Before describing the mechanistic models for sodium entrainment, droplet diameter and heat transfer a simple model [4] for an isentropic expansion of the two-phase fuel from known initial conditions to a final volume at slug impact is presented. With this basic model of the expansion work in mind, the results of the subsequent analyses using different heat transfer models can be easily contrasted and compared.

To perform this analysis a few simplifying assumptions are employed:

(1) The fuel vapor behaves as a perfect gas.
(2) The fuel thermophysical properties are constant (Appendix A).
(3) The slope of the saturation curve is approximated by the Clasium Clapeyron relation.
(4) The volume occupied by the liquid fuel is small in comparison to that occupied by the vapor.

The thermodynamic state principle requires that

$$Tds = dh_f - v_f dP_f \tag{6.1}$$

and in an isentropic expansion ds = 0 which gives

$$dh_f = v_f dp_f \tag{6.2}$$

where

$$h = X_f h_{fg_f} + c_{l_f}(T_f - T_{ref}) + h_{ref} \tag{6.3.1}$$

$$dh_f \doteq h_{fg_f} dX_f + c_{l_f} dT_f \tag{6.3.2}$$

The fuel specific volume (v_f) can be approximated by

$$v_f = (1-X_f)v_{l_f} + X_f v_{gf} \doteq X_f v_g \simeq X_f \frac{R_f T_f}{P_f} \tag{6.4}$$

When this is substituted into the right-hand side of Equation 6.2 with the ClausiusClapeyron relation, the result is

$$v_f dP_f \doteq \left(\frac{X_f R_f T_f}{P_f}\right)\frac{dp_f}{dT_f} dT_f = \left(\frac{X_f R_f T_f}{P_f}\right)\left(\frac{h_{fg_f}}{v_{fg} T_f}\right) dT_f$$

therefore

$$v_f dP_f \doteq \frac{h_{fg_f} X_f dT_f}{T_f} \tag{6.5}$$

If Equation 6.3 and 6.5 are equated, the result is

$$h_{fg_f} dX_f + c_{l_f} dT_f = h_{fg_f} X_f \frac{dT_f}{T_f}$$

which by rearranging and dividing by T_f gives

$$h_{fg_f}\left(\frac{dX_f}{T_f} - \frac{X_f dT_f}{T_f^2}\right) = -c_{l_f}\frac{dT_f}{T_f}$$

$$h_{fg_f} d\left(\frac{X_f}{T_f}\right) = -c_{l_f}\frac{dT_f}{T_f} \tag{6.6}$$

Now if this relation is integrated from the initial conditions (i) to those at any T_f and X_f at a larger expansion volume, the result is

$$\frac{X_f}{T_f} = \frac{X_{fi}}{T_{fi}} + \frac{c_{l_f}}{h_{fg_f}} \ln \frac{T_{fi}}{T_f} \tag{6.7}$$

This relation gives us the thermodynamic properties at the end state for a specified final volume. The energy equation can now be utilized to obtain the expansion work as

$$(U_{f_i} - U_f) = -\Delta W$$

or

$$\Delta W = m_f[(h_f - P_f v_f) - (h_{f_i} - P_{f_i} v_{f_i})] \quad (6.8)$$

Substituting in the definitions for h_f (Equation 6.3) and v_f (Equation 6.4) the result is

$$\Delta W = m_f[(X_{f_i} - X_f)h_{fg_f} + c_{l_f}(T_{f_i} - T_f) + R_f(X_f T_f - X_{f_i} T_{f_i})] \quad (6.9)$$

Using the initial conditions given in Table 6.2 the work derived from an isentropic expansion of the core materials is depicted in Figure 6.4. These can be compared to the upper and lower bounds on the expected expansion based upon estimates described in the following sections. These limits are not based on mechanistic heat transfer models but rather on known limits to the possible effects of sodium entrainment.

6.2.2 Vaporization Potential of the Sodium Coolant

The effect of sodium entrainment and heat transfer on the expansion work of the vapor bubble is highly dependent upon the amount of sodium which is vaporized during the process. This was emphasized in Chapter 1 and 2 where the results of Cho and Epstein's work [3] demonstrated that sodium could be a work enhancing fluid given a small amount of sodium mass entrained, a small drop diameter (100μm) and a large heat flux (black body radiation). At a given temperature sodium has a higher vapor pressure than does UO_2 (see Table 6.3). Thus the expansion characteristics of the two-phase fuel given the three conditions of the Cho and Epstein analysis vaporized a substantial

fraction of the entrained sodium coolant causing the expanding bubble to have a higher pressure and a larger work output at slug impact.

If a large enough fraction of the entrained sodium is vaporized because of heat transfer, then the expansion would be nearly at constant pressure. This behavior would occur because of two counter-balancing effects: (1) As the two-phase bubble expanded the fuel partial pressure would decrease due to the expansion and heat transfer. However, subsequent sodium vaporization would raise its partial pressure in the bubble, keeping the total pressure high; (2) The pressure would not greatly exceed the core pressure because if it did, the flow of the two-phase fuel out of the core into the expanding bubble would cease halting the energy supply for further sodium vaporization and keeping the pressure near that of the core.

Given this unusual coupling of two substances with quite different thermodynamic properties, the adverse effect on the expansion work due to sodium entrainment can be given an upper limit as Figure 6.4 illustrated.

A lower bound on the expansion work results if all the sodium entrained were assumed to be brought to its saturation temperature instantaneously but did not vaporize. This lower bound is a function of how much liquid sodium is entrained and the initial conditions and geometry, and an example of its effect is shown in Figure 6.4. The models and governing equations used to get this lower bound will be presented in the following sections.

The effect of sodium entrainment and heat transfer using the more mechanistic models detailed in the following sections will then fall within this bounding envelope of possible vapor expansion work.

6.2.3 Coolant Entrainment Rate

As in the past analyses of small scale experiments in Chapters 3, 4 and 5, it is believed that a dominant mechanism of coolant entrainment is Taylor Instabilities. The general result from the experiments performed in this work indicated that the entrainment rate could be modeled as

$$\dot{V}_e = A_p[C_1\sqrt{a\lambda_c} + C_2\sqrt{aD_p}] \qquad (3.28)$$

where the length scales are the critical Taylor instability wavelength, λ_c, and a characteristic geometrical size of the system, D_p. The relative entrainment velocity, $v_r \sim\sqrt{a\lambda_c}$, would represent a local entrainment mechanism dominated by instabilities of the size of λ_c, while $v_r \sim \sqrt{aD_p}$ would represent a global entrainment mechanism where much larger instabilities, a fraction of the system size, D_p, would contribute to entrainment.

This question of dominate length scales was a moot point for analysis of SRI and Purdue tests because the cylindrical size of the upper plenums in these small scale experiments (8-20 cm) were close in size to the width of the experimental apparatus used to correlate the Taylor entrainment phenomenon. Thus the predicted entrained coolant would not change significantly using either view with the appropriate correlated constants. However, if this model is to be applied now for full scale calculations, the resolution of which mechanism may be dominant is necessary. To answer this question an analysis of two-dimensional tests performed by Rothrock [54] was done. The characteristic width of this system was larger than previous experiments ($D_p \sim 30.5$ cm) and the acceleration range was quite different ($1<a/g<50$). The results indicated that the local mechanism entrainment model ($\dot{V}_e \sim A_p\sqrt{a\lambda_c}$) showed good agreement with experimental results while the other global model was in error by 50% which was outside the expected error of the experiment.

Therefore, the local entrainment mechanism was used in the analysis of the small scale tests of SRI [21,26] and Purdue [28]. The tests by Rothrock may be considered as not completely definitive because the change in scale for the acceleration or the diameter was not large. However, it does give the indication that the proper model to use with a large change in scale is

$$\dot{V}_e = 4.65\ A_p \sqrt{a\lambda_c} \tag{6.10}$$

This local model will be used in the full scale calculations presented. It should be noted though that the usage of this local model is conservative because it will predict entrainment rates at full scale condition smaller than those of the global model. The reason is that the global model behaves as

$$\dot{V}_e / A_p \sim D_p^{\frac{1}{2}} \tag{6.11}$$

and thus with an order of magnitude or more change in the scale of the system from small (1/30) to full scale, it increases drastically in its prediction of the magnitude of coolant entrainment. Later in the heat transfer analysis the effect of this difference will be illustrated.

6.2.4 Relative Velocity and Characteristic Size of Entrained Sodium Droplet

The relative velocity between the entrained droplet and the vapor is modeled in a one dimensional manner identical to that used in Chapters 4 and 5. The relative velocity (see Figure 6.5) is the difference between the vapor velocity (v_g) and the drop velocity and is given by

$$v_{rel} = v_g - v_d$$

$$v_{rel}(x,t) = \frac{x}{x_{slug}} \left(v_{slug}(t) + C\sqrt{a\lambda_c}\right) - v_d(x,t) \tag{6.12}$$

The drop is initially born at the slug velocity ($v_{slug}(t_o)$) at a past time (t_o) and accelerates due to the frictional drag of the vapor described by the

momentum equation as

$$\frac{dv_d}{dt} = \frac{3}{4} C_d \frac{\rho_g}{\rho_l} (v_{rel}(x,t))^2 \qquad (6.13)$$

The relative velocity is different for each drop born at a different x at time t_o. Again in utilizing this concept of the relative velocity some approximations are made. These approximations again are identical to those utilized in modeling the small scale SRI and Purdue tests in Chapters 4 and 5 and will be described when the heat transfer models are presented in Section 6.5.2. The order of magnitude of v_{rel} initially for each set of initial conditions is given in Table 6.4 by the relation

$$v_{rel_i} \sim 4.65 \sqrt{a\lambda_c}$$

This initial value for the relative velocity will decrease as the expansion proceeds because the drag forces will accelerate the drop and reduce v_{rel} by at least a factor of about 5-10.

The droplet diameter is assumed to be equal to the critical Taylor instability wavelength, λ_c, given by

$$D_d = \lambda_c = 2\pi\sqrt{\frac{\sigma}{a(\rho_l-\rho_g)}} \qquad (6.14)$$

The reason for this choice is that for all of the small scale experiments of SRI and Purdue the model analysis qualitatively and quantitatively exhibited good agreement with the data when $\lambda_c \leq D_d \leq \lambda_m$ ($\sqrt{3}\lambda_c$). This occurred even when the characteristic Weber number was slightly above its critical values ($We - 30 \sim 100$ vs. $We_{crit} - 7\text{-}20$). The reason for this behavior was attributed to the fact that the drops did not have sufficient time to break up.

The droplet diameters and their Weber numbers when $\lambda_c = D_d$ for the range of full scale initial conditions are listed in Table 6.4. Again it

appears that as v_{rel} decreases, the Weber number approaches We_{crit} and $D_d = \lambda_c$ is stable and will not breakup. This conclusion is also substantiated by computing the time for droplet breakup (τ_{br}) from Sonin's [62] and Gordon's [66] analysis and comparing it to a characteristic expansion time up to slug impact. The time τ_{br} is given as

$$\tau_{br} = C \frac{D_d}{v_{rel}} \sqrt{\frac{\rho_l}{2C_d \rho_g}} \tag{6.15}$$

where $C \sim 10$. These results are also given in Table 6.4. The results for $T_f = 7000^{o}K$ indicate that some of the initial drops may breakup because $\tau_{br} \sim .5\ \tau_{exp}$. However, for the lower fuel temperatures $\tau_{br} \geq \tau_{exp}$, the indication being that the droplets once born do not significantly breakup in the allotted time. Based upon these results the droplet diameter is taken to be λ_c.

6.2.5 Mass Flow Rate of Two-Phase Fuel From Core

The phenomenon of a blowdown of a two-phase mixture from the core is quite different for the full scale than the small scale experiments of SRI and Purdue. The Purdue tests had an orifice installed between the core and the upper plenum, and the SRI tests were a non-equilibrium expansion. Both these situations are not expected at the full scale and, therefore, as a reasonable model for two-phase mass flow from the core a homogeneous equilibrium model is employed where

$$G_{fco} = \rho_{ex_f} \sqrt{2(h_{core} - h_{ex})} \quad \text{if } P_b < P_{fco} \tag{6.16.1}$$

$$G_{fco} = 0 \quad \text{if } P_b > P_{fco} \tag{6.16.2}$$

where $1/\rho_{ex_f} = v_{f_{ex}} = (1-X_{ex})v_f + X_{ex_f} v_g$ (6.16.3)

$$X_{ex} = X(s_{ex} = s_{core}) \quad (6.7)$$

and the subscript ex denotes the isentropic exit conditions. A description of this model in more detail and the other two-phase models is given in Appendix E.

6.2.6 Order of Magnitude Analysis of the Heat Flux by Various Sources

In the small scale experiments of SRI and Purdue one major mechanism dominated the heat transfer process; noncondensible gas tests - forced convection, condensible tests - condensation on the entrained droplets. The situation is quite different for full scale conditions where more than one mechanism for heat transfer must be considered: radiation, vaporization of sodium due to UO_2 condensation, conduction. An estimate of the magnitude of these heat fluxes using their characteristic Nusselt numbers can be made (see Table 6.5.).

The radiation heat flux assuming black bodies is given by

$$\dot{q}/A|_{rad} = \sigma_r(T_f^4 - T_l^4) \quad (6.17)$$

where the Nusselt number is

$$Nu = \frac{\bar{h}D_d}{k_g} = \frac{\sigma_r(T_f^4 - T_l^4)}{(T_f - T_l)} \frac{D_d}{k_g} \quad (6.18)$$

The conduction heat flux for a sphere is given by [59]

$$\dot{q}/A|_{cond} = \frac{k_g}{D_d} Nu\ (T_f - T_l) \quad (6.19)$$

where Nu = 2. The maximum heat flux caused by UO_2 condensation and subsequent sodium vaporization is much harder to estimate. One possible mechanism could be the situation where UO_2 condensation supplies the energy for the sodium droplet vaporization. Lee and Ryley [74] performed an experiment with a water droplet vaporizing into superheated steam and proposed

for vaporization the Nusselt number as

$$Nu = 2 + .74\ Re^{.5} Pr^{.33} \tag{6.20}$$

where

$$\dot{q}/A\Big|_{vap} = \frac{k_g}{D_d} Nu\ (T_f - T_l) \tag{6.21}$$

This can be used as an estimate of the heat transfer due to this mechanism where

$$Re = \frac{\rho_g\ v_{rel}\ D_d}{\mu_g} \tag{6.22}$$

and

$$Pr = \frac{c_{p_g}\ \mu_g}{k_g} \tag{6.23}$$

Table 6.5 indicates that, for full scale initial conditions, the fuel vapor radiation and sodium vaporization - UO_2 condensation processes will dominate the heat transfer process.

6.3 Possible Physical Mechanisms for Two-Phase Fuel and Coolant Heat Transfer

Consideration of the vaporization potential of the sodium coolant led to a non-mechanistic upper bound on the adverse effect of sodium entrianment and vaporization (see Figure 6.4). If the possible mechanisms for this heat transfer process can be more clearly defined, then the bounds on its effect on expansion work up to slug impact could be narrowed. To examine some of these mechanisms remember some of the key variables that can affect this heat transfer process (Figure 6.2):

(1) The relative amount of coolant entrained and its droplet size.

(2) The controlling heat flux for energy transfer.

(3) The effect of noncondensible gases.

Cho and Epstein [3] proposed a conservative heat transfer model which predicted a large amount of sodium vaporization based upon certain assumptions for each of these three factors: (1) small parametric amounts of sodium

coolant entrained with a fixed droplet size; (2) instantaneous achievement of the saturation temperature of the sodium droplets and black body radiation controlled vaporization; (3) non-condensible gas present and UO_2 condensation in a fog around the drop [79-85]. This model will give an upper bound on the expansion work due to the heat transfer mechanisms assumed.

This model can be initially used in this analysis for two purposes:

(1) To establish the consistency of this analysis with past work [3]

(2) To see the effect of replacing the parametric entrainment rates with the mechanistic Taylor Instability entrainment model for V_e and D_d.

All other physical processes are kept the same in the model (see Table 6.6, model 1).

This model can be altered (Table 6.6, model 2) by accounting for the radiation properties of the two fluids [76,77]. In particular, the reflectivity of a clean sodium surface is quite high (~96%). This fact, in conjunction with the view of the model that the UO_2 will condense in a fog around the drop, as the drop is vaporizing, suggests that the sodium surface during the accident will be clean and the heat flux mechanistically would be reduced by this radiative factor. Again the other assumptions remain the same as in the first model.

Another possible mechanism that could cause sodium vaporization given a saturated coolant droplet is UO_2 condensation near the drop, and forced convection effects replenishing the hot fuel vapor and sweeping away the condensate near the sodium droplet surface sustaining its vaporziation (Table 6.6, model 3). As Section 6.2.6 indicated using a Nusselt number from water vaporization experiments, the heat flux by this mechanism is comparable to the radiation heat flux (Table 6.5).

These three models are conservative in the modeling of heat transfer in that the sodium droplet is assumed to come instantaneously to its satura-

temperature and vaporization begins immediately. The total pressure in the expanding bubble due to both sodium and fuel vapor will be increased above realistic values because the sodium vaporization rate is large.

In a similar fashion a highly optimistic heat transfer model can be constructed to give a lower bound on the expansion work by considering the case where the entrained coolant is brought instantaneously to its saturation point but no vaporization occurs (Table 6.6, model 4). This would represent the maximum quenching effect of the sodium coolant as Section 6.2.2 initially indicated.

Given these models for the heat transfer process, upper and lower bounds on the expansion work can be identified. To obtain a realistic estimate of the sodium entrainment effect, the final two assumptions of the Cho and Epstein analysis should be investigated mechanistically: (1) What is the characteristic time for the bulk of the sodium droplet to come to its saturation temperature and is vaporization precluded during this interval; (2) What effect does noncondensible gas have on these phenomena and the mechanism for heat transfer. Figure 6.6 addresses these questions by listing two alternative concepts depending upon noncondensible gas effects.

If the mole fraction of noncondensible gas is large (mole fraction $\sim$ .1) and the entrained sodium droplet is not saturated, then the UO_2 vapor will probably condense away from the sodium droplet surface as a fog [79-81,84], leaving the surface clean (Figure 6.7). The most probable mechanism for heat transfer is then due to radiation from the liquid UO_2 fog in the vicinity of the droplet to the coolant surface (Table 6.6, model 5). If the time (τ_{sat}) for the drop to heat up to its saturation temperature is longer than the characteristic expansion time (τ_{exp}), then the sodium droplet will not vaporize.

On the other hand, if noncondensible gases are not present, then UO_2 vapor could condense on the sodium droplet (Table 6.6, model 6). However, due to the unusual mismatch of the thermophysical properties for these two materials and the high fuel vapor temperatures, the instantaneous interface temperature is quite large and is above the homogeneous nucleation point of the sodium [82]. Some of the sodium surface would vaporize pushing the condensate away while the remaining energy transferred during the contact goes into heating the bulk of the droplet. After the UO_2 vapor has diffused back to the sodium liquid surface, the cycle will repeat itself. This sputtering phenomenon (Figure 6.8) may continue causing two events to occur simultaneously; (1) heating the drop up to saturation, (2) vaporizing some of the coolant droplet. The rates of both of these processes in comparison to τ_{exp} and the conservative sodium vaporization rates of past models will determine if the sputtering process mitigates or enhances the fuel vapor expansion work. The phenomenon can be self-limiting in that as sodium vapor is generated the UO_2 cannot diffuse through it fast enough to significantly vaporize more sodium.

These last two physical mechanisms of vapor-liquid heat transfer embody the realistic models of the effect on sodium entrainment on the expansion work. The next section presents the governing equations used to analyze the expansion followed by a detailed mathematical description of each model and its effect on the vapor work.

6.4 Governing Equations for Expansion Process

The governing equations used in the analysis of this two-phase expansion are similar in approach to that used in Chapter 5. Two lumped parameter volumes are utilized in modeling the expanding two-phase mixture (Figure 6.5); one constant volume for the core region (adiabatic) containing only the

two-phase fuel, and one for the expanding bubble where sodium entrainment occurs. The two volumes are coupled by the mass flow rate of two-phase fuel from the core into the bubble. The dependent variables chosen to describe the fuel behavior in the core are the quality, X_{fco}, and the temperature, T_{fco}. The bubble expansion behavior is dependent on the fuel mass, m_{f_b}, and the sodium mass, m_{c_b}, thus the bubble pressure, P_b, and fuel temperature, T_{f_b}, are used to describe the state of the bubble. The assumptions utilized in the analysis are:

(1) The thermophysical properties of UO_2 and sodium are assumed to be constant and are listed in Appendix A.

(2) Sodium and fuel vapor can be modeled as perfect gases.

(3) The mass flow rate out of the core is based on a homogeneous equilibrium model.

(4) The bubble expansion is modeled with a one dimensional momentum equation.

(5) The liquid and vapor expelled from the core are equilibrium and saturated.

(6) The saturated liquid volume in the expanding bubble is assumed to be small in comparison to the vapor volume.

(7) The Clausius Clapeyron relation is used to describe the slope of the saturation line.

(8) No thermal interaction occurs between entrained sodium drops and UO_2 liquid from the core.

(9) The rate of change of kinetic and potential energy are negligible.

(10) The energy transferred by viscous dissipation is neglected.

Assumptions 3 and 4 and their validity will be discussed later with the results of the analysis. The remainder of the assumptions deal with the properties of the two reactor materials. Research is still actively underway to obtain more complete thermodynamic and thermophysical properties; therefore, these standard assumptions can be considered a first estimate to more detailed analysis.

For the core region the equation for the conservation of mass is

$$\frac{d}{dt}(m_{fco}) = -\dot{m}_f \tag{6.24}$$

or

$$\frac{1}{v_{fco}}\frac{dv_{fco}}{dt} = \frac{1}{m_{fco}}\dot{m}_f \tag{6.25}$$

where $m_{fco} = V_{co}/v_{fco}$

and $\dot{m}_f/A_{core}$ is given by Equations 6.15 - 6.17. Now the left-hand side of the equation can be rearranged in a similar manner to that done in Equations 5.31 to 5.35 by noting

$$v_{fco} = v_{l_f} + X_{fco}(v_g - v_{lf}) \doteq v_{l_f} + X_{fco}\frac{R_f T_{fco}}{P_{fco}} \tag{6.26}$$

to give

$$\frac{1}{v_{fco}}\frac{dv_{fco}}{dt} = \frac{1}{v_{fco}}\left[\frac{dX_{fco}}{dt}\left(\frac{R_f T_{fco}}{P_{fco}}\right) + X_{fco}\left[\frac{R_f}{P_{fco}}\frac{dT_{fco}}{dt} - \frac{R_f T_{fco}}{P_{fco}^2}\frac{dP_{fco}}{dt}\right]\right] \tag{6.27}$$

The Clausius Clapeyron relation can be utilized where

$$\frac{dP_{fco}}{dt} = \frac{dP_{fco}}{dT_{fco}}\frac{dT_{fco}}{dt} = \frac{h_{fg_f}}{v_g T_{fco}}\frac{dT_{fc}}{dt} \tag{6.28}$$

Inserting this into Equation 6.27 and solving for the rate of change of the fuel quality ($\dot{X}_{fco}$) the result is

$$\dot{X}_{fco} = \frac{P_{fco}}{R_f T_{co}}\left[\frac{v_{fco}}{m_{fco}}\dot{m}_f + \left[\frac{X_{fco} h_{fg_f}}{P_{fco} T_{fco}} - \frac{X_{fco} R_f}{P_{fco}}\right]\dot{T}_{fco}\right] \tag{6.29}$$

The energy equation for the core can be expressed as

$$\frac{d}{dt}(m_{fco} u_{fco}) = -\dot{m}_f(h_{fco}) \tag{6.30.1}$$

$$u_{fco} = X_{fco} u_{fg_f} + c_{l_f}(T_{fco} - T_{ref}) + u_{ref} \tag{6.31.1}$$

$$h_{fco} = u_{fco} + P_{fco}\, v_{fco} \tag{6.31.2}$$

By rearranging this equation and noting the continuity equation (6.24), the result is

$$m_{fco} u_{fg_f} \dot{X}_{fco} + m_{fco} c_{l_f} \dot{T}_{fco} = \dot{m}_{fco} P_{fco} v_{fco} \tag{6.30.2}$$

again noting that $P_{fco} = P_{sat}\ (T_{fco})$. There are two unknowns (T_{fco}, X_{fco}) given as derivatives of time and two equations which describe their behavior. The core is coupled to the two-phase bubble by $\dot{m}_f$ and thus must be solved simultaneously with the governing equations for the bubble.

The conservation of mass equations for the bubble for the fuel and coolant are given as

$$\frac{dm_{fb}}{dt} = \dot{m}_f \tag{6.32}$$

where $\dot{m}_f$ is from Equations 6.15-6.17

$$\dot{m}_e = \frac{dm_{fb}}{dt} = \rho_c \dot{V}_e \tag{6.33}$$

where $\dot{V}_e$ is from Equation 6.10.

A one dimensional momentum equation is utilized to describe the bubble expansion and is given by

$$a = \frac{dv_{slug}}{dt} = \frac{d^2x}{dt^2} = \frac{(P_b - P_\infty)\, A_p}{M_{slug}} \tag{6.34}$$

where the bubble pressure (P_b) is composed of the fuel vapor partial pressure (P_{f_b}) and the sodium vapor partial pressure if there is vaporization.

The energy equation for the fuel can be written as

$$\frac{d}{dt}(m_{fb} u_{fb}) = -\dot{q}_l - P_b \frac{d}{dt}(V_{fb}) + \dot{m}_f (u_{fc} + P_{fc}\, v_{fc}) \tag{6.35}$$

This can be rearranged to give

$$\frac{d}{dt}(m_{fb} h_{fb}) = -\dot{q}_l + V_{fb} \frac{dP_b}{dt} + \dot{m}_f\, h_{fc} \tag{6.36}$$

where $$h_{fb} = X_{fb} h_{fg_f} + c_{l_f} (T_{fb} - T_{ref}) + h_{ref} \quad (6.37)$$

The partial volume of the fuel in the bubble (V_{fb}) can be expressed in terms of the partial pressure of the fuel in the bubble by

$$V_{fb} = V_b \frac{P_{fb}}{P_b} \quad (6.38)$$

where $$V_b = A_p x \quad (6.39)$$

$$P_{fb} = P_{sat} (T_{fb}) \quad (6.40)$$

for a mixture of gases. Now the derivative on the left-hand side can be evaluated and the resulting equation is

$$m_{fb} \frac{dh_{fb}}{dt} = \dot{q}_1 + V_b \frac{P_{fb}}{P_b} \frac{dP_b}{dt} + \dot{m}_f (h_{fco} - h_{fb}) \quad (6.41)$$

or expanding

$$m_{fb}(h_{fg_f} \frac{dX_{fb}}{dt} + c_p \frac{dT_{fb}}{dt}) = -\dot{q}_1 + V_b \frac{P_{fb}}{P_b} \frac{dP_b}{dt} + \dot{m}_f (h_{fco} - h_{fb}) \quad (6.42)$$

The fuel quality (X_{fb}) is expressed in terms of the partial pressure and temperature of the fuel and is given by

$$X_{fb} = \frac{v_{fb} - v_{lf}}{v_g - v_{lf}} \doteq \frac{v_{fb}}{v_g} = \frac{P_{fb} V_b}{m_{fb} R_f T_{fb}} \quad (6.43)$$

The time derivative of the fuel quality can be found by taking the derivative of each variable on the right-hand side of Equation 6.43 as

$$\frac{dX_{fb}}{dt} = X_{fb} [\frac{-\dot{m}_f}{m_{fb}} - \frac{\dot{T}_{fb}}{T_{fb}} + \frac{\dot{x}}{x} + \frac{\dot{P}_{fb}}{P_{fb}}] \quad (6.44)$$

where $\frac{dP_{fb}}{dt}$ can be approximated using the Clausius Clapeyron relation as

$$\dot{P}_{fb} = \frac{dP_{fb}}{dT_{fb}} \frac{dT_{fb}}{dt} = (\frac{h_{fg_f}}{v_g T_{fb}})_{fuel} \dot{T}_{fb} = (\frac{h_{fg_f} P_{fb}}{R_{fb} T_{fb}^2}) \dot{T}_{fb} \quad (6.45)$$

Now the energy equation contains two new variables of time, P_b, and T_{fb}, in addition to the past variables of x, X_{fco}, T_{fco}. This now gives us

five unknowns with four equations. The core fuel mass flow rate, $\dot{m}_f$ (Equation 6.15-6.17), the coolant entrainment rate, $\dot{V}_e$ (Equation 6.10), and the fuel equation of state, $P_{fb} = P_{sat}(T_{fb})$ (Appendix A), are specified. The heat transfer rate model ($\dot{q}_l(t)$) will be described later. If there is sodium vaporization $P_b \neq P_{fb}$ and a coolant energy equation is needed for the sodium saturated vapor and liquid to determine P_b and T_{fb}. This would then give an equal amount of unknowns (5) and equations (5).

The coolant energy equation can be written in a similar fashion to Equation 6.35 as

$$\frac{d}{dt}(m_{cb}u_{cb}) = +\dot{q}_l - P_b\frac{d}{dt}(V_{cb}) + \dot{m}_{cb}(h_{ent}) \tag{6.46}$$

The energy equation can be rearranged using the concept of Equations 6.38 - 6.40 for V_{cb} to give

$$m_{cb}\frac{dh_{cb}}{dt} = \dot{q}_l + \frac{(P_b-P_{fb})}{P_b}V_b\frac{dP_b}{dt} + \dot{m}_{cb}(h_e-h_{cb}) \tag{6.47}$$

where

$$V_{cb} = V_b\frac{(P_b-P_{fb})}{P_b} \tag{6.48}$$

and where

$$h_{cb} = X_{cb}\left[c_{p_{cg}}(T_{fb}-T_{sat}) + h_{fg_c}\right] + c_{lc}(T_{sat}-T_{ref}) + h_{ref} \tag{6.49}$$

and

$$T_{sat} = T_{sat}(P_b) \tag{6.50}$$

is given in Appendix A. The sodium quality in the bubble is given by

$$X_{cb} \doteq \frac{(P_b-P_{fb})V_b}{m_{fc}R_cT_{fb}} \tag{6.51}$$

In the derivative of the coolant enthalpy ($\frac{dh_{cb}}{dt}$) the term $\frac{dT_{sat}}{dt}$ will appear and again the Clausius Clapeyron relation can be used to approximate this as

$$\frac{dT_{sat}}{dt} = \frac{dT_{sat}}{dP_b}\frac{dP_b}{dt} = \left(\frac{v_g T_{sat}}{h_{fg_c}}\right)_{coolant}\frac{dP_b}{dt} = \frac{R_c T_{fb}}{(P_b - P_{fb})}\frac{T_{sat_c}}{h_{fg_c}}\frac{dP_b}{dt} \tag{6.52}$$

This set of governing equations, once mathematical models for $\dot{q}_1$ are presented, comprise a set of ordinary non-linear differential equations with time as the independent variable. As in Chapter 3, 4 and 5 this system is solved using a numerical integration technique available as a library subroutine for the MIT IBM 370/168 computer. A more detailed description of the solution technique is given in Appendix F. The method used to solve this system of equations is the same as that used in Chapter 5 because this system of equations is again a "stiff" system.

In the following section the mathematical formulations of the heat transfer models are presented. Then the effects of each heat transfer model upon the two-phase expansion work up to slug impact will be evaluated.

6.5 Effect of Fuel Vapor-Liquid Coolant Heat Transfer on the Bubble Expansion Work

6.5.1 Maximum Heat Transfer Model - No Sodium Vaporization (Model 4)

A non-mechanistic lower bound of the effect of heat transfer on the expansion work can be found by assuming that the sodium coolant entrained is heated up instantaneously to its saturation temperature, but does not vaporize. Maximum energy is transferred from the UO_2 two-phase bubble without the adverse effects of sodium vaporization. The heat transfer rate is given by

$$\dot{q}_1 = \dot{m}_{cb} c_{l_c} (T_{sat} - T_1) \tag{6.53}$$

where

$$\dot{m}_{cb} = \dot{m}_e = \rho_c \dot{V}_e \tag{6.54}$$

and $\dot{V}_e$ is from Equation 6.10. This simple model can be included into Equations 6.36 and 6.47 and the system of governing equations previously

described in Section 6.4 can be solved. The results for each of the three geometric initial conditions (see Figure 6.3) are illustrated in Figures 6.9 to 6.11.

The reduced expansion work due to heat transfer can be compared to the isentropic expansion work. The amount of work reduction is proportional to the amount of sodium mass entrained. For the case of no above-core structure, the amount of sodium entrained depends on whether or not the sodium is in or out of the fission gas plenum. If the sodium is out of the fission gas plenum region, the expansion will be initially spherical then planar and the acceleration will be from the fuel vapor into the sodium liquid throughout the expansion (i.e., positive). This physical situation will allow Taylor Instability entrainment throughout the expansion and this has been modeled by a one-dimensional expansion in the upper plenum. The amount of sodium entrained is large because the area for entrainment is large (see Table 6.7) and the acceleration is positive. This causes a work reduction by a factor of 5-10 (Figure 6.11).

Conversely if the sodium is in the fission gas plenum region, the acceleration initially is positive due to its planar growth and some coolant is entrained. However, once the bubble emerges from this region with a high velocity and starts to grow in an initially spherical fashion, the acceleration will be from the coolant into the vapor (i.e., negative) and no coolant entrainment will occur due to Taylor Instabilities. This behavior continues as long as there is spherical growth. Once the expanding bubble senses the surrounding walls, the expansion begins a transition to planar growth and the acceleration now would turn positive and entrainment will begin again. This spherical-planar growth transition point for small scale experiments in Chapter 3 and 5 was predicted using the analysis by Christopher [28] as outlined in Appendix D. For the fuel scale geometry

of the CRBR, the transition should occur after 1/3 of the expansion time to impact has elapsed. However, for the results given in Figure 6.10, it was conservatively assumed that no sodium entrainment occurred after the two-phase bubble expands out of the fission gas plenum region. This assumption tacitly assumes that the spherical to planar transition does not occur until after slug impact. This is not a best estimate assumption but because this transition is not well known at this time, this conservative bound is used for all the full scale calculations where the above-core structure is out and the sodium is in the fission gas plenum (see Table 6.7). As Figure 6.10 indicates the maximum work reduction due to this entrainment is still large, reducing the work from an isentropic expansion by a factor of 2-3.

When the above-core structure is in place and the sodium is in the fission gas plenum, the two-phase fuel expansion will be planar throughout the majority of the expansion to slug impact ($\Delta V_b \doteq 15m^3$ where cover gas volume = $20.5m^3$). Only at the end of the expansion when the bubble emerges from the flow guide tubes is the expansion spherical ($\Delta V_b \doteq 5.5m^3$) and no coolant entrainment will occur due to Taylor Instabilities. At the beginning of the expansion the fuel vapor and liquid will expand through the fission gas plenum where the fuel rod spacing is quite small (e.g. for P/D ≃ 1.25, the gap is approximately 1.5 - 3mm) and is the same order of magnitude as the size of a Taylor Instability critical wavelength (λ_c = 1-10mm). Therefore, it was assumed that no sodium entrainment occurred due to Taylor Instabilities during this part of the volume expansion ($\Delta V \simeq 1.9m^3$). The amount of sodium entrained is not as large as the sodium out-structure out case (see Table 6.7) because the entrainment cross sectional area is now the guide tube flow area not the whole vessel area, a reduction by a factor of eight. Nevertheless, the expansion work is reduced by a large factor of 3-8 for this non-mechanistic

model (Figure 6.9). Some sodium will be left on the structure as a film as it is pushed out of the fission gas region. When this amount was estimated [69] and included as part of the sodium coolant, it was found to have a small effect on the expansion work. This effect is discussed in more detail in the next section.

6.5.2 Rate Models for Sodium Coolant Vaporization Upper Bounds (Models 1,2,&3)

The heat transfer models to be described, mechanistically model the rate of sodium vaporization assuming that the sodium droplet has come to its saturation temperature instantaneously. The relative velocity and diameter of the entrained sodium droplet are given in Equations 6.12-6.15. The relative velocity (v_{rel}) used in the following calculations employs the same approximation as that modeled in Chapter 5 and is given in Equations 5.23 and 5.24 as

$$v_{rel}(x,t) = \frac{x}{x_{slug}}(v_{slug}(t) + c\sqrt{a\lambda_c}) + (1 - \frac{x}{x_{slug}})v_{core}$$

$$- \left[\frac{x - x(t=0)}{x_{slug} - x(t=0)}\right]^{\frac{1}{2}} v_{slug}(t) - \int_o^t \left\langle \frac{dv_d}{dt} \right\rangle dt \qquad (6.55)$$

where

$$\left\langle \frac{dv_d}{dt} \right\rangle = \sum_{\Delta x_i} \frac{\frac{dv_d}{dt}\Delta x_i}{\Delta x_i} \qquad (6.56)$$

and where from momentum equation for the entrained drop the drag force is

$$\frac{dv_d}{dt} = \frac{3}{4}\frac{C_d}{D_d}\frac{\rho_g}{\rho_l}(v_{rel}(x,t))^2 \qquad (6.57)$$

These heat transfer models all assume that the entrained sodium is instantaneously brought up to its saturation temperature and some rate mechanism determines the amount of sodium vaporization ($\dot{m}_{vap}$). Thus all three models can be represented as

$$\dot{q}_l = \dot{m}_{cb} c_{l_c} (T_{sat_c} - T_l) + \dot{m}_{vap} (h_{fg_c} + c_{vg_c} (T_{fb} - T_{sat_c})) \quad (6.58)$$

where

$$\dot{m}_{vap}(t) = \frac{1}{h_{fg_c}} \left[\sum_{\text{All drops}} \dot{q}_{drop}(x,t) \right] \quad (6.59)$$

The heat transfer rate from each drop ($\dot{q}_{drop}(x,t)$) is dependent upon the governing rate mechanism.

In heat transfer models 1 and 2 (see Table 6.6) radiation is considered to be the controlling rate mechanism and the heat transfer to the drop is given as

$$\dot{q}_{drop} = \pi D_d(x,t)^2 \left(\varepsilon_r \sigma_r (T_{fb}^4 - T_{sat_c}^4)\right) \quad (6.60)$$

where $\varepsilon_r = 1$ for a black body (model 1)

$\varepsilon_r = .04$ for a clean sodium surface (model 2)

and where D_d is born at $D_d = \lambda_c$ at a distance $x(t_o)$ and decreases as the droplet vaporizes. This model conveys the physical picture that the UO_2 vapor has condensed in a fog near the drop and radiates energy to it. The number of sodium droplets entrained and the heat transferred to them in the bubble can be found by finding the number in an axial increment in distance (Δx_i)

$$\text{No } (\Delta x_i) = \frac{\Delta V_e(\Delta x_i)}{\frac{\pi D_d(x)^3}{6}} \quad (6.61)$$

where ΔV_e is given by Equation 6.10 and $D_d(x)$ is the size when the droplet is born $D_d = \lambda_c$ at a given x. Then summing over all Δx_i from $0<x<x_{slug}$ at each time, t, we get

$$\dot{m}_{vap} = \frac{1}{h_{fg_c}} \left[\sum_{\Delta x_i} \frac{6\Delta V_e(\Delta x_i)}{D_d(x)^3} (D_d(x,t))^2 \left(\varepsilon_r \sigma_r (T_{fb}^4 - T_{sat_c}^4)\right) \right] \quad (6.62)$$

An approximation of this expression can be made by finding the spatially averaged drop diameter D_d and then using it in an overall heat transfer rate

model for vaporization. This is the same approximation utilized in Chapters 4 and 5 and gave good results when compared to the experimental results. The expression for the average diameter is then

$$\langle D_d \rangle = \sum_{\Delta x_i} \frac{No(\Delta x_i) D_d(\Delta x_i) \Delta x_i}{No(\Delta x_i) \Delta x_i} \tag{6.63}$$

where $D_d(x)$ is the drop diameter born at x at a past time t_o given by Equation 6.15. The rate of vaporization then becomes

$$\dot{m}_{vap} = \frac{1}{h_{fg_c}} \left[\frac{6\Delta V_e (1-X_{cb})}{\langle D_d \rangle} (\varepsilon_r \sigma_r (T_{fb}^4 - T_l^4)) \right] \tag{6.64}$$

In Equation 6.64 it has been also assumed that the evaporating drop diameter, $D_d(x,t)$, is approximately equal to

$$D_d^2(x,t) = D_d^2(x) \left[\frac{\rho_c D_d(x,t)}{\rho_c D_d(x)} \right]^3 \frac{D_d(x)}{D_d(x,t)} = D_d^2(x)(1-X_{cb}) \frac{D_d(x)}{D_d(x,t)} \doteq D_d^2(x)(1-X_{cb}) \tag{6.65}$$

where X_{cb} is the mass quality of the sodium vapor. By this assumption the same limits are kept for $D_d(x,t)$, and the ratio $\frac{D_d(x)}{D_d(x,t)}$ is assumed to be near one. This is a good assumption because this ratio lies between 1.02-1.11 for the initial droplets being vaporized at the time of slug impact.

The heat transfer model 3 considers that the sodium vaporization occurs in a moving system where the UO_2 condensation causes the vaporization. A Nusselt number for vaporization by Lee and Ryley [74] is used in this model to describe the heat transfer coefficient as

$$Nu = \frac{\bar{h} D_d}{k_g} = 2 + .74\ Re^{.5} Pr^{.33} \tag{6.66}$$

where

$$Re = \frac{\rho_g v_{rel}(x,t) D_d}{\mu_g} \tag{6.67}$$

and

$$Pr = \frac{c_p \mu_g}{k_g} \tag{6.68}$$

This correlation is the result of experiments involving water droplet

vaporization by superheated steam and assumes the effect of transpiration cooling is negligible because the degree of superheat is small. El-Wakil [75] developed a correction factor to the vaporization Nusselt number which accounts for the reduction in the temperature gradient and, therefore, $\bar{h}$ due the effect of transpiration cooling. The magnitude of the reduction is estimated to be small (.3-.5) for UO_2/sodium system and is only a second order effect in reducing the heat transfer coefficient and is conservatively neglected. The model for sodium droplet vaporization becomes then

$$\dot{q}_{drop} = \pi D_d^2 \left(\frac{k_g}{D_d}\right) Nu \left(T_{fb} - T_{sat_c}\right) \qquad (6.69)$$

and total vaporization rate is given by

$$\dot{m}_{vap} = \frac{1}{h_{fg_c}} \left[\sum_{\Delta x_i} \frac{6\Delta V_e(\Delta x_i)(1-X_{cb})}{D_d(\Delta x_i)} \frac{k_g \, Nu}{D_d(x)} \left(T_{fb} - T_{sat_c}\right) \right] \qquad (6.70)$$

where the approximation of Equation 6.65 is again utilized. This vaporization rate can also be expressed using average values of D_d and v_{rel}. The spatially averaged diameter D_d can be found for this model as before using the averaging technique of

$$\langle D_d \rangle = \left[\sum_{\Delta x_i} \frac{No(\Delta x_i) \, D_d(\Delta x_i)^{1.5} \Delta x_i}{No(\Delta x_i)\Delta x_i} \right]^{\frac{2}{3}} \qquad (6.71)$$

The exponent 1.5 is used here because the diameter appears in the model to the 1.5 power. Spatially averaged value of v_{rel} can be found by

$$\langle v_{rel} \rangle = \left[\sum_{\Delta x_i} \frac{v_{rel}(\Delta x_i)^{.5} \Delta x_i}{\Delta x_i} \right]^2 \qquad (6.72)$$

Again the exponent .5 is used because the relative velocity appears in Nusselt No. to the .5 power. Now the rate of vaporization can be rewritten for a spatially averaged $\langle D_d \rangle$ and $\langle v_{rel} \rangle$ as

$$\dot{m}_{vap} = \frac{1}{h_{fg_c}} \left[\frac{6\Delta V_e (1-X_{cb})}{\langle D_d \rangle} \frac{k_g}{\langle D_d \rangle} Nu \, (T_{fb} - T_{sat_c}) \right] \tag{6.73}$$

where

$$Nu = 2 + .74 \left[\frac{\rho_g \langle v_{rel} \rangle \langle D_d \rangle}{\mu_g} \right] \left[\frac{c_{p_g} \mu_g}{k_g} \right]^{.33}$$

These models were individually inserted into Equations 6.36 and 6.47 to complete the set of governing differential equations to predict the expansion behavior of the bubble.

The results of the analysis for each of the three geometric initial conditions are shown in Figures 6.9 - 6.11 and tabulated as example cases in Table 6.7 at the time of coolant slug impact. A few general observations can be made after viewing Figures 6.9-6.11 and Table 6.7:

(1) The expansion work at slug impact with the inclusion of any of the three heat transfer models is increased above the work of an isentropic UO_2 expansion. This work increase due to sodium vaporization is anywhere from 2 - 30%, which offsets the effect of UO_2 condensation.

(2) The model of sodium vaporization due to radiation onto a clean sodium surface (ε = .04) consistently gives the lowest expansion work increase (2 - 10%) for both the sodium in and sodium out cases without the above-core- structure.

(3) As the amount of sodium vaporized is predicted to increase by using more conservative models (e.g. black body radiation) the amount of UO_2 left in the vapor phase in the bubble and the bubble temperature decrease markedly. This indicates that even when the entrained sodium does not act as a quenching liquid, it does have a positive radiological effect on the initial conditions of the bubble after slug impact.

The reason for the small increase in the expansion work at slug impact using all three models is due to the effects of two countervailing processes. As the sodium became entrained, it was raised to its saturation temperature which caused a lowering of the bubble pressure due to UO_2 vapor condensation. However, as the sodium was vaporized the sodium vapor replaced the condensing UO_2 vapor at a much higher pressure. Remember that at a given temperature the vapor pressure of sodium is much higher than UO_2, thus the pressure of the

bubble is increased. The net effect of this was that the sodium vapor held the pressure near the core pressure for much longer times throughout the expansion and thus provided an almost constant pressure expansion.

For the initial condition with the above-core structure in place if the sodium left on fission gas structure is estimated and included in the analysis the effect is minimal. Using the results of Ozgu [69], the sodium left on the structure is estimated and considered as part of the entrained volume. This adds approximately 200 kg of entrained sodium but only reduces the expansion work by less than 5% ($\Delta W \sim 85$ megajoules).

The reason that the radiation model with an assumed clean sodium surface ($\varepsilon_r = .04$) gave expansion work results close to those of the black body model is again a matter of two counterbalancing effects. As the rate of sodium vaporization is reduced due to a lower radiative emissivity, the amount of sodium vapor and its partial pressure decrease while the temperature of the bubble and the amount of UO_2 vapor remain at much higher levels (see Table 6.7). Therefore, the partial pressure of the UO_2 vapor is much higher due both to a higher temperature and a larger vapor mass fraction. The net effect is that the total pressure is lower than the total pressure values for black body radiation or forced convection vaporization but not significantly lower (see Table 6.7).

Another effect to note is that as the initial core temperature is reduced, these models for sodium vaporization cause the expansion work to come close to the upper bound of a constant pressure expansion. The reason for this is that as the core temperature decreases, the expansion time increases to slug impact. Therefore, there is more time for heat transfer and thus more sodium is vaporized holding the bubble pressure nearly constant.

The final point to note is that the amount of UO_2 vapor and the bubble temperature is much lower as the rate of sodium vaporization increases (Table

6.7). The reason for this lies in the fact that there is a large enthalpy gain to the sodium as it is vaporized and thus a large loss to the UO_2. Because the UO_2 is saturated not superheated the temperature of bubble falls markedly as $\dot{m}_{vap}$ increases, and this causes X_{fb} to decrease also. Also as the sodium vaporization rate increases, the higher bubble pressure holds more of the two-phase UO_2 in the core and decreases the mass ejected into the bubble (m_{fb}).

The mass of the entrained sodium in the bubble is more affected by the initial geometry of the expansion than the details of the expansion process as Table 6.7 depicts. This occurs because all the characteristic pressures and accelerations of these expansions are approximately the same for the conservative models and thus only the geometry affects the result, due to area for entrainment and acceleration magnitude and direction. For the optimistic model (#4) the acceleration decreases as pressure goes down but the expansion time to slug impact increases and thus the net effect results in almost the same amount of coolant entrained.

In the past sections two other effects upon the expansion work have been mentioned and should be repeated here. If the coolant entrainment is partially governed by a global entrainment mechanism of Taylor Instabilities ($V_e \sim A_p \sqrt{aD_p}$), then the amount of coolant entrainment would be much greated (i.e., by a factor of 2-5) and the possible effect on reducing the work expansion is much greater (see Figure 6.11). This behavior is not confirmed by entrainment data of the small scale experiments with a change in scale (Chapter 3) but should be investigated in larger scale experiments. The second important effect is the amount of saturated liquid UO_2 which is ejected into the bubble. It has been assumed that a homogeneous mixture is ejected from the core and this is conservative in that a maximum amount

of UO_2 liquid is ejected into the bubble, keeping the bubble pressure high with heat transfer due to the fuel liquid flashing into vapor. However, if there is mainly vapor in the expansion as in the SRI small scale water tests, the bubble pressure will not be maintained as the UO_2 condenses and thus the pressure will decrease more dramatically and the sodium will definitely act as a quenching liquid.

Given these upper and lower bounds on the expansion work, two best estimate models are now presented which look at the two possible cases of the presence of noncondensible gases.

6.5.3 Radiation Heat Transfer Model with no Sodium Vaporization (Model 5)

The more realistic situation during the two-phase expansion is that the entrained sodium droplet heats up to its saturation temperature at a mechanistic rate and not instantaneously. The rate mechanism which governs this heat up is dependent upon a number of factors, one of which is the amount of noncondensible gases present. The thinking in the reactor safety community has changed over the last few years in regard to this. Cho and Epstein [82] originally considered the UO_2 vapor and sodium interaction without consideration of noncondensibles. Their conclusion was that stable UO_2 condensation on a liquid sodium surface is dependent upon the interface temperature of the constituents and, therefore, their initial conditions and thermophysical properties. Later work by Epstein and others [79-81,84] on the role of fog formation and noncondensible gases in the condensation process introduced another view of the subject. If noncondensible gases are present in the vapor (mole fraction $\Psi \geq .01$) and the interface temperature of the sodium droplet is low ($T_I < 3200^{\circ}K$) [84], then the UO_2 will condense in a fog near the sodium surface but not upon it. Therefore, the main mechanism for energy transfer will be due to radiation heat

transfer from the vapor to the surface. This is the view that Cho and Epstein [3] used in their model, because in the realistic LMFBR environment some noncondensibles will be present, and will impede surface condensation. Finally, Condiff and Chan [83,85] examined parametrically the vaporization behavior of a saturated sodium droplet controlled by a radiation heat flux. The fuel vapor is predicted to condense in a fog away from the sodium surface for two reasons: (1) As before noncondensibles inhibit fuel vapor diffusion and help create a fog; (2) The fog formation is also enhanced because the radiation flux is so large that the vapor literally condenses before it can diffuse the distance to the sodium surface. Their conclusion was that the sodium vapor will periodically sweep away the fog reducing the rate of vaporization by an order of magnitude and yet the radiation mechanism still will dominate the vaporization process over conduction.

All this previous analysis by investigators at Argonne seems to indicate that the realistic situation for sodium - UO_2 vapor heat transfer during the expansion lies somewhere in between the two extremes (see Figure 6.6). On one hand enough noncondensible gas may be present to impede UO_2 condensation on an entrained sodium droplet and the heat transfer will be from a radiating fog of some unknown emittance around the droplet onto the sodium surface. Alternately, no noncondensible gases may be present and then UO_2 condensation will occur at the surface. The real situation lies in the middle and is a very complex process, thus the two extremes are modeled here to give best estimate bounds on the probable types of heat transfer behavior and the effect on the expansion work.

The case where noncondensible gases are present in large proportions precludes any significant contacts between condensing UO_2 and liquid sodium. The heat transfer mechanism, as Section 6.3 briefly described, is radiation,

where the UO_2 condenses in a fog around the droplet and radiates energy to it. The first question to address is what are likely radiation properties of the sodium surface, UO_2 fog and vapor. Chan [76,77] has suggested that the reflectivity for a clean sodium surface is similar to that of polished silver (.8-.96) and assuming a gray surface the emissivity would be ε_r=.04-.2. Now this value will increase if the sodium surface becomes dirty due to some UO_2 condensation upon it. The amount of UO_2 condensate needed for this to occur and the resultant emissivity would be difficult to determine. It will be initially assumed that ε_r = .04 for the sodium surface. Later in the discussion the results of the analysis will indicate that this emissivity can rise by a factor of five and the conclusions will not change. The spectral properties of the UO_2 vapor and fog are more complex. Hottel [63] uses the emittance, an engineering factor for a polar radiating gas, to characterize these spectral properties but for UO_2 the experimental data is nonexistant and this approach cannot be used. Chan [85] suggests that the fog may be swept away when the saturated sodium droplet vaporizes effectively reducing radiation flux by the vapor and fog by an order of magnitude. This conclusion is not useful here because the sodium enters highly subcooled. Thus the possible range of spectral properties may be broad for the UO_2 vapor and fog but in this analysis it is conservatively assumed that they behave as a black gas.

The heat transfer process from the two-phase fuel to the entrained sodium droplets is realistically composed of two periods: (1) Heat transfer as the initially entrained droplets heat up to their saturation temperature in some time τ_{sat}; (2) Heat transfer as some of the droplets now saturated begin to vaporize as others are heated up to T_{sat_c}. The important point here is that in the expansion time of the bubble up to coolant slug impact (τ_{exp})

only the first phase of heat transfer occurs and the initially entrained sodium droplets do not come up to their saturation temperature. To show this consider a simple lumped parameter energy balance for the drop being entrained at $D_d = \lambda_c$ and at initial temperature T_1,

$$\rho_c \frac{\pi}{6} D_d^3 c_l \frac{dT_1}{dt} = \pi D^2 \varepsilon_r \sigma_r (T_f^4 - T_1^4) \qquad (6.74)$$

where for $T_f \geq 2T_1$ the approximation can be made

$$\rho_c \frac{\pi D_d^3}{6} \frac{dT_1}{dt} \doteq \pi D^2 \varepsilon_r \sigma_r T_f^4 \qquad (6.75)$$

Now this expression can be algebraically simplified and integrated from T_1 to T_{sat} for $0<t<\tau_{sat}$ to give

$$(T_{sat} - T_1) = \left(\frac{6\varepsilon_r \sigma_r T_f^4}{D_d \rho_c}\right) \tau_{sat} \qquad (6.76)$$

This expression is a valid apprxoimation for the initial droplet heat up because the Biot is small (see Table 6.8) where it is defined as

$$Bi = \frac{\bar{h} D_d}{2k_c} = \frac{D_d}{2k_c} \left(\frac{\varepsilon_r \sigma_r T_f^4}{T_f - T_1}\right) \qquad (6.77)$$

The results of this simple calculation (Table 6.8) indicates that $\tau_{sat} >> \tau_{exp}$ and thus no sodium vaporization would occur. The major reason for this conclusion is that the most likely sodium drop diameter ($D_d = \lambda_c$) is quite large in comparison to that assumed in past analysis (e.g. Cho and Epstein [3], D_d = 100μm). Therefore, the time to raise the bulk of the droplet to T_{sat} is not instantaneous, but quite long. This conclusion does not change even if the sodium surface emissivity (absorptivity) increases by a factor of five.

Therefore, a simple best estimate model for heat transfer from the UO_2 vapor and fog to the sodium droplet would be

$$\dot{q}_{drop} = \pi D_d(x)^2 \varepsilon_r \sigma_r (T_{fb}^4 - T_l^4) \qquad (6.78)$$

where $D_d(x) = \lambda_c$, the droplet born at that axial distance (x) at a past time (t_o). The total heat transfer rate from all the entrained coolant droplets summing over the whole bubble in discrete axial increments (Δx_i) would be

$$\dot{q}_l = \sum \Delta x_i \left[\frac{\Delta V_e(\Delta x_i)}{\frac{\pi D_d(\Delta x_i)}{6}} 3\pi D_d(\Delta x_i)^2 \varepsilon_r \sigma_r (T_{fb}^4 - T_l^4) \right]$$

or simplifying

$$\dot{q}_l = \sum \Delta x_i \left[\frac{6\Delta V_e(\Delta x_i)}{D_d(\Delta x_i)} \varepsilon_r \sigma_r (T_{fb}^4 - T_l^4) \right] \qquad (6.79)$$

Now the same approximation can be made here as in the past where the spatial average of $\langle D_d \rangle$ is utilized, given by Equation 6.63. The total heat transfer rate then becomes

$$\dot{q}_l = \frac{6\Delta V_e}{\langle D_d \rangle} \varepsilon_r \sigma_r (T_{fb}^4 - T_l^4) \qquad (6.80)$$

Again it should be noted that $T_f^4 >> T_l^4$ and thus the changing drop temperature has a negligible effect. Sodium vaporization does not occur, and the coolant energy equation (Equation 6.46) is drastically simplified to a differential equation monitoring the temperature of the initially entrained droplet, given by

$$\frac{dT_l}{dt} \doteq \frac{6\varepsilon_r \sigma_r T_{fb}^4}{D_d \rho_c} \qquad (6.81)$$

Thus the bubble pressure (P_b) is the saturation pressure of the UO_2 vapor (P_{fb}).

This heat transfer model (Equation 6.80) was inserted into the fuel energy equation (Equation 6.41) and the system of equations was again solved. The overall effect on the expansion work up to slug impact is shown in Figure 6.12. The UO_2 vapor pressure in the expanding bubble decreases

and the expansion work is reduced by a factor of 1.2 to 2.5. The variance in the work at impact is totally dependent on the value of the radiative absorptivity of the sodium surface. If it is low (ε_r = .04), then a small amount of the fuel energy is transferred to the sodium liquid and the work reduction is only 20%. If the surface is partially dirty causing a higher ε_r, then more energy is transferred to the sodium without vaporization. This is shown by Figure 6.12 for ε_r = .2 which represents a best estimate for the absorptivity of the sodium surface based upon conversations with Chan [76], and still no sodium vaporization. Although this does not represent an order of magnitude reduction in the work, it does represent enough of a reduction so that it should be considered as equally important as other possible mitigating effects as identified by the SIMMER calculations [10]. The final point to emphasize is that this represents one possible scenario if noncondensible gases successfully impede UO_2 condensation on the liquid droplet. The other possible alternative if no noncondensible gases are now presented to get a best estimate of the heat transfer and expansion behavior for the other realistic situation.

6.5.4 Diffusion Controlled Sodium Vaporization Model (Model 6)

If no noncondensible gases are present, the UO_2 vapor will begin to condense on an entrained sodium droplet (Figure 6.8). This condensation may result in two processes: (1) The bulk of the drop heats up to its saturation temperature and some vaporization may occur at the surface of the droplet if $T_I >> T_{sat_c}$; (2) Once the bulk of the droplet is at T_{sat_c}, it will vaporize continuously. The intent of this section is to quantitatively show the possible effects of this heat transfer model on sodium droplet heat up, vaporization and the expansion work at slug impact.

The process as described in Section 6.3 is initially conceived to be

a sputtering phenomenon (for $t < \tau_{sat}$; Figure 6.8), where a cyclic process initially occurs: (1) the UO_2 vapor condenses on the droplet in a characteristic time, τ_{cont}; (2) causes some sodium vaporization because $T_I > T_{HN}$ in a time, τ_{vap}; (3) then after the sodium vapor expansion, the UO_2 diffuses back to the sodium surface to recondense in a time, $\tau_{recount}$. There are three ingredients in this proposed model:

(1) The interface temperature as the UO_2 condenses on the sodium liquid surface is above the homogeneous nucleation temperature of the sodium coolant causing rapid vaporization after τ_{cont}.

(2) The characteristic times of the initial sputtering process can be estimated and seem to be dominated by the time for the sodium vapor to expand and the UO_2 vapor to diffuse back to the sodium surface.

(3) As time progresses, the sodium vaporization caused by this process is controlled by the rate at which the UO_2 vapor can diffuse to the surface of the droplet.

To determine the interface temperature as the UO_2 condenses on the surface is not a straightforward process. The saturation and homogeneous nucleation temperature of the sodium is much lower than the melting temperature of the UO_2 for the range of fuel vapor pressures. Therefore, when the UO_2 condenses, it may solidify on the sodium surface. The interface temperature between the sodium and UO_2 changes depending on whether the UO_2 is condensing or both condensing and freezing. Appendix H presents in detail the models needed to determine T_I and the results are presented here (see Table 6.9). It has been assumed in these models that the thermophysical properties are constant. This becomes a bad assumption near the critical point of the coolant fluid (in this case for sodium) and, therefore, the results of the analysis for $T_f = 7000^{\circ}K$ should be considered very tentative. The interface temperature if the UO_2 is simply condensing on the sodium surface is given by

$$\frac{T_I - T_1}{T_f - T_1} = \frac{1}{\beta}\left[\frac{1}{\beta} + \text{erf}\kappa_1\right]^{-1} \tag{6.82}$$

where κ_1 is found by trial and error from the expression

$$\frac{c_{l_f}(T_f - T_1)}{\sqrt{\pi}\, h_{fg_f}} = \kappa_1 e^{\kappa_1^2}\left[\frac{1}{\beta} + \text{erf}\,\kappa_1\right] \tag{6.83}$$

and where

$$\beta = \sqrt{\frac{k_c \rho_c c_{l_c}}{k_f \rho_f c_{l_f}}} \simeq 2 \tag{6.84}$$

The interface temperature if the UO_2 is condensing and freezing on the sodium surface is given by

$$\frac{T_I - T_1}{T_{m_f} - T_1} = \frac{1}{1 + (\text{erf}\kappa_s)\beta} \tag{6.85}$$

where κ_s is found by trial and error from the expression

$$\frac{\kappa_s e^{\kappa_s^2} L_s \sqrt{\pi}}{c_{s_f}(T_{m_f} - T_1)} = \left[\frac{\beta}{1+\beta\text{erf}\kappa_s} - \left(\frac{T_f - T_{m_f}}{T_{m_f} - T_1}\right)\frac{1}{\text{erf}\kappa_1 - \text{erf}\kappa_s}\right] \tag{6.86}$$

and κ_1 is found by trial and error from

$$\frac{\kappa_1 e^{\kappa_1^2} h_{fg_f} \sqrt{\pi}}{c_{l_f}(T_f - T_{m_f})} = \left[\frac{1}{\text{erf}\kappa_1 - \text{erf}\kappa_s}\right] \tag{6.87}$$

The determination of which model was appropriate depends on whether the interface temperature is above or below the homogeneous crystallization point for solidifcation (T_{HC}). Cronenberg [149] indicates that this temperature for UO_2 and sodium is approximately 2600°K. This temperature is analogous to the homogeneous nucleation temperature in that it is at or below this temperature that solidifcation occurs very rapidly ($t \simeq 10^{-12}$ sec) as predicted by kinetic theory. If $T_I > T_{HC}$ as predicted by Equation 6.82, then the condensate will not crystallize as a solid and grow in the short amount of time of the expansion. If $T_I < T_{HC}$ then the condensate will

crystallize into a solid very quickly and the process is considered to be instantaneous. The application of this criteria to this problem indicates that for $T_{HC} = 2600^{o}K$, solidification occurs below a fuel vapor temperature of $5500^{o}K$ and this is the dividing line for application of Equation 6.82 or 6.85. The interface temperatures are shown in Table 6.9. The important point to note is that this interface temperature is always higher than the saturation temperature (T_{sat_c}) and the homogeneous nucleation temperature of the sodium (T_{HN}). The homogeneous nucleation temperature designates the point above which nucleation of vapor from the coolant will occur quite rapidly due to molecular density fluctuations in the liquid. When the coolant temperature is above this point, the major vapor nucleation mechanism is due to this process. The rate of nucleation [134] is again given by kinetic theory as

$$J(s^{-1}cm^{-3}) = A(T)\ N \exp\left(-\frac{W}{k_B T_g}\right) \tag{6.88}$$

where

$$W = \frac{-16\pi\sigma^3}{3(P_g - P)^2} \tag{6.89}$$

$$A(T) = \left(\frac{2\sigma}{\pi m_{molec}}\right)^{\frac{1}{2}} \simeq 10^{-11}\text{-}10^{-12}s^{-1} \tag{6.90}$$

$$N(\text{liquid number density } -cm^{-3}) = \frac{6.02(10^{-23})\rho_c}{MW_c} = 10^{22}cm^{-3} \tag{6.91}$$

and for this application

$$T_g = T_I \tag{6.92.1}$$

$$P_g = P_{sat}(T_I) \tag{6.92.2}$$

$$P = P_f = P_{sat}(T_f) \tag{6.92.3}$$

Even if this interface temperature due to UO_2 condensation existed over a long time ($t \simeq \tau_{exp}$), the bulk of the sodium drop does not heat up

instantaneously to T_{sat}. To get a conservative value of τ_{sat}, we can assume that $T_I = T_{HN}$ over the whole heating period. This will not physically occur because the sodium will vaporize in a sputtering fashion, and T_I will decrease during each cycle. With this constant temperature boundary condition, the shortest time for τ_{sat} can be found from the transient conduction tables for a sphere [59]. This characteristic time, τ_{sat}, is given in Table 6.9 for the average sphere temperature ($\frac{2r}{D_d} = .5$) to rise to T_{sat_c}. Even with this conservative estimate, $\tau_{sat} \simeq \tau_{exp}$.

Therefore, this sputtering heat transfer process to the sodium cannot be realistically assumed to cause instantaneous heat up of the droplet to T_{sat}. The next important question to answer is how much sodium vaporizes ($\dot{m}_{vap}$) during this time due to the UO_2 condensation on the sodium surface. If $\dot{m}_{vap}$ is large and comparable to the rates predicted by the black body radiation model or the other conservative models in Section 6.5.2, the expansion work of the process will be greater than an isentropic expansion. However, if $\dot{m}_{vap}$ is much lower, then the expansion work should be reduced relative to isentropic. This conclusion would imply that for both extremes of the expected accident condition, the entrained sodium coolant has a quenching effect on the two-phase UO_2 expansion.

To determine this vaporization rate, the sputtering process will be described: (1) First, as the process initially begins, the characteristic times of the first sputtering cycles are estimated; (2) Secondly as time progresses, the analysis indicates a reduction of the vaporization rate due to vapor diffusion effects. During this initial sputtering process it is assumed the heat transferred to the droplet by contact is much greater than that due to radiation. This is a good assumption for the initial sputtering cycles but after many cycles fuel vapor diffusion to the surface

decreases the UO_2 vapor contact rate and both heat transfer processes must be considered. The initial process is composed of three characteristic times (see Figure 6.8).

The time during the UO_2 condensation on the sodium surface up to sodium vaporization can be estimated to be of the order of the molecular collision frequency for homogeneous nucleation

$$\tau_{cont} = A(T) \doteq 10^{-12} \text{ sec} \tag{6.94}$$

where A(T) is given in Equation 6.90. During this time the sodium droplet is heated by the UO_2 condensate with the surface temperature at T_I. Because the time is so short a simple semi-infinite mass model for the temperature distribution [70] can be used to find the depth within the sodium (x_{pent}) where the sodium temperature is greater than T_{sat_c}, and the relation is

$$\frac{T_{sat} - T_I}{T_1 - T_I} = \text{erf}\left(\frac{x_{pent}}{2\sqrt{\alpha_c \tau_{cont}}}\right) \tag{6.95}$$

The time for vaporization of the sodium can be estimated by

$$\tau_{vap} \doteq \frac{\Delta m_{vap}}{\dot{m}_{vap}}$$

The quantity, m_{vap}, is the amount of sodium that could be vaporized due to the energy transferred into the droplet for temperatures $T_{sat} < T < T_I$. This can be found by a simple energy balance

$$\Delta m_{vap} h_{fg_c} = \text{mass}(T > T_{sat})(\text{average energy})$$

$$\Delta m_{vap} = \frac{1}{h_{fg_c}} \left[(\rho_c D_d^2 x_{pent}) c_{l_c} \left(\frac{T_I - T_{sat}}{2}\right)\right] \tag{6.96}$$

where the average energy per unit mass is approximated by $\frac{c_{l_c}}{2}(T_I - T_{sat})$. The rate of sodium vaporization would be high because $T_I \simeq T_{HN}$, and can be approximated by a kinetic theory model [59] for vaporization

$$\frac{\dot{m}_{vap}}{A} = \frac{1}{\sqrt{2\pi R_c}} \frac{P(T)}{\sqrt{T}}$$

and, therefore, for this case $\dot{m}_{vap}$ is

$$\dot{m}_{vap} = \frac{\pi D_d^2}{\sqrt{2\pi R_c}} \frac{P(T_I)}{\sqrt{T_I}} \tag{6.97}$$

The time for the UO_2 to recontact the sodium surface to condense is determined by the time (τ_{mom}) for the sodium vapor, initially at a high pressure ($P_{sat_c}(T_I) > P_f = P_{sat}(T_f)$), to expand to a pressure equal to P_f and the time (τ_{diff}) for the UO_2 to diffuse back to the surface. It is assumed that these processes occur in sequence

$$\tau_{recount} = \tau_{mom} + \tau_{diff} \tag{6.98}$$

The time for the sodium expansion (τ_{mom}) can be found by a simple one dimensional kinematic equation for the inertial growth of the sodium vapor layer as

$$\tau_{mom} \doteq \left[\frac{2(x_{exp} - x_{pent})}{a}\right]^{\frac{1}{2}} \tag{6.99}$$

where x_{exp} is the final expanded distance of the sodium vapor. The acceleration (a) is given by an approximation to the spherical momentum again because $x_{pent} << \frac{D_d}{2}$

$$\frac{d^2r}{dt^2} = \frac{(P_c - P_f)}{r\,\rho_f} - \frac{3}{2}\left(\frac{dr}{dt}\right)^2 \tag{6.100}$$

Since $r = \frac{D_d}{2} + x$, the above equation reduces to

$$a \doteq \frac{d^2x}{dt^2} \doteq \left(\frac{P_c - P_f}{\frac{D_d}{2}\,\rho_f}\right) \tag{6.101}$$

where $\frac{dx}{dt}$ is assumed to be negligible. This will give the smallest value of τ_{mom} because the acceleration is a maximum. The final expanded distance (τ_{exp}) is found by assuming that the sodium vapor behaves like a perfect

gas, therefore,

$$x_{exp} = x_{pent} \frac{P_{sat}(T_I)}{P_{sat}(T_f)} \left(\frac{T_f}{T_I}\right) \qquad (6.102)$$

The characteristic time for the fuel vapor to diffuse back to the surface (τ_{diff}) is estimated from simple diffusion theory [60] to be the time when the fuel vapor has diffused across the expansion distance of the sodium vapor (x_{exp}), and is given as

$$\tau_{diff} \doteq \frac{x_{exp}^2}{4\, D_{f\,c}} \qquad (6.103)$$

where $D_{f\,c}$ is the diffusion coefficient for UO_2 and sodium vapor. This physical property is not known for UO_2/sodium so it is assumed as is commonly done for gases [60] that the Lewis number ($\frac{D_{f\,c}}{\alpha_c}$) is one and the coolant thermal diffusivity is used in Equation 6.103.

When all of these characteristic times are estimated for the initial sputtering cycles (see Table 6.10), it is found that the time required for the UO_2 vapor to recontact the sodium surface governs the sodium vaporization. Specifically in these early stages of the sputtering process $\tau_{mom} > \tau_{diff}$ and the sodium vapor pushes away the UO_2 vapor and condensate. The sodium vaporization flux ($\frac{\dot{m}_{vap}}{A}$) due to this initial sputtering process is predicted to be the same order of magnitude as that due to black body radiation (Table 6.10). This would imply that if this vaporization rate were continued throughout the time that the droplet is heated up to its saturation point (τ_{sat}) the effect on the expansion work would be similar to that of the conservative radiation models. However, this realistically cannot occur, because as the sodium vaporizes over many cycles, the UO_2 vapor will be pushed further and further away from the droplet, and a larger layer of sodium vapor will build up. A complex diffusion process of sodium vapor diffusing away from the surface as the UO_2 vapor diffuses toward the droplet will then govern the sodium vaporization. After many sputtering

cycles (10^3-10^5) which would only constitute a fraction of a millisecond, the mole fraction (Ψ) of sodium vapor in the expanding bubble is significant ($\Psi > .01$). The sodium vapor then conceptually behaves as a noncondensible gas inhibiting the UO_2 fuel vapor from diffusing to the cold sodium droplet and condensing upon it. Thus the UO_2 vapor must diffuse through the sodium vapor and condense to vaporize any more sodium. The maximum rate of UO_2 vapor diffusion ($\frac{\dot{m}_{fg}}{A}$) can be approximated by a simple diffusion rate of a gas diffusing toward a spherical surface at a steady state, and is given by [59,60]

$$\frac{\dot{m}_{fg}}{A} = \frac{D_{fc}}{R_f T} \left(\frac{\Delta P}{1}\right) \tag{6.104}$$

The mass diffusion properties are not known for UO_2 and sodium, and thus the diffusion coefficient (D_{fc}) is found by assuming Lewis No. $= \frac{D_{fc}}{\alpha_{cg}} = 1$. This is a good estimate for gases [60]. To get the maximum rate of fuel vapor diffusion, let us assume that $\Delta P = P_f$ and $1 \simeq \frac{D_d}{2}$, because we know that the maximum partial pressure difference over the characteristic heat transfer size is represented by this ratio.

The highest rate of sodium vaporization ($\dot{m}_{vap}$) will occur if all the UO_2 vapor, diffusing to the surface, is assumed to condense upon it and vaporizes sodium while the radiation heat flux from the vapor goes into heating the droplet up to T_{sat_c}. This is a very conservative assumption because it neglects the possibility that the UO_2 vapor could also condense in a fog around the drop without contact as would happen if a noncondensible were present. This is likely because the sodium droplet surface is cold and the sodium vapor mole fraction is large enough ($\Psi \geq .01$ [85]) not only to inhibit UO_2 vapor diffusion but to cause fog formation. This vaporization rate can be found by a simple steady state energy balance as

$$\frac{\dot{m}_{vap}}{A}\left(c_{pg_c}(T_f-T_{sat})+h_{fg_c}+c_{l_c}(T_{sat}-T_l)\right)$$

$$=\frac{\dot{m}_{fg}}{A}\,h_{fg_f}$$

or

$$\frac{\dot{m}_{vap}}{A}=\frac{\dot{m}_{fg}}{A}\left[\frac{h_{fg_f}}{c_{pg_c}(T_f-T_{sat})+h_{fg_c}+c_{l_c}(T_{sat}-T_l)}\right]$$

(6.105)

This vaporization rate, as Table 6.10 illustrates, is significantly less than the initial rate and the rates of vaporization due to both conservative models of radiation heat flux.

In addition the time for the droplet to come to its saturation point (τ_{sat}) is much longer than the smallest value previously calculated in Table 6.9, because a much lower heat flux would be controlling the heat up rate. This heat flux is composed of the energy deposited due to fuel vapor condensation at this much lower $\frac{\dot{m}_{vap}}{A}$ and radiation to the drop from the fuel vapor (Equation 6.80). A simple calculation can show that, at these low diffusion controlled sodium vaporization rates, the radiation heat flux is of the same order of magnitude and larger than that from this fuel condensation and must be included in the analysis. The radiation heat flux is

$$\dot{q}''|_{rad}=\varepsilon_r\sigma_r(T_f^4-T_l^4) \qquad (6.106)$$

and for $T_f \simeq 4000^{o}K$

$$\dot{q}''|_{rad}=5.6(10^5)w/m^2$$

The energy delivered by fuel vapor condensation and causing the subsequent sodium vaporization is

$$\dot{q}''|_{cond}=\frac{\dot{m}_{fg}}{A}\,h_{fg_f} \qquad (6.107)$$

and for $T_f = 4000$, $\frac{\dot{m}_{fg}}{A} = .028\ k_g/m^2 s$

$$\dot{q}'' \Big|_{cond} = .5(10^5)\ w/m^2$$

Thus both must be included in the analysis, and for the possible fuel temperature ranges $\dot{q}'' \Big|_{rad} > \dot{q}'' \Big|_{cond}$. The time for the bulk of the droplet to come to its saturation temperature (τ_{sat}) is now mainly controlled by the radiation heat flux (see Table 6.8) and $\tau_{sat} > \tau_{exp}$. Thus this diffusion controlled sodium vaporization and radiation energy transfer will occur throughout the bubble expansion.

This sodium vaporization and fuel vapor-liquid heat transfer model can be included in the governing equations to assess the effect upon the expansion work up to slug impact. Only two modifications to the governing equations (Equations 6.24 - 6.52) need to be made. First, the rate of coolant entrained ($\dot{m}_e$, Equation 6.33) is quite different from the amount that appears as the bubble as sodium vapor caused by fuel vapor diffusion and condensation ($\dot{m}_{fb} = \dot{m}_{vap}$). For this heat transfer model the relations are

$$\dot{m}_e = \rho_c \dot{V}_e \tag{6.108}$$

where $\dot{V}_e$ is from Equation 6.10, and the amount vaporized in the coolant energy equation is

$$\dot{m}_{fb} = \left(\frac{\dot{m}}{A}_{vap}\right) A_{drops} \tag{6.109}$$

where $\frac{\dot{m}}{A}_{vap}$ is given by Equation 6.105 and $A_{drop} = \frac{6\Delta V_e}{\langle D_d \rangle}$. The heat transfer mechanism is now a combination of radiation heat flux (Equation 6.80) to heat up the bulk of the droplet and fuel vapor condensation on the drop causing sodium vaporization. The expression ($\dot{q}_1$) is given as

$$\dot{q}_1 = \frac{6\Delta V_e}{\langle D_d \rangle} \left[\varepsilon_r \sigma_r (T_{fb}^4 - T_1^4) + \frac{\dot{m}_{fg}}{A} h_{fg_f}\right] \tag{6.110}$$

This new heat transfer model can be included with the governing equations and the expansion work for the two-phase fuel up to slug impact

predicted (see Figure 6.12). The results indicate that the bubble expansion work is still reduced from an isentropic expansion by a factor of 1.2 to 2.5 again depending on ε_r. The major reason for this similarity to model 5 is due to the small amount of sodium vaporization predicted by the model. The partial pressure of the fuel vapor is reduced due to vapor condensation and radiative energy transfer to the sodium droplets, and the partial pressure of the sodium vapor remains low although higher than UO_2 because the mass of sodium vaporized is quite small in contrast to that predicted by the conservative heat transfer models (models 1-3, Table 6.6).

6.6 Summary

The conclusion from this analysis is that if realistic heat transfer models are considered (models 5 and 6, Table 6.6) and included in the two-phase fuel expansion process, the expansion work could be reduced by a factor of 1.2 to 2.5. The difference in expansion work between the best estimate model including sodium vaporization and that with no sodium vaporization is small because fuel vapor diffusion limits the sodium vaporization rate. Thus ultimately the heat transfer rate is governed by radiation. The range of work effects is totally dependent upon the radiative properties of the sodium droplet surface, where the fuel vapor is conservatively considered to act as a black gas. It should be reemphasized though that this conclusion is based upon the initial conditions presented and the conservative assumptions concerning the core mass flow rate into the upper plenum and the amount of sodium coolant entrained.

TABLE 6.1

SUMMARY OF FULL SCALE CRBR GEOMETRIC PARAMETERS [9,10]

CORE* VOLUMES (m^3)	FUEL	- .846
	STEEL	- .6214
	GAS GAP	- .045
	SODIUM	- 1.055
	TOTAL	- 2.56

*INNER & OUTER CORE COMBINED - DIAMETER - 1.88 m

UPPER BLANKET (m^3)	FUEL	- .326
	STEEL	- .254
	GAS GAP	- .022
	SODIUM	- .392
	TOTAL	- .993

FISSION GAS PLENUM (m^3)	STEEL	- .929
	GAS GAP	- .977
	SODIUM	- 1.486
	TOTAL	- 3.392

COLLECTOR VOLUME (m^3)	STEEL	- .358
	SODIUM	- .56
	TOTAL	- .918

FLOWGUIDE TUBES+ (m^3)	STEEL	- 1.372
	SODIUM	- 12.348
	TOTAL	- 13.72

+ LENGTH - 3.2 m; DIAMETER - 2.2 m

COVER GAS VOLUME - 20.44 m^3

TABLE 6.2

INITIAL CONDITIONS FOR THE TESTS TO BE ANALYZED

INITIAL CORE				
AVERAGE TEMP (T_{f_c} - ^{o}K)	4000	5000	6000	7000
CORE FUEL QUALITY (X_{fc})				
SODIUM IN FGP*	.0003	.00418	.0204	.0588
SODIUM OUT FGP	.00175	.0247	.121	.35
CORE FUEL MASS (m_{fc} - k_g)		7500		
CORE CROSS SECTIONAL AREA (A_{core} - m^2)		2.77		
VESSEL CROSS SECTIONAL AREA (A_p - m^2)		29.2		
SODIUM SLUG MASS (M_{slug} - k_g)				
IN UPPER PLENUM		156,000		
IN FGP		4,400		

*FGP - FISSION GAS PLENUM REGION

TABLE 6.3

COMPARISON OF THE VAPOR PRESSURE FOR UO_2 AND SODIUM

T_f (^oK)	$P_{sat}(UO_2)$ (MPa)	P_{sat}(Sodium) (MPa)
1000		.02
1500	$2(10^{-13})$	1.1
2000	$2(10^{-8})$	8.1
2500	$2(10^{-5})$	27.1
2733‡		40.8
3070*	.002	
4000	.26	
5000	4.6	
6000	27.2	
7000	86.8	

‡ CRITICAL TEMPERATURE OF SODIUM

* FREEZING POINT OF UO_2

TABLE 6.4

SUMMARY OF THE EXPANSION PARAMETERS FOR CRBR

$T_f(^oK)$		4000	5000	6000	7000
$P_{f_i} = P_{sat}(T_f)$(MPa)		.26	4.6	27.2	86.8
$T_{sat}\|_{sodium} = T_{sat}(P_{f_i})(^oK)$		1272	1828	2502	2733
a*	(m/s^2)	49.3	866	5090	16250
$D_d \simeq \lambda_c$	(μm)	11200	2713	1240	854
$v_{rel_i} \simeq v_r$ †	(m/s)	3.5	7.1	11.7	17.3
$v_{rel_m} \simeq .2\ v_{rel_i}$ ǂ	(m/s)	.7	1.4	2.3	3.4
$We_i(v_{rel_i})$	(msec)	2	31	190	790
$We_m(v_{rel_m})$	(msec)	.08	1.3	7.5	30
τ_{br}		65-300	20-100	2.5-13	1-5
τ_{exp} +		168	40	16.5	9.3

* $a = \frac{(P_f - P_\infty)\ A_p}{M_{slug}}$; $A_p = 29.2\ m^2$; $M_{slug} = 156{,}000\ k_g$

† $v_r = 4.65\ \sqrt{a\lambda_c}$

ǂ This relative velocity occurs soon after the expansion begins.

+ $\tau_{exp} = \left(\frac{2(\text{Cover Gas Vol.})}{A_p\ a}\right)^{\frac{1}{2}}$

TABLE 6.5

COMPARISON OF HEAT FLUXES BY VARIOUS MECHANISMS

T_f	RADIATION Nu	CONDUCTION Nu	CONDENSATION (SODIUM VAPORIZATION) Nu
4000	1500	2	32
5000	690	2	62
6000	278	2	91
7000	144	2	124

$T_1 = 800^{\circ}K$

TABLE 6.6

SUMMARY OF THE HEAT TRANSFER MODELS UTILIZED

MODEL	COOLANT ENTRAINMENT MODEL	COOLANT DROPLET DIAMETER	COOLANT DROPLET TIME TO SATURATION	HEAT TRANSFER MECHANISM
ISENTROPIC EXPANSION	NO SODIUM ENTRAINED	N.A.	N.A.	NONE - ADIABATIC
CHO - EPSTEIN [3]	PARAMETRIC	ASSUMED 100 μm	INSTANTANEOUS	SODIUM VAPORIZATION CONTROLLED BLACK-BODY RADIATION DUE TO UO_2 FOG AROUND DROP DUE TO NONCONDENSIBLE GASES
1. BLACK BODY RADIATION	TAYLOR INSTABILITY	$D_d = \lambda_c$	INSTANTANEOUS	SAME AS CHO AND EPSTEIN
2. RADIATION CLEAN SODIUM SURFACE	TAYLOR INSTABILITY	$D_d = \lambda_c$	INSTANTANEOUS	SAME AS CHO AND EPSTEIN BUT NOW RADIATION FLUX ON CLEAN SODIUM; REFLECTIVITY=96%
3. UO_2 CONDENSATION AND SODIUM VAPORIZATION	TAYLOR INSTABILITY	$D_d = \lambda_c$	INSTANTANEOUS	UO_2 CONDENSATION IN VICINITY OF DROP CAUSES SODIUM VAPORIZATION DESCRIBED BY A NUSSELT NO. FOR VAPORIZATION
4. MAXIMUM HEAT TRANS. NO SODIUM VAPORIZATION	TAYLOR INSTABILITY	$D_d = \lambda_c$	INSTANTANEOUS	ASSUME NO SODIUM VAPORIZATION
BEST ESTIMATE				
5. RADIATION HEAT TRANS NO SODIUM VAPORIZATION	TAYLOR INSTABILITY	$D_d = \lambda_c$	RADIATION RATE CONTROLLED HEAT UP	NONCONDENSIBLE GASES CAUSE UO_2 CONDENSATION IN A FOG NEAR THE DROP & RADIATION FLUX ON A CLEAN SODIUM SURFACE
6. RADIATION HEAT TRANSFER, DIFFUSION CONTROLLED SODIUM VAPORIZATION	TAYLOR INSTABILITY	$D_d = \lambda_c$	CONDENSATION CONTROLLED HEAT UP	NO NONCONDENSIBLE GASES ALLOW UO_2 CONDENSATION ON SODIUM SURFACE & SODIUM SPUTTERING VAPORIZATION

TABLE 6.7

FINAL CONDITIONS OF THE BUBBLE AT SLUG IMPACT FOR SELECTED CASES

HEAT TRANSFER MODELS ASSUMING INSTANTANEOUS DROPLET SATURATION

ABOVE-CORE STRUCTURE IN PLACE	1	2	3	4
T_{f_i} (^{o}K)			6000	6000
T_{f_b} (^{o}K)			3360	5033
P_b (MPa)			24.5	4.9
m_{fb} (k_g)			2884	7200
X_{fb}			.00076	.09
m_{cb} (k_g)			1300	1600
X_{cb}			.37	0
NO ABOVE-CORE STRUCTURE-SODIUM IN				
T_{f_i} (^{o}K)	5000	5000		5000
T_{f_b} (^{o}K)	3200	4115		4625
P_b (MPa)	4.8	3.8		1.75
m_{fb} (k_g)	1000	2241		3030
X_{fb}	.0013	.0246		.0372
m_{cb} (k_g)	761	801		685
X_{cb}	.11	.048		0

TABLE 6.7 (CONTINUED)

NO ABOVE-CORE STRUCTURE-SODIUM OUT	1	2	3	4
T_{f_i} (^{o}K)	7000	7000	7000	7000
T_{f_b} (^{o}K)	3000	4310	4345	5200
P_b (MPa)	54.0	35.5	36.7	7.1
m_{fb} (k_g)	3570	5050	4960	5150
X_{fb}	.000018	.034	.026	.175
m_{cb} (k_g)	3500	3500	3500	3500
X_{cb}	.33	.134	.137	0

TABLE 6.8

CHARACTERISTIC TIME FOR A SODIUM DROPLET TO HEAT UP TO ITS SATURATION TEMPERATURE BY RADIATION HEAT TRANSFER

T_{f_i} (^{o}K)	4000	5000	6000	7000
$P_f = P_{sat}(T_f)$ (MPa)	.26	4.6	27.2	86.8
T_{sat_c} (^{o}K)	1272	1828	2502	2733
D_d^* (μm)	11200	2713	1240	854
$B_i (\varepsilon_r = .04)$	.016	.007	.008	.008
Radiation τ_{sat} (msec)	1640	356	129	55
τ_{exp}^* (msec)	168	40	16.5	9.3

* See Table 6.4 for calculational scheme.

TABLE 6.9

CHARACTERISTIC TIME FOR A SODIUM DROPLET TO HEAT UP TO ITS SATURATION TEMPERATURE BY UO_2 CONDENSATION ON SODIUM SURFACE

$T_f(^oK)$	4000	5000	6000	7000
$P_f = P_{sat}(T_f)$(MPa)	.26	4.6	27.2	86.8
$D_d(\lambda_c)(\mu m)$	11200	2713	1240	854
$T_1(^oK)$	800	800	800	800
$T_{sat_c}(^oK)$	1272	1828	2502	2733*
$T_{HN}(^oK)$	2100	2175	2600	2733*
$T_I(^oK)$	2200	2595	2900	3150
$T_{HC}(^oK)$	2673	2673	2673	2673
$\Theta = \frac{T_{sat}-T_{HN}}{T_1-T_{HN}}$	.64	.25	.055	0
$Fo = \frac{4\alpha_c \tau_{sat}}{D_d^2}$ $(\frac{r}{r_o} = .5)$	.075	.25	.35	-
FASTEST DROPLET HEAT UP TIME (τ_{sat}) FOR CONSTANT TEMPERATURE BOUNDARY CONDITION [59]				
τ_{sat}(msec)	158	21	9	-
$\tau_{exp}^{\ddagger}$ (msec)	168	40	16.5	9.3

*$T = T_{crit}$

‡ calculated from expression in Table 6.4

TABLE 6.10

CHARACTERISTIC TIMES AND SODIUM VAPORIZATION RATES
FOR THE SPUTTERING HEAT TRANSFER PROCESS

$T_f(^oK)$	4000	5000	6000
$D_d(m)$	$1.12(10^{-2})$	$2.7(10^{-3})$	$1.24(10^{-3})$
SODIUM VAPORIZATION RATE FOR THE INITIAL SPUTTERING PROCESS			
$\tau_{cont}(sec)$	10^{-12}	10^{-12}	10^{-2}
$x_{pent}(m)$	10^{-8}	$.5(10^{-8})$	$.3(10^{-8})$
$\Delta m_{vap}(k_g)$	$2.6(10^{-10})$	$1.6(10^{-11})$	$1.2(10^{-12})$
$\tau_{vap}(sec)$	$1.3(10^{-11})$	10^{-11}	$4(10^{-12})$
$x_{exp}(m)$	10^{-6}	$7(10^{-8})$	$8.5(10^{-9})$
$\tau_{mom}(sec)$	$1.7(10^{-9})$	$8(10^{-10})$	$6(10^{-11})$
$\tau_{diff}(sec)$	$5.8(10^{-8})$	$2(10^{-8})$	$7(10^{-9})$
$\tau_{recount} = \tau_{mom} + \tau_{diff}$	$5.97(10^{-8})$	$2(10^{-8})$	$7(10^{-9})$
$\tau_{sp} = \tau_{cont}+\tau_{vap}+\tau_{recont}$	$5.97(10^{-8})$	$2(10^{-8})$	$7(10^{-9})$
$\frac{\dot{m}_{vap}}{A_{drop}} = \frac{\Delta m_{vap}}{\tau_{sp}\pi D_d^2}\left(\frac{k_g}{m^2 s}\right)$	11	35	36
SODIUM VAPORIZATION RATE FOR SPUTTERING PROCESS AFTER MANY CYCLES			
$\frac{\dot{m}_{fg}}{A}\ (k_g/m^2 s)$	.028	.095	.178
$\frac{\dot{m}_{vap}}{A_{drop}}(k_g/m^2 s)$	.0045	.011	.018

TABLE 6.10 (Continued)

SODIUM VAPORIZATION RATE DUE TO RADIATION HEAT FLUX ON SATURATED DROPLET

$\frac{\dot{m}_{vap}}{A_{drop}}$	$(\varepsilon_r=1)(\frac{k_g}{m^2 s})$	5	12.3	25
$\frac{\dot{m}_{vap}}{A_{drop}}$	$(\varepsilon_r=.04)(\frac{k_g}{m^2 s})$	.2	.5	1

FIGURE 6.1

SCHEMATIC PICTURE OF THE CRBR REACTOR VESSEL

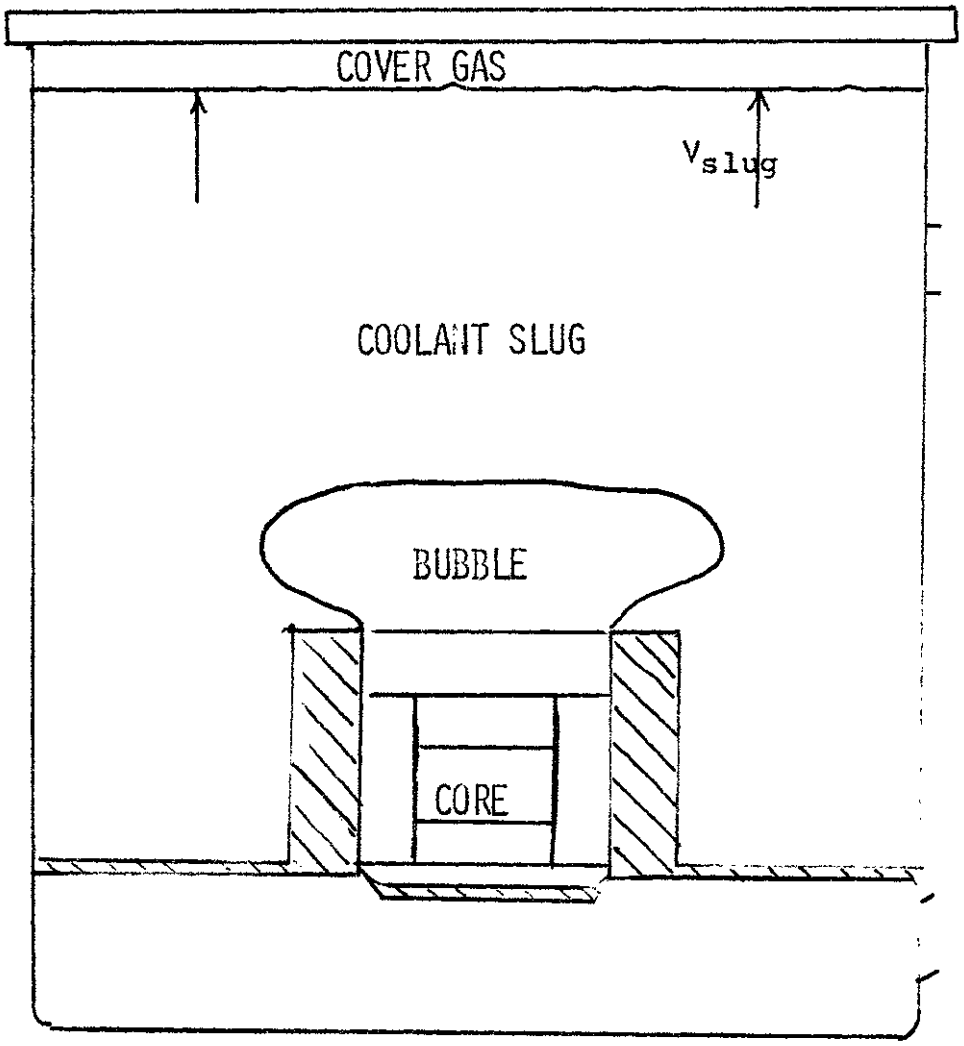

FIGURE 6.2

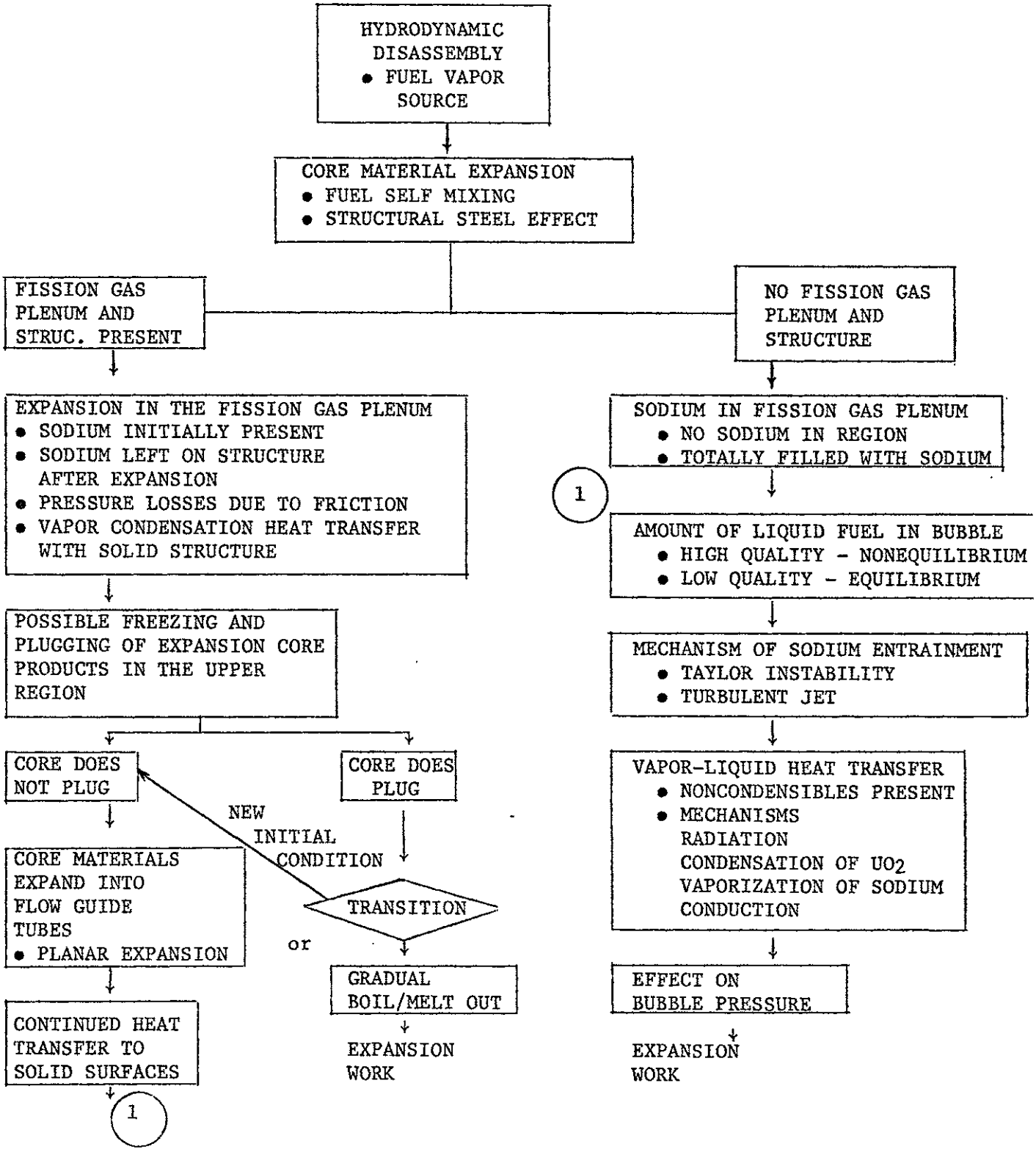

POSSIBLE EVENT TREE FOR A HYDRODYNAMIC DISASSEMBLY

FIGURE 6.3

THREE GEOMETRIC CONFIGURATIONS USED TO ANALYZE THE TWO-PHASE FUEL EXPANSION

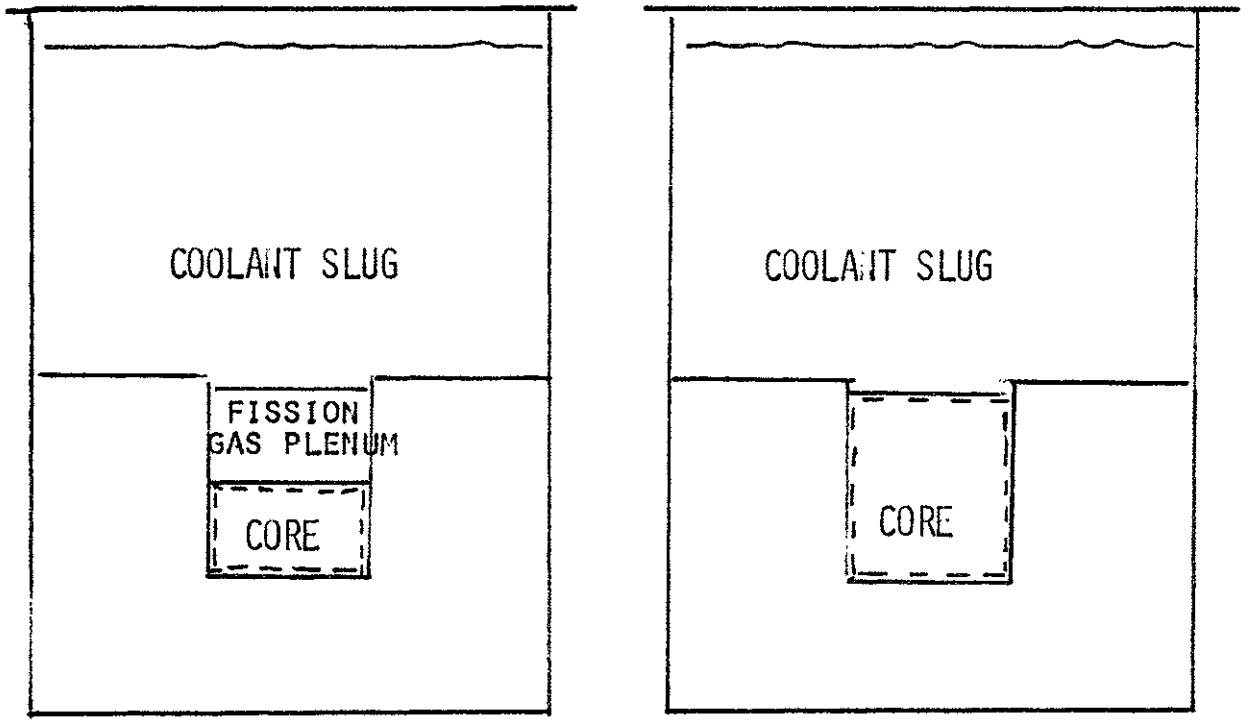

ABOVE-CORE STRUCTURE OUT
SODIUM IN THE FISSION GAS PLENUM

ABOVE-CORE STRUCTURE OUT
SODIUM OUT OF THE FISSION GAS PLENUM

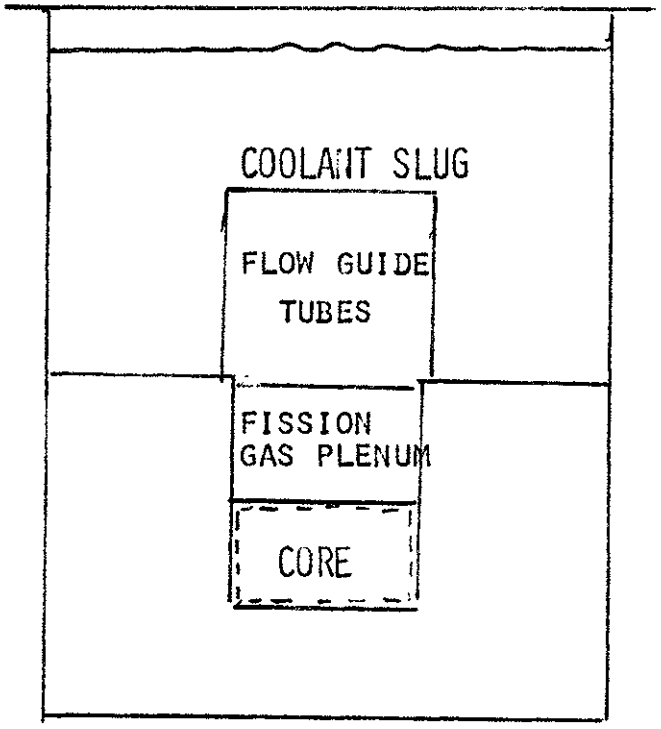

ABOVE-CORE STRUCTURE IN PLACE
SODIUM IN THE FISSION GAS PLENUM

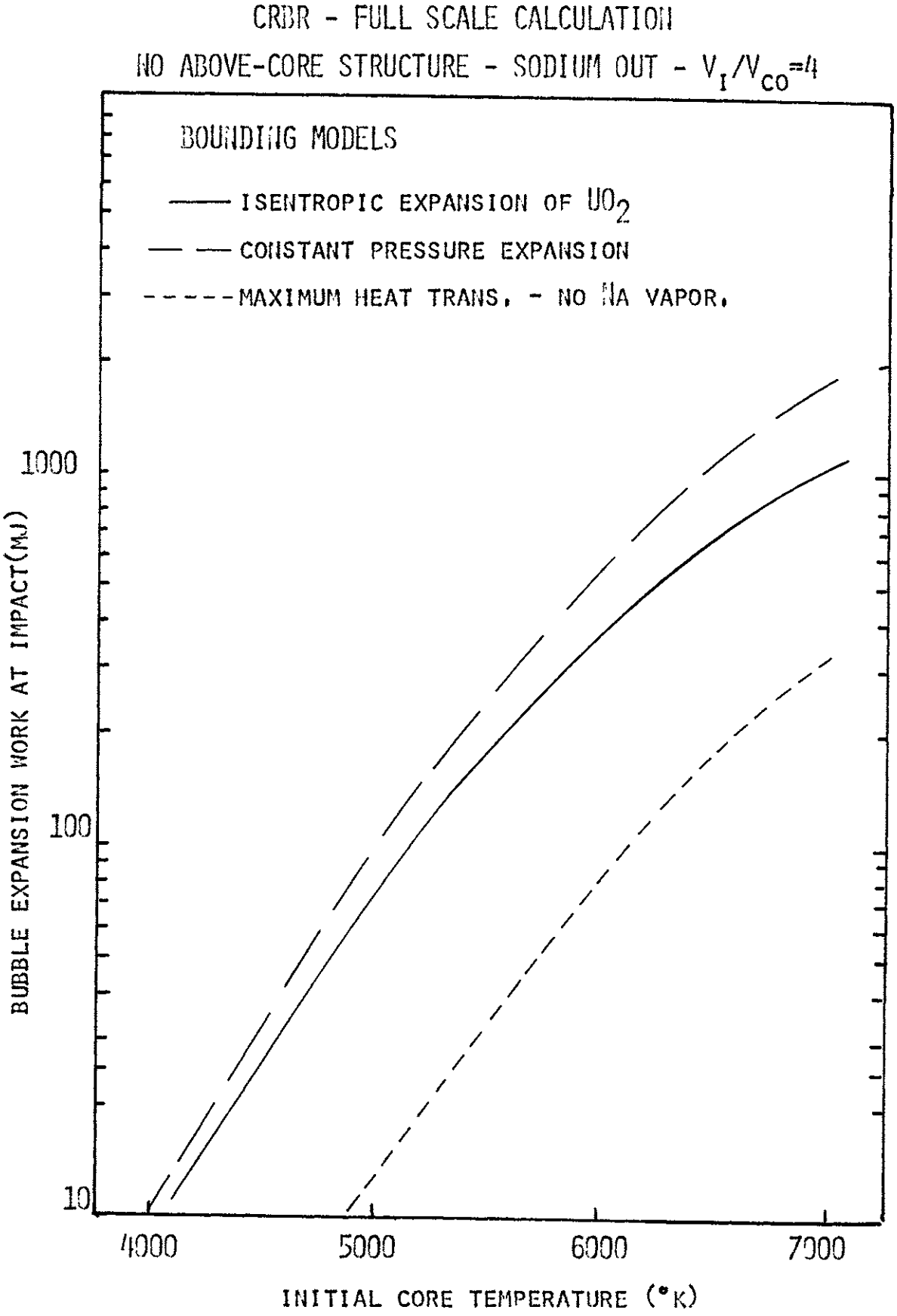

FIGURE 6.4 ISENTROPIC FUEL EXPANSION UP TO SLUG IMPACT COMPARED TO NON-MECHANISTIC BOUNDS ON THE EFFECT OF SODIUM ENTRAINMENT

FIGURE 6.5

CONCEPTUAL MODEL OF THE TWO-PHASE BUBBLE EXPANSION

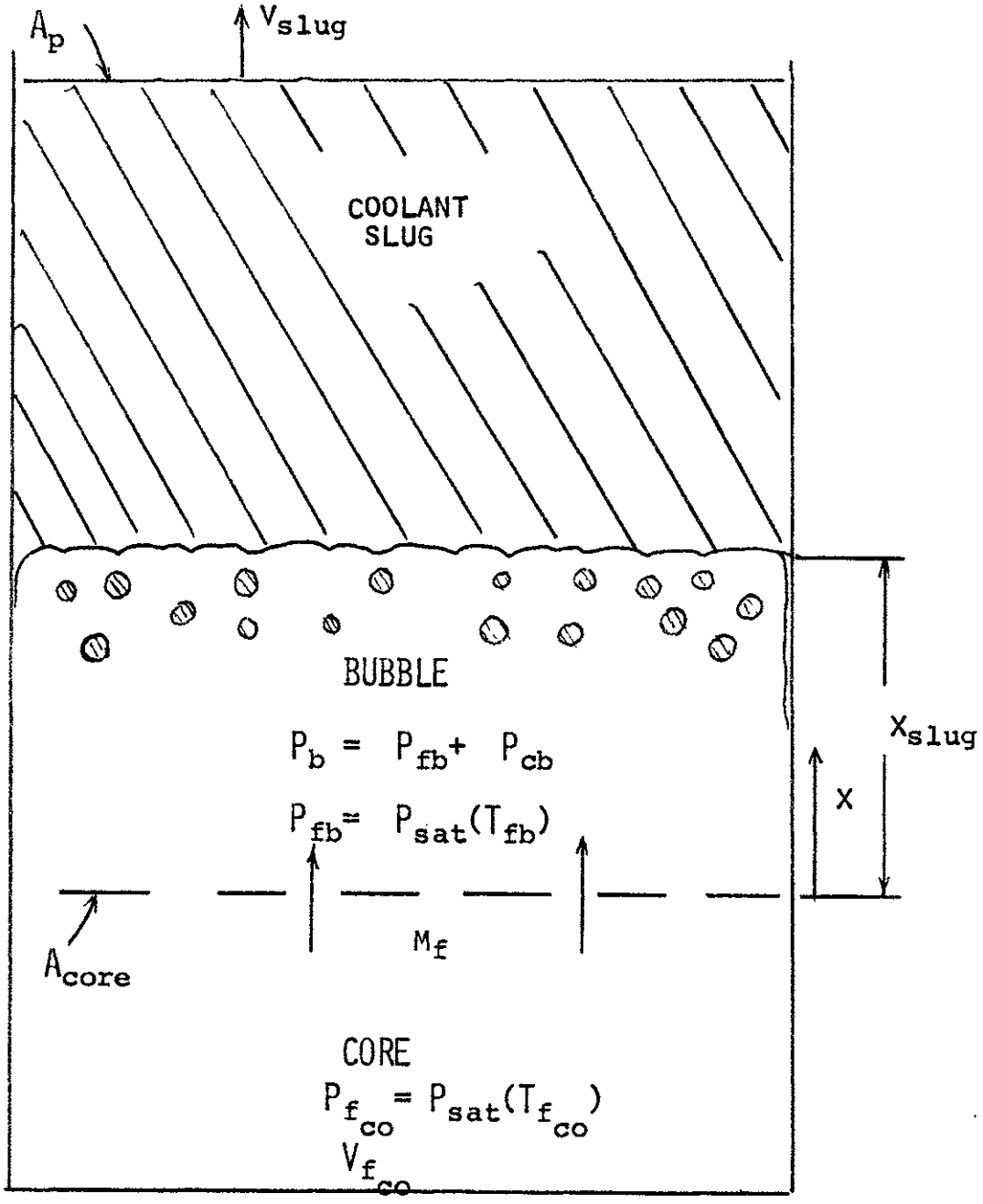

FIGURE 6.6

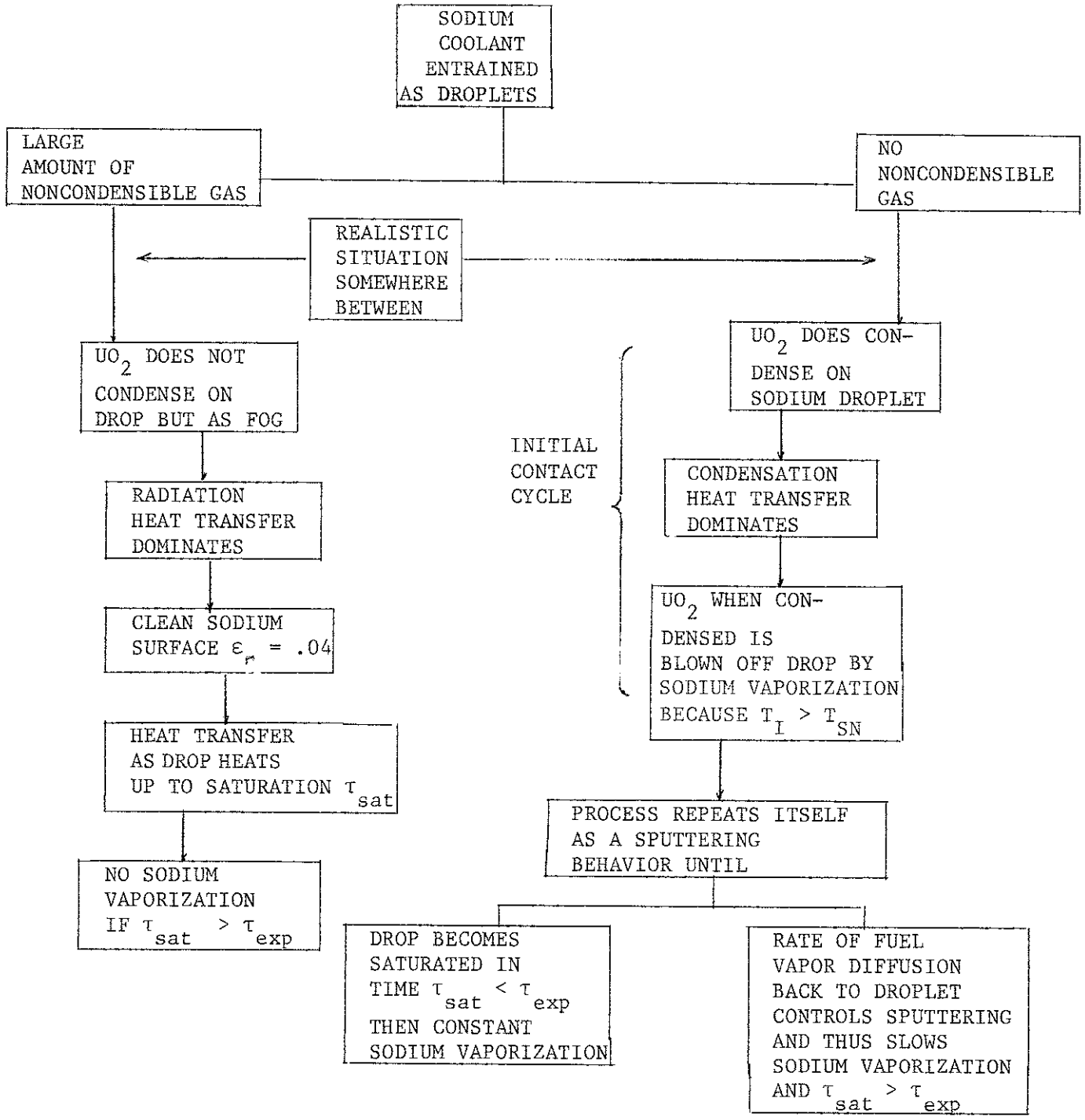

BLOCK DIAGRAM OF POSSIBLE MECHANISTIC HEAT TRANSFER MODELS AS EFFECTED BY INITIAL CONDITIONS

FIGURE 6.7

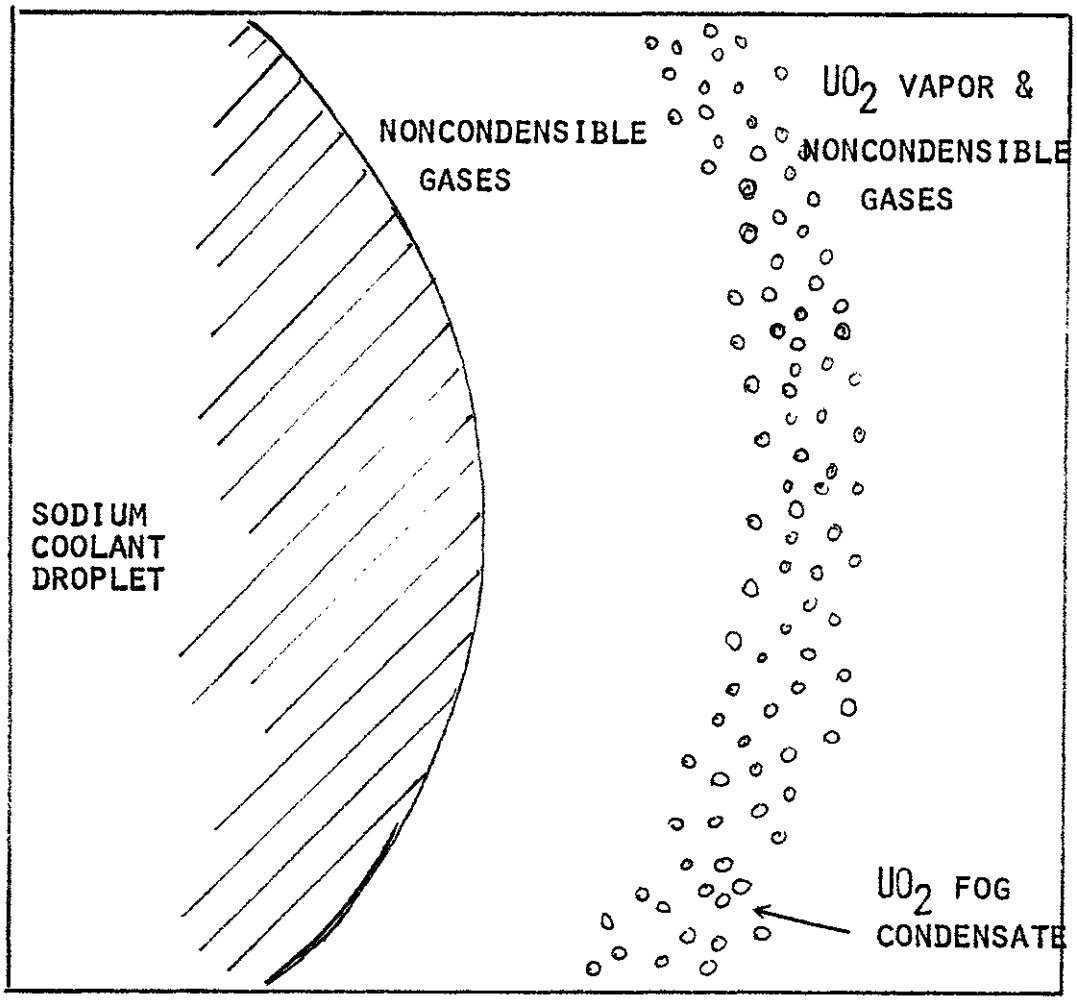

CONCEPTUAL VIEW OF RADIATION HEAT TRANSFER MODEL
NO SODIUM VAPORIZATION

FIGURE 6.8

CONCEPTUAL VIEW OF DIFFUSION CONTROLLED SODIUM VAPORIZATION MODEL

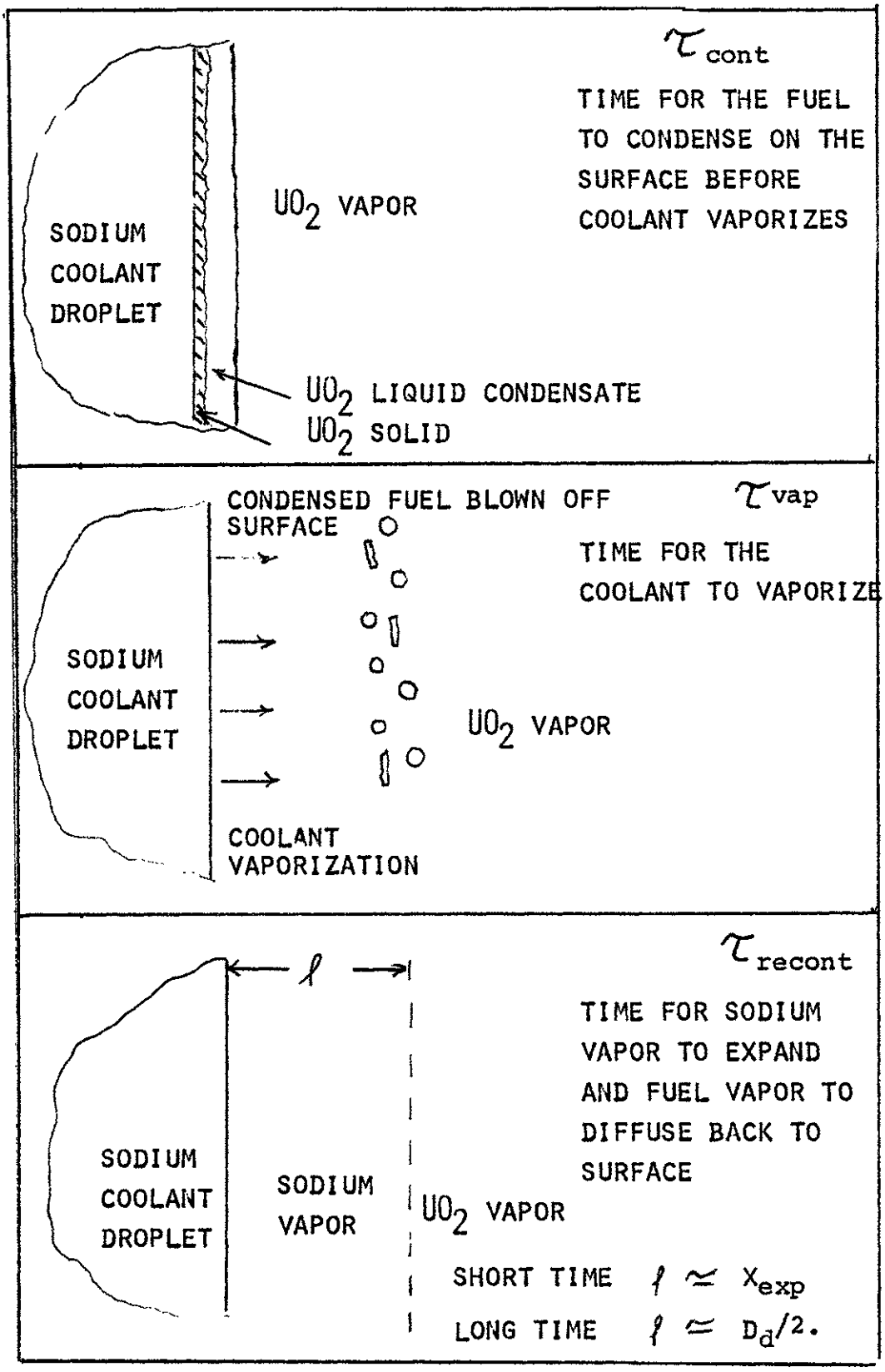

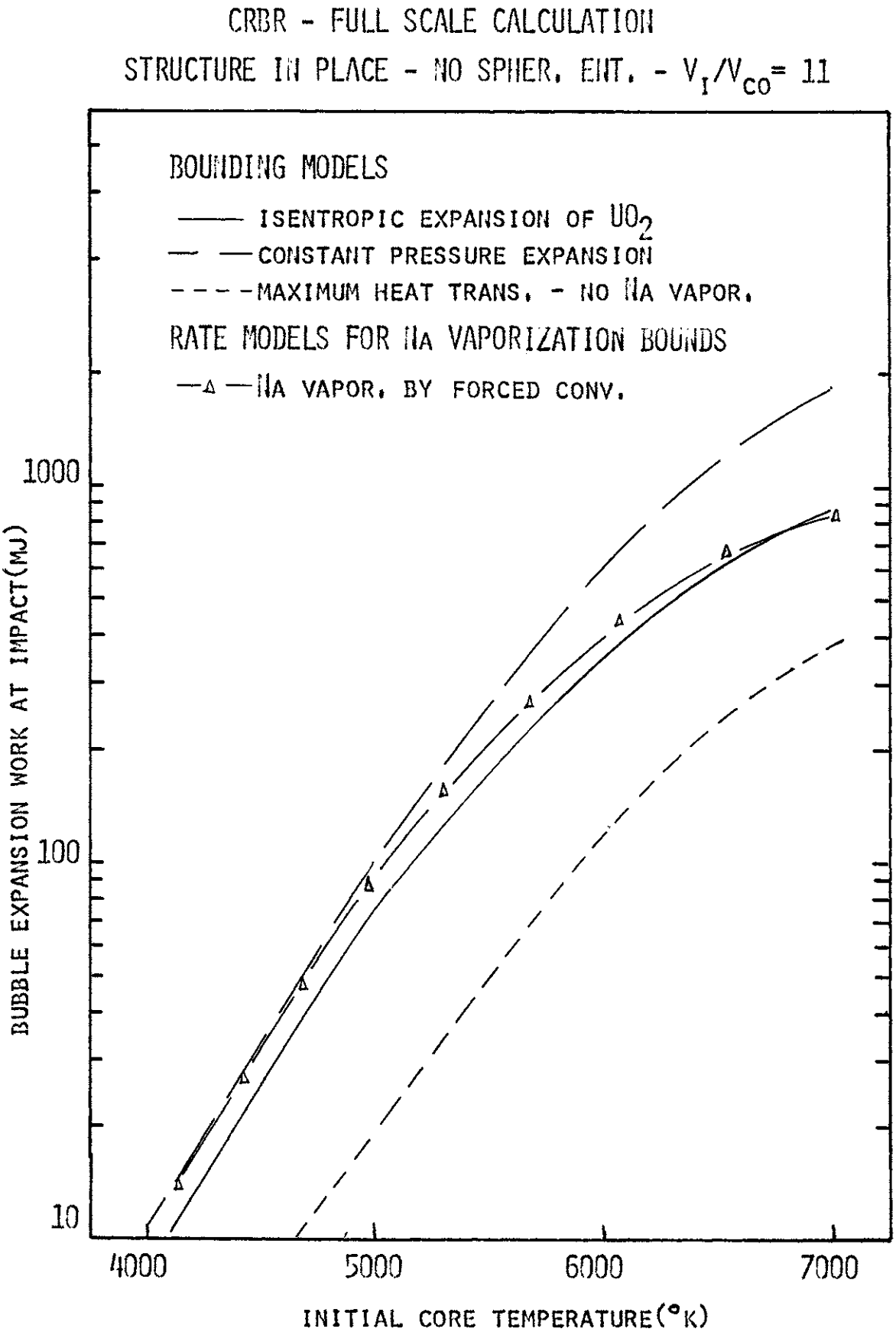

FIGURE 6.9 EXPANSION WORK AT SLUG IMPACT WITH THE ABOVE-CORE STRUCTURE AND SODIUM IN THE FISSION GAS PLENUM

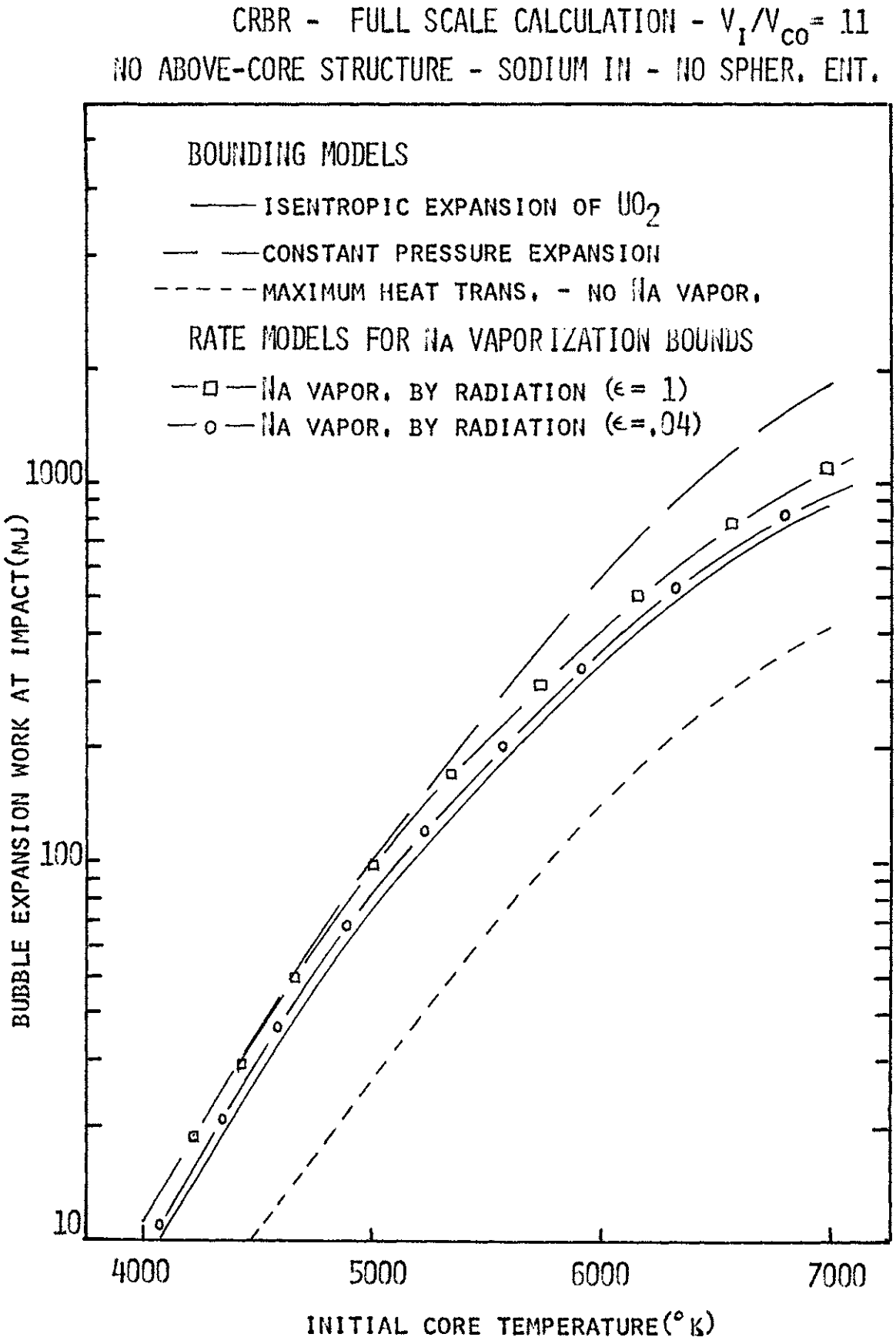

FIGURE 6.10 EXPANSION WORK AT SLUG IMPACT WITHOUT THE ABOVE-CORE STRUCTURE AND SODIUM IN THE FISSION GAS PLENUM

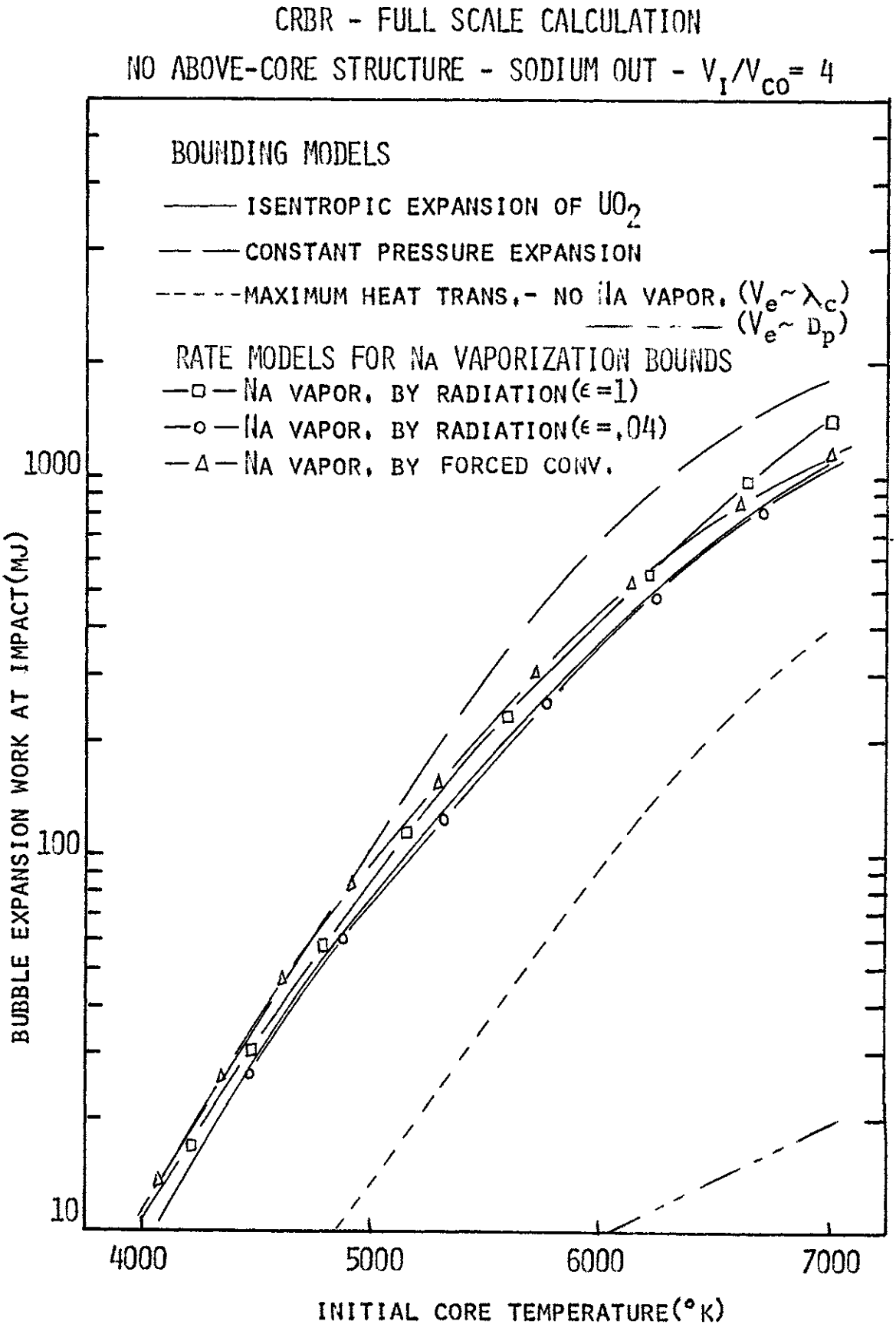

FIGURE 6.11 EXPANSION WORK AT SLUG IMPACT WITHOUT THE ABOVE-CORE STRUCTURE AND SODIUM OUT OF THE FISSION GAS PLENUM

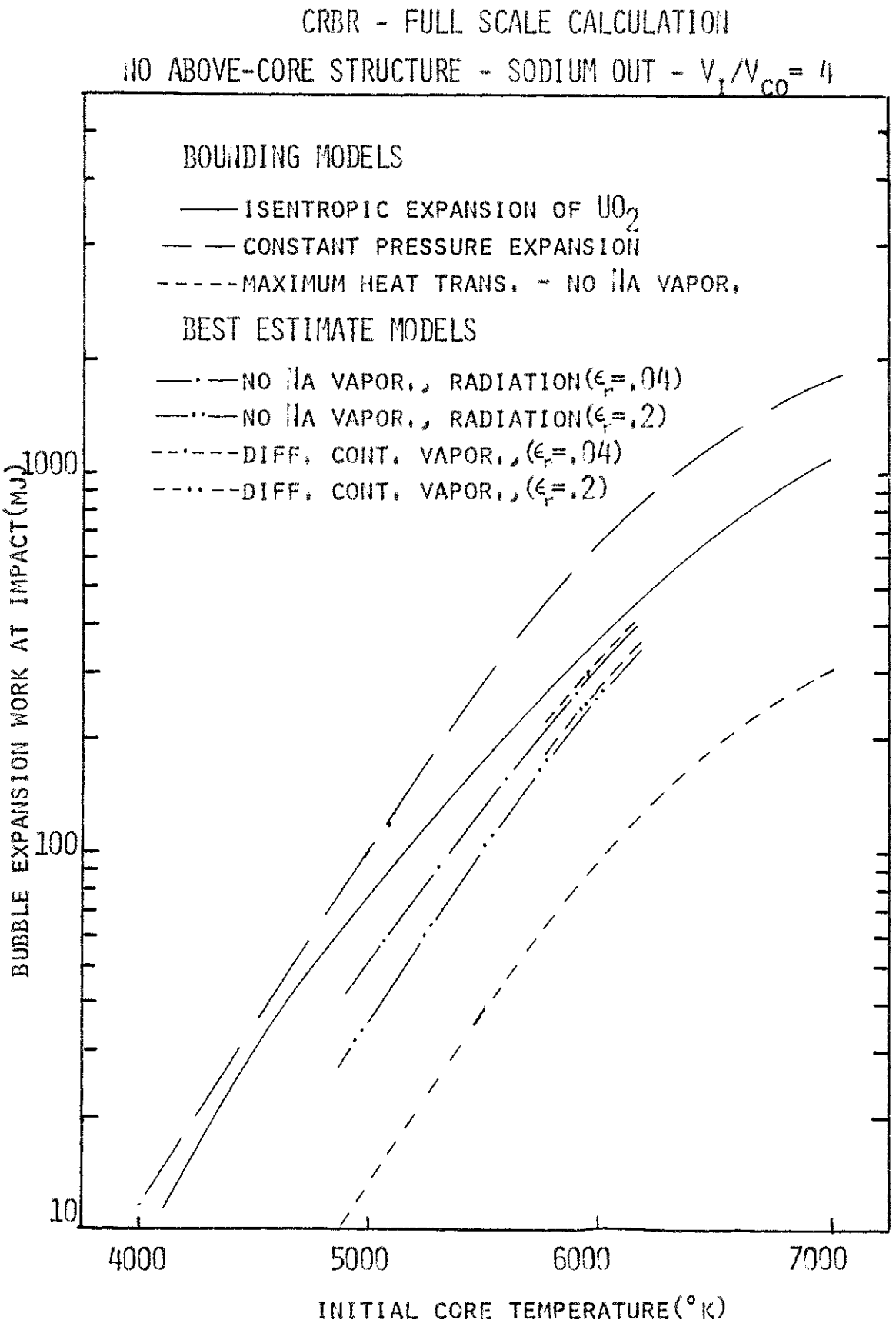

FIGURE 6.12 BEST ESTIMATE HEAT TRANSFER MODELS EFFECT ON THE EXPANSION WORK AT SLUG IMPACT

7. DIMENSIONAL ANALYSIS OF FULL SCALE HEAT TRANSFER PROCESS

7.1 Introduction and Basic Review of Dimensional Analysis

The purpose of this chapter is two-fold: (1) to determine the dimensionless groups which govern the vapor-liquid heat transfer process and bubble expansion for the full scale situation as presented in Chapter 6; (2) to recommend possible simulant fluid pairs that may show similar behavior to the full scale constituents. In a sense this section is part of the recommendations for future work. To really show the reduction in the expansion work due to sodium entrainment, some simulant system or reactor materials experiments must be done, and this analysis is needed as an aid in properly designing and scaling the experiments.

The basic theory of dimensional analysis is not complex although its application to complicated phenomena is quite challenging. A good review of the methods of dimensional analysis is given in references 59, 87, and 88, and only a brief overview is given here. The methods of dimensional analysis are based upon the principle of dimensional uniformity, which means that all governing equations of a phenomenon should be dimensionally consistent. If the equations are known and nondimensionalized, the predicted behavior of the phenomena is based upon a set of dimensionless groups which are part of the equations. The behavior is valid for any geometry, set of fluids and properties, boundary and initial conditions, as long as the values of the dimensionless groups remain the same. If the governing equations are unknown, the independent variables could be intuitively deduced and dimensional analysis again aids in forming the dimensionless groups that can be used as the basis for experimentation, and the parameters useful in empirical correlations. There are two methods utilized in employing dimensional

analysis: (1) the Buckingham Pi Theorem; (2) Nondimensionalizing the governing differential equations.

If the governing equations are unknown or the equations are too complex, the dimensionless grouping of quantities can be done using the Pi Theorem. A simple example will demonstrate its usefulness. Suppose we want to obtain the dimensionless quantities governing the pressure drop (ΔP) in a circular pipe in order to use these groupings as the independent variables in experimentation. First, some intuitive physical reasoning or past experience is drawn upon to give the independent variables on which ΔP depends, for example

$$\Delta P = f(\rho, v, D, \mu, e) \tag{7.1}$$

where e is a length parameter describing the roughness of the pipe, which may be important for rough inner surfaces. Now in this functional equation there are three primary dimensions--length (l), mass (m), and time (t)--used. The Pi Theorem states that the number of dimensionless groupings is equal to the number of variables (independent and dependent) minus the number of primary dimensions, or in this case, 6-3 = 3 groups. Now these groupings can be found by inspection or algebraically by choosing three of the independent variables as the factors which will nondimensionalize the other three. For example, if ρ, v,D are chosen as the variables which will nondimensionalize the others, the requirement is that the dimensions of this group of three variables be the same as those of the other three variables, i.e.,

$$\rho^a v^b D^c \sim \Delta p \tag{7.2.1}$$

$$\rho^d v^e D^f \sim \mu \tag{7.2.2}$$

$$\rho^3 v^h D^i \sim e \tag{7.2.3}$$

and the three dimensionless groups become

$$\pi_1 = \frac{\Delta P}{\rho^a v^b D^c}, \quad \pi_2 = \frac{\mu}{\rho^d v^e D^f}, \quad \pi_3 = \frac{e}{\rho^g v^h D^i} \tag{7.3}$$

The exponents can be found by inspection as

$$\frac{\frac{\Delta P}{\rho}}{v^2} = f\left(\frac{\rho v D}{\mu}, \frac{e}{D}\right) \tag{7.4.1}$$

$$\frac{\Delta P}{\rho v^2} = f(\text{Re, roughness}) \tag{7.4.2}$$

Now experiments can be undertaken to determine the functional relationships of these quantities reducing the independent variables from 5 to 2.

If the governing equations are known then the equations themselves can be nondimensionalized. From this process nondimensional groups will appear in the equations. The application of this analysis to the full scale phenomena of Chapter 6 will serve as the example, and will be done for two reasons:

1. The dimensionless groups which are found for the governing equations and the heat transfer models by this process give the characteristics of the full scale expansion which should be matched in experimentation to adequately assess the proposed models;

2. The same dimensionless groups can be determined for a series of candidate simulant fluid pairs to assess which ones may be useful in experimentally modeling the heat transfer and expansion phenomenon.

7.2 Dimensionless Groups of the Governing Equations

The independent variable in the governing equations is time, t. The dependent variables are:

CORE REGION

mass of fuel - m_{fco}
mass quality of fuel - X_{fco}
temperature of fuel - T_{fco}

EXPANDING BUBBLE REGION

expansion distance - $x = V_b/A_p$

mass of fuel - $m_{f_b} = m_{f_{coi}} - m_{fco}$

entrained mass of coolant - m_e

pressure - $P_b = P_f + P_c$

temperature - $T_{f_b} = T_{sat}(\text{fuel})$

These variables are initialized at the start of the transient calculation (e.g. $T_{fco} = T_{fi}$).

The governing equations for the two-phase fuel expansion process have been presented in Chapter 6 and consist of: the mass of the fuel and energy conservation equation for the core region (Equation 6.29 and 6.30); the axial momentum equation for the bubble (Equation 6.34); the fuel and coolant mass and energy conservation equations for the bubble (Equation 6.32, 6.33, 6.42, 6.47 respectively). The equations of state and caloric equation for the enthalpy for the fuel and coolant are given in Chapter 6 and Appendix A.

The independent and dependent variables and the governing equations are nondimensionalized to determine the dimensionless groupings which govern the phenomena. The choice of which parameters are used to non-dimensionalize the equations can be made arbitrarily using constant physical values because they are known and easily controlled for a process. To motivate the choice of these parameters, let us consider the axial momemtum equation for the process (Equation 6.34)

$$\frac{d^2x}{dt^2} = \frac{(P_b - P_\infty)A_p}{M_{slug}} \tag{7.5.1}$$

and nondimensionalize it. Dividing through by the right-hand side and substituting in for M_{slug} and A_p we get

$$\frac{\rho_c V_{slug}}{(P_b - P_\infty)\frac{\pi}{4} D_p^2} \frac{d^2x}{dt^2} = 1 \tag{7.5.2}$$

where

$$M_{slug} = \rho_c V_{slug}$$

$$A_p = \frac{\pi}{4} D_p^2$$

Now by some algebraic rearrangement we get

$$\frac{P_i}{(P_b - P_\infty)} \frac{V_{slug}}{\frac{\pi}{4} D_p^3} \frac{d^2\left[\frac{x}{D_p}\right]}{d\left[\frac{t^2}{\rho_c D_p^2 / P_i}\right]} = 1 \qquad (7.5.3)$$

where P_i is introduced as the initial pressure of the expansion $P_i = P_{fco}(t=0) = P_b(t=0)$. By inspection we observe that three parameters, ρ_c, D_p, P_i can be used nondimensionalize the equation because they contain three of the four primary dimensions (mass, time, length, temperature). Therefore, these three paraemters along with a temperature, T_{fi}, (the initial core and bubble temperature) are used to nondimensionalize the variables and governing equations.

Now we can write the variables in dimensionless form as follows. The independent variable is

$$t^* = t \Big/ \sqrt{\frac{\rho_c D_p^2}{P_i}} = t/\tau \qquad (7.6.1)$$

The dependent variables are

CORE REGION

$$m^*_{fco} = \frac{m_{fco}}{\rho_c D_p^3} \qquad (7.6.2)$$

$$X^*_{fco} = X_{fco} \qquad (7.6.3)$$

$$T^*_{fco} = T_{fco}/T_{fi} \qquad (7.6.4)$$

BUBBLE REGION

$$x^* = x/D_p \qquad (7.6.5)$$

$$m^*_{fb} = m^*_{fco_i} - m^*_{fco} \qquad (7.6.6)$$

$$m_e^* = V_e/D_p^3 \tag{7.6.7}$$

$$P_b^* = P_b/P_i \tag{7.6.8}$$

$$T_{fb}^* = T_{fb}/T_{fi} \tag{7.6.9}$$

Now each governing equation will be nondimensionalized.

For the core region the conservation of mass equation (6.29) and energy equation (6.30.1) describe the transient behavior of the core as the hot two-phase fuel is ejected into the upper plenum. The mass equation is

$$\frac{dX_{fco}}{dt} = \frac{P_{fco}}{R_f T_{fco}} \left[\frac{v_{fco}}{m_{fco}} \dot{m}_f + \left(\frac{X_{fco} h_{fg_f}}{P_{fco} T_{fco}} - \frac{X_{fco} R_f}{P_{fco}} \right) \frac{dT_{fco}}{dt} \right] \tag{7.7}$$

The mass equation can be nondimensionalized to give,

$$\frac{dX_{fco}^*}{dt^*} = \left(\frac{P_{fco} v_{fco} \dot{m}_f \tau}{R_f T_{fco} m_{fco}} \right) + \left[\frac{X_{fco}^* h_{fg_f}}{R_f T_{fco} T_{fco}^*} - \frac{X_{fco}^*}{T_{fco}^*} \right] \frac{dT_{fco}^*}{dt^*} \tag{7.8}$$

where two dimensionless groups are formed and are given by

$$\dot{m}_f^* = \left(\frac{P_{fco} v_{fco}}{R_f T_{fco}} \frac{\dot{m}_f \tau}{m_{fco}} \right) = \frac{P_{fco} v_{fco}}{R_f T_{fco}} \left(\frac{\tau}{m_{fco}} A_{core} \rho_{ex} \sqrt{2\Delta h} \right) \tag{7.9}$$

$$\left(\frac{dP_f}{dT_{fco}} \right)^* = \frac{h_{fg_f}}{R_f T_{fco} T_{fco}^*} \tag{7.10}$$

again noting that $P_{fco} = P_{sat}(T_{fco})$. For the possible range of full scale initial conditions of the UO_2 two-phase fuel, the quantitive values of these groups are given in Table 7.1. Specifically, the initial values of m_{fco} (~7500 kg) and $\dot{m}_f$ (Appendix E - critical flow) are used here to provide a basis for future comparison.

The energy equation for the two-phase fuel in the core is

$$\frac{d}{dt}(m_{fco}u_{fco}) = -\dot{m}_f h_{fco} \tag{7.11.1}$$

where

$$h_{fco} = u_{fco} + P_{fco} v_{fco} \tag{7.11.2}$$

and

$$u_{fco} = X_{fco} u_{fg_f} + c_{l_f}(T_{fco}-T_{ref}) + u_{ref} \tag{7.11.3}$$

This equation can be rearranged as in Equation 6.30.2 and made dimensionless to give

$$\frac{dX^*_{fco}}{dt^*} + \frac{c_{l_f}T_{fi}}{u_{fg_f}} \frac{dT^*_{fco}}{dt^*} = \left(\frac{-\dot{m}_f \tau}{m_{fco}} \frac{P_{fco}v_{fco}}{R_f T_{fco}}\right)\left(\frac{R_f T_{fco}}{u_{fg_f}}\right) \tag{7.12}$$

or

$$\frac{dX^*_{fco}}{dt^*} + \frac{c_{l_f}T_{fi}}{u_{fg_f}} \frac{dT^*_{fco}}{dt^*} = -\dot{m}^*_f \left(\frac{R_f T_{fco}}{u_{fg_f}}\right) \tag{7.13}$$

where the new dimensionless groupings are

$$u^*_{fsub} = \frac{c_{l_f}T_{fi}}{u_{fg_f}} \tag{7.14.1}$$

$$u^*_{g_f} = \frac{R_f T_{fco}}{u_{fg_f}} \tag{7.14.2}$$

The internal energy can be written in terms of the enthalpy, to be consistent with the remaining governing equations, where the enthalpy appears due to the convective energy terms. Now within Equations 7.14.1 and 7.14.2 using the definition of the enthalpy (Equation 7.11.2), the dimensionless groups become,

$$u^*_{fsub} = \left(\frac{c_{l_f}T_{fi}}{h_{fg_f} - P_{fco}(v_{fg})}\right) \tag{7.15.1}$$

$$u^*_{g_f} = \left(\frac{R_f T_{fco}}{h_{fg_f} - P_{fco}(v_{fg})}\right) \tag{7.15.2}$$

The reference enthalpy for the fuel (T_{ref} = 298°K) is neglected in this analysis for two reasons: (1) The properties of UO_2 are not well established and at the present time, h_{ref} is assigned a value of zero [144]; (2) Actually h_{ref} is not zero compared to a temperature of 0°K, but its value will be small (~100,000 $\frac{w-s}{k_g}$) compared to operational enthalpies (~2,000,000 $\frac{w-s}{k_g}$) and thus can be neglected. The initial numerical values of these groups for the components of the two-phase fuel enthalpy are given in Table 7.1. The values for the fuel vapor quality are dependent upon the initial geometric conditions of the accident because the core initial volume may be altered. For the values listed in Table 7.1, the above-core structure and sodium in the fission gas plenum are not considered to be present.

The axial momentum equation (Equation 6.34) for the expanding bubble has been already made dimensionless to find the constant parameters to be used in the remaining equations. The resulting momentum equation is

$$\frac{d^2x^*}{dt^{*2}} = a^* \tag{7.16}$$

where the dimensionless group a^* is

$$a^* = \frac{(P_{fb} - P_\infty)\ A_p \tau^2}{M_{slug}\ D_p} \tag{7.17}$$

The initial dimensionless acceleration (a^*) can be found when $P_{fb} = P_i$. Also a characteristic expansion time up to slug impact ($\tau^*_{exp} = \tau_{exp}/\tau$) can be found by using a constant pressure expansion. The expansion time is

$$\tau_{exp} = \left(\frac{2 \text{ cover gas volume}}{a}\right)^{\frac{1}{2}} \tag{7.18}$$

The numerical values for these groups are given in Table 7.1.

The conservation of mass (Equation 6.32) and energy equations (Equation 6.41) for the two-phase fuel in the expanding bubble can be nondimensionalized in a similar manner as before. The result for the mass

equation is

$$\frac{dm^*_{fb}}{dt^*} = \frac{\dot{m}_f \tau}{\rho_c D_p^3} \tag{7.19}$$

where the groups have been previously defined (Equation 7.5.6, 7.8).

The energy equation (Equation 6.41) can be nondimensionalized by $\frac{\tau^3}{\rho_c D_p^5}$ to give

$$m^*_{fb} \frac{\tau^2}{D_p^2} \frac{dh_{fb}}{dt^*} = \frac{-\tau^3 \dot{q}_l}{\rho_c D_p^5} + \frac{\tau^3 V_b P_{fb}}{\rho_c D_p^5 P_b} \frac{dP_b}{dt}$$

$$+ \dot{m}^*_{fb} \frac{\tau^2}{D_p^2}(h_{fco} - h_{fb}) \tag{7.20.1}$$

where $h_f = f(X_f, T_f) = X_f h_{fg_f} + c_{l_f}(T_f - T_{ref}) + h_{ref}$ (7.20.2)

for either $h_{fco}(X_{fco}, T_{fco})$ or $h_{fb}(X_{fb}, T_{fb})$. The heat transfer from the fuel to the entrained sodium ($\dot{q}_l$) will not be specified here but rather is examined separately in the next section, with the dimensionless group defined as

$$\dot{q}^* = \frac{-\tau^3 \dot{q}_l}{\rho_c D_p^5} \tag{7.21}$$

The enthalpy of the fuel both in the bubble, (h_{fb}), and in the core, (h_{fco}), is modeled by Equation 7.20.2 and the nondimensional groups for this property is given by

$$\frac{\tau^2 h_f}{D_p^2} = h^*_f = \frac{\tau^2 h_{fg_f}}{D_p^2}\left[X_f + \frac{c_{l_f}(T_f - T_{ref})}{h_{fg_f}} + \frac{h_{ref}}{h_{fg_f}}\right] \tag{7.22.1}$$

or

$$h^*_f = h^*_{fg_f}[X^*_f + h^*_{fsub}] \tag{7.22.2}$$

where h_{ref} has been neglected.

The time derivative of the enthalpy in Equation 7.20.1 also gives a dimensionless group which describes the expansion

$$\frac{\tau^2}{D_p}\frac{dh_{fb}}{dt^*} = \frac{dh^*_{fb}}{dt^*} = h^*_{fg_f}\left[\frac{dX^*_{fb}}{dt^*} + \frac{c_{l_f}T_{fi}}{h_{fg_f}}\frac{dT^*_{fb}}{dt^*}\right] \tag{7.23.1}$$

where by Equation 6.43

$$X_{fb} = \frac{P_{fb}V_b}{m_{fb}R_fT_{fb}} \tag{7.23.2}$$

and

$$P_{fb} = P_{sat}(T_{fb}) \tag{7.23.3}$$

If these relations are inserted into $\frac{dX^*_{fb}}{dt^*}$, and if the Clausius Clapeyron relation (Equation 6.45) is again used for P_{fb}, the result is

$$\frac{dX^*_{fb}}{dt^*} = X^*_{fb}\left[\frac{1}{x^*}\frac{dx^*}{dt^*} + \left(\frac{dP_f}{dT_{fb}}\right)^*\frac{dT^*_{fb}}{dt^*} - \frac{\dot{m}_f\tau}{m_{fb}} - \frac{1}{T^*_{fb}}\frac{dT^*_{fb}}{dt^*}\right] \tag{7.23.4}$$

The only new dimensionless group obtained from the time derivative is $c_{l_f}T_{fi}/h_{fg_f}$, and this is very similar to the group, h^*_{fsub}, given in Equation 7.22.7.

The pressure behavior of the bubble is given by the third term in Equation 7.20.1 as

$$\frac{V^*_b}{P_b}\frac{dP^*_b}{dt^*} = \left(\frac{\tau^2V_bP_{fb}}{\rho_cD_p^5}\right)\left(\frac{P_i}{P_b}\right)\frac{dP^*_b}{dt^*} \tag{7.24}$$

where P_b is dependent upon the partial pressure of the fuel and coolant vapor in the bubble. The quantitative values for all these dimensionless groups for fuel in the bubble are given in Table 7.1, using the initial conditions for a variety of fuel temperatures.

The coolant which is entrained in the expanding bubble is continually heated by the two-phase fuel and may be vaporized. The conservation of mass and energy equations for the coolant (Equations 6.33 and 6.47) are

$$\frac{dm_e}{dt} = \rho_c \dot{V}_e \tag{7.25}$$

where $\dot{V}_e$ is given in Equation 6.10, and

$$\frac{dh_{cb}}{dt} = \frac{\dot{q}_l}{m_{cb}} + \left(\frac{P_b - P_{fb}}{P_b}\right) \frac{V_b}{m_{cb}} \frac{dP_b}{dt} + \frac{\dot{m}_{cb}}{m_{cb}} (h_e - h_{cb}) \tag{7.26.1}$$

where $$h_{cb} = X_{cb}[c_{pg_c}(T_{fb} - T_{sat_c}(P_b)) + h_{fg_c}] + c_{l_c}(T_{sat_c}(P_b) - T_{ref}) \tag{7.26.2}$$

Now $\dot{m}_e$ is not necessarily equal to $\dot{m}_{cb}$, and depends upon the heat transfer model utilized as Chapter 6 indicated. If Equation 7.25 is nondimensionalized, the result is

$$\dot{m}_e^* = \frac{\dot{V}_e \tau}{D_p^3} \tag{7.27}$$

and the result is given in Table 7.1 for the initial conditions.

The energy equation (Equation 7.26.1) may be nondimensionalized as before by $\tau^3/\rho_c D_p^5$ giving

$$\frac{\tau^2}{D_p^2} \frac{dh_{cb}}{dt^*} = \frac{\dot{q}^*}{m^*_{cb}} + \frac{\tau^3 (P_b - P_{fb}) V_b}{D_p^2 P_b m_{cb}} \frac{dP_b}{dt} + \frac{\dot{m}^*_{cb}}{m^*_{cb}} \frac{\tau^2}{D_p^2} (h_e - h_{cb}) \tag{7.28}$$

where $\dot{q}^*$ and m^*_{cb} have been previously defined. The enthalpy of the coolant in the bubble, h_{cb}, and the entrained value, h_e, can be given as

$$\frac{\tau^2}{D_p^2} h_{cb} = h^*_{cb} = \frac{\tau^2}{D_p^2} h_{fg_c} \left[X_{cb} \left(\frac{c_{pg_c}(T_{fb} - T_{sat})}{h_{fg_c}} + 1 \right) + \frac{c_{l_c}(T_{sat} - T_{ref})}{h_{fg_c}} + \frac{h_{ref}}{h_{fg_c}} \right] \tag{7.29.1}$$

or

$$h^*_{cb} = h^*_{fg_c} \left[X^*_{cb} (h^*_{csup} + 1) + h^*_{csub} + h^*_{ref} \right] \tag{7.29.2}$$

and

$$\frac{\tau^2}{D_p^2} h_e = h^*_e = \frac{\tau^2}{D_p^2} h_{fg_c} \left[\frac{c_{l_c}(T_l - T_{ref})}{h_{fg_c}} + \frac{h_{ref}}{h_{fg_c}} \right] \tag{7.30}$$

The numerical values of each group are given in Table 7.1, except X_{cb} which is dependent on the expansion process starting at t=0 @ $X_{cb} = 0$. The enthalpy of sodium is known down to 0^oK, where $h_{ref} = 0$. The pressure behavior is given by the third term in Equation 7.28 as

$$\frac{\tau^3 V_b (P_b - P_{fb})}{\rho_c D_p^5 P_b m_{cb}} \frac{dP_b}{dt} = \frac{V_b^*}{m^*_{cb}} \left(\frac{P_i}{P_{fb}} - \frac{1}{P^*_b} \right) \frac{dP^*_b}{dt^*} \tag{7.31}$$

Initially for no sodium vaporization $P_{fb} = P_b$ and this term is zero in the coolant energy equation. As time progresses and vaporization occurs, this will become non-zero and positive. As in the case of Equation 7.24, the values of this term depend upon the transient expansion and the partial pressures of the fuel and coolant.

The time derivative of the coolant enthalpy in Equation 7.28 also designates some nondimensional groups

$$\frac{\tau^2}{D^2} \frac{dh_{cb}}{dt^*} = \frac{dh^*_{cb}}{dt^*} = h^*_{fg_c} \left[X^*_{cb} \frac{c_{pg_c}}{h_{fg_c}} T_{fi} \left(\frac{dT^*_{fb}}{dt^*} - \frac{1}{T_{fi}} \frac{dT_{sat}}{dP^*_b} \frac{dP^*_b}{dt^*} \right) \right.$$
$$\left. + \frac{c_{l_c}}{h_{fg_f}} \frac{dT_{sat}}{dP^*_b} \frac{dP^*_b}{dt^*} + (h^*_{csup} + 1) \frac{dX^*_{cb}}{dt^*} \right] \tag{7.32.1}$$

where X_{cb} is defined by Equation 6.51 and when substituted in $\frac{dX^*_{cb}}{dt}$ becomes

$$\frac{dX^*_{cb}}{dt^*} = X^*_{cb}\left[\frac{1}{x^*}\frac{dx^*}{dt^*} + \frac{1}{P^*_b}\frac{dP^*_b}{dt^*} - \left(\frac{dP^*_{fb}}{dT_{fb}}\right)\frac{dT^*_{fb}}{dt^*} - \frac{\dot{m}_{cb}}{m_{cb}} - \frac{1}{T^*_{fb}}\frac{dT^*_{fb}}{dt^*}\right] \tag{7.32.2}$$

Using the Clausius-Clapeyron relation with the groups for dT_{sat}/dP_b, the resulting new dimensionless groups are

$$h^*_{g_c} = \frac{c_{pg_c}T_{fi}}{h_{fg_c}} \tag{7.33.1}$$

$$\left(\frac{dT_{sat}}{dP_b}\right)^* = \frac{P_i}{T_{fi}}\frac{dT_{sat}}{dP_b} = \left(\frac{P_i}{P_b - P_{fb}}\right)\left(\frac{R_c T_{fb}}{h_{fg_c}}\right)\left(\frac{T_{sat_c}}{T_{fi}}\right) \tag{7.33.2}$$

$$(h_c dT_{sat})^* = \frac{c_{l_c}T_{fi}}{h_{fg_c}}\left(\frac{dT_{sat}}{dP_b}\right)^* \tag{7.33.3}$$

The values for these three new quantities are given in Table 7.1, where it is assumed that $\left(\frac{P_i}{P_b - P_{fb}}\right) = 1$.

The dimensionless groups describing the governing equations have been derived and estimated for possible full scale reactor conditions. In the next section the heat transfer models are nondimensionalized following Equation 7.21 and numerically estimated for the full scale conditions.

7.3 Dimensionless Groups for Heat Transfer Models

The heat transfer models presented in Chapter 6 entail a wide spectrum of assumptions about the energy exchange phenomenon. The upper and lower bound heat transfer rates employ non-mechanistic models for the entrained coolant heat up of the droplet to its saturation temperature. The use of such modeling does not produce different dimensionless groups from those of the previous section. For example, if instantaneous saturation of the

coolant drop is assumed, the form of this portion of the heat transfer model ($\dot{q}_1^*|_{sat}$) is

$$\dot{q}_1^*|_{sat} = \frac{\tau^3 \dot{q}_1}{\rho_c D_p^5} = \left(\frac{\dot{m}_e}{\rho_c D_p^3}\right)\left(\frac{\tau^2 h_{fg_c}}{D_p^2}\right)\left(\frac{c_{l_c}(T_{sat}-T_l)}{h_{fg_c}}\right) \tag{7.34}$$

As is evident this term is simply a product of past dimensionless groupings. Therefore, in this section emphasis is placed on the two realistic models for vapor-liquid heat transfer.

If a large mole fraction of noncondensible gases is initially present, then the fuel vapor will not condense upon the droplet surface and a radiation heat flux from the condensed UO_2 fog and vapor onto the clean sodium surface is the probable heat transfer mechanism. The mathematical formulation of this model (Equation 6.80) can be nondimensionalized by $\tau^3/\rho_c D_p^5$ and becomes

$$\dot{q}_1^*|_{rad} = \frac{6\,\Delta V_e\,\tau^3}{\rho_c D_p^5 D_d}\,\varepsilon_r \sigma_r (T_{fb}^4 - T_l^4) \tag{7.35}$$

Numerical values of this quantity can be found by taking the initial values for the temperatures and drop diameter (Equation 6.14) and estimating ΔV_e as

$$\Delta V_e \doteq \frac{\dot{m}_e}{\rho_c}\tau = \dot{V}_e \tau \tag{7.36}$$

Table 7.2 gives the values of this quantity to be used for future comparison in scaling.

The sputtering contact model described in Chapter 6 consisted of two parts. Initially when no sodium vapor is present in the bubble, the sodium vaporization rate due to UO_2 vapor condensation on the droplet surface is high. However, after a short time (less than 1 msec), the mole fraction of sodium vapor around the drop is not negligible and the UO_2 vapor must diffuse through the sodium vapor to condense on the drop, thus the sodium vaporization rate should be drastically reduced. The droplet will be heated up over the

expansion time up to slug impact by the radiation heat flux from the vapor. Therefore, the heat transfer model for the entrained sodium droplets heating up to T_{sat_c} is given by Equations 7.35 and 7.36.

The initial sputtering process is important because it generates the sodium vapor which insulates the droplets at later times from significant UO_2 condensation and sodium vaporization. The initial sputtering process is dependent upon a few specific physical processes: (1) The interface temperature at UO_2 - sodium contact gives the condition $T_I > T_{HN}$; (2) The characteristic times for the sputtering cycle are short and generate a large vaporization rate. The interface temperature for the whole range of fuel vapor temperatures of interest should be above the sodium homogeneous nucleation temperature. Depending upon the fuel vapor temperature range two different models were used to predict this temperature (Equations 6.82 to 6.87). Both, however, contain similar dimensionless groups, therefore, these groupings can be quantitatively estimated to ensure in future experimentation that $T_I > T_{HN}$. The interface temperature can be represented by

$$\frac{T_I - T_1}{T_{fb} - T_1} > \frac{T_{HN} - T_1}{T_{fb} - T_1} \tag{7.37}$$

as the governing criterion.

If the fuel vapor condenses but does not freeze on the liquid surface, then T_I is given by Equations 6.82 and 6.83 as

$$\frac{T_I - T_1}{T_{fb} - T_1} = \frac{1}{\beta}\left[\frac{1}{\beta} + \text{erf}\ \kappa_1\right]^{-1} \tag{7.38}$$

whereby Equation 6.38

$$\kappa_1 = f\left(\beta, \frac{c_{1_f}\ (T_{fb} - T_1)}{\sqrt{\pi}\ h_{fg_f}}\right) \tag{7.39}$$

and β is given by Equation 6.84.

If the fuel vapor condenses and freezes on the liquid coolant surface, then the dimensionless groups are slightly different and are given by

$$\frac{T_I - T_l}{T_{mf} - T_l} = \frac{1}{1 + \beta \, \text{erf} \, \kappa_s} \tag{7.40}$$

where κ_s and κ_l are dimensionless parameters determined by the dimensionless quantities

$$\kappa_s, \kappa_l = f\left(\frac{c_{l_f}(T_f - T_{mf})}{\sqrt{\pi}\, h_{fg_f}}, \frac{T_f - T_{mf}}{T_{mf} - T_l}, \frac{c_{s_f}(T_{mf} - T_l)}{\sqrt{\pi}\, L_s}\right) \tag{7.41}$$

The numerical values of these parameters for both models are given in Table 7.2 for the range of full scale fuel vapor temperatures. When scaling the phenomenon for different fluids, the important factor to ensure is that $T_I > T_{HN}$ and either model may be appropriate to predict this.

The characteristic times for the initial sputtering process in Equations 6.94 - 6.10.3 (τ_{sat}, τ_{vap}, τ_{recont}) determine the initial rate of coolant vaporization $\left(\frac{\dot{m}_{vap}}{A_{drop}}\right)$. The nondimensional relationship is given by

$$\frac{\dot{m}^*_{vap_i}}{A} = \frac{\Delta m_{vap} \tau}{\pi D_d^2 \rho_c D_p \tau_{sp}} \tag{7.42}$$

where $\tau_{sp} = \tau_{cont} + \tau_{vap} + \tau_{recont} \simeq \tau_{recont}$. Although $\tau_{sp} \simeq \tau_{recont}$, the other characteristic times enter into the calculation of Δm_{vap}. The dimensionless value of these parameters are given in Table 7.2 and it should be emphasized that this phenomenon seems to be valid only for the initial part of the vaporization process. After this the quasi-steady state diffusion process will control the sodium vaporization rate (Equation 6.104 and 6.105). This process will probably occur over the majority of the expansion and thus scaling this phenomenon is more crucial than the initial vaporization rate. The nondimensional grouping is given as

$$\frac{\dot{m}^*_{cb}}{A} = \frac{\dot{m}^*_{vap_f}}{A} = \frac{\tau\, \dot{m}_{fg}}{\rho_c D_p A}\left[\frac{h_{fg_f}}{c_{pc_g}(T_{fb}-T_{sat}) + h_{fg_c} + c_{l_f}(T_{sat}-T_l)}\right] \qquad (7.43)$$

where

$$\frac{\dot{m}_{fg}}{A} \doteq \frac{D_{fc}}{R_f T_{fb}}\left[\frac{P_f}{\frac{D}{2^d}}\right] \qquad (7.44)$$

This is also tabulated in Table 7.2.

Given the identification of the dimensionless groups and their full scale numerical values, two tasks can now be undertaken: (1) The scaling laws of other experimental groups (SRI, Purdue Univ.) investigating the vapor-liquid heat transfer process and its effect on the bubble expansion work can be checked for their consistency for future tests; (2) The numerical values for these nondimensional groups can be determined for simulant fluid pairs to determine if this heat transfer and two-phase expansion process can be simulated, at least to some extent, in small-scale experiments.

7.4 Purdue and SRI Scaling Laws

The ongoing experimental programs at Purdue University by Christopher and Theofanous [28] and at SRI International by Cagliostro [26] are conducted in small scale apparatus. To accurately assess the possible full scale effect of the vapor-liquid heat transfer as well as other possible mitigating phenomena (e.g. solid-vapor heat transfer and frictional drag) on the expansion work, these experimental tests must be based upon a consistent set of scaling laws. Scaling laws designate the required values of the many independent variables and fluid properties necessary in the small-scale experiments to achieve behavioral similarity between the full scale prototype and the small-scale test. A scaling law can be defined like in Chapter 4, as

$$B_i = \frac{\text{value of parameter i at full scale}}{\text{value of parameter i at small-scale}} \qquad (7.45)$$

Table 7.3 lists the assumed scaling laws of P_i, D_p and ρ_c for both experimental programs. With these given as independent parameters, the values of all the other scaling laws for the other variables and properties can be found from the dimensionless groups derived in the previous sections and are also listed in Table 7.3. To illustrate how this is done, consider the dimensionless time, $t^* = t/\tau$, and how B_t can be found by the requirement that

$$t^*\Big|_{\substack{\text{full}\\\text{scale}}} = t^*\Big|_{\substack{\text{small}\\\text{scale}}} \tag{7.46}$$

$$\frac{t}{\tau}\Big|_{\substack{\text{full}\\\text{scale}}} = \frac{t}{\tau}\Big|_{\substack{\text{small}\\\text{scale}}}$$

$$B_t = B_\tau \tag{7.47}$$

Now B_τ is determined from the chosen scaling laws of P_i, D_p and ρ_c (Equation 7.6) giving

$$B_\tau = \sqrt{\frac{B_{\rho_c} B_{Dp}^2}{B_p}} \tag{7.48}$$

where if SRI scaling laws are used

$$B_\tau = \frac{1\ b^2}{1} = b \tag{7.49}$$

Therefore, the scaling law for time for SRI tests

$$B_t = b \tag{7.50}$$

This same procedure can be done for each of the independent variables and fluid properties. The results are shown in Table 7.3. The specific scaling laws for the various components of the heat transfer model are not given because they are dependent upon the fluids chosen and this task has not been done by either investigator. Rather the point of this section is to illustrate the scaling laws that are inherently implied given the initial assumption of B_p, B_D, and B_ρ. If the phenomenon modeled in these experiments

is to be similar to the full scale, then an attempt to satisfy these scaling laws must be made.

7.5 Estimates of Numerical Values for the Dimensionless Groups of Candidate Simulant Fluids

The fluids which are used to simulate the full scale phenomenon in small-scale experiments should have the same quantitative values for the nondimensional groups.

Given the initial choice of the scaling laws for the pressure, coolant density and the characteristic diameter, the values for the nondimensional groups can be calculated for the small-scale experiments. There are two important points to be made.

1. The small-scale experiments currently planned by SRI and Purdue to investigate the vapor-liquid heat transfer and other phenomena anticipated during the HCDA have not yet been scaled for heat transfer effects. Also experiments begun by Rothrock [54] at MIT could also be used to investigate the vapor-liquid heat transfer phenomenon. The previous dimensional analysis can be utilized for all these experiments. It can aid in determining the simulant fluids to use in demonstrating the behavior that is expected at full scale conditions.
2. The major phenomenon that cannot be scaled during this heat transfer process is the contribution of the radiation heat flux to the energy transfer process. This fact can be used as an advantage in the small-scale experiments. By choosing simulant fluids properly, the temperatures can be kept low in comparison to the full scale case. Then the two possible processes of contact sputtering controlled by fuel vapor

diffusion and radiation heat transfer are separated. The diffusion and vaporization process can be investigated without the complicating effect of radiation.

A determination of which simulant pairs are suited to model the vaporization-condensation of the UO_2-sodium system is difficult. The only way to approach it is to use past experience in scaling and calculate the numerical values of dimensionless groups for some candidate fluids and compare the results to those of the UO_2-sodium system. Refrigerants were considered to be the most useful candidate fluids for two reasons: (1) The variety of fluid types offered a large spectrum of different combinations of pressures, temperatures and properties for the fuel and the coolant; (2) The fluid would be easy to handle because the operating temperatures would be not far ($\pm 100^0$C) from the ambient, and the fluids are transparent for easy visual observations. Water was not considered a good simulant fluid for the fuel because the latent heat of vaporization is so large (~600-1000 BTU/lbm). If it is used in a small-scale experiment, the dimensionless group $h^*_{fg_f}$ always is a factor of 10-50 higher than what is needed to accurately model the fuel.

The numerical values for the designated nondimensional groups are given for some possible refrigerant simulant fluids in Tables 7.4 and 7.5 (properties from Ref. 152). The results illustrate that for the given scaling laws for pressure, density and diameter, the simulant pair of Freon-113 or Freon-11 (fuel) and Freon 13 (coolant) seems to give numerical values closest to the full scale conditions (Table 7.1 and 7.2). The major reason for this conclusion can be demonstrated by examining the dimensionless groups for the interface temperature. For example, the parameter β should be large (near 2) to ensure that the initial interface temperature is

above T_{HN} of the coolant but below T_{crit}. This then will cause the initial large coolant vaporization process and the diffusion controlled coolant vaporization throughout the remainder of the expansion. This interface condition is not satisfied when the simulant refrigerants (R-11 and R-12 or R-22) have boiling points which are close in their range as Table 7.4 depicts. However, when the simulant fluids have large differences in their boiling points as the R-113/R-13 system, then the fuel-coolant behavior of the full scale can be more accurately modeled (see Table 7.5). Appendix C gives details of the other possible refrigerant system (R-11/R-13) that could be used to model the heat transfer process.

TABLE 7.1

NUMERICAL VALUES OF DIMENSIONLESS GROUPS OF THE GOVERNING EQUATIONS AT FULL SCALE CONDITIONS USING INITIAL CONDITIONS

ASSUMED				
T_{f_i} (^{o}K)	4000	5000	6000	7000
P_i (MPa)	.263	4.61	27.2	96.8
D_p (m)	6.1	6.1	6.1	6.1
ρ_c (k_g/m^3)	835	835	835	835
τ (sec)	.344	.082	.034	.019
DERIVED				
m^*_{fco}	.04	.04	.04	.04
X^*_{fco} (sodium out)	.00175	.0247	.121	.35
a*	.59	.93	.96	.96
τ^*_{exp}	.49	.49	.49	.49
$(\frac{dP_f}{dT_{fco}})^*$	13.8	9.74	6.93	5.01
$\dot{m}^*_{f\ crit}$	$4(10^{-4})$	.007	.0524	.161
u^*_{fsub}	1.5	2.19	3.23	4.78
$u^*_{g_f}$	.078	.114	.169	.25
V^*_b ($V_b = 20.44m^3$)	.09	.09	.09	.09
$\frac{c_{l_f} T_{fi}}{h_{fg_f}}$	1.4	1.97	2.76	3.85
h^*_{fsub}	1.3	1.85	2.63	3.66
$h^*_{fg_f}$	5410	271	40	10.5

TABLE 7.1 (Continued)

$\dot{m}^*_e$ (use a*)	.153	.075	.0505	.042
$h^*_{fg_c}$	11450	578	53	31‡
h^*_{csub}	.352	.622	1.69	
h^*_{csup}	1.82	2.38	4.94	99‡
h^*_c	3307	188	32.3	10
$h^*_{g_c}$	2.66	3.75	8.44	
$(\frac{dT_{sat}}{dP_b})^*$	.128	.206	.53	
$(h_c dT_{sat})^*$	.184	.42	2.42	

‡ The coolant is above its critical temperature (T_{crit}) at contact and $T_{HN} = T_{crit}$. Thus the enthalpies are referenced to

$$h^* = \frac{\tau^2}{D_p^2} h$$

for $(h^*_{sub} + h^*_{fg_c})$ and $h^*_{c_{sup}}$.

TABLE 7.2

NUMERICAL VALUES FOR FULL SCALE HEAT TRANSFER NONDIMENSIONAL GROUPS

	DERIVED				
	T_f	4000	5000	6000	7000
	RADIATION MODEL FOR NO FUEL VAPOR CONDENSING ON DROP SURFACE				
	$\dot{q}_l^*\|_{rad}$ (ε_r = .04)	62.4	4.06	.89	.35
	SPUTTERING MODEL FOR FUEL VAPOR CONDENSING ON DROP SURFACE				
	$T_I > T_{HN}$				
	β	2	2	2	2
FUEL DOES NOT FREEZE	$\frac{c_{l_f}(T_f-T_l)}{\sqrt{\pi}\, h_{fg_f}}$	.64	.85	1.38	1.94
FUEL DOES FREEZE	$\frac{T_f-T_{mf}}{T_{mf}-T_l}$	.41	.85	1.29	1.73
	$\frac{\alpha_{s_f}}{\alpha_{\rho_c}}$				
	$\frac{c_{s_f}(T_{m_f}-T_l)}{\sqrt{\pi}\, L_s}$	2.74	2.74	2.74	2.74
	$\frac{c_{l_f}(T_f-T_{mf})}{\sqrt{\pi}\, h_{fg_f}}$	.18	.43	.77	1.23
	$\frac{\dot{m}^*_{vap_i}}{\bar{A}}$	$7.4(10^{-4})$	$5.63(10^{-4})$	$2.4(10^{-4})$	
	$\frac{\dot{m}^*_{vap_f}}{\bar{A}}$	$3.03(10^{-7})$	$1.77(10^{-7})$	$1.2(10^{-7})$	

TABLE 7.3

SCALING LAWS FOR PURDUE AND SRI EXPERIMENTS

SCALING LAWS B_i	SCALING FACTORS b	
ASSUMED	SRI	PURDUE
Pressure B_p	1	b
Diameter B_D	b	b
Density B_ρ	1	1
DERIVED		
Time B_t	b	$b^{\frac{1}{2}}$
Mass B_m	b^3	b^3
Distance B_x	b	b_1
Velocity B_v	1	$b^{\frac{1}{2}}$
Acceleration B_b	1/b	1
Enthalpy B_h	1	b
Mass Quality B_x	1	$1_{\frac{7}{2}}$
Power $B_{\dot{w}}$	b^2	$b^{\frac{7}{2}}$
Heat Transfer Rate $B_{\dot{q}}$	b^2	$b^{\frac{7}{2}}$
where b = 30		b = 7

FULL SCALE - CRBR UPPER PLENUM AND FISSION GAS REGION

TABLE 7.4

NUMERICAL VALUES FOR NONDIMENSIONAL GROUPS USING SMALL-SCALE SIMULANT FLUIDS

ASSUMED			
FUEL	R-11	R-11	R-11
COOLANT	R-22	R-22	R-12
$T_f(^oK)$ - FULL SCALE	5000	6000	5000
B_ρ	1.5	1.5	1.6
B_p	7	7	7
B_D	7	7	7
HEAT TRANSFER SCALING OF FUEL-COOLANT INTERFACE TEMPERATURE			
P_f(MPa)	.66	3.9	.66
$T_f(^oK)$	362	458	362
$T_l(^oK)$	233	233	243
$c_{l_f}(\frac{w-s}{k_g\ ^oK})$	880	880	880
FUEL CONDENSES BUT DOES NOT FREEZE			
β	1.35	1.35	1.02
$\frac{c_{l_f}(T_f-T_l)}{\sqrt{\pi}\ h_{fg_f}}$	.42	3.9	.4
κ_l	.35	1	.3
T_I^* (^oK)	316	333	329
T_{HN}^* (^oK)	335	345	350

*$T_I < T_{HN}$: THEREFORE, THESE SIMULANT FLUIDS DO NOT MATCH THE EXPECTED BEHAVIOR OF UO_2 VAPOR AND SODIUM LIQUID

TABLE 7.5

NUMERICAL VALUES FOR NONDIMENSIONAL GROUPS USING SMALL-SCALE SIMULANT FLUIDS

FUEL - R-113

COOLANT - R-13 (ρ_c - 1520 k_g/m^3)

ASSUMED			
T_f (^oK) FULL SCALE	5000	6000	6000
B_p	7	20	30
B_D ‡	7	20	30
τ	.0405	.01	.0083
DERIVED			
$\dot{m}^*_{f_{crit}}$	.021	.105	.107
$(\frac{dP_f}{dT_{fco}})^*$	7.04	5.14	6.31
$h^*_{fg_f}$	259	105	188
$h^*_{fsub}(T_{ref} - 0^oK)$	2.76	3.8	3.1
$u^*_{g_f}$	.165	.202	.224
$h^*_{csub}(T_{ref} - 0^oK)$	1.69	2.25	1.81
$h^*_{fg_c}$	265	113	194
h^*_{csup}	.66	.88	.74
h^*_e $(T_1 - 188^oK)$	363	182	283
$\dot{m}^*_e$	.099	182	283
$h^*_{g_c}$	1.71	2.23	1.90
$(\frac{dT_{sat}}{dP_b})^*$	.152	.197	.169

TABLE 7.5 (CONTINUED)

$(h_c dT_{sat})^*$	.297	.502	.37
FUEL DOES NOT FREEZE			
$\dot{q}_l^*\|_{rad}$ $(\varepsilon_r = 1)$	.067	.032	.038
β	1.25	1.25	1.25
$\frac{c_{l_f}(T_f - T_l)}{\sqrt{\pi}\, h_{fg_f}}$	.87	1.26	.98
	T_I (~300°K) > T_{HN} (~280°K)		
$\frac{\dot{m}^*_{vap_i}}{\bar{A}}$	$5.68(10^{-4})$	$6.8(10^{-4})$	$8.9(10^{-4})$
$\frac{\dot{m}^*_{vap_f}}{\bar{A}}$	$2.2(10^{-7})$	$5.7(10^{-7})$	$8.7(10^{-7})$

ǂ THESE SCALING LAWS WERE CHOSEN ARBITRARILY TO MATCH THE EXPERIMENTAL APPARATUS ALREADY BUILT AND IN OPERATION AT PURDUE [28] (B_D = 7), MIT [54] (B_D = 20), AND SRI [26] (B_D = 30).

8. CONCLUSIONS AND RECOMMENDATIONS FOR FUTURE WORK CONCERNING TWO-PHASE FUEL AND COOLANT HEAT TRANSFER

8.1 Conclusions

The investigation of two-phase fuel and coolant heat transfer, as envisioned in the LMFBR (seeFigures 2.1 and 6.1) during a postulated Hypothetical Core Disruptive Accident (HCDA), has led to a number of conclusions about the physical phenomena involved for both past small-scale experiments (SRI, Purdue) and the full scale reactor situation:

1. It appears that a dominant mechanism for coolant entrainment (volumetric rate - $\dot{V}_e$) into the expanding fuel bubble prior to slug impact is due to Taylor Instabilities. A model for this entrainment rate was developed ($\dot{V}_e = 4.6\ A_p \sqrt{a\lambda_c}$) based upon simple one-dimensional experiments where the acceleration (a) and the critical Taylor instability wavelength (λ_c) form the correlation for the entrainment velocity. This model was verified by agreement with data from transient unheated experiments performed at MIT [54] and at SRI [26] (see Figure 3.22 and 3.28). The use of the characteristic length, λ_c, in the correlation appears warranted based upon the data of these tests although no experiments have been performed where the scale of the system, D_p, has been increased by an order of magnitude to conclusively disprove the alternate hypothesis that entrainment scales with D_p. However, use of the λ_c correlation is conservative in full scale calculations because it underestimates the entrained coolant volume if it is in error thereby reducing the heat transfer rate.

2. Modeling of small-scale heated experiments for both non-condensible gases (PETN) [22] and condensible two-phase water sources [26,28] indicate that the characteristic size of the entrained coolant in droplet form lies between the critical Taylor Instability wavelength ($D_d = \lambda_c$) and the fastest growing Taylor wavelength ($D_d = \lambda_m = \sqrt{3}\lambda_c$), as Figures 4.11, 5.9, and 5.18 illustrate. The dominant heat transfer mechanism differs for the noncondensible gas source (Chapter 4 - forced convection heat transfer between gas and drop), and the condensible water source (Chapter 5 - condensation heat transfer controlled by the water droplet). However, in both sets of experiments, the drop size used to match experimental results is $\lambda_c \leq D_d \leq \lambda_m$.

3. The coolant entrainment rate ($\dot{V}_e$) and droplet size (D_d) as previously determined are used in full scale calculations to model two-phase UO_2 and sodium heat transfer. The results indicate that radiation heat transfer controls the energy transfer process, and the bubble expansion work at slug impact is reduced by a factor of 1.2 to 2.5 (Figure 6.12) due to this heat transfer process. The amount of the work reduction is dependent upon the radiative absorptivity of the sodium surface (in this analysis $.04 < \varepsilon_r < .2$ [76]). The amount of sodium vaporized during the expansion is predicted to be small for two major reasons: a) The droplet size, $D_d = \lambda_c$, is large enough so that the bulk of the coolant droplet does not reach its

saturation temperature during the expansion time; b) During the heatup of the coolant droplet to T_{sat}, some sodium vaporization occurs, but remains small because it is controlled by the rate of fuel vapor diffusing to the drop surface. Therefore, the mitigating effect of sodium entrainment and heat transfer on the expansion work is just as significant as other possible effects suggested by the SIMMER - I code [10].

4. The full scale behavior predicted in Chapter 6 must be verified by experimentation. Scaling analysis in Chapter 7 indicates that small scale simulant tests using refrigerants, R-11 or R-113 (fuel) and R-13 (coolant), can be used to model the two-phase expansion and coolant vaporization but without the effects of radiation heat transfer. This similarity in scaling is illustrated in Figures 8.1 and 8.2 where dimensionless pressure ($P_b^* = P_b/P_i$) and volume ($V_b^* = V_b/D_p^3$) versus time ($t^* = t/\sqrt{\rho_c D_p^2/P_i}$) are plotted for full scale reactor materials, UO_2/sodium, and small-scale simulant materials of R-11/R-13, using the heat transfer and expansion models from Chapter 6. The only way to investigate radiation heat transfer effects is to employ reactor materials in experiments and the scaling analysis provided in Chapter 7 can also be useful.

8.2 Recommendations

Future investigations into these phenomena should be in three general areas: a) phenomenological models used in the analysis

b) initial and boundary conditions for the expansion

c) inclusion of the proposed model into SIMMER.

The first area involves the phenomenological models used in the analyses in the present work. There are four specific recommendations:

1) Hydrodynamic unheated experiments should be performed at larger scales (1/5 - 1/10 of CRBR) to verify that the model of coolant entrainment based on Taylor Instabilities ($\dot{V}_e \sim A_p \sqrt{a\lambda_c}$) is adequate. With a change in scale of an order of magnitude new entrainment mechanisms may be observed as significant; (e.g. relative velocity of entrainment, $\dot{V}_e/A_p \sim \sqrt{a\lambda_c}$, may be larger at larger scales indicating that the length scale, λ_c, is not totally appropriate). The tests planned at Purdue by Christopher and Theofanous [28] are at 1/7 scale of the CRBR and may be suitable for this purpose. Also the basic behavior of Taylor Instabilities over a larger range of accelerations (1 - 10000 g) should continue to be investigated for the purpose of assessing the phenomena with new initial conditions.

2) The heat transfer size ($\lambda_c \leq D_d \leq \lambda_m$) empirically found from the analysis of the small scale experiments from SRI and Purdue [22,26,28] and used in the full scale analysis should be verified by hydrodynamic tests at small (1/20 - 1/30) and large-scale (1/7). The only method seen as feasible to accomplish this is visual measurements perhaps by stroboscopic photography. For this purpose two-dimensional rather than three-dimensional tests should be performed to facilitate the photography methods.

3. Small scale simulant heated experiments should be performed using the simulant fluids designated in Chapter 7 (R-11 or R-113 as fuel, R-13 as coolant), to assess the vaporization potential of the coolant. These experiments could verify the diffusion controlled vaporization model presented in Chapter 6. As Figures 8.1 and 8.2 indicate, these simulant fluids best model the UO_2/sodium system excluding radiation heat transfer at 1/7 scale (future Purdue tests) while a good simulation is also predicted for 1/20 (MIT [54]) and 1/30 scales [26].

4. Small-scale experiments should also be performed using reactor materials to assess the role of radiation in the expansion process. This avenue of work is only possible at a laboratory equipped to handle high temperature materials; however, the scaling analysis presented in Chapter 7 can be used as a part of the experimental preparation.

The second area of work involves the initial and boundary conditions assumed in these analyses. There are three specific recommendations:

1. The discharge of two-phase fuel from the core was assumed to be homogeneous and equilibrium giving the maximum flow rate from the core and the maximum amount of saturated liquid ejected into the bubble. This is conservative because the pressure in the bubble is predicted to be higher during the expansion increasing the expansion work. An assessment of the core discharge behavior under different initial conditions should be conducted. One possibility could be simple blow-down experiments using different scales for the fuel ejection time

and the initial geometries above the core. This study is also needed to assess the proper design of small-scale experiments. For example, SRI condensible water tests [26] experienced a nonequilibrium discharge which may or may not be prototypic of the full scale accident events.

2. If the fission gas plenum region remains, sodium coolant will be left on this structure as the core materials expand. The effect on the expansion of this coolant should be assessed. The first unknown is how much is left on solid structure as a film. No experiments have been carried out at these high accelerations [69]. If it is a very thin film (10 μm), then it could be neglected, but if it is thick (~ 500 μm), then it is the same thickness as the clad, and it may be a nonnegligible heat sink. Also entrainment of this coolant in the expanding fuel is possible and its thermal effect unknown.

3. The radiative properties of sodium and fuel predicted by theory [76] should be compared to experimental results of sodium and fuel depending upon the commercial purity of the materials and the effect of possible reactor environment impurities. For example, sodium radiative properties could be tested from samples extracted from EBR II and FFTF after various operation time intervals.

The final area of work involves the coupling of this full scale analysis with the other possible phenomena that could occur during the core material expansion. The computer code SIMMER I [10] was developed to mechanistically describe the LMFBR HCDA from the time after the initiation phase up to sodium

slug impact on the reactor vessel and its structural response. Although all the possible mechanisms are included (an assumed above-core structure in place), the physical mechanisms for many of the thermal hydraulic phenomena are absent with rate coefficients installed as first order estimates for various processes. This present work provides a phenomenological model for the inclusion of the effects of sodium coolant entrainment and two-phase fuel and coolant heat transfer into this computer code. Its effect on the expansion work and the interplay with other possible processes can be better determined by inclusion of these models into the SIMMER-I code.

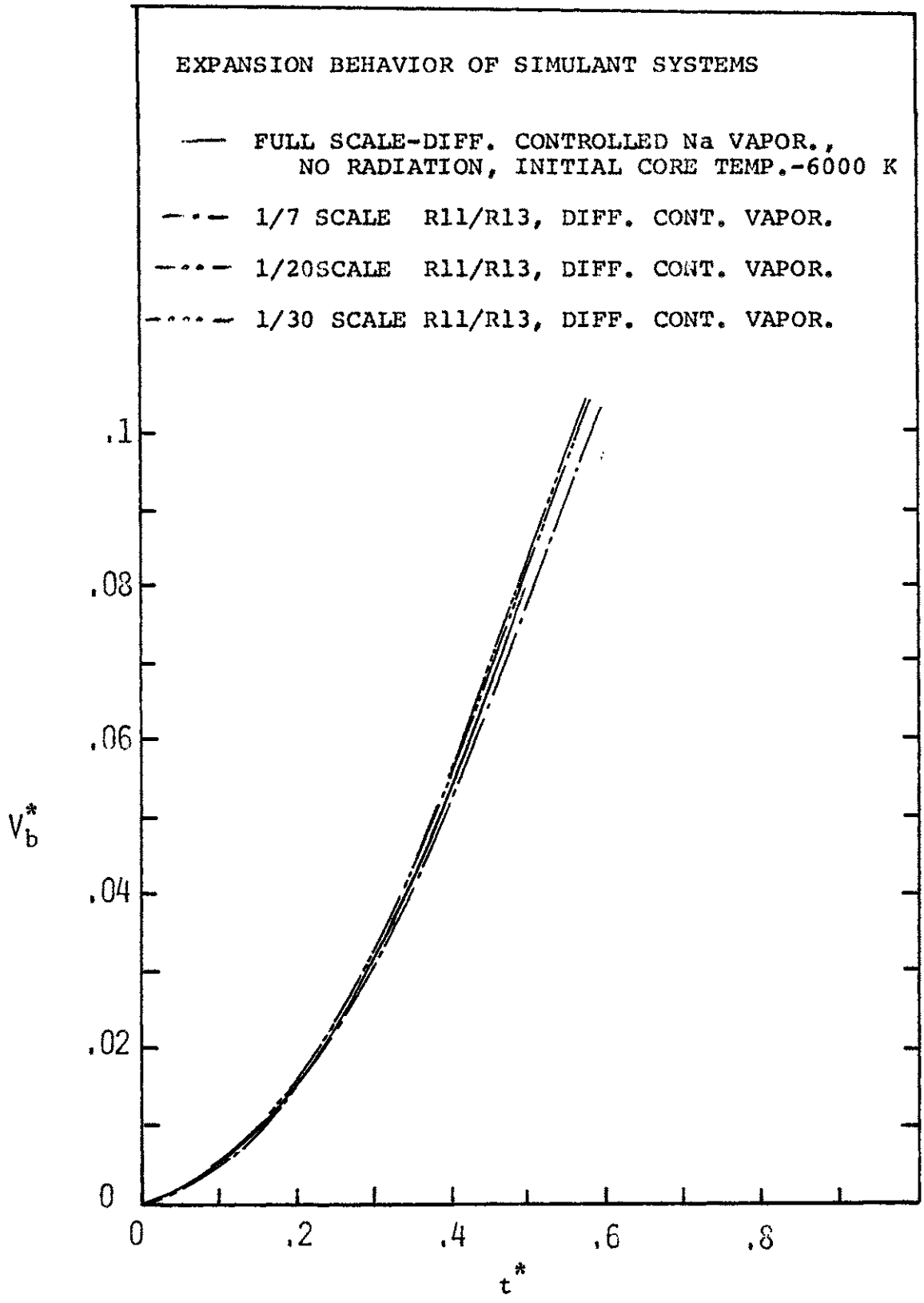

FIGURE 8.1 DIMENSIONLESS TRANSIENT EXPANSION BEHAVIOR FOR SIMULANT FUEL-COOLANT SYSTEMS WITHOUT RADIATION HEAT TRANSFER

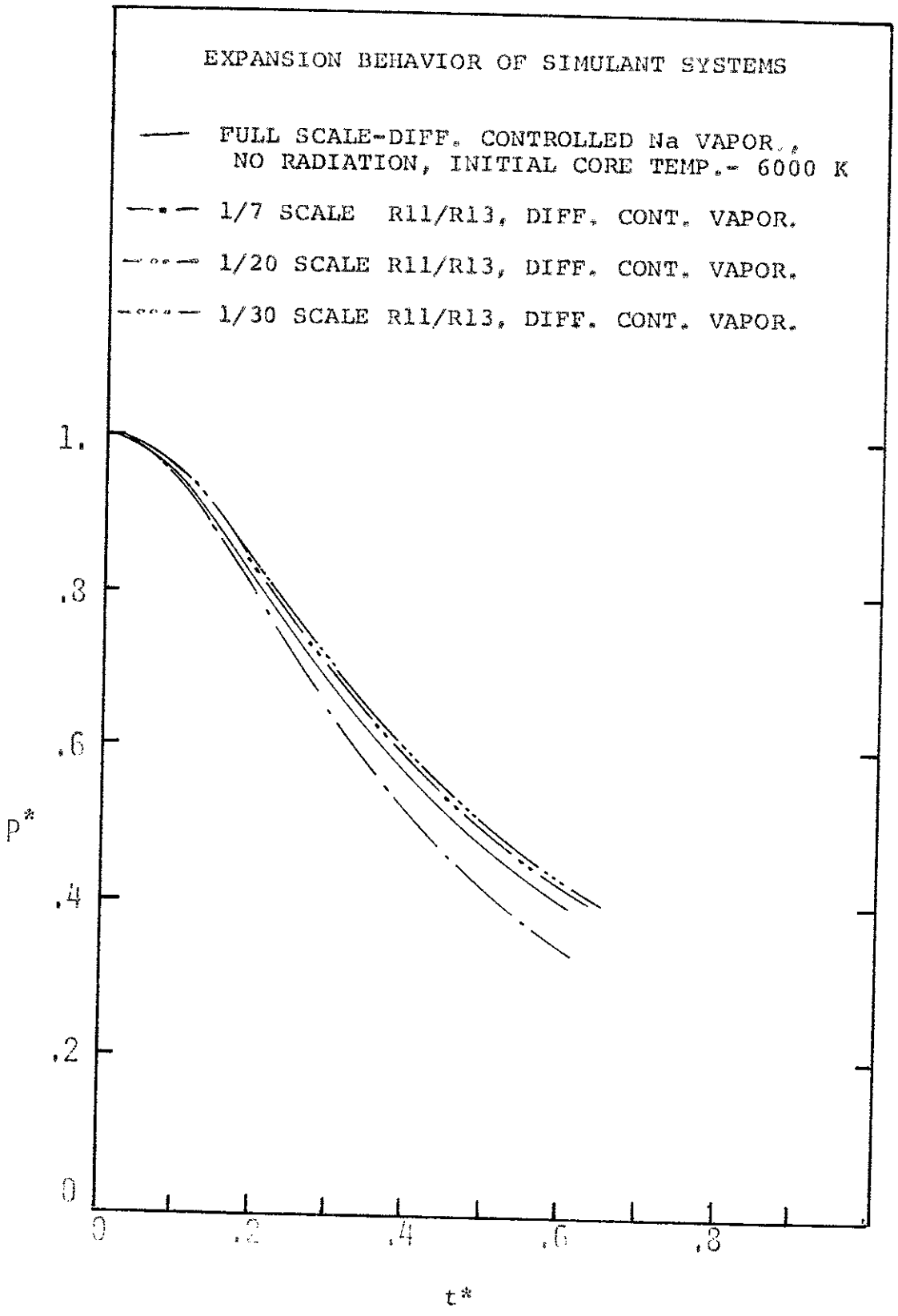

FIGURE 8.2 DIMENSIONLESS TRANSIENT PRESSURE BEHAVIOR FOR SIMULANT FUEL-COOLANT SYSTEMS WITHOUT RADIATION HEAT TRANSFER

PART II

MOLTEN FUEL AND COOLANT HEAT TRANSFER

9. GENERAL REVIEW OF LITERATURE CONCERNING MOLTEN FUEL-COOLANT INTERACTIONS IN EXPERIMENTS AND THEORY

9.1 Introduction

The possible consequences of a thermal interaction between hot molten fuel and a cold coolant can be dangerous and are of concern to many industries including the nuclear industry. This molten fuel-coolant interaction phenomenon (MFCI) involves the transfer of energy from the hot fuel to the coolant, and the rate of this heat transfer determines if the process is energetic and possibly destructive.

An idealized picture of the process is depicted in Figure 9.1. Molten fuel and coolant are brought into physical contact, perhaps due to one of a number of possible modes of contact; dropping, injection, shock tube acceleration. Each constituent has its own set of initial conditions (mass, temperature, size, velocity) and its properties which can affect the outcome of the interaction. The fuel and coolant become coarsely intermixed and although $T_H >> T_c$, the mechanism for this intermixing (e.g. coolant film boiling) could minimize any significant heat transfer from one constituent to another. The transient heat transfer process is now triggered by some random or external source somewhere in the mixture (e.g. pressure pulse). The possibility of damage due to this interaction occurs when the coolant is more volatile than the fuel, that is when the vapor pressure of the coolant at a given temperature is higher than that of the fuel at the same temperature. In this situation the triggering of the heat transfer interaction could vaporize some of the coolant, if the fuel is hot enough, at pressures greater than the ambient. The final stage of the interaction is when this heat transfer process propagates and fuel and coolant become more finely

intermixed and the pressure generated by the vaporization exerts its influence on the environment.

If the pressure generated is large in comparison to the ambient pressure and the characteristic time for the process is short in comparison to time for pressure relief ($\tau_{exp} << \frac{2D_c}{c_a}$), then the liquid masses could be accelerated against the structure and this energetic MFCI could cause disruptive mechanical energy effects.

If either the pressure generated is small or the characteristic time for its formation is long in comparison to the pressure relief time, then the coolant vaporization can occur without a large conversion of the thermal energy into disruptive mechanical energy and the MFCI would be incoherent. The initial conditions of the constituents and the geometry of the system will determine the consequences of the process, but up to the present time, the physical phenomena of each stage of this process are not well understood and possible theories are still in dispute. A brief review of the extensive amount of experimentation and analysis done on this topic is presented. First, the experimental experience concerning MFCI's is given to present the results of not only the nuclear industry but of other industries. Special emphasis is given to the large body of data for small scale simulant material experiments (specifically molten metal-water systems). It is for these series of experiments that a model is proposed in Chapter 10 that describes the self-triggering behavior of the interaction. Secondly, the contemporary theoretical concepts are described with particular emphasis on two theories which are being presently debated in the technical community. A more extensive review of these topics is given by Reid [6] and Board [7].

9.2 Experimental Studies

Before reviewing industrial MFCI experience some clarification of terms is necessary to aid in the classification of the experiments. The manner in which the fuel and coolant initially come into contact is governed by the accelerations or velocity at which each fluid approaches the other. Four general categories are:

(1) Shock tube: In this situation the fuel or coolant is accelerated into the other constituent due to a pressure difference across the mass of the fluid. This could be considered the most disruptive mode of contact since the constituents are brought together at high accelerations and velocities.

(2) Injection: The fuel or coolant is introduced into the other constituent through a pipe or opening whereby the one fluid appears as a turbulent jet entering the reservoir of the other fluid.

(3) Drop: The fuel or coolant is dropped into the other constituent and only gravitational acceleration affects the rate of contact.

(4) Static: The fuel and coolant may be coexistant in a system with little relative motion. This may be due to a drop into a shallow tank or disruption of a physical boundary where both fluids existed previously.

9.2.1 Non-Nuclear Industrial Experience, Experiments and Accidents

A summary of some of the industrial tests and accidents is given in Table 9.1. The foundry accidents [6] involving molten metals and water for large masses were mainly caused by the failure of the ingot cooling systems. The copper crucible which held the molten metal also contained outer water cooling coils which failed and caused the water to become intermixed with the metal. An energetic event occurred when some extraneous events caused a random pressure disturbance in the vicinity of the ingot and triggered the vapor explosion. The same phenomenon was noted for the matte industry where accidental pouring of the sulfide compounds onto water (even snow) caused this vapor explosion.

Experiments performed by Alcoa Aluminum attempted to get a qualitative understanding of the phenomenon [90]. Vapor explosions could be suppressed if the aluminum could be dropped from a large distance, broken into small drops, or solidified before reaching the bottom of the coolant tank. In addition, the explosion magnitude changed when the steel tank was lined with different chemicals (lime-more violent, oil-less violent), or if the chemicals were dissolved in the water. This evidence suggested to the investigators that the vapor explosion was triggered near the tank walls perhaps at the bottom. This explosion behavior is now controlled in the aluminum industry by the coating of an oil (Tarset) on the tank walls to reduce the explosion hazard.

The paper pulp industry also investigated these phenomena after large scale accidents occurred during industrial operation [91]. Small scale experiments [92] investigated the temperature thresholds for these interactions and determined an upper and lower fuel temperature threshold for constant coolant temperatures. These boundaries were qualitatively noted to change as the injection rate, water subcooling and fuel composition were altered. Nelson suggested that the mechanism for these explosions was that the superheat limit for the water coolant had been reached (homogeneous nucleation). This theory has been suggested by others and will be examined later.

9.2.2 A Summary of MFCI Accidents in the Nuclear Industry

There have been accidents and destructive tests involving the vapor explosion phenomenon in the nuclear research industry. A comprehensive review of these nuclear incidents is given by Thompson [93]. In 1952 the Canadian research reactor NRX experienced a melt down accident, and one of the conclusions of the follow up investigation was that the pressure

tube of the primary system failed due to a stem explosion when the water contacted the molten fuel. The SL-1, a navy research reactor in Washington state, experienced a melt down accident due to an operator manually removing a control rod and causing a transient prompt burst condition. The accident caused the aluminum clad fuel elements to melt in the water coolant, causing a steam vapor explosion, disrupting the reactor and killing the operator.

The Borax-I facility conducted an early destructive test and produced a very energetic interaction (~10,000 psia) when metallic fuel elements were melted in the water coolant. Also the Spert-1D test was a design transient overpower experiment where the aluminum clad fuel was melted in the water coolant. This experiment again produced an energetic vapor explosion when the aluminum clad fuel (uranium) melted in the presence of the water coolant.

9.2.3 In Pile Tests with Reactor Materials

A summary of more recent experiments concerning the MFCI phenomenon in the LMFBR is given in Table 9.2. Experiments which investigate the failure of the fuel rod in a reactor environment have been conducted over the past few years. The experiments at Argonne [94, 95, 96] were performed in the TREAT reactor and investigated fuel pin failure, movement of fuel and coolant masses, and possible MFCI behavior in single and seven pin fuel bundles (UO_2 - sodium) when subjected to overpower transients (TOP $\doteq$ 23 msec) and loss of flow (LOF) conditions. The LOF tests (L and R series) did not observe any MFCI phenomenon because at the time of fuel melting and failure, the sodium had boiled out of the fuel channels and no sodium reentry occurred. Transient overpower tests were conducted in a flowing sodium loop (E and H series) where the fuel failure resulted in pin failure (1 or 7 pin bundle) and the molten fuel being ejected into the liquid sodium. The experimental data indicated that large pressure spikes occurred during the interaction

($\lesssim$5.0 MPa) and they were mainly attributed to the fission gas pressure and fuel vapor pressure. The associated expansion work output of the vapor and fission gas was quite small compared to the thermal energy input to the fuel pin ($\lesssim$ .3%), and much smaller than the maximum 30% conversion ratio of Hicks and Menzies [4]. The conclusion drawn from these tests was that the MFCI's were incoherent and nonenergetic events. Subsequent TREAT tests in TOP conditions using a fuel pin in a stagnant sodium column (S-series) led to similar conclusions by ANL. However, in this set of experiments the experimental results were different from the past tests in that the magnitude of the pressure spikes were larger (2.5 - 20.0 MPa), and the delay time between the transient and these recorded pulses was long (.2 to 2.4 secs). This behavior has been interpreted by others [7] to be due to energetic MFCI's in localized areas of the test assembly. Their reasoning suggested that if localized MFCI's could occur in small scale tests, the actual reactor full scale geometry could also have an energetic MFCI which could be more coherent because of the larger masses involved. This conclusion is not unrealistic in the light of the pressure behavior although the ratio of the vapor and gas expansion work to the thermal energy input again remained at an extremely low value as in past E and H series tests ($\lesssim$ .3%). Thus although the tests were invaluable in examining fuel and coolant dynamics the possibility of an energetic MFCI in the LMFBR environment was not firmly excluded by the results.

Sandia Laboratories have conducted similar TOP tests in the ACPR reactor [97]. The main characteristic which differs in these series of tests is that the power pulse given to the test fuel pin is much larger than the TREAT tests over shorter amounts of time (~ 1.4 msec) which give very large and fast thermal energy deposition. This power profile creates

initial conditions at the time of fuel pin failure such that some of the fuel is in a two-phase state and not totally molten. Thus these tests are more characteristic of the phenomena in Part I of this investigation although observation of the MFCI behavior was initially one of the test objectives. The pressure spikes created by these tests were large (~60 MPa) and were attributed to the fuel vapor pressure (~50 - 80 MPa) not MFCI's, while the energy conversion ratio was again very small ($\lesssim$ .1%). However, when uranium carbide fuel (UC) not UO_2 was used in the fuel pin, the pressure pulses increased in magnitude and duration significantly, indicating an energetic MFCI. The interpretation of this behavior by Fauske [98] was that the spontaneous nucleation criterion for energetic MFCI's was satisfied for the UC fuel but not for the UO_2 fuel with sodium coolant, and thus the experimental results can be regarded as further proof of this theory.

9.2.4 Out of Pile Tests with Reactor Materials

Large scale tests out of pile using reactor materials have been conducted by Argonne [102] to investigate possible MFCI's and fuel freezing behavior when a molten slug of UO_2 (>5kg) is injected into a subassembly structure filled with sodium. The molten UO_2 was injected using a thermite chemical reaction ($U + M_o + O_2 \rightarrow UO_2 + M_o$ + gases + energy) into the structure with and without sodium present. No large pressure pulses or large energy conversion ratios were measured, rather in both cases the UO_2 simply began to freeze as it traveled through the cold sodium and structure. Dropping experiments using large masses of UO_2 (~50 kg) are now underway at Sandia Labs [99]; however, no results have been reported.

Small scale static experiments conducted at the Karlsruhe in Germany and at the JEF facility in France [6] using UO_2 in a stagnant sodium pool did not produce any energetic MFCI's. All the pressure pulses measurements were small ($\leq$ 5.MPa) with low energy conversion ratios. The same behavior was noted when UO_2 and stainless steel (~25 gm) was dropped into sodium by Armstrong [100]. However, small scale vapor explosions were produced after long dwell times (~100 msec) by injecting small amounts of sodium (~5 gm) into a container of molten UO_2 [101]. The explanation for this behavior covers a large spectrum of theories. For example, Fauske [133] concluded that this behavior is due to the sodium in droplet form heating up to its spontaneous nucleation temperature without significant vaporization, and then rapidly vaporizing at high pressures. Given this explanation, this phenomenon could not escalate into a large scale energetic MFCI because of the dwell time needed for the coolant drop to reach its explosive vaporization point. However, Board and Caldarola [7] have interpreted the same data for the sodium-UO_2 system as displaying behavior similar to a film boiling regime before the explosion. They assert that perhaps other hydrodynamic mechanisms are responsible for the energetic event and not a temperature threshold.

9.2.5 Simulant Material Systems - Large Scale Experiments

One experimental procedure that was developed [110] to investigate the thermal interaction behavior of the hot and cold pair, consists of impacting the fluids together in a shock tube arrangement. The cold water was held above the fuel in a long cylindrical column by a diaphragm and accelerated downward onto the fuel by a pressure difference across the coolant column. Wright [110] used different hot liquids (aluminum, silver) and the MFCI's were quite energetic (~40 MPa). The question though that can immediately be raised is whether these molten metals and water adequately

simulate the behavior of UO_2 and sodium or for that matter UO_2 and water. The answer to this was not clear at the time of these experiments because no plausible theory was being advanced that could be used as a basis for developing scaling laws or premises for simulant system choices. Probably the main reason for the choice of these simulant systems (molten metals - water) and the others to be described is that they consisted of materials which had lower melting points than UO_2, the ease of handling the materials in smaller laboratory scale was enhanced without the use of sodium and UO_2, and most important, coherent energetic MFCI's could be reliably obtained giving a large body of experimental data and behavior. The theoretical models described in the following section will give further direction as to what are the necessary characteristics of simulant systems. At this point it would be accurate to observe that the simulant systems used are useful in observing the variable dependencies of vapor explosions, which when determined tend to exclude the UO_2-sodium system from coherent energetic MFCI's.

Henry [109] performed a series of experiments (240) in shock tube geometries where the simulant materials, the initial temperatures and the initial driving pressures were varied. Henry reached two main conclusions from the results: (1) There is a temperature threshold to these interactions which corresponds to the spontaneous nucleation temperature ($T_I > T_{SN}$), above which the detect interaction pressures increase substantially above hydrodynamic levels, indicating energetic MFCI's; (2) These energetic interactions can be suppressed by increasing the ambient pressure in the shock tube; this behavior is similar to the results reported by Henry [105,107] in dropping experiments.

A test program is presently underway in the United Kingdom at Winfrith [103] where a number of simulant fuels (aluminum, steel, tin) at large scales (20 kg) are dropped into water. As in past tests in American industry, the interactions obtained can be quite energetic ($\gtrsim$20 MPa). One major difference in these experiments is that the behavior of the interaction is more closely observed for analysis by pressure measurements and hi speed photography. The general behavior of the interaction is that the fuel enters the water and falls to the bottom of the tank in a dispersion (coarse intermixing) with probable film boiling between the constituents. A random self-trigger at the base of the tank begins the rapid water vaporization and a high pressure front ("explosion front") propagates upward quite rapidly (~200 m/s) with rapid fuel-coolant mixing, expelling the tank contents. Board [104] has also conducted experiments using molten tin in water and has observed this propagation behavior. The trigger in Board's experiments was not left to the randomness of the interaction but triggered by an external pressure pulse. This qualitative MFCI description fits the view given in Figure 9.1 quite well, and in fact, the purpose of these tests at Winfrith seem to be directed at gaining information on the propagation phase of the interaction.

Large scale dropping experiments have been conducted at Argonne [105,107,108] and by Board [106] over the past few years using water or light oils as the fuel and freon refrigerants (R-12, R-22) as the coolant to study the behavior of vapor explosions with a variance in the initial temperatures. Armstrong's apparatus (Figure 9.2) is characteristic of the test geometries where the size of the system is of the same order of magnitude as the size of the fluid masses. A compendium of the resulting

interaction pressures from many experimenters is given in Figure 9.3 [108]. As the plot illustrates when the interface temperature between the fuel and coolant exceeds the spontaneous nucleation temperature (for perfect wetting this is the homogeneous nucleation temperature), the peak reaction pressure rises markedly indicating a temperature threshold for energetic MFCI's. Henry and Fauske [107] have used these observations in support of the spontaneous nucleation theory.

Henry [107] varied both the initial hot and the cold temperatures for the R-22 and mineral oil pair and again verified this temperature threshold for coherent energetic MFCI's (Figure 9.4). Board [106] has disputed this experimental evidence and has contended that this temperature threshold is only significant in that it allows a large mass of the cold and the hot liquid to come into a coarse mixture because this temperature (T_{SN}) denotes the stable film boiling limit for these liquid-liquid pairs. He maintains that the mechanism for the trigger and propagation of the explosion is not necessarily the same as that for coarse intermixing of the pair. His point is that there may be a mechanism that could permit this coarse intermixing below this film boiling threshold (e.g. premixing of fuel and coolant in LMFBR geometry) and thus the MFCI could occur below this limit. This line of reasoning was tested by Armstrong [108] by dropping R-22 into water by two means. The first consisted of simply pouring the R-22 into the water. The second method consisted of dropping into the water R-22 contained in a plastic sack, and the sack was then ruptured while in the water. The second method provided the coarse intermixing without the possible dependence on temperature. As Figure 9.5 indicates, the test results did not change at all from past results and this suggests that this temperature threshold is linked not only with the intermixing phase but with the trigger and propagation phase of the energetic MFCI.

9.2.6 Simulant Material Systems - Small Scale Experiments - Non-Metallic

Some small scale experiments using the injection mode of mixing have been performed at Argonne by Anderson [111] for the purpose of observing the MFCI trigger mechanism. This geometry of the water coolant being injected into the molten salt produced violent MFCI's (~10 MPa) with characteristically long dwell times as the water traveled through the salt in a film boiling regime. Again the coarse premixing preceded the randomly triggered event. The rapid water vaporization, pressure pulse, and expulsion began over a short time span (40 μsec) indicating the truly explosive character of the interaction.

Henry [107] performed a series of small scale experiments (Figure 9.6) where Freon droplets were placed on a hot oil surface. A drop capture model was proposed based on the spontaneous nucleation theory which predicted the hot fuel temperature ranges and droplet sizes when the falling droplets would wet the oil surface and quickly vaporize on the oil or slowly evaporate while in a film boiling mode. Figure 9.7 shows the good agreement between the model and the experiments. Henry incorporated this model into an energetics model for an energetic MFCI. This model will be reviewed later.

Experiments are being conducted at Sandia Labs by Nelson and Buxton [112,113] in regard to the MFCI problem in Light Water Reactors. They have used a system of molten oxides (iron and oxygen) and water which is quite similar to the reactor materials. The reported results have not been extensive as of yet but two major observations have been reported up to this present time: (1) The system does undergo energetic MFCI's only when the interaction is started by an external pressure pulse. This may indicate that film boiling which is the initial boiling regime between the constituents

is a thick film and does not collapse due to a random trigger but needs external assistance; (2) The interaction can be suppressed even with an initial pressure pulse by decreasing the oxygen content of the fuel material. This has been interpreted by the investigators to mean that the vaporization trigger for these interactions may be due to a dissolved gas release mechanism. With a decrease in the oxygen gas content, the latent gas pressure driving force for fragmentation and intermixing decreases thereby stopping the interaction.

9.2.7 Simulant Material Systems - Small Scale Experiments - Molten Metals

The overwhelming majority of small scale experimentation for MFCI's has been done using molten metals as the fuel and water as the coolant.

For the experiments to be reviewed, the drop mode of contact was used to insert the fuel into the coolant and small fuel masses ($m < 25$ gm) were utilized. The fuel-coolant interactions (vapor explosions) to be described consisted of small pressure pulses (3 bar at the pressure transducer) and varying degrees of fuel fragmentation. The various research groups have deduced the severity of the interaction in different ways:

(1) Pressure pulses measured by transducer at different distances from the drop path [119,120, 122-124].

(2) Hot fuel fragmentation determined: by qualitative visual inspection [115-117, 119,120, 122-124]; by ratio of fragmented surface area to original surface area of the drop; by photographic [118] or chemical measurements [126]; by the ratio of the mass of fragmented fuel to the original mass [125].

These various measurements lead to slightly different conclusions regarding the conditions for the threshold of fuel-coolant interactions, particularly for the threshold at the lower hot fuel temperatures.

Experimental data has been accumulated for molten metals dropped into water over a wide range of coolant and fuel temperatures [114-126]. Let us view the behavior of the experimental results in light of the independent variables; initial coolant temperature, initial fuel temperature, size of the fuel mass, drop height, shape of the fuel mass and the type of trigger which initiated the interaction. Table 9.3 gives a brief summary of the experiments and the range of the independent variables utilized.

Swift and Pavlik [115] found that tin, bismuth and lead (at 800°C) would fragment in water near 0°C but remained intact at a water temperature of 60°C, whereas, zinc, gold, silver and aluminum did not fragment at all. Ivins [114] observed an enhancement of the fuel fragmentation with an increase of the Weber number (We>60) above the critical value (We = 10-20). This effect gave an indication of the influence of a hydrodynamic mode of fragmentation. To illustrate this Ivins dropped mercury into water under isothermal conditions and produced similar results.

Fragmentation can also be due to thermal effects. As the initial temperature of the coolant (T_{c_i}) is increased at a fixed initial fuel temperature (T_{H_i}), the amount of fragmentation of the fuel drop increases to a maximum and then falls to zero as Figure 9.8 illustrates. The experiments of Dullforce [125] quantified the fragmentation by the "percentage disintegration," PD, defined as the mass of comminuted fuel to the original mass. Similar behavior is noted for the data of Cho [118] (Figure 9.9) although the peak fragmentation occurred at much lower coolant temperatures (4-20°C) with the cutoff for fragmentation also occurring sooner (70°C). Cho used a photographic method to measure the projected area of the fragmented drop and formed a ratio of this area to the original projected area. This may

account for some of the difference in the results but the general behavior is similar. As the initial temperature of the fuel is increased at a fixed T_{c_i}, the fragmentation of the fuel drop again reaches a maximum and then decreases markedly. This is demonstrated for the tin/water system in Figure 9.9 for Cho's data, Figure 9.10 for Dullforce's data, on Figure 9.11 for MIT data, and on Figure 9.12 for Frohlich's lead/water data [126]. MIT [122,124] recorded the violence of the interaction by visual fragmentation inspection and recording the transient pressure in the vicinity of the interaction. As Figure 9.13 illustrates, the transient peak pressure of the interaction has a behavior similar to fuel fragmentation. The point through where the detected pressure becomes small is at a slightly lower fuel temperature than the fragmentation cutoff. In addition, it should be noted that as the size of fuel droplet increases, the detected pressure increases. This trend is more pronounced than Figure 9.13 depicts, because the transducer in Arakari's experiments [119] at UCLA was farther from the fuel droplet than in MIT experiments. Because the pressure intensity is known to decrease in strength by $\frac{1}{r}$ [128], the comparative pressures at the same distance from the fuel would show a larger difference.

Another dependent variable to consider is the dwell time (τ_D) to the interaction. Initially when the fuel is dropped into the water coolant, nothing occurs. There is a characteristic time (τ_D) before the interaction begins. This dwell time is accompanied by a small amplitude high frequency pressure oscillation as Bjornard at MIT observed [122]. When the interaction occurs, the frequency of recorded pressure peaks slows to a few Hertz and the peak pressure depicted on Figure 9.13 is recorded. As the interaction continues, a cyclic nature is noted until the fuel droplet appears fragmented and the detected pressure falls to zero. As Figure 9.14 illustrates,

as the initial fuel temperature increases for a fixed T_{c_i}, the dwell time increases. Similar behavior is noted for a fixed initial fuel temperature (T_{H_i}). The effect of the size of the mass on this dependent variable is difficult to determine. For Bjorkquist's data at MIT [123] using droplet masses of .8 gm and 6.2 gm, the dwell times at a fixed T_{H_i} and T_{c_i} showed no change within the scatter of the data. The overall behavior for τ_D can be linked to the fuel droplet fragmentation behavior to observe that as fragmentation becomes small (T_{H_i} increasing or T_{c_i} increasing) τ_D becomes large. Thus there is a characteristic upper boundary for these self-triggered interactions.

This notion of a self-triggered fragmentation zone was identified by Dullforce [125] for the tin/water system as Figure 9.15 illustrates. The lower boundary ($T_{c_i} = 0^{\circ}C$) represents the freezing point of water and no thermal fragmentation is observed below this limit. The vertical left hand boundary for fragmentation of tin/water varies, depending on the experimental investigator, from 300-375°C. Dullforce [125] attributes this left boundary to the point where the contact interface temperature ($T_i = 250^{\circ}C$) goes above the melting temperature of the fuel ($T_{mel} = 232^{\circ}C$). As Figure 9.10 illustrates though the extent of fragmentation becomes significant above $T_{H_i} = 400^{\circ}C$. This corresponds to a condition where the contact interface temperature ($T_I = 330^{\circ}C$) is above the homogeneous nucleation temperature of water ($T_{HN} = 305^{\circ}C$). Thus there is a region of small fragmentation when $T_{mel} < T_I < T_{HN}$ and much greater fragmentation when $T_I > T_{HN}$. The data of Cho at Argonne [118] (Figure 9.9) and Bjorkquist at MIT [11] (Figure 9.11) seem to support this general trend.

As the fuel (or coolant) temperature continues to rise, the degree of fragmentation of the fuel droplet goes through a maximum for self-

triggered interactions and then decreases to an insignificant amount (Figure 9.8). There is an upper diagonal cutoff for self-triggered interactions as Figure 9.15 illustrates. What is significant to note here is that for different investigators with different independent variables such as size of fuel droplet and drop height, the boundary for self-triggered interactions changes markedly. Dullforce [125] has theorized that this diagonal boundary is a transition point from thin film boiling behavior to thick film boiling. This transition inhibits the destabilization of the film boiling regime and thereby precludes a self-triggered interaction.

Board [121] investigated the relationship of externally triggered interactions to the body of data in the self-triggered mode. He demonstrated that at a fuel and coolant temperature combination where no self-triggered event occurred, an applied external pressure pulse triggered an interaction. This was accomplished by dropping molten tin into water (2-5 cm above the water) and letting it come to rest on a crucible ($T_{H_i} = 800^{o}C$) $T_{c_i} = 80^{o}C$). A pressure pulse was applied in two ways. First, the ambient pressure of the experiment was increased causing the film boiling mode to be destabilized and an interaction occurred. Secondly, an external rod was used to generate a pressure pulse by rapping the side of the test chamber. This again resulted in an interaction. Board concluded that fragmentation is triggered by a mechanism that leads to unstable film boiling between the fuel and coolant. This experiment graphically illustrates that there can be more than one way to trigger a vapor explosion. The model to be described in the next chapter only applies to the self-triggered interaction in the drop mode of contact.

9.3 Theoretical Studies

The analysis employed to describe the molten fuel-coolant interaction have evolved over time from parametric models, to various models which have proposed MFCI mechanisms to predict the various experimental parameters (peak pressure, fragmentation, expansion work) which measure the strength of the interaction. A good review is given by Reid and Caldarola [6,7] and only a brief review is presented here for the two major models that are advanced for energetic MFCI's (Table 9.4).

The most important point to make when looking at these two models is that each one was developed with a different purpose in mind and, therefore, are only applicable to certain parts of the MFCI phenomenon. The spontaneous nucleation theory originally proposed by Fauske [129,132-134] and later expanded by Henry and Bankoff [130,131,135] has mainly addressed the necessary (but not sufficient) requirements for coarse intermixing and triggering of an energetic MFCI. This theory is then applicable to both large and small scale systems and all material combinations because these phases of the interaction exist for all scales. However, the theory does not present a comprehensive model for the observed suppression of vapor explosions and fragmentation seen in the small scale simulant material experiments. This, in fact, is where the model proposed in Chapter 10 fits into the overall theory of spontaneous nucleation and vapor explosions. In addition, this model has not addressed the phenomenon of the propagation of the MFCI and the possible role of spontaneous nucleation. The detonation wave model proposed originally by Board [139] and now being expanded by Williams [136], Bankoff [137], and Theofanous [138] has exclusively dealt with the dynamic characteristics of the propagation phase of a large energetic MFCI. This theory is then applicable only to large scale systems where

propagation is really relevant and only where the initial phases of the interaction have occurred. Thus this model will be briefly described here but it has no relevance to the small scale experiments modeled in Chapter 10.

9.3.1 Spontaneous Nucleation Theory

One of the possible mechanisms for vapor bubble nucleation in a liquid is homogeneous nucleation. A vapor bubble can be nucleated in the bulk of the liquid when a vapor nuclei greater or equal to the critical size (r_{crit})

$$P_v - P_l = \frac{2\sigma}{r_{crit}} \tag{9.1}$$

is formed due to molecular density fluctuations in the liquid. Now this process is possible at all times in the liquid but the probability of such a nucleation mechanism becomes important when the bulk temperature of the fluid is heated above T_{sat} to a temperature (T_{HN}) where the predicted rate of nucleation by this mechanism is large. The rate of bubble nucleation is given from kinetic theory as [134]

$$J = A(T)N \exp\left(-\frac{W}{k_B T}\right) \left[\frac{1}{cc\ sec}\right] \tag{9.2}$$

where A(T) is the collision frequency of the liquid molecules and is a function temperature with a value nearly constant at 10^{12} s^{-1}. N is the number density of the liquid moelcules ($N \sim 10^{22}$ cm^{-3}), and W is the work needed to form a spherical vapor bubble of radium, T_{crit}, given by

$$W = 4\pi r_{crit}\sigma + \frac{4}{3}\pi r_{crit}^3 \left[P_l - P_g(T)\right] \tag{9.3}$$

where using Equation 9.1 for T_{crit}, the work is given as

$$W = \frac{16\pi\sigma^3}{3(P_g(T)-P_l)^2} \tag{9.4}$$

The value of J will change almost ten orders of magnitude when the homogeneous nucleation temperature is reached (T_{HN}). For example, for water $T_{HN} = 305^{o}C$ compared to $T_{sat} = 100^{o}C$. Now if this nucleation takes place at an interface (liquid-liquid in this case), the work to form the bubble is decreased as the wettability of the surfaces decreases. Therefore, as W goes down, smaller temperatures are needed to keep the nucleation rate large. The spontaneous nucleation temperature (T_{SN}) accounts for this wetting effect. The lower limit for this temperature (T_{SN}) is the saturation point (T_{sat}); thus for a perfect wetting fluid pair (contact angle = 0), $T_{SN} = T_{HN}$, and for a non-wetting pair (contact angle = 180^{o}), $T_{SN} = T_{sat}$. For most fluids the steady state contact angle is between 0 and 90^{o}, thus Fauske [134] has pointed out that $T_{SN} \simeq T_{HN}$.

The original model proposed by Fauske was simply that a necessary criterion for an energetic MFCI is that upon liquid-liquid contact, the instantaneous interface temperature

$$T_I = \frac{T_H}{1+\beta} + \frac{\beta T_c}{1+\beta}$$

where

$$\beta = \sqrt{\frac{K\rho C_c}{K\rho C_H}} \tag{9.5}$$

must be greater than T_{SN}. Fauske has more recently suggested [98] that the spontaneous nucleation mechanism may be part of the propagation mechanism but this contention has not been analytically modeled.

Henry [129] proposed a drop capture model using the concept of spontaneous nucleation to model the Freon-Oil results he had obtained [105]. The model

takes the view that the coarse intermixing of the fuel and coolant is facilitated by film boiling because $T_I > T_{SN}$ and during this time the coolant continually touches the fuel liquid surface in a droplet form [130]. The coolant and fuel are then fragmented and mixed due to the explosive boiling phenomenon of spontaneous nucleation until the droplets are small enough to wet the fuel surface and then can coherently vaporize. The observed experimental pressure of the interactions is predicted to be the saturation pressure of the instantaneous interface temperature above T_{SN}. The model as this qualitative description indicates deals with the lower threshold ($T_I \geq T_{SN}$) for random self-triggered vapor explosions. Henry further theorizes that an upper limit exists for self-triggered interactions, $T_I \leq T_{crit}$, where T_{crit} is the critical temperature of the coolant. The physical reason for this upper limit is that the random liquid-liquid touching cannot exist above T_{crit}, thus no self-trigger will exist.

Bankoff [131] has proposed a model similar to Henry's in its result but with a slightly different physical view. The film boiling regime is again seen as the mechanism for coarse intermixing where the regime is stable for $T_I > T_{SN}$. Also the liquid-liquid contacts that Henry proposes is assumed in this model [130]. The difference lies in the fact that Bankoff views each "splash" contact between the liquids as a possibility for this vaporization event to escalate into an explosive rapid vaporization rather than the view of Henry's of coolant and fuel fragmentation down to a critical size then the explosive interaction. The model then views the self-triggered event as a continually escalating process with the observed experimental pressure to be predicted by the local saturation pressure statistically weighted by the contact frequency.

Both models it should be emphasized try to model the observed pressure pulses and account for the lower temperature threshold $T_I > T_{SN}$. The model proposed in Chapter 10 looks more closely at the upper threshold for self-triggered interactions that Henry has suggested $T_I \leq T_{crit}$ and the experimental evidence for the upper fragmentation boundary for molten metal/water systems.

9.3.2 Detonation Wave Model

The propagation phase of the energetic MFCI is the focus of this theory by Board [139]. The coarse mixture and sufficiently energetic trigger are assumed. Originally, these assumptions placed the model out of the realm of reality for the LMFBR because the necessary trigger strength was enormous (e.g. a required pressure pulse or shock wave: tin - water ~ 100 MPa, UO_2 - Na ~ 1500 MPa). The necessity for such large triggers was based on the physical view that a traveling shock through a coarse fuel-coolant mixture would be maintained by hydrodynamic fragmentation of the fuel and coolant behind the shock to small sizes, allowing a large amount of heat transfer to the coolant. The coolant would then vaporize without the need of spontaneous nucleation and sustain the shock wave intensity. Board assumed values necessary for hydrodynamic fragmentation due to Taylor and Helmholtz instabilities from a gas liquid system which gave large pressure pulse trigger values. Theofanous [138] has since shown that these values are high by at least an order of magnitude, making the assumed trigger more realistic. Additionally, Theofanous and others [137] have suggested that the hydrodynamic fragmentation may not govern the rate of propagation of the energetic high pressure front. Fauske [98] has suggested that the necessary criteria for large scale propagation may be the spontaneous nucleation criteria.

TABLE 9.1

MFCI ACCIDENT/EXPERIMENTAL SUMMARY

INDUSTRIAL OVERVIEW

INDUSTRY	FUEL-COOLANT MATERIAL	MODE OF CONTACT	SCALE	REMARKS
FOUNDRY-CASTING INDUSTRY [6]	STEELS WATER TITANIUM ZIRCONIUM TUNGSTEN	STATIC-DROP	LARGE (>50 kg)	FAILURE OF COPPER CRUCIBLE JACKET AROUND MOLTEN INGOT, WATER COOLED; EXTERNAL TRIGGER NECESSARY FOR ENERGETIC MFCI
MATTE PREPARATION INDUSTRY [6]	COPPER WATER COBALT SULFIDES	STATIC-DROP	LARGE	ACCIDENTAL DROP OF MATTE INTO WATER POOL
ALUMINUM CAST INDUSTRY [90]	ALUMINUM WATER	STATIC-DROP	LARGE SMALL (<1 kg)	EXPERIMENTS MAINLY DONE BY ALCOA INDICATE THERMAL AS WELL AS POSSIBLY CHEMICAL INTERACTION OCCURRED AT CONTAINER BOTTOM; SURFACE OR STATIC TRIGGER
	MOLTEN SALT WATER	DROP/INJ.	SMALL	EXPLOSIONS OCCURRED IN BULK OF WATER; NO LINE R CHANGE HELPED, EXPLOSIONS HAD LONG DWELL TIME AND SHORT RISE TIMES;
PAPER PULP INDUSTRY [91, 92]	SMELT WATER	STATIC DROP/INJ.	LARGE SMALL	WATER COOLING JACKET FAILURE EXPERIMENTAL DROP IN WATER NOTED AN UPPER AND LOWER TEMPERATURE THRESHOLD; FUNCTION OF INJECTION RATE, COMPOSITION, & WATER TEMP.
NUCLEAR INDUSTRY [93]	U — WATER ALUMINUM	STATIC DROP	LARGE	SL-1, SPERT, BORAX ALL TOPS & MELTDOWNS IN WATER

TABLE 9.2

MFCI EXPERIMENTAL SUMMARY
NUCLEAR INDUSTRY

		STATIC - DROPPING	INJECTION	SHOCK
REACTOR MATERIAL	IN PILE (IN REACTOR EXPERIMENT)	• TREAT TEST - ANL [94,95,96] - LOF - L&R SERIES - TOP - E&H SERIES - FLOWING S SERIES - STAGNANT • ACPR TESTS - SANDIA [97] ALL UO_2 MFCI's - NONENERGETIC		
	OUT OF PILE LARGE SCALE (m_f > 1 kg)	• SANDIA EXPER. ONGOING [99] m_f > 25 kg INTEGRAL TEST & MEASUREMENTS	• ANL - [102] THERMITE INJECTION UO_2 INTO Na, NO^2 EXPLOSIONS	
	SMALL SCALE (m_f < 1 kg)	• KARLSRUHE - TOP SIMULATION [7] - 1 & 7 PIN BUNDLE ≤ 50 g • JEF - TOP SIMULATION [7] - SINGLE PIN ~ 7.2 gm ALL MFCI's: INCOHERENT - NON-ENERGETIC	• ANL - DROP & INJ. EXPER. SS & UO_2 into Na [100] (25gm & 300g) Na into UO_2 [101] (5gm & 100gm)	
SIMULANT MATERIAL	LARGE SCALE (m_f > 1 kg)	• FREON - OIL/WATER [105-108] - DEFINITE TEMPERATURE THRESHOLD FOR ENERGETIC MFCI's - SPONTANEOUS NUCLEATION THEORY • ALUMINUM - WATER [103] - COHERENT MFCI - TRIGGERED AT BASE • STEEL & TIN - WATER [103] - SIMILAR TO Al-H_2O RANDOM TRIGGER • TIN - WATER [104] - PRESSURE TRIGGER GIVES ENERGETIC MFCI		• WRIGHT [110] - LARGE PRESSURE PULSES 200 BARS - COHERENT MFCI's - HIGH CONV. RATIO 10%
	SMALL SCALE (m_f < 1 kg)	• LIGHT WATER EXPERIMENT - SANDIA NELSON & BUXTON [112,113] CORIUM, Fe - WATER PRESSURE TRIGGER GIVES ENERGETIC MFCI • FREON - H_2O [107] - SHOW SMALL SCALE FILM BOILING BEHAVIOR • MOLTEN METAL - H_2O [114-128] - TEMPERATURE THRESHOLD SHOWN	• ANL - ANDERSON [111] - MOLTEN SALT & WATER - ENERGETIC MFCI - LONG DWELL TIMES - RAPID MIXING ~ 200 μsec	• ANL - HENRY [109] - MANY MAT'L COMBINATIONS - ENERGETIC MFCI's WHEN $T_I > T_{HN}$

TABLE 9.3

SMALL SCALE MFCI PARAMETERS FOR MOLTEN METAL-WATER EXPERIMENTS

SIMULANT SYSTEM	N	M_D (GM)	D_D (CM)	H_D (CM)	WE	RE	T_{CI} (°C)	T_{HI} (°C)	COVER GAS
TIN/WATER									
CHO(6)	27	.14-.5	.35-.52	5	6.5-10	288	4-70	230-700	AIR
CHO(6)	31	.14-.5	.35-.52	5- 300	6.5-550	288-2250	22	230-900	AIR
WITTE(4)	10	2.1-5.6	.85-1.2	10	33-46	904	28-42	335-700	AIR
DULLFORCE	300	12	1.5	3	17.5	736	0-80	300-1000	N_2
BJORK.(11)	65	.8	.6	6.8	16	450	20-23	300-1100	AIR
BJORK.(11)	48	6.2	1.2	6.8	32	900	20-23	300-1100	AIR
SHIRAL.(12)	18	2	.82	2.54	8	370	22	400-650	N_2
ARAKERI(7)	48 12	25	1.9	11.25	25	1830	10-70 STRATIFIED	300-800	AIR
YASIN (8)	8	25	1.9	7	25	1438	STRATIFIED	480-735	AIR
BISMUTH/WAT.									
CHO(6)	24	.09-.5	.25-.46	5	6.7-13	228	4-50	300-800	AIR
WITTE(4)	7	.8-1.6	.54-1.1	10	30-63	1290	23-34	450-740	AIR
BJORK.(11)	27	9.7	1.2	6.8	64	891	20-23	300-700	AIR
YASIN(8)	7	41	1.9	2.5	19	904	18-50 STRATIFIED	370-790	AIR
LEAD/WATER									
CHO(6)	7	.13-.5	.29-.45	5	6.6-11	253	22	350-700	AIR
WITTE(4)	4	2-9	.72-1.2	10	35-53	904	26-43	425-590	AIR
FROHLICH(14	39	.67	.35	1	8	107	0-40	300-750	AIR
SWIFT PAVKIK(3)	VARIOUS METALS		.83	71	290	2000	0, 60	800	

TABLE 9.4

MAJOR CONTEMPORARY
THEORIES FOR
COHERENT ENERGETIC MFCI's

SPONTANEOUS NUCLEATION MODEL [129-135]

- Physically, it is known $T_{sat} < T_{SN} < T_{HN}$
  where T_{SN} = f(wetting angle; $T_{SN} = T_{sat}$ @ 180^{o}; $T_{SN} = T_{HN}$ @ 0^{o})
  0 to 90^{o} $T_{SN} \simeq T_{HN}$
- Necessary not sufficient criterion for energetic MFCI that $T_I \geq T_{SN} \simeq T_{HN}$:
- This threshold temperature is:
  - the coarse interviewing mechanism by film boiling with $T_{HN} \simeq T_{min}$ film
  - not necessarily the trigger mechanism
  - involved in the propagation phase of the event
- HENRY - DROP CAPTURE MODEL [129,135]
  - coolant - fuel fragmentation and mixing coincident with film boiling to allow interpenetration
  - for $T_I > T_{HN}$ the superheat limit is reached for small drops that wet the fuel surface (Figure 9.7) with a coherent explosion
- BANKOFF - SPLASH THEORY [130-131]
  - random liquid-liquid contacts give local vaporization and only can escalate when $T_I > T_{HN}$.

DETONATION WAVE MODEL [136-139]

- The initial conditions for coarse intermixing and a sufficiently energetic trigger are assumed to exist and the propagation phase is modeled.
- The propagation is viewed as a traveling shock wave where its disruptive strength is maintained by the rapid fragmentation of the fuel and heat transfer behind the shock front
- Rapid fragmentation and mixing could be caused by
  - purely hydrodynamic forces [136-139]
  - vapor collapse
  - rapid vaporization due to spontaneous nucleation

FIGURE 9.1

CONCEPTUAL VIEW OF MOLTEN FUEL-COOLANT INTERACTIONS

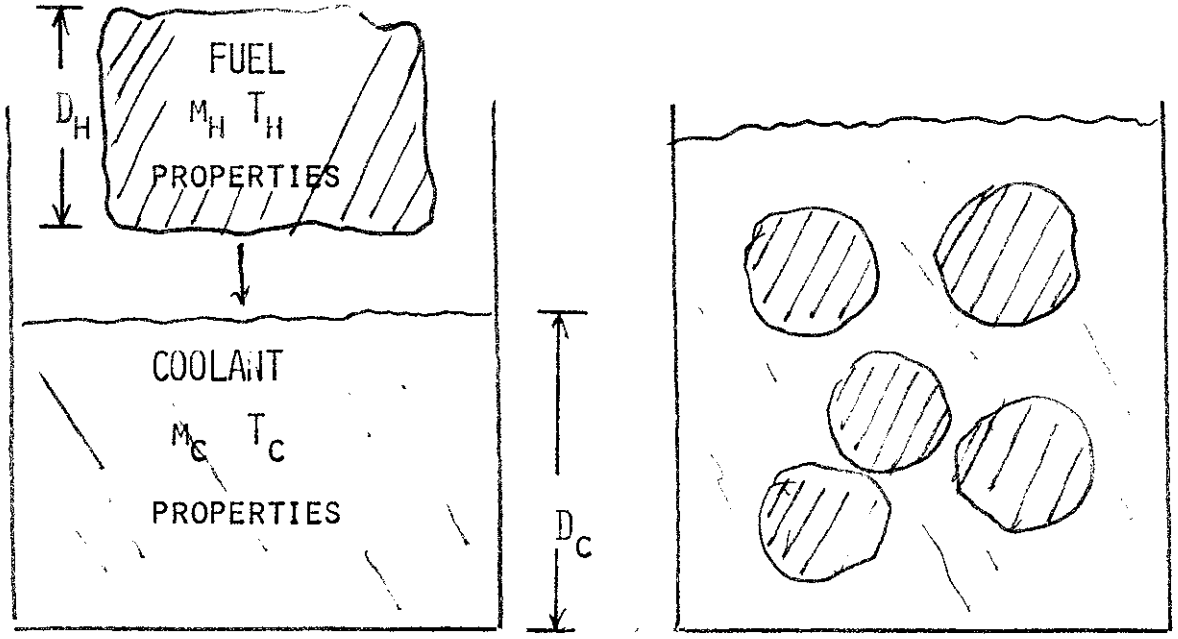

FUEL AND COOLANT CONTACT

(t=0)

COARSE INTERMIXING

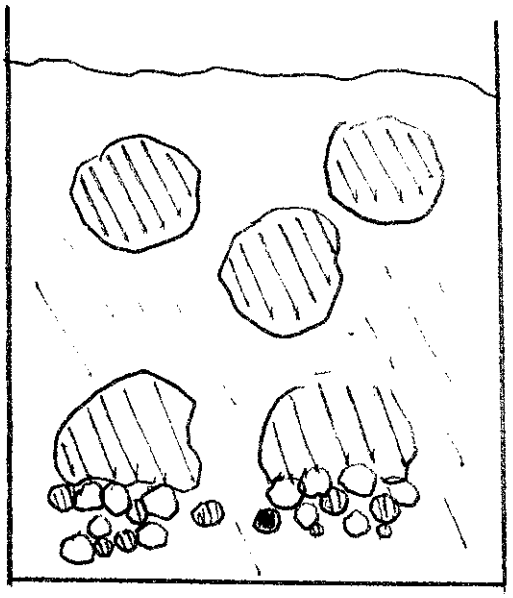

TRIGGER

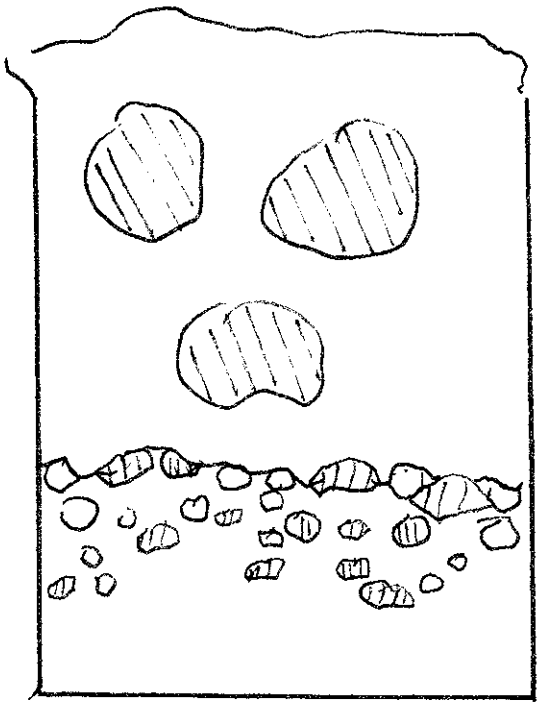

PROPAGATION

($t=\tau_{exp}$)

FIGURE 9.2 ARMSTRONG's EXPERIMENTAL APPARATUS FOR R22/H_2O TESTS

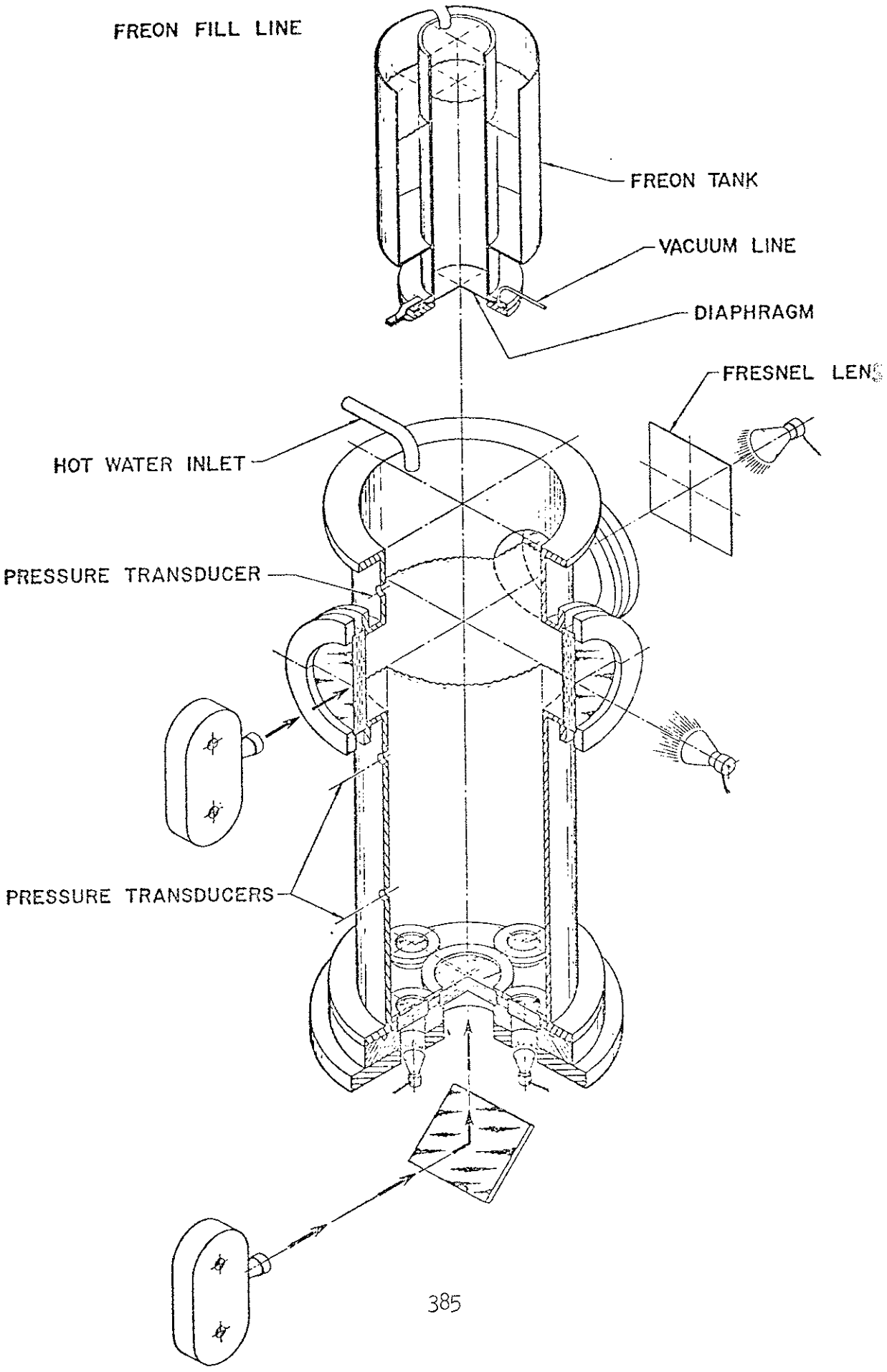

FIGURE 9.3 COMPENDIUM OF R22/WATER DATA ON PEAK INTERACTION PRESSURE

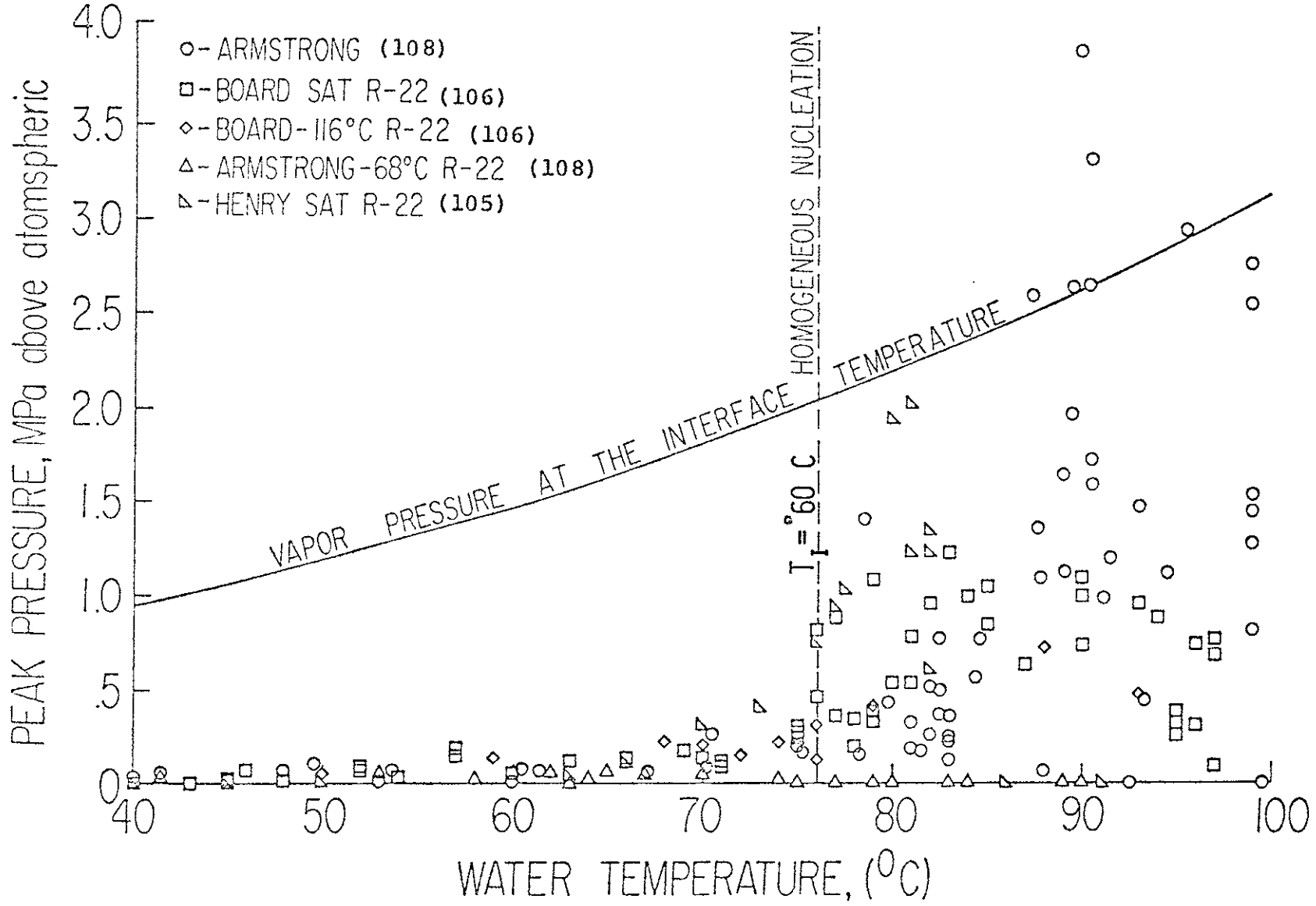

FIGURE 9.4 HENRY'S EXPERIMENTAL DATA FOR R22/OIL INTERACTIONS INDICATING A LOWER TEMPERATURE THRESHOLD

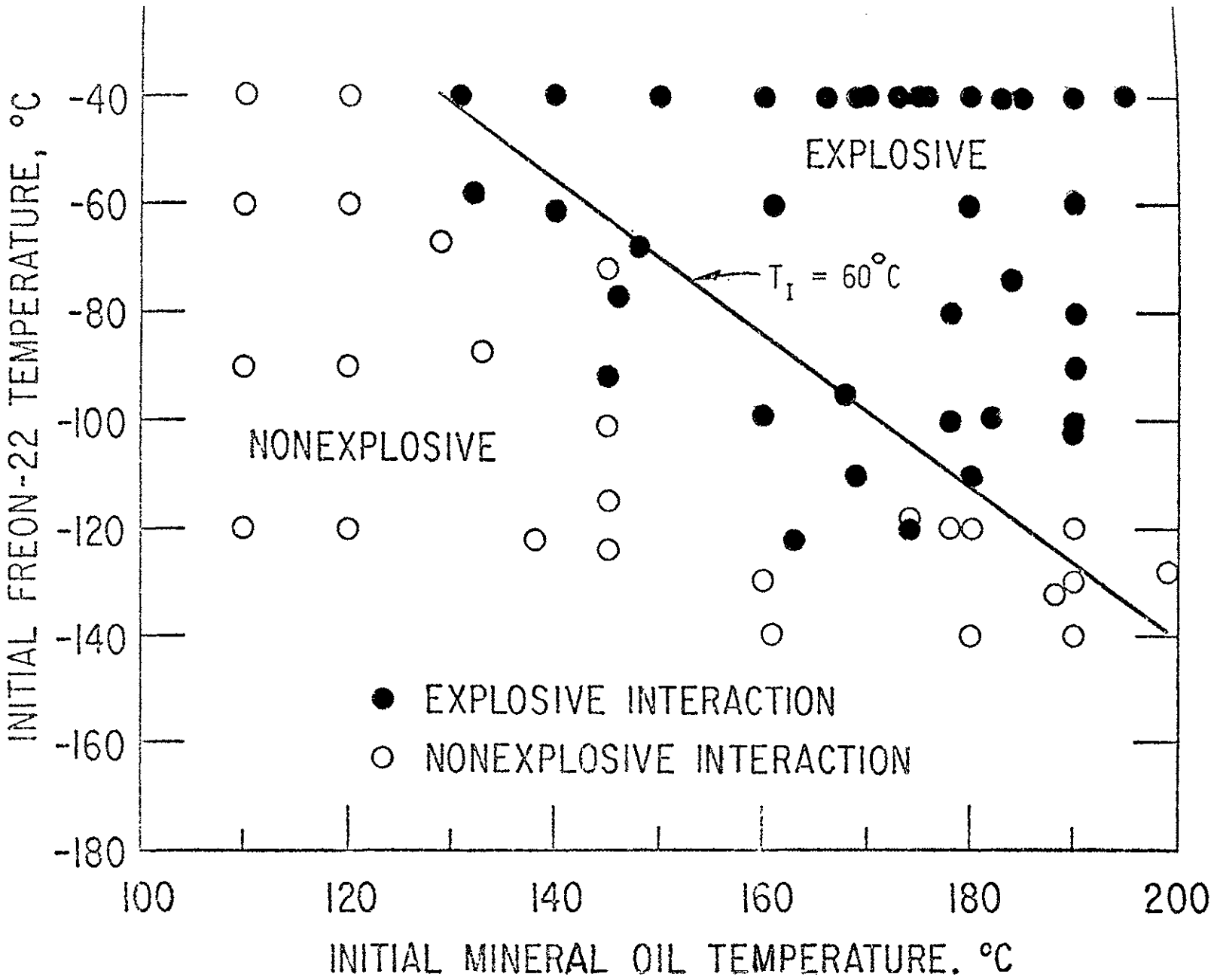

FIGURE 9.5 ARMSTRONG'S RESULTS FOR A CONSTRAINED INTERACTION

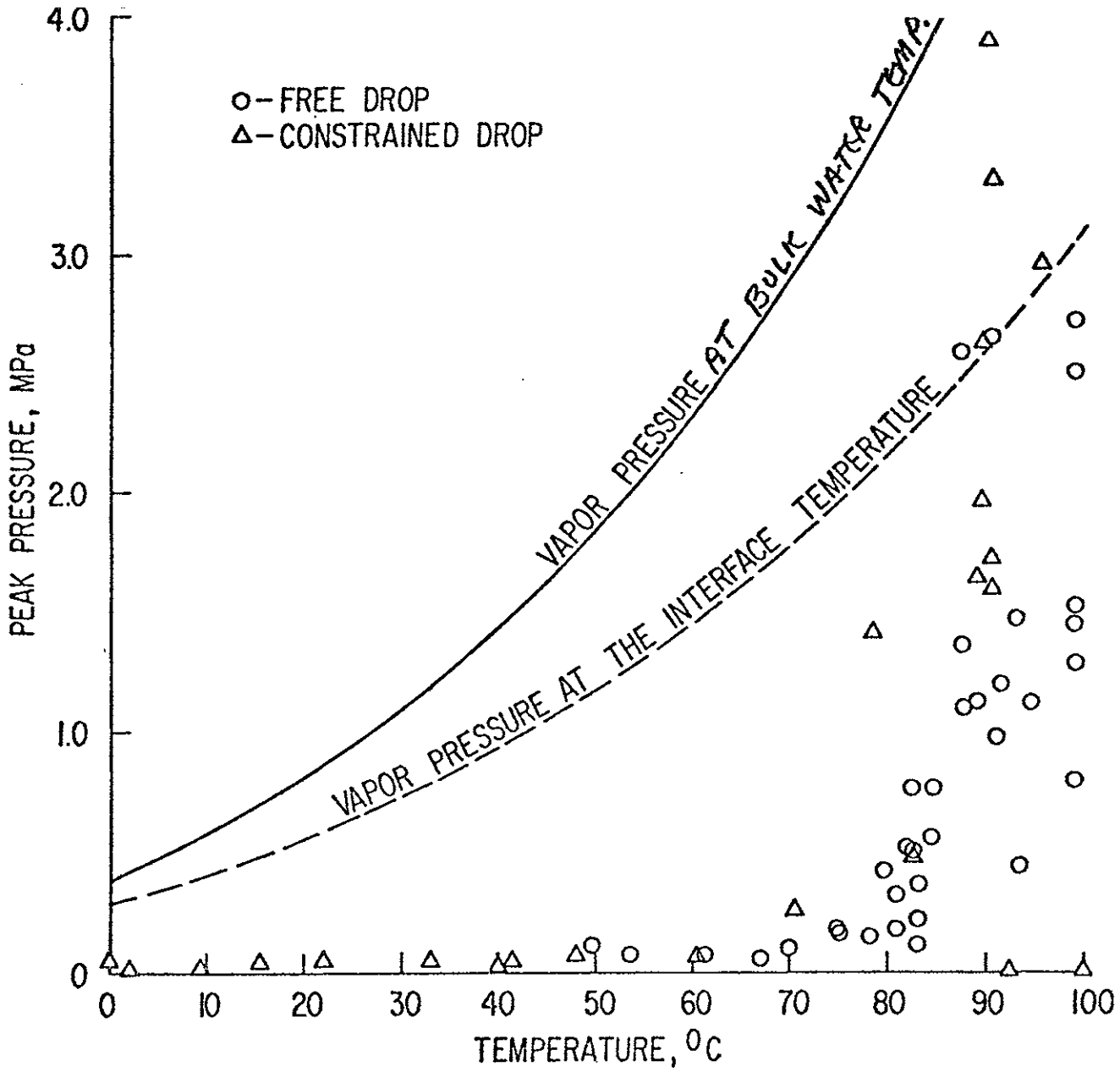

FIGURE 9.6 EXPERIMENTAL APPARATUS FOR SMALL SCALE R22 DROP TESTS

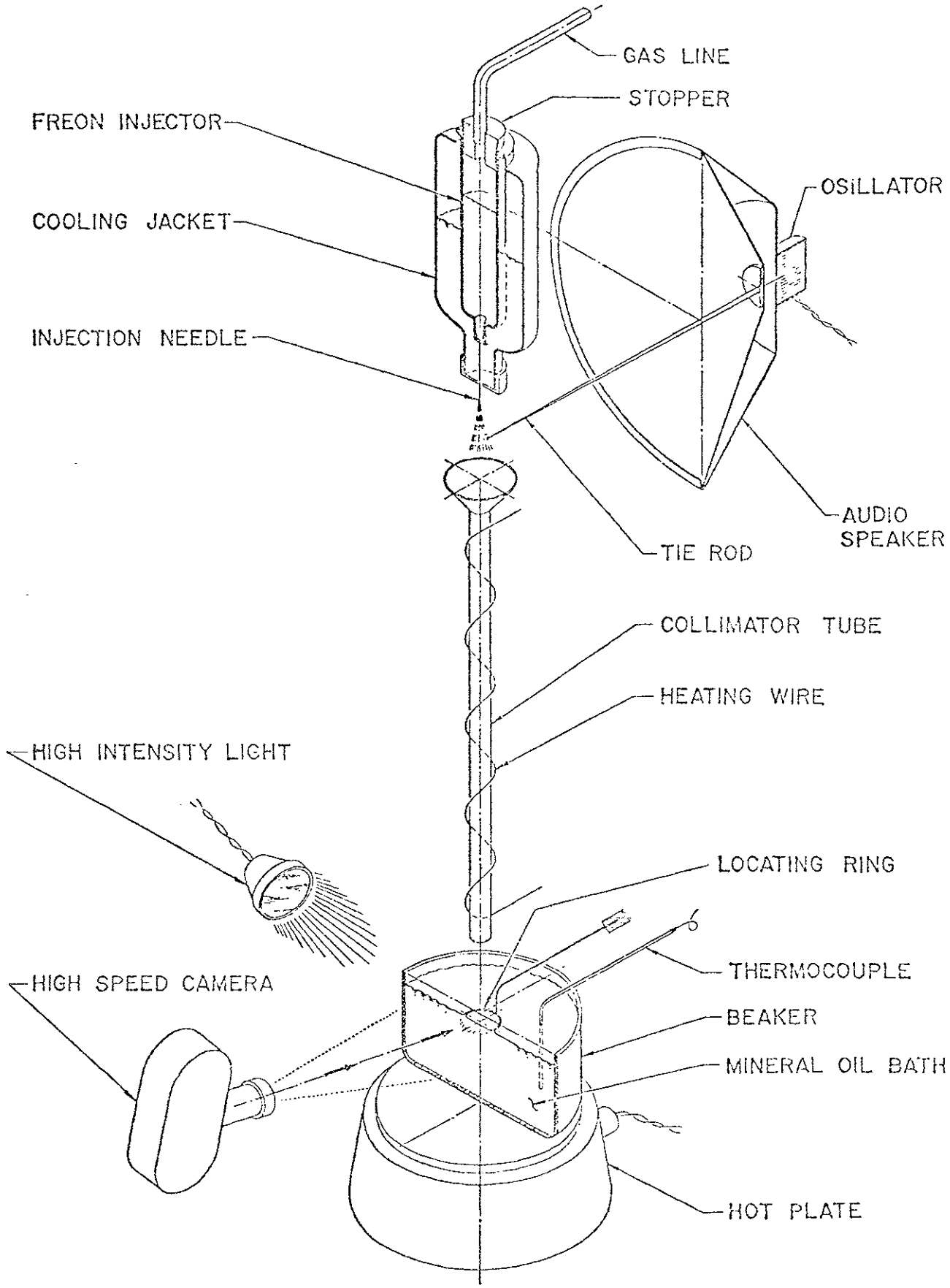

FIGURE 9.7 COMPARISON BETWEEN SMALL SCALE R22 DATA AND HENRY'S DROP CAPTURE MODEL

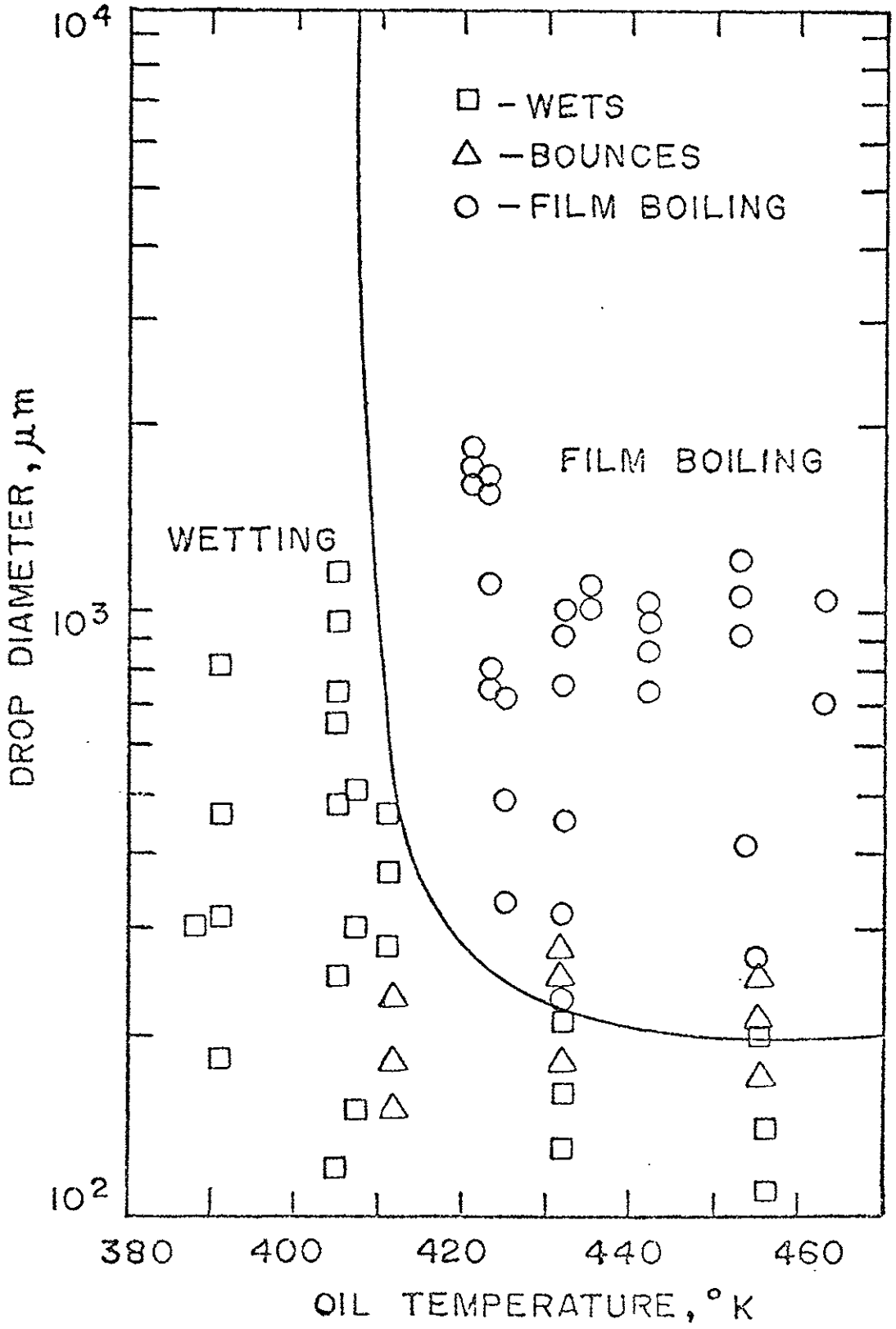

FIGURE 9.8

DULLFORCE'S EXPERIMENTAL FRAGMENTATION BEHAVIOR FOR T_{ci}

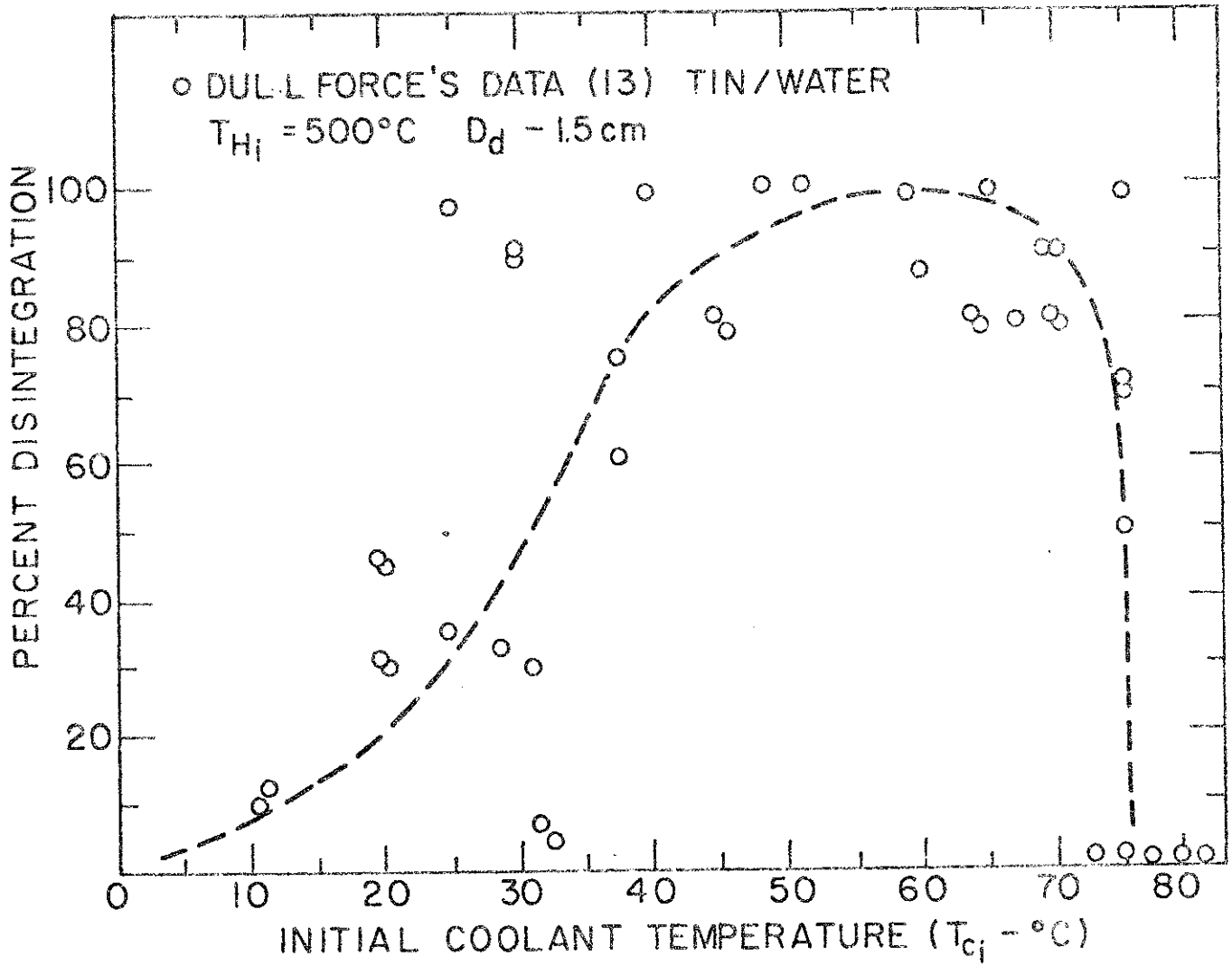

FIGURE 9.9

CHO'S EXPERIMENTAL FRAGMENTATION BEHAVIOR

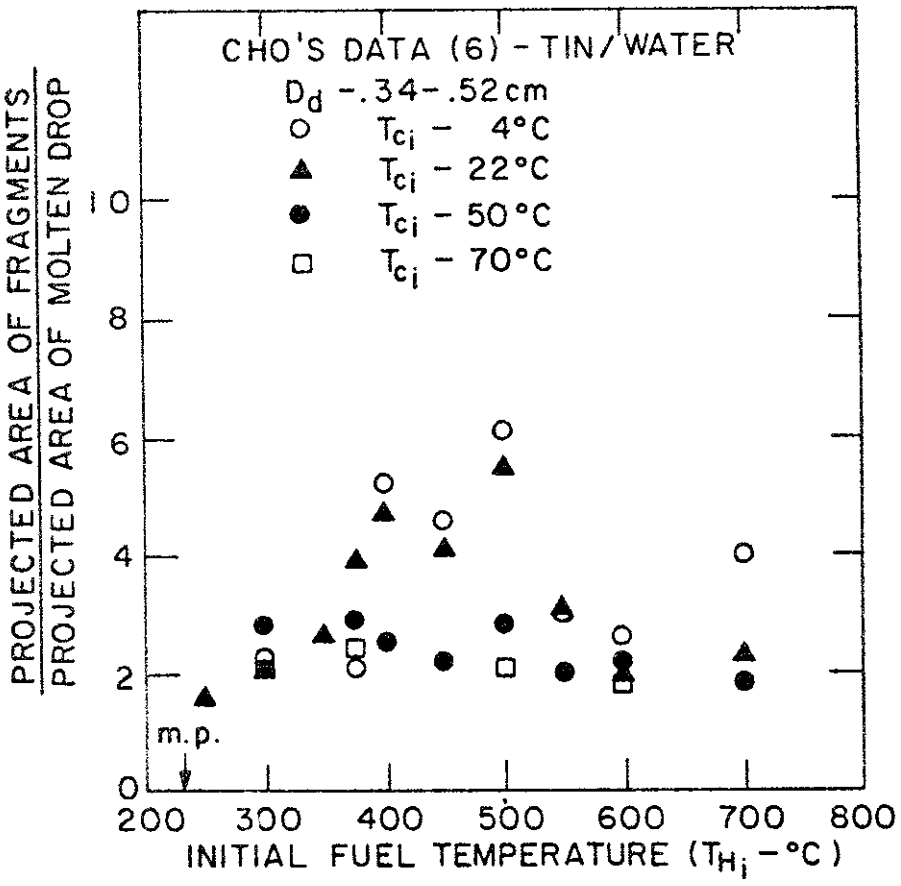

FIGURE 9.10

DULLFORCE'S EXPERIMENTAL FRAGMENTATION BEHAVIOR FOR T_{Hi}

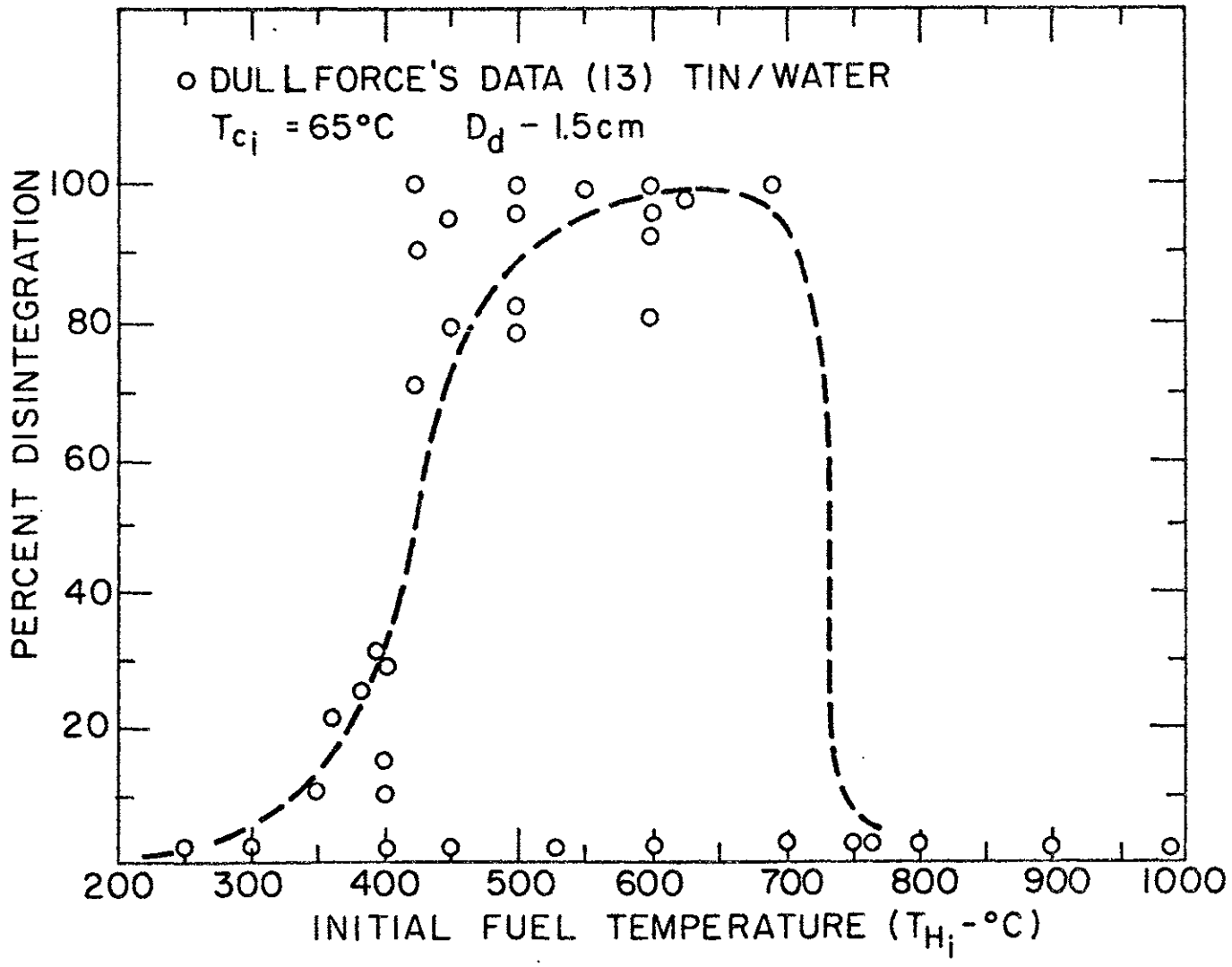

FIGURE 9.11

MIT EXPERIMENTAL FRAGMENTATION BEHAVIOR FOR T_{Hi}

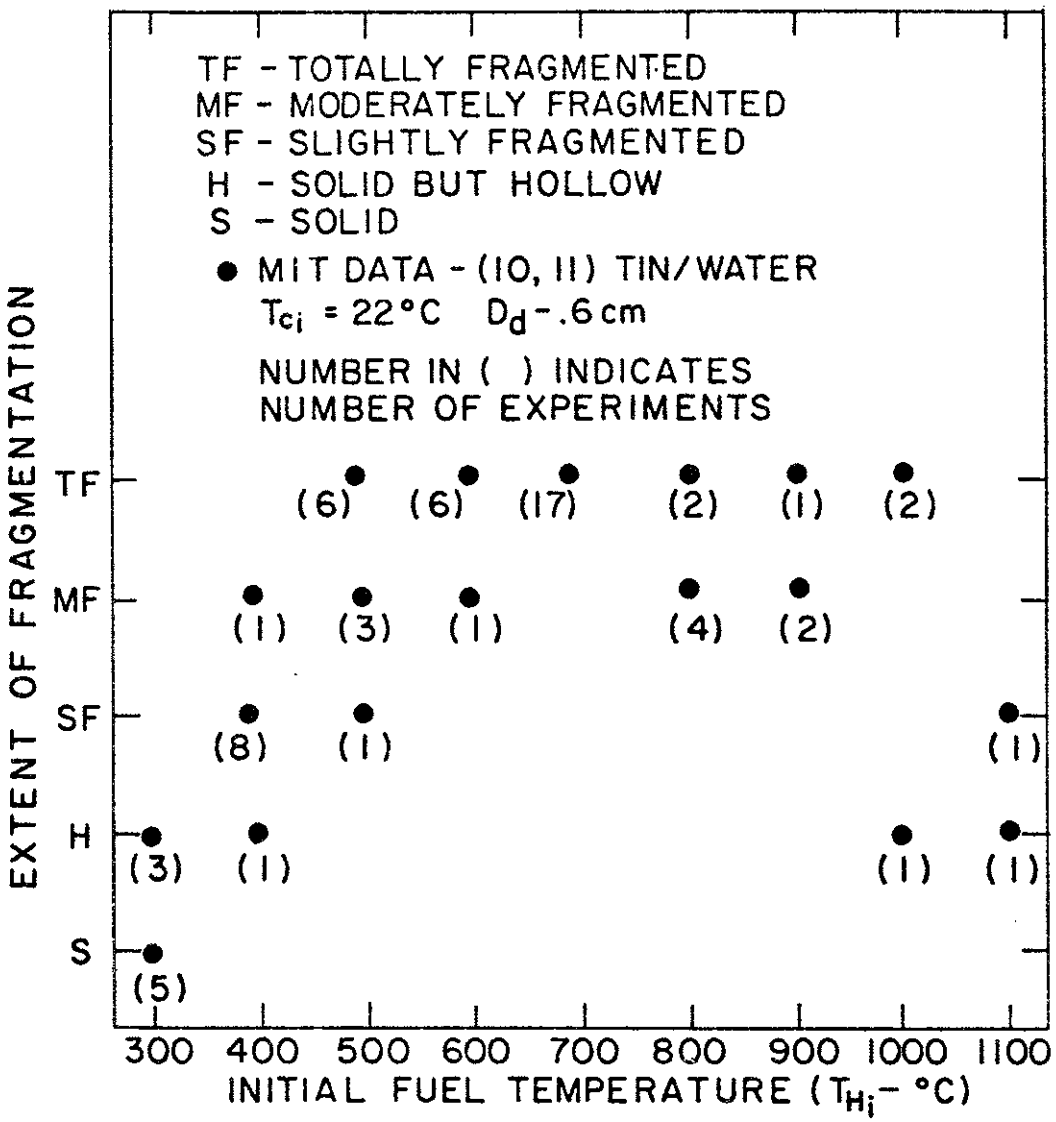

FIGURE 9.12

FROHLICH'S EXPERIMENTAL FRAGMENTATION BEHAVIOR

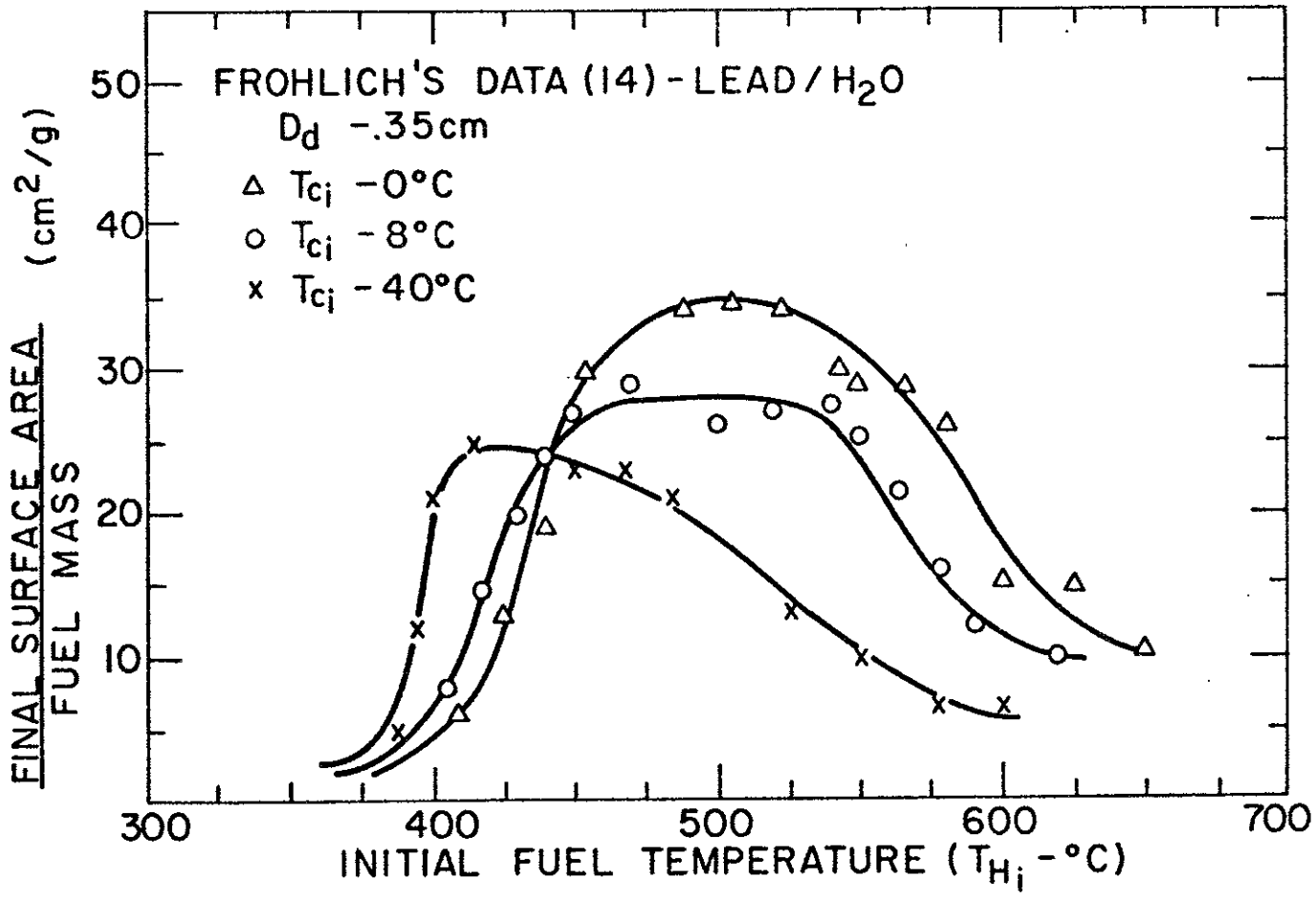

FIGURE 9.13

TRANSDUCER PEAK PRESSURE BEHAVIOR

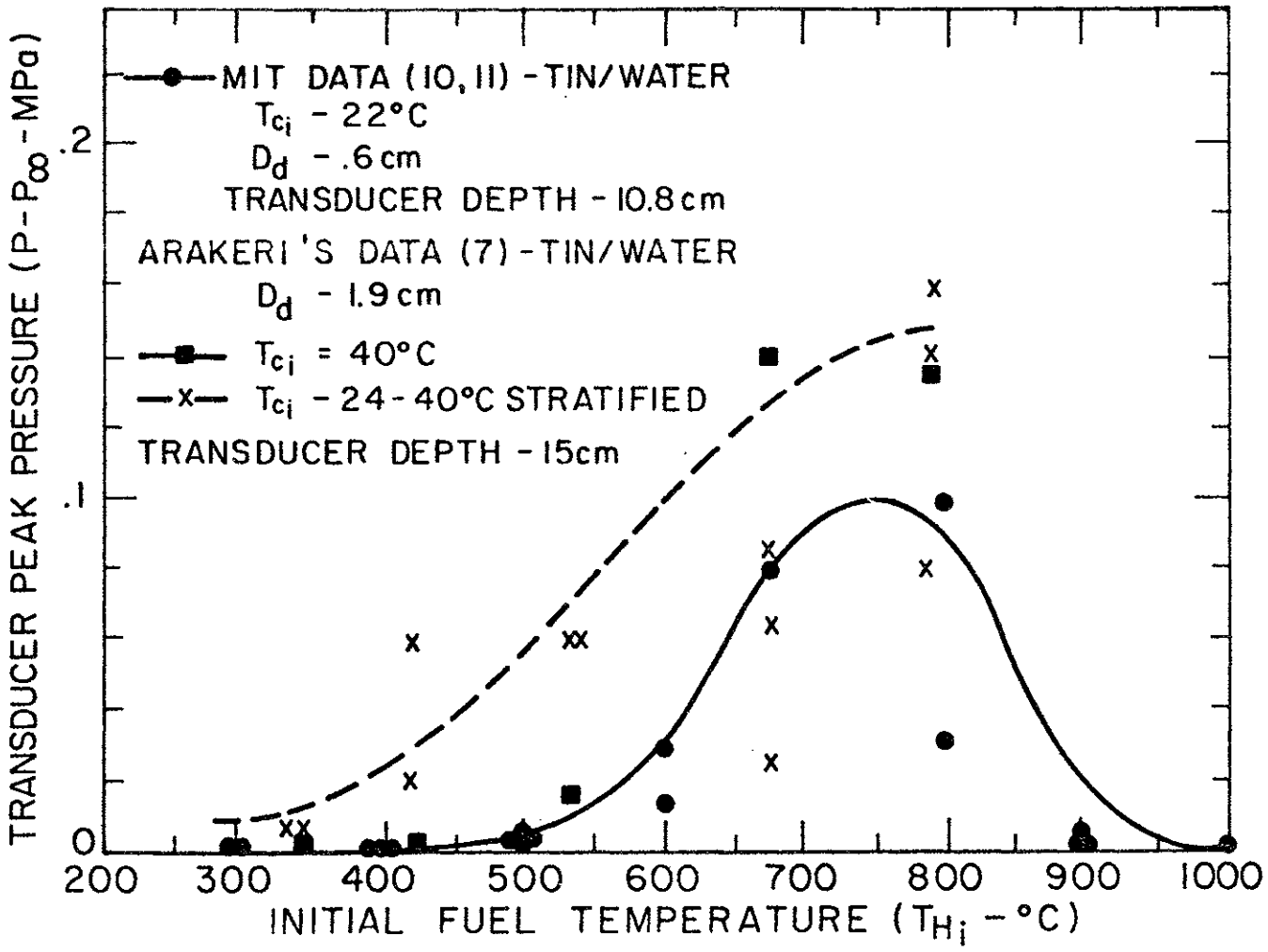

FIGURE 9.14

EXPERIMENTAL DWELL TIME BEHAVIOR

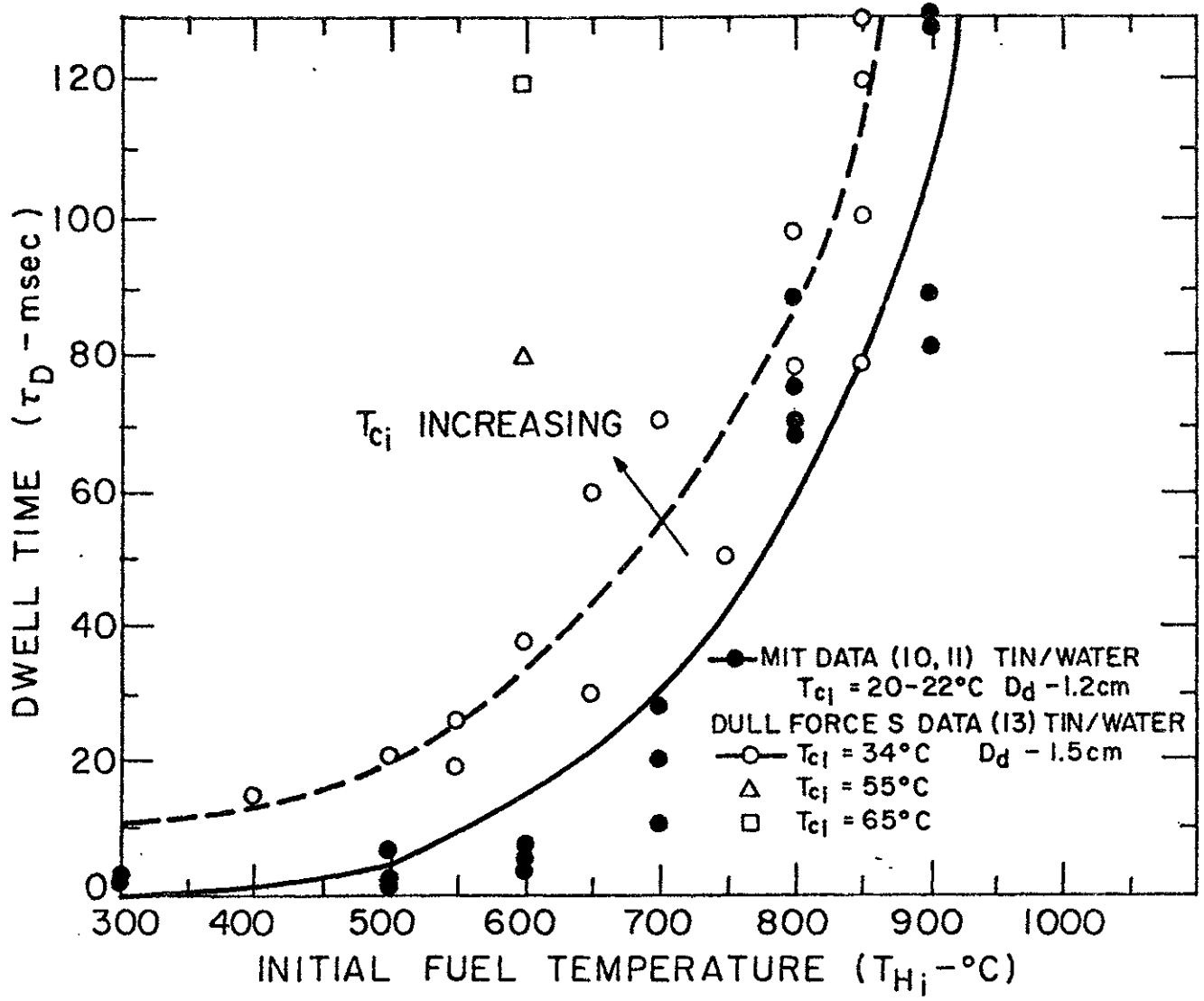

FIGURE 9.15

TIN/WATER EXPERIMENTAL FRAGMENTATION BOUNDARIES

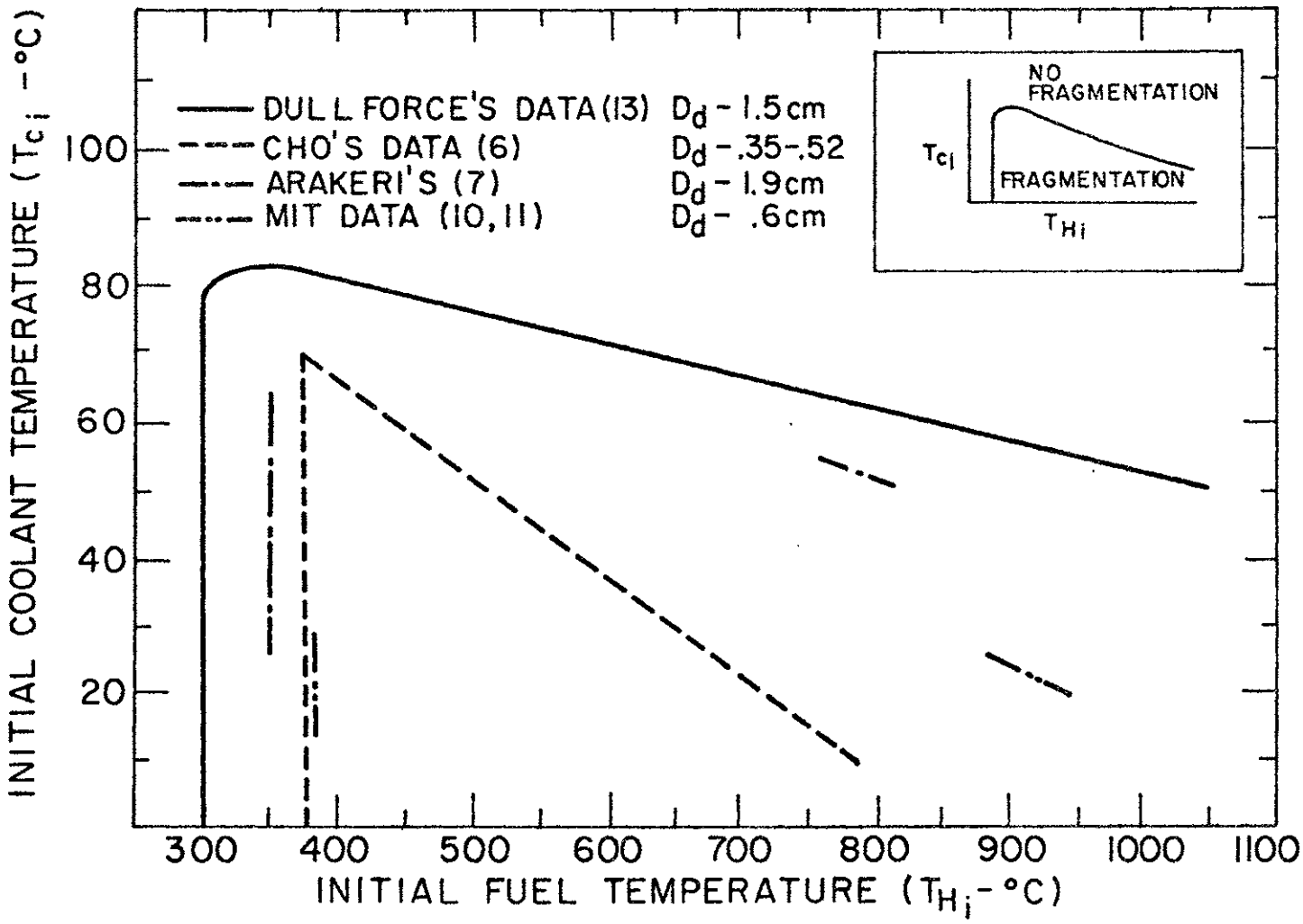

10. PROPOSED MODEL FOR SELF-TRIGGERED INTERACTIONS IN MOLTEN METAL-WATER SMALL SCALE EXPERIMENTS

10.1 Overview

The model for self-triggered interactions to be proposed is based on a mechanistic view of film boiling. Yao and Henry [130] performed a series of experiments where water (or ethanol) was put on a heated copper plate in a steady state film boiling mode. It was shown, using electrical resistance probes, that the liquid in the film boiling region randomly touched the solid surface. These random contacts decreased in frequency and duration as the copper plate temperature was increased, although they still existed when the interface temperature exceeded the homogeneous nucleation temperature of water.

This view of film boiling was used in the energetics model for liquid-liquid systems in the spontaneous nucleation theory by Henry, [129] as the basis for the self-trigger of energetic interactions, where $T_I > T_{HN}$. Bankoff [131], in his splash theory for liquid-liquid vapor explosions, also viewed film boiling as being accompanied by many random liquid-liquid contacts that could escalate into the self-trigger mechanism of the interaction.

Similarly, in the molten metal/water experiments this qualitative view of film boiling seems to be valid as the mechanism for the self-trigger. When the molten metal enters the coolant pool, a film boiling regime is eventually initiated between the constituents. When the temperature combination of the fuel and coolant lie within the self-triggered interaction zone, the film boiling regime is viewed as one where random

liquid-liquid contacts between the fuel and coolant can occur. These contacts during the film boiling process are probably the mechanism for the self-trigger. In these small scale experiments the fuel is dropped through a noncondensible gas environment (air or nitrogen). These gases can be trapped as an initial film between the fuel and coolant. This film, though, would begin to collapse in some characteristic time (τ_{coll}). If the characteristic time (τ_{sat}) for the coolant interface temperature to heat to its ambient saturation temperature is longer than τ_{coll}, then the gas film will begin to collapse, initiating these random liquid-liquid contacts. These contacts and the associated coolant vapor generation will generate a film boiling regime, where continued random liquid-liquid contacts could generate a self-triggered interaction after the experimentally observed dwell time (τ_D). This type of behavior would be characteristic of fuel and coolant temperature combinations within the self-triggered zone.

Extending this mechanistic view, the upper diagonal boundary for self-triggered interaction would represent the condition where the relation $\tau_{sat} > \tau_{coll}$ changes to $\tau_{sat} < \tau_{coll}$. At these temperature combinations the time (τ_{sat}) for the coolant interface to come to its ambient saturation temperature would be equal to or smaller than the characteristic time (τ_{coll}) for the noncondensible film to begin to collapse. The coolant would then vaporize into the film and increase its thickness before a significant amount of random liquid-liquid contacts occur. Since these contacts would be dramatically reduced, the self-triggered interaction would not occur.

10.2 Cooling Analysis Within the Self-Triggered Interaction Zone

This section of the analysis is repeated from the work of Corradini [141] to give the complete physical picture for the molten metal-water interactions. The self-triggered interaction occurs after a characteristic dwell time (τ_D). Originally, Bjorkquist at MIT [123] performed a cooling analysis of the fuel at the time of interaction. To estimate the heat transfer coefficient for film boiling, results of Stevens' and Witte's experiment [140] for a moving solid silver sphere (D = 1.9 cm) in water were used. The tin was modeled as a sphere, and using the experimental dwell times it was found that the tin did not cool substantially and all interactions (T_{Hi}>400°C) occurred at predicted tin surface temperatures greated than the critical temperature of the water coolant (400°C<T<650°C). In experiments by Arakeri at UCLA [119] stroboscopic photography was used to observe the detailed movements of the tin before and during the interaction. The photographs indicated quite clearly that in almost all dropping experiments the tin mass in film boiling became distorted, and a small projection grew out from the bulk of the mass. The interaction consistently seemed to start at this projection and proceed upwards to the bulk of tin engulfing it. Arakeri [119] concluded that the start of the interaction at the projection suggests a destablized film boiling regime.

A possible explanation of the experimental observation is that the fuel projection acted as a cooling fin, cooling down the fuel in the projection to a temperature lower than the bulk. To determine the temperature at the tip of the fin at the time of the interaction, a transient fin cooling analysis was performed. Bjorkquist's data [123] for D_d = 1.2 cm were used for both temperatures and dwell times because both sets of data were consistently available. The drop was modeled as a sphere with a

fixed length fin attached (Figure 10.1). The size of the fin is determined from UCLA photographs as

$$\frac{\text{Diameter of Fin}}{\text{Diameter of Drop}} = \frac{D_F}{D_d} = \frac{1}{5}$$

$$\frac{\text{Diameter of Fin}}{\text{Length of Fin}} = \frac{D_F}{L_F} = \frac{1}{3}$$

These fixed ratios were assumed to be applicable to the MIT large tin drop data. The justification of this assumption is based on the possible origin of the observed deformation. Arakeri's drop experiments were conducted with drop Weber numbers of 84, and Bjorkquist's experiments at Weber numbers of 32. Both of these are above the range of critical Weber number values $7.5<We<15$, so that each would be expected to deform with time. To estimate a characteristic time for the drop to deform a distance equal to the initial radius of the sphere [67], we can write a momentum equation for the drop as

$$\rho_H \frac{Dv}{Dt} \simeq \nabla P \tag{10.1}$$

Now a representative velocity of the deforming molten metal can be the radius $(\frac{D_d}{2})$, divided by the characteristic time for drop deformation (τ_{def})

$$\frac{Dv}{Dt} \simeq (\frac{D_d}{2})(\frac{1}{\tau_{def}})^2 \tag{10.2}$$

The pressure gradient can be estimated by

$$\nabla P = 2\Delta P/D_d \tag{10.3}$$

Therefore, we can write

$$\tau_{def} = \frac{D_d}{2}\sqrt{\frac{\rho_H}{\Delta P}} \tag{10.4}$$

The pressure drop for deformation can be estimated by

$$\Delta P = \frac{C_D \rho_c V_{ent}^2}{2} \tag{10.5}$$

where

C_D - drag coefficient = .5

V_{ent} - drop entrance velocity

Using this approximation it is found that

τ_{def} = 27 msec for MIT data

τ_{def} = 32 msec for UCLA data

Thus it appears that for proportionately the same drop deformation, each drop requires the same amount of time. Thus it would be reasonable to assume MIT drop experiments would produce projections of the same ratios as in UCLA experiments.

The heat transfer coefficient used for this analysis is taken from the experimental findings of Stevens and Witte [140]. The transient governing energy equation for the fin is given by

$$\frac{\partial T_H}{\partial t} = \alpha \frac{\partial^2 T_H}{\partial x^2} - \frac{\bar{h} Per}{\rho_H c_H A_{cs}} (T_H - T_c) \tag{10.6}$$

where boundary conditions

(i) $T_H = T_{H_i}$ for x at the root of the fin in the bulk mass for $t \geq 0$ (10.7)

(ii) $\frac{\partial T_H}{\partial x} = 0$ for x at the tip of the fin for $t \geq 0$ (10.8)

Initial condition for all x

(iii) $T_H = T_{H_i}$ for $t = 0$ (10.9)

A classical solution for this is given in Carslaw and Jaeger [70] for the temperature at the tip of the fin (T_{tip}) as,

$$T_{tip}(t) = \frac{2\,[T_{Hi} - T_{ci}]}{L_F} \sum_{n=0}^{\infty} e^{-(\nu+\alpha\beta^2)} (G_n(t)) \tag{10.10}$$

where

$$G_n(t) = \frac{\alpha\,\beta_n (-1)^n\,(e^{-(\nu+\alpha\beta^2)\,t} - 1)}{\nu + \alpha\,\beta_n^2} + \frac{(-1)^n}{\beta_n}$$

$$\beta_n = \frac{(2n+1)\,\pi}{L_F}$$

$$\nu = \frac{hPer}{\rho_H c_H A_{cs}}$$

$$\alpha = \frac{K_H}{\rho_H c_H}$$

Using this expression, the temperature at the tip in the region of the self-triggered interaction of the fin can be determined for the range of experimental fuel temperatures and dwell times. Constant thermophysical properties are used and are listed in Appendix A. As Table 10.1 indicates, the temperatures of the fin tip before liquid-liquid contact are approximately constant. When the coolant attempts to wet the surface in a random contact, the surface temperature is reduced further to the contact interface value of

$$T_I = \frac{T_{tip}(\tau_D)}{1+\beta} + \frac{\beta T_{c_i}}{1+\beta} \tag{10.11}$$

where

$$\beta = \sqrt{\frac{k_c \rho_c c_c}{k_H \rho_H c_H}}$$

Given the uncertainties of the thermophysical properties near the critical point, the application of this conduction solution gives a rough indication of the actual temperature after liquid-liquid contact seems to fall near or below the critical temperature of the water coolant ($T_{crit} = 375^{o}C$).

Henry [129] has asserted in his spontaneous nucleation energetics model that in the drop mode of contact a vapor explosion can only occur if $T_{SN}<T_{I}<T_{crit}$. It appears that this analysis indicates that self-triggered interactions of the tin/water system are consistent with the upper boundary of this spontaneous nucleation model. It must be noted, though, that in the self-triggered region the surface temperature is near or below T_{crit}, while the remaining tin mass is significantly above T_{crit}. This situation seems to imply that the self-trigger has a definite temperature threshold; whereas, the continued propagation or continuance of the fragmentation does not.

10.3 Model for the Prediction of the Self-Triggered Fragmentation Upper Boundary

The physical reason for this upper fragmentation boundary (Figure 10.2) has been cast as the comparison of two characteristic times (τ_{sat} and τ_{coll}). If $\tau_{sat}>\tau_{coll}$, then the initial noncondensible gas film will begin to collapse first and eventually initiate a film boiling regime where random liquid-liquid contacts can occur and can lead to a self-triggered interaction. If $\tau_{sat}<\tau_{coll}$, then the coolant interface temperature reaches T_{sat} before the collapse begins. The coolant can then vaporize and feed the film, increasing its thickness before the random contacts occur, and thus self-triggered interactions cease.

The characteristic collapse time (τ_{coll}) is viewed as being caused by oscillations of the coolant or fuel interface due to Taylor Instabilities. Consider Figure 10.3 where the noncondensible film is between the fuel and coolant and the upper surface has a slight undulation of size η_o and wavelength λ. This situation is unstable and the initial wavelength will grow with time according to the relation [40],

$$\eta = \eta_o \cosh (n\ t) \tag{10.12}$$

where

$$n = \sqrt{\frac{2\pi}{\lambda} \frac{g\ (\rho_\ell - \rho_g)}{\rho_\ell}} \tag{10.13}$$

for

$$\eta_o << \lambda$$

The initial wavelength which oscillates can be estimated to be near the critical Taylor Instability wavelength of [41],

$$\frac{\lambda}{2\pi} \doteq \frac{\lambda c}{2\pi} = \sqrt{\frac{(\sigma_\ell)}{g(\rho_\ell - \rho g)}}$$

The characteristic time (τ_{coll}) is the time for η to grow from its initial amplitude (η_o) to the film thickness (δ). This is under the assumption that $\delta << \lambda$. The resulting expression is

$$\tau_{coll} = \frac{1}{n} \cosh^{-1} \left(\frac{\delta}{\eta_o}\right) \tag{10.15}$$

The solution to this is plotted in Figure 10.4 in a dimensionless form, and values of n can be calculated using properties listed in Appendix A. The values of n calculated are approximately the same for all the liquid constituents, and, therefore, the question is what should be used for δ/η_o. This will be addressed later.

To estimate the characteristic time (τ_{sat}) for the coolant interface to be heated to its ambient saturation temperature, let us consider the conceptual view of Figure 10.5. We geometrically model the initial heat

transfer from the fuel to the coolant as two semi-infinite masses at different temperatures, separated by a noncondensible gas film of thickness δ. This geometry is valid for the fuel droplet if the thermal penetration depth is less than the radius

$$\sqrt{\alpha_H t} < \frac{D_d}{2}$$

which for this application corresponds to $t < 150$ msec. Only conduction heat transfer is considered during this time. This is a reasonable first approximation because δ is small and the heat flux due to conduction is substantially larger than the radiation. This will be illustrated later. The gas film during this transient heat transfer process is assumed to be of negligible thermal capacity and having a constant thickness δ. Thermophysical properties are assumed to be constant for this analysis. The governing energy equation for each region is

$$\frac{\partial T}{\partial t} = \alpha \frac{\partial^2 T}{\partial x^2} \tag{10.16}$$

where the boundary conditions and initial conditions are

$$\text{(i)} \quad T_H = T_{Hi}; \text{ for } t > 0 \quad x \to -\infty \tag{10.17}$$

$$\text{(ii)} \quad T_c = T_{c_i}; \text{ for } t > 0 \quad x \to \infty \tag{10.18}$$

$$\text{(iii)} \quad -k_H \, \partial T_c / \partial x \big|_{x=0} = q'' (t); \; t > 0 \tag{10.19}$$

$$\text{(iv)} \quad -k_c \, \partial T_c / \partial x \big|_{x=0} = q'' (t); \; t > 0 \tag{10.20}$$

where

$$q'' (t) = \frac{(k_g)}{\delta} \left(T_H (0,t) - T_c (0,t)\right)$$

$$\text{(v)} \quad T_H = T_{H_i}; \; t = 0 \quad x < 0$$

$$T_c = T_{c_i}; \; t = 0 \quad x > 0 \tag{10.21}$$

this problem can be solved by taking the LaPlace transform, solving the resulting ordinary differential equation, and taking the inverse transform. Appendix G details the solution procedure and the resulting expression for the coolant interface temperature is given by

$$\Theta_m = \frac{T_c\,(0,t) - T_{c_i}}{T_{H_i} - T_{c_i}} = (1 + \beta)\left[1 - e^{w^2}\,(\text{erfc}\;\; w)\right] \tag{10.22}$$

where

$$w = C_1\,(\alpha_c\, t)^{\frac{1}{2}} \tag{10.23}$$

$$C_1 = \frac{k_g\,(1 + \beta)\sqrt{\alpha_H}}{k_H\,\beta\,\delta\,\sqrt{\alpha_c}} \tag{10.24}$$

$$\beta = \sqrt{\frac{k_c \rho_c c_c}{k_H \rho_H c_H}} \tag{10.25}$$

The solution to this equation is shown graphically in the dimensionless form in Figure 10.6 where

$$\Theta_m = \frac{T_c\,(0,\, t) - T_{c_i}}{T_{H_i} - T_{c_i}}$$

The characteristic time (τ_{sat}) is that time when

$$\Theta_m = \frac{T_{sat}\,(\tau_{sat}) - T_{c_i}}{T_{H_i} - T_{c_i}}$$

that is when the coolant interface temperature has reached its saturation temperature.

10.4 Determination of the Initial Gas Film Thickness

Two physical parameters remain to be estimated before this model can be utilized, δ and δ/η_o. The ratio of the initial noncondensible gas film

thickness (δ) to the initial amplitude (η_o) of a wavelength at the gas-liquid interface is an unknown. Physically, though, reasonable limits can be put on it to obtain an estimate. It is expected that in comparison to the initial wavelength of the instability at the gas-liquid interface that

$$\delta << \lambda$$

and that

$$\eta_o << \lambda$$

It is a reasonable first approximation to assume that η_o is of the same order of magnitude as δ such that

$$1 < \delta/\eta_o < 10$$

As Figure 10.4 indicates, this represents the knee of the curve between a large and a small change in $n\tau_{coll}$ given δ/η_o. For this analysis, it has been assumed that

$$\delta/\eta_o = 2 \qquad (10.26)$$

Depending on the liquid considered (molten metal or water) this corresponds to a τ_{coll} of approximately 20 msec. This value seems physically reasonable because the characteristic time to collapse of the film is not a function of temperature. Thus for low fuel or coolant temperatures within the self-triggered fragmentation zone, the collapse time should be of the same order of magnitude as the smaller dwell times prior to an interaction. This is because the collapse process is viewed as the start of the random contacts which eventually are the cause of the self-triggered interaction.

When the fuel droplet falls into the water pool at the start of each experiment, some noncondensible gas is carried in with it. The gas film

is probably some fraction of the low velocity boundary layer that is formed around the fuel droplet as it falls through the cover gas into the water. Thus the thickness of the gas film is modeled as

$$\frac{\delta}{D_d} = \frac{C}{(Re_g)^{\frac{1}{2}}} \tag{10.27}$$

where

$$Re_g = \frac{\rho_g \, v_{ent} \, D_d}{\mu_g}$$

which is similar in functional form to the thickness of a laminar boundary layer.

10.5 Calculation of Θ_m

The upper diagonal boundary in Figure 10.1 represents the upper limit above which self-triggered interactions cease. Along this upper limit line it is observed that the experimental value of

$$\Theta_{exp} = \frac{T_{sat} - T_{c_i}}{T_{H_i} - T_{c_i}} \tag{10.28}$$

is essentially constant. The model presented gives a prediction of this boundary if we take $\tau_{sat} = \tau_{coll}$. Thus for an experimental set of initial conditions, the value for τ_{coll} can be determined from Equation 10.15 and substituted into Equation 10.22, with a value for δ, and Θ_m is calculated where

$$\Theta_m = \frac{T_{sat}\,(\tau_{coll}) - T_{c_i}}{T_{H_i} - T_{c_i}}$$

With this dimensionless temperature, an upper boundary line for self-triggered interactions can be constructed where

$$T_{H_i} = T_{c_i} + \frac{T_{sat} - T_{c_i}}{\Theta_m} \tag{10.29}$$

Using various values for the constant C in Equation 10.27 to determine δ, Θ_m was calculated from Equations 10.22 to 10.25 with $\tau_{sat} = \tau_{coll}$ for the experimental conditions listed in Table 9.3. A single value of C was chosen, which gave the best agreement between Θ_m and Θ_{exp}, Figure 10.10 and the relation is

$$\frac{\delta}{D_d} = 2.5 \left[\frac{\rho_g}{\rho_\ell} \frac{1}{Re}\right]^{\frac{1}{2}} \qquad (10.27)$$

A comparison of the prediction of the model of the upper boundary and experimental values for the tin/water system is given in Figure 10.7. The agreement between the model and experiment is good. The data of Swift and Pavlik [115] and Witte [116] were omitted because not enough experiments were performed to discern a sharp upper fragmentation boundary.

The model accurately predicts the shifts in the boundary from one set of experimental initial conditions to another. The two main variables which change are the diameter of the fuel drop and the entrance velocity. As the size of the fuel mass increases, the size of δ increases. This in turn demands more time for the coolant interface at $T_c(0,t)$ to reach its saturation temperature T_{sat}. Thus the boundary for equality between τ_{sat} and τ_{coll} is moved upward to larger fuel and coolant temperature combinations. In the limit, as the size becomes much bigger in this contact mode, the boundary becomes almost horizontal at $T_{c_i} = T_{sat}$ and almost any fuel temperature is predicted to be able to have a self-triggered vapor explosion. For large scale dropping experiments (tin/H_2O, steel/H_2O) this model would not be applicable because the size of the system is the same order of magnitude as the size of fuel mass, thus the explosion characteristics would change. An increase in the entrance velocity has the

opposite effect on δ, causing a decrease. Thus, the zone of self-triggered interactions would be reduced in size. In both cases, though, an increase in v_{ent} or D_d would increase the Weber number and thus give rise to an increase in hydrodynamically induced fragmentation [114,118].

One assumption of this model was to ignore radiation heat transfer. To show the adequacy of this assumption, let us calculate the effective heat transfer coefficient for conduction and black body radiation (as maximum) at a high fuel droplet temperature ($1000^{o}C$). The heat transfer coefficient for conduction is

$$\bar{h}_c = \frac{k_g}{\delta} = \frac{(R_e)^{\frac{1}{2}} k_g}{.079 D_d}$$

for the UCLA data [119], this gives us the smallest value of $\bar{h}_c$ as $1060 \frac{W}{m^{2}{}^{o}k}$. The heat transfer coefficient for radiation is given by

$$\bar{h}_r = \sigma_r \frac{(T_{H_i}^4 - T_{c_i}^4)}{(T_{H_i} - T_{c_i})}$$

which for $T_{c_i} = 20^{o}C$ gives us $\bar{h}_r = 151\ W/_{m}21^{o}K$. Thus at the largest fuel temperature, the heat transfer coefficient from radiation is small compared to conduction and can be neglected.

This model can be extended to other molten metal/water systems. Figure 10.8 illustrates the model prediction for the lead/water system in comparison to the recent data of Frohlich [126]. Although the agreement is not as good as tin/water predictions, the general trend of the data is followed by the prediction. Frohlich used small diameter fuel droplets, thus the upper cutoff temperatures for fragmentation were quite low.

Figure 10.9 depicts the prediction of the fragmentation boundary model for the bismuth/water system. The agreement between UCLA data and the prediction of the model is good. MIT experiments were conducted at coolant temperatures of 20-22°C and bismuth temperatures up to 700°C. In this range no decreasing trend in the extent of fragmentation was noted, and the prediction of the model is consistent with this observation, placing the boundary at $T_{H_i} = 900^{\circ}C$ for $T_{c_i} = 20^{\circ}C$. The worst agreement between model and experiment was for the bismuth experiments of Cho. The model predicts a low boundary due to the small diameter fuel drop reportedly used, yet the observed cutoff at $T_{c_i} = 50^{\circ}C$ was at a much higher fuel temperature. Given the range of fuel droplet diameters used, the boundary may correspond to a larger droplet diameter. This would tend to shift the prediction of the model in the correct direction.

To compare the relative error between the experiment and the model, consider Figure 10.10 and 10.11. This error results from equating the predicted collapse time for the gas film (τ_{coll}) to the characteristic time (τ_{sat}) for the coolant interface to come to its saturation temperature. The model uses τ_{coll} to calculate a predicted dimensionless temperature Θ_m. Figure 10.10 compares this with the value (Θ_{exp}) determined from experiments. Excluding the bismuth/water data of Cho, the relative error of the model does not exceed 30%. As Figure 10.11 illustrates, this error results from a difference between τ_{coll} and the characteristic time (τ_{sat}) obtained from experimental results. The error of these two characteristic times results in the smaller error between Θ_m and Θ_{exp} (Figure 10.10) because the time enters Equations 10.22 and 10.23 as $t^{\frac{1}{2}}$. Thus a larger error in the time to saturation temperature at the coolant interface has a reduced effect.

Although this simple model shows good agreement with the experimental results, it must be emphasized that it is an initial approach motivated to explain the striking observation of the nearly constant behavior of Θ_{exp}. There are a number of specific assumptions in the model that cannot be considered totally valid:

(1) The model for the initial size of the noncondensible film (δ) was empirically found to be adequate although it is not based on detailed fluid mechanics analysis.

(2) The model for τ_{coll} employs the amplitude growth rate from Taylor's original linear analysis and does not contain the effects of viscosity or surface tension.

(3) There may be other fluid instability mechanisms operative that could also aid in the noncondensible gas film breakdown (e.g. Kevin-Helmholtz Instabilities). These have not been specifically analyzed.

(4) The analysis is a quasi-steady analysis for constant δ. This is not the real situation during the droplet's impact into the water and thus a more detailed analysis of the droplet's entrance could be done. In such an analysis δ would be taken as a function of time and the complete model could be upgraded.

The present analysis then is just a first step in presenting one possible explanation for the observed experimental results, and could be re-examined in view of items (1) through (4) above to explore other possible explanations.

TABLE 10.1

TIN COOLING ANALYSIS

MIT DATA $m = 6.2$ gm.

$D_d = 1.2$ cm.

$\frac{D_f}{D_d} = .2$ $\qquad$ $\frac{D_f}{L_f} = .33$

T_{H_i} (°C)	T_{c_i} (°C)	$\bar{h}$ $(\frac{w}{cm^2 k°})$	τ_D (msec)	Fin Tip Temperature before liquid-liquid contact	$T_{tip}(\tau_D)$ °C after liquid-liquid contact
500	23	1	5	472	395
600	23	.9	15	455	381
700	23	.75	35	460	386
800	23	.7	70	463	388
900	23	.6	100	440	369
1000	23	.5	150	380	320

FIGURE 10.1

CONCEPTUAL MODEL OF FUEL MASS PROJECTION

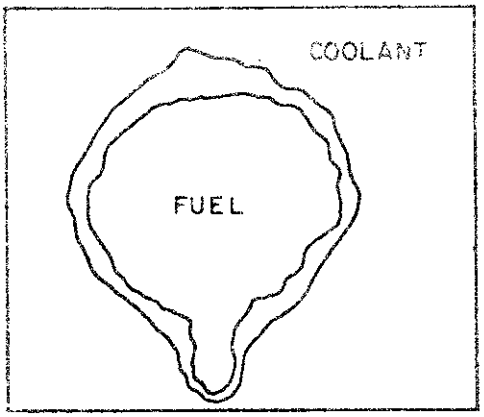

POSSIBLE SHAPE OF FUEL MASS

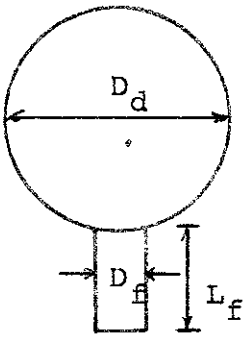

MODEL OF FUEL MASS

FIGURE 10.2

FRAGMENTATION BOUNDARY FOR SMALL SCALE MOLTEN METAL/WATER INTERACTIONS

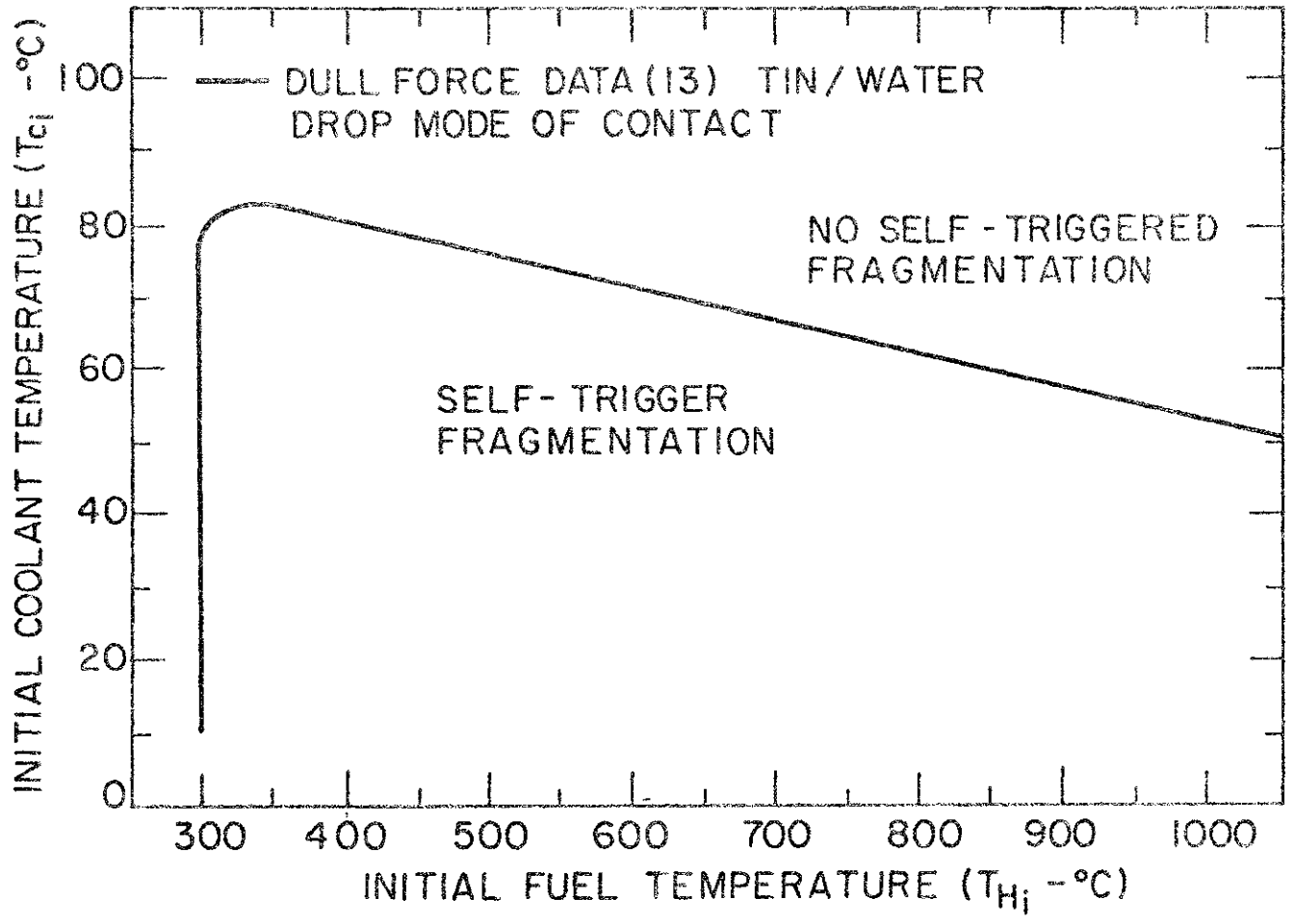

FIGURE 10.3

CONCEPTUAL VIEW OF INSTABILITY AT FUEL-COOLANT INTERFACE

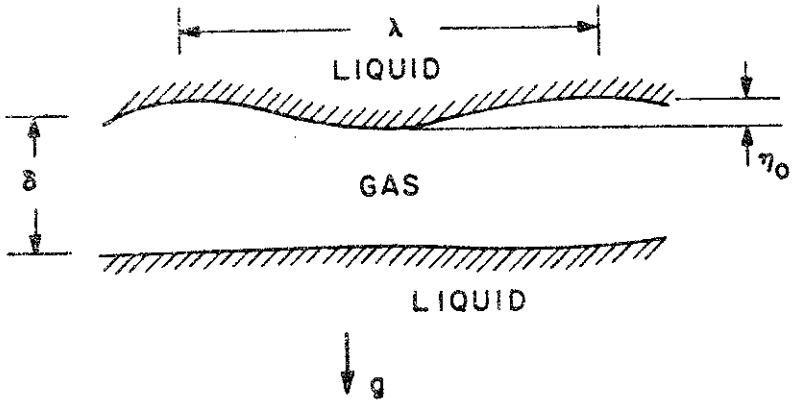

FIGURE 10.4

VALUES FOR DIMENSIONLESS COLLAPSE TIME

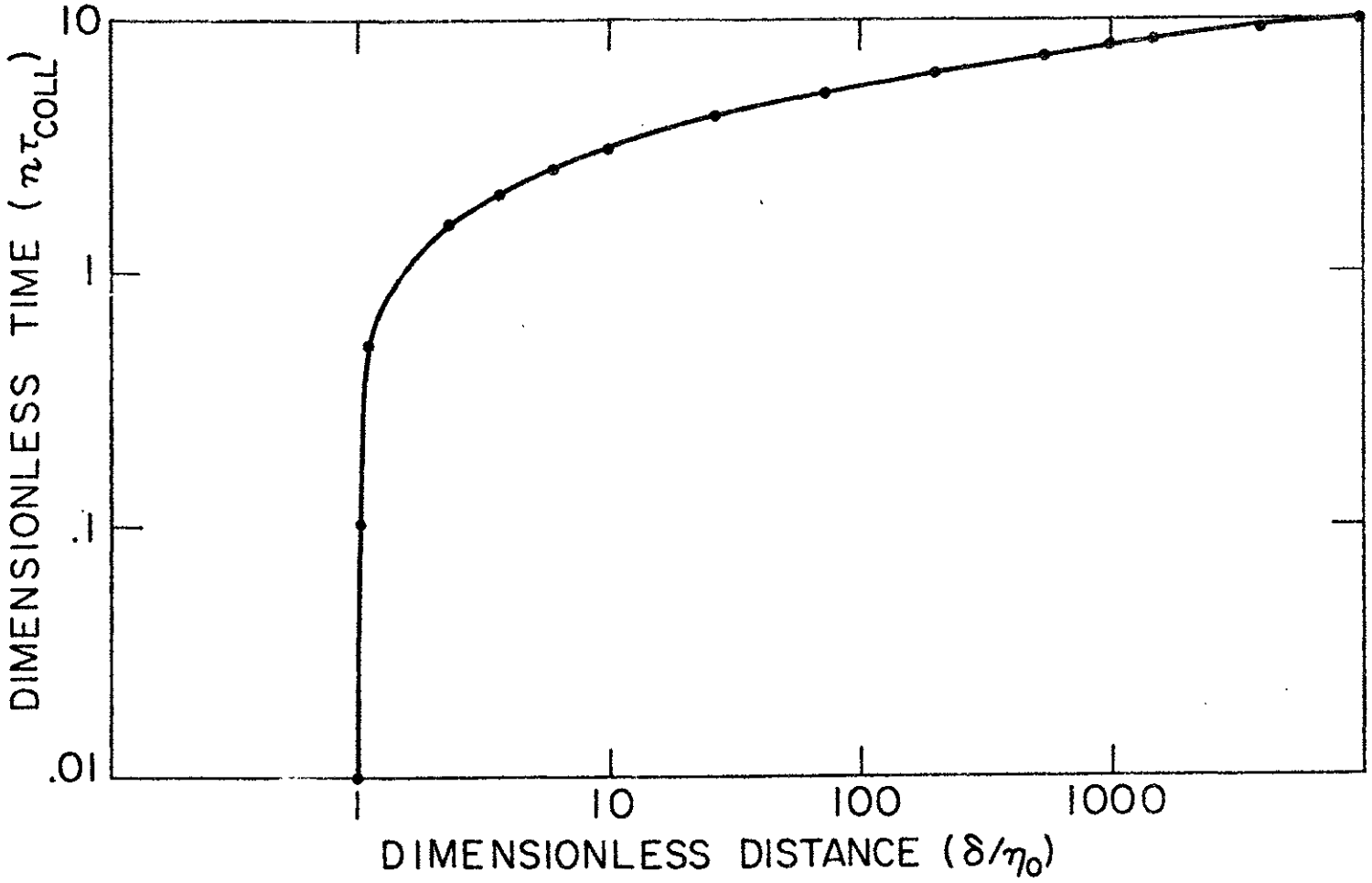

FIGURE 10.5

CONCEPTUAL VIEW OF FUEL-COOLANT INTERFACE

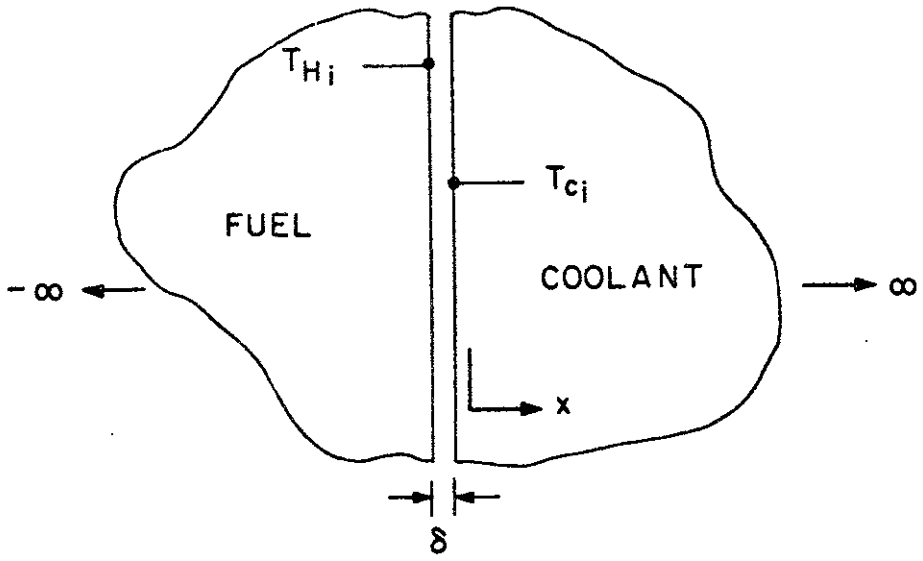

FIGURE 10.6

VALUES FOR DIMENSIONLESS COOLANT INTERFACE TEMPERATURE

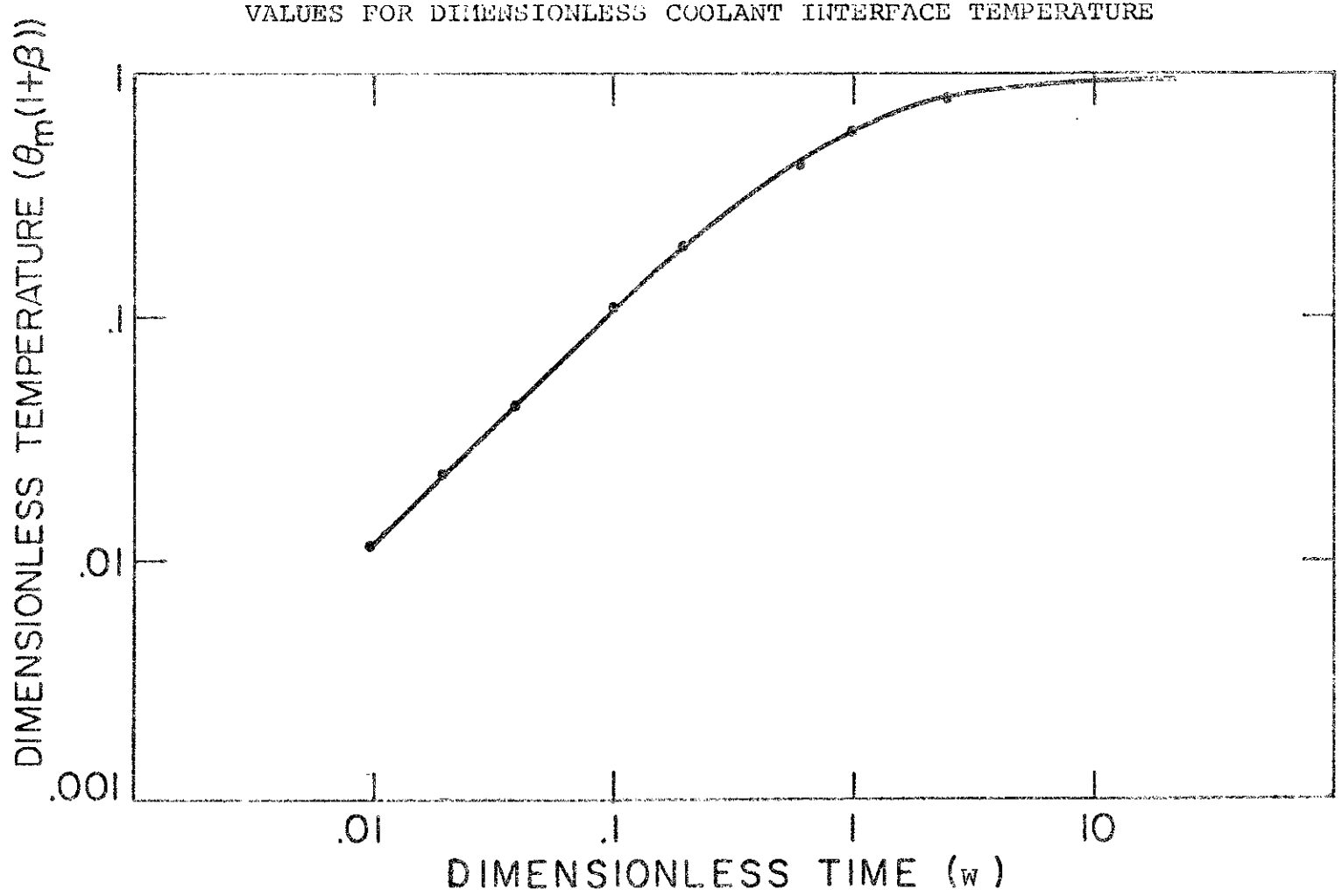

FIGURE 10.7

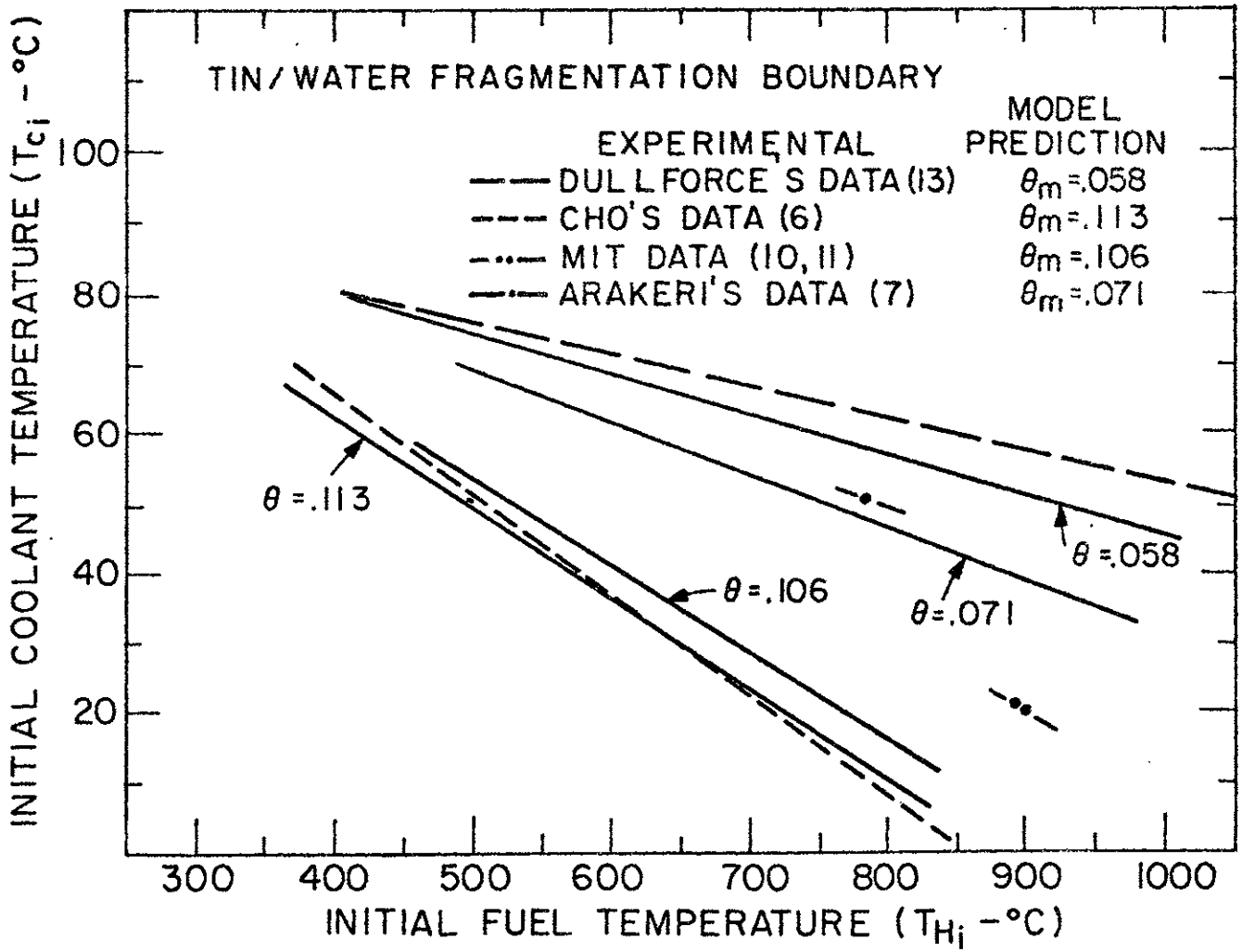
TIN/WATER FRAGMENTATION BOUNDARY
EXPERIMENTAL
MODEL PREDICTION
DULLFORCE'S DATA (13) θm=.058
CHO'S DATA (6) θm=.113
MIT DATA (10, 11) θm=.106
ARAKERI'S DATA (7) θm=.071
θ=.113
θ=.106
θ=.071
θ=.058
INITIAL COOLANT TEMPERATURE (Tci - °C)
INITIAL FUEL TEMPERATURE (THi - °C)
20
40
60
80
100
300
400
500
600
700
800
900
1000

FIGURE 10.8

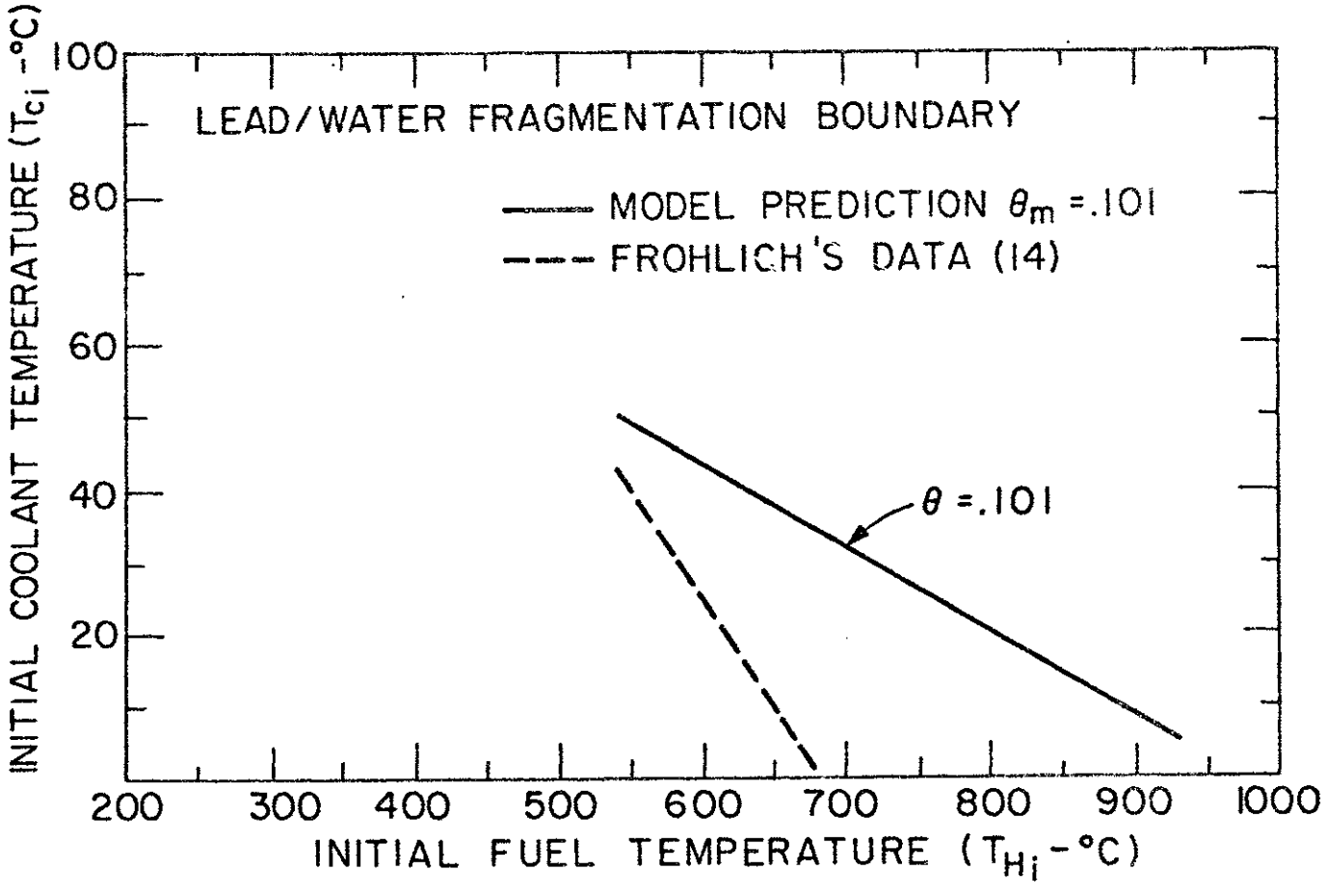
LEAD/WATER FRAGMENTATION BOUNDARY
MODEL PREDICTION θ_m =.101
FROHLICH'S DATA (14)
θ =.101
INITIAL COOLANT TEMPERATURE (T_{ci} -°C)
INITIAL FUEL TEMPERATURE (T_{Hi} -°C)
100
80
60
40
20
200
300
400
500
600
700
800
900
1000

FIGURE 10.9

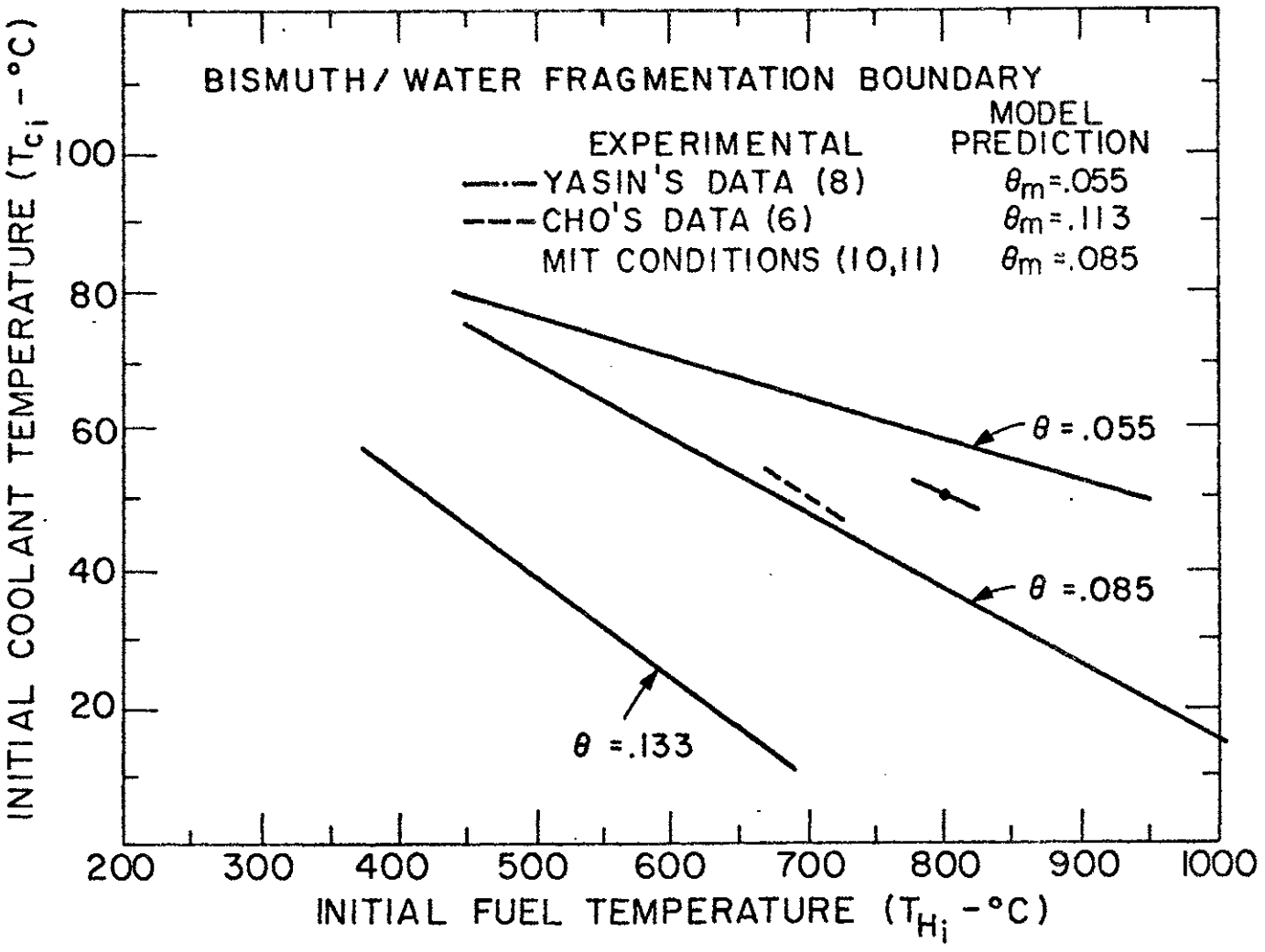
BISMUTH / WATER FRAGMENTATION BOUNDARY
EXPERIMENTAL
YASIN'S DATA (8)
CHO'S DATA (6)
MIT CONDITIONS (10,11)
MODEL PREDICTION
θ_m=.055
θ_m=.113
θ_m=.085
θ =.055
θ =.085
θ =.133
INITIAL COOLANT TEMPERATURE (T_{ci} - °C)
INITIAL FUEL TEMPERATURE (T_{Hi} - °C)
100
80
60
40
20
200
300
400
500
600
700
800
900
1000

FIGURE 10.10

RELATIVE ERROR BETWEEN θ_{exp} AND θ_m

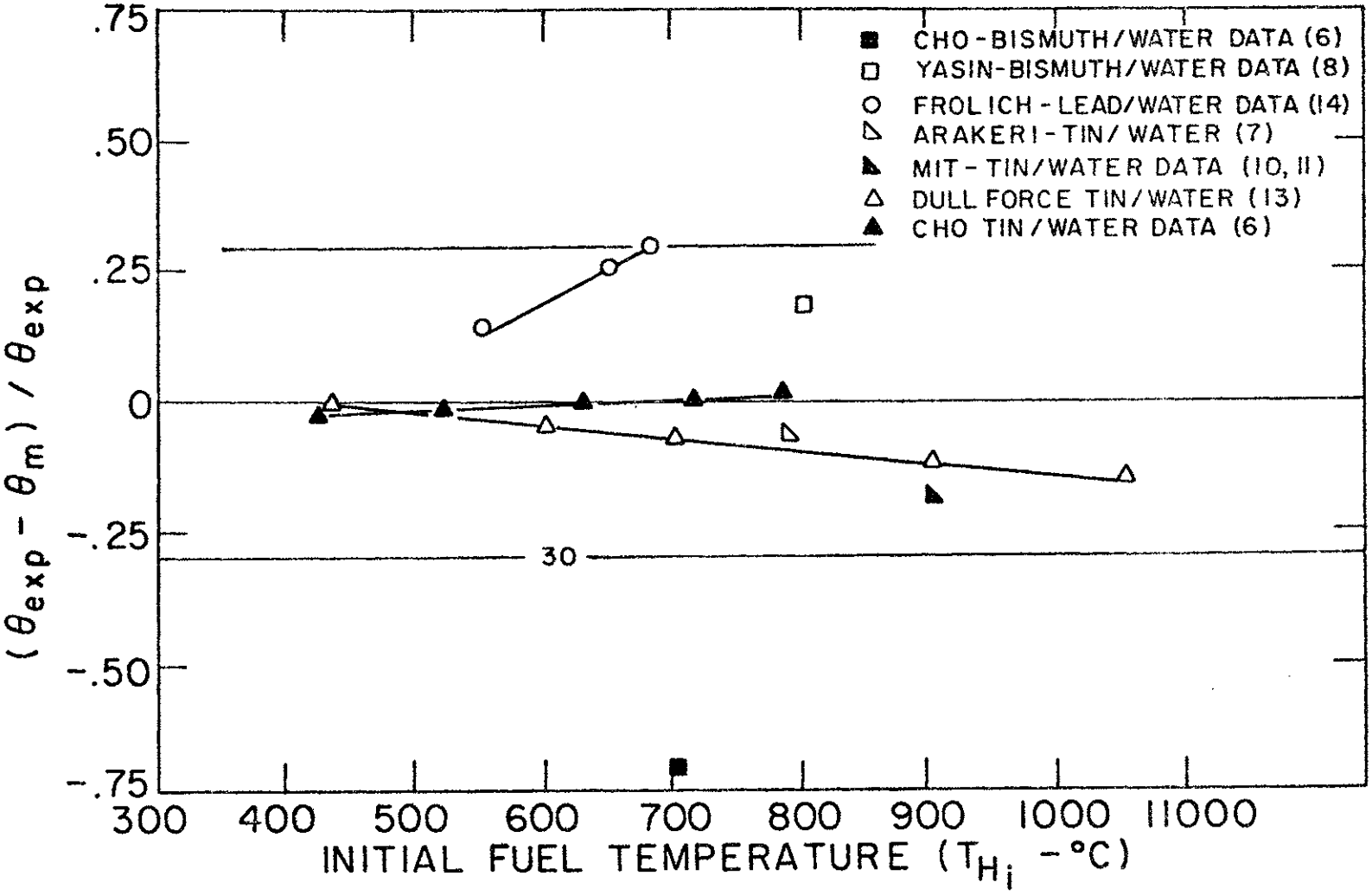

FIGURE 10.11

RELATIVE ERROR BETWEEN EXPERIMENTAL τ_{sat} VALUES AND CALCULATED τ_{coll}

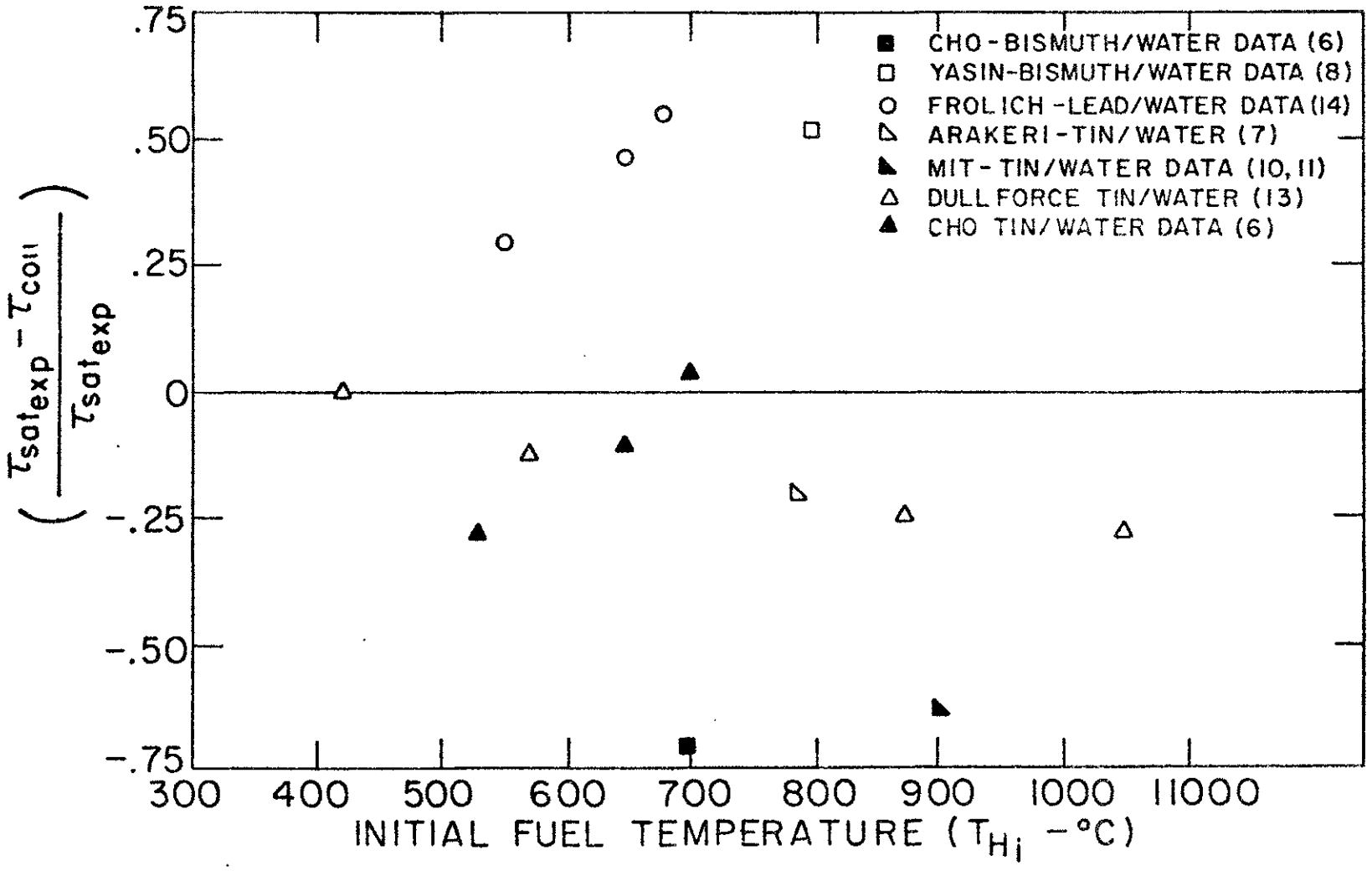

11. CONCLUSIONS AND RECOMMENDATIONS FOR FUTURE WORK CONCERNING MOLTEN FUEL-COOLANT INTERACTIONS (MFCI)

11.1 Conclusions

It has been experimentally observed that for some simulant materials (e.g. tin/water, bismuth/water, lead/water) random self-triggered interactions only occur in a specific region of fuel and coolant initial temperatures, for small scale experiments (fuel mass < 100 gm) in the drop mode of contact. The model presented in Chapter 10 for these interactions indicates:

1. The fuel surface temperature in the region where a self-triggered interaction begins is near or below the critical temperature of the coolant as investigated for the tin/water system (see Table 10.1). This analysis seems to be consistent with the upper boundary ($T_I < T_{crit}$) of the spontaneous nucleation theory of Henry [129] for a self-triggered interaction, although the bulk of the fuel mass is above this limit.

2. The upper diagonal cutoff on a T_{c_i} vs. T_{H_i} plot for these self-triggered interactions can be explained by the initial presence of a noncondensible gas film. This gas allows a thick stable film boiling regime to develop at a point when the characteristic time (τ_{sat}) for the coolant interface to heat up to T_{sat}, is less than the time (τ_{coll}) for the hydrodynamic collapse of the gas film. This breakpoint ($\tau_{sat} = \tau_{coll}$) is used in a model to predict the constant dimensionless temperature

$$\Theta_m = \frac{T_{sat} - T_{c_i}}{T_{H_i} - T_{c_i}}\ \text{model} = f(\tau_{sat}) \qquad (11.1)$$

where self-triggered framgentations cease. This prediction shows good agreement with molten metal/water data (see Figure 10.7) for the experimentally observed cutoff temperature

$$\Theta_{exp} = \frac{T_{sat} - T_{c_i}}{T_{H_i} - T_{c_i}}\ \text{experiments}$$

This proposed model implies that the phenomenon of the small-scale self-triggered interaction, although quite interesting academically, seems to be an anomalous event in relation to larger scale MFCI's. There are two reasons for this conclusion.

First, the proposed model indicates that as the scale of the system increases (i.e., larger fuel and coolant masses), the predicted boundary for self-triggered interactions rises to the saturation temperature of the coolant (i.e., $\Theta_m = 0$). This points out that at large system scales a self-triggered MFCI is always possible, regardless of the initial coolant temperature (T_{c_i}). The magnitude of the hot fuel temperature (T_{H_i}) in conjunction with T_{c_i} will determine if the MFCI is energetic (e.g. energetic MFCI if $T_I > T_{SN}$). Therefore, small-scale experiments are not well suited to investigate large-scale triggering events because of the possible anomalous results at large values of T_{c_i} or T_{H_i}.

The second reason is based upon the belief that realistic large-scale MFCI's will always have an external disturbance associated with them that could serve as the trigger to an interaction. Thus sole reliance or research into the self-trigger to generate an MFCI is not a prudent position for safety analysis. Random external triggers caused by ambient pressure changes,

pressure pulses (shocks) or solid surface phenomenon may be more realistic triggers and more effective in beginning an interaction. Investigations of these external trigger mechanisms and their relation to large and small MFCI's appears to be a more important avenue for future research.

11.2 Recommendations

To advance recommendations for future work in the area of MFCI's is a difficult task. At the present time, experimental research at various laboratories throughout the country and the world is continuing on this phenomenon (see Table 9.2) and not only in the nuclear industry (e.g. Aluminum, LNG industry). In r gard to a realistic assessment of the hazard of energetic MFCI's, the role of the university (particularly MIT) does not seem to be conducting integral experiments. Rather its most effective place lies in phenomenological modeling of the fuel-coolant interaction in its various phases, and some confirmatory experimentation for individual phenomena (see Table 11.1). There are three areas of work that I would recommend.

An initial requirement for an energetic MFCI that is recognized by a concensus of investigators [103,104,132] is coarse premixing of fuel and coolant. One method for coarse premixing is a film boiling regime between the fuel and coolant. However, the mechanism for this coarse premixing is in dispute (see Table 11.1). The spontaneous nucleation theory [132] identifies the spontaneous nucleation temperature ($T_{SN} \simeq T_{HN}$ for a well wetted system) as the minimum temperature (T_{min}) for film boiling in a liquid-liquid system and the temperature necessary to exceed for coarse premixing. Other investigators do not equate $T_{SN} = T_{min}$ and feel that T_{min} and coarse intermixing can occur below T_{SN}. Thus one useful task for the

future would be modeling film boiling and its destabilization for liquid-liquid systems. In conjunction with this some experimental work could be done to observe liquid-liquid film boiling behavior. Two important questions could be answered in conjunction with this work: (1) For various fluid pairs does T_{min} (defined traditionally as the point of $\dot{q}/A$ min) equal the spontaneous nucleation temperature of the coolant ($T_{SN} \simeq T_{HN}$); (2) Does the analysis and experimentation indicate any similarities between liquid-liquid film boiling and solid-liquid film boiling behavior. Initially a steady state experiment could be designed most likely in a planar geometry to observe the liquid-liquid film boiling. Molten metal/water fluid pairs as well as refrigerant (R-11, R-22)/oil pairs could be used to investigate the phenomena of wetability, coolant subcooling, ambient pressure variations, and liquid-liquid contacts (frequency, duration) during the film boiling process.

A second task concerning coarse intermixing would be to answer the question is film boiling the only mechanism for premixing. This general question can be refined to ask if a noncondensible gas can be used as a premixing mechanism for the fuel and coolant. Simple unheated experiments could be designed to inject fuel into the coolant to visually observe the intermixing behavior of fuel and coolant with and without the gas present. Heated experiments could repeat this process with the initial temperature combinations changed such that the $T_I = T_{SN}$ boundary is deliberately crossed. The resulting interaction could be monitored visually as well as with dwell time, and pressure measurements.

The final recommended task for future work involves modeling the trigger and propagation phase of a postulated MFCI together in a mechanistic and coherent fashion. At the present time, models do exist separately for both the trigger and propagation phase (see Table 11.1). The major drawbacks are:

1. Although the models for the trigger of large and small scale systems are based on physical mechanisms, there is no link at the present on how this trigger couples with the propagation phase to affect the environment (e.g. pressure-volume expansion, shockwaves, etc.).

2. Although the propagation models do have dynamic analysis and some work energy assessment of an MFCI, there exists no mechanism for the propagation in the models.

At the present time Board [7] contends that the key for efficient propagation is governed by rapid fragmentation and hydrodynamic mixing, while Fauske [98] seems to uphold the belief that spontaneous nucleation threshold is the necessary ingredient. However, neither theory has incorporated proposed mixing, fragmentation, and heat transfer mechanisms into a propagation and expansion model. Thus the need in the future in this area is to couple the mechanistic trigger with a mechanism for these processes, to assess the overall behavior of an MFCI. It is felt that the actual mechanism for coherent propagation is based on both rapid hydrodynamic mixing (Taylor Instabilities) and explosive boiling (spontaneous nucleation). Both processes must occur simultaneously and quickly ($\tau << 1$ msec) to allow for mixing and heat transfer, before the coolant and fuel can greatly expand stopping the energy transfer process.

These recommendations should be put into perspective in regard to the needs of reactor safety. For the LMFBR the thermophysical properties and initial conditions of UO_2 and sodium put the characteristic interface temperature below T_{SN} for sodium. Thus it is felt that the coarse intermixing phase is the first consideration here, not the propagation phase. For the LWR (and the LNG and molten metal/water industries), the thermo-

physical properties and initial conditions of UO_2 and water put the characteristic interface temperature much higher than T_{SN} and T_{crit} for water. The propagation phase is much more important for this safety application.

TABLE 11.1

PHENOMENOLOGICAL MODELING OF MFCI'S

A. COARSE INTERMIXING

SPONTANEOUS NUCLEATION THEORY - FAUSKE [132-134]

1. Small- & Large-Scale Systems
2. Coherent MFCI When $T_I > T_{SN}$
3. Empirically a Necessary Criterion for Energetic MFCI

Wet & Capture Model-Henry [129,130,135]

Splash Model-Bankoff [137]

T_{min} - MINIMUM FILM BOILING POINT - VAPOR COLLAPSE - [125]

1. Small-Scale Systems
2. Film Boiling Destabilization Causes Fragmentation
3. Hard to Verify Because $T_{min} \simeq T_{SN}$ so Effect Could be Masked

- IS FILM BOILING THE ONLY MECHANISM FOR COARSE INTERMIXING
- Exper. on Noncondensible Gas Effect on Premixing

- IS $T_{min} = T_{HN}$
- Exper. for Liquid-Liquid Film Boiling
- Model for Film Boiling Destabilization

B. TRIGGER

SELF-TRIGGER MFCI MODEL CORRADINI-PROPOSED-CHAP. 10

1. Small-Scale Systems
2. Upper Frag. Cutoff Expl. By Noncondensible Gases
3. Good Data Agreement Given Empirical Constant

GAS RELEASE/ACOUSTIC CAVITATION MODELS [124,112,113]

1. Small-Scale Systems
2. Dissolved Gas Triggers Frag. Perhaps Helped by Acoustic Pulse From External Press. Pulse
3. Data Shows Good Trend for Fe_xO_y Sandia Tests

C. PROPAGATION

DETONATION WAVE MODEL - BOARD - [136-139]

1. Large-Scale Systems Assuming Parts A&B
2. Coherent MFCI by Rapid Hydrodynamic Mixing
3. First Step in Propagation Modeling - No Proven Mechanisms for Propagation of a Coherent MFCI

Theofanous - Patel [138] contend Fragmentation By Taylor Instab.

Bankoff - Propagation Model [137]

PARAMETRIC MODELS FOR MFCI'S

1. Small-& Large-Scale Systems
2. No Mechanisms - Parametric
3. Can be Made To Fit Data

e.g. - Caldarola Model
- Cho-Wright Model

TRIGGER - PROPAGATION MODEL

- Given a Trigger (Random, Pressure, Shock, Gas Release, Cavitation)
- Trigger is Stochastic By Nature so Cannot Link with Premixing
- What is Role of Spontaneous Nucleation in Propagation

1. Area of Application
2. Essence of the Model
3. Experimental Verification and/or Technical Assistance

_____ PREVIOUSLY PROPOSED MODELS

_ _ _ RECOMMENDED FOR FUTURE

REFERENCES

(1) Reactor Safety Study, WASH - 1400, NUREG 75/014, October, 1975.

(2) Clinch River Breeder Reactor Plant Safety Study, Westinghouse Advanced Reactor Division, June, 1976.

(3) Cho, D.H., Epstein, M., "Work Potential from a Mechanical Disassembly of the Voided FFTF Core," ANL/RAS 74-17, Aug., 1974.

(4) Hicks, E.P., Menzies, D.C., "Theoretical Studies of the Fast Reactor Maximum Accident," Proc. of the Conf. on Safety, Fuels, and Core Design in the LMFBR, ANL-7120, 1965.

(5) Armstrong, D.R., Anderson, R.P., "R-22 Vapor Explosions," presented at the ASME Winter Annual Meeting, Atlanta, Ga., December, 1977.

(6) Reid, R.C., "Superheated Liquids: A Laboratory Curiosity and Possibly, and Industrial Curse," MIT Chem. Eng. Dept., submitted for publication December, 1977.

(7) Board, S.J., Caldarola, L., "Fuel Coolant Interaction in Fast Reactors," presented at the ASME Winter Annual Meeting, Atlanta, Ga., December, 1977.

(8) Final Safety Analysis Report, Fast Flux Test Facility, Energy Research and Development Administration, 1975.

(9) Preliminary Safety Analysis Report, Clinch River Breeder Reactor Plant, Energy Research and Development Administration, 1975.

(10) Charles Bell, Los Alamos Scientific Laboratory, private communication, October, 1977.

(11) Vaughn, G.J., Caldarola, L., Todreas, N.E., "A Model for Fuel Fragmentation During Molten Fuel-Coolant Thermal Interactions," Fast Reactor Safety Conference, Chicago, Illinois, October, 1976.

(12) Fauske, H.K., "On the Mechanism of Uranium Dioxide - Sodium Explosive Interactions," Nuclear Science and Eng., V.51, p. 95, 1973.

(13) Board, S.J., et al, "Detonation of Fuel-Coolant Explosion," Nature, V. 254, p. 319-321, 1975.

(14) Board, S.J., Hall, R.W., "An Explosion Propagation Mechanism," Proc. of the Second Specialist Meeting on Sodium - Fuel Interactions in Fast Reactors, Ispra, It., Nov., 1973.

(15) Armstrong, D.R., et al, "Interaction of Sodium with Molten UO_2 and Stainless Steel Using a Dropping Mode of Contact," ANL - 7890, Dec., 1971.

(16) Armstrong, D.R. et al, "Explosive Interaction of Molten UO_2 and Liquid Sodium," ANL-76-24, March, 1976.

(17) Fauske, H.K., Lecture at the MIT Summer Reactor Safety Course, July, 1977.

(18) Epstein, M., Cho, D. "Fuel Vaporization and Quenching by Cold Sodium; Interpretation of TREAT TEST S11," Proc. Fast Reactor Safety Meeting, CONF - 740401 - PL, Bev. Hills, April, 1974.

(19) Schmidt, T.R., "LMFBR Prompt Burst Excursion (PBE) Experiments in the Annular Core Pulse Reactor (ACPR)," Proc. Intl. Meeting on Fast Reactor Safety and Related Physics, CONF-761001, Chicago, Ill., October, 1976.

(20) Wright, T., Kress, T., Fuel Aerosol Simulation - Fast Plan, ORNL-NUREG-TN-129, 1977.

(21) Chang, Y.W., Gvildys, J., "REXCO-HEP. Hydrodynamic-Elastic-Plastic Computer Code for Fast Reactor Containment," ANL-73-24, 1973.

(22) Cagliostro, D.J., Florence, A.L., Characterization of an Energy Source for Modeling HCDA's in Nuclear Reactors, First Interim Report, PYU-1960, October, 1972.

(23) Florence, A.L., Abrahamson, G.R., Simulation of a HCDA in the Fast Flux Test Facility, Second Interim Report, PYU 1109, Nov., 1971.

(24) Florence, A.L., Abrahamson, G.R., Simulation of a HCDA in a Fast Flux Test Facility, Final Report, HEDL-SRI-1 May, 1973.

(25a)-(25j) Cagliostro, D.J., et al, "Experimental Studies in Reactor System Response to Core Disassembly Accidents," Quarterly Progress Report, No. 1 through 10, August, 1977.

(26) Ploeger, D. W., Cagliostro, D.J., Development and Characterization of a Liquid-Vapor Bubble Source for Modeling HCDA Bubbles, Technical Report 2, PYU-2939, March, 1977.

(27) Theofanous, T.G. et al, "LMFBR/HCDA Energy Field and Core Material Transport," presented at Fifteenth National Heat Transfer Conference, San Francisco, 1975.

(28) Christopher, D.M., Transient Development of a Two-Phase Jet, Master's Thesis, Purdue Univ., May, 1977.

(29) Chen, W.L., Cho, D.H., "Heat Loss to Cold Structure During a MFCI," ANL/RAS-73-9, April, 1973.

(30) Theofanous, T.G., Fauske, H.K., "An Energy Dissipation Mechanism Due to the Cladding of the Fission - Gas Plenum during an NCDA," ANL/RAS-72-31, Sept., 1972.

(31) Epstein, M., Private communication, June, 1976.

(32) Tobin, R., Private communication, October, 1977.

(33) Schlichting, H., Boundary Layer Theory, McGraw Hill Pub., New York, 1968.

(34) Ricou, F.P., Spalding, D.B., "Measurements of Entrainment by Axisymmetrical Turbulents Jets," Journal of Fluid Mechanics, V.11, p. 21, 1961.

(35) Chawla, T.C., "An Analysis of the Kevin-Helmholtz Instability at the Gas-Liquid Interface of Liquid-Submerged Sonic Gas Jets Relative to Fission-Gas Jet Impingement in LMFBR Subassemblies," ANL-8094, 1974 (as well as Journal of Fluid Mechanics, V. 67, Pt. 3, p. 513, 1975).

(36) Chawla, T.C., "Equations of Motion of a Liquid-Submerged Sonic Gas Jet Relative to Fission Gas Jet Impingement in Subassemblies of the LMFBR," Nuclear Science and Engineering, V. 53, p. 466, 1974.

(37) Chawla, T.C., "Rate of Liquid Entrainment at the Gas-Liquid Interface of a Liquid Submerged Sonic Gas Jet," Nuclear Science and Engineering, V. 56, p. 1, 1975.

(38) Bell, R. et al, Journal of the British Nuclear Energy Society, V 11, p. 183, 1972.

(39) Abramovich, S., Solan, A., "The Initial Development of a Submerged Laminar Round Jet," Journal of Fluid Mechanics, V. 59, p. 791, 1973.

(40) Taylor, G.I., "The Instability of Liquid Surfaces when Accelerated in the Direction Perpendicular to Their Planes I," Proceedings of the Royal Society of London, A, V. 201, p. 92, 1950.

(41) Bellman, R., Pennington, R.H., "Effects of Surface Tension and Viscosity on Taylor Instability," Quarterly Journal of Applied Math., V. 12, p. 151, 1954.

(42) Birkhoff, G., "Note on Taylor Instability," Quarterly of Applied Math., V. 12, p. 306, 1955.

(43) Birkhoff, G., "Stability of Spherical Bubbles," Quarterly of Applied Math., V. 13, p. 451, 1956.

(44) Nayfeh, A. H., "On the Non-Linear Lamb-Taylor Instability," Journal of Fluid Mechanics, V. 38, Pt. 3, p. 619, 1969.

(45) Daly, B.J., "Numerical Study of Two Fluid Rayleigh-Taylor Instability," Physics of Fluids, V. 10, No. 2., Feb., 1967.

(46) Daly, B.J., "Numerical Study of the Effect of Surface Tension on Interface Stability," Physics of Fluids, V. 12, No. 7, July, 1969.

(47) Kiang, R.L., "Non-Linear Theory of Inviscid Taylor Instability Near the Cutoff Wave Number," Physics of Fluids, V. 12, No. 7, July, 1969.

(48) Birkhoff, G., Taylor Instability, Report for LASL, No. LA-1862, 1954.

(49) Taylor, G.I., Davies, R.M., "The Mechanics of Large Bubbles Rising Through Extended Liquids and Through Liquids in Tubes," Proceedings of the Royal Society of London A, V. 200, p. 375, 1950.

(50) Lewis, D.J., "The Instability of Liquid Surfaces when Accelerated... II," Proceedings of the Royal Society of London A, V. 202, p. 81, 1950.

(51) Allred, J. et al, Experimental Studies of Taylor Instability, Report for LASL, No. LA-1600.

(52) Emmons, H.W., et al, "Taylor Instability of Finite Surface Waves," Journal of Fluid Mechanics, V. 7, p. 177, 1960.

(53) Cole, R.L., Tankein, R.S., "Experimental Study of Taylor Instability," Physics of Fluids, V. 16, No. 11, Nov., 1973.

(54) Rothrock, R., Kazimi, M.S., "Experimental Investigation of a Gas Jet Expansion in a Two-Dimensional Liquid Pool," to be published by MIT Dept. of Nuclear Engineering as NU-REG report, 1978.

(55) Holten, R.A., Heat Transfer Effects in the FFTF Scale Model Experiments, MIT-M.S. Thesis, Nuclear Engineering Dept., 1971.

(56) Corradini, M., Sonin, A.A., Todreas, N.E., "Proposed Model for Vapor Bubble - Slug Heat Transfer During LMFBR HCDA's, Trans. of the ANS, Vol. 26, p. 367, June, 1977.

(57) Corradini, M., Sonin, A.A., Todreas, N.E., Proposed Heat Transfer Model for the Gas-Liquid Heat Transfer Effects Observed in the SRI Scaled Tests, MIT-COO-2781-9TR, Dec., 1976.

(58) Sonin, A.A., MIT, Private communication, June, 1976.

(59) Rohsenow, W.M., Choi , H., Heat, Mass and Momentum Transfer, Prentice Hall, New York, 1961.

(60) Bird, R.B., Stewart, W.E., Lightfoot, E.N., Transport Phenomena, Wiley and Sons Pub., New York, 1960.

(61) Kreith, F., Principles of Heat Transfer, Wiley, New York.

(62) McAdams, W.H., Heat Transmission, McGraw-Hill, 1942, New York.

(63) Hottel, H.C., Sarofin, A.F., Radiative Transfer, McGraw Hill, New Jersey, 1967.

(64) Hinze, J.O., "Fundamentals of the Hydrodynamic Mechanism of Splitting in Dispersion Processes," A.I.Ch.E. Journal, V.1, No. 3, p. 289, 1951.

(65) Hinze, J.O., "Forced Deformations on Viscous Globules," Applied Scientific Research, V. A1, p. 263, 1948.

(66) Gordon, G.D., "Mechanism and Speed of Breakup of Drops," Physics of Fluids, V. 30, No. 4, No.11, 1969.

(67) Sonin, A.A., MIT, Private communication, October, 1977.

(68) Cagliostro, D.J., SRI, Private communication, October, 1977.

(69) Ozgu, R., Chen, J.C., "Local Film Thickness During Transient Voiding of a Liquid Filled Channel," ASME Winter Annual Meeting, Houston, 1975, 75-WA/HT-27.

(70) Carslaw, H.S., Jaeger, J.C., Conduction of Heat in Solids, Clarendon Press, Oxford, 1959.

(71) Mikic, B.J., MIT, Private communication, September, 1977.

(72) Henry, R.E., Fauske, H.K., "The Two-Phase Critical Flow of One-Component Mixtures in Nozzles, Orifice, and Short Tubes," Journal of Heat Transfer, V. 93, No. 6, May, 1971.

(73) Fauske, H.K., "Critical Two-Phase, Steam Water Flows," Proceedings of the Heat Transfer and Fluid Mechanics Institute, Stanford, Calif., Stanford Univ. Press, 1961.

(74) Lee, K., Ryley, R.I., "The Evaporation of Water Droplets in Superheated Steam," Journal of Heat Transfer, V. 90, p. 445, November, 1968.

(75) El-Wakil, M.M., "A Theoretical Investigation of the Heating-Up Period of Injected Fuel Droplets Vaporizing in Air," Technical Note 3179, Nat. Advisory Committee for Aeronautics, May, 1954.

(76) Chan, S.H., Univ. of Wisc. - Milw., Private communication, April & Aug., 1978.

(77) Cho, D.H., Chan, S.H., "Transient Energy Transfer by Conduction and Radiation for a Sudden Contact between Molten UO_2 and Sodium," ANL/RAS 77-51, November, 1977.

(78) Erdman, C.A., et al, "Condensation of Fuel onto the Above-Core Structure During an LMFBR CDA, "NUREG-0344, October, 1977.

(79) Rosner, D.E., Epstein, M., "Fog Formation Conditions Near Coal Surfaces," Journal of Colloid Interface Science, V. 28, p. 60, 1968.

(80) Toor, H.L., "Fog Formation in Boundary Value Problems," Al.Ch.E.Journal, V. 17, No. 1, p. 5, Jan., 1971.

(81) Theofanous, T.G., Fauske, H.K., "The Effect of Noncondensibles on the Rate of Sodium Vapor Condensation from a Single Rising HCDA Bubble," Nuclear Technology, V. 19, p. 132, 1973.

(82) Epstein, M., Cho, D.H., "Transient Phenomena at the UO_2 Vapor-Liquid Sodium Interface, "Transactions of Amer. Nuc. Soc., V. 18, p. 222, 1974.

(83) Chan, S.H., Cho, D.H., "A Calculational Method for Transient Radiation Heat Transfer in an Absorbing-Emitting Medium and its Application to LMFBR Accident Analysis," Trans. of Amer. Nuc. Soc., V. 21, p. 323, 1975.

(84) Epstein, M., Cho, D.H., "Fog Formation in Hypothetical LMFBR Accidents," Transactions of Amer. Nuc. Soc., V. 21, p. 324, 1975.

(85) Condiff, D.W., Chan, S.H., "Studies of Radiation - Controlled Fog Formation," Transaction of the Amer. Nuc. Soc., V. 22, p. 452, 1975.

(86) Cho, D.H., Argonne Nat'l. Lab., Private communication, June, 1968.

(87) Sedov, L.I., Similarity and Dimensional Methods in Mechanics, Academic Press, New York, 1959.

(88) Langhaar, H.L., Dimensional Analysis and the Theory of Models, Wiley New York, 1951.

(89) Bridgeman, P.W., Dimensional Analysis, Yale Univ. Press, New Haven, 1931.

(90) Long, G., "Explosions of Molten Aluminum in Water - Cause and Prevention," Metal Progress, V. 71, p. 107, May, 1957.

(91) Nelson, W., Kennedy, E.H., "What Causes Kraft Dissolving Tank Explosions," Paper Trade Jnl., July 16, 1950, July 23, 1956, p. 30.

(92) Nelson, W., "A New Theory to Explain Physical Explosions," Black Liquor Recovery Boiler Adv. Comm. Meeting, Atl., Ga., Oct., 1972.

(93) Thompson, T. J., "Accidents and Destructive Tests," The Technology of Nuclear Reactor Safety, Vol. 1, Ed. T. J. Thompson, J.G. Beckerley, MIT Press, Camb., Ma., 1964.

(94) Doerner, R.C. et al, "Final Summary of Fuel Dynamics Test H2 and E4," ANL 76-16, 1976.

(95) Wright, R.W. et al, "Summary of Autoclave Treat Tests on Molten Fuel Coolant Interactions," CONF-740401., p. 254, 1974.

(96) Barts, E.W. et al, "Summary and Evaluation - Fuel Dynamics Loss of Flow Experiments," ANL 75-57.

(97) Schmidt, T.R., "LMFBR Prompt Burst Excursion (PBE) Experiments in the Annular Core Pulsed Reactor (ACPR)," Conf. 76001, ANS/ENS meeting on Fast Reactor Safety, Chicago, October, 1976.

(98) Fauske, H., State of the Art on Fuel-Coolant Interactions, U.S.D.O.E., 1978.

(99) Camp, B., Sandia Lab., Private communication, 1978.

(100) Armstrong, D., et al, "Interaction of Sodium with Molten UO_2 and Stainless Steel Using a Drop Mode of Contact," ANL 7890, 1971.

(101) Armstrong, D. et al "Explosive Interaction of Molten UO_2 and Liquid Sodium," ANL 76-24, March, 1976.

(102) Henry, R.E. et al, "Experiments on Pressure Driven Fuel Compaction with Reactor Materials," CONF-761001, ANS/ENS meeting on Fast Reactor Safety, Chicago, October, 1976.

(103) Briggs, A.J., "Experimental Studies of Thermal Interactions at AEE Winfrith," Third Specialist Meeting on Sodium Fuel Interactions, Tokyo, PNC-N251, 76-12, 1976.

(104) Board, S.J., Hall, R.W., "Recent Advances in Understanding Large Scale Vapour Explosions," Third Specialist Meeting on Sodium Fuel Interactions, Tokyo, PNC-N251, 76-12, 1976.

(105) Henry, R.E. et al "Large Scale Vapor Explosion," CONF-740401-P3, Fast Reactor Safety Meeting, Beverly Hills, April, 1974.

(106) Board, S.J., et al "The Role of Spontaneous Nucleation in Thermal Explosions - Freon/Water Experiments," CONF-840401-P3, Fast Reactor Safety Meeting, Beverly Hills, April, 1974.

(107) Henry, R.E., Fauske, H.K., "Vapor Explosions and Simulant Fluids," CONF-761001, ANS/ENS Fast Reactor Safety Meeting, Chicago, October, 1976.

(108) Armstrong, D., Anderson, R. "R-22 Explosions," presented at ASME Winter Meeting, Dec., 1977.

(109) Segev, A., Henry, R.E., "Thermal and Hydrodynamic Interactions in Shocktube Configurations," ASME Winter Meeting, San Francisco, 1978.

(110) Wright, R.W., et al, "Kinetic Studies of Heterogeneous Water Reactors," USAEC Rep. STL 372-22 July, 1965, STL-30, 1965.

(111) Anderson, R.P., Bova, L., "Final Report on the Small Scale Vapor Explosion Experiment with Na Cl - H_2O System," ANL-76-57, 1976.

(112) Nelson, L. , Buxton, L., "Impulse Initiated Gas Release - A Possible Trigger for Vapor Explosions," Trans. of ANS, V. 26., June, 1977.

(113) Nelson, L., Buxton, L., "The Thermal Interaction of Molten LWR Core Materials with Water," Trans. of ANS, Vol. 26, June, 1977.

(114) Ivins, R.O. and Baker, L., "Chemical Engineering Division Semiannual Report, Jan.-June 1964" ANL-6900, 270-280, August, 1964.

(115) Swift, D. and Pavlik, J., "Chemical Engineering Division Semiannual Report, July-December 1965," ANL-7125, p. 187-193, May, 1966.

(116) Witte, L.C. et al, "Heat Transfer and Fragmentation During Molten Metal/Water Interaction," Journal of Heat Transfer, p. 251, November, 1973.

(117) Bradley, R.H. et al "Investigation of the Vapor Explosion Phenomena Using a Molten-Metal Jet Injection into Distilled Water" ORO-3936-7, October, 1971.

(118) Cho, D.H., Gunther, W.H., "Fragmentation of Molten Materials Dropped into Water," Reactor Development Program Progress Report, ANL, 1973.

(119) Arakeri, V.H. et al, "An Experimental Study of the Thermal Interaction for Molten Tin Dropped into Water," UCLA-ENG-7502, December, 1975.

(120) Yasin, J., "A Simulation of Thermal Phenomenon Expected in Fuel - Coolant Interactions in LMFBR's., UCLA-ENG-76100, September 1976.

(121) Board, S.J., et al, "Fragmentation in Thermal Explosions," International Journal of Heat and Mass Transfer, Vol. 17, p. 331, 1974.

(122) Bjornard, T.A., "An Experimental Investigation of Acoustic Cavitation as a Fragmentation Mechanism of a Molten Tin Droplet in Water" MIT-COO-2831-3TR, 1975.

(123) Bjorkquist, G.M., "An Experimental Investigation of the Fragmentation of Molten Metals in Water," TID-26820, 1975.

(124) Shiralker, Gautam, S. "An Investigation of the Fragmentation of Molten Metal Dropped into Cold Water," MIT-COO-2781-7TR, 1976.

(125) Dullforce, T.A. et al, "Self-Triggering of Small Scale Fuel-Coolant Interactions," CLM-P424, AKAEA Res. Group, 1975.

(126) Frohlich, G. et al, "Experiments with Water and Hot Melts of Metal," Journal of Non Equil. Thermodym., Vol 1, p. 91, 1976.

(127) Vaughn, G.J., Caldarola, L., Todreas, N.E., "A Model for Fuel Fragmentation During Molten Fuel/Coolant Thermal Interactions," Fast Reactor Safety Conference, Chicago, October, 1976.

(128) Morse, P.M., Ingard, K.L., Theoretical Acoustics, p. 240, McGraw Hill, New York, 1968.

(129) Henry, R.E., Fauske, H.K., "Energetics of Vapor Explosions," AICHE-ASME Heat Transfer Conference, San Francisco, August, 1975, 75-HT-66.

(130) Yao, S.C., Henry, R.E., "Hydrodynamic Instability Induced Liquid-Solid Contacts in Film Boiling," ASME-Winter Annual Meeting, Dec., 1976, 76-WA/HT-25.

(131) Ochai, M., Bankoff, S.G., "A Local Propagation Theory for Vapor Explosions," 3rd Specialists Meeting on Sodium - Fuel Interactions, Tokyo, March, 1976.

(132) Fauske, H.K., "On the Mechanism of Uranium Dioxide - Sodium Explosive Interactions," Nuclear Science and Engineering, V. 51, p. 95, 1971.

(133) Fauske, H.K., "Mechanisms of Liquid-Liquid Contact and Heat Transfer Related to Fuel-Coolant Interactions," EUR 5309, p. 201, Nov., 1973.

(134) Fauske, H.K., "Some Aspects of Liquid-Liquid Heat Transfer and Explosive Boiling," CONF 740401, April, 1974.

(135) Henry, R.E., Fauske, H.K., "Nucleation Characteristics in Physical Explosions," Third Specialist Meeting on Sodium Fuel Interactions, PNC-N251, 76-12, Tokyo, 1976.

(136) Williams, D.C., "A Critique of the Board-Hall Model for Thermal Detonations in UO_2-Na Systems," CONF-761001, ANS/ENS Fast Reactor Safety Meeting, October, 1976.

(137) Bankoff, S.G. et al, "On the Existence of Steady State Fuel-Coolant Detonation Waves," Third Specialist Melting on Sodium Fuel Interactions PNC-N251, 76-12, Tokyo, 1976.

(138) Patel, P.D., Theofanous, T.G., "Fragmentation Requirements for Detonating Vapor Explosions," PNE-78-122, Purdue University, Jan., 1978.

(139) Board, S.J. et al, "Detonation of Fuel-Coolant Explosions," Nature, V. 254, No. 5498, p. 319, March, 1975.

(140) Stevens, J.W., Witte, L.C., "Destabilization of Vapor Film Boiling around Spheres," Int. Journal of Heat and Mass Transfer, V. 16, p. 669, 1973.

(141) Tills, J.L. et al, "A Prediction of the Thermal Conductivity of UO_2 Vapor," Journal of Nuclear Materials, V. 67, p. 1, 1977.

(142) Golden, G.H., et al, "Thermophysical Properties of Sodium," ANL-7323, August, 1967.

(143) Chasanov, M.G., et al, "Chemical Engineering Div. - Annual Report July 1973 - June 1974," ANL-8120, June, 1974.

(144) Liebowitz, L. et al, "Properties for LMFBR Safety Analysis," ANL-CEN-RSD-76-1, April, 1976.

(145) Keenan, J., Keyes, L. Steam Tables, Wiley Co., New York, 1961.

(146) McNallon, M., "Fluid Dynamics and Mass Transfer in Vertical Submerged Gas Jets," Ph.D. Thesis, February, 1977.

(147) Tsai, S.S., Kazimi, M.S., "The Potential for Penetration of a Hot Vapor Jet into a Subcooled Liquid," 76-WA/H7-78, ASME Winter Annual Meeting, Dec., 1976.

(148) Miller, F., Probability and Statistics for Engineers, McGraw Hill, New York, 1970.

(149) Cronenberg, A.W., Coats, R.L., "A Comparison of Solidification Phenomena for UO_2, UC, and UN, Relative to Quenching in Sodium Coolant," Nuclear Engineering and Design, V. 25 , 1975.

(150) Arapaci, V.S., Conduction Heat Transfer, Addison-Wesley, New York, 1966.

(151) Kazimi, M.S. et al, "The Instantaneous Interface Temperature of Suddenly Contacting UO_2 and Sodium," Transactions of Amer. Nuc. Soc., V. 21, p. 321, 1975.

(152) Bolz, R.E., Ture, G.L., Editors, Handbook of Tables for Applied Engineering Science, CRC Press, Cleveland, 1976.

APPENDIX A

THERMODYNAMIC AND THERMOPHYSICAL PROPERTIES

PROPERTIES OF FULL SCALE FUEL-COOLANT SYSTEM

PROPERTY	UO_2	Ref	Sodium	Ref
Saturation curve	$P = \frac{1}{10}\exp(A - \frac{B}{T} - C\ln T)$ P - Pascals T - ^oK A = 69.979 B = 76800 C = 4.34 Menzies' Equation	(144)	$\log P = A - \frac{B}{T}$ P = atm. T = ^oK A = 10.40861 B = 12016.6	(142)
Heat of Vaporization h_{fg} - w-s/kg	$1.7(10^6)$	(144)	$2.9(10^6)$	(144)
Enthalpy h	$X_f h_{fg_f} + c_{l_f}(T_{sat} - T_{ref}) + h_{ref}$		$X_c[c_{p_g}(T_f - T_{sat}) + h_{fg_c}]$ $+ c_{l_c}(T_{sat} - T_{ref}) + h_{ref}$	
Specific Heat Ratio $\gamma = c_{pv}/c_{v_v}$	1.07	(143)	1.15	(144)
Gas Constant $R - \frac{w\text{-}s}{kg\,^oK}$	30.8		361	
Vapor Specific Heat $c_g - \frac{w\text{-}s}{kg\,^oK}$	503	(143)	2140	(142)
Vapor Thermal Cond. $k_g - \frac{w}{m\,^oK}$	.033 @ 5000^{o}K	(141)	.066	(142)
Vapor Viscosity μ_g - kg/m-s	$1.5(10^{-4})$	(78)	$2.1(10^{-4})$	(142)
Liquid Density ρ_l kg/m^3	8000	(144)	835	(142)
Liquid Specific Heat $c_l - \frac{w}{m\,^oK}$	550	(144)	1300	(142)

APPENDIX A (CONTINUED)

PROPERTY	UO_2	Ref	Sodium	Ref
Liquid Thermal Cond. $k - \frac{w}{m\,^oK}$	4	(144)	65	(142)
Liquid Surface Tension σ - nt/m	.475	(144)	.13	(144)
Heat of Fusion L_s $(\frac{w-s}{kg})$	280000	(144)		
CRITICAL PARAMETERS	8000^oK 200 MPa	(144)	2733^oK 41.5 MPa	(142)

$T_{melt} = 3073^oK$ $T_{HN} = 2100^oK$

APPENDIX A (CONTINUED)

PROPERTIES OF PETN EXPLOSIVE AND WATER

Property	PETN	Ref	Water	Ref (145)
Heat of Combustion $(\frac{cal}{gm})$	841	(24)	-	
Molecular Weight (gm)	161 explosive 28.8 gases	(34)	18	
Specific Heat of Gas (vapor) c_{p_g} $\frac{w-s}{kg\,^oK}$	1844 @ 3400^{o}K	(55)	2500	
Thermal Cond. of Gas (vapor) k_g $\frac{w}{m\,^oK}$	.240 @ 3400^{o}K .10 @ 1000^{o}K	(60)	-	
Viscosity of Gas (vapor) μ_g $\frac{kg}{m-s}$	$7.8(10^{-5})$ @ 3400^{o}K $3.9(10^{-5})$ @ 1000^{o}K	(60)	$1.6(10^{-5})$	
Gas Constant R_g - $\frac{w-s}{kg\,^oK}$	290		462	
$\gamma_g = c_{pv} / c_{v_v}$	1.2	(55)	1.3	
Heat of Vaporization h_{fg} - $\frac{w-s}{kg}$	-		$2.12(10^6)$@420^{o}K $1.66(10^6)$@534^{o}K	

APPENDIX A (CONTINUED)

		Tin*	Lead*	Bismuth*	Water	Ref(145)
Melt. Temp.	$T_{mel}(^{o}C)$	232	325	270	0	
Homogeneous Nuc. Temp.	$T_{HN}(^{o}C)$	---	---	---	305	
Critical Temp.	$T_{crit}(^{o}C)$	---	---	---	375	
Sat. Temp. @ 1MPa	$T_{Sat}(^{o}C)$	---	---	---	100	
Thermal Cond. of liquid	$k(\frac{w}{m^{o}K})$	32.5	15	15	.62	
Density of liquid	$\rho(^{kg/}_{m}3)$	6800	10250	9700	1000	
Specific Heat of liquid	$c(\frac{w-s}{kg^{o}K})$	250	150	150	4184	
Surface Tension	$\sigma(^{nt}/m)$	.495	.423	.352	.073	

*Ref. 61

Thermal conductivity of gas film (k_g) = .035 $^{w}/m^{o}K$

APPENDIX B

TAYLOR INSTABILITY EXPERIMENT - APPARATUS AND DATA REDUCTION

The Taylor Instability experiment which was discussed in Chapter 3 was fashioned after the design principle of Lewis' experiment [50]. The major reason for this was that the experimental designs of Emmons [52] and Cole [53] did not seem adaptable to the high accelerations (100 - 1000g) that the instability behavior was to be observed at. The basic intent was to build an experimental apparatus that was simple and could be used to investigate the instability growth behavior as a function of high accelerations and develop an entrainment model based upon the results. The geometry chosen was a rectangular channel (Figure B.1), where the width (12.7 cm) was made much larger than the critical wavelengths of the planned accelerations and the thickness (1.9 cm) was kept small to aid in visually observing the growth of the instabilities. More detailed drawings of the apparatus, including dimensions are given in Figures B.2 to B.4.

The principle of operation was quite simple. The liquid slug to be accelerated was held in the upper chamber by an aluminum foil sheet and air was introduced on both sides of it. The upper air-liquid interface was given an initial standing wave of some known wavelength, and then accelerated by a pressure difference downward through the lower chamber where hi-speed photographs could be taken to view the growth behavior of the instability. The standing wave was imposed by a motorized paddle. The pressure difference was created with the use of a double rupture disk assembly. The upper and lower chambers were both pressurized to the initial high pressure and the space between the rupture disks to half this value. The experiment was started by opening a solenoid valve which depressurized the space between

the rupture disks, and because neither disk could support the entire pressure difference between the chamber and the ambient, both break simultaneously and create a rarefaction wave ($\sim 10^{-4}$ sec). The lower chamber is then depressurized by this rarefaction wave as it travels up the channel. This sets up the initial pressure differential across the liquid slug causing it to break the foil and be accelerated downward as the instability grows on the upper surface.

The materials used in the construction of the apparatus were carbon steel rectangular posts and plates as the structural members and plexiglas as the transparent material for the viewing windows. As Figures B.2 and B.3 indicate, the upper and lower chamber is composed of welded rectangular steel posts which form the frame for the plexiglas windows. The windows are attached by simply drilling holes through the steel and plexiglas, and bolting the windows on either side of the steel in a "sandwich" configuration. Paper gasket seals are inserted between the steel and plastic to assure pressure integrity at high pressures (~200psia). The inner rectangular channel does not have any projections or protusions that would disturb the passage of the liquid. The plexiglas is milled to exactly fit the steel frame form. The lower double rupture disk assembly and rupture disks are a manufactured unit purchased from the Fike Company in St. Louis, Missouri. Replacement disks are also purchased from Fike. Each rupture disk is rated at a specific bursting pressure determined at the factory and has an error estimated at 5-10% with a failure rate of 10%. Both of these specifications are furnished by the company.

The steel chamber above the upper plexiglas viewing chamber contains the motor and paddle which are used to give the initial standing wave to the liquid. A Bodine motor turns a camshaft which generates an oscillatory

motion in the paddle creating the standing waves. The size of this initial wavelength (λ_i) can be adjusted by changing the rpm of the motor. This is easily accomplished by the use of a rheostat to control the supply voltage to the motor. This upper volume is large enough to also serve as a pressure reservoir so that during the experiment the high pressure does not decrease rapidly, and thus provides a near constant value of acceleration to the liquid slug.

The parameters of interest in the experiment are: (1) the distance traveled by the liquid slug (D_t) to determine velocity and acceleration (a); (2) the growth behavior of the instability measured by the change in the depth of the water slug with time ($\Delta d_i = d_i - d$, d_i - initial depth, d - depth at any time). The experiment is photographed by a Hy-Cam Hi-speed Movie Camera (~5000 frames/sec) to visually measure these quantities, and an internal timer in the camera automatically marks the film at set intervals (every msec) to synchronize the distance measurements. The camera also contains an internal electrical circuit which is used to start the experiment by opening the solenoid valve between the rupture disks at a prescribed point during the filming.

One particular problem that was experienced in these tests was the high failure rate and the unpredictability of the breaking characteristics of the foil and the rupture disks. Forty tests were attempted but only twenty-three of these tests gave adequate results to identify them as a success, and include them as part of the data base. In fact, two of these runs (see Table B.1) #5 and #15, did show some signs that these starting mechanisms interfered with the results. These two runs can be used as prime examples of some of the adverse starting characteristics of this experiment which can affect the results.

In every experimental run the test starts by the breaking of the pair of rupture disks almost simultaneously and then the foil supporting the liquid slug. If the rupture disks do not break cleanly, then the lower chamber will not depressurize as fast as it should, thereby lowering the acceleration. In addition, the acceleration can increase dramatically once the chamber is further depressurized by another rarefaction wave and the slug is partially down the channel. This appears to be one of the factors in the results of Run #5. The observed acceleration was low (140g = a) yet the initial pressure and liquid depth should have produced an acceleration near 500g. The foil can also break unevenly which gives the liquid slug an uneven acceleration. This occurs because some of the liquid is ejected before the foil breaks completely, and the instability growth is affected. Therefore, it is unclear what is the penetration velocity of the instability or what is the proper reference point to measure the acceleration (Figure B.5). This uneven foil breakage is the major fault observed in Runs #5 and #15. The foil initially breaks in one region (near the wall) and not the other. Subsequently, the whole foil breaks but now the lower surface is uneven. Only after these effects have damped out and the slug lower interface is essentially flat can the data be considered useful. Most runs with this problem could not be analyzed. A number of materials were tested as the support membrane for the liquid slug; waxed paper, plastic wrap, thick aluminum sheets, Mylar plastic sheets of various thicknesses. However, only the aluminum foil membrane worked with any amount of success.

The inherent error in the visual measurement of the distances and times for the experimental runs can be estimated by the experience of the observer. Because the timing mechanism is internal to the camera and its

accessories it is not expected that the error is large (<1%). The major error in this experiment is in the visual measurement of the travel distance (D_t) and the penetration depth ($\Delta d_i = d_i - d$). The distance measurement marks are at 1/2 inch spacings on the apparatus; therefore, the maximum error is 1/2 inch ($s_e \simeq 1/2"$) over a total distance of 10" (~5%) for the slug travel distance, and 2" - 6" (8-25%) for the water depth. The error then in the determination of the acceleration (a) and the instability penetration velocity (v_r) can be estimated by propagation of the error in the functions

$$a \simeq \frac{2D_t}{t^2} \tag{B.1}$$

$$v_r \simeq \frac{\Delta d}{t} \tag{B.2}$$

where

$$D_t = \bar{D}_t \pm s_{e_D}^2$$

$$\Delta d = \Delta d \pm s_{e_{\Delta D}}^2$$

$$\text{and } s_{e_t}^2 = 0.$$

The principle of propagation of errors is

$$s_{e_f}^2 = \sum_i \frac{\partial f_i}{\partial x_i} s_{e_{x_i}}^2 \tag{B.3}$$

where

$$s_{e_a}^2 \simeq s_{e_D}^2 \left[\frac{\bar{a}}{\bar{D}_t}\right]^2 \tag{B.4.1}$$

$$s_{e_{v_r}}^2 \simeq s_{e_{\Delta d}}^2 \left[\frac{\bar{v}_r}{\bar{\Delta d}}\right]^2 \tag{B.4.2}$$

The data was recorded by replaying the film of the experiment and measuring the distances as a function of the time marks. Again, the travel distance (D_t) and the relative penetration distance of the instability were

measured ($d_i = d_i - d$). These quantities are plotted as a function of time and shown in Figures B.6 to B.27. The measurements were repeated on two different occasions to minimize the possibility of random errors.

To determine the average acceleration $(\bar{a})$ and the penetration velocity of the instability $(\bar{v}_r)$ for each run, two different methods were used. First, the travel distance was plotted as

$$\sqrt{2D_t} \text{ vs } \Delta t \tag{B.5}$$

and the change in the water slug depth as

$$\Delta d_i \text{ vs } \Delta t \tag{B.6}$$

The quantities $(\bar{a})^{\frac{1}{2}}$ and $(\bar{v}_r)$ are the slope of these plots and can be estimated by a simple calculation. The second method was to fit each set of data for each run with a least squares fit assuming the functional form of (a) and (v_r) to be

$$D_t = C\ t^m \tag{B.7}$$

$$\Delta d_i = D\ t^o \tag{B.8}$$

The principles of least squares is outlined in Reference 148. The constants (C, D, m, o) were determined statistically by averaging the data. The equations were represented as

$$\log(D_t) = \log C + m \log t \tag{B.9}$$

$$\log (\Delta d_i) = \log D + o \log t \tag{B.10}$$

This is of the form of the linear equation

$$y = A + B\ x \tag{B.11}$$

The partial differences were found by the formulas [148]

$$S_{xx} = n \sum_{i=1}^{n} x_i^2 - \left(\sum_{i=1}^{n} x_i \right)^2 \tag{B.12}$$

$$S_{yy} = n \sum_{i=1}^{n} y_i^2 - \left(\sum_{i=1}^{n} y_i \right)^2 \qquad \text{(B.13)}$$

$$S_{xy} = n \sum_{i=1}^{n} x_i y_i - \left(\sum_{i=1}^{n} x_i \right) \left(\sum_{n=1}^{n} y_i \right) \qquad \text{(B.14)}$$

where n is the number of data points for each run. The values of m and o are found by

$$B = \log (m \text{ or } o) = S_{xy}/S_{xx} \qquad \text{(B.15)}$$

The value of C and D are found by

$$A = \bar{y} - B\,\bar{x} = \log (C \text{ or } D) \qquad \text{(B.16.1)}$$

where

$$\bar{y} = \frac{1}{n} \sum_{i=1}^{n} y_i \text{ (same for } \bar{x}) \qquad \text{(B.16.2)}$$

Now the acceleration ($\bar{a}$) and instability penetration velocity ($\bar{v}_r$) is given by

$$\bar{a} = \frac{\frac{dD_t}{dt}/t_f - \frac{dD_t}{dt}/t_o}{t_f - t_o} \qquad \text{(B.17)}$$

$$\bar{v}_r = \frac{\Delta d(t_f) - \Delta d(t_o)}{t_f - t_o} \qquad \text{(B.18)}$$

where t_f is the time at the end of the experiment and t_o is the start of the experiment. Both methods gave similar results and the statistically average results are reported in Chapter 3.

This same method can be used to determine the functional dependence of $\bar{v}_r$ on $\bar{a}$ by assuming a form of the equation

$$\bar{v}_r = C\,\bar{a}^{\,m} \qquad \text{(B.19)}$$

and the logarithm is again taken to give

$$\log \bar{v}_r = \log C + m \log \bar{a} \qquad \text{(B.20)}$$

$$y = a + bx$$

The same procedure is followed to find the empirical constants (C, m). To determine the statistical confidence interval (95%) for these constants, the equations below were used: (1) The variance is given by [148]

$$s_e^2 = \frac{S_{xx}S_{yy} - (S_{xy})^2}{n(n-2)S_{xx}} \tag{B.21}$$

(2) The constants are known within a range of values given by

$$b \pm t_{\alpha/2}\, S_e \frac{S_{xx} + n\bar{x}}{nS_{xx}} \tag{B.22}$$

$$a \pm t_{\alpha/2}\, S_e \sqrt{\frac{n}{S_{xx}}} \tag{B.23}$$

where $t_{\alpha/2}$ is the 95% confidence interval coefficient assuming the statistical distribution for C and m are normal distributions. The results of these least square fits to the data are given in Table 3.3.

RUN	Film Sp(fps)	Time Sp(mps)	P_{max}(MPa)	λ_i(cm)	λ_{o_e}(cm)	d_i(cm)	d_e(cm)	$\bar{v}_r$	$\bar{a}$
2	2500	1000	.405	1.27	4.45	6.35	.95	827	442
3	4500	1000	.432	1.27	5.72	11.43	1.91	1100	439
4	4500	1000	.678	1.27	5.08	13.97	1.43	1063	511
5	4500	1000	.652	--	6.99	11.43	.94	1200	143
6	4900	1000	.680	.64	4.45	10.16	5.72	860	380
7	4500	1000	.687	.64	3.18	8.89	1.91	969	778
8	4750	1000	.687	.64	4.45	7.62	2.14	650	132
9	4500	1000	.687	.64	4.76	6.35	1.19	1190	994
10	4750	1000	.653	2.54	6.35	15.24	8.10	670	103
11	4900	1000	.673	2.54	6.35	10.16	2.54	950	527
12	5000	1000	.667	2.54	4.45	6.35	1.91	537	215
15	5000	1000	.639	1.27	5.08	15.24	--	450	148
16	4000	1000	.653	1.27	7.62	10.48	1.91	687	380
17	3500	1000	.687	1.27	5.08	6.67	1.43	1085	1021
18	3800	1000	.667	1.27	6.99	12.7	2.86	760	135
19	3500	1000	.660	2.54	5.40	12.7	1.43	926	631
20	4000	1000	.653	2.54	5.08	8.26	1.43	1300	1425
21	3800	1000	.660	1.27	5.08	8.26	1.43	868	227
22 G	4000	1000	.653	1.27	5.08	7.62	.48	472	150
23 G	4000	1000	.653	1.27	6.99	12.07	2.86	455	120
25	5000	1000	.391	1.27	5.08	6.99	0	400	117
26 P	5000	1000	.391	1.27	3.81	6.99	1.19	455	126
27 P	5000	1000	.391	1.27	5.08	10.48	.95	580	75

G - AIR - GLYCERINE
P - AIR - PHOTOFLOW

TABLE B.1

SUMMARY OF RESULTS FOR THE TAYLOR INSTABILITY EXPERIMENT

FIGURE B.1 EXPERIMENTAL APPARATUS

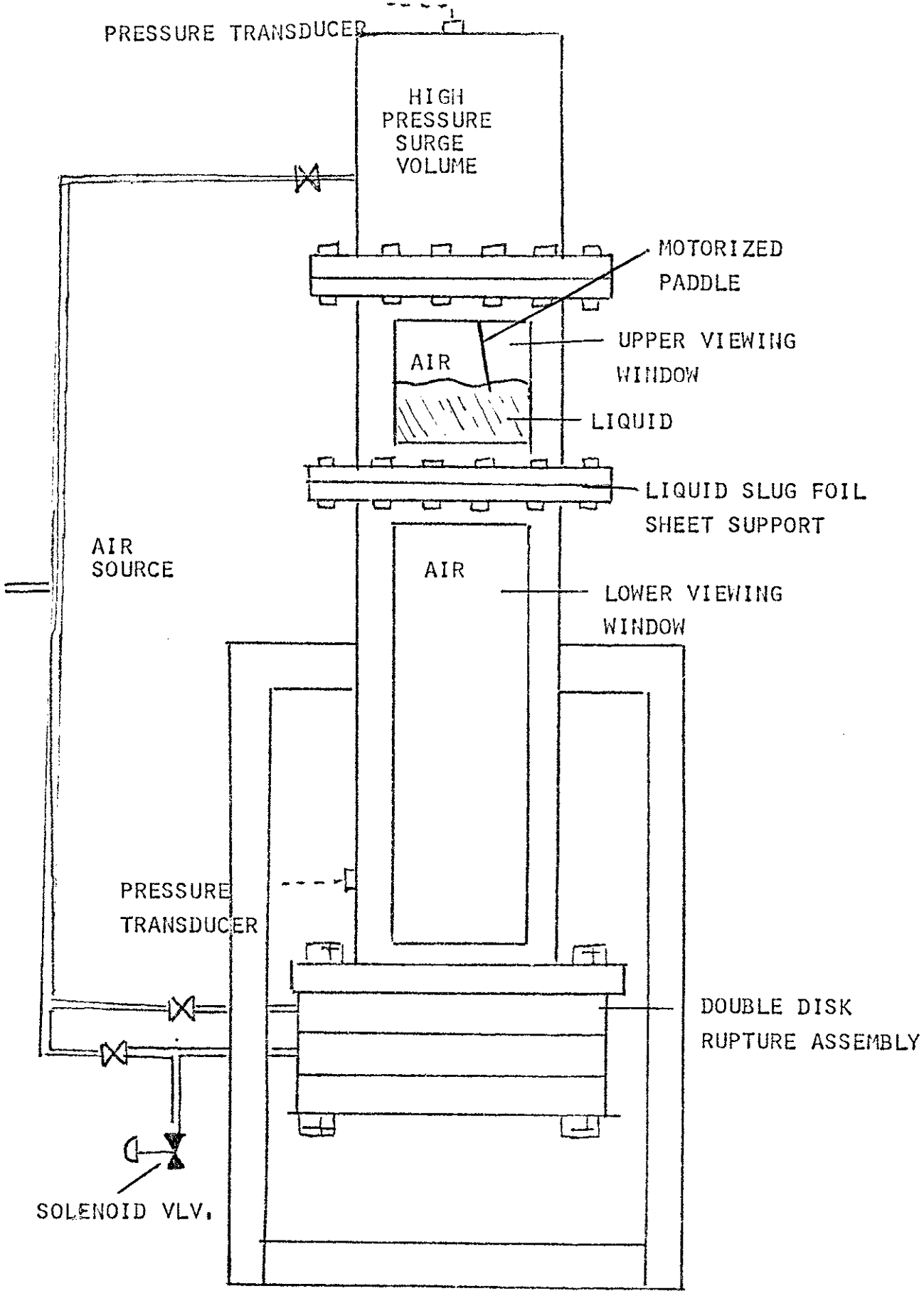

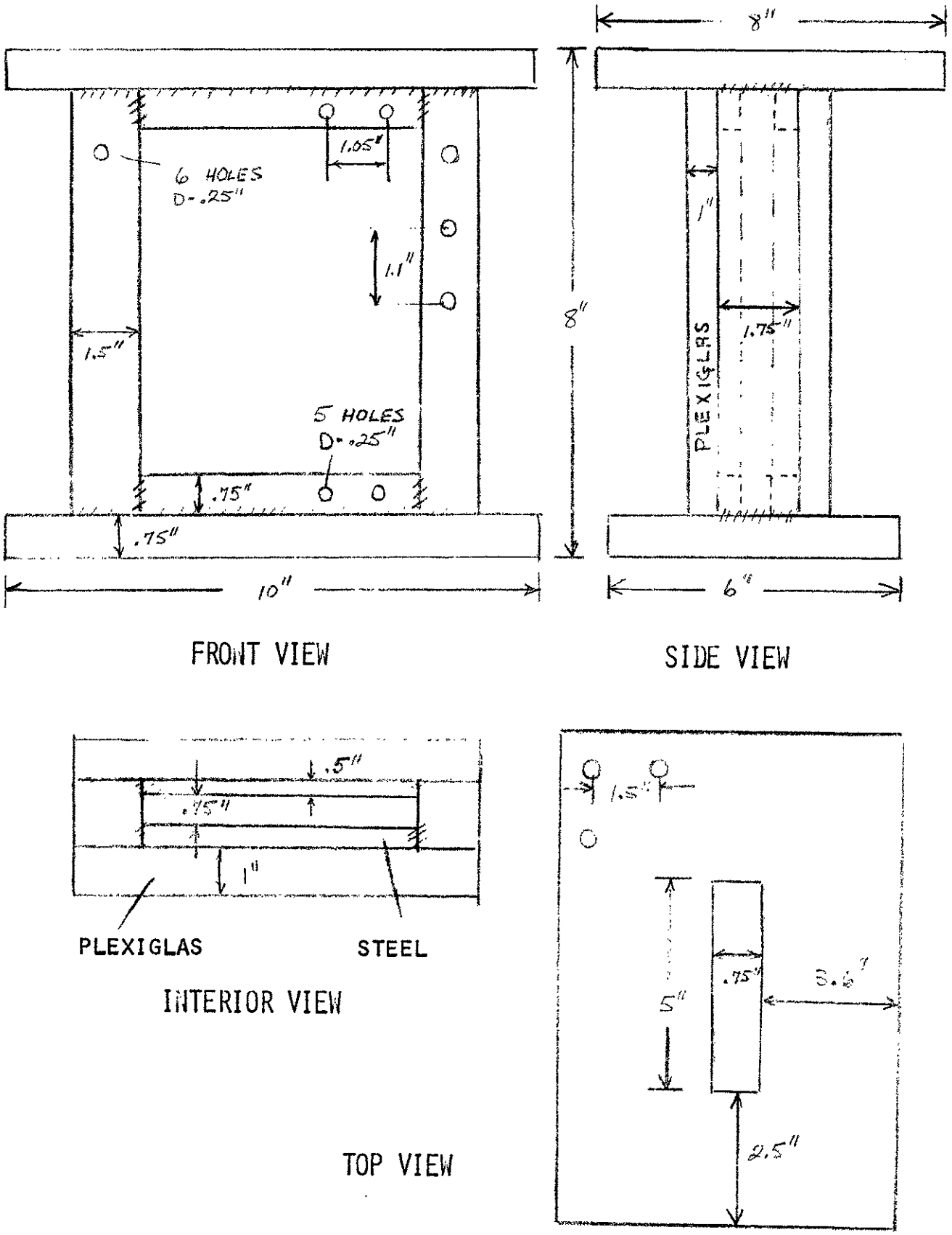

FIGURE B.2 TOP ASSEMBLY SCHEMATIC PICTURE

FIGURE B.3 LOWER ASSEMBLY SCHEMATIC PICTURE

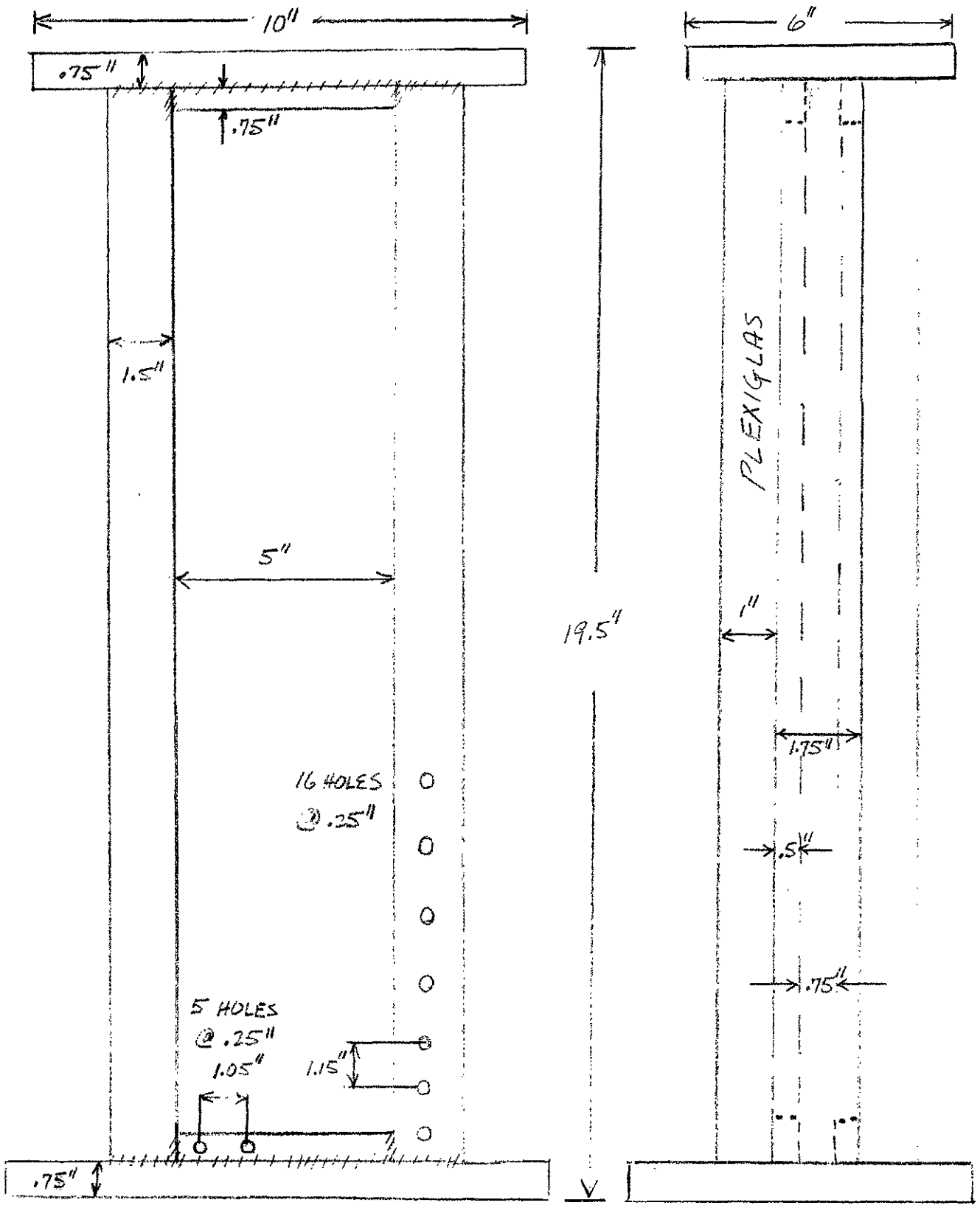

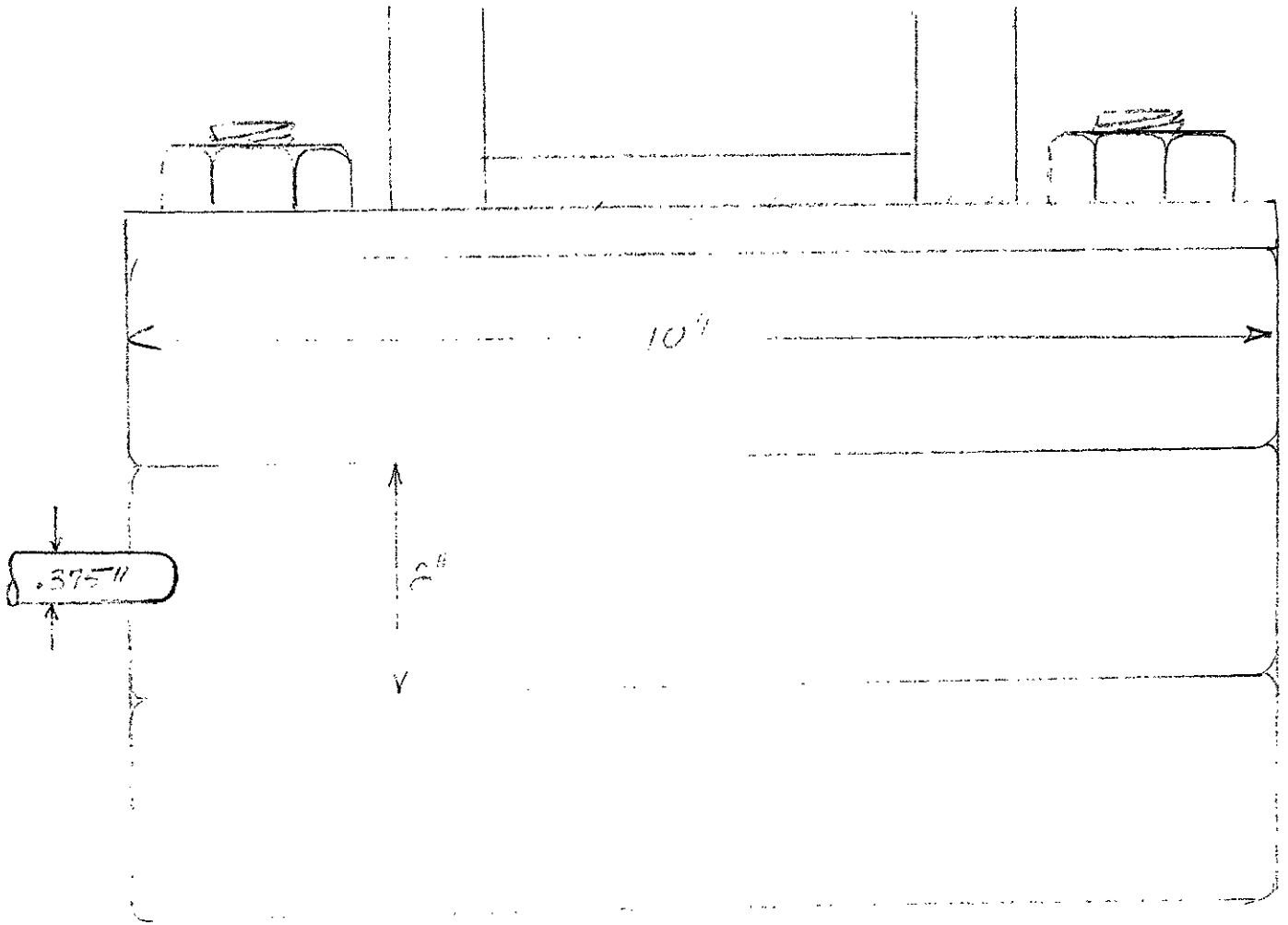

DOUBLE RUPTURE DISK ASSEMBLY

FIGURE B.4

FIGURE B.5

EXPERIMENTAL BEHAVIOR FOR IMPROPER FOIL BREAKAGE

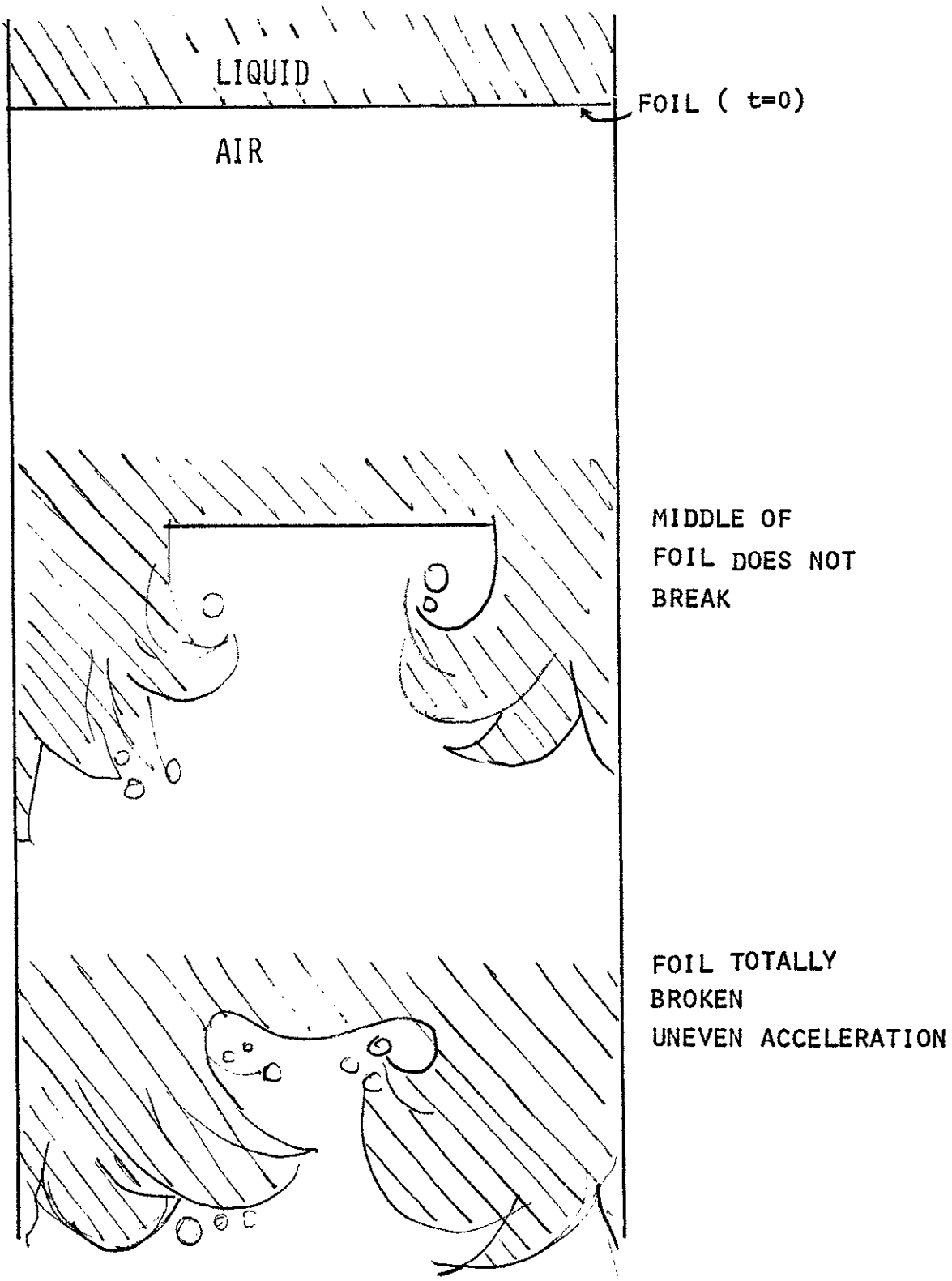

FIGURE B.6

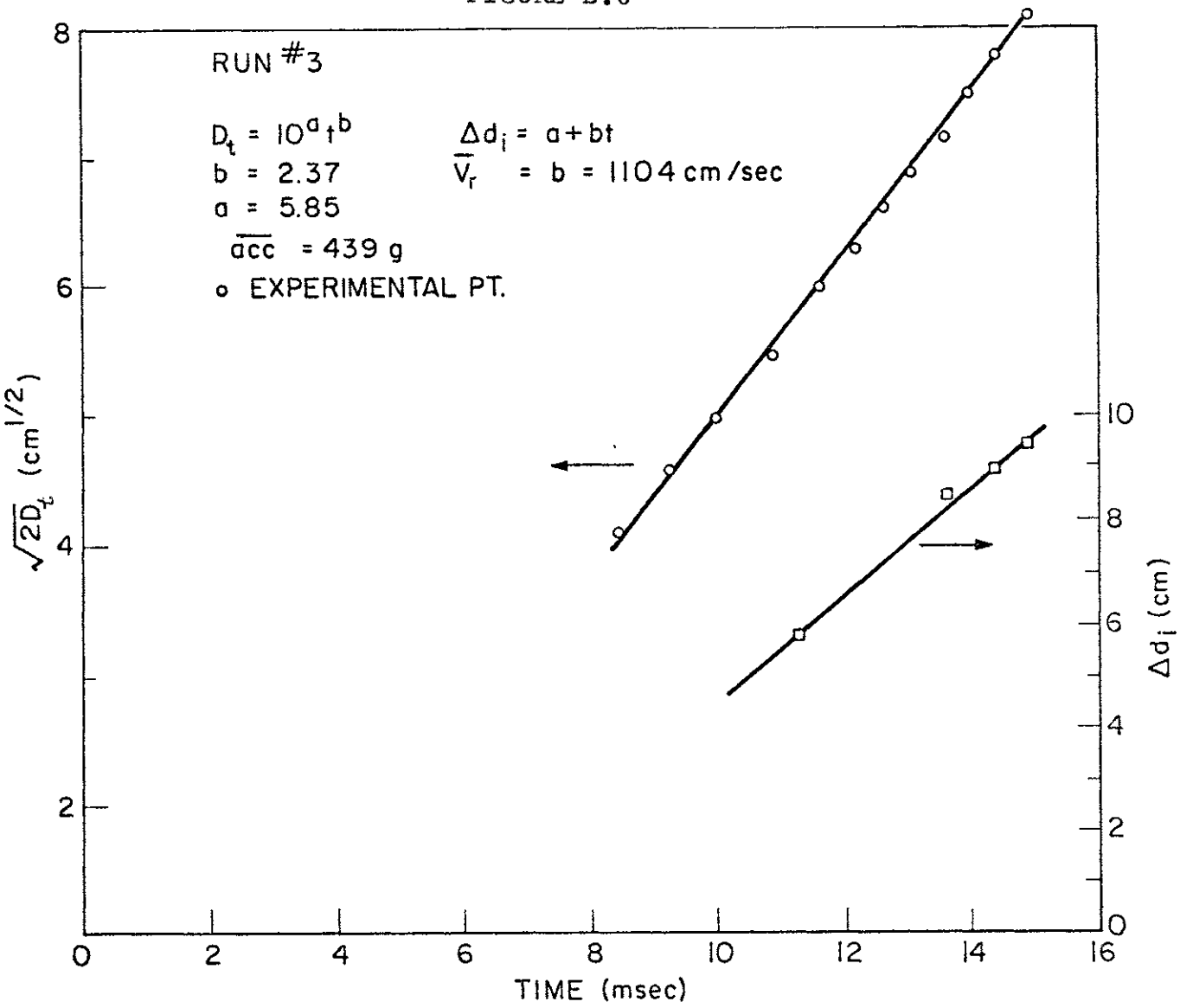
RUN #3
$D_t = 10^a t^b$
b = 2.37
a = 5.85
$\overline{acc}$ = 439 g
o EXPERIMENTAL PT.
$\Delta d_i = a + bt$
$\overline{V_r}$ = b = 1104 cm/sec
$\sqrt{2D_t}$ (cm$^{1/2}$)
Δd_i (cm)
TIME (msec)
0
2
4
6
8
10
12
14
16

FIGURE B.7

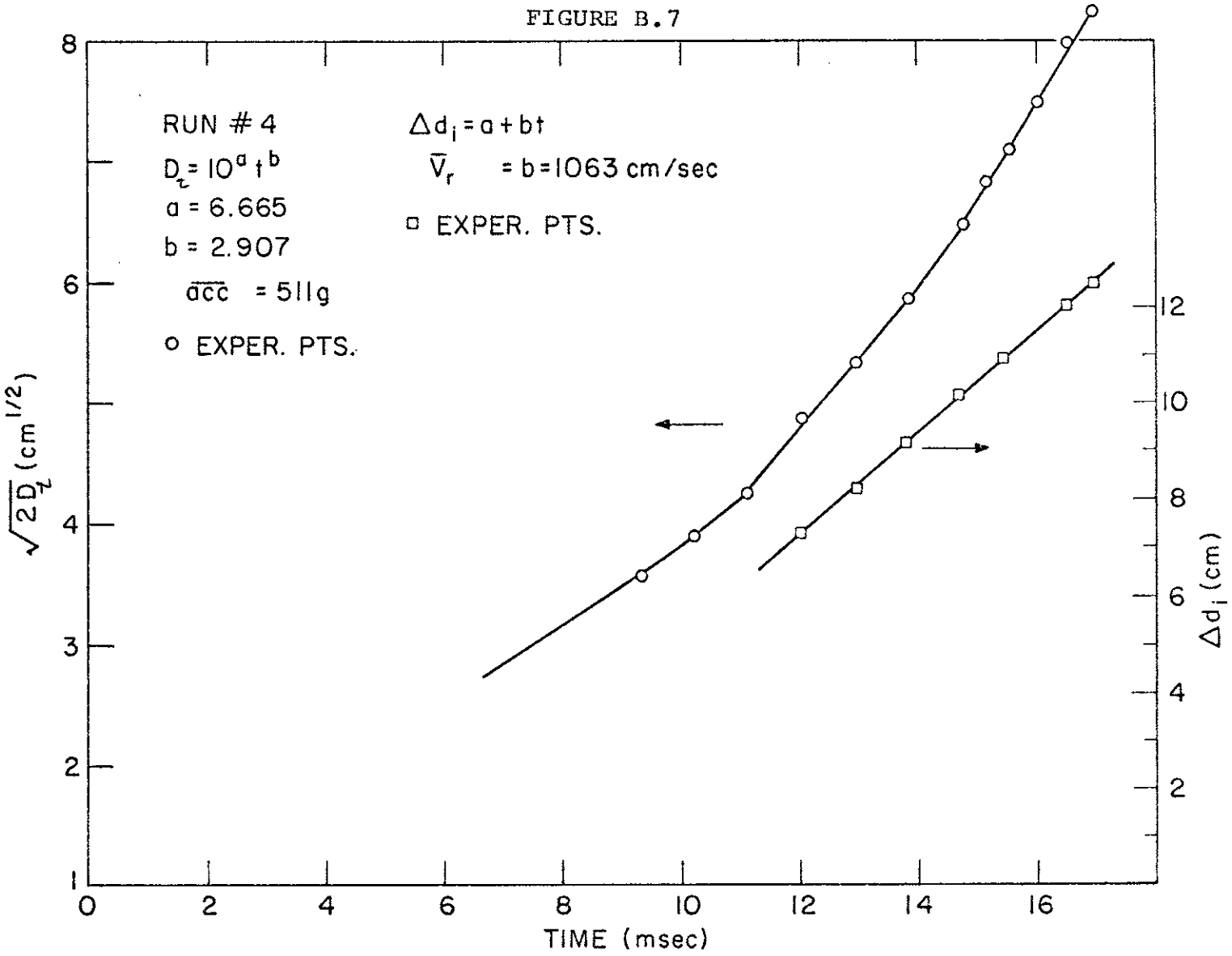
RUN # 4
$D_z = 10^a t^b$
a = 6.665
b = 2.907
$\overline{acc}$ = 511g
○ EXPER. PTS.
$\Delta d_i = a + bt$
$\bar{V}_r$ = b = 1063 cm/sec
□ EXPER. PTS.
$\sqrt{2D_z}$ (cm$^{1/2}$)
Δd_i (cm)
TIME (msec)
0
2
4
6
8
10
12
14
16
1
2
3
4
6
8
2
4
6
8
10
12

FIGURE B.8

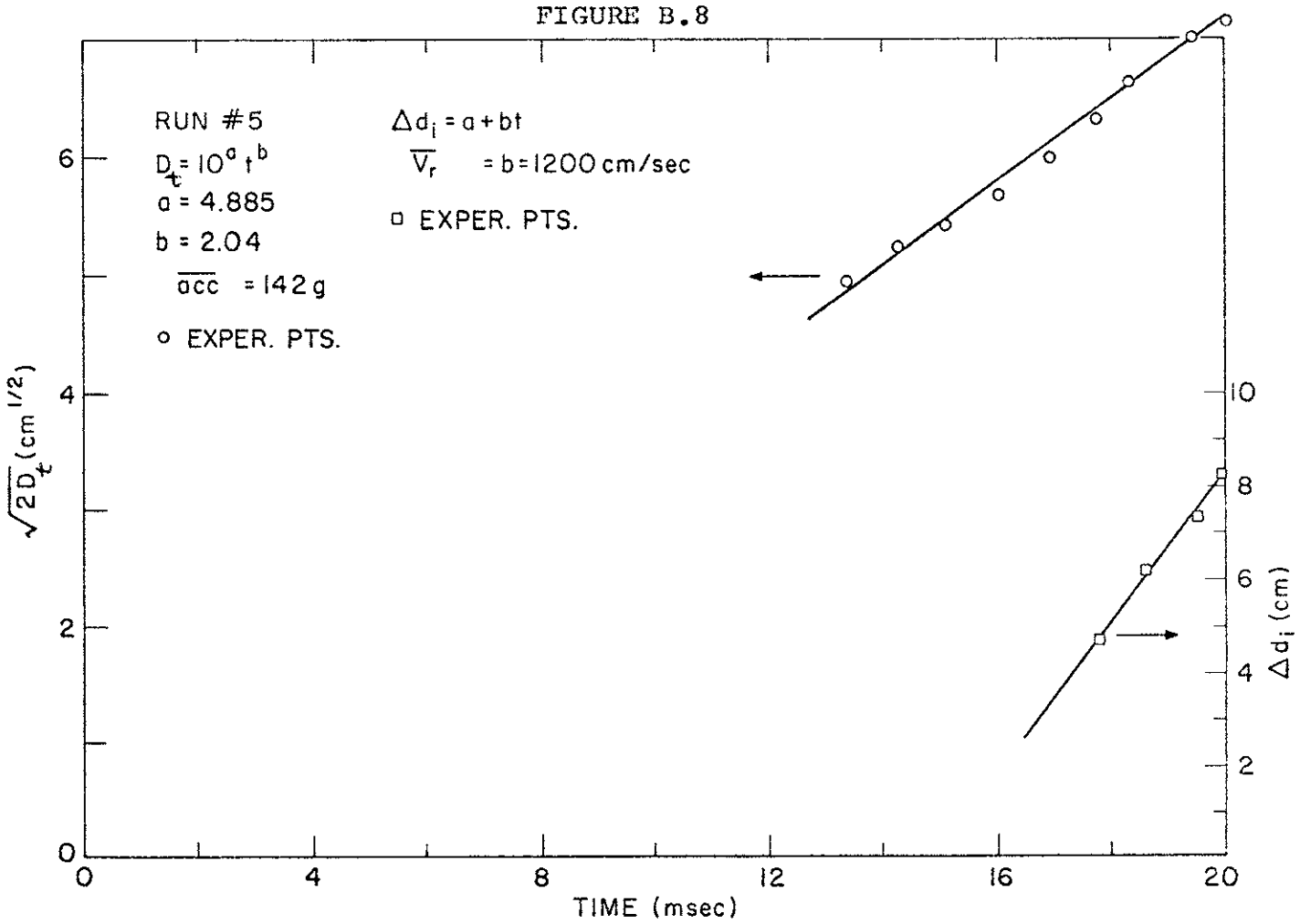
RUN #5
$D_t = 10^a t^b$
a = 4.885
b = 2.04
$\overline{acc}$ = 142 g
o EXPER. PTS.
$\Delta d_i = a + bt$
$\overline{V_r}$ = b = 1200 cm/sec
□ EXPER. PTS.
$\sqrt{2D_t}$ (cm$^{1/2}$)
Δd_i (cm)
TIME (msec)
0
2
4
6
8
10
12
16
20

FIGURE B.9

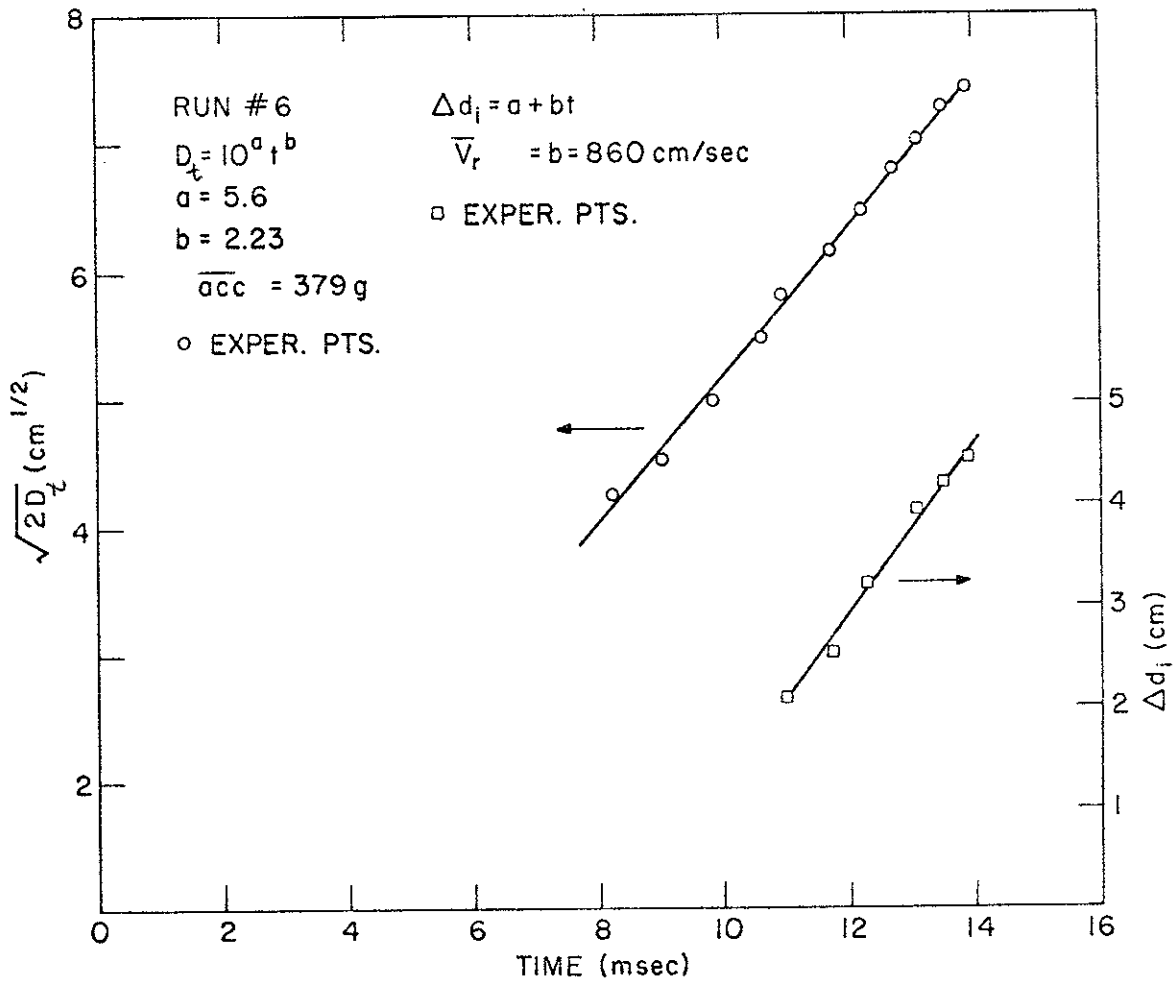
RUN #6
$D_t = 10^a t^b$
a = 5.6
b = 2.23
$\overline{acc}$ = 379 g
○ EXPER. PTS.
$\Delta d_i = a + bt$
$\overline{V_r}$ = b = 860 cm/sec
□ EXPER. PTS.
$\sqrt{2D_t}$ (cm$^{1/2}$)
Δd_i (cm)
TIME (msec)
0
2
4
6
8
10
12
14
16
1
2
3
4
5
6
8

FIGURE B.10

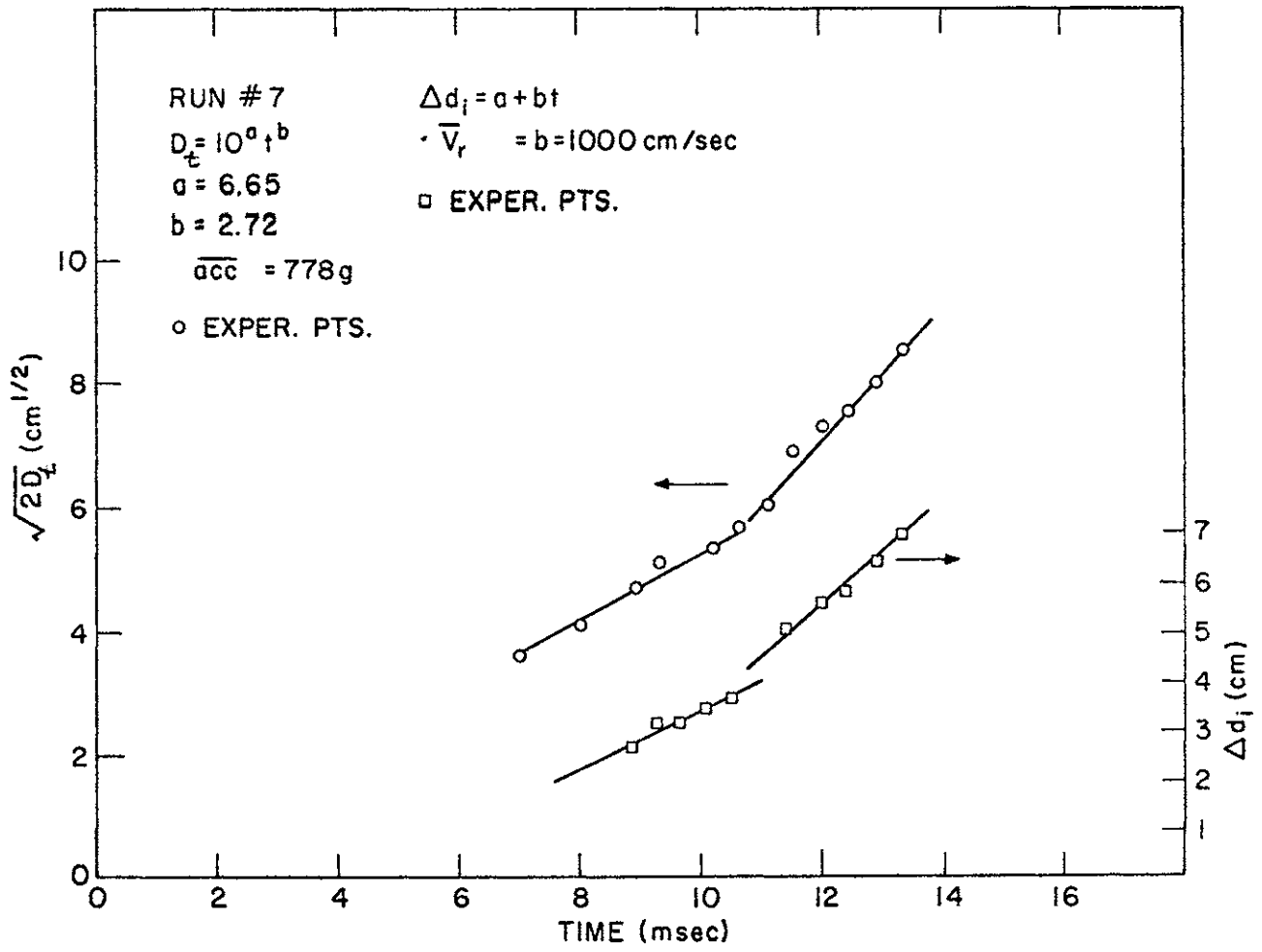
RUN #7
$D_t = 10^a t^b$
a = 6.65
b = 2.72
$\overline{acc}$ = 778g
o EXPER. PTS.
$\Delta d_i = a + bt$
$\overline{V_r}$ = b = 1000 cm/sec
□ EXPER. PTS.
$\sqrt{2D_t}$ (cm$^{1/2}$)
Δd_i (cm)
TIME (msec)
0
2
4
6
8
10
12
14
16
1
2
3
4
5
6
7

FIGURE B.11

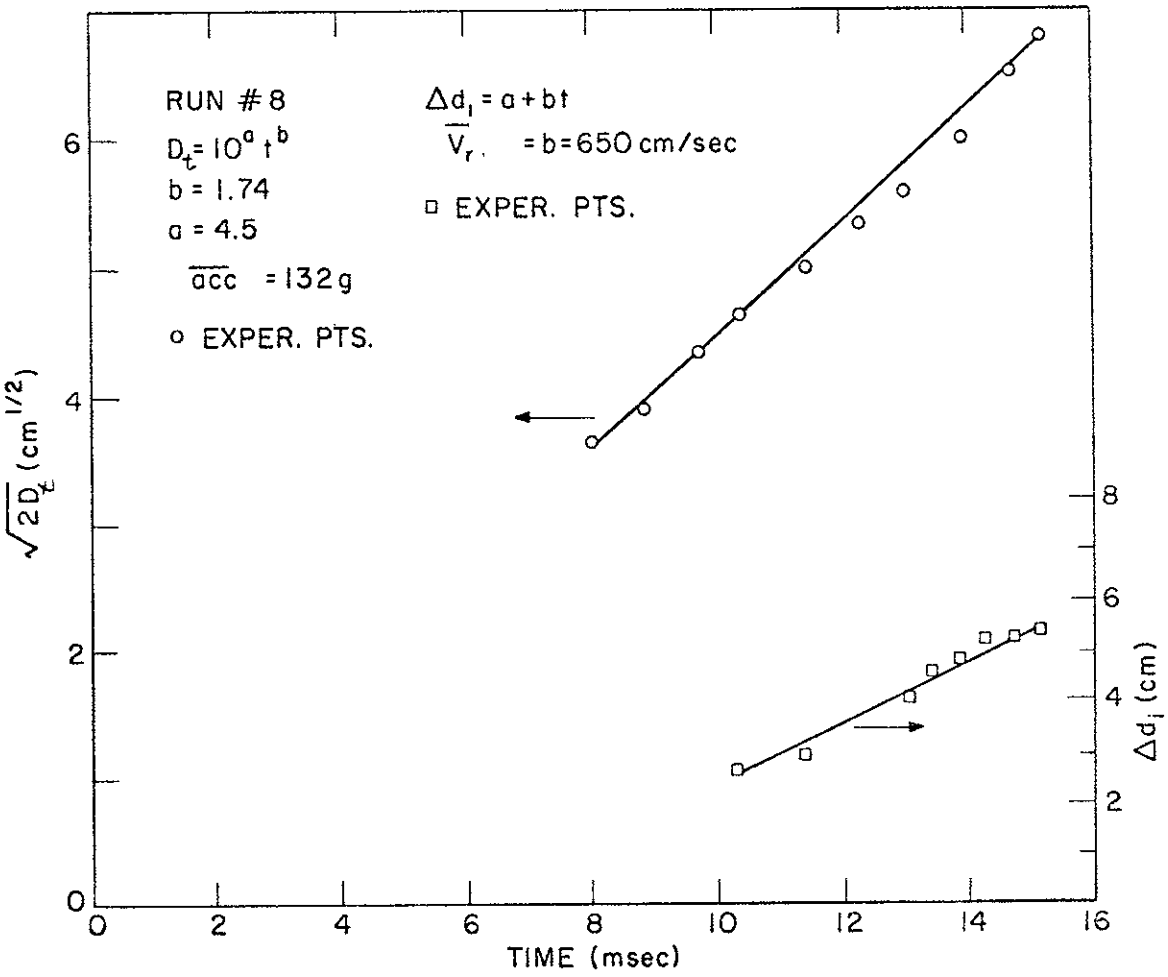
RUN #8
$D_t = 10^a t^b$
b = 1.74
a = 4.5
$\overline{acc}$ = 132 g
o EXPER. PTS.
$\Delta d_i = a + bt$
$\overline{V_r}$ = b = 650 cm/sec
□ EXPER. PTS.
$\sqrt{2D_t}$ (cm$^{1/2}$)
Δd_i (cm)
TIME (msec)
0
2
4
6
8
10
12
14
16

FIGURE B.12

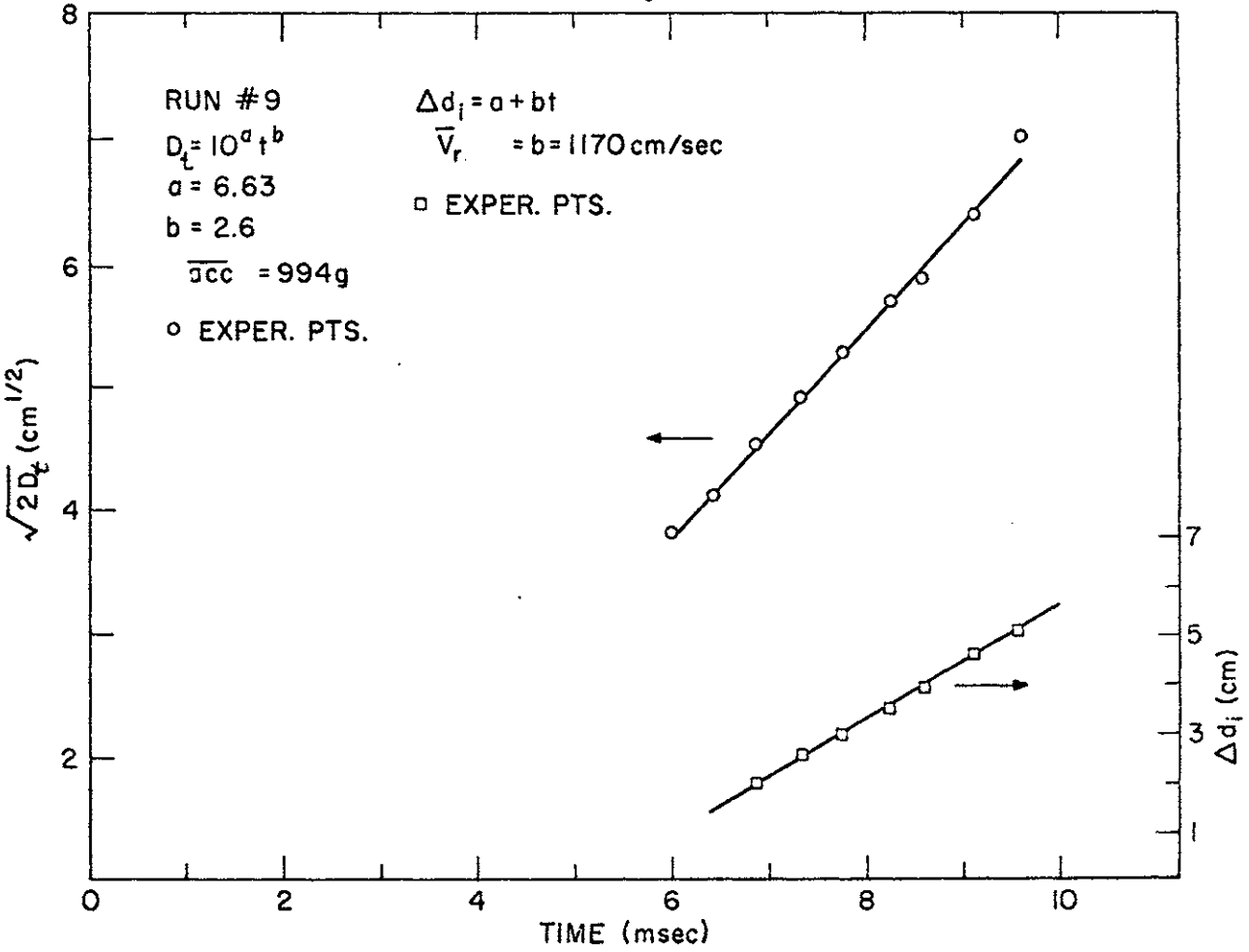
RUN #9
$D_t = 10^a t^b$
a = 6.63
b = 2.6
$\overline{acc}$ = 994g
o EXPER. PTS.
$\Delta d_i = a + bt$
$\bar{V}_r$ = b = 1170 cm/sec
□ EXPER. PTS.
$\sqrt{2D_t}$ (cm$^{1/2}$)
Δd_i (cm)
TIME (msec)
0
2
4
6
8
10
2
4
6
8
1
3
5
7

FIGURE B.13

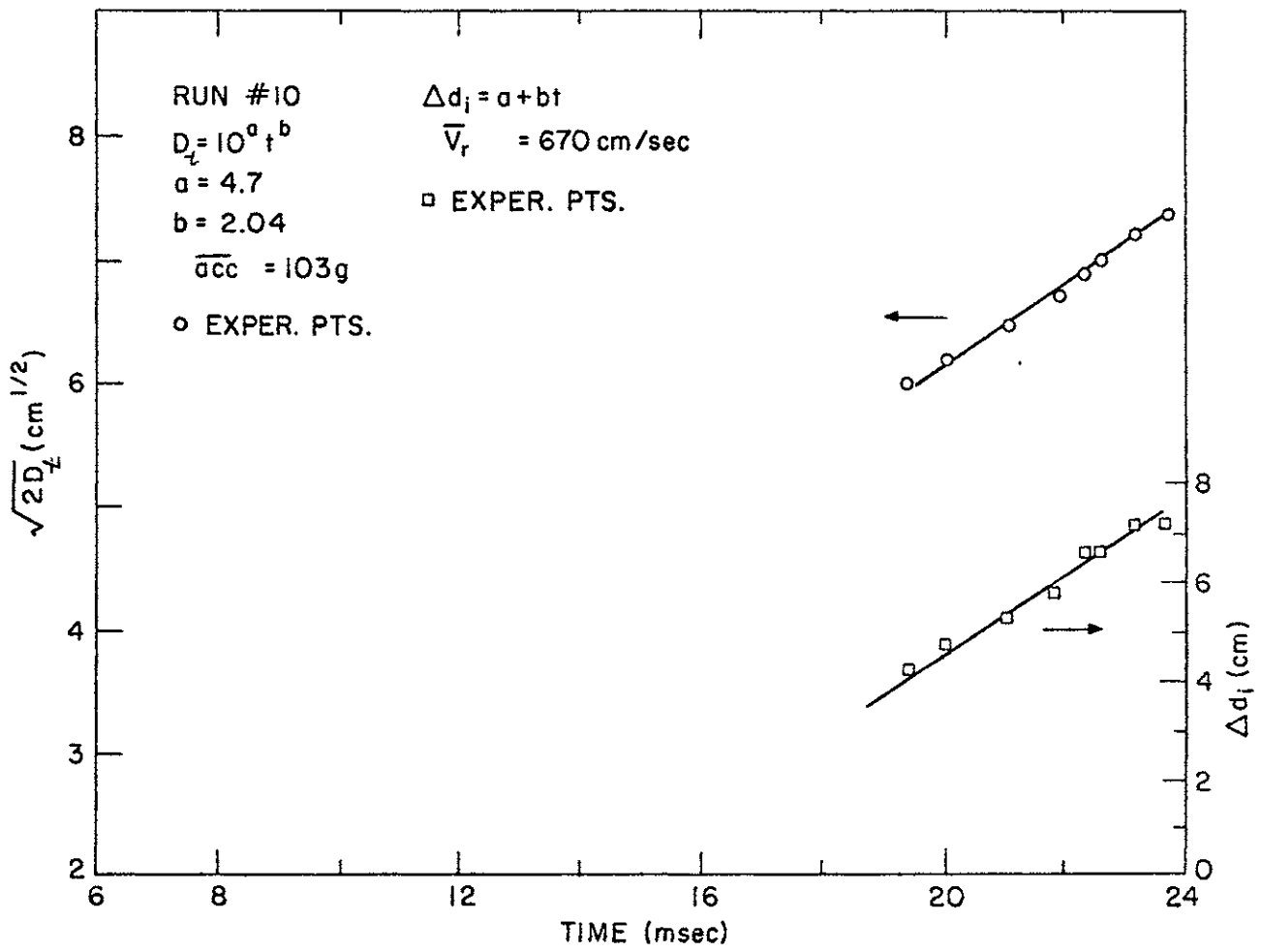
RUN #10
$D_\ell = 10^a t^b$
a = 4.7
b = 2.04
$\overline{acc}$ = 103g
o EXPER. PTS.
$\Delta d_i = a + bt$
$\overline{V}_r$ = 670 cm/sec
□ EXPER. PTS.
$\sqrt{2D_\ell}$ (cm$^{1/2}$)
Δd_i (cm)
TIME (msec)
2
3
4
6
8
0
2
4
6
8
12
16
20
24

FIGURE B.14

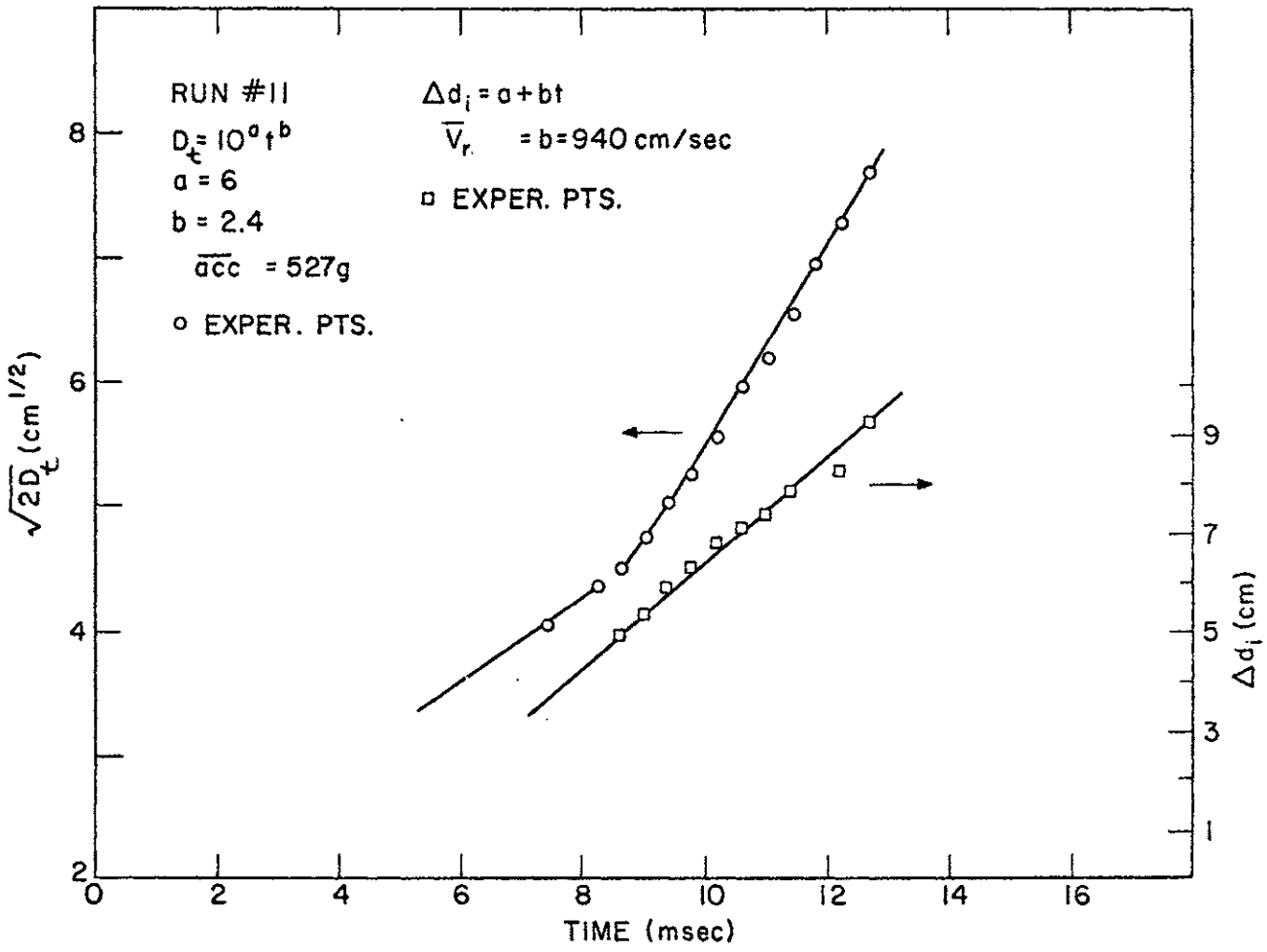
RUN #11
$D_t = 10^a t^b$
a = 6
b = 2.4
$\overline{acc}$ = 527g
o EXPER. PTS.
$\Delta d_i = a + bt$
$\overline{V}_r$ = b = 940 cm/sec
□ EXPER. PTS.
$\sqrt{2D_t}$ (cm$^{1/2}$)
Δd_i (cm)
TIME (msec)
0
2
4
6
8
10
12
14
16
2
4
6
8
1
3
5
7
9

FIGURE B.15

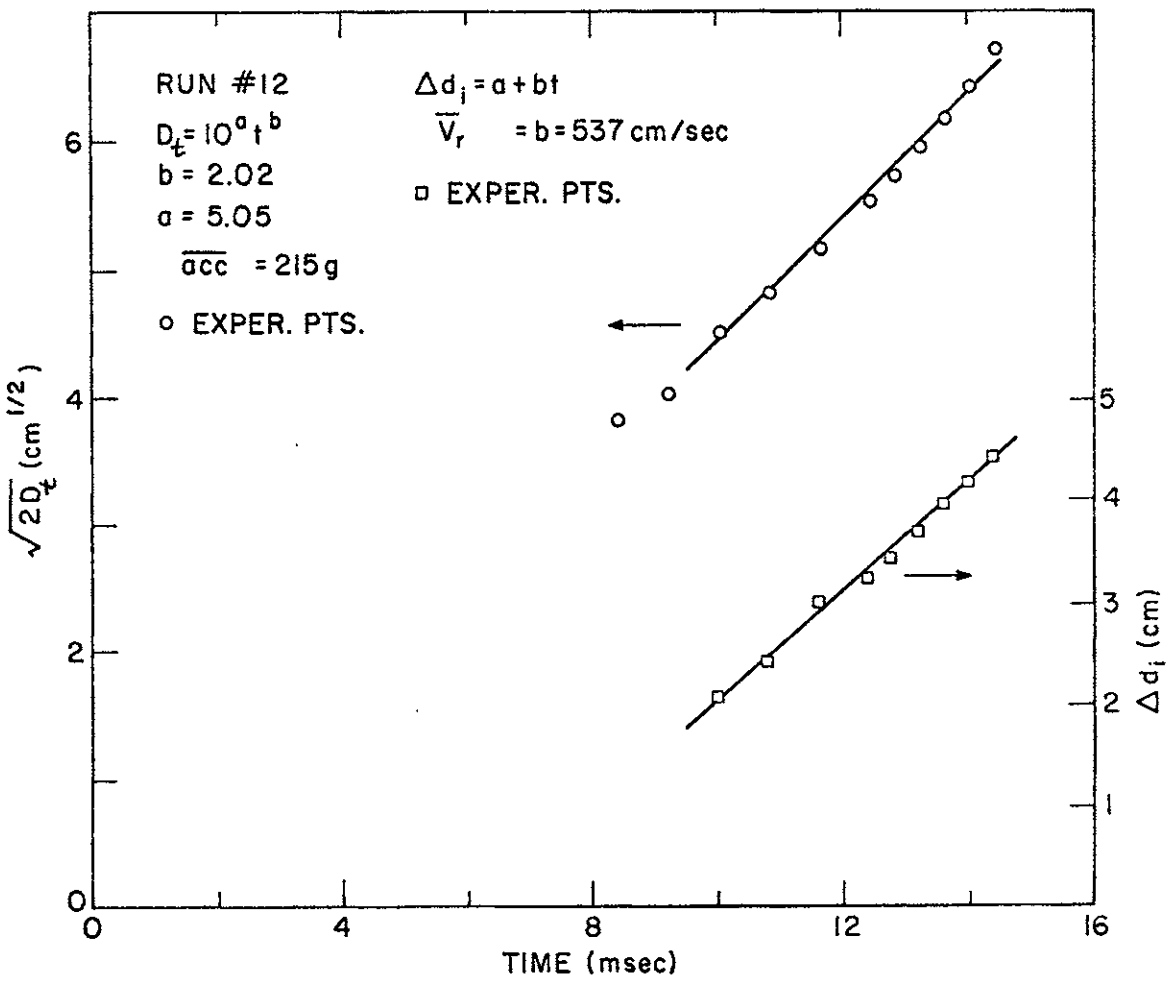
RUN #12
$D_t = 10^a t^b$
b = 2.02
a = 5.05
$\overline{acc}$ = 215 g
o EXPER. PTS.
$\Delta d_i = a + bt$
$\overline{V_r}$ = b = 537 cm/sec
□ EXPER. PTS.
$\sqrt{2D_t}$ (cm$^{1/2}$)
Δd_i (cm)
TIME (msec)
0
2
4
6
8
12
16
1
3
5

FIGURE B.16

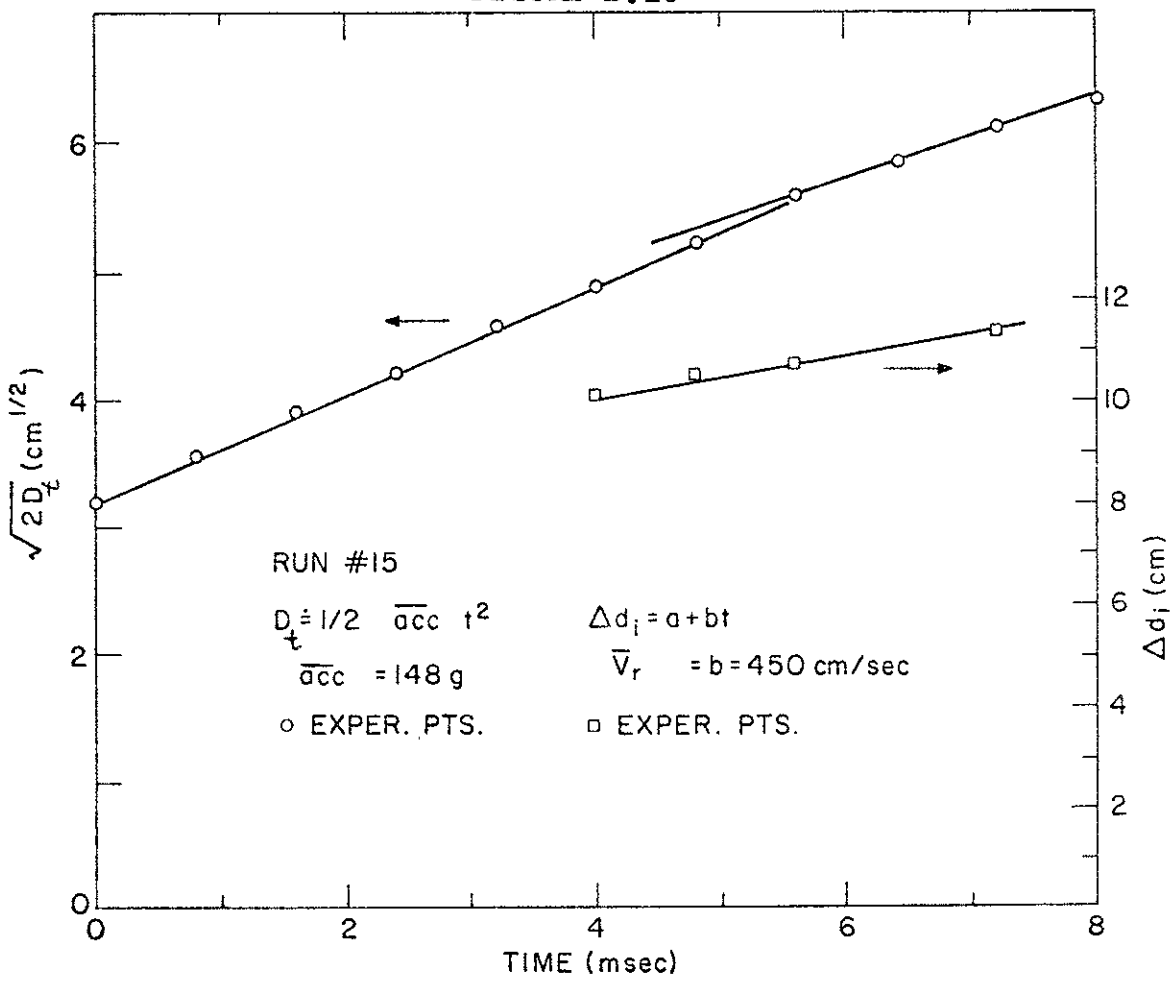
RUN #15
$D_t \doteq 1/2 \ \overline{acc} \ t^2$
$\overline{acc} = 148$ g
o EXPER. PTS.
$\Delta d_i = a + bt$
$\overline{V}_r = b = 450$ cm/sec
□ EXPER. PTS.
$\sqrt{2D_t}$ (cm$^{1/2}$)
Δd_i (cm)
TIME (msec)
0
2
4
6
8
10
12

FIGURE B.17

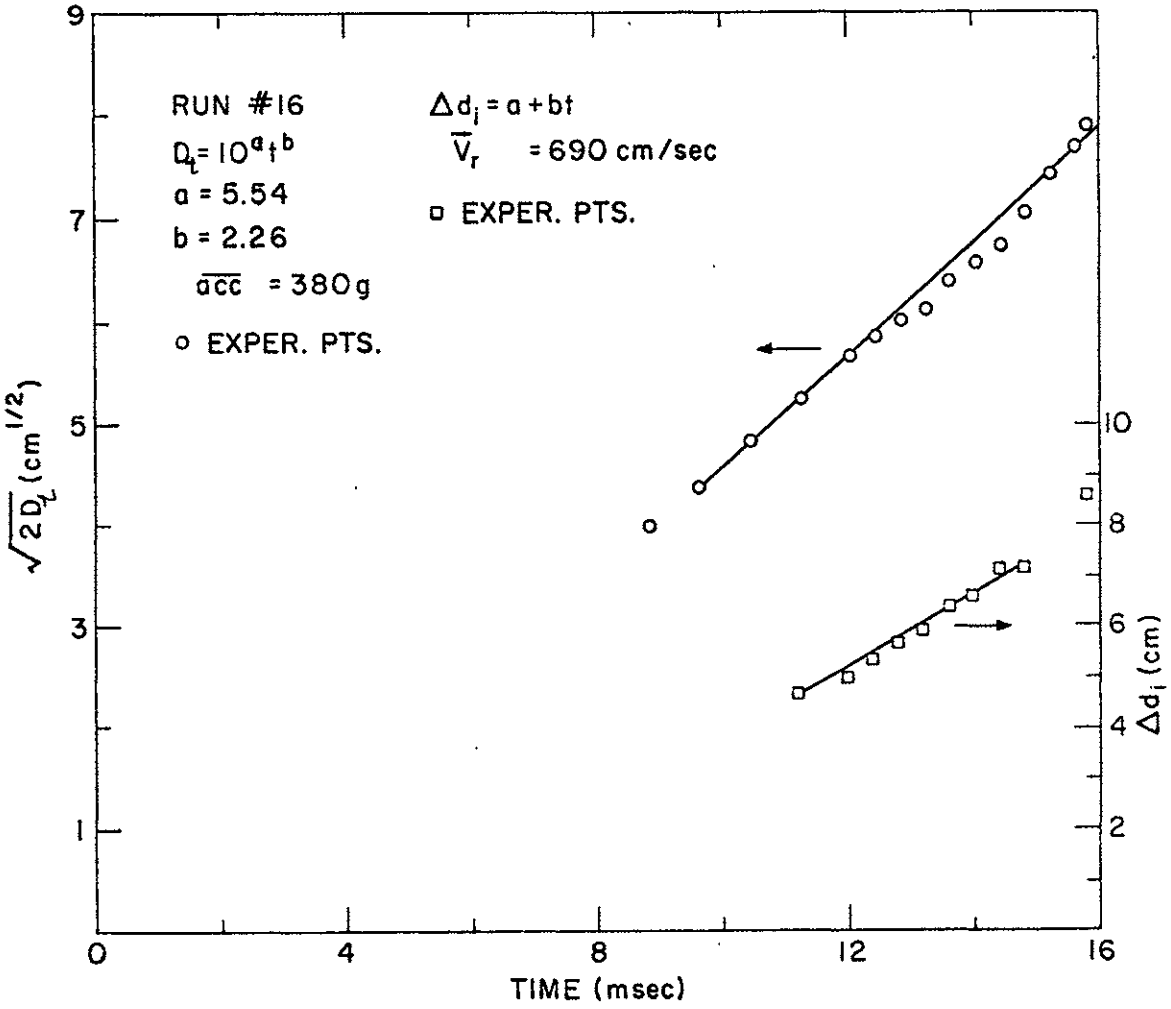
RUN #16
$D_\ell = 10^a t^b$
a = 5.54
b = 2.26
$\overline{acc}$ = 380g
o EXPER. PTS.
$\Delta d_i = a + bt$
$\overline{V}_r$ = 690 cm/sec
□ EXPER. PTS.
$\sqrt{2D_\ell}$ (cm$^{1/2}$)
Δd_i (cm)
TIME (msec)
0
4
8
12
16
1
3
5
7
9
2
4
6
8
10

FIGURE B.18

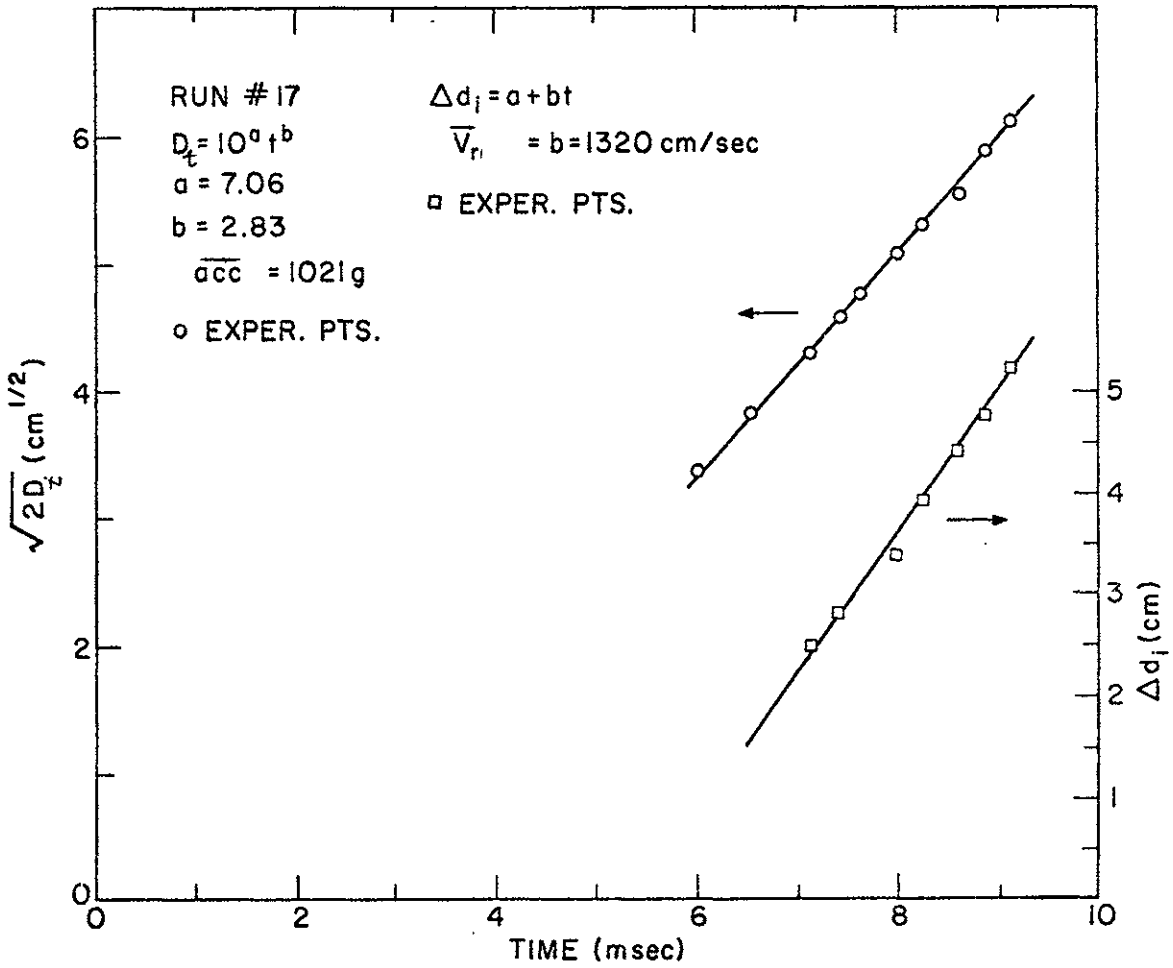
RUN #17
$D_t = 10^a t^b$
a = 7.06
b = 2.83
$\overline{acc}$ = 1021 g
o EXPER. PTS.
$\Delta d_i = a + bt$
$\overline{V}_{ri}$ = b = 1320 cm/sec
□ EXPER. PTS.
$\sqrt{2D_z}$ (cm$^{1/2}$)
Δd_i (cm)
TIME (msec)
0
2
4
6
8
10

FIGURE B.19

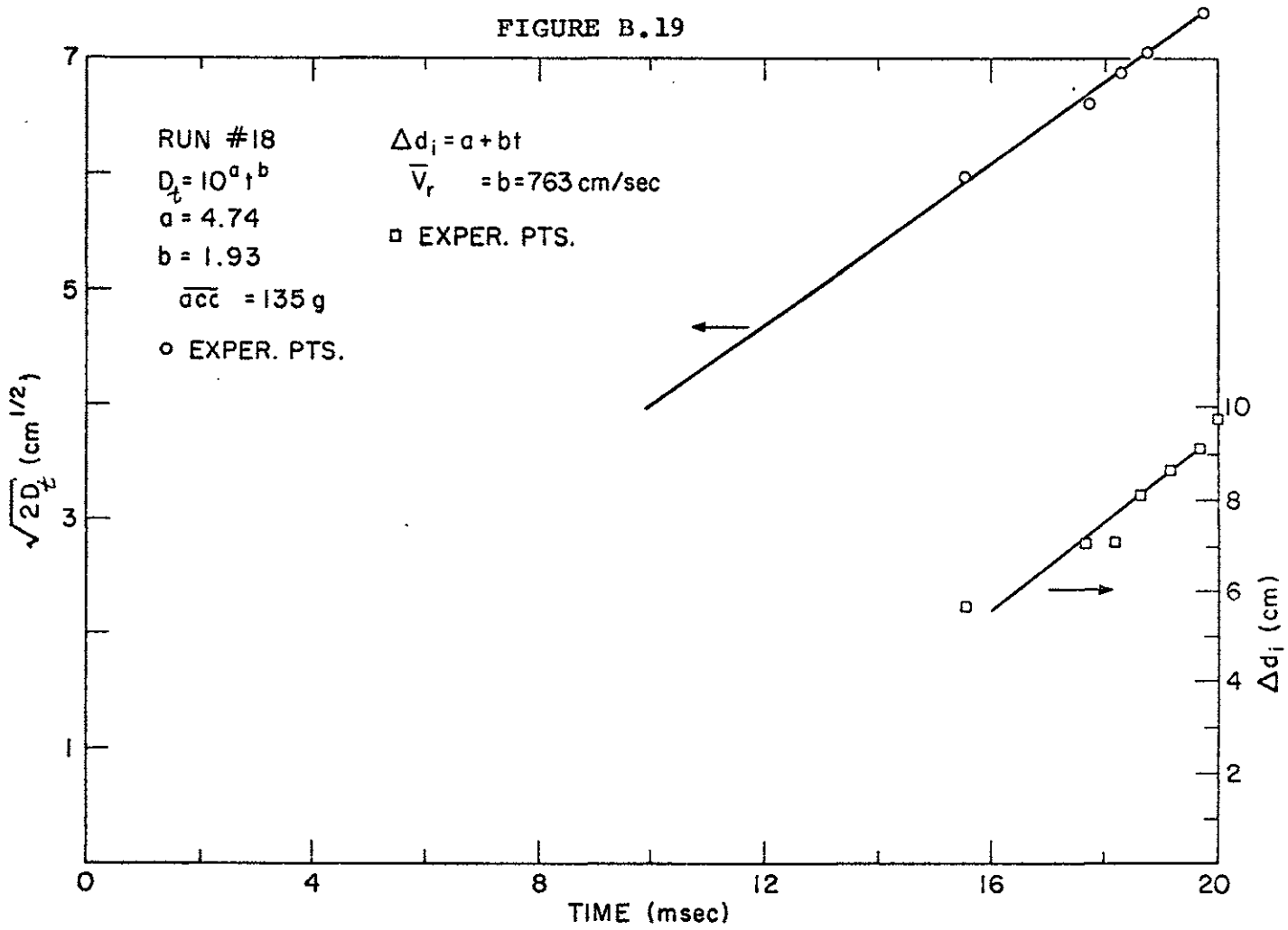
RUN #18
$D_t = 10^a t^b$
a = 4.74
b = 1.93
$\overline{acc}$ = 135 g
o EXPER. PTS.
$\Delta d_i = a + bt$
$\overline{V}_r$ = b = 763 cm/sec
□ EXPER. PTS.
$\sqrt{2D_t}$ (cm$^{1/2}$)
Δd_i (cm)
TIME (msec)
0
4
8
12
16
20
1
3
5
7
2
4
6
8
10

FIGURE B.20

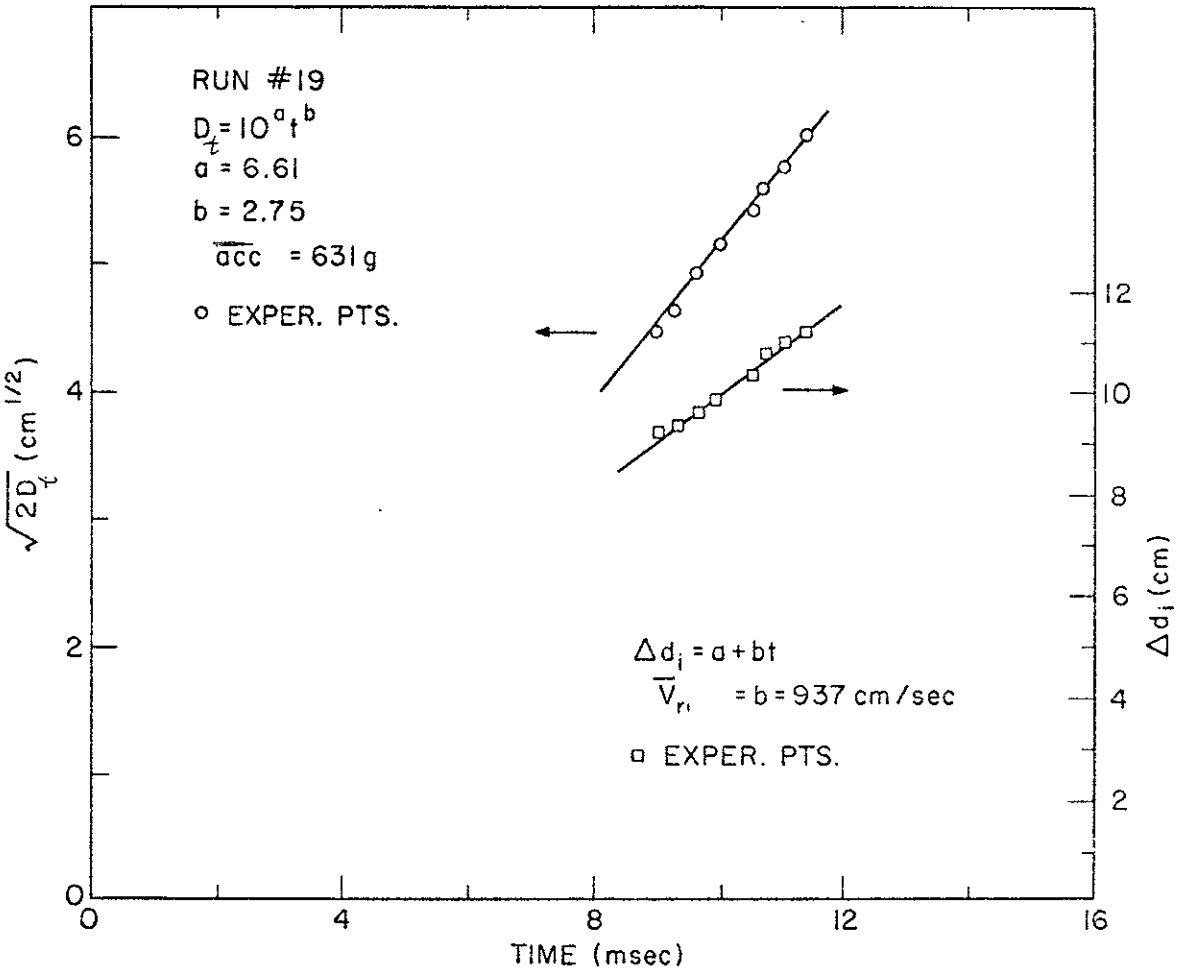
RUN #19
$D_t = 10^a t^b$
a = 6.61
b = 2.75
$\overline{acc}$ = 631 g
o EXPER. PTS.
$\Delta d_i = a + bt$
$\overline{V}_{ri}$ = b = 937 cm/sec
□ EXPER. PTS.
$\sqrt{2D_t}$ (cm$^{1/2}$)
Δd_i (cm)
TIME (msec)
0
2
4
6
8
10
12
16

FIGURE B.21

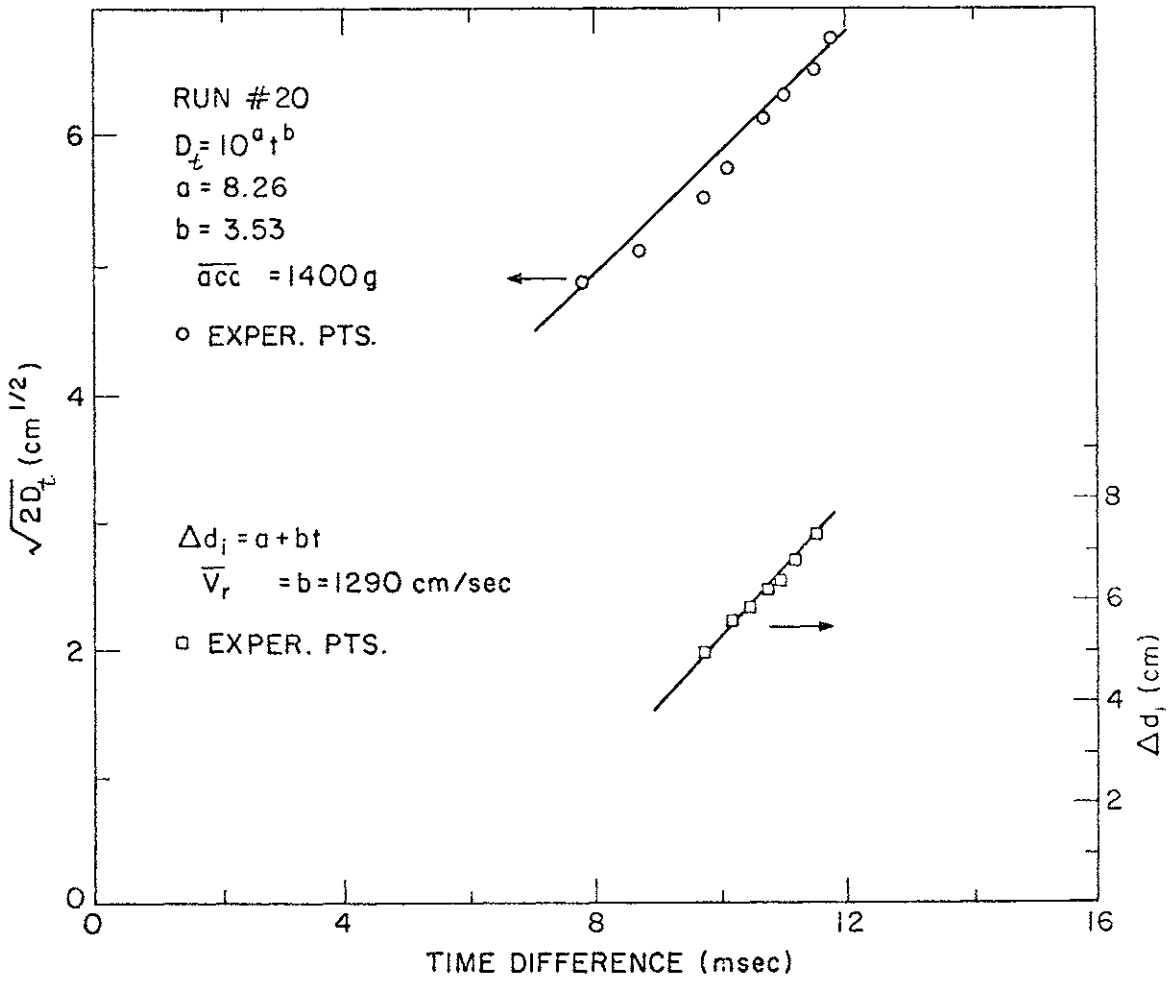
RUN #20
$D_t = 10^a t^b$
a = 8.26
b = 3.53
$\overline{acc}$ = 1400 g
o EXPER. PTS.
$\Delta d_i = a + bt$
$\overline{V_r}$ = b = 1290 cm/sec
□ EXPER. PTS.
$\sqrt{2D_t}$ (cm$^{1/2}$)
Δd_i (cm)
TIME DIFFERENCE (msec)
0
2
4
6
8
12
16

FIGURE B.22

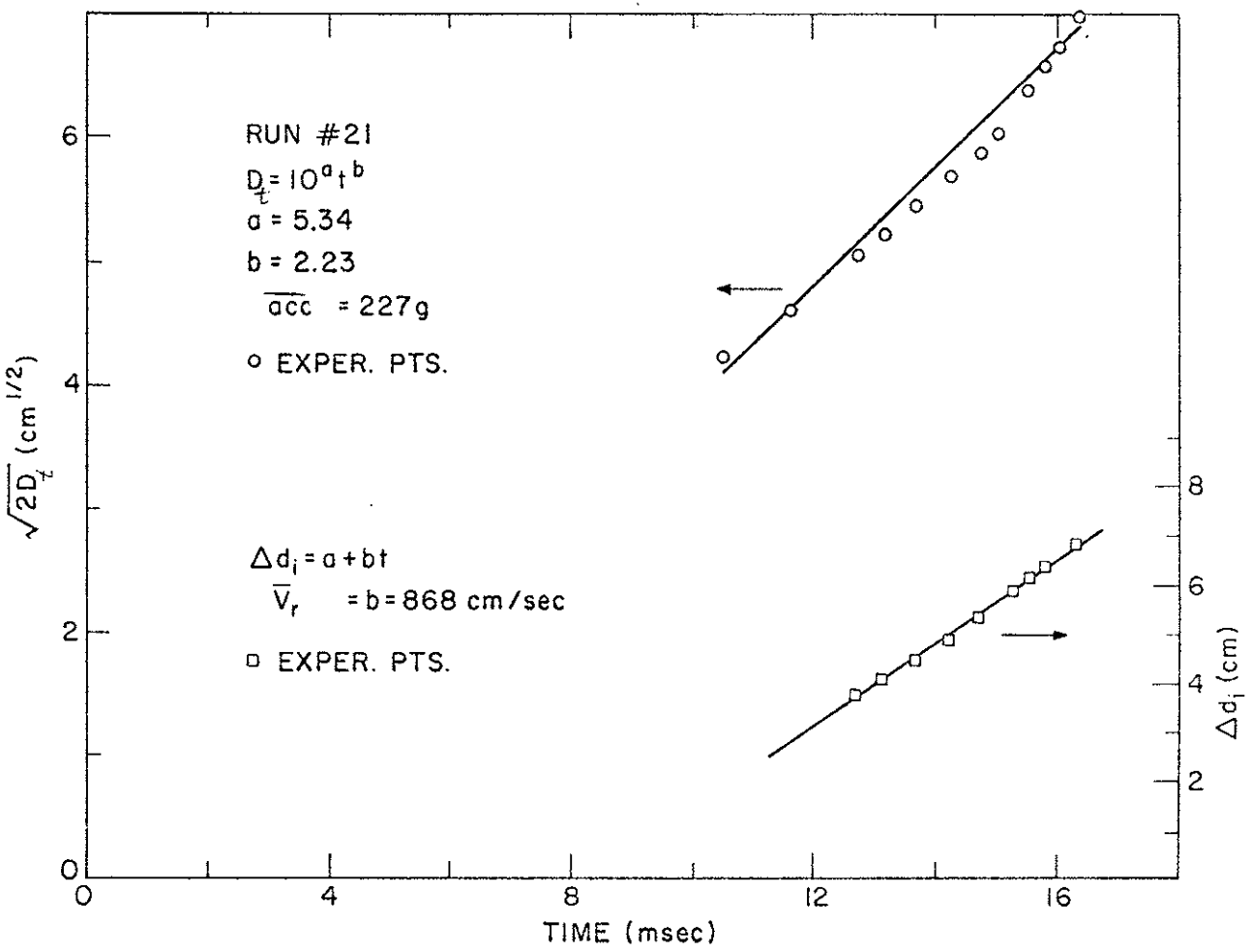
RUN #21
$D_t = 10^a t^b$
a = 5.34
b = 2.23
$\overline{acc}$ = 227g
o EXPER. PTS.
$\Delta d_i = a + bt$
$\overline{V}_r$ = b = 868 cm/sec
□ EXPER. PTS.
$\sqrt{2D_t}$ (cm$^{1/2}$)
Δd_i (cm)
TIME (msec)
0
2
4
6
8
12
16

FIGURE B.23

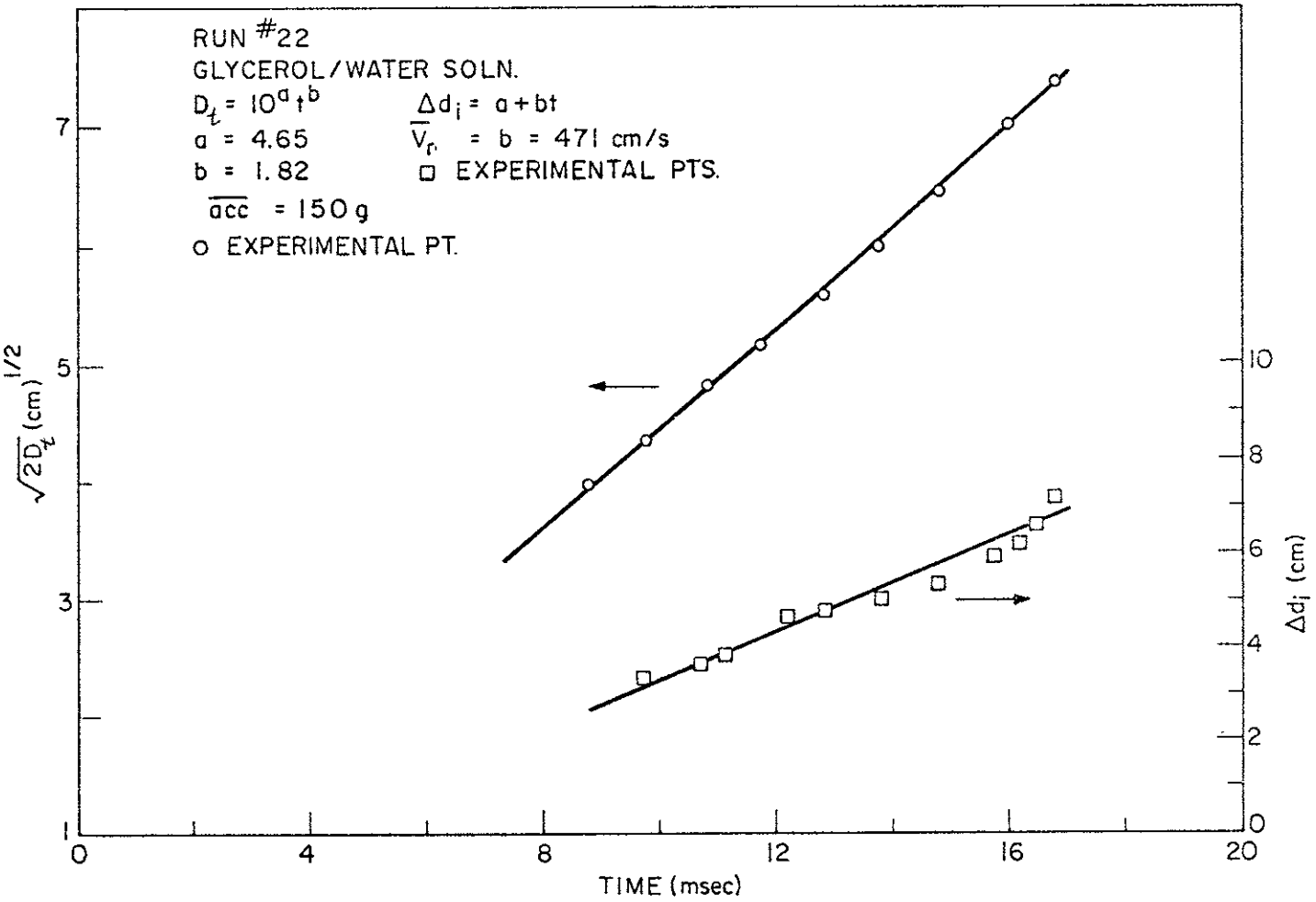
RUN #22
GLYCEROL/WATER SOLN.
$D_t = 10^a t^b$
a = 4.65
b = 1.82
$\overline{acc}$ = 150 g
o EXPERIMENTAL PT.
$\Delta d_i = a + bt$
$\overline{V_r}$ = b = 471 cm/s
□ EXPERIMENTAL PTS.
$\sqrt{2D_t}$ (cm)$^{1/2}$
Δd_i (cm)
TIME (msec)
1
3
5
7
0
2
4
6
8
10
0
4
8
12
16
20

FIGURE B.24

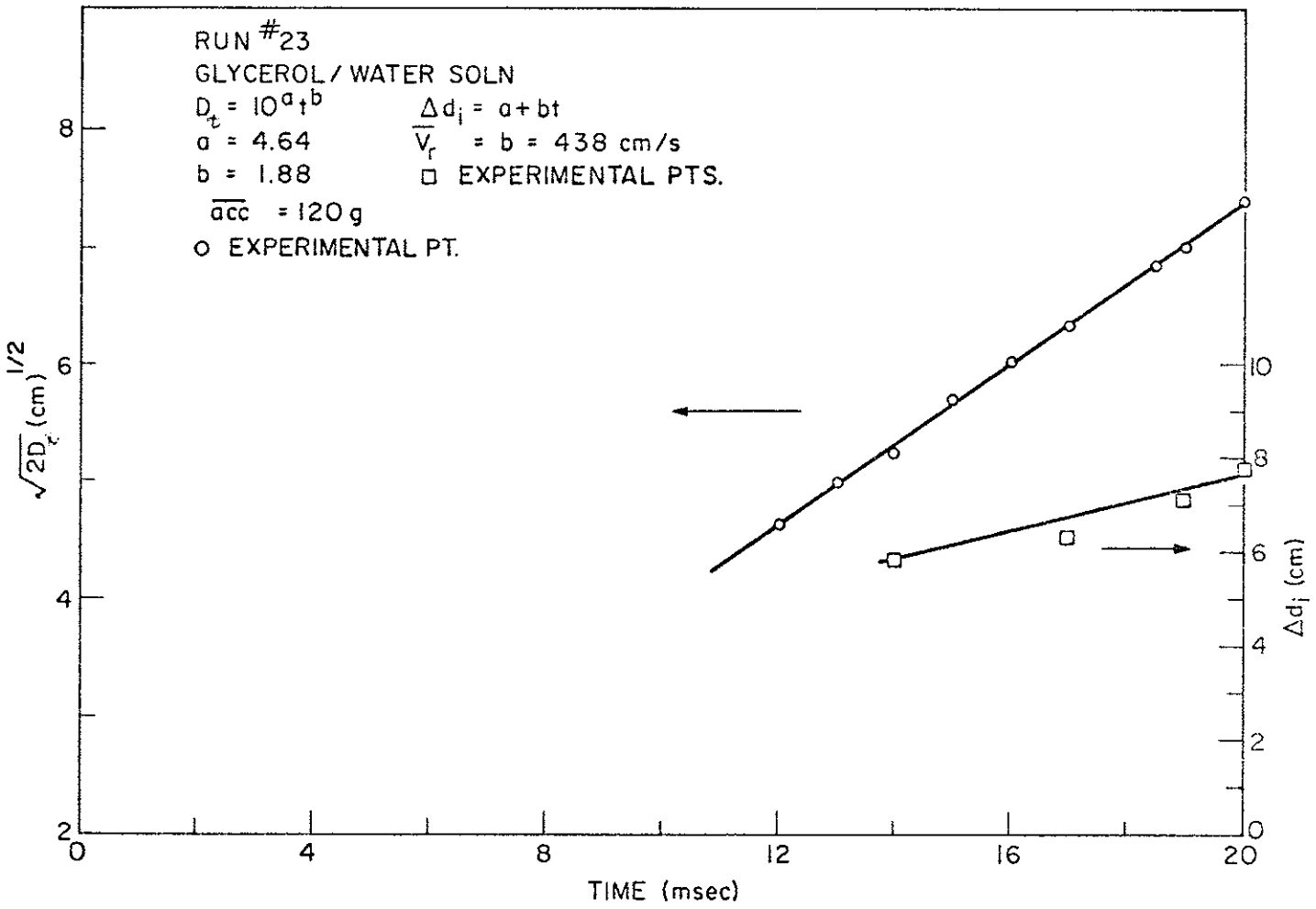
RUN #23
GLYCEROL / WATER SOLN
$D_t = 10^a t^b$
a = 4.64
b = 1.88
$\overline{acc}$ = 120 g
o EXPERIMENTAL PT.
$\Delta d_i = a + bt$
$\overline{V_r}$ = b = 438 cm/s
□ EXPERIMENTAL PTS.
$\sqrt{2D_t}$ (cm)$^{1/2}$
Δd_i (cm)
TIME (msec)
0
4
8
12
16
20
2
4
6
8
0
2
4
6
8
10

FIGURE B.25

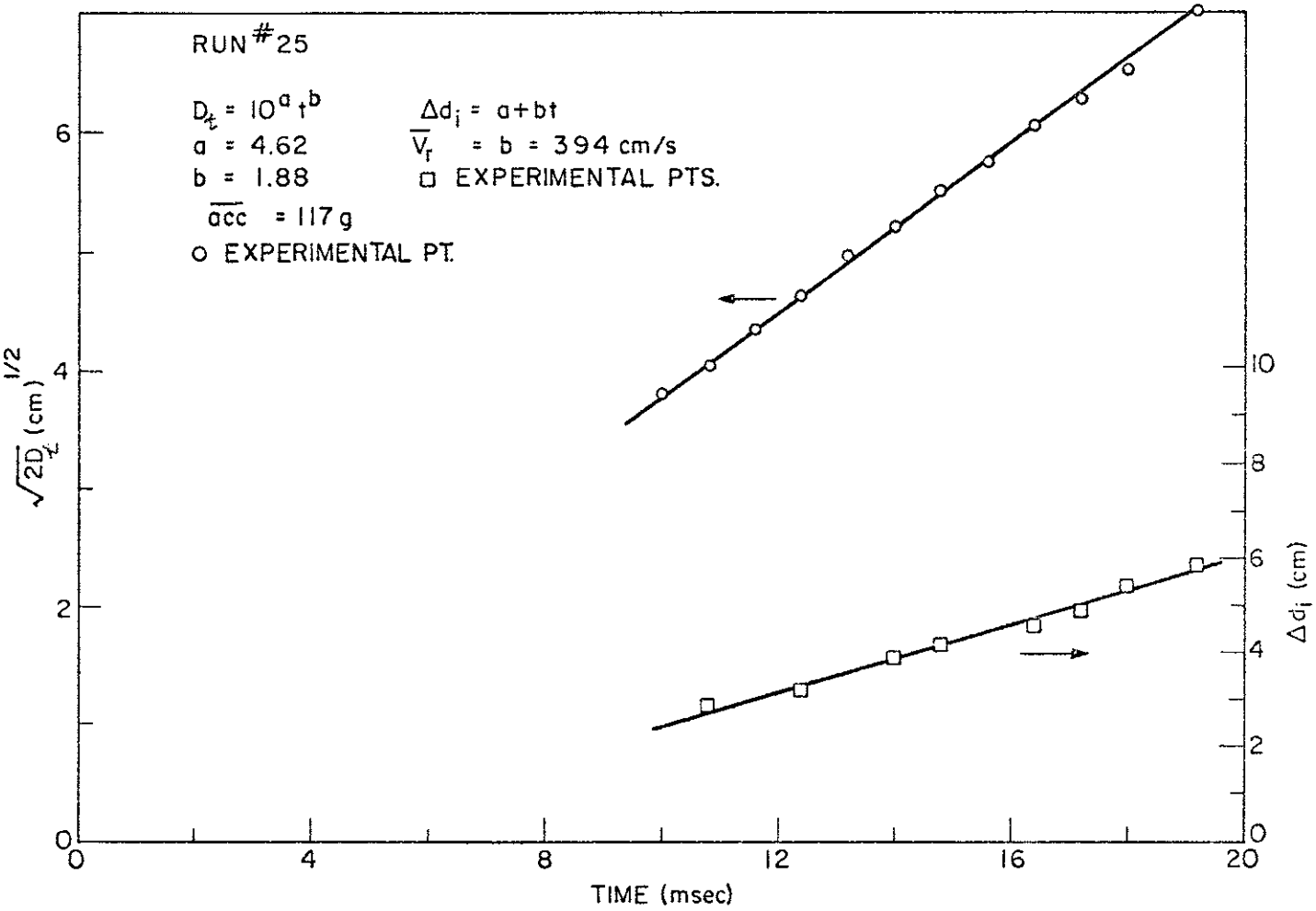
RUN # 25
$D_t = 10^a t^b$
a = 4.62
b = 1.88
$\overline{acc}$ = 117 g
O EXPERIMENTAL PT.
$\Delta d_i = a + bt$
$\overline{V_t}$ = b = 394 cm/s
□ EXPERIMENTAL PTS.
$\sqrt{2D_t}$ (cm)$^{1/2}$
Δd_i (cm)
TIME (msec)
0
2
4
6
8
10
12
16
20

FIGURE B.26

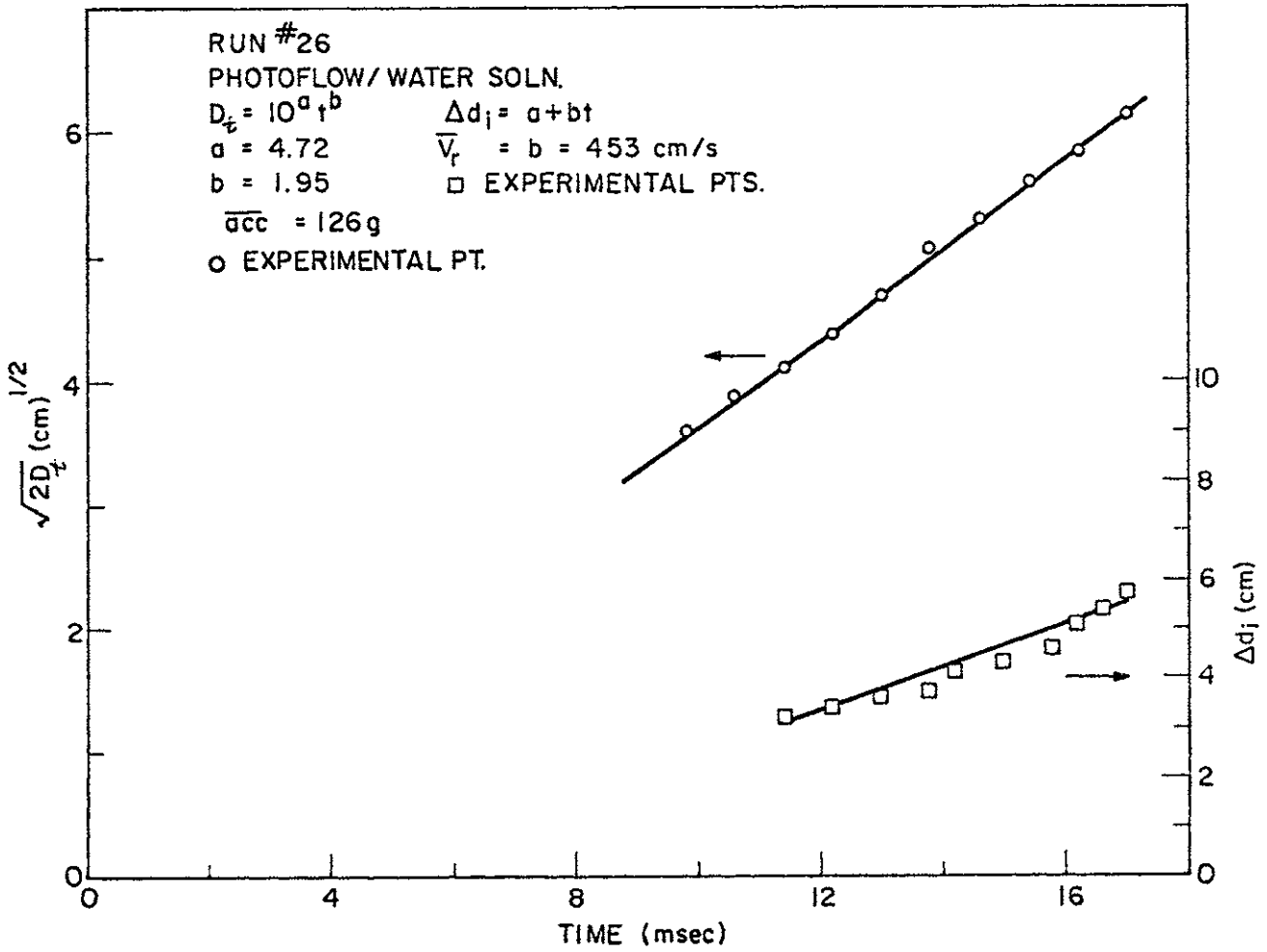
RUN #26
PHOTOFLOW/ WATER SOLN.
$D_t = 10^a t^b$
$\Delta d_j = a + bt$
a = 4.72
$\overline{V_t}$ = b = 453 cm/s
b = 1.95
□ EXPERIMENTAL PTS.
$\overline{acc}$ = 126 g
o EXPERIMENTAL PT.
$\sqrt{2D_t}$ (cm)$^{1/2}$
Δd_j (cm)
TIME (msec)
0
2
4
6
8
10
12
16

FIGURE B.27

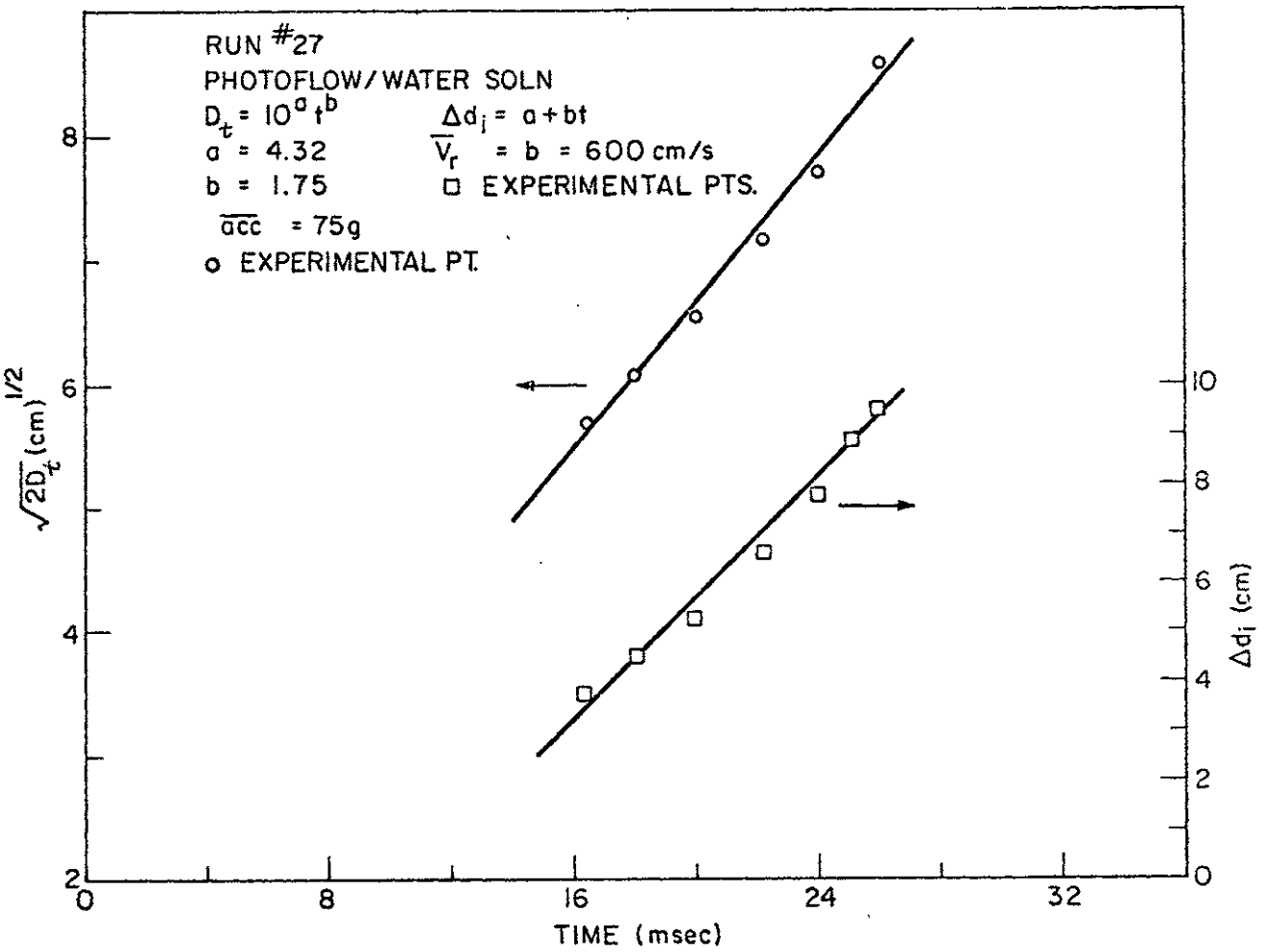
RUN #27
PHOTOFLOW/WATER SOLN
$D_t = 10^a t^b$
a = 4.32
b = 1.75
$\overline{acc}$ = 75g
o EXPERIMENTAL PT.
$\Delta d_j = a + bt$
$\overline{V_r}$ = b = 600 cm/s
□ EXPERIMENTAL PTS.
$\sqrt{2D_t}$ (cm)$^{1/2}$
Δd_j (cm)
TIME (msec)
0
8
16
24
32
2
4
6
8
0
2
4
6
8
10

APPENDIX C

CHARACTERISTIC DIMENSIONLESS PARAMETERS

Overview

The purpose of this appendix is to give estimates of important dimensionless parameters which may govern the heat transfer and vapor (gas) expansion characteristics of the small scale experiments and the full scale reactor situation. These estimates are useful in determining which phenomena may govern the expansion process and how possible scaling of the key phenomenon may be done.

Noncondensible SRI Heated Experiments [22], SRI and PU Condensible Tests [26,28]

The important parameters considered for these tests are the entrained droplet Reynolds number (Re), vapor (gas) Prandtl number (Pr), droplet Weber number (We), gas (vapor) Nusselt number (Nu), and the ratio of the characteristic time for drop breakup (τ_{br}) to the characteristic expansion time of the experiment (τ_{exp}). To estimate these values the approximate relative velocity between the entrained droplet and the gas (vapor) as envisioned in Figures 4.5 and 5.5 is needed as well as the droplet diameter. Utilizing these quantities with properties from Appendix A and the dimensionless groups, the estimates can be made. To get an approximate relative velocity, the relation

$$v_{rel} \simeq 4.65 \sqrt{a\lambda_c} \qquad (C.1)$$

where

$$\lambda_c = 2\pi \sqrt{\frac{\sigma}{\Delta\rho a}} \qquad (C.2)$$

is used. This value represents the initial relative velocity the droplets experience. To obtain the acceleration the one dimensional momentum equation can be used giving

$$a = \left[\frac{(P_{g_i} - P_\infty) A_p}{M_{slug}} \right] \tag{C.3}$$

where the initial conditions are found from Tables 4.4 and 5.2. The size of the entrained water droplet in these experiments can be estimated by the Taylor Instability critical wavelength ($D_d = \lambda_c$ - Equation C.2). The droplet Reynolds number is then defined as

$$Re = \frac{\rho_g v_{ref} D_d}{\mu_g} \tag{C.4}$$

The droplet Weber number is defined as

$$We = \frac{\rho_g v_{rel}^2 D_d}{\sigma} \tag{C.5}$$

For the noncondensible SRI tests the Nusselt number was determined by the correlation of McAdams

$$Nu = \frac{\bar{h} D_d}{kg} = .33\ Re^{.6} \tag{C.6}$$

for $Pr \simeq 1$

For the condensible tests the heat transfer coefficient ($\bar{h}$) was dominated by the heat transfer resistance of the entrained water droplet (semi-infinite geometry) and the condensate water film (thickness -δ) giving us

$$\bar{h} = \frac{k_c}{(\delta + \frac{\sqrt{\pi 2_c t}}{4}} \tag{C.7}$$

where

$$\delta = \frac{2k_c(T_{sat} - T_l)\Delta t}{(\rho h_{f_g} \sqrt{\pi \alpha_c t})} \tag{C.8}$$

and, therefore, the Nusselt number is given by

$$Nu = \frac{D_d}{(\delta + \frac{\sqrt{\pi \alpha_c t}}{4})} \tag{C.9}$$

The characteristic time for droplet breakup due to Weber forces was estimated [66] by the relation

$$\tau_{br} = \frac{C\, D_d}{v_{rel}} \sqrt{\frac{\rho_l}{\rho_g 2 C_d}} \qquad (C.10)$$

where $C_d = .5$ and the constant of proportionality ~ 10 [67]. This can be compared to the experimental expansion times (τ_{exp}) and is useful in assessing if the droplet can indeed breakup in the time allotted $\tau_{br}/\tau_{exp} << 1$.

The values of these dimensionless groups are given in Table C.1 using the initial conditions (Table 4.4 and 5.2) of the tests. The Weber numbers for the droplets in the Purdue tests are below the critical values and thus the droplets do not breakup. For the SRI tests, it can be seen that $We > We_{crit}$; however, the time for breakup is about 10-30% of the expansion time, thus it is not clear if the droplets can breakup. The average droplet size of $\lambda_c \leq D_d \leq \lambda_m$ is needed to successfully match the experimental data and, therefore, it appears the majority of the droplets do not breakup.

Numerical Values of Full Scale Dimensionless Groups

In Chapter 7 the nondimensional groups were derived from the governing equations and heat transfer models. The numerical values of these groups were estimated for the range of anticipated fuel temperatures and are given in Table C.2 and C.3.

Numerical Values of Full Scale Dimensionless Groups Using Simulant Fluids at Small Scale

Chapter 7 also indicates that a simulant pair of Freon-113 (fuel) and Freon-13 (coolant) could be used to model the UO_2-sodium system except for radiation effects. The intent of this section is to present the details on which this conclusion is based.

The possible modeling of this phenomenon using simulant fluids at small scales enables a larger variety of parameters to be measured: pressure, temperature, coolant entrainment, perhaps coolant droplet size, bubble expansion characteristics. To accomplish this, some criteria and constraints must be put on the simulant fluids that are chosen: (1) The fluids should be transparent if possible to allow visual observation of the phenomenon; (2) The temperature and pressure regimes of the constituents should be small enough to allow ease in handling and data acquisition; (3) The fluids should not be exotic so that basic thermodynamic and thermophysical properties are readily available in the literature [152]. With these requirements, it was felt that refrigerants would be the best simulant fluid candidates. All the properties were obtained from Reference 152 for consistency.

The numerical values for these dimensionless groups are given in Tables C.4 to C.7, for various refrigerants. The first requirement of this scaling process is that the interface temperature of the fuel and coolant as the fuel condenses is above T_{HN} for the coolant. As Table C.4 and C.5 indicate, this eliminates most of the possible refrigerant combinations. However, if R-11 or R-113 is used as the fuel and R-13 is used as the coolant, then the initial interface requirement is satisfied (see Table C.6 and C.7). Both R-11 and R-113 have similar thermodynamic and thermophysical properties and thus either one could be used with R-13 as a simulant pair to compare with the UO_2/sodium system.

The complete calculation of all the dimensionless groups is given in Table C.7 at three scales for R-113 and R-13. The choice of the scaling laws for pressure and geometric size is arbitrary and coincides with the experimental setups at Purdue (1/7 scale), MIT (1/20 scale), and SRI (1/30 scale). A different choice of these scaling laws may give even better

agreement between small and full scale values but even with these choices, the agreement is good. It appears that the worst agreement occurs between R-13 and sodium for the subcooled enthalpy (h^*_{csub}) and entrainment values (h^*_e). However, the similarity between the small and full scale dimensionless values is good enough so that use of these fluids would give an indication of the possible effects at full scale for the coolant vaporization and sputtering process. Remember that the radiation heat transfer process cannot be modeled and only tests with reactor materials will confirm the modeling in this area, and these possible heat transfer effects.

TABLE C.1

SUMMARY OF DIMENSIONLESS GROUPS FOR SMALL SCALE EXPERIMENTS(SRI,Purdue)

Test	v_{rel} (m/s)	D_d (μm)	Re	Pr	Nu	We	τ_{br}/τ_{exp}
SRI AVG2	17.7	200	1100	.85	22	25	.8/2.3
SRI A134	20	155	1600	.84	27.5	35	.4/1.9
SRI A132	21	145	1835	.84	30	42	.3/1.7
SRI A143	15	300	700	.90	17	11	1.7/3.4
SRI - condensible	13	375	6650	.86	20.5	17	1./3.
PU - 3V	6.6	1400	1350	.95	14	1.9	-
PU - 4L	6.6	1400	1360	.95	14	1.9	-

TABLE C.2

SUMMARY OF DIMENSIONLESS GROUPS FOR POSSIBLE FULL SCALE CONDITIONS

T_{f_i} (^oK)	4000	5000	6000	7000
$P_i = P_{f_i}$ (MPa)	.26	4.63	27.2	86.8
$D = D_p$ (m)	6.1	6.1	6.1	6.1
ρ_c (kg/m^3)	835	835	835	835
τ (sec)	.344	.082	.034	.019
$\tau^*_{exp} = \tau_{exp}/\tau$	.49	.49	.49	.49
a*	.59	.93	.96	.96
$\dot{m}_f^*$ crit		.0101	.0152	.0171
m^*_{fco}	.04	.04	.04	.04
X_{fco} (sodium out)	.00175	.0247	.121	.35
$h^*_{f_{sub}} = \frac{c_{\rho_f} \Delta T}{h_{fg_f}}$	1	1.44	2.05	2.85
$h^*_{fg_f} = \frac{\tau^2}{D_p^2}(h_{fg_f})$	5410	271	40	10.5
$Pv^*_f = \frac{\tau^2}{D_p^2}(P_{fco} v_{fco})$	.78	.78	.78	.78
V^*_b ($V_b = 20.44 m^3$)	.09	.09	.09	.09
$\dot{m}^*_e$ (@ a*)	.153	.0752	.0505	.042
$h^*_{sub} = \frac{c_{\rho_c} \Delta T}{h_{fg_c}}$	.352	.622	1.69	
$h^*_{fg_c} = \frac{\tau^2 h_{fg_c}}{D_p^2}$	11450	578	52.8	31‡

TABLE C.2 (CONTINUED)

$h^*_{c_{sup}} = \frac{c_{p_{g_c}} T}{h_{fg_c}}$	1.82	2.38	4.94	99‡
h^*_e	3307	188	32.3	10

‡ The coolant is above its critical temperature (T_{crit}) at contact and $T_{HN} = T_{crit}$. Thus the enthalpies are referenced to

$$h^* = \frac{\tau^2}{D_p^2} h$$

for $(h^*_{sub} + h^*_{fg_c})$ and $h^*_{c_{sup}}$.

TABLE C.3

SUMMARY FO DIMENSIONLESS GROUPS FOR POSSIBLE FULL SCALE CONDITIONS

T_f	4000	5000	6000	7000
RADIATION MODEL FOR NO FUEL VAPOR CONDENSING ON DROP SURFACE				
$\dot{q}_l\big\|_{rad}$ $(\varepsilon_r = .04)$	62.4	4.06	.89	.35
SPUTTERING MODEL FOR FUEL VAPOR CONDENSING ON DROP SURFACE				
$T_I > T_{HN}$				
β	2	2	2	2
FUEL DOES NOT FREEZE $\dfrac{c_{l_f}(T_f - T_l)}{\sqrt{\pi}\, h_{fg_f}}$	.64	.95	1.38	1.94
FUEL DOES FREEZE $\dfrac{T_f - T_{m_f}}{T_{m_f} - T_l}$	.41	.85	1.29	1.73
$\dfrac{c_{s_f}(T_{m_f} - T_l)}{\sqrt{\pi}\, L_s}$	2.74	2.74	2.74	2.74
$\dfrac{c_{l_f}(T_f - T_{m_f})}{\sqrt{\pi}\, h_{fg_f}}$	.18	.43	.77	1.23
$\dot{\frac{m}{A}}_{vap_i}$	$7.4(10^{-4})$	$5.63(10^{-4})$	$2.4(10^{-4})$	
$\dot{\frac{m}{A}}_{vap_f}$	$3.03(10^{-7})$	$1.77(10^{-7})$	$1.2(10^{-7})$	

TABLE C.4

SUMMARY OF DIMENSIONLESS GROUPS FOR SIMULANT FLUID SYSTEMS

FUEL	R-11	R-11	R-11
COOLANT	R-22	R-22	R-12
T_f(^oK) - FULL SCALE	5000	6000	5000
B_P	7	7	7
B_D	7	7	7
HEAT TRANSFER SCALING OF FUEL-COOLANT INTERFACE TEMPERATURE			
P_f(MPa)	.66	3.9	.66
T_f(^oK)	362	458	362
T_l(^oK)	233	233	243
c_{l_f} ($\frac{w-s}{kg\,^oK}$)	880	880	880
FUEL CONDENSES BUT DOES NOT FREEZE			
β	1.35	1.35	1.02
$\frac{c_{l_f}(T_f - T_l)}{\sqrt{\pi}\, h_{fg_f}}$	.42	3.9	.4
λ_l	.35	1	.3
T_I^+ (^oK)	316	333	329
T_{HN}^+ (^oK)	335	345	350

+ $T_I < T_{HN}$: THEREFORE, THESE SIMULANT FLUIDS DO NOT MATCH THE EXPECTED BEHAVIOR OF UO_2 VAPOR AND SODIUM LIQUID.

TABLE C.5

SUMMARY OF DIMENSIONLESS GROUPS FOR SIMULANT FLUID SYSTEMS

FUEL - R-113

COOLANT - R-22

T_f(^oK) FULL SCALE	5000	6000	6000
B_P	7	20	30
B_D	7	20	30
HEAT TRANSFER SCALING OF FUEL-COOLANT INTERFACE TEMPERATURE			
P_f(MPa)	.66	1.36	.9
T_f(^oK)	385	426	401
T_l(^oK)	233	233	233
c_{l_f} ($\frac{w-s}{kg\,^oK}$)	922	922	922
FUEL CONDENSES BUT DOES NOT FREEZE			
β	1.42	1.42	1.42
$\frac{c_{l_f}(T_f - T_l)}{\sqrt{\pi}\, h_{fg_f}}$	.66	1.03	.78
λ_l	.45	.55	.5
T_I + (^oK)	323	340	330
T_{HN} + (^oK)	335	345	335

+ $T_I > T_{HN}$: THEREFORE, THESE SIMULANT FLUIDS DO NOT MATCH THE EXPECTED BEHAVIOR OF UO_2 VAPOR AND SODIUM LIQUID.

TABLE C.6

SUMMARY OF DIMENSIONLESS GROUPS FOR SIMULANT FLUID SYSTEMS

FUEL - R-11

COOLANT - R-13

T_f(^oK) FULL SCALE	5000	6000	7000	6000
B	7	7	30	30
B_D	7	7	30	30
HEAT TRANSFER SCALING OF FUEL-COOLANT INTERFACE TEMPERATURE				
P_f (MPa)	.66	3.9	2.9	.9
T_f (^oK)	362	459	439	375
T_l(^oK)	188	188	188	188
c_{l_f} ($\frac{w-s}{kg\,^oK}$)	880	880	880	880
FUEL CONDENSES BUT DOES NOT FREEZE				
β	1.14	1.14	1.14	1.14
$\frac{c_{l_f}(T_f - T_l)}{\sqrt{\pi}\, h_{fg_f}}$	.57	4.7	1.7	.64
λ_l	.4	1	.7	.42
T_I^+ (^oK)	304	326	329	311
T_{HN}^+ (^oK)	280	302	285	280

+ $T_I > T_{HN}$: THEREFORE, THE FIRST REQUIREMENT FOR SIMILARITY WITH THE UO_2 VAPOR AND SODIUM SYSTEM IS SATISFIED. R-11 and R-113 ARE THERMODYNAMICALLY SIMILAR, THUS IT APPEARS BOTH ARE COMPATIBLE AS THE SIMULANT FUEL.

TABLE C.7

SUMMARY OF DIMENSIONLESS GROUPS FOR SIMULANT FLUID SYSTEMS

FUEL - R-113

COOLANT - R-13

T_f (^oK) FULL SCALE	5000	6000	6000
B_P	7	20	30
B_D ‡	7	20	30
τ	.0405	.01	.0083
a* (set by M_{slug})	.93	.96	.96
$\dot{m}^*_{f\ crit}$	.024	.009	.0145
$h^*_{fg_f}$	259	105	188
$h^*_{f_{sub}}$ (T_{ref}-0^oK)	2.76	3.8	3.1
$h^*_{c_{sub}}$ (T_{ref}-0^oK)	1.69	2.25	1.81
$h^*_{fg_c}$	265	113	194
$h^*_{c_{sup}}$	.66	.88	.74
h^*_e (T_1 - 188^oK)	363	182	283
$\dot{m}^*_e$	.099	.11	.13
FUEL DOES NOT FREEZE			
$\dot{q}^*_{1\|_{rad}}$ (ε_r = 1)	.067	.032	.038
β	1.25	1.25	1.25

TABLE C.7 (CONTINUED)

$\frac{c_{l_f}(T_f - T_l)}{\sqrt{\pi}\, h_{fg_f}}$	.87	1.26	.98

T_I ($\sim 300^{\circ}K$) > T_{HN} ($\sim 280^{\circ}K$)

$\frac{\dot{m}^*}{A}_{vap_i}$	$5.68(10^{-4})$	$6.8(10^{-4})$	$8.9(10^{-4})$
$\frac{\dot{m}^*}{A}_{vap_f}$	$2.2(10^{-7})$	$5.7(10^{-7})$	$8.7(10^{-7})$

APPENDIX D

SPHERICAL TO PLANAR TRANSITION FOR SUBMERGED JETS

A single or two-phase bubble which emerges into a larger liquid pool initially will grow in a spherical manner and then at some transition point will grow preferentially upward in a one dimensional manner (Figure 3.2 and 3.24). This transition behavior of a transient submerged jet will be affected by the geometry of the system in that as the characteristic diameter of the upper pool is increased for a fixed discharge diameter, the transition point will occur later in the expansion [28]. Also, this behavior will be affected by the relative densities of the ejected fluid and the liquid in the pool [27]. If the density of the ejected fluid is much greater than the liquid density of the pool, then the spherical growth will be small and the ejected fluid will penetrate as a jet into the upper fluid. The momentum of the ejected fluid ($\rho_g v^2 A$) is much greater than the inertia of the pool (ρ_lVol g)) and, therefore, will penetrate it. If the reverse situation is the case, the spherical growth will deominate the expansion. These qualitative physical facts aid in the understanding of the phenomenon but do not help in predicting this transition point. Specifically in the small scale experiments modeled in Chapters 3 and 5 and in the full scale accident scenario for the CRBR without the above-core structure in Chapter 6, this transition may be important. The reason is that if the Taylor Instability phenomenon is the dominant mechanism for coolant entrainment, the spherical growth phase could suppress coolant entrainment depending upon the initial conditions of the bubble as it emerges into the upper pool. If the bubble attains a high entrance velocity into the

upper pool (e.g. this occurs when the coolant is initially in the fission gas plenum region), then the spherical growth has a characteristic acceleration which is negative (i.e., directed from the coolant into the vapor bubble) as shown by the Rayliegh equation

$$a = \ddot{R}_b = \frac{1}{R_b}\left[\frac{\Delta P}{\rho_1} - 1.5\,\dot{R}_b^{\,2}\right] \qquad (D.1)$$

where $\dot{R}_b > 0$ and $\dot{R}_b^{\,2} > \Delta P/\rho_1$. For this inward directed acceleration Taylor Instability will not occur. Once the transition to planar growth occurs, the acceleration then becomes positive again and Taylor Instability entrainment is operative.

There has been some research into the behavior of transient submerged jets [28,36,146,147] and there are some recommendations as to the point of transition and its dependence on the geometry and density ratio. These are presented here briefly to see which one is applicable to the experiments and full scale conditions considered.

There have been a couple of models developed which are based on steady state analyses to determine the characteristic shape of the emerging bubble and the transition point. McNallon [146] developed a steady state model to predict the transition point of a bubble from spherical to jet-like growth for a steady flow of gas into a liquid pool with no wall effects. The basis of the model is a steady state momentum balance of the bubble at the radium (R_b) of transition (Figure D.1). The momentum balance of forces gives

$$\underbrace{\frac{\rho_g(\dot{V}_g)^2}{\pi r_o^{\,2}}}_{\text{Momentum flux}} + \underbrace{g(\rho_1 - \rho_g)\frac{4}{3}\pi R_b^{\,3}}_{\text{byoyancy force}} = \underbrace{\frac{.01\,\rho_1(\dot{V}_g)^2}{\pi R_b^{\,2}}}_{\text{inertial force}} + \underbrace{\frac{.2\rho_1(\dot{V}_g)^2}{\pi R_b^{\,2}}}_{\text{viscous force}} + \underbrace{2\pi r_o\sigma}_{\text{surface tension}} \qquad (D.2)$$

This is a fifth order equation in R_b but can be simplified for the application here where the bubble is big (surface tension is negligible) and the gas volumetric flow rate ($\dot{V}_g$) is large (neglect the buoyancy effect). These simplifications give us

$$R_b = (.2\frac{\rho_l}{\rho_g})^{\frac{1}{2}} r_o \qquad (D.3)$$

Note that this criterion has the dependence on the density ratio that is qualitatively expected. This model can be applied to the transient jets of the CRBR geometry for the SRI and Purdue small scale tests and the full scale conditions. The results are given in Table D.1. Because wall effects are neglected, the relevance of the criterion to the reactor situation is quite limited because it appears that wall effects may dominate.

Tsai and Kazimi [147] developed a steady state model to predict the shape of a submerged two-phase jet being ejected into a liquid under steady flow conditions without a consideration of the wall effects. This model fundamentally differs from McNallon in that it inserts not a fluid mechanics criterion for the bubble shape (ρ_g/ρ_l) but a heat transfer criterion (SB) and the model applies to a two-phase jet condensing on the surface (A_b) of the liquid-vapor interface (Figure D.1). The dimensionless group that determines the shape is

$$SB = \frac{\bar{h}_{cond}(T_g - T_l)}{X_g G_g (h_{fg})_g} \doteq (\frac{A_{core}}{A_b}) \qquad (D.4)$$

if $SB \to 0$ JET-LIKE

$SB \to 1$ SPHERE

If the condensation heat transfer coefficient ($\bar{h}_{core}$) is high or the vapor mass flux is low ($X_g G_g$), the area necessary for condensation heat transfer decreases (A_b), thus the SB tends toward one and $l \simeq D$. If the reverse situation exists, the $l >> D$. Note that the $\bar{h}$ used here is based upon the

surface area of the bubble not on the possible additional area due to liquid entrainment. Using this physical basis, the area ratio is geometrically related to 1/D to predict the bubble shape and is compared to steam-water experiments in a large water pool and shows good agreement. This model again does not appear to be as relevant criterion in this case. The lack of consideration of density ratio and wall effects hamper its use because it is not known which phenomenon may dominate the transition process, and it appears that heat transfer effects may be the least important and wall effects the most important for the CRBR geometry. This can be seen again by the sample calculation in Table D.1. The values do not match the small scale results and the reason again appears to be the geometry effect when the walls are close to the throat size.

Abramovich [36] investigated the behavior of unheated submerged laminar jets in air-water experiments in a large pool of liquid and correlated the velocity of advance of the jet-like part of the bubble (u_J^*) and its spherical front (u_b^*). The results indicated that again the density ratio criterion qualitatively described the transient behavior observed. No wall effects were investigated, thus the results would not be useful here.

Christopher and Theofanous [28] did perform a theoretical analysis of the potential flow behavior of a constant pressure jet being expelled into an upper pool of the CRBR scaled size and their own experimental size. The results indicated that approximately one third of the expansion time up to the time of slug impact, the bubble grows in a spherical manner and the remainder of the time begins a transition to a one-dimensional constraint. The analysis emphasized that the growth transition was not definite

but existed over a span of time. In addition, because the ratio of vessel diameter to the core diameter (D_p/D_{core}) in their own tests was slightly smaller than the CRBR ratio, the transition would be predicted to be sooner. The wall effects do dominate the transition point and this is demonstrated again by the results of the MIT tests [54] in Chapter 3. The ratio D_p/D_{core} in this 2-D experiment was 4 and it was observed for $\rho_g/\rho_l \simeq .002 - .01$ that all the transient expansions grew spherically for much longer times ($2R_b/D_{core} \sim 1.7$) than in the SRI or Purdue scaled tests, before a transition to a one dimensional constraint occurred. This ratio of the bubble size at the transition point (R_b) to the core diameter (D_{core}) can be calculated from the Purdue results if a sharp transition at $t/\tau_{exp} = 1/3$ is assumed. The results are shown in Table D.1. The agreement between the SRI test results and the model is good. The SRI experimental point of transition was chosen based on the entrainment behavior. At this ratio of $2R_b/D_{core}$, the water entrainment began in the upper plenum suggesting positive acceleration (Taylor Instability operative) and planar growth. This criterion was used in the prediction of the transition point for the small scale tests of Purdue and SRI.

For the full scale conditions there are two geometric extremes to the possible spectrum of initial conditions that the accident could have: (1) The above-core structure is present; and, therefore, the expansion to slug impact is mainly planar, and the transition point is irrelevant; (2) The above-core structure is not present due to some accident circumstance and the initial condition can be with the sodium coolant in or out of the fission gas plenum region. If the coolant is out of this region, then the initial spherical growth velocity is zero and the acceleration will be positive up to slug impact regardless of the growth behavior. In this

case a one dimensional model is sufficient. If the sodium is in the plenum region, the initial velocity for spherical growth will be high and thus the acceleration is negative suppressing Taylor Instability entrainment. Using the Purdue criterion then, this will continue for at least 1/3 of the expansion time. Thus, it is in this specific initial condition for the full scale that the criterion of Christopher is given consideration.

TABLE D.1

SPHERICAL TO JET-LIKE GROWTH TRANSITION POINT PREDICTIONS

$(2R_b/D_{core})$

	McNallon	Christopher	Kazimi	Exper.
SRI [26]	1.33	.95	2.04	1.036
$D_v D_{core} = 3.4$				
Purdue [28] 3V	5.3	.93	1.5	
$D_v/D_{core} = 3.1$				
Full Scale Conditions	.6	.95	1.5 - 4.	
$D_v/D_{core} = 3.3$				
UO_2 - Na (P_{g_i} - 20.0 MPa)				

FIGURE D.1

CONCEPTUAL MODELS FOR SPHERICAL-JETLIKE BUBBLE TRANSITION

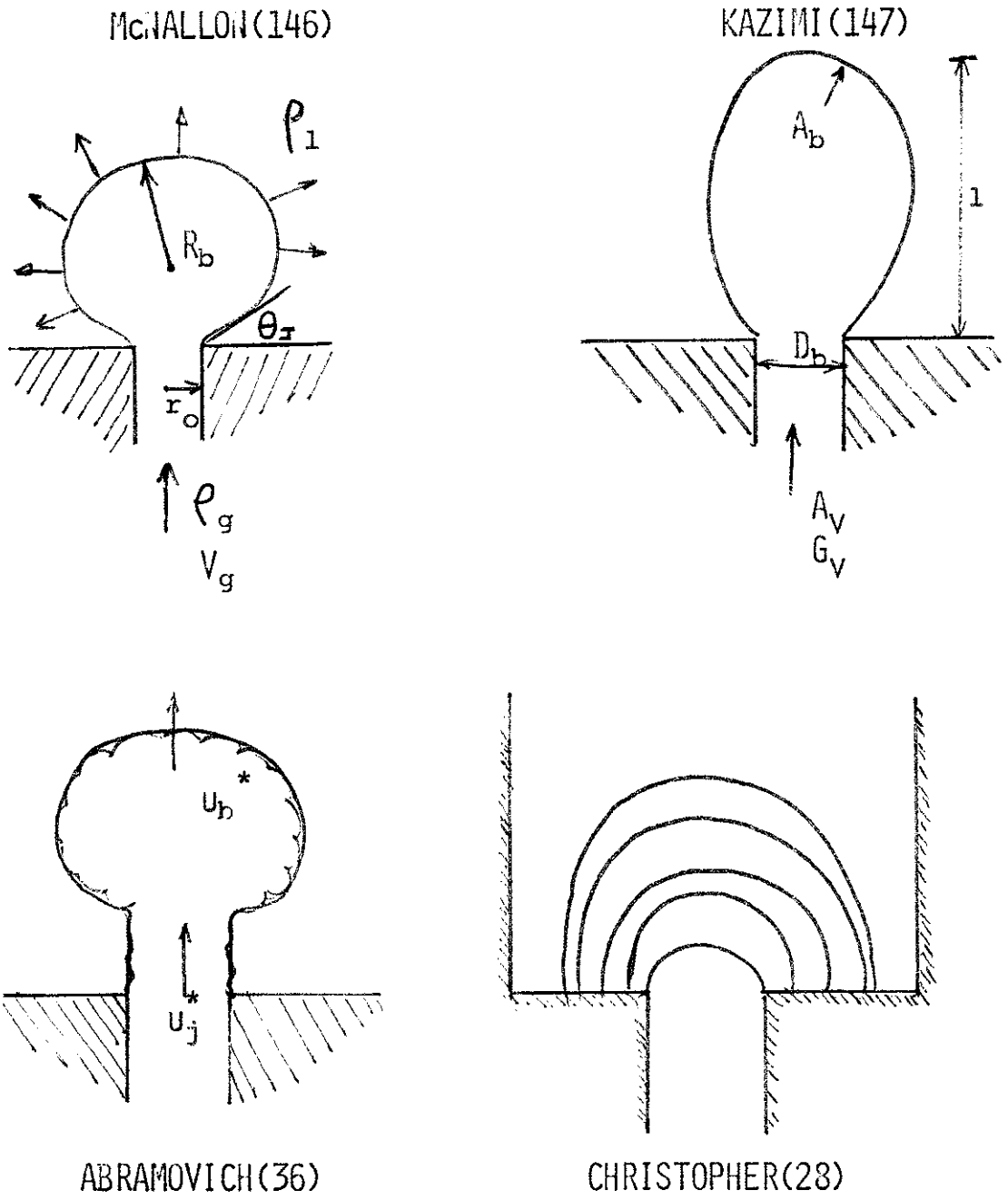

APPENDIX E

Two-Phase Critical Flow of One Component Mixtures

In the modeling of the small scale experiments in Chapter 5 and the full scale calculations in Chapter 6 models are needed to specify the rate of two-phase mass flow of fuel from the core region to the expanding bubble. The geometric characteristics of the experimental system or the full scale reactor are important in determining what models are suitable. For both the small scale experiments and the CRBR geometry (Figure E.1), the geometry resembles a short tube or an orifice with $L/D \lesssim 1$. There are a few models which are applicable to this situation as outlined by Henry [72] and Fauske [73]. These are presented briefly here as a background to what is used in the analysis of the experiments.

For the situation of equilibrium flow of the two-phase fuel where an orifice exists as in the Purdue tests, or where a short tube exists with $L/D \lesssim 1$ as in the case of the SRI tests, Fauske suggests the use of the orifice equation given by

$$G = .61 \sqrt{2 \rho_{core} (P_{core} - P)} \qquad (E.1)$$

where ρ_{core}, P_{core} are the density and pressure of the two-phase fuel mixture in the core and

$P = P_{res}$ - reservoir pressure when $P_{core} \geq P_{res} \geq .55 P_{core}$

$P = .55\ P_{core}$ - choked flow condition when $P_{res} \leq .55\ P_{core}$

This simple quasi-steady state model is found by an application of Bernoulli's equation to the short tube geometry

$$\Delta P \sim \frac{\rho v^2}{2} \qquad (E.2.1)$$

$$v \sim \frac{2\Delta P}{\rho} \qquad \text{(E.2.2)}$$

$$\therefore \quad G = C_o \sqrt{2\rho\Delta P} \qquad \text{(E.2.3)}$$

This model is used for the Purdue tests because it appears that the blowdown from the core is equilibrium in nature and an orifice was used. For the SRI tests the blowdown pressure traces indicated a definite non-equilibrium condition where it appears only saturated vapor exits the core. Thus this orifice model is inapplicable and a flashing model is used instead, and is described in Chapter 5.

For the situation of the full scale conditions, the possibility of an orifice situation is not ruled out but in general the size could not be known a priore and thus the blowdown area is assumed to be the entire core cross-sectional area, and the orifice model is inapplicable. Henry [72] outlines two other models which are based on the physical view of the two-phase fuel being ejected out of the core as a homogeneous mixture of liquid and vapor in the core and blowdown tube. This situation is applicable to the full scale condition because the energy deposition from the hydrodynamic disassembly would be somewhat homogeneous thus fuel vapor and liquid would be initially intermixed.

One model is a homogeneous "frozen" flow model where the two phases are physically pictured to be ejected at the same velocity but no heat or mass transfer occurs between the phases, and the vapor controls the blowdown and is modeled as an isentropic perfect gas. This type of non-equilibrium expansion gives a critical mass flux of [72]

$$G_{crit} = \frac{1}{v}\left[2x_{core}\, v_{g_{core}} P_{core} \left(\frac{\gamma}{\gamma-1}\right)\left[1 - \eta\,\frac{\gamma-1}{\gamma}\right]\right]^{\frac{1}{2}} \qquad \text{(E.3)}$$

where

$$v = (1 - X_{core})v_{fcore} + X_{core}v_{gcore}\eta^{\frac{1}{\gamma}} \quad (E.4)$$

$$\eta = \text{critical pressure ratio } [\frac{2}{\gamma+1}]^{\frac{\gamma}{\gamma-1}} \quad (E.5)$$

γ is ratio of vapor specific heats

Now this model would be applicable at full scale conditions if in the time of the expansion (τ_{exp}) the saturated liquid fuel does not evaporate due to pressure wave relief ($21/c_a \sim \tau_{exp}$). An estimate of this time ($21/c_a$) can be made where c_a is the acoustic velocity of the two-phase medium assumed to be near that of the vapor phase (~350m/s). The core size is approximately a meter in height and thus $21/c_a \sim 6$ msec. This can be compared with probable expansion times of 17-160 msec over the range of initial full scale conditions. Therefore, it appears that the blowdown is more equilibrium in nature and the "frozen" flow model is inapplicable.

The second model is the homogeneous equilibrium model, where it is assumed the blowdown is isentropic and the two phases are always in thermodynamic equilibrium with the same velocities. The mass flux can be found by a steady state energy balance

$$\dot{m} h_{core} = \dot{m} h_{ex} + \dot{m} \frac{v_{ex}^2}{2} \text{ ; ex-exit conditions}$$

$$v_{ex} = \sqrt{2(h_{core} - h_{ex})}$$

$$G_{ex} = \rho_{ex} \sqrt{2(h_{core} - h_{ex})} \quad (E.6)$$

where

$$1/\rho_{ex} = v_{ex} = (1 - X_{ex})\, v_f + X_{ex}\, v_g \quad (E.7)$$

and $$X_{ex} = \frac{s_{core} - s_f}{s_{fg}}$$

$$X_{ex} = X_{core} \left(\frac{T_{ex}}{T_{core}}\right) + \frac{c_p T_{ex}}{h_{fg}} \ln \frac{T_{core}}{T_{ex}} \qquad \text{(E.8)}$$

The critical mass flux occurs where G is maximum, near pressure ratios of $.55 \leq P_b/P_{core}$. This model is utilized in the full scale calculations to predict the mass flow rate out of the core into the expanding bubble.

One final note should be made. Although these three models differ in the physical description of the process, the mass fluxes each one predicts for typical full scale conditions are not in large disagreement, thus any could be used without dramatic differences in the results (Table E.1).

TABLE E.1

COMPARISON OF TWO-PHASE MASS FLUX MODELS

$G - (^{kg}/_{m^2 s})$

	P_{core} (MPa)	86.8	27.2	4.63
	T_{core} (^{o}K)	7000	6000	5000
MODEL	P_{res}/P_{core}			
ORIFICE	.55	125000	70100	29000
EQUIL	.55	174000	85000	23400
FROZEN	.55	190000	108000	45000
ORIFICE	.7	102200	57200	23700
EQUIL	.7	173000	81300	23300
ORIFICE	.8	84000	46700	19300
EQUIL	.8	159000	77000	23200
ORIFICE	.9	59000	33000	14000
EQUIL	.9	121000	65000	21700

FIGURE E.1

CONCEPTUAL VIEW OF GEOMENTRIC EFFECTS OF TWO-PHASE CRITICAL FLOW

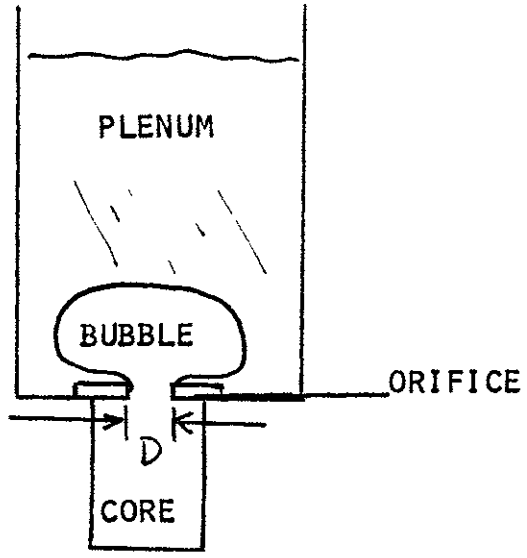

PURDUE TESTS

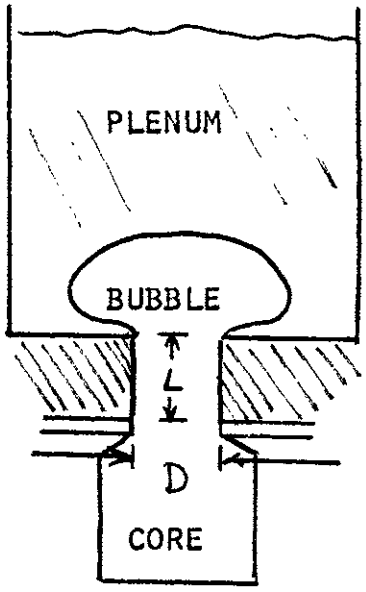

SRI TESTS

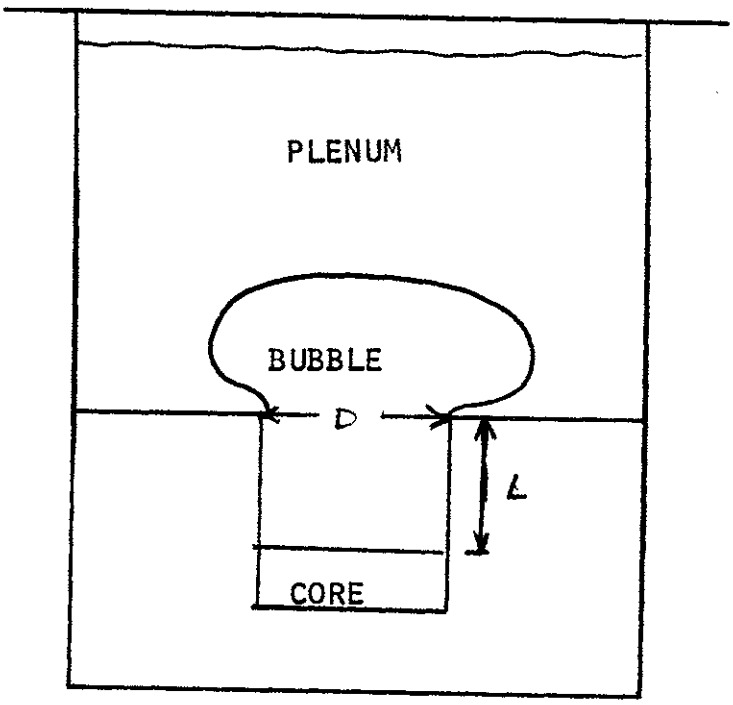

FULL SCALE GEOMETRY

APPENDIX F

NUMERICAL SOLUTION OF A SYSTEM OF NON-LINEAR DIFFERENTIAL EQUATIONS

Numerical Methods Utilized in the Analysis

To solve the non-linear system of differential equations presented in Chapters 3, 4, 5, and 6, two numerical techniques were employed. Both are incorporated in the mathematical subroutine library for the MIT-IBM 370/168 computer. Each one has a different method of solution which is suitable for a different type of system of equations. In Chapters 3 and 4 the system was composed of a group of up to eight non-linear ordinary differential equations, with time as the independent variable. Once the initial condition for each of the dependent variables is specified the system can be numerically integrated to determine the transient behavior of each of the dependent variables. One mathematical property of this system was that it was not "stiff." The term, "stiff," describes the situation where the characteristic period ($e^{w_1 t}$) for the variance of one dependent variable ($x_1 = f_1(t)$) is orders of magnitude different from the period ($e^{w_n t}$) of another dependent variable ($x_n - f_n(t)$). In other words, the variables in the equations describing the physics of the experiments in Chapters 3 and 4 had similar rates of change. This permitted the use of a simple integration technique, Euler predictor corrector. The subroutine name for this technique was DVOGER and was quite fast and inexpensive to use. The system of equations in Chapters 5 and 6 was stiff and this required a more elaborate numerical integration technique, DVDQ solution method utilizing Adams-Falkner prediction and Adams-Moulton corrector

coefficients. The subroutine name for this technique was DQSYK, and proved to be quite expensive to use for the large full scale problems (11 equations ~ 50 msec transient ~ 2-4 cpu minutes).

Usage of DVOGER was quite straight forward, requiring the coding of a main program which consisted of four major sets of input information:

(1) A matrix (Y) is supplied containing the initial conditions for all the depednent variables.

(2) A functional subroutine (DFUN) is supplied which contains the system of non-linear ordinary differential equations arranged such that the time derivatives (DY(I)) appear alone on the left hand side of the equations.

(3) The desired time step size (H) is input along with upper (HMAX) and lower bounds (HMIN) to designate the desired range over which the optimum time step is chosen.

(4) The maximum relative error (EPS) desired for the dependent variables is supplied. This is determined by comparing the value of the variable at a time using one time step size and then the value at the same time using a smaller time step size. If the difference divided by the value of the variable is smaller then EPS, then the integration proceeds. If not, the time step size is reduced until EPS is satisfied.

The solution of the system of equations in Chapter 3 and 4 utilized a maximum error of 1%.

Usage of the subroutine DQSYK proved to be more difficult because the behavior of the system of equations used with the models of Chapter 6 proved to be quite stiff. This resulted in long computer running times to solve the transient cases of interest for the full scale calculations. Again the same four categories of input were necessary:

(1) A matrix (X) containing the initial conditions of the dependent variables.

(2) A matrix (F) containing the set of non-linear ordinary differential equations.

(3) The desired time step size (H) with upper and lower bounds.

(4) A vector (EPS(I)) containing the maximum absolute errors for each dependent variable.

This last option is included in this technique to facilitate the convergence of the solution for a stiff system of equations. Each variable has its own maximum error and this can be made large (5%) for variables where the rate of change is small (e.g. core temperatures and qualities) and can be made small (1%) for variables where the rate of change is large (e.g. heat transfer, distance, velocity). The technique was utilized to try to minimize the running time of the transient calculations. Difficulty was encountered especially in the transient equations for bubble expansion in Chapter 6 where the sodium coolant is substantially vaporized. In this case the core temperature and quality decrease slowly as does the pressure in the expanding bubble because of coolant vaporization. This is contrasted by the high rate of change of the heat transfer between the vapor and liquid which controls the rate of vaporization and the axial expansion velocity.

Spatial Averaging Techniques for Heat Transfer Model Variables (v_{rel}, D_d, dv_d/dt)

For all three types of heat transfer models presented in Chapters 4, 5 and 6 (small scale noncondensible heated, small scale condensible heated - no vaporization, full scale condensible UO_2 fuel - vaporizing sodium), the quantities for the relative velocity (v_{rel}), the droplet diameter (D_d) and the average drop acceleration (dv_d/dt) must be spatially averaged. The method utilized to average these quantities was to find the values of each one at axial intervals (Δx_i) and find the average value at every time step. A simple flow chart of the process is given in Table F.1. The only difficulty that is posed by this scheme is to provide adequate storage space for the values at each axial interval; (approximately 100 were used in the analyses.) The storage space for the computer code was modest (~ 400k bytes), but the

computer execution time was approximately doubled due to this averaging technique. This was noticeably more expensive for the full scale calculations in Chapter 6.

For the more approximate rate models (#2 & #3) outlined in the chapters, the droplet diameter and heat transfer coefficient were estimated by hand calculations and inserted as constant values in the computer program.

TABLE F.1

SPATIAL AVERAGING TECHNIQUE - LOGIC FLOW CHART

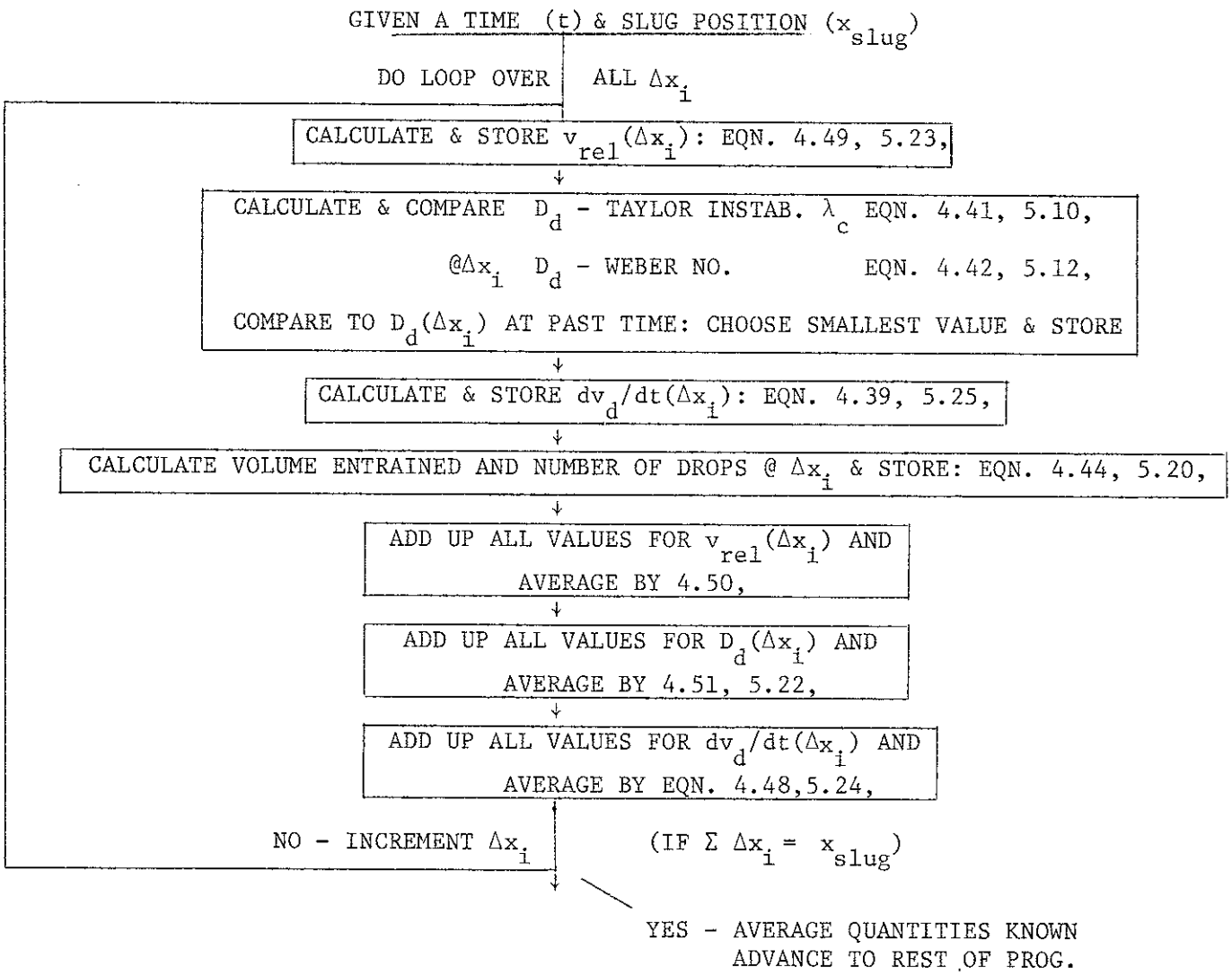

APPENDIX G

SOLUTION OF THE ENERGY EQUATION IN CHAPTER 10

The governing equation given in equation 10.16 is

$$\frac{\partial T}{\partial t} = \alpha \frac{\partial^2 T}{\partial x^2} \tag{G-1}$$

with boundary condition

$$\text{(i)} \quad T_H = T_{H_i}; \; t > 0 \quad x \to -\infty \tag{G-2}$$

$$\text{(ii)} \quad T_c = T_{c_i}; \; t > 0 \quad x \to \infty \tag{G-3}$$

$$\text{(iii)} \quad -k_H \left.\frac{\partial T_H}{\partial x}\right|_{x=0} = q''(t); \quad t \tag{G-4}$$

$$\text{(iv)} \quad -k_c \left.\frac{\partial T_c}{\partial x}\right|_{x=0} = q''(t); \quad t > 0 \tag{G-5}$$

$$q''(t) = \frac{k_g}{\delta} [T_H(0,t) - T_c(0,t)]$$

and initial condition

$$\text{(v)} \quad T_c = T_{c_i}; \; x > 0, \; t = 0 \tag{G-6}$$
$$T_H = T_{H_i}; \; x < 0, \; t = 0$$

If we define

$\Theta = T - T_{c_i}$ and take the Laplace Transform, we obtain

Hot region

$$S\,\overline{\Theta}_H - (T_{H_i} - T_{c_i}) = \alpha_H \frac{d^2\overline{\Theta}_H}{dx^2} \tag{G-7}$$

cold region

$$S\bar{\theta}_c = \alpha_c \frac{d^2\bar{\theta}_c}{dx^2} \tag{G-8}$$

$$\text{(i)} \quad \bar{\theta}_H = \left(\frac{T_{H_i} - T_{c_i}}{S}\right); \quad x \to -\infty \tag{G-9}$$

$$\text{(ii)} \quad \bar{\theta}_c = 0 \; ; \quad x \to +\infty \tag{G-10}$$

$$\text{(iii)} \quad -K_H \left.\frac{d\bar{\theta}_H}{dx}\right|_{x=0} = \left.\frac{k_g}{\delta} \left(\bar{\theta}_H - \bar{\theta}_c\right)\right|_{x=0} \tag{G-11}$$

$$\text{(iv)} \quad -K_c \left.\frac{d\bar{\theta}_c}{dx}\right|_{x=0} = \left.\frac{k_g}{\delta} \left(\bar{\theta}_H - \bar{\theta}_c\right)\right|_{x=0} \tag{G-12}$$

for the hot region we obtain a homogenous and particular solution. Upon applying boundary condition (i)

$$\bar{\theta}_H = \left(\frac{T_{H_i} - T_{c_i}}{S}\right) + B_e^{Q_H x};$$

where

$$Q_H = \sqrt{\frac{S}{\alpha_H}}$$

B = undetermined coefficient

for the cold region after applying boundary condition (ii)

we obtain

$$\bar{\theta}_c = E_e^{Q_c x}$$

where $Q_c = \sqrt{\frac{S}{\alpha_c}}$

E = undetermined coefficient

The two remaining coefficients are found by applying boundary conditions (iii) and (iv) and we obtain after some albegra

$$B = \frac{-\beta(T_{H_i} - T_{c_i})}{S(1+\beta + Q_H(\frac{k_H \delta}{k_g}\beta))}$$

$$E = \frac{(T_{H_i} - T_{c_i})}{S(1+\beta+ Q_H(\frac{k_H \delta \beta}{k_g}))}$$

where

$$\beta = \sqrt{\frac{k_c \rho_c c_c}{k_H \rho_H c_H}}$$

Thus the expression for $\overline{\Theta}_c(x)$ at $x = 0$ is

$$\overline{\Theta}_c(0) = \frac{(T_{H_i} - T_{c_i})}{(\frac{k_H \delta}{k_g}\beta)} \left[\frac{1}{\frac{k_g(1+\beta)}{k_H \beta} + Q_H}\right]$$

$$= \frac{(T_{H_i} - T_{c_i})}{\frac{k_H \delta \beta \sqrt{\alpha_c}}{k_g \sqrt{\alpha_H}}} \left[\frac{1}{S(C_1 + Q_c)}\right] \qquad \text{(G-13)}$$

where

$$C_1 = \frac{(1+\beta)\sqrt{\alpha_H}}{\beta\frac{k_H\delta}{k_g}\sqrt{\alpha_c}}$$

Now the inverse transform can be taken from Arpaci [150] and we obtain equation 10.1b solution as

$$\left(\frac{T_c(0,t) - T_{c_i}}{T_{H_i} - T_{c_i}}\right) = \left(\frac{1}{1+\beta}\right)\left[\left[1 - e^{w^2}\operatorname{erfc} w\right]\right] \qquad (G\text{-}14)$$

where $w = C_1(\alpha_c t)^{\frac{1}{2}}$

APPENDIX H

INTERFACE TEMPERATURE BETWEEN THE FUEL AND COOLANT

One major parameter that is of importance in the sputtering contact model is the instantaneous interface temperature between the fuel and coolant. As the UO_2 fuel vapor initially contacts the sodium droplet surface at the beginning of the expansion and condenses upon it, the temperature of the interface begins to rise to a constant value caused by the energy being transferred across it due to the sensible heat of the fuel and the latent heat of vaporization. After a time the UO_2 may also begin to freeze on the surface and this will also increase the interface temperature because of the latent heat of fusion. This complex process is quite difficult to model precisely to determine the interface temperature as a function of time for short times (10^{-10} - 10^{12}s). However, the importance of the interface temperature in this application is to determine if it exceeds the homogeneous nucleation temperature of the sodium coolant (T_{HN}). The reason for this is that if $T_I > T_{HN}$, then the sodium near the surface will almost instantaneously vaporize (10^{-12} sec) and this would represent the maximum rate of sodium vaporization as the bulk of the entrained sodium droplet is being heated to T_{sat}. Therefore, in trying to predict T_I from a model, it is conservative to assume that T_I reaches its constant value instantaneously so that if $T_I > T_{HN}$ the maximum amount of sodium liquid near the surface will be above T_{sat} and give the largest sodium vaporization rate. This should give a higher bubble pressure during the initial expansion and a larger work value. There are four conduction models that could be utilized to predict the instantaneous interface temperature (Figure H.1). Each will be

examined briefly to determine which is appropriate to use in this portion of the analysis.

The classical model for the interface temperature of two semi-infinite masses each at different temperatures (Figure H.1(a)) is given by the relation [70]

$$T_I = \frac{T_f}{1+\beta} + \frac{\beta T_1}{1+\beta} \tag{H.1}$$

where

$$\beta = \sqrt{\frac{k_c \rho_c c_{1c}}{k_f \rho_f c_{1f}}} \tag{H.2}$$

This model is not appropriate here because the fuel vapor is condensing on the sodium and may be solidifying, therefore no account is taken in this model for the increase in the interface temperature due to the latent heat of vaporization or fusion. In fact, the predicted interface temperature using this model is much lower than T_{HN} (e.g. $T_f = 6000^{\circ}K$, $T_{HN} = 2600^{\circ}K$, $T_I = 2273^{\circ}K$) due to the neglect of the latent heats.

Given this same geometry Kazimi [151] extended this analysis to very short times ($<10^{-11}$ sec) and found, by using the hyperbolic heat conduction equation for energy flow, that the interface temperature is much higher initially for semi-infinite geometries and generally the interface temperature can be given by

$$T_I = A_1 e^{-at} + A_2(1 - e^{-at}) \tag{H.3}$$

where

$$a = \frac{\Lambda_c + \beta_t \Lambda_f}{2(1 + \beta_t)} \tag{H.4}$$

$$A_1 = \frac{T_f}{1+\beta_t} + \frac{\beta_t T_c}{1+\beta_t} \tag{H.5}$$

$$A_2 = \frac{T_f}{1+\beta} + \frac{\beta_t T_c}{1+\beta_t} \qquad (H.6)$$

$$\Lambda_i = c_a^2/\alpha \quad i \text{ - fuel or coolant} \qquad (H.7)$$

$$\beta_t = \frac{\rho_c c_{\rho_c} c_{a_c}}{\rho_f c_{l_f} c_{a_f}} \qquad (H.8)$$

and where the heat transport speed is approximated by the acoustic velocity in the medium (c_a). Physically, this model says that energy cannot be transported away from the interface infinitely fast at short times and the speed of this heat transport is near c_a. Thus initially the temperature near the interface is higher (i.e., $T_I = A_1$ @ $0 < t < 10^{-11}$ sec) until the heat transport speed allows the energy to diffuse away from the vicinity of the interface (i.e., $T_I = A_2$ which is Equation H.1 @ $t > 10^{-11}$ sec). This model is not applicable here, although it predicts $T_I > T_{HN}$, because enough UO_2 fuel vapor cannot condense in such a short time to cause it to act as a semi-infinite body of hot liquid. Only after condensation has begun could these "instantaneous" models apply and even then they neglect h_{fg_f} and L_s. To illustrate this consider that the fastest rate of condensation expected is [59]

$$\frac{\dot{m}_f}{A}_{cond} = \frac{P_{sat}(T_f)}{\sqrt{2\pi R_f T_f}} \qquad (H.9)$$

Now in 10^{-11} seconds the amount condensed is, e.g. $T_f = 6000^oK$,

$$\frac{\dot{m}_f}{A}_{cond} = 2.5\ (10^{-7})\ kg/m^2$$

This carried with it enough energy to raise the liquid coolant at the surface and down to a depth (d) controlled by the heat transport speed

$$d = c_a(10^{-11}) \quad c_a \sim 1500\ m/s$$
$$= 1.5(10^{-8})m$$

to an average temperature of only ($T_l \sim 800^oK$)

$$T = \frac{\frac{\Delta m_f}{A}_{cond} h_{fg_f}}{\rho_c c_{l_c} d} + T_l = 826^{o}K$$

In the time of the predicted high interface temperature of the model from $0 < t < 10^{-11}$ sec, not enough vapor has condensed. Thus realistically T_I rises from T_l to a temperature higher than T_{HN} caused by the condensation and possible solidification of the fuel in finite depths.

The second classical model (Figure H.1(b)) used to determine the interface temperature considers the solidification of the liquid (UO_2) and treats the condensate as a semi-infinite mass. Carslaw and Jaeger [70] give the interface temperature as

$$\frac{T_I - T_l}{T_{m_f} - T_l} = \frac{1}{1 + \beta \operatorname{erf} \kappa_s} \tag{H.10}$$

where κ_s is found by trial and error from

$$\frac{L_s \sqrt{\pi}}{c_{l_f}(T_{m_f} - T_l)} = \frac{1}{\kappa_s} \left[\frac{\beta e^{-\kappa_s^2}}{1+\beta \operatorname{erf} \kappa_s} - \left(\frac{T_f - T_{m_f}}{T_{m_f} - T_l}\right) \frac{k_{f_l}\sqrt{\alpha_{f_s}}}{k_{f_s}\sqrt{\alpha_{f_l}}} \frac{e^{-\kappa_s^2 \frac{\alpha_{f_s}}{\alpha_{f_l}}}}{\operatorname{erfc} \kappa_s} \right] \tag{H.11}$$

assuming $\rho_{f_s} = \rho_{f_l}$.

For UO_2 fuel solid and liquid

$$k_{f_l} \doteq k_{f_s}$$

$$\alpha_{f_l} \doteq \alpha_{f_s}$$

and therefore the result is

$$\frac{L_s \sqrt{\pi}}{c_{l_f}(T_{m_f} - T_l)} = \frac{1}{\kappa_s} e^{\kappa_s^2} \left[\frac{\beta}{1+\beta \operatorname{erf} \kappa_s} - \left(\frac{T_f - T_{m_f}}{T_{m_f} - T_l}\right) \frac{1}{\operatorname{erfc} \kappa_s} \right] \tag{H.12}$$

This model is not appropriate for this situation primarily because it neglects h_{fg_f} and this latent heat energy is much larger than L_s ($h_{fg_f} \simeq 6\ L_s$).

Another tacit assumption here is that solidification instantaneously begins upon condensate contact with the cold sodium (i.e., $t < 10^{-12}$ sec). This is only true if the interface temperature between the sodium and fuel liquid is below the homogeneous crystallization temperature, T_{HC}. This is below T_{m_f} and is determined from kinetic theory as is the homogeneous nucleation temperature. Cronenberg (149) utilized this criteria for UO_2 with the rate equation

$$J_c(cc^{-3}s^{-1}) = 10^{33}(cc^{-1}s^{-1})\exp\left(\frac{-16\pi\ \bar{\sigma}_{ls}^{\ 3}}{3(\rho_f L_s)^2}\left(\frac{T^2}{(T_{m_f}-T)^2 k_B T}\right)\right) \tag{H.13}$$

and found that $T_{HC} \simeq 2673^{\circ}K$. This temperature corresponds to the temperature when the crystallization rate J_c becomes large (i.e. J_c changes from 10^{-12} to 10^{+12} in a span of ten degrees). This criteria is used to determine if the fuel solidifies instantaneously given the interface temperature for fuel and sodium liquid.

The model utilized to find the interface temperature considering fuel condensation and neglecting fuel solidification is an extension of the principles outlined in Carslaw and Jaeger [70] (seeFigure H.1(c)). The governing energy equation for each region is

$$\frac{\partial T}{\partial t} = \alpha \frac{\partial^2 T}{\partial x^2} \tag{H.14}$$

where the initial conditions are @ $t = 0$

$$T = T_1;\ x < 0 \tag{H.15.1}$$

$$T = T_f;\ x > 0 \tag{H.15.2}$$

and the boundary conditions for all time are

$$T_c = T_1;\ x \to -\infty \tag{H.16.1}$$

$$T_c = T_{f_1}; \; x = 0 \tag{H.16.2}$$

$$-k_c \frac{\partial T}{\partial x}\Big|_c = -k_{f_1} \frac{\partial T}{\partial x}\Big|_{f_1}; \; x = 0 \tag{H.16.3}$$

$$T_{f_1} = T_f; \; x = \delta_1(t) \tag{H.16.4}$$

$$k_{f_1} \frac{\partial T}{\partial x}\Big|_{f_1} = \rho_f \, h_{fg_f} \frac{d\delta_1}{dt}; \; x = \delta_1(t) \tag{H.16.5}$$

Similar to Carslaw's technique the solution is assumed to be of the form

$$T - T_1 = A\left[1 + \operatorname{erf} \frac{x}{2\sqrt{(\alpha_c t)}}\right]; \; x \leq 0 \tag{H.17}$$

$$T - T_1 = B + C \operatorname{erf}\left[\frac{x}{2\sqrt{(\alpha_{f1} t)}}\right]; \; x \geq 0 \tag{H.18}$$

where boundary condition H.16.1 is satisfied. Now if the rest of the boundary conditions are applied, the constants can be found and the interface temperature is

$$T_I - T_1 = \frac{1}{\beta} (T_f - T_1) \left[\frac{1}{\beta} + \operatorname{erf} \kappa_1\right]^{-1} \tag{H.19}$$

where κ_1 is found by the expression

$$\frac{c_{l_f} (T_f - T_1)}{\sqrt{\pi} \, h_{fg_f} \kappa_1 e^{\kappa_1^2}} = \left[\frac{1}{\beta} + \operatorname{erf} \kappa_1\right] \tag{H.20}$$

Chapter 6 utilizes this expression to find T_I and the result is that this expression is valid for $T_f > 5500^{\circ}K$. For initial fuel temperatures below this limit, the interface temperature is predicted to be below T_{HC} and therefore, the condensate of the fuel solidifies in a very short time ($t < 10^{-12}$ sec) and thus must be considered.

The final model developed for the interface temperature takes into account the finite depth of solid UO_2 and liquid UO_2 (see Figure H.1(d)). The governing equation is again Equation H.14. The initial conditions are again

the same and the new boundary conditions [82] are

$$T_c = T_1; \quad x \to -\infty \tag{H.21.1}$$

$$T_c = T_{f_s}; \quad x = 0 \tag{H.21.2}$$

$$-k_c \left.\frac{\partial T}{\partial x}\right|_c = -k_{f_s} \left.\frac{\partial T}{\partial x}\right|_{f_s}; \quad x = 0 \tag{H.21.3}$$

$$T_{f_1} = T_{m_f}; \quad x = \delta_s(t) \tag{H.21.4}$$

$$T_{f_s} = T_{m_f}; \quad x = \delta_s(t) \tag{H.21.5}$$

$$-k_{f_s} \left.\frac{\partial T}{\partial x}\right|_{f_s} = k_{f_1} \left.\frac{\partial T}{\partial x}\right|_{f_1}; \quad x = \delta_s(t) \tag{H.21.6}$$

$$T_{f_1} = T_f; \quad x = \delta_1(t) \tag{H.21.7}$$

$$-k_{f_1} \left.\frac{\partial T}{\partial x}\right|_{f_1} = \rho_f h_{fg_f} \frac{d\delta_1}{dt}; \quad x = \delta_1(t) \tag{H.21.8}$$

The solution is assumed to be of the form [70]

$$T - T_1 = A\left(1 + \operatorname{erf} \frac{x}{2(\alpha_c t)^{\frac{1}{2}}}\right); \quad x \leq 0 \tag{H.22}$$

$$T - T_1 = B + C \operatorname{erf} \frac{x}{2(\alpha_{f_1} t)^{\frac{1}{2}}}; \quad 0 \leq x \leq \delta_s^{(+)} \tag{H.23}$$

$$T - T_1 = D + E \operatorname{erf} \frac{x}{2(\alpha_{f_s} t)^{\frac{1}{2}}}; \quad \delta_s(t) \leq x \leq \delta_1(t) \tag{H.24}$$

where Equation H.21.1 is satisfied. The rest of the boundary conditions can be applied to find the other constants and the interface temperature is given by

$$\frac{T_I - T_1}{T_{m_f} - T_1} = \frac{1}{1 + \beta \operatorname{erf} \kappa_s} \tag{H.25}$$

where for $k_{f_s} \doteq k_{f_l}$

$\alpha_{f_s} \doteq \alpha_{f_l}$

which are good approximations, κ_s and κ_l are given by

$$\frac{\sqrt{\pi}\, L_s}{c_{l_f}(T_{m_f} - T_l)} = \frac{1}{\kappa_s e^{\kappa_s^2}} \left[\frac{\beta}{1+\beta}\, \mathrm{erf}\, \kappa_s - \left(\frac{T_f - T_{m_f}}{T_{m_f} - T_l}\right) \frac{1}{\mathrm{erf}\, \kappa_l - \mathrm{erf}\, \kappa_s} \right] \tag{H.26}$$

$$\frac{\sqrt{\pi}\, h_{fg_f}}{c_{l_f}(T_f - T_{m_f})} = \frac{1}{\kappa_l e^{\kappa_l^2}} \left[\frac{1}{\mathrm{erf}\, \kappa_l - \mathrm{erf}\, \kappa_s} \right] \tag{H.27}$$

The interface temperature is found using this model for $T_f < 5500^{\circ}K$ because the resulting interface temperature is below T_{HC} and the fuel will solidify. The interface temperature is slightly higher due to the energy of the latent heat of fusion released during solidification.

FIGURE H.1

CONCEPTUALS MODELS FOR FUEL-COOLANT INTERFACE TO DETERMINE THE INTERFACE TEMPERATURE

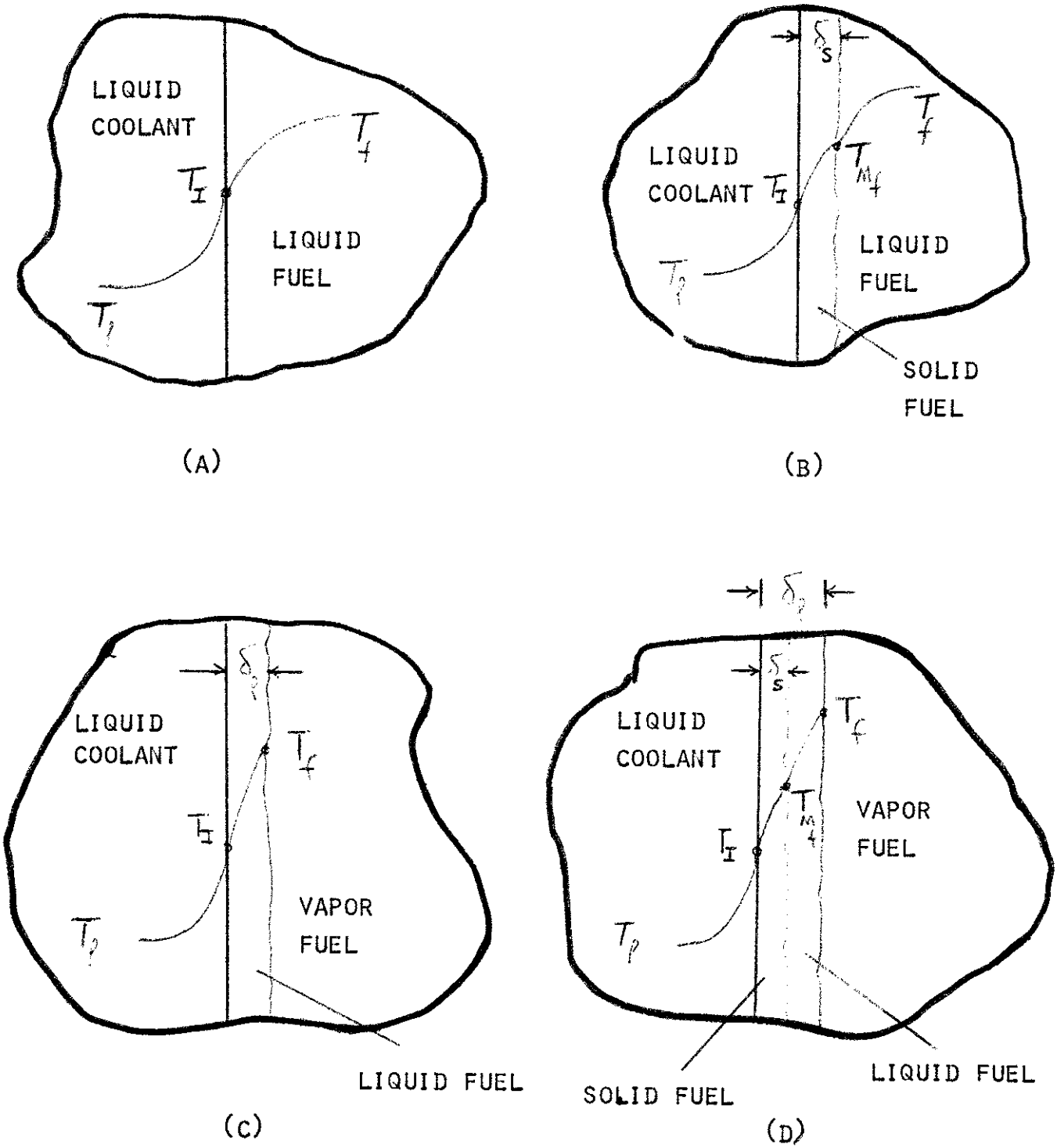

$$\delta_l = 2\kappa_l (\alpha_{fl} t)^{1/2}$$

$$\delta_s = 2\kappa_s (\alpha_{fs} t)^{1/2}$$